HAL open science

Fonctionnelles d'energie non-empiriques pour la structure nucleaire

Vincent Rotival

To cite this version:

Vincent Rotival. Fonctionnelles d'energie non-empiriques pour la structure nucleaire. Physique Nucléaire Théorique [nucl-th]. Université Paris-Diderot - Paris VII, 2008. Français. NNT : . tel-00409482

HAL Id: tel-00409482

https://theses.hal.science/tel-00409482v1

Submitted on 8 Aug 2009

HAL is a multi-disciplinary open access archive for the deposit and dissemination of scientific research documents, whether they are published or not. The documents may come from teaching and research institutions in France or abroad, or from public or private research centers.

L'archive ouverte pluridisciplinaire **HAL**, est destinée au dépôt et à la diffusion de documents scientifiques de niveau recherche, publiés ou non, émanant des établissements d'enseignement et de recherche français ou étrangers, des laboratoires publics ou privés.

Université Paris.Diderot (Paris VII)
Commissariat à l'Energie Atomique

Thèse de Doctorat de Physique Nucléaire

présentée pour obtenir le grade de

Docteur en Sciences de l'Université Denis Diderot - Paris VII

Spécialité Champs, Particules, Matière

par

Vincent Rotival

Fonctionnelles d'énergie non-empiriques pour la structure nucléaire

Soutenue publiquement le 29 septembre 2008
à l'amphithéatre Claude Bloch (IPhT - CEA Saclay)
devant la commission d'examen composée de :

M. Pierre Binétruy, Univ. Paris VII ..... Président
M. Jean-François Berger, CEA/DAM/DPTA/SPN ..... Directeur de Thèse
M. Thomas Duguet, CEA/DSM/Irfu/SPhN ..... Co-Directeur de Thèse
M. Luis Miguel Robledo, Universitad Autónoma de Madrid ..... Rapporteur
M. Achim Schwenk, TRIUMF ..... Rapporteur
M. Karim Bennaceur, IPN Lyon, Université Lyon I ..... Examinateur
M. Andreas Nogga, Forschungszentrum Jülich ..... Examinateur

Thèse préparée au sein du Service de Physique Nucléaire,
CEA/DAM Bruyères-Le-Châtel

It's been about 9 months since I have, some people might say, "defected to the western capitalist world", and now seems to be as good a time as another to put the final touch to this work. There are so many people I'd like to thank that this would require at least an additional tome and yet this section would remain incomplete. Being not as prolixe as some of my fellow PhD students, I really hope that no one will hold me any grudge if this foreword pales with respect to the sheer size of this manuscript.

I am pretty sure that Jean-François will understand if my first lines of acknowledgements are for Thomas, who would have deserved more recognition than the unofficial "Co-Director" title that some stubborn people even refused to award him. He found the right words, alongside with Jean-Luc, to convince me to come and work in theoretical nuclear physics and I will never regret this decision, in terms of the challenges that I was offered or the people I got to meet. I hope that he appreciated working together as much as I did, and I think that our work reflects the good fit we have been, being both workaholics with a keen sense for politically incorrect humor. But beside being a brilliant scientist, who also knew how to cope with my mood swings, most of all I want to thank him and his wife Violaine for their welcome and hospitality during the year I spent at MSU. I particularly enjoyed this relationship that went beyond a simple student-advisor hierarchy, and I'll always remember the two epic World Cups we watched over there, in particular a phenomenal France-NZ in rugby, but also an soccer qualification game seen during a conference on a 5" poor streaming in Chinese.

I am also very grateful towards Jean-François who trusted me enough to let me go away for more than half of my PhD and work with Bruyères-Le-Châtel's nemesis team, but was always here with his natural kindness when I needed reassurance or fresh perspectives on what I was doing. The long discussions we had not only taught me a "little bit" of physics, but also really mattered in the end when it came to putting together all the pieces that we had thrown away in every possible direction. I only regret not having been able to follow all the leads he gave me which still represent challenging work for 50 more students.

My next words are for my jury, who all manifested a great interest for this project and almost immediately accepted to take a part in it. Maybe their courage faltered when they got the final version of the dissertation with only a few weeks to read it, for which I'll always be both respectful and grateful, but their encouragements and very positive reviews helped me through the final phase of my PhD. We were very proud with Thomas and Jean-François for having such a jury of experts in various domains. I just might apologize to Karim for the little bloody scare I gave him at MSU, and remind Achim that I actually did not need his help to meet my girlfriend!

This joint project would not have taken shape without the contribution from many more people that all deserve kudos, from the people in Bruyères-Le-Chatel (in particular my officemate Noël who surprinsingly knew as much as I did about crappy late-night TV shows), Saclay, Lyon and Bordeaux, to oversea connections in Michigan State, Ohio State or Vancouver. I was given the opportunity to interact with a lot of great people, academically and humanly-speaking, and I don't want to risk forgetting even one of them by by trying to name them all. Nevertheless, I really consider that this PhD fed from all these fruitful collaborations, which did not only fueled my Frequent Flyer card and granted me access in airport lounges during my holidays, but also can be seen throughout this manuscript.

I just need to add a few words of gratitude to one of Physical Review C' editors, John Millener, that allowed us to set a record in terms of paper submission. Our submission status

speaks for itself [1]

Part I

CORRESPONDENCE

SENT	*RCVD*	*DESCRIPTION*
11May09		**Published, PRC 79, 054308, Issue 5**
09Apr09	13Apr09	Proofs sent
27Mar09		Sent for publication
27Mar09		Editorially accepted, authors informed
26Mar09		Correspondence (miscellaneous) to authors
25Mar09	25Mar09	Correspondence to authors; response received
24Mar09		Correspondence (miscellaneous) to authors
26Jan09	24Mar09	On hold by editors
23Dec08		Correspondence (miscellaneous) to authors
04Dec08	23Dec08	Correspondence to authors; response received
22Oct08		Correspondence (miscellaneous) to authors
24Sep08	22Oct08	Correspondence to authors; response received
28Apr08		Correspondence (miscellaneous) to authors
24Apr08	27Apr08	Correspondence to authors
24Apr08		Correspondence (miscellaneous) to authors
24Apr08		Correspondence (miscellaneous) to authors
08Apr08	23Apr08	Editorial decision to authors
26Feb08	02Apr08	Sent to referee; report received
02Apr08		Reminder to referee
13Mar08	17Mar08	Correspondence to authors
25Feb08	25Feb08	Correspondence to authors; response received
12Feb08		Correspondence (miscellaneous) to authors
24Jan08	12Feb08	Editorial decision to authors
21Nov07	16Jan08	Sent to referee; report received
11Jan08		Reminder to referee
04Jan08	04Jan08	Reminder to referee; response received
14Nov07		Acknowledgment of receipt to authors
08Nov07		Correspondence (miscellaneous) to authors
08Nov07		**Submission received**

Part II

CORRESPONDENCE

SENT	*RCVD*	*DESCRIPTION*
11May09		**Published, PRC 79, 054309, Issue 5**
06May09		Proofs sent
08Apr09	13Apr09	Proofs sent
27Mar09		Sent for publication
27Mar09		Editorially accepted, authors informed
26Mar09		Correspondence (miscellaneous) to authors
25Mar09	25Mar09	Correspondence to authors
24Mar09		Correspondence (miscellaneous) to authors
24Mar09		Correspondence (miscellaneous) from authors
18Mar09		Correspondence (miscellaneous) to authors
17Mar09	18Mar09	Editorial decision to authors
27Jan09	17Mar09	Sent to referee; report received
10Mar09	12Mar09	Reminder to referee; response received
03Mar09		Reminder to referee
23Dec08		Correspondence (miscellaneous) to authors
24Sep08	23Dec08	Editorial decision to authors
04Dec08		Correspondence (miscellaneous) to authors
04Sep08	18Sep08	Correspondence to referee; response received
04Sep08		Correspondence (miscellaneous) to authors
09Jul08	02Aug08	Sent to referee; report received
21May08	19Jun08	Sent to referee; report received
12Jun08	13Jun08	Reminder to referee; response received
14May08		Correspondence (miscellaneous) to authors
06May08	13May08	Editorial decision to authors
05Mar08	28Apr08	Sent to referee; report received
17Apr08	21Apr08	Reminder to referee; response received
10Apr08		Reminder to referee
05Mar08		Correspondence (miscellaneous) to authors
25Jan08	20Feb08	Sent to referee; report received
15Jan08		Correspondence (miscellaneous) to authors
02Jan08	15Jan08	Editorial decision to authors
21Nov07	20Dec07	Sent to referee; report received
13Dec07	13Dec07	Reminder to referee; response received
14Nov07		Acknowledgment of receipt to authors
08Nov07		Correspondence (miscellaneous) to authors
08Nov07		**Submission received**

In spite of some political/not-so-clever referee comments, he really believed in what we were doing even when we were wondering if trying to reason with stubborn people about basic physics was worth it at all. Thanks to him, and my laziness to finish this dissertation, I can finally refer to our halo papers as something else that "submitted to PRC" pre-prints.

Though I am sure that most of them will never go beyond this page, there are many more people close to me that I think of when it comes to the people that mattered in my life these last 3 years. If it is a shame that I lost contact with some of them, they all got, maybe unwillingy, involved at some point in the mix and helped me realize that life was not always about halos and v_{BDRS}. In an order which does not reflect any kind of hierarchy, I thank with all my heart my family, that supported me in every decision I made, my second family from Polytechnique which is getting bigger everyday and harder to gather but with always the same joy, my dear friends from the CPM grad school (the memorable, but through fuzzy memories, school trips and the stupid ideas we seemed to never run short of) and I am not forgetting MSU's french connection that gave me a little glimpse of the American Pie way of life. A special dedication goes to the (happy few?) ones that chose to stay in their respective fields of research. Apart from the fact that most of them have already, or will soon, found permanent positions (which proves in all modesty that our DEA class was just "F#$% brilliant"), I really wish all of them the best, and I am just sorry that I won't be able to join them for the 6pm apéro any more, some people having real work to do...

While I may be done with my PhD, I obviously think of a special someone who should also soon (the sooner the better) put the finishing touch to hers. Cheer up Alice, soon we'll stop sponsoring Thalys and I'll be able to take care of you as well as you did so far with me, for better things await...

[1] Thanks a lot to Christopher Wesselborg who managed to dig up this souvenir from PRC's archives.

I really hope that at least some people will enjoy reading this manuscript as much as I did working on this project, and I think that this shows through the (many) pages hereafter. We shared with Thomas and Jean-François a common desire to be as exhaustive as possible, and maybe we took some kind of wicked pleasure when we settled for a two-volume dissertation... On the other hand, while I am really proud of what we have accomplished, this must still be considered as an unfinished with a lot of loose ends that I hope some people will feel interested in pursuing. In spite of being an unfinished work, this does not prevent Thomas from holding his words concerning a "two-in-one bet"...

Contents

Acknowledgements i

Table of contents v

List of figures xi

List of tables xv

Introduction 3

Conventions and notations 11

1 Energy density functional formalism 15
- 1.1 Single- and multi-reference formulations . . . 16
  - 1.1.1 Density functional theory . . . 16
  - 1.1.2 Energy density functional method for the nuclear problem . . . 18
- 1.2 Hartree-Fock-Bogoliubov realization . . . 21
  - 1.2.1 Symmetries of single-particle states . . . 21
  - 1.2.2 Generalized density matrix . . . 22
  - 1.2.3 Hartree-Fock-Bogoliubov equations . . . 22
  - 1.2.4 Coordinate space . . . 25
  - 1.2.5 Bases of interest . . . 25
  - 1.2.6 Bardeen-Cooper-Schrieffer approximation . . . 27
  - 1.2.7 Hartree-Fock realization . . . 28
  - 1.2.8 Spontaneous symmetry breaking and single-particle basis . . . 28
  - 1.2.9 Constrained HFB calculations . . . 30
- 1.3 Existing empirical models . . . 30
  - 1.3.1 Skyrme energy density functionals . . . 32
  - 1.3.2 Gogny energy density functional . . . 38
  - 1.3.3 Successes and limitations of existing empirical EDF models . . . 40
- 1.4 Pairing correlations for zero-range EDFs . . . 42
  - 1.4.1 UV divergences for contact pairing functionals . . . 42
  - 1.4.2 Regularization scheme . . . 44
  - 1.4.3 Vacuum and in-medium renormalization schemes . . . 44
  - 1.4.4 Gap in symmetric nuclear matter . . . 46
  - 1.4.5 Low-density behaviors and BCS-BEC crossover . . . 47
  - 1.4.6 Consequences for finite nuclei . . . 51
  - 1.4.7 Discussion . . . 55

I Halo phenomenon in medium- and heavy-mass nuclei **57**

Introduction **61**

2 Phenomenology of halo systems **63**
2.1 Basic features . . . 63
2.1.1 Importance of low angular-momentum orbits . . . 63
2.1.2 Role of pairing correlations . . . 64
2.2 Existing investigations and analysis methods . . . 65
2.2.1 First characterizations . . . 65
2.2.2 The Helm model . . . 69

3 Quantitative analysis of halo properties **75**
3.1 Properties of the one-body density . . . 76
3.1.1 Definitions and notations . . . 76
3.1.2 Decomposition of the N-body wave function . . . 77
3.1.3 Asymptotics of overlap functions . . . 77
3.1.4 Internal density . . . 78
3.2 Crossing pattern in $\rho^{\infty}_{[1]}(r)$ . . . 80
3.3 Halo characterization . . . 81
3.3.1 Spatial definition . . . 81
3.3.2 Relevant energy scales . . . 81
3.3.3 Definition of the halo region . . . 82
3.3.4 Quantitative halo criteria . . . 87

4 Results **91**
4.1 Implementation of the method . . . 92
4.1.1 Intrinsic overlaps in EDF calculations . . . 92
4.1.2 Numerical implementation of halo criteria . . . 94
4.2 Formation of halos in medium-mass nuclei . . . 94
4.2.1 Results for specific isotopic series . . . 94
4.2.2 Convergence of the calculations . . . 105
4.3 Impact of the Skyrme EDF . . . 110
4.4 Large-scale calculations . . . 111
4.5 Role of pairing correlations . . . 116
4.5.1 Pairing anti-halo effect . . . 116
4.5.2 Decorrelation from pairing field . . . 119
4.5.3 Importance of low densities . . . 120
4.6 Model-independence of the method . . . 124
4.6.1 Light nuclei . . . 124
4.6.2 Atom-positron/ion-positronium complexes . . . 126
4.6.3 Universality of the phenomenon . . . 127

Conclusions **131**

II Ab-initio approach to the nuclear many-body problem **135**

Introduction **139**

5 Vacuum nuclear interactions **141**
5.1 Bare nucleon-nucleon forces . . . 142
5.1.1 General expression from fundamental symmetries . . . 142
5.1.2 High-precision parametrizations . . . 143
5.2 Three-nucleon interaction . . . 147
5.3 Properties of bare nucleon-nucleon forces . . . 151
5.3.1 Momentum space . . . 152
5.3.2 Partial wave decomposition . . . 153
5.3.3 Scattering phase shifts . . . 154
5.3.4 Deuteron properties . . . 161
5.3.5 Weinberg eigenvalues . . . 162
5.4 Vacuum NN forces from renormalization group techniques . . . 164
5.4.1 Low-momentum nucleon-nucleon forces . . . 165
5.4.2 Properties of $V_{\text{low}\,k}$ . . . 170

6 Many-body problem **177**
6.1 Introduction . . . 177
6.2 Treatment of in-medium correlations . . . 178
6.2.1 Goldstone-Brueckner formalism . . . 178
6.2.2 Expansion of the ground-state wave-function and energy . . . 180
6.2.3 Choice of the one-body potential Γ . . . 181
6.3 Pairing correlations within a diagrammatic framework . . . 182
6.3.1 Conventions . . . 182
6.3.2 Compensation of dangerous diagrams . . . 183

7 Nuclear matter **185**
7.1 Introduction . . . 186
7.2 Conventions . . . 187
7.3 Averaged three-body vacuum interaction . . . 188
7.3.1 Decomposition of the three-body Hamiltonian . . . 188
7.3.2 Three-body contributions to the effective two-body interaction . . . 189
7.3.3 Expressions for $v^{\overline{\text{NNN}}}$ with low-momentum interactions . . . 191
7.4 Nuclear matter equation of state . . . 191
7.4.1 Introductory remarks . . . 192
7.4.2 Kinetic energy . . . 192
7.4.3 Correlation energy: generalities . . . 193
7.4.4 Correlation energy: partial wave expansion . . . 194
7.4.5 Correlation energy: MBPT calculations . . . 195
7.4.6 Infinite matter properties . . . 196
7.4.7 Results . . . 197
7.5 Pairing gaps . . . 207
7.6 Quantitative characterization of perturbative behaviors . . . 210

III Non-empirical effective forces **213**

Introduction **217**

8 Defining non-empirical vertices **219**
8.1 Non-empirical effective vertices for the EDF formalism . . . 219
8.2 Long-term strategies . . . 222
8.2.1 Strategy 1: representation of the vacuum NN interaction . . . 222
8.2.2 Strategy 2: representation of the vacuum NN + $\overline{\text{NNN}}$ interaction . . . 223
8.2.3 Strategy 3: representation of the in-medium effective vertices . . . 223
8.3 Expression and key features . . . 224
8.3.1 Analytical operatorial form . . . 226
8.3.2 Tensor interaction . . . 228
8.3.3 Various remarks . . . 229
8.4 Useful expressions for $v^{[X]}_{\text{BDRS}}$ . . . 230
8.4.1 Momentum space . . . 230
8.4.2 Infinite matter: vertices . . . 231
8.4.3 Infinite matter: correlation energy . . . 232
8.4.4 Partial wave decomposition . . . 233
8.5 Adjustment procedure . . . 237

9 Stochastic model optimization **239**
9.1 Introduction . . . 239
9.2 Nelder-Mead method . . . 241
9.3 Canonical genetic algorithms . . . 245
9.4 Simplex-coded genetic algorithms . . . 247
9.5 The FITPACK fit module . . . 250
9.5.1 Efficiency benchmarking . . . 250
9.5.2 Performance optimization . . . 252
9.6 Confidence intervals . . . 263
9.6.1 Linear model . . . 263
9.6.2 Non-linear model . . . 265

10 Results: bare nucleon-nucleon force **269**
10.1 $^1\text{S}_0$ channel: separable representation . . . 270
10.2 Explicit inclusion of renormalization group cutoffs . . . 270
10.2.1 Motivations . . . 270
10.2.2 One-dimension toy model . . . 276
10.2.3 Applications . . . 278
10.2.4 Realistic RG-induced vertices . . . 284
10.3 Results for $v^{[\text{bare}(2)]}_{\text{BDRS}}$: $^1\text{S}_0$ channel with RG cutoffs . . . 286
10.3.1 Fit setup . . . 286
10.3.2 Convergence issues . . . 287
10.3.3 First results . . . 292
10.3.4 Evolution with the RG cutoff Λ . . . 296
10.3.5 Representation accuracy . . . 298
10.3.6 Impact of the RG cutoff function . . . 299
10.3.7 Evolution with the number of gaussians . . . 303
10.3.8 Isospin-symmetry breaking . . . 304
10.3.9 Comparison with separable interactions . . . 306
10.3.10 Uncertainties analysis . . . 307
10.4 Results for $v^{[\text{bare}(2)]}_{\text{BDRS}}$: $L \leq 2$ partial waves with RG cutoffs . . . 313
10.5 Results for $v^{[\text{bare}(2)]}_{\text{BDRS}}$: no RG cutoffs in the $^1\text{S}_0$ channel . . . 316

Conclusions 321

Bibliography 327

List of Figures

1 Coordinate space matrix elements of the bare NN force Argonne V18 3
2 Pictorial view of a nucleus 4
3 Low-energy static and dynamical nuclear properties 5
4 Worldwide existing and upcoming radiactive nuclear beam facilities 5
5 The chart of nuclides 6
6 Halo parameters for drip-line chromium isotopes and different Skyrme EDFs . . 7
7 Schematic representation of the main objective of the present work 9
8 Conventions for the labeling of individual states 13

1.1 Illustration of the two-step EDF method 19
1.2 Properties of the HFB quasiparticle spectrum 24
1.3 Neutron pairing field in ^{120}Sn from Skyrme-EDF calculations 37
1.4 Properties of the HFB quasiparticle spectrum 40
1.5 Illustration of the asymptotic freedom of phenomenological EDF models 41
1.6 Pairing strength for regularized and renormalized pairing functionals 44
1.7 Pairing gap in symmetric nuclear matter for empirical pairing functionals . . . 47
1.8 BCS-BEC Crossover diagram for surface regularized pairing functionals 49
1.9 BCS-BEC Crossover diagram for renormalized pairing functionals 50
1.10 BCS and crossover phase diagrams 51
1.11 Neutron densities for ^{80}Cr and several regularized pairing functionals 52
1.12 Neutron canonical occupations in Cr isotopes (regularized pairing) 53
1.13 Neutron densities for ^{80}Cr and several renormalized pairing functionals 54
1.14 Neutron canonical occupations for Cr isotopes (renormalized pairing) 54
1.15 Ajusted density-dependent coupling strengths of local pairing functionals 55

2.1 Neutron canonical energies for Cr isotopic isotopes from EDF calculations . . . 66
2.2 Proton, neutron and charge r.m.s. radii for Cr isotopes from EDF calculations . 67
2.3 Two-neutron separation energies for Cr isotopes from EDF calculations 67
2.4 Neutron canonical energies for Sn isotopic isotopes from EDF calculations . . . 68
2.5 Proton, neutron and charge r.m.s. radii for Sn isotopes from EDF calculations . 68
2.6 Two-neutron separation energies for Sn isotopes from EDF calculations 69
2.7 Geometric and Helm radii for Cr and Sn isotopes 71
2.8 Realistic and Helm form factors of ^{54}Cr and ^{80}Cr 71
2.9 Realistic and Helm densities of ^{54}Cr and ^{80}Cr 72
2.10 Neutron Helm radii and halo parameters for Cr isotopes 72
2.11 Realistic and Helm densities of ^{54}Cr and ^{80}Cr with a different fit protocol . . . 73

3.1 Solutions of a finite spherical well 80
3.2 "Core+tail" simplified models for the choice of halo parameters 82
3.3 Energy scales relevant for the appearance of halos 83
3.4 Ankle in the log-density due to the presence of a low-lying state 84
3.5 Ratio between the second-order log-density and its peak value 86
3.6 Definition of r_0 through the second derivative of the log-density 87
3.7 Consequences of the definition of r_0 on the density profile 88

3.8 Evolution of r_0 along the Cr isotopic chain . . . 89

4.1 Neutron quasiparticle occupation in ^{80}Cr . . . 93
4.2 Neutron separation energies Cr isotopic chain . . . 95
4.3 Average number of nucleons participating in the halo for Cr isotopes . . . 96
4.4 Neutron densities for even-even Cr isotopes . . . 97
4.5 Halo factor parameter δR_{halo} for Cr isotopes . . . 97
4.6 Total neutron root-mean-square radius and core contribution for Cr isotopes . . . 98
4.7 Decomposition of the halo region for Cr isotopes . . . 100
4.8 Neutron densities for even-even Sn isotopes . . . 100
4.9 Neutron separation energies Sn isotopic chain . . . 102
4.10 Decomposition of the halo region for Sn isotopes . . . 102
4.11 Average number of nucleons participating in the halo for Sn isotopes . . . 104
4.12 Halo factor parameter δR_{halo} for Sn isotopes . . . 104
4.13 Total neutron root-mean-square radius and core contribution for Sn isotopes . . . 105
4.14 Evolution of N_{halo} and δR_{halo} as a function of the box radius for ^{80}Cr . . . 106
4.15 Evolution of different radii as a function of the box radius . . . 107
4.16 Neutron canonical states for ^{80}Cr with renormalized pairing functionals . . . 108
4.17 Neutron canonical states for ^{80}Cr with regularized pairing functionals . . . 108
4.18 Evolution of N_{halo} and δR_{halo} for different angular momentum truncations . . . 109
4.19 Properties of ^{80}Cr as a function of $J_{\max}$ for regularized pairing functionals . . . 110
4.20 Properties of ^{80}Cr as a function of $J_{\max}$ for renormalized pairing functionals . . . 110
4.21 Single-particle and halo properties for ^{80}Cr with different pairing functionals . . . 112
4.22 Neutron densities for ^{80}Cr with refits of the Skyrme parameters . . . 112
4.23 N_{halo} parameter for about 500 spherical nuclei . . . 113
4.24 δR_{halo} parameter for about 500 spherical nuclei . . . 114
4.25 Correlation between N_{halo} and δR_{halo} . . . 114
4.26 Canonical spectrum and halo factors of the best halo candidates . . . 115
4.27 Neutron canonical energies for Cr isotopes with and without pairing . . . 116
4.28 Halo criteria for Cr isotopes and spherical HF/HFB calculations . . . 117
4.29 Contributions of individual orbitals to the halo with and without pairing . . . 119
4.30 Neutron canonical occupations for drip-line Cr isotopes . . . 120
4.31 Individual neutron canonical gaps for drip-line Cr isotopes . . . 121
4.32 Single-particle energies in ^{80}Cr and renormalized pairing functionals . . . 121
4.33 Single-particle energies in ^{80}Cr and regularized pairing functionals . . . 122
4.34 N_{halo} parameter for Cr isotopes using different pairing form factors . . . 122
4.35 δR_{halo} parameter for Cr isotopes using different pairing form factors . . . 123
4.36 Individual halo contributions for ^{80}Cr and renormalized pairing functionals . . . 124
4.37 Core, halo and total neutron densities for light nuclei . . . 125
4.38 Valence electron, positron, core and total density for e^++A complexes . . . 127
4.39 Universality of halos formation . . . 128

5.1 Structure of the bare two-body force in terms of meson exchanges . . . 144
5.2 Iterative and non-iterative diagrams for meson exchanges . . . 146
5.3 Hierarchy of nuclear forces from Chiral Perturbation Theory . . . 148
5.4 The Tjon line for two-body forces . . . 150
5.5 Three-body force matrix diagrams from chiral EFT at N^{2}LO . . . 150
5.6 Illustration of the principle of a partial wave expansion . . . 153
5.7 Deuteron wave functions for N^{3}LO . . . 161
5.8 Illustration of the renormalization group formalism . . . 164
5.9 $V_{\text{low}\,k}$ matrix elements in the ^{1}S$_0$ channel for different values of Λ . . . 166
5.10 $V_{\text{low}\,k}$ matrix elements in all $L \leq 2$ partial waves (2D) . . . 168
5.11 $V_{\text{low}\,k}$ matrix elements in all $L \leq 2$ partial waves (specific values) . . . 169
5.12 Cutoff functions $f(k)$ for the renormalization flow equations . . . 170

5.13 $^1S_0$ phase shifts for Argonne V18 and $V_{\text{low}\,k}$ . . . 171
5.14 $^1S_0$ matrix elements for $V_{\text{low}\,k}$ from different realistic NN forces . . . 172
5.15 $V_{\text{low}\,k}$ scattering phase shifts in all $L \leq 2$ partial waves . . . 173
5.16 Weinberg eigenvalues for $V_{\text{low}\,k}$ starting from Argonne V18 . . . 175
5.17 Weinberg eigenvalues for $V_{\text{low}\,k}$ starting from N^{3}LO . . . 175

6.1 Ground-state and single-particle energies written in terms of the G-matrix . . . 180
6.2 Perturbation theory for ground-state and single-particle energies . . . 181
6.3 Propagators and contractions involved in MBPT with pairing correlations . . . 182
6.4 Diagrammatic representation of the compensation of dangerous diagrams . . . 183
6.5 One-body fields at lowest order in two-particle-irreducible vertices . . . 184

7.1 Nuclear matter phases . . . 186
7.2 Bare NN + $\overline{\text{NNN}}$ force from chiral-EFT diagrams . . . 190
7.3 Two-body vertices at various levels of MBPT ($^1S_0$ channel) . . . 198
7.4 Two-body vertices at various levels of MBPT ($^3S_1$-$^3D_1$ channel) . . . 199
7.5 Symmetric nuclear matter equation of state with $V_{\text{low}\,k}$ . . . 201
7.6 Symmetric nuclear matter equation of state from MBPT calculations . . . 202
7.7 (S, T) channels decomposition of nuclear matter equation of state . . . 204
7.8 Partial wave decomposition of nuclear matter equation of state . . . 205
7.9 Convergence of MBPT calculations: partial wave decomposition . . . 206
7.10 Neutron gap obtained from $V_{\text{low}\,k}$ for different RG cutoffs Λ . . . 209
7.11 Neutron gap with HF self-energies . . . 209
7.12 Correlation between coupling ranges and Weinberg eingenvalues . . . 211
7.13 Correlation between coupling ranges and the RG cutoff . . . 211
7.14 Correlation between matrix elements and Weinberg eingenvalue for $V_{\text{low}\,k}$ . . . 212

8.1 Effective MBPT vertex in the particle-hole channel . . . 221
8.2 Effective MBPT vertex in the particle-particle channel . . . 221
8.3 Diagrammatic representation of the SR-EDF energy . . . 222
8.4 Long-term strategy to construct microscopic bare/effective vertices $v^{[X]}_{\text{BDRS}}$ . . . 225

9.1 Illustration of the limitations of very simple optimization techniques . . . 240
9.2 Diagrams for a flow representation of an algorithm . . . 241
9.3 Diagramatic representation of the simplex algorithm . . . 242
9.4 Diagramatic representation of the Nelder-Mead step . . . 243
9.5 Nelder-Mead algorithm in two dimensions . . . 244
9.6 Diagramatic representation of a generic algorithm algorithm . . . 245
9.7 Mutation step in a hybrid genetic algorithm . . . 248
9.8 Crossover step in a hybrid genetic algorithm . . . 249
9.9 Diagramatic representation of the hybrid simplex-genetic algorithm . . . 249
9.10 Scaling properties of FITPACK as a function of the dimensionality . . . 253
9.11 Scaling properties of FITPACK as a function of the population size . . . 254
9.12 Scaling properties of FITPACK as a function of the merit evaluation time . . . 254
9.13 Hybrid simplex-genetic algorithm: first parallelization strategy . . . 255
9.14 Profiling of FITPACK using brute-force parallelization . . . 256
9.15 Conventions for the JUMPSHOT profiling program . . . 256
9.16 Profiling of FITPACK using brute-force parallelization: evolution phase . . . 257
9.17 Profiling of FITPACK using brute-force parallelization: aggregates . . . 258
9.18 Hybrid simplex-genetic algorithm: second parallelization strategy . . . 259
9.19 Connection grid for threads in the IPGA approach . . . 260
9.20 Profiling of FITPACK using island parallelization . . . 261
9.21 Profiling of FITPACK using island parallelization: evolution phase . . . 262
9.22 Profiling of FITPACK using island parallelization: aggregates . . . 262
9.23 Linear model used to illustrate the construction of confidence intervals . . . 268

10.1 Matrix elements for a separable representation of $V_{\text{low}\,k}$ in the $^1\text{S}_0$ channel . . . 271
10.2 $^1\text{S}_0$ phase shifts of $V_{\text{low}\,k}$ and its separable representation . . . 271
10.3 Matrix elements in momentum space of a simple gaussian . . . 272
10.4 Gaussian reconstruction from a partial wave expansion . . . 273
10.5 Gaussian reconstruction from a sharp RG-truncated partial wave expansion . . 274
10.6 Gaussian reconstruction from a smooth RG-truncated partial wave expansion . 275
10.7 RG cutoff functions in momentum and coordinate spaces . . . 281
10.8 RG-induced non-local vertex for an exponential RG cutoff function . . . 282
10.9 RG-induced non-local vertex for a sharp RG cutoff function . . . 283
10.10 Sharp RG cutoff function in coordinate space for the 3D and 1D cases . . . 285
10.11 Smooth RG exponential cutoff functions in coordinate space for the 3D case . . 286
10.12 Definition of theoretical uncertainties on $V_{\text{low}\,k}$ . . . 288
10.13 Results for 30 different fits of $V_{\text{low}\,k}$: naive case . . . 290
10.14 Zero-momentum coupling constants and relative strengths: naive case . . . 291
10.15 Results for 30 different fits of $V_{\text{low}\,k}$: improved case . . . 291
10.16 Results for 30 different fits of $V_{\text{low}\,k}$: optimal case . . . 292
10.17 Matrix elements for $V_{\text{low}\,k}$ and $v_{\text{BDRS}}^{[\text{bare}(2)]}$ . . . 294
10.18 Scattering phase shifts and INM gap equation for $V_{\text{low}\,k}$ and $v_{\text{BDRS}}^{[\text{bare}(2)]}$ . . . 294
10.19 Matrix elements of $v_{\text{BDRS}}^{[\text{bare}(2)]}$ with and without the RG cutoff functions . . . 295
10.20 Properties of $V_{\text{low}\,k}$ and $v_{\text{BDRS}}^{[\text{bare}(2)]}$ for $\Lambda = 2.1$ fm^{-1} . . . 296
10.21 Parameters of $v_{\text{BDRS}}^{[\text{bare}(2)]}$ at different Λ . . . 297
10.22 Zoomed matrix elements of $V_{\text{low}\,k}$ for different RG cutoffs Λ . . . 297
10.23 Rescaled theoretical error bars on $V_{\text{low}\,k}$ for a statistically accurate $v_{\text{BDRS}}^{[\text{bare}(2)]}$ . . 299
10.24 Average error on $V_{\text{low}\,k}$ for statistical accuracy as a function of Λ . . . 299
10.25 Matrix elements of $v_{\text{BDRS}}^{[\text{bare}(2)]}$ at $\Lambda = 2.1$ fm^{-1} with different cutoff schemes . . . 301
10.26 Parameters of $v_{\text{BDRS}}^{[\text{bare}(2)]}$ with different RG cutoff functions . . . 302
10.27 Form factors of $v_{\text{BDRS}}^{[\text{bare}(2)]}$ in the $^1\text{S}_0$ channel . . . 302
10.28 Diagrammatic representation of $V_{\text{low}\,k}$ at small Λ . . . 303
10.29 Parameters of $v_{\text{BDRS}}^{[\text{bare}(2)]}$ with different number of gaussians N . . . 304
10.30 $v_{\text{BDRS}}^{[\text{bare}(2)]}$ residuals in the $^1\text{S}_0$ channel for different numbers of gaussians . . . 305
10.31 Matrix elements for $V_{\text{low}\,k}$, v_{sep} and fitted $v_{\text{BDRS}}^{[\text{bare}(2)]}$ at $\Lambda = 1.8$ fm^{-1} . . . 307
10.32 Matrix elements differences between $v_{\text{sep/BDRS}}$ and $V_{\text{low}\,k}$ . . . 307
10.33 Fit accuracy as a function of the convergence threshold of FITPACK . . . 308
10.34 Parameters of $v_{\text{BDRS}}^{[\text{bare}(2)]}$ at different Λ including error bars . . . 312
10.35 $^1\text{S}_0$ Matrix elements of $v_{\text{BDRS}}^{[\text{bare}(2)]}$ including error bars . . . 313
10.36 $^1\text{S}_0$ scattering phase shifts of $v_{\text{BDRS}}^{[\text{bare}(2)]}$ including error bars . . . 314
10.37 $^1\text{S}_0$ gap equation of $v_{\text{BDRS}}^{[\text{bare}(2)]}$ including error bars . . . 314
10.38 χ^2 of the $L \leq 2$ model as a function of the number of FITPACK iterations . . . 315
10.39 Phase shifts of $v_{\text{BDRS}}^{[\text{bare}(2)]}$ in various partial waves using RG cutoffs . . . 316
10.40 $v_{\text{BDRS}}^{[\text{bare}(2)]}$ matrix elements using RG cutoffs in all $L \leq 2$ partial waves . . . 317
10.41 Matrix elements of the full gaussian $v_{\text{BDRS}}^{[\text{bare}(2)]}$ in the $^1S_0$ channel . . . 318
10.42 $^1S_0$ scattering phase shifts of the full gaussian $v_{\text{BDRS}}^{[\text{bare}(2)]}$ . . . 319
10.43 $^1S_0$ gap equation in symmetric nuclear matter of the full gaussian $v_{\text{BDRS}}^{[\text{bare}(2)]}$ . . . 319

List of Tables

1.1 Symmetries broken/restored in the two-step EDF approach . . . 19
1.2 Infinite matter properties of Skyrme functionals used in the present study . . . 35
1.3 Existing parametrizations for the Gogny forces . . . 39
1.4 Refit of DDDI parameters to reproduce microscopic results for the pairing gap . 56

4.1 Neutron canonical energies in ^{80}Cr and separation energies . . . 95
4.2 Single-particle contributions to the halo for Cr isotopes . . . 99
4.3 Neutron canonical energies in ^{174}Sn and separation energies . . . 101
4.4 Single-particle contributions to the halo for Sn isotopes . . . 103
4.5 Anti-halo effect: single-particle contributions to the neutron halo in ^{80}Cr . . . 118
4.6 Values of N_{halo} and δR_{halo} for ^{13}C and ^{11}Be . . . 125
4.7 Results of the halo analysis for various atom-positron systems . . . 126

5.1 Accuracy of modern models for the two-body bare interaction . . . 149
5.2 Parameters for the bare chiral three-nucleon force . . . 151
5.3 Block representation of the two-body nuclear interaction . . . 155
5.4 Non-zero partial waves for a nuclear interaction with tensor correlations . . . 155
5.5 Scattering parameters for $V_{\text{low}\,k}$ . . . 174
5.6 Deuteron properties for $V_{\text{low}\,k}$ . . . 174

6.1 Conventions for the lines and diagrams involved in MBPT calculations . . . 178

7.1 Empirical values for infinite nuclear matter properties . . . 197
7.2 Saturation properties for the equation of state in MBPT calculations . . . 200

8.1 Additional conventions for the effective vertices . . . 220

9.1 Mutation step in a canonical genetic algorithm . . . 246
9.2 Crossover step in a canonical genetic algorithm . . . 247
9.3 Convergence rate for the simplex and genetic algorithms . . . 250
9.3 (Continued) Convergence rate for the simplex and genetic algorithms . . . 251
9.4 Quantiles for normal and Student laws . . . 265
9.5 Confidence intervals obtained with two different methods . . . 268

10.1 Parameters for a separable representation of $V_{\text{low}\,k}$ at two cutoffs Λ . . . 271
10.2 Control parameters that enter the fitting procedure . . . 288
10.3 Initial limits used in the fit of $V_{\text{low}\,k}$ with three gaussians . . . 289
10.4 Optimization results for 30 fits with different procedures . . . 293
10.5 Weinberg eigenvalues and scattering parameters for $V_{\text{low}\,k}$ and $v_{\text{BDRS}}^{[\text{bare}(2)]}$ . . . 294
10.6 Optimization results for different RG cutoff Λ . . . 298
10.7 Optimization results for different RG cutoff functions for $V_{\text{low}\,k}$ . . . 303
10.8 Optimization results for different isospin projections . . . 306
10.9 Representation error for the parameters of $v_{\text{BDRS}}^{[\text{bare}(2)]}$ . . . 310
10.10 90% Confidence intervals for the parameters of $v_{\text{BDRS}}^{[\text{bare}(2)]}$ . . . 311

10.11 Fitted values of $v_{\mathrm{BDRS}}^{[\mathrm{bare}(2)]}$ 320
10.12 Physical properties of $v_{\mathrm{BDRS}}^{[\mathrm{bare}(2)]}$ 320

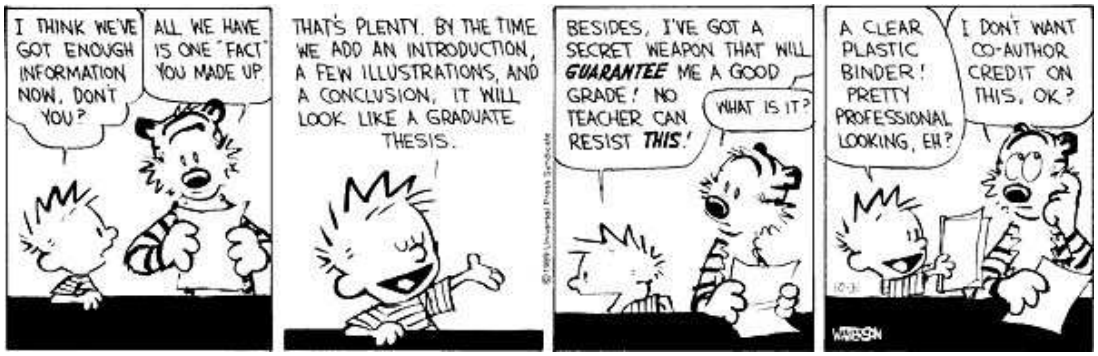
I THINK WE'VE GOT ENOUGH INFORMATION NOW, DON'T YOU?
ALL WE HAVE IS ONE "FACT" YOU MADE UP.
THAT'S PLENTY. BY THE TIME WE ADD AN INTRODUCTION, A FEW ILLUSTRATIONS, AND A CONCLUSION, IT WILL LOOK LIKE A GRADUATE THESIS.
BESIDES, I'VE GOT A SECRET WEAPON THAT WILL GUARANTEE ME A GOOD GRADE! NO TEACHER CAN RESIST THIS!
WHAT IS IT?
A CLEAR PLASTIC BINDER! PRETTY PROFESSIONAL LOOKING, EH?
I DON'T WANT CO-AUTHOR CREDIT ON THIS, OK?

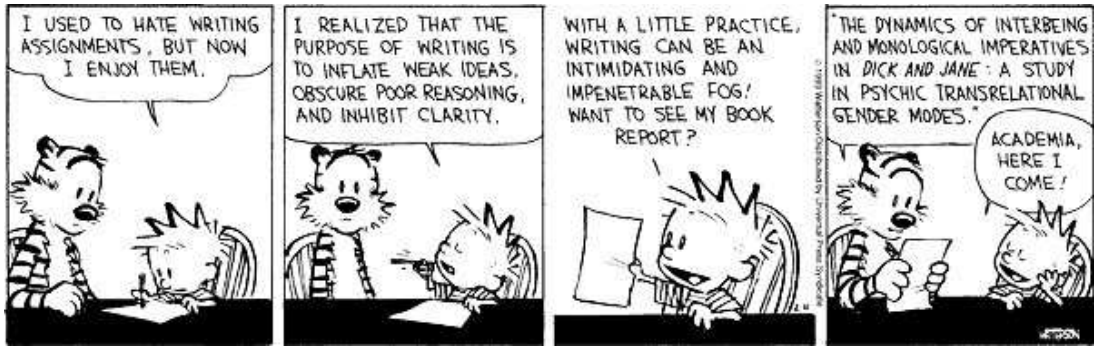
I USED TO HATE WRITING ASSIGNMENTS, BUT NOW I ENJOY THEM.
I REALIZED THAT THE PURPOSE OF WRITING IS TO INFLATE WEAK IDEAS, OBSCURE POOR REASONING, AND INHIBIT CLARITY.
WITH A LITTLE PRACTICE, WRITING CAN BE AN INTIMIDATING AND IMPENETRABLE FOG! WANT TO SEE MY BOOK REPORT?
"THE DYNAMICS OF INTERBEING AND MONOLOGICAL IMPERATIVES IN DICK AND JANE: A STUDY IN PSYCHIC TRANSRELATIONAL GENDER MODES."
ACADEMIA, HERE I COME!

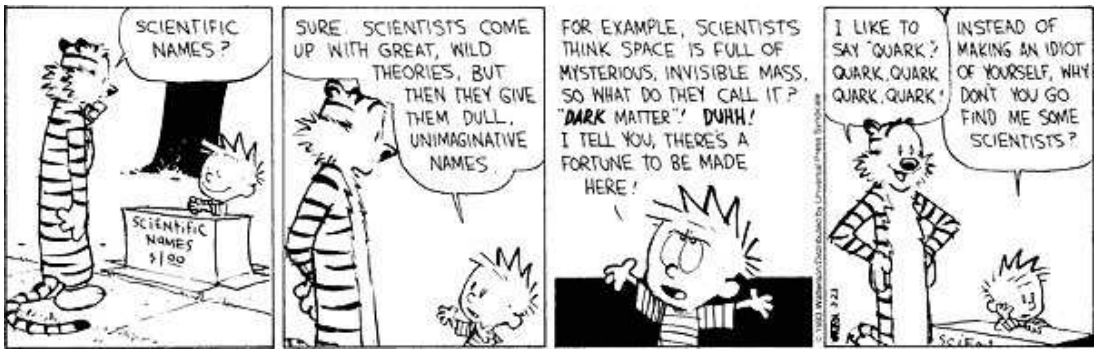
SCIENTIFIC NAMES?
SCIENTIFIC NAMES $1.00
SURE. SCIENTISTS COME UP WITH GREAT, WILD THEORIES, BUT THEN THEY GIVE THEM DULL, UNIMAGINATIVE NAMES.
FOR EXAMPLE, SCIENTISTS THINK SPACE IS FULL OF MYSTERIOUS, INVISIBLE MASS. SO WHAT DO THEY CALL IT? "DARK MATTER"! DUHH! I TELL YOU, THERE'S A FORTUNE TO BE MADE HERE!
I LIKE TO SAY "QUARK? QUARK, QUARK QUARK, QUARK!"
INSTEAD OF MAKING AN IDIOT OF YOURSELF, WHY DON'T YOU GO FIND ME SOME SCIENTISTS?

Introduction

In spite of over fifty years of theoretical and experimental studies, low-energy nuclear structure remains an open and difficult problem. While extensive progress has been made, for instance concerning the understanding of the shell structure, or the impact of nucleon superfluidity on low-energy properties, an accurate and universal description of nuclei from first principles is still beyond reach because of the specificities of the nuclear quantum many-body problem.

First of all, and in opposition to systems governed by quantum electrodynamics (QED), the strong nucleon-nucleon interaction cannot be derived yet from a gauge theory of interacting quarks and gluons, that is quantum chromodynamics (QCD) describing the intrinsic stucture of hadrons and their interaction. The inter-nucleon interaction can only be effectively modelized in the low-energy domain, in terms of a very complicated structure [1; 2]. Nucleons are assigned to both spin and isospin SU(2) doublets, i.e. 4-component fermions interacting in various configurations stemming from general invariances of the problem, e.g. spin-orbit, tensor, quadratic spin-orbit... couplings. As an example, Fig. 1 displays in coordinate space the state-of-the-art two-nucleon (NN) Argonne V18 [3] potential in the four two-body spin/isospin channels. Beyond its complex structure, the NN force presents bound (deuteron np in the coupled $^3S_1$-$^3D_1$ channels) and virtual (di-neutron nn in the $^1S_0$ channel) states. The associated large scattering lengths, together with the short-range repulsion between nucleons closer than their classical hard sphere radii makes the nuclear many-body problem highly non-perturbative. Finally, a treatment of three-body (NNN) interactions in a theory of point-like nucleons is unavoidable, as has been quantitatively confirmed by modern calculations such as (i) differential nucleon-deuteron cross-sections [4–6], (ii) the under-estimation of the triton and light nuclei binding energies [7], (iii) the Tjon line [8], (iv) the violation of the Koltun sum rule [9], (v) the non-saturation of symmetric nuclear matter [10–15], or more generally the Coester line problem [16–18].

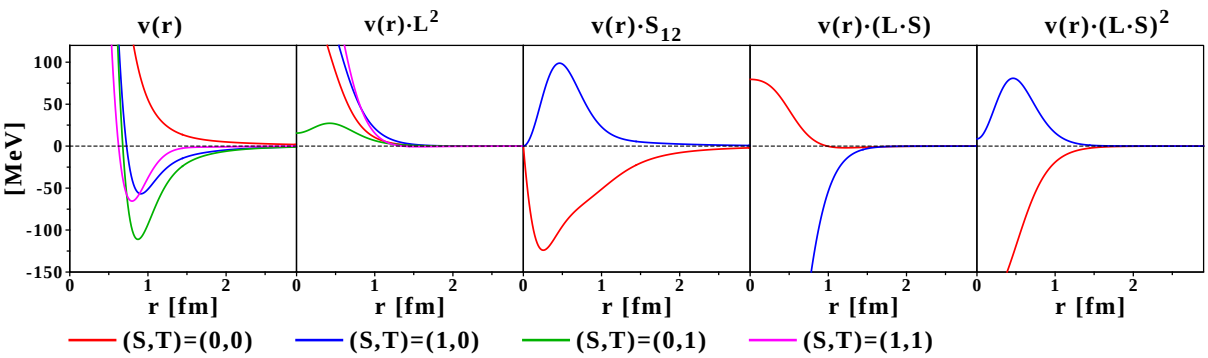

Figure 1: Coordinate space matrix elements of the bare NN force Argonne V18 provided in the four spin/isospin channels and separated in various components: central $\mathbb{I}$, centrifugal $\vec{\mathbf{L}}^2$, tensor S_{12}, spin-orbit $(\vec{\mathbf{L}}\cdot\vec{\mathbf{S}})$ and quadratic spin-orbit $(\vec{\mathbf{L}}\cdot\vec{\mathbf{S}})^2$.

At the same time, most nuclei (i.e. nuclei with masses typically between 40 and 350) are by essence intermediates between few- and many-body systems, as pictured in Fig. 2. That is (i) ab initio techniques that describe the interacting system in terms of basic two- and three-body vacuum forces find rapidly their theoretical and computational limits, while at the same time (ii) finite-size effects play a significant part, which prevents any statistical treatment. Furthermore, a unified view of low-energy nuclear structure implies a coherent description of (i) small- and large-amplitude collective motions, (ii) closed and open systems, that is a description of the structure-reaction interface (fission, fusion, nucleon emission at the drip-line...), and (iii) stable and exotic systems, e.g. systems with large isospin asymmetry, for which peculiar behaviors are already experimentally observed (see below). Finally, pairing correlations are essential to describe low-energy bulk properties of nuclei, but their explicit treatment complexifies the formulation of the many-body problem.

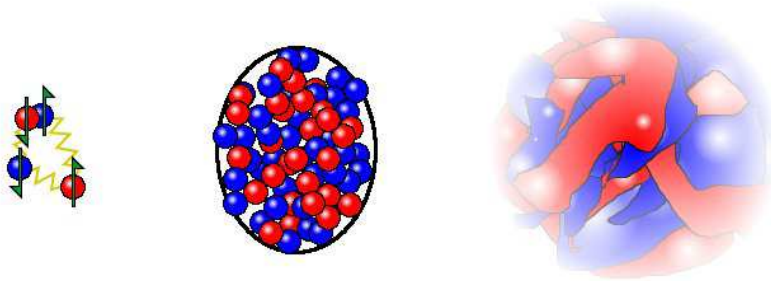

Figure 2: Pictorial view of a nucleus, as an intermediate between pure few-body and many-body systems.

The treatment of the nuclear many-body problem aims at a description of ground (masses, radii, deformation and multipolar moments...) and excited (single-particle, vibrational, shape and spin isomers, high-spin and super-deformed rotational bands...) state properties over the whole nuclear chart, both for the ∼3100 already observed nuclei [19] and the thousands which are still to be discovered. Fig. 3 presents the diversity of low-energy properties that one aims to describe. In that respect, a cross-fertilization between theoretical and experimental studies is more topical than ever, with the apparition of (i) new generations of radioactive ion beam (RIB) facilities producing very short-lived weakly-bound systems with acceptable yields, and (ii) high-precision detectors which allow precise measurements in low statistics and high noise-to-signal ratios.

Existing and upcoming facilities [20; 21] (see Fig. 4), based either on in-flight fragmentation [22; 23] (FAIR (GSI) [24], RIBF (RIKEN) [25], EURISOL [26], A1200 (NSCL) [27]...) or reaccelerated beams [28] (ARENAS^3 (Louvain-La-Neuve) [29], ISAC (TRIUMF) [30], REX-ISOLDE (CERN) [31], SPIRAL/SPIRAL2 (GANIL) [32], HRIBF (ORNL) [33]...) can/will explore further the nuclear chart towards the limits of stability against nucleon emission, the so-called nucleon drip-lines. For instance, the study of the terra incognita in the neutron-rich region may allow a better comprehension of the astrophysical nucleosynthesis of about half of the nuclei heavier than iron, i.e. through the r-process, which is one of the "Eleven science questions for the next century", as ranked by the American National Research Council [34]. The proximity of the Fermi energy to the particle continuum for large isospin asymmetry gives rise to new phenomena, such as the opening or quenching of magic numbers [35], or the formation of neutron halos, that is systems with anomalously large extensions due to the presence of weakly bound neutrons [36; 37]. While the latter phenomenon is observed in several light nuclei such as ^{11}Be [38; 39] or ^{11}Li [40; 41], and theoretically well understood, extrapolations towards

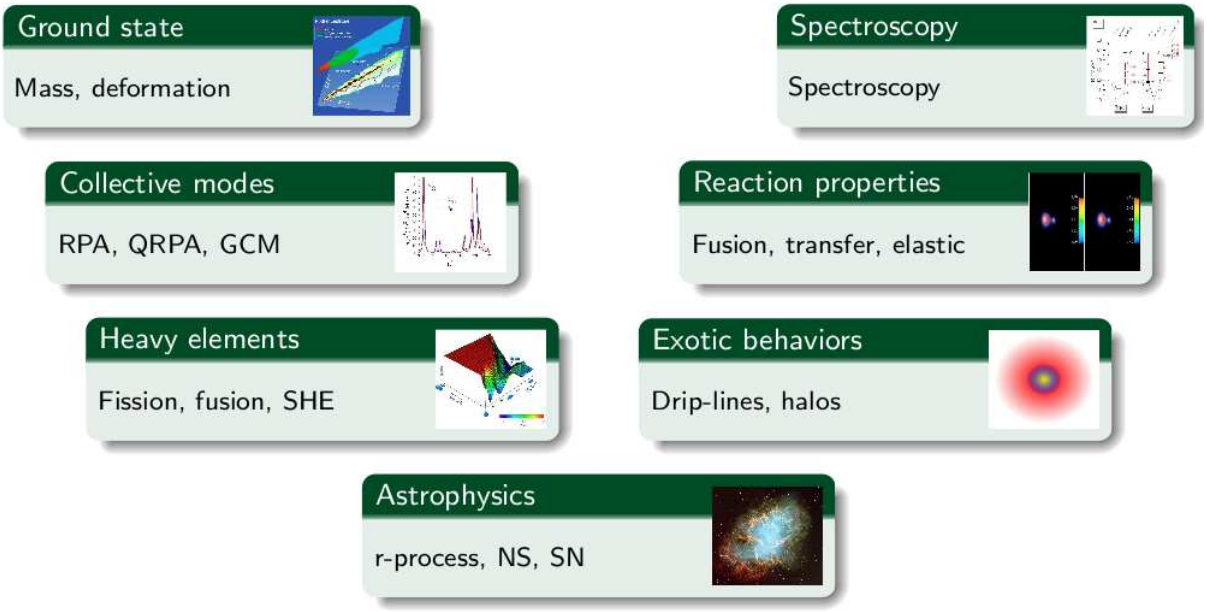

Figure 3: Low-energy static and dynamical nuclear properties to be obtained within a coherent theoretical framework.

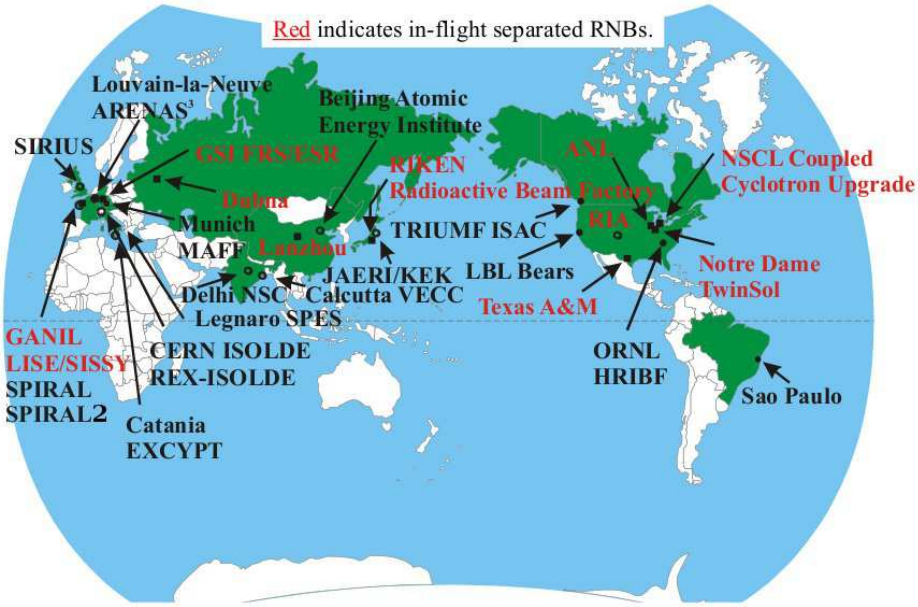

Figure 4: Worldwide existing and upcoming radiactive nuclear beam facilities.

higher masses remain beyond experimental reach, and only based on approximate/misleading theoretical predictions. The problem of a quantitative and model-independent characterization of the formation of nuclear halos [42; 43] will constitute the first part of this dissertation. The proposed method will allow the identification of shortcomings of existing methods and the lack of predictive power of empirical nuclear forces under extreme conditions.

In addition to studying exotic nuclei, experiments close to the valley of stability still provide critical information. For instance, precise mass measurements using Penning traps [44; 45] or Schottky spectrometry [46] refine and extend mass difference formulæ, leading to a better understanding of pairing correlations. At the same time, the study of Wigner energy [47], that is a surstability for $N = Z$ elements, might give leads concerning the importance of $T = 0$ proton-neutron pairing. One may also, among other topics of interest, mention recent experiments concerning rotational or vibrational bands [48], shape coexistence [49; 50], fission properties of actinides [51], collective modes [52], or the quest for superheavy elements and a potential island of stability beyond the $Z = 82$ magic number [53].

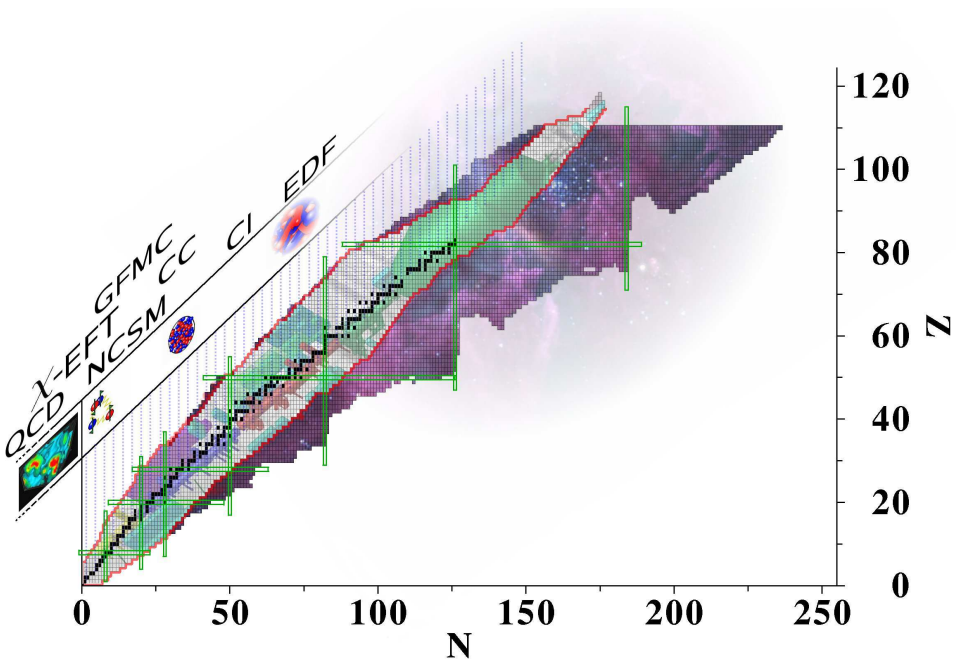

Figure 5: The chart of nuclides. Stable nuclei are represented in black with traditional magic numbers in green, while experimentally known nuclei are delimited by the red curve. Theoretically predicted nuclei by energy density functional calculations in the terra incognita are also represented. The domains of application of standard nuclear structure methods can be found in the upper part of this chart.

While bulk properties of nuclei can be roughly explained using macroscopic approaches such as the liquid drop model (LDM) [54; 55], microscopic techniques are the tool of choice for a coherent description of all static and dynamical nuclear properties, while keeping as much as possible a connection with the initial vacuum two- and three-body interactions at the same time. However, because the numerical complexity of the nuclear problem increases exponentially with the number of nucleons, necessary approximations lead to models that gradually lose the connection with bare forces as one goes from few- to many-body systems by (i) restricting the Hilbert space in which nucleons evolve, (ii) approximating the treatment of correlations, and/or (iii) using phenomeno-

logical corrections or full approximations based on empirical assumptions and experimental data. This is illustrated by Fig. 7. For three- or four-nucleon systems, essentially exact solutions of the Faddeev or Yakubowski equations can be found using realistic forces [56–58]. Likewise, in the case of very light nuclei ($A \lesssim 12$) Green function Monte-Carlo (GFMC) calculations [59–61] can describe the fully correlated few-body problem starting from realistic two- and three-body forces, using the exact evolution operator, but are restricted to local potentials and face already huge numerical challenges for ^{12}C. Other ab initio methods allow the treatment of nuclei up to $A \approx 16$ using vacuum NN and NNN forces, e.g. (i) the stochastic variational method (SVM) based on an expansion of the true many-body wave function in gaussian wave packets [62–64], or (ii) the no-core shell model (NSCM) [65–68] which projects the interacting problem on a given model space defined through a harmonic oscillator basis. Coupled-cluster (CC) theory [69–73], which constructs the correlated state from a product state using a cluster expansion, truncated to B-body operators (typ. $B \sim 1-4$), renders possible calculations up to $A \approx 50$ around magic shells. Note that all these methods, while giving essentially exact results, still use a truncation of some sort while preserving an explicit connection with vacuum nuclear forces. To go to heavier systems, an approximate treatment of both the interacting problem and the interaction is needed. For instance, the configuration interaction (CI) model [74; 75], or shell model (SM), constructs a model space within which valence nucleons interact through an effective interaction. Even though the latter is usually obtained as a microscopic G-matrix, certain combinations of its matrix elements (monopolar terms...) are partly refitted on experimental data within a given model space (sd, pf...). Proceeding this way, spectroscopic properties within the considered model space are described with an excellent accuracy [74; 76]. Finally, the theoretical tool of choice for the microscopic description of all medium- and heavy-mass nuclei is the Energy Density Functional (EDF) method [77], often referred to as "self-consistent mean-field method". Based on relativistic or non-relativistic frameworks, it allows a unified description of nuclei over the whole nuclear chart. However, state-of-the-art calculations are based on empirical energy functionals (Skyrme, Gogny) adjusted on exprimental data, which raises the question of (i) the connection with underlying vacuum NN and NNN forces, and (ii) the predictive power of extrapolated EDF results in the terra incognita, as illustrated in Fig. 6. A detailed presentation of the EDF method, of its successes and limitations, is given later on as this formalism is used throughout the present dissertation.

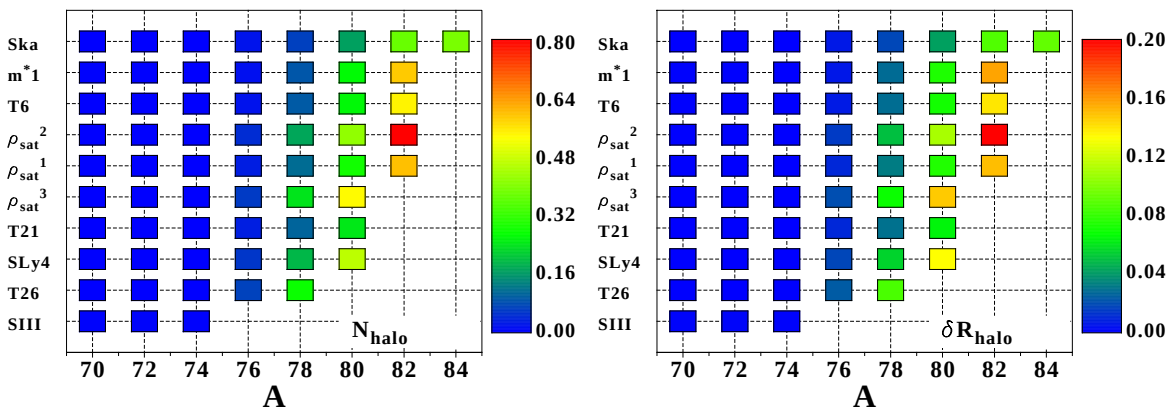

Figure 6: Halo parameters N_{halo} and δR_{halo} (see Part I) for drip-line chromium isotopes computed for different Skyrme EDFs. Large discrepancies between all of these empirical models are seen for the drip-line position and halo parameters.

Thus, the connection between the effective interaction used in approximate many-body calculations and the vacuum NN (and NNN, NNNN...) force is not always explicit. Still, several high-precision models for those potentials are available. Based on an operatorial expansion [3], a meson exchange model [78; 79], or a simple parametrization [80], NN models constitute phenomenological anzätze that are adjusted such that high-precision nucleon-nucleon scattering data are reproduced with an almost perfect precision ($\chi^2/N_{\rm dof} \approx 1$). The recent development of chiral effective field theory (χ-EFT) has made possible the connection between the low-energy nucleon-nucleon force and QCD, whose relevant high-energy effects are extracted through fitted contact terms [81–84]. The hierarchy between two-, three-, four-... nucleon forces is also naturally explained within the context of χ-EFT. QCD lattice calculations are now ongoing and will soon explicitly constrain the low-energy coupling constants that appear in χ-EFT [85; 86]. While chiral forces are not at the level of precision of state-of-the-art phenomenological models yet, they represent an essential step towards a unified description of nuclear interactions.

The main topic of the present dissertation constitutes an attempt towards an explicit and quantitative connection between high-precision NN and NNN models and EDFs used for the description of heavy nuclei, as illustrated by Fig. 7. Indeed, empirical models used in EDF calculations are crude, and limitations come from (i) their (too) simple analytical expressions, and/or (ii) their adjustement procedure. This connection is now possible thanks to the new paradigm set by low-momentum vacuum interactions coming from the application of the renormalization group. Such soft-core vacuum low-energy potentials are constructed from hard-core models [87], under the constraint of preserving low-energy physical observables such as scattering phase shifts and bound states. As these potentials are by essence soft and perturbative, they allow a treatment of the nuclear system in the framework of many-body perturbation theory (MBPT) [88; 89], which is applied on a daily basis to QED [90; 91], condensed matter [92], atomic or molecular [93–97] systems. For the first time, EDF calculations of medium- and heavy-mass nuclei with explicit connections to underlying nuclear forces can thus be envisioned. Nevertheless, MBPT calculations of self-bound superfluid heavy nuclei in terms of complex resonant interactions, even restricted to second order, constitute a theoretical challenge.

This dissertation is organized as follows. The bases of the EDF formalism and its specificities are recalled in Chap. 1. In particular, a presentation of existing phenomenological models will highlight their lack of connection with vacuum nuclear potentials. To illustrate extreme behaviors that can be tackled with EDF methods, e.g. at large isospin asymmetry, the formation of medium-mass nuclear halos is investigated in Part I using a brand-new analysis method. Such a method provides a coherent framework for a quantitative characterization of halo systems and is used to perfom a detailed analysis of the impact that EDF ingredients may have on predictions of their appearance. In the second half of the document, the construction of non-empirical effective vertices for EDF calculations is initiated. Firstly, Part II presents the necessary grounds for such an approach, that is a detailed study of the properties of vacuum nuclear forces followed by a discussion concerning the inclusion of in-medium effects. In particular, standard benchmarks for NN and NNN models such as the scattering phase shifts, the nuclear matter equation of state, deuteron properties or Weinberg eigenvalues, are presented, before initiating the construction of the new non-empirical effective vertex $V_{\rm BDRS}$ at different levels of (many-body) complexity. In Part III, the analytical expression of this new milestone is given and justified, before the adjustment procedure using artificial intelligence methods is presented. The optimization process is then carried on under different approximations, leading to high-precision analytical representations of low-momentum in-medium vertices that can be used for EDF calculations. Properties of such non-empirical in-medium vertices are characterized through calculations of infinite nuclear matter.

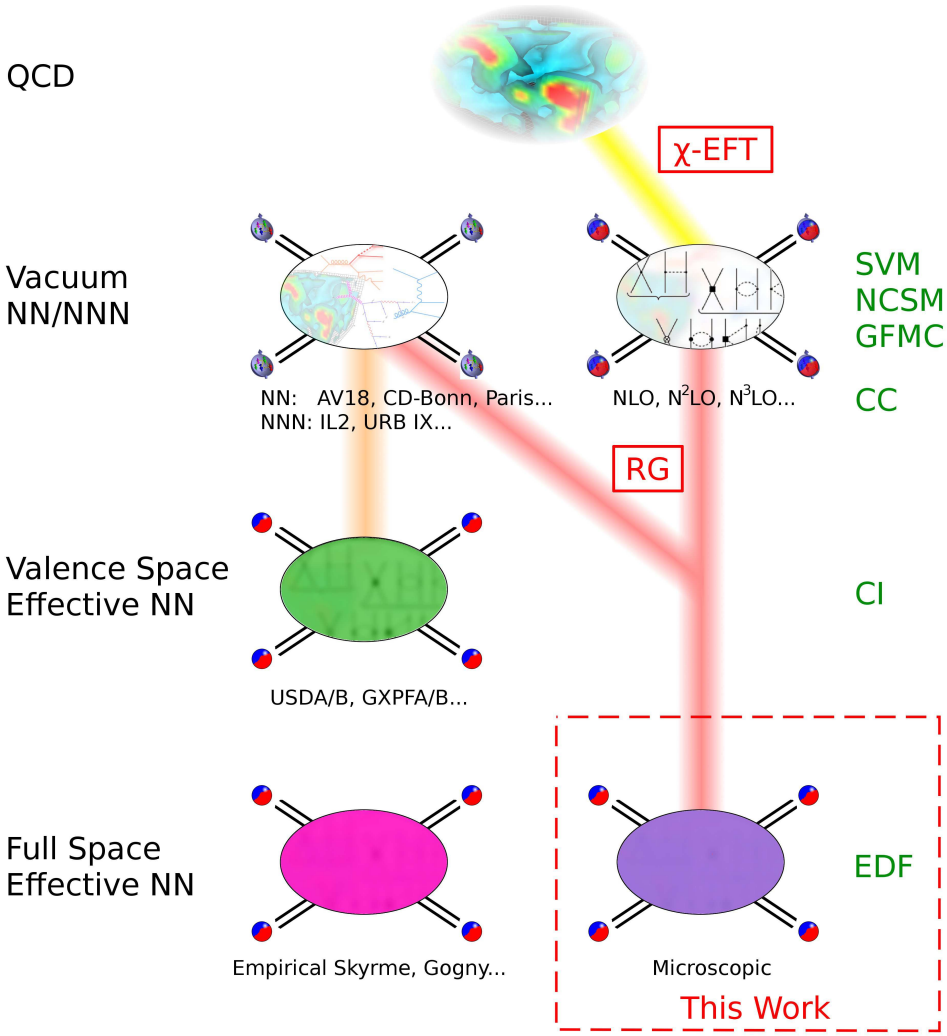

Figure 7: Schematic representation of the main objective of the present work. While χ-EFT allows for the first time an explicit connection between QCD and high-precision NN/NNN forces, state-of-the-art effective functionals used for EDF calculations are at this point empirical expressions adjusted on experimental data and carry very little information from underlying vacuum NN and NNN interactions. The use of low-momentum interactions based on the renormalization group provides the opportunity to realize an explicit and quantitative connection.

Conventions and notations

The principal acronyms and notations used throughout this manuscript are summarized below. In particular, standard definitions (common variable changes, usual operators...) are explicited here.

Acronyms

BEC	Bose-Einstein condensate
BCS	Bardeen-Cooper-Schrieffer
CI/SM	configuration interaction / shell model
χ-PT	chiral perturbation theory
c.o.m.	center-of-mass
DDDI	density-dependent delta interaction
DFT	density functional theory
DME	density matrix expansion
(SR/MR-)EDF	(single-reference/multi-reference) energy density functional
(χ-)EFT	(chiral) effective field theory
GA	genetic algorithm
GCM	generator coordinate method
GFMC	Green function Monte-Carlo
HF(B)	Hartree-Fock(-Bogoliubov)
(T)HO	(transformed) harmonic oscillator (basis)
IPGA	island-parallel genetic algorithm
INM/SNM	infinite/symmetric nuclear matter
MBPT	many-body perturbation theory
NCSM	no-core shell model
NN/NNN	two-nucleon/three-nucleon (interaction)
N^{n}LO	next-to-next-to-... leading order (in χ-PT)
PNM	pure neutron matter
PNR	particle number restoration
REG/REN-X	regularized/renormalized density-dependent pairing functional
RIB/RNB	radioactive ion beam/radioactive nuclear beam
RG	renormalization group
r.m.s.	root-mean-square (radius)
(Q)RPA	(quasi-)random phase approximation

SA	simplex algorithm
$V_{\mathrm{low}\,k}$	low-momentum bare NN force
WS	Woods-Saxon

Relative coordinates

From initial nucleon positions $\vec{r}_{1234}$, it is common to use the standard variable change leading to center-of-mass and relative coordinates as following:

$$\left[\begin{array}{rcl} \vec{r} & = & \vec{r}_2 - \vec{r}_1 \\ \vec{r}\,' & = & \vec{r}_4 - \vec{r}_3 \end{array}\quad \begin{array}{rcl} \vec{R} & = & \frac{1}{2}(\vec{r}_1 + \vec{r}_2) \\ \vec{R}\,' & = & \frac{1}{2}(\vec{r}_3 + \vec{r}_4) \end{array}\right. \Leftrightarrow \left[\begin{array}{rcl} \vec{r}_1 & = & \vec{R} - \frac{r}{2} \\ \vec{r}_3 & = & \vec{R}\,' - \frac{\vec{r}\,'}{2} \end{array}\quad \begin{array}{rcl} \vec{r}_2 & = & \vec{R} + \frac{r}{2} \\ \vec{r}_4 & = & \vec{R}\,' + \frac{\vec{r}\,'}{2} \end{array}\right. \tag{1}$$

Likewise, in momentum space

$$\left[\begin{array}{rcl} \vec{K} & = & \vec{k}_1 + \vec{k}_2 \\ \vec{K}\,' & = & \vec{k}_3 + \vec{k}_4 \end{array}\quad \begin{array}{rcl} \vec{k} & = & \frac{1}{2}(\vec{k}_1 - \vec{k}_2) \\ \vec{k}\,' & = & \frac{1}{2}(\vec{k}_3 - \vec{k}_4) \end{array}\right. \Leftrightarrow \left[\begin{array}{rcl} \vec{k}_1 & = & +\vec{k} + \frac{\vec{K}}{2} \\ \vec{k}_3 & = & +\vec{k}' + \frac{\vec{K}\,'}{2} \end{array}\quad \begin{array}{rcl} \vec{k}_2 & = & -k + \frac{\vec{K}}{2} \\ \vec{k}_4 & = & -k' + \frac{\vec{K}\,'}{2} \end{array}\right. \tag{2a}$$

$$\left[\begin{array}{rcl} \vec{q} & = & \vec{k} - \vec{k}\,' \\ \vec{q}\,' & = & \vec{k} + \vec{k}\,' \end{array}\right. \Leftrightarrow \left[\begin{array}{rcl} \vec{k} & = & \frac{1}{2}(\vec{q}\,' + \vec{q}) \\ \vec{k}\,' & = & \frac{1}{2}(\vec{q}\,' - \vec{q}) \end{array}\right. \tag{2b}$$

Operators, product states and wave functions

$\hat{a}_i^\dagger/\hat{a}_i$	Particle creation/annihilation operator in an arbitrary configuration basis
$\varphi_i(\vec{r}\,\sigma\,q)$	Single-particle wave function in an arbitrary basis
$\hat{a}_{\vec{r}\sigma q}^\dagger/\hat{a}_{\vec{r}\sigma q}$	Particle creation/annihilation operator in position$\otimes$spin$\otimes$isospin space $\hat{a}_i^\dagger = \sum_{\sigma\,q} \int d\vec{r}\,\varphi_i(\vec{r}\,\sigma\,q)\,\hat{a}_{\vec{r}\sigma q}^\dagger$
$\psi_i(\vec{r}\,\sigma\,q)$	Single-particle wave function in the HF basis
$\hat{c}^\dagger/\hat{c}$	Particle creation/annihilation operator in the canonical basis
$\phi_i(\vec{r}\,\sigma\,q)$	Single-particle wave function in the canonical basis
$\hat{\beta}^\dagger/\hat{\beta}$	Particle creation/annihilation operator in the quasiparticle basis
$\mathcal{U}_\mu(\vec{r}\,\sigma\,q)/\mathcal{V}_\mu(\vec{r}\,\sigma\,q)$	Quasiparticle spinors
$\lvert 1:i, 2:j\rangle$	Normalized non-antisymmetrized two-particle product state
$\lvert i\,j\rangle$	Normalized antisymmetrized two-particle product state $\lvert i\,j\rangle = \hat{a}_i^\dagger\,\hat{a}_j^\dagger\,\lvert 0\rangle = \frac{\lvert 1:i, 2:j\rangle - \lvert 1:j, 2:i\rangle}{\sqrt{2}}$
$P_{\vec{r}/\sigma/\tau}$	Position/spin/isospin-flip operator $P_{\vec{r}}\,\lvert 1:\vec{r}\,\sigma\,q, 2:\vec{r}\,'\,\sigma'\,q'\rangle = \lvert 1:\vec{r}\,'\,\sigma\,q, 2:\vec{r}\,\sigma'\,q'\rangle$ $P_\sigma\,\lvert 1:\vec{r}\,\sigma\,q, 2:\vec{r}\,'\,\sigma'\,q'\rangle = \lvert 1:\vec{r}\,\sigma'\,q, 2:\vec{r}\,'\,\sigma\,q'\rangle$ $P_\tau\,\lvert 1:\vec{r}\,\sigma\,q, 2:\vec{r}\,'\,\sigma'\,q'\rangle = \lvert 1:\vec{r}\,\sigma\,q', 2:\vec{r}\,'\,\sigma'\,q\rangle$
P_{12}	Two-particle exchange operator $P_{12} = P_{\vec{r}}\,P_\sigma\,P_\tau$ $P_{12}\,\lvert 1:i, 2:j\rangle = \lvert 1:j, 2:i\rangle$

$\mathcal{A}_{12}$	Two-particle antisymmetrization operator $\mathcal{A}_{12} = \mathbb{I} - P_{12}$
$\mathcal{A}_{123}$	Three-particle antisymmetrization operator $\mathcal{A}_{123} = (\mathbb{I} + P_{23}P_{12} + P_{31}P_{12})(\mathbb{I} - P_{12})$
$\prod_{S/T/S_z/T_z}$	Projector on a specific two-body spin/isospin state $\prod_S = \left[\frac{1+(-1)^{1-S}P_\sigma}{2}\right]$ $\prod_{S_z} = \left[(1-S_z^2) + \frac{1}{2}S_z\,S_z + (\frac{3}{2}S_z^2 - 1)\,S_z^2\right]$

Labeling of single-particle states

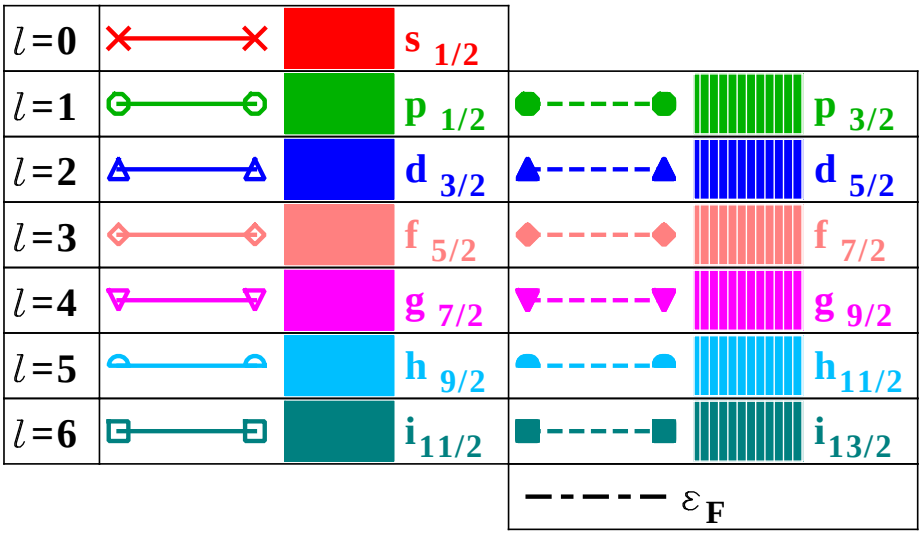

Figure 8: Conventions used in all the figures for the labeling of individual states and of the chemical potential.

Short notations

$\bar{f}(r)$	Radial part of an arbitrary function $f(\vec{r})$
$[L]$	Degeneracy $[L] = 2L+1$
$L^{\pm}$	Shortcut for $L \pm 1$

Dirac notations for two-body matrix elements

To keep track of all angular momenta, the following short notations will be used in place of Dirac ones for a given operator O, where Υ denotes all other dependencies beyond the relative momenta $\vec{k}$ and $\vec{k}\,'$

$$\langle k\,(LS)JS_z\,TT_z|O(\Upsilon)|k'\,(L'S)JS_z\,TT_z\rangle \equiv \langle k\,|O_{LL'}^{JSS_zTT_z}(\Upsilon)|k'\,\rangle \equiv O_{LL'}^{JST}(k,k';\Upsilon)\,, \tag{3a}$$

$$\langle k\,(LS)J\,T|O(\Upsilon)|k'\,(L'S)J\,T\rangle \equiv \langle k\,|O_{LL'}^{JST}(\Upsilon)|k'\,\rangle \equiv O_{LL'}^{JST}(k,k';\Upsilon)\,, \tag{3b}$$

$$O_{LL}^{LST}(k,k';\Upsilon) \equiv O_{L}^{JST}(k,k';\Upsilon)\,. \qquad \text{(Uncoupled channels)} \tag{3c}$$

Chapter 1

Energy density functional formalism

Abstract: This chapter briefly presents the formalism used for calculations of finite medium- and heavy-mass nuclei, that is the self-consistent energy density functional (EDF) framework, in particular in its single-reference (SR) Hartree-Fock-Bogoliubov (HFB) realization. Full sets of equations relative to several situations of interest (systems breaking time-reversal invariance, $\tilde{\rho}$ and κ representations, restriction to spherical systems) can be found in Appendix B, and only the main results are presented in the present chapter. The two major families of energy functionals employed in non-relativistic calculations, i.e. Skyrme or Gogny functionals, are presented, alongside with specific points which will be important later on, e.g. the treatment of ultraviolet divergences for quasi-local pairing functionals. It will eventually be shown that the combination of a (too) simple fitting procedure and a naive regularization of the pairing problem leads to spurious phase transitions in weakly bound nuclei.

Contents

1.1 Single- and multi-reference formulations **16**
1.1.1 Density functional theory 16
1.1.2 Energy density functional method for the nuclear problem 18
1.2 Hartree-Fock-Bogoliubov realization **21**
1.2.1 Symmetries of single-particle states 21
1.2.2 Generalized density matrix 22
1.2.3 Hartree-Fock-Bogoliubov equations 22
1.2.4 Coordinate space 25
1.2.5 Bases of interest 25
1.2.5.1 Canonical basis 25
1.2.5.2 HFB quasiparticle basis 27
1.2.6 Bardeen-Cooper-Schrieffer approximation 27
1.2.7 Hartree-Fock realization 28
1.2.8 Spontaneous symmetry breaking and single-particle basis 28
1.2.9 Constrained HFB calculations 30
1.3 Existing empirical models **30**
1.3.1 Skyrme energy density functionals 32
1.3.1.1 Particle-hole functional 32
1.3.1.2 Existing parametrizations 35
1.3.1.3 Particle-particle functional 35
1.3.1.4 Nuclear structure with Skyrme functionals 36

1.3.2 Gogny energy density functional 38
1.3.2.1 Existing parametrizations 39
1.3.2.2 Nuclear structure calculations with Gogny forces 39
1.3.3 Successes and limitations of existing empirical EDF models 40
1.4 Pairing correlations for zero-range EDFs 42
1.4.1 UV divergences for contact pairing functionals 42
1.4.2 Regularization scheme 44
1.4.3 Vacuum and in-medium renormalization schemes 44
1.4.4 Gap in symmetric nuclear matter 46
1.4.5 Low-density behaviors and BCS-BEC crossover 47
1.4.6 Consequences for finite nuclei 51
1.4.7 Discussion 55

1.1 Single- and multi-reference formulations

For a N-body system interacting in the presence of two-, three-... body forces $v^{\mathrm{NN,NNN,\cdots}}$, the total Hamiltonian reads

$$H^N = \sum_{i=1}^{N} t_i + \sum_{\substack{i,j=1\\ i<j}}^{N} v^{\mathrm{NN}}(r_{ij}) + \sum_{\substack{i,j,k=1\\ i<j,i<k}}^{N} v^{\mathrm{NNN}}(r_{ij}, r_{ik}) + \dots \tag{1.1}$$

where $\vec{r}_{ij} = \vec{r}_j - \vec{r}_i$ and t_i is the free kinetic operator. As soon as the number of particles exceeds a few units and/or the structure of the interactions becomes complicated, exact solutions of the N-body problem become very difficult to find. This is the case for most many-body electronic, molecular or nuclear systems, which require to design consistent approximation schemes.

1.1.1 Density functional theory

Density functional theory (DFT) is one of the most popular and successful ab initio approaches to the structure of quantum many-body electronic systems (atoms, molecules, solids...). The basic concept is that **ground-state observables of a many-body system can be represented by a functional of the ground-state density** $\rho(\vec{r})$ [98–102]. The two building blocks of DFT are

- the Hohenberg-Kohn theorem [103], which states the existence of a functional $F[\rho]$ such that the energy of a system of N particles in a one-body external potential $u(\vec{r})$ can be written as
$$E_u[\rho] = F[\rho] + \int \mathrm{d}\vec{r}\, u(\vec{r})\, \rho(\vec{r})\,, \tag{1.2}$$
where $F[\rho]$ only depends on the Hamiltonian of the interacting system, thus is independent of the external potential u, while it might depend on the particle number N. The ground-state density $\rho_0(\vec{r})$ and energy $E_0 = E_u[\rho_0]$ are then obtained by minimizing $E_u[\rho]$ with respect to a variation of the density $\rho(\vec{r})$ under the constraints that ρ is positive and $\int \mathrm{d}\vec{r}\, \rho(\vec{r}) = N$.

- the Kohn-Sham implementation [104; 105], which asserts that for any interacting system, there exists a unique local single-particle potential $u_{KS}(\vec{r})$ such that the ground-state

density of the interacting system equals the ground-state density of the auxiliary non-interacting system in the external potential $u_{KS}(\vec{r})$, that is

$$\rho(\vec{r}) = \rho_{KS}(\vec{r}) = \sum_{i=1}^{N} \sum_{\sigma} |\phi_i(\vec{r}\sigma)|^2 \,, \tag{1.3}$$

expressed using the lowest N single-particle orbitals $\phi_i(\vec{r})$ solutions of the one-body Kohn-Sham equation

$$\left[-\frac{\nabla^2}{2m} + u_{KS}(\vec{r})\right] \phi_i(\vec{r}) = \epsilon_i \, \phi_i(\vec{r}) \,. \tag{1.4}$$

In the Kohn-Sham scheme, F is split into

$$F[\rho] \equiv T[\rho] + U[\rho] + E_{xc}[\rho] \,, \tag{1.5}$$

where (i) $T[\rho]$ is the universal (kinetic) energy functional of the non-interacting system, (ii) $U[\rho]$ is the Hartree functional depending on the two-body interaction potential $v^{\mathrm{NN}}(\vec{r}_i, \vec{r}_j)$, and (iii) $E_{xc}[\rho]$ is the so-called exchange-correlation functional, including the Fock term and all remaining many-body correlations. When $E_{xc}[\rho]$ is neglected, the Kohn-Sham equations reduce to the standard self-consistent Hartree ones. Additionally, the Kohn-Sham potential is given through the condition that ground-state energies of the interacting and non-interacting problem ($U[\rho] = E_{xc}[\rho] = 0$) are met for the same density $\rho(\vec{r})$, i.e.

$$u_{KS}(\vec{r}) \equiv u(\vec{r}) + \frac{\partial E_{xc}[\rho]}{\partial \rho(\vec{r})}(\vec{r}) \,. \tag{1.6}$$

While the Kohn-Sham potential is local/multiplicative, the exchange-correlation functional might be largely non-local. The main difficulty for DFT practitioners lies in the fact that no prescription is given to construct F, i.e. the universal exchange-correlation part E_{xc}. Several levels of realization exist to construct

$$E_{xc}^{x}[\rho] \equiv \int \mathrm{d}\vec{r}\, \mathcal{E}_{xc}(\vec{r}) \,, \tag{1.7}$$

and they correspond to adding more complex dependencies in the functional $\mathcal{E}_{xc}$. The standard classification separates, from the most simple to the most involved level of description [106] :

1. the local density approximation (LDA), where $\mathcal{E}_{xc}$ only depends on the local density $\rho(\vec{r})$ and is matched onto the energy per unit volume of the corresponding infinite homogenous system,

2. the generalized gradient approximation (GGA), where additional specific dependencies on the gradient $\nabla \rho(\vec{r})$ are added to $\mathcal{E}_{xc}$,

3. the meta-GGA, which introduces as an additional degree of freedom the kinetic energy density of occupied Kohn-Sham orbitals

$$\tau(\vec{r}) = \sum_{i=1}^{N} \sum_{\sigma} |\nabla \phi_i(\vec{r}\sigma)|^2 \,, \tag{1.8}$$

4. the hyper-GGA, which takes also into account dependencies of $\mathcal{E}_{xc}$ on single-particle energies ϵ_i and occupations ρ_i,

5. the last ladder, called generalized random phase approximation (RPA), which involves unoccupied Kohn-Sham orbitals, and can be seen as the ultimate goal in terms of global accuracy.

1.1.2 Energy density functional method for the nuclear problem

In nuclear physics, DFT-like approaches have been used for the past twenty years with great success [77], but have usually been formulated in terms of wave-function-/effective Hamiltonian-based methods. Recently, a shift towards a more general functional theory has been intitiated, leading to the notion of energy density functional (EDF) methods, although a comprehensive connection between nuclear EDF and DFT methods, if it exists, is far from being achieved yet. Important theoretical efforts are currently dedicated to understanding such a connection, if any, especially as far as symmetries are concerned. Such a connection is complexified by the fact that, while the nuclear EDF method strongly relies on the concept of symmetry breaking and restoration (see below), the standard Hohenberg-Kohn theorem is a symmetry-conserving approach.

An important duty of the EDF method is to take into account specific aspects of the nuclear many-body problem, that is (i) the fact that a nucleus is self bound, (ii) the presence of the isospin degree of freedom alongside with the spin one, and (iii) the necessity to account for pairing correlations from the outset. Indeed, pairing correlations are not only known for a long time to play a significant role in finite nuclei, e.g. they explain the observed odd-even mass staggering [107–109] or the increase of the moment of inertia as a function of spin, but they are also important for nuclear astrophysics [110]. Indeed, neutrino cooling mechanisms are driven by nucleonic superfluidity in the interior of neutron stars [111–114], in such a way that pairing has a major effect on the thermal evolution of a star right after its creation (suppression of the neutron emission process [115]). In that respect, nucleon-nucleon superfluidity, which occurs with gaps of the order of a few MeVs [116], is of very interest. The treatment of pairing correlations has been formulated within the DFT framework [117], although that corresponds to a system coupled to a particle reservoir. This is relevant for an isolated nucleus.

The essence of the nuclear EDF formalism is a two-step approach where the concept of symmetry breaking plays an essential role: (a) the single-reference (SR) formulation that incorporates static collective correlations associated with symmetry-breaking modes, beyond bulk correlations that are incorporated into the functional itself, and (b) the multi-reference (MR) formulation that further includes correlations associated with quantum collective fluctuations of the order parameters $q \equiv |q|e^{i\varphi}$ associated with all symmetries broken at the SR-EDF level[1], as schematically exemplified in Fig. 1.1. Doing so, one incorporates fluctuations of (i) the phase φ, i.e. large-amplitude fluctuations with no restoring force that recover the invariants of the problem as in the case of angular momentum restoration (AMR) or particle number restoration (PNR), and of (ii) the magnitude $|q|$, i.e. large-amplitude motions handled by the symmetry-restored generator coordinate method (GCM). At the SR-EDF level, the basic fields the energy is functional of (see below) break symmetries of the exact energy in such a way that the latter is a scalar, e.g. the SR-EDF energy is degenerated relative to φ[2]. Order parameters associated with standard broken symmetries at the SR-EDF level can be found in Tab. {1.1}.

To summarize, SR-EDF is the best approximation of the interacting problem that incorporates static correlations, whereas the full solution is only obtained after the MR-EDF step. This indicates that a comparison of current EDF approaches to DFT is only meaningful at the MR-EDF level. Note that, given that there is no obvious separation of scales regarding excitation

[1] Taking a single order parameter of the form $q = |q|e^{i\varphi}$ corresponds to the situation where the considered symmetry group can be parametrized by a single continuous parameter φ. In the case of rotational symmetry, the $SO(3)$ non-abelian Lie group is parametrized by three Euler angles (α, β, γ).

[2] This constrains the expression of the EDF. Taking the example of the $U(1)$ group associated with the particle number symmetry, only products $\kappa^q \kappa^{q*}$ can appear in the definition of $\mathcal{E}[\rho, \kappa, \kappa^*]$ as $\kappa^q \sim e^{2i\varphi}$ and $\kappa^{q*} \sim e^{-2i\varphi}$.

energies associated with all different categories of correlations in the system, this empirical two-step approach is not a priori free from double countings. Indeed correlations mentioned above, i.e. (i) bulk correlations resummed into the EDF, (ii) static correlations brought in via symmetry breaking at the SR-EDF level, and (iii) dynamical correlations brought about by MR-EDF calculations, are not necessarily non-orthogonal.

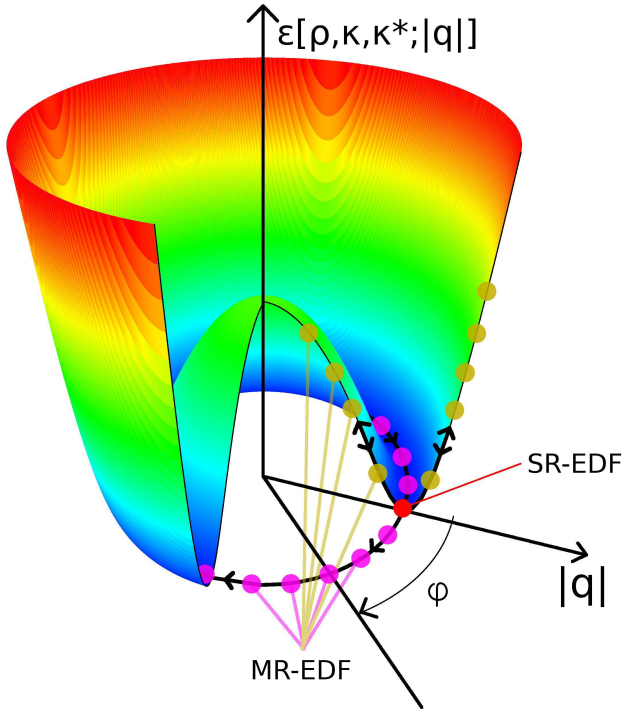

Figure 1.1: Illustration of the two-step EDF method. The multi-reference level corresponds to including fluctuations on the magnitude $|q|$ and phase φ of the order parameter associated with the symmetries that are broken at the SR-EDF level.

	Symmetry Group		Order parameter	
	Label	Casimir	"Phase"	"Magnitude"
PNR	$U(1)$	Particle number $\hat{N}$	Gauge angle φ	$\lvert\kappa\rvert$
AMR	$SO(3)$	Angular momentum $\hat{J}^2$	Euler angles (α, β, γ)	$\langle r^\lambda Y^\mu_\lambda\rangle(\lambda > 1)$
COMR	$T(3)$	Linear momentum $\hat{P}$	c.o.m. coordinates (R_x, R_y, R_z)	$\langle r^\lambda\rangle(\lambda > 1)$

Table 1.1: Symmetries that are broken at the SR-EDF level and restored at the MR-EDF level plus associated order parameters and Casimir invariants defining the irreducible representations of the symmetry group. The magnitude of the order parameter is defined as (i) the norm of the pairing tensor κ for PNR, (ii) multipoles of the density with $\lambda > 1$ for AMR, and (iii) radial moments of the density for center-of-mass (c.o.m.) restoration (COMR).

Multi-reference calculations allow the incorporation of dynamical correlations into the ground state, but also to study spectroscopic properties of nuclei. Different realizations are then possible, such as the quasiparticle random phase approximation (QRPA) which can be seen as a harmonic

limit of a complete MR-EDF framework [118; 119].

Let us now make explicit the nuclear EDF. At the SR-EDF level, which will be the scope of the present work, the $U(1)$ gauge symmetry breaking is explicitly included by considering the most general[3] energy functional for the ground state $\mathcal{E}[\rho^q, \kappa^q, \kappa^{q*}]$ that depends on the one-body density ρ and pairing tensor κ defined for isospin q as

$$\rho^q_{\nu\mu} \equiv \langle\Phi|\hat{a}^\dagger_\mu\,\hat{a}_\nu|\Phi\rangle\,, \qquad \kappa^q_{\nu\mu} \equiv \langle\Phi|\hat{a}_\mu\,\hat{a}_\nu|\Phi\rangle\,, \tag{1.9}$$

where $\{\hat{a}/\hat{a}^\dagger\}$ are standard particle creation and annihilation operators, and $|\Phi\rangle$ is an auxiliary reference state to be specified. In the present approach, fermions always carry a good isospin q. That is, the nuclear EDF is not only a functional of the local one-body density $\rho(\vec{r})$ but depends a priori on the full density matrix ρ and pairing tensor κ. At the SR-level, $|\Phi\rangle$ is usually taken as a product state. As in the DFT case, $\mathcal{E}$ splits into the uncorrelated kinetic energy and the remaining correlation energy. Using anticommutation properties for the set $\{\hat{a}/\hat{a}^\dagger\}$, only half of the matrix elements of ρ and κ are shown to be linearly independent. Indeed

$$\rho^{q\,*}_{ij} = \rho^q_{ji}\,, \qquad \kappa^q_{ij} = -\kappa^q_{ji}\,, \qquad \kappa^{q\,*}_{ij} = -\kappa^{q\,*}_{ji}\,. \tag{1.10}$$

One can thus choose the irreducible set of independent variables

$$\left\{\{\rho^q_{ij}, \rho^{q\,*}_{ij}, \kappa^q_{ij}, \kappa^{q\,*}_{ij}\}, j<i\}, \{\rho^q_{ii}\}, \forall i\right\}. \tag{1.11}$$

In the same spirit as in DFT, the nuclear SR-EDF method will rely on a minimization principle, that is one will here evaluate the variation of $\mathcal{E}[\rho, \kappa, \kappa^*]$ with respect to the set of independent variables defined above to obtain

$$\begin{aligned}\delta\mathcal{E} =& \sum_q \sum_{j<i} \left(\frac{\delta\mathcal{E}}{\delta\rho^q_{ij}}\,\delta\rho^q_{ij} + \frac{\delta\mathcal{E}}{\delta\rho^{q\,*}_{ij}}\,\delta\rho^{q\,*}_{ij} + \frac{\delta\mathcal{E}}{\delta\kappa^q_{ij}}\,\delta\kappa^q_{ij} + \frac{\delta\mathcal{E}}{\delta\kappa^{q\,*}_{ij}}\,\delta\kappa^{q\,*}_{ij} \right) + \sum_q \sum_i \frac{\delta\mathcal{E}}{\delta\rho^q_{ii}}\,\delta\rho^q_{ii} \\ \equiv& \frac{1}{2} \sum_q \sum_{ij} \left(h^q_{ji}\delta\rho^q_{ij} + h^{q\,*}_{ji}\delta\rho^{q\,*}_{ij} - \Delta^{q\,*}_{ji}\delta\kappa^q_{ij} - \Delta^q_{ji}\delta\kappa^{q\,*}_{ij} \right) \\ =& \frac{1}{2}\,\mathrm{Tr}\left\{h\delta\rho + h^*\delta\rho^* - \Delta^*\delta\kappa - \Delta\delta\kappa\right\}\,,\end{aligned} \tag{1.12}$$

where we have introduced, for $j \leq i$, the hermitian one-body field h and the skew symmetric pairing field Δ as

$$h^q_{ji} \equiv \frac{\delta\mathcal{E}}{\delta\rho^q_{ij}} = h^{q\,*}_{ij}\,, \qquad \Delta^q_{ij} \equiv \frac{\delta\mathcal{E}}{\delta\kappa^{q\,*}_{ij}} = -\Delta^q_{ji}\,, \tag{1.13a}$$

$$h^{q\,*}_{ji} \equiv \frac{\delta\mathcal{E}}{\delta\rho^{q\,*}_{ij}} = h^q_{ij}\,, \qquad \Delta^{q\,*}_{ij} \equiv \frac{\delta\mathcal{E}}{\delta\kappa^q_{ij}} = -\Delta^{q\,*}_{ji}\,. \tag{1.13b}$$

In the nuclear EDF method, the minimization of $\mathcal{E}[\rho, \kappa, \kappa^*]$ is not related to the Rayleigh-Ritz variational principle as (i) the ground-state energy is not computed as the average value of the nuclear Hamiltonian in a trial state, and (ii) there is no such thing as a Hohenberg-Kohn theorem that underlines such a minimization. That is, depending on the content of $\mathcal{E}$, one could find an energy that is below the actual ground-state eigenenergy.

There is a second so-called $\tilde{\rho}$, or "Russian", representation for the SR-EDF, where the pairing tensor is replaced by the pair density matrix

$$\tilde{\rho}(\vec{r}\,\sigma\,q, \vec{r}\,'\,\sigma'\,q') \equiv -2\sigma'\,\kappa(\vec{r}\,\sigma\,q, \vec{r}\,'\,-\sigma'\,q')\,. \tag{1.14}$$

[3] Under the constraint that $\mathcal{E}[\rho^q, \kappa^q, \kappa^{q\,*}]$ is a scalar with respect to all broken symmetries at the SR-EDF level.

There are subtleties regarding the relationship between κ and $\tilde{\rho}$ representations, in particular when writing the self-consistent equations in coordinate space. Of course, these representations are fully equivalent, but one or the other may present advantages under certain circumstances. The pair density matrix is particularly suited for quasi-local pairing functionals, in particular when the corresponding effective pairing vertex is limited to the spin-singlet/isospin-triplet channel (cf Sec. 1.3.1.3). When the system is invariant under the time-reversal symmetry, the pair density $\tilde{\rho}$ becomes hermitian which leads to further simplifications. While the κ representation will be used for most of the following derivations, intermediate results will also be expressed in the $\tilde{\rho}$ representation. When necessary, superscripts $[\tilde{\rho}/\kappa]$ will distinct the two conventions.

The following derivations will be applied to the case of time-reversal invariant systems. A complete set of derivations including time-reversal symmetry-breaking states can be found in Appendix B.

1.2 Hartree-Fock-Bogoliubov realization

We now define a practical application of the SR-EDF by specifying the form of the auxiliary state $|\Phi\rangle$ from which the density matrices ρ and κ are constructed.

1.2.1 Symmetries of single-particle states

Single-nucleon spinors $\{\varphi_\mu\}$ have good isospin projections and are represented by

$$\langle \vec{r}\,|\,\mu\rangle \equiv \varphi_\mu(\vec{r}\,q) = \begin{pmatrix} \langle \vec{r}\;\sigma = +1/2\,q|\,\mu\rangle \\ \langle \vec{r}\;\sigma = -1/2\,q|\,\mu\rangle \end{pmatrix} = \begin{pmatrix} \varphi_\mu(\vec{r}+1/2\,q) \\ \varphi_\mu(\vec{r}-1/2\,q) \end{pmatrix} . \tag{1.15}$$

Symmetries and associated quantum numbers μ used to designate single-particle states depend on the situation and cannot be given once and for all (see Sec. 1.2.8). As it will be seen later, the introduction of pairing correlations requires at least the existence of one good quantum number (beyond isospin) to split the basis into two halves that are coupled by the special part of the Bogoliubov transformation. Because it is general enough to cover most of the situations of interest, the z-signature ζ will be used as the transformation that provides this quantum number [120]. Signature transformations correspond to rotations by an angle π around the reference axes, i.e.

$$\hat{R}_j = e^{i\pi\hat{J}_j} = e^{i\pi\hat{L}_j}\,e^{i\pi\hat{S}_j} = i\,e^{i\pi\hat{L}_j}\,\hat{\sigma}_j \qquad \text{for } j = x,\,y,\,z\,, \tag{1.16}$$

for spin 1/2 particles, where $\hat{\sigma}_j$ are the Pauli spin-matrices. One finds that $\hat{R}_i^2 = -1$, that is single-particle eigenstates of $\hat{R}_z$ have eigenvalues $i\zeta_\mu = \pm i$ (thus $\zeta_\mu = \pm 1$). As said above, the basis will be split into two halves according to the z-signature quantum number and pairing is assumed to take place between states of opposite signature. They will be characterized by the notation $(\mu, \hat{\nu})$, where the negative signature state is not specified.

For the present discussion, it is also relevant to introduce the time-reversal operator $\hat{\mathcal{T}} = e^{i\,\pi\,\hat{S}_y}\,\hat{K}$, where $\hat{K}$ is an operator which associates to a wave function its complex conjugate and $\hat{S}_y$ is the spin-projection operator of the N-body system on the y axis. For single-nucleon spinors the time-reversal operator reduces to $i\,\hat{\sigma}_y\,\hat{K}$. For time-reversal invariant systems, i.e. $\hat{\mathcal{T}}|\Phi\rangle = |\Phi\rangle$, all single-particle bases of interest are closed under the action of $\hat{\mathcal{T}}$. Thus, one can always find a state $\varphi_{\tilde{\mu}}(\vec{r}\sigma q)$ in the basis fulfilling

$$\varphi_{\bar{\mu}}(\vec{r}\,\sigma\,q) \equiv (\hat{\mathcal{T}}\,\varphi)_\mu(\vec{r}\,\sigma\,q) \equiv \eta_\mu\,\varphi_{\tilde{\mu}}(\vec{r}\,\sigma\,q)\,, \tag{1.17}$$

where $\eta_{\tilde{\mu}} = -\eta_\mu$ and $|\eta_\mu| = 1$ (this quantum number can be taken real), with the additional result that $\varphi_{\tilde{\mu}}$ has an opposite signature to φ_μ. In such a basis, matrix elements of the time-reversal operator read as $\mathcal{T}_{\mu\hat{\nu}} \equiv \langle\mu|\mathcal{T}\,\hat{\nu}\rangle = \eta_{\hat{\nu}}\,\delta_{\tilde{\mu}\hat{\nu}}$.

A subtlety is that, for a given pair $(\mu, \tilde{\mu})$, the quantum number ζ_μ originally used to separate the basis into two halves coupled by the Bogoliubov transformation is not necessarily the same as the (real) phase η_μ, i.e. $\eta_\mu\,\zeta_\mu = \pm 1$ depending on the quantum number μ. For time-reversal systems, it might thus be useful, as we will do, to reorder each pair of conjugated states $(\mu, \tilde{\mu})$ according to η_μ and not ζ_μ as done in general.

1.2.2 Generalized density matrix

In the Hartree-Fock-Bogoliubov (HFB) realization of the SR-EDF formalism [121–123], the density matrices ρ and κ are provided by a reference state $|\Phi\rangle$ built as an independent quasiparticle state, that is a vacuum for a set of quasiparticle operators $\{\hat{\beta}/\hat{\beta}^\dagger\}$ defined as linear combinations of $\{\hat{a}/\hat{a}^\dagger\}$:

$$\begin{pmatrix} \hat{\beta}^q \\ \hat{\beta}^{q\dagger} \end{pmatrix} \equiv W^{q[\kappa]^\dagger} \begin{pmatrix} \hat{a}^q \\ \hat{a}^{q\dagger} \end{pmatrix} \equiv \begin{pmatrix} \mathcal{U}^{q[\kappa]^\dagger} & \mathcal{V}^{q[\kappa]^\dagger} \\ \mathcal{V}^{q[\kappa]^{\mathrm{T}}} & \mathcal{U}^{q[\kappa]^{\mathrm{T}}} \end{pmatrix} \begin{pmatrix} \hat{a}^q \\ \hat{a}^{q\dagger} \end{pmatrix} . \tag{1.18}$$

One has then

$$\forall\,\nu, q\,, \qquad \hat{\beta}^q_\nu\,|\Phi\rangle \equiv 0\,, \qquad |\Phi\rangle \equiv \prod_q \prod_{\nu[q]} \hat{\beta}^q_\nu\,|0\rangle\,. \tag{1.19}$$

Since the many-body auxiliary HFB state is an independent-quasiparticle state, the normal density matrix ρ does not contain enough information to characterize $|\Phi\rangle$. The generalized one-body density matrix which does so is defined in the traditional representation as

$$\mathcal{R} \equiv \begin{pmatrix} \rho & \kappa \\ -\kappa^* & 1-\rho^* \end{pmatrix} = \begin{pmatrix} \langle\Phi|\hat{a}^\dagger\,\hat{a}|\Phi\rangle & \langle\Phi|\hat{a}\,\hat{a}|\Phi\rangle \\ \langle\Phi|\hat{a}^\dagger\,\hat{a}^\dagger|\Phi\rangle & \langle\Phi|\hat{a}\,\hat{a}^\dagger|\Phi\rangle \end{pmatrix}, \tag{1.20}$$

and is idempotent since $|\Phi\rangle$ is an independent quasiparticle state, that is $\mathcal{R}^2 = \mathcal{R}$. This leads to relations between ρ and κ of the form

$$\rho\cdot\rho - \kappa\cdot\kappa^* = \rho\,, \qquad \rho\cdot\kappa - \kappa\cdot\rho^* = 0\,, \tag{1.21a}$$

$$\kappa^*\cdot\rho - \rho^*\cdot\kappa^* = 0\,, \qquad \rho^*\cdot\rho^* - \kappa^*\cdot\kappa = \rho^*\,. \tag{1.21b}$$

1.2.3 Hartree-Fock-Bogoliubov equations

Equations of motion for single-particle states and Bogoliubov amplitudes are determined self-consistently from the variation of the total energy under the constraints

$$\mathrm{Tr}\{\rho^q\} = \mathrm{Tr}\{\rho^{q\,*}\} = \langle\hat{N}_q\rangle = \langle\hat{N}_q^\dagger\rangle = N_q\,, \tag{1.22a}$$

$$\mathcal{R}^{q\,2} - \mathcal{R}^q = 0\,, \tag{1.22b}$$

which are to be met by adjusting Lagrange parameters λ^q and Λ^q accordingly. The second constraint (Eq. (1.22b)) makes the many-body state to remain a quasiparticle vacuum with even number parity whereas the first one (Eq. (1.22a)) fixes the average particle number to the actual number of particles. This is the minimum set of constraints. The minimization reads then

$$\delta\Big(\mathcal{E}[\rho,\kappa,\kappa^*] - \frac{1}{2}\sum_q \lambda^q(\mathrm{Tr}\{\rho^q\} + \mathrm{Tr}\{\rho^{q\,*}\}) - \sum_q \mathrm{Tr}\{\Lambda^q(\mathcal{R}^{q\,2} - \mathcal{R}^q)\}\Big) = 0\,. \tag{1.23}$$

The variation is expressed through a variation of the matrix elements of $\mathcal{R}^q$, which can be written as

$$\delta\mathcal{R}^q_{kl} = \begin{pmatrix} \delta\rho^q_{kl} & \delta\kappa^q_{kl} \\ -\delta\kappa^{q\,*}_{kl} & -\delta\rho^{q\,*}_{kl} \end{pmatrix} . \tag{1.24}$$

Introducing the generalized HFB matrix $\mathcal{H}^q$, in analogy to $\mathcal{R}^q$, as

$$\mathcal{H}^q \equiv \begin{pmatrix} h^q & \Delta^q \\ -\Delta^{q\,*} & -h^{q\,*} \end{pmatrix} , \tag{1.25}$$

the variation of the energy given by Eq. (1.12) can be rewritten as

$$\delta\mathcal{E} = \sum_{ijq} \mathcal{H}^q_{ij}\delta\mathcal{R}^q_{ji} = \mathrm{Tr}\{\mathcal{H}\delta\mathcal{R}\} . \tag{1.26}$$

Taking into account the variation of the constraints, the variational equation finally reads

$$\mathrm{Tr}\{\left(\mathcal{H}'^q - \mathcal{R}^q\Lambda^q - \Lambda^q\mathcal{R}^q + \Lambda^q\right)\delta\mathcal{R}^q\} = 0 , \tag{1.27}$$

where

$$\mathcal{H}'^q \equiv \begin{pmatrix} h^q - \lambda^q & \Delta^q \\ -\Delta^{q\,*} & -(h^{q\,*} - \lambda^q) \end{pmatrix} . \tag{1.28}$$

Eliminating the Lagrange parameters Λ^q yields to

$$0 = [\mathcal{H}'^q, \mathcal{R}^q] , \tag{1.29}$$

that is, the solution of the minimization problem is a basis which diagonalizes simultaneously $\mathcal{H}'^q$ and $\mathcal{R}^q$. Finally, Eq. (1.29) can be transformed into the HFB eigenvalue problem which, in the κ representation, takes the form

$$\begin{pmatrix} h^q - \lambda^q & \Delta^q \\ -\Delta^{q\,*} & -h^{q\,*} + \lambda^q \end{pmatrix} \begin{pmatrix} \mathcal{U}^{q\,[\kappa]} \\ \mathcal{V}^{q\,[\kappa]} \end{pmatrix}_\mu = E^q_\mu \begin{pmatrix} \mathcal{U}^{q\,[\kappa]} \\ \mathcal{V}^{q\,[\kappa]} \end{pmatrix}_\mu , \tag{1.30}$$

where $(\mathcal{U}^q_\mu, \mathcal{V}^q_\mu)$ are the upper and lower components of the quasiparticle eigenstate μ expanded in the single-particle basis of interest one starts from, whereas E^q_μ denotes the corresponding quasiparticle energy. Quasiparticle energies E^q_μ are the eigenvalues of the generalized HFB matrix $\mathcal{H}'^q$, and the associated (column) matrices $\mathcal{U}^q_\mu$ and $\mathcal{V}^q_\mu$ define the corresponding quasiparticle states. If the single-particle basis has a dimension M, the previous diagonalization leads to $2M$ eigenvalues/eigenvectors. These eigenstates are separated into two groups with opposite eigenvalues $\{E^q_\mu : (\mathcal{U}^q_\mu, \mathcal{V}^q_\mu)\}$ and $\{-E^q_\mu : (\mathcal{V}^{q\,*}_\mu, \mathcal{U}^{q\,*}_\mu)\}$. Usually one only selects quasiparticle with positive energies, while different conventions are possible. It can be shown that the system is bound if $\lambda^q < 0$, and that the quasiparticle spectrum (i) is continuous if the chemical potential λ^q is positive, and (ii) is partly continuous for $|E^q_\mu| > -\lambda^q$ and partly discrete for $|E^q_\mu| < -\lambda^q$ when $\lambda^q \leq 0$. Such properties are illustred in Fig. 1.2. The proper selection of only one half of the HFB wave functions allows to construct localized one-body and pairing densities, although some individual quasiparticle wave functions belong to the continuum [124]. When the Fermi level tends to zero, the quasiparticle spectrum becomes more continuous which indicates the presence of a strong coupling with the continuum induced by pairing correlations.

The normal density matrix and pairing tensor can be expressed in terms of the amplitudes of all quasiparticle states with positive energy E^q_μ as

$$\rho^q = \mathcal{V}^{q\,[\kappa]\,*}\,\mathcal{V}^{q\,[\kappa]\,\mathrm{T}} , \qquad \kappa^q = \mathcal{V}^{q\,[\kappa]\,*}\,\mathcal{U}^{q\,[\kappa]\,\mathrm{T}} = -\mathcal{U}^{q[\kappa]}\,\mathcal{V}^{q\,[\kappa]\,\dagger} . \tag{1.31}$$

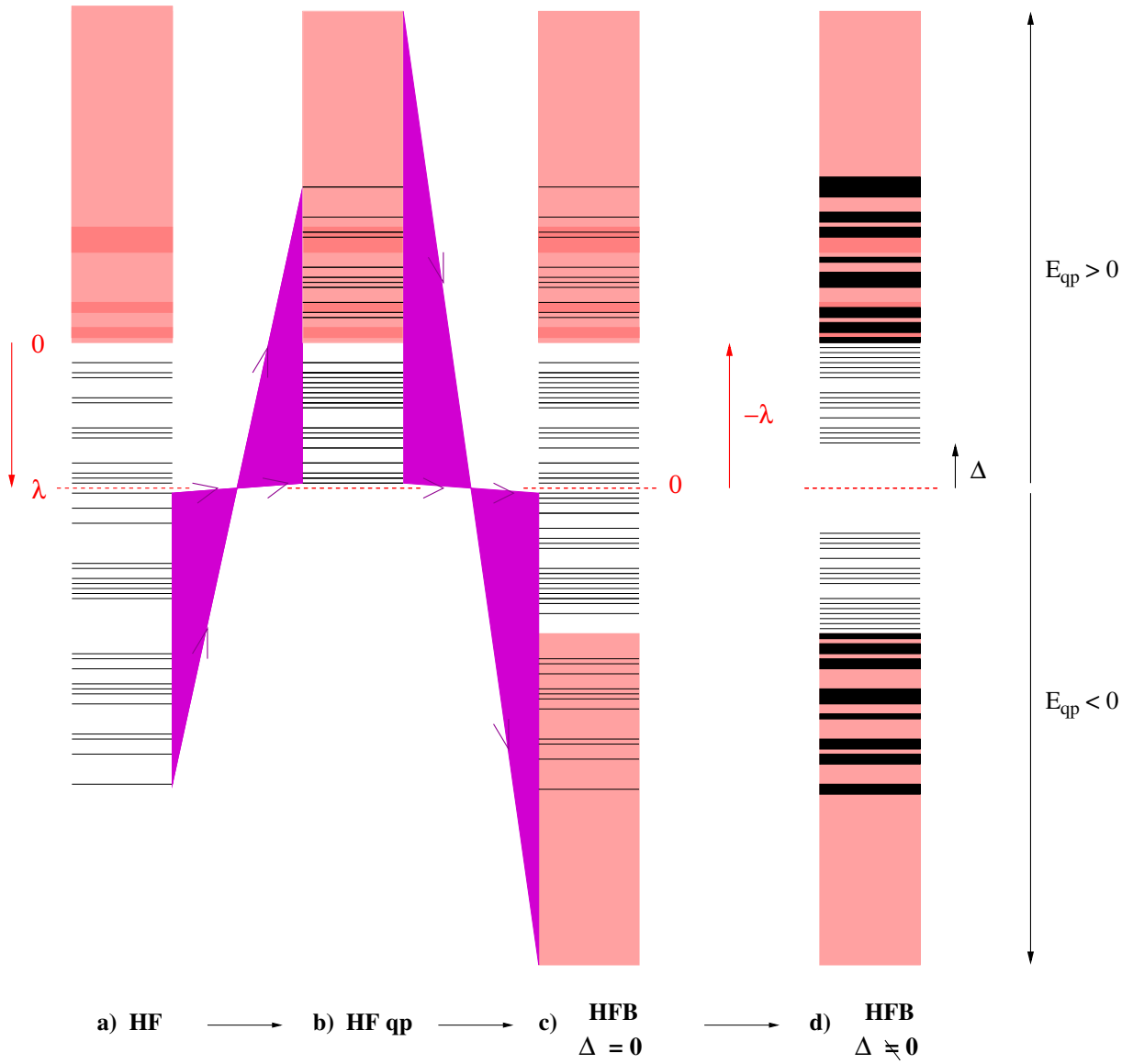

Figure 1.2: Construction of the HFB quasiparticle spectrum from the HF one:
a) Single-particle spectrum ϵ^q_μ: discrete bound states in black and energy continuum in red. Continuum resonances are represented with their width on top of the continuum background.
b) Corresponding positive quasiparticle spectrum, i.e. $E^q_\mu = |\epsilon^q_\mu - \lambda^q|$.
c) Corresponding quasiparticle spectrum in doubled basis, $\pm|\epsilon^q_\mu - \lambda^q|$
d) Corresponding quasiparticle spectrum in doubled basis including pairing correlations. Resonances coming from deeply-bound single-particle states have now a finite width because of their coupling to the energy continuum.

1.2.4 Coordinate space

Starting from the HFB equations in an arbitrary configuration basis (Eq. (1.30)), one can obtain their expression in coordinate⊗spin⊗isospin space

- for the κ representation as

$$\int \mathrm{d}\vec{r}\,' \sum_{\sigma'} \begin{pmatrix} h'^q(\vec{r}\,\sigma,\vec{r}\,'\,\sigma') & \Delta^q(\vec{r}\,\sigma,\vec{r}\,'\,\sigma') \\ -\Delta^{q*}(\vec{r}\,\sigma,\vec{r}\,'\,\sigma') & -h'^{q\,*}(\vec{r}\,\sigma,\vec{r}\,'\,\sigma') \end{pmatrix} \begin{bmatrix} \mathcal{U}_\mu^{q\,[\kappa]}(\vec{r}\,'\,\sigma'\,q) \\ \mathcal{V}_\mu^{q\,[\kappa]}(\vec{r}\,'\,\sigma'\,q) \end{bmatrix} = E_\mu^q \begin{bmatrix} \mathcal{U}_\mu^{q\,[\kappa]}(\vec{r}\,\sigma\,q) \\ \mathcal{V}_\mu^{q\,[\kappa]}(\vec{r}\,\sigma\,q) \end{bmatrix}, \tag{1.32}$$

where

$$h'^q(\vec{r}\,\sigma,\vec{r}\,'\,\sigma') \equiv h^q(\vec{r}\,\sigma,\vec{r}\,'\,\sigma') - \lambda^q\,\delta_{\sigma\sigma'}\,\delta(\vec{r}-\vec{r}\,')\,. \tag{1.33}$$

- for the $\tilde{\rho}$ representation as

$$\int \mathrm{d}\vec{r}\,' \sum_{\sigma'} \begin{pmatrix} h'^q(\vec{r}\,\sigma,\vec{r}\,'\,\sigma') & \tilde{h}^q(\vec{r}\,\sigma,\vec{r}\,'\,\sigma') \\ \tilde{h}^q(\vec{r}\,\sigma,\vec{r}\,'\,\sigma') & -h'^q(\vec{r}\,\sigma,\vec{r}\,'\,\sigma') \end{pmatrix} \begin{bmatrix} \mathcal{U}_\mu^{q\,[\tilde{\rho}]}(\vec{r}\,'\,\sigma'\,q) \\ \mathcal{V}_\mu^{q\,[\tilde{\rho}]}(\vec{r}\,'\,\sigma'\,q) \end{bmatrix} = E_\mu^q \begin{bmatrix} \mathcal{U}_\mu^{q\,[\tilde{\rho}]}(\vec{r}\,\sigma\,q) \\ \mathcal{V}_\mu^{q\,[\tilde{\rho}]}(\vec{r}\,\sigma\,q) \end{bmatrix}, \tag{1.34}$$

where the pair field $\tilde{h}^q$ is defined through

$$\tilde{h}_{ij}^q \equiv \frac{\delta\mathcal{E}}{\delta\tilde{\rho}_{ij}^{q\,*}}\,. \tag{1.35}$$

1.2.5 Bases of interest

The transformation matrix W^q from Eq. (1.18) may be decomposed into a set of three consecutive transformations using the Bloch-Messiah-Zumino theorem [125–127] as

$$W^{q\,\dagger} = \begin{pmatrix} C^{q\,\dagger} & 0 \\ 0 & C^{q\,\mathrm{T}} \end{pmatrix} \begin{pmatrix} \bar{\mathcal{U}}^{q\,\dagger} & \bar{\mathcal{V}}^{q\,\dagger} \\ \bar{\mathcal{V}}^{q\,\mathrm{T}} & \bar{\mathcal{U}}^{q\,\mathrm{T}} \end{pmatrix} \begin{pmatrix} D^{q\,\dagger} & 0 \\ 0 & D^{q\,\mathrm{T}} \end{pmatrix}, \tag{1.36}$$

where D^q and C^q are unitary, and $\bar{\mathcal{U}}^q$ and $\bar{\mathcal{V}}^q$, which define the special Bogolyubov transformation

$$\begin{pmatrix} \hat{\alpha}^q \\ \hat{\alpha}^{q\dagger} \end{pmatrix} = \begin{pmatrix} \bar{\mathcal{U}}^{q\,\dagger} & \bar{\mathcal{V}}^{q\,\dagger} \\ \bar{\mathcal{V}}^{q\,\mathrm{T}} & \bar{\mathcal{U}}^{q\,\mathrm{T}} \end{pmatrix} \begin{pmatrix} \hat{c}^q \\ \hat{c}^{q\dagger} \end{pmatrix} = \begin{pmatrix} \bar{\mathcal{U}}^{q\,\dagger} & \bar{\mathcal{V}}^{q\,\dagger} \\ \bar{\mathcal{V}}^{q\,\mathrm{T}} & \bar{\mathcal{U}}^{q\,\mathrm{T}} \end{pmatrix} \begin{pmatrix} D^{q\,\dagger} & 0 \\ 0 & D^{q\,\mathrm{T}} \end{pmatrix} \begin{pmatrix} \hat{a}^q \\ \hat{a}^{q\dagger} \end{pmatrix}, \tag{1.37}$$

are respectively diagonal and canonical (see Sec. 1.2.5.1). This transformation leads, from the so-called canonical basis $\{\hat{c}/\hat{c}^\dagger\}$, to a set of quasiparticle states $\{\hat{\alpha}/\hat{\alpha}^\dagger\}$ which diagonalizes the generalized density matrix $\mathcal{R}^q$ with eigenvalues of 1 (0) for occupied (unoccupied) quasiparticle states. In general, this basis will not yet diagonalize the HFB Hamiltonian $\mathcal{H}'^q$. The decomposition of the matrix W^q establishes several bases of interest that we now characterize.

1.2.5.1 Canonical basis

The unitary transformation D^q among single-particle states leads from the original basis $\{\hat{a}/\hat{a}^\dagger\}$ to the canonical basis $\{\hat{c}/\hat{c}^\dagger\}$ [122; 128]. The latter diagonalizes the one-body density matrix according to the transformation

$$\rho_{\nu\mu}^q = \left(D^q\rho^q D^{q\,\dagger}\right)_{\nu\mu} = \rho_{\mu\mu}^q\,\delta_{\nu\mu}\,, \tag{1.38}$$

and puts the pairing tensor in its canonical form $\kappa_{\mu\tilde{\nu}}^q = \kappa_{\mu\tilde{\mu}}^q\,\delta_{\nu\mu}$. The canonical basis is the name given to the *natural basis* in the context of HFB calculations. This basis has the important

property that all the states ϕ_μ constituting it are localized in coordinate space, although they are defined as linear combinations of original single-particle wave functions which might partly belong to a continuum [124]. That makes it an adequate representation for the HFB solutions and densities [129; 130]. If the canonical basis is ordered in such a way that pairs of conjugated states $(\mu, \tilde{\mu})$ come next to each other, the special Bogoliubov transformation matrices $(\bar{\mathcal{U}}^q, \bar{\mathcal{V}}^q)$ become 2×2 block diagonal, with blocks having the structure

$$\bar{\mathcal{U}}^{q\,[\kappa]} \equiv \begin{pmatrix} u^q_\mu & 0 \\ 0 & u^q_{\tilde{\mu}} \end{pmatrix} \quad = \quad u^q_\mu \begin{pmatrix} 1 & 0 \\ 0 & 1 \end{pmatrix}, \tag{1.39a}$$

$$\bar{\mathcal{V}}^{q\,[\kappa]} \equiv \begin{pmatrix} 0 & \eta_\mu\, v^q_\mu \\ \eta_{\tilde{\mu}}\, v^q_\mu & 0 \end{pmatrix} = \eta_\mu\, v^q_\mu \begin{pmatrix} 0 & 1 \\ -1 & 0 \end{pmatrix}, \tag{1.39b}$$

where u^q_μ and v^q_μ are real coefficients. Explicit expressions of (u^q_μ, v^q_μ) can be obtained by using the fact that the minimization principle amounts to canceling vacuum-to-two-quasiparticle diagrams (see Sec. 6.3)

$$\mathcal{H}^{q\,20} = \bar{\mathcal{U}}^{q\,[\kappa]\dagger}\,(h^q - \lambda^q)\,\bar{\mathcal{V}}^{q\,[\kappa]*} - \bar{\mathcal{V}}^{q\,[\kappa]\dagger}\,\left(h^{q\,\mathrm{T}} - \lambda^q\right)\bar{\mathcal{U}}^{q\,[\kappa]*} + \bar{\mathcal{U}}^{q\,[\kappa]\dagger}\,\Delta^q\,\bar{\mathcal{U}}^{q\,[\kappa]*} - \bar{\mathcal{V}}^{q\,[\kappa]\dagger}\,\Delta^{q\,*}\,\bar{\mathcal{V}}^{q\,[\kappa]*} = 0\,. \tag{1.40}$$

For a specific matrix element in the canonical basis, the previous identity leads to the well-known BCS-like expressions

$$\begin{bmatrix} u^{q\,2}_\mu \\ v^{q\,2}_\mu \end{bmatrix} = \frac{1}{2}\left(1 \pm \frac{h^q_{\mu\mu} - \lambda^q}{\sqrt{\left[h^q_{\mu\mu} - \lambda^q\right]^2 + \Delta^{q\,2}_{\mu\tilde{\mu}}}}\right), \tag{1.41}$$

which leaves the sign of v^q_μ undecided. Usually one takes $u^q > 0$, while the sign of v^q is fixed such that the pairing gap is positive for an attractive pairing interaction. As a result, the one-body density matrix and the pairing tensor read

$$\rho^q_{\mu\mu} = \quad \rho^q_{\tilde{\mu}\tilde{\mu}} = v^{q\,2}_\mu\,, \qquad\qquad \kappa^q_{\mu\tilde{\mu}} = -\kappa^q_{\tilde{\mu}\mu} = u^q_\mu\, v^q_\mu\,. \tag{1.42}$$

In the Russian representation, $\tilde{\rho}^q$ becomes diagonal in the canonical basis for time-reversal invariant systems, that is

$$\tilde{\rho}^q(\vec{r}, \vec{r}\,') = \sum_\mu \phi^\dagger_\mu(\vec{r}\,'\,q)\,\phi_\mu(\vec{r}\,q)\,u^q_\mu\,v^q_\mu\,, \tag{1.43}$$

where ϕ_μ denotes a canonical basis wave function. The amplitudes of the special Bogoliubov transformation written in the $\tilde{\rho}$ representation take the form

$$\bar{\mathcal{U}}^{q\,[\tilde{\rho}]} = u^q_\mu \begin{pmatrix} 1 & 0 \\ 0 & 1 \end{pmatrix}, \qquad\qquad \bar{\mathcal{V}}^{q\,[\tilde{\rho}]} = v^q_\mu \begin{pmatrix} 1 & 0 \\ 0 & 1 \end{pmatrix}. \tag{1.44}$$

Even though the HFB realization of the SR-EDF method is **not** an independent quasiparticle theory, it is convenient to use the canonical basis for analysis purposes as it provides the best approximate single-particle picture and allows one to define individual "energies" and "pairing gaps" through

$$e_i \equiv h_{ii}\,, \qquad\qquad \Delta_i \equiv |\Delta_{i\tilde{i}}|\,. \tag{1.45}$$

1.2.5.2 HFB quasiparticle basis

The unitary transformation C^q among quasiparticle states

$$\begin{pmatrix} \hat{\beta}^q \\ \hat{\beta}^{q\dagger} \end{pmatrix} = \begin{pmatrix} C^{q\,\dagger} & 0 \\ 0 & C^{q\,\mathrm{T}} \end{pmatrix} \begin{pmatrix} \hat{\alpha}^q \\ \hat{\alpha}^{q\dagger} \end{pmatrix} , \tag{1.46}$$

leads to a final set of quasiparticle states which solve the HFB equation $[\mathcal{R}^q, \mathcal{H}'^q] = 0$, and therefore diagonalise $\mathcal{R}^q$ and the HFB matrix $\mathcal{H}'^q$ at the same time. Equivalently as in the canonical basis, quasiparticle occupations can be defined as

$$N^q_\nu \equiv \sum_k \left|\mathcal{V}^q_{\nu k}\right|^2 . \tag{1.47}$$

However, those occupations are not eigenvalues of the density matrix ρ^q.

1.2.6 Bardeen-Cooper-Schrieffer approximation

The Bardeen-Cooper-Schrieffer (BCS) approximation corresponds to a particular Bogoliubov transformation where the unitary transformation C^q is trivial ($C^q = \mathbb{I}$), that is when the quasiparticle basis $\{\hat{\alpha}/\hat{\alpha}^\dagger\}$ already diagonalizes the generalized HFB matrix $\mathcal{H}'^q$. In this case, only matrix elements $\Delta^q_{\mu\tilde{\mu}}$ of the pairing field are non-zero in the basis $\{\hat{c}/\hat{c}^\dagger\}$. The HFB transformation takes then the form

$$\hat{\beta}^{q\,\dagger}_\mu = \sum_j \sum_k D^q_{jk} \bar{\mathcal{U}}^q_{k\mu}\, \hat{a}^{q\dagger}_j + D^{q\,*}_{jk}\, \bar{\mathcal{V}}^q_{k\mu}\, \hat{a}^q_j = \sum_j D^q_{j\mu}\, u^q_\mu\, \hat{a}^{q\dagger}_j + D^{q\,*}_{j\tilde{\mu}}\, v^q_{\tilde{\mu}}\, \hat{a}^q_j , \tag{1.48}$$

which allows to rewrite the BCS ground state as

$$|\Phi^{\mathrm{BCS}}\rangle = \prod_q \prod_{\mu>0} \left(u^q_\mu + v^q_{\tilde{\mu}}\, \hat{c}^{q\,\dagger}_\mu\, \hat{c}^{q\,\dagger}_{\tilde{\mu}}\right) |0\rangle = \prod_q \prod_{\mu>0} \left(u^q_\mu + v^q_\mu\, \hat{c}^{q\,\dagger}_\mu\, \hat{c}^{q\,\dagger}_{\bar{\mu}}\right) |0\rangle . \tag{1.49}$$

The BCS approximation amounts then to only considering pairing correlations between time-reversed states $\mu/\bar{\mu}$. One can observe that when C^q is non-trivial the full HFB state takes a similar expression in the canonical basis, i.e.

$$|\Phi^{\mathrm{HFB}}\rangle = \prod_q \prod_{\mu>0} \left(u^q_\mu + v^q_\mu\, \hat{c}^{q\,\dagger}_\mu\, \hat{c}^{q\,\dagger}_{\bar{\mu}}\right) |0\rangle , \tag{1.50}$$

but in this case the canonical basis is not assimilated to the HF one that contains continuum states.

Another definition for the BCS approximation consists of taking a local and constant pairing field in coordinate space [124], that is

$$\tilde{h}^{q\,\mathrm{BCS}}(\vec{r}\,\sigma, \vec{r}\,'\,\sigma') \equiv \tilde{h}^{q\,\mathrm{BCS}}\, \delta(\vec{r} - \vec{r}\,')\, \delta_{\sigma\sigma'} . \tag{1.51}$$

Quasiparticle wave functions become then, in the $\tilde{\rho}$ representation, proportional to canonical basis wave functions, i.e.

$$\mathcal{U}^{q\,[\tilde{\rho}]}_\mu(\vec{r}\,\sigma\, q) = u^q_\mu\, \phi_\mu(\vec{r}\,\sigma\, q) , \qquad \mathcal{V}^{q\,[\tilde{\rho}]}_\mu(\vec{r}\,\sigma\, q) = v^q_\mu\, \phi_\mu(\vec{r}\,\sigma\, q) . \tag{1.52}$$

As a consequence, canonical wave functions in the BCS approximation are localized for $e^q_\mu < 0$ and non-localized for $e^q_\mu > 0$, in opposition to the HFB formalism. BCS densities are thus in general non-localized and the nucleus is surrounded by an unphysical nucleon gas [124] caused by the coupling to the continuum due to the monopolar pairing interaction. This phenomenon is not important for nuclei in the valley of stability, where it can be numerically kept under control. However for exotic nuclei the BCS theory breaks down, as loosely bound nuclei are strongly coupled to the single-particle continuum.

1.2.7 Hartree-Fock realization

In the Hartree-Fock (HF) realization of the SR-EDF method, the reference state $|\Phi\rangle$ is a Slater determinant. This corresponds to eliminating all dependencies of the EDF on the anomalous density and thus the *explicit* treatment of pairing correlations. However, it is important to stress that, at least in principle, this does not mean that the effect of superfluidity could not be accounted for in such a realization of the EDF method. It would however certainly require to design very complex energy functionals $\mathcal{E}[\rho]$. Anomalous contractions of $\{\hat{a}\,\hat{a}/\hat{a}^\dagger\hat{a}^\dagger\}$ pairs, thus the pairing tensor, are therefore zero, and so is the pairing gap Δ^q. According to Eq. (1.41), occupations in the canonical basis become

$$\begin{bmatrix} u_\mu^{q\,2} \\ v_\mu^{q\,2} \end{bmatrix} = \begin{bmatrix} 0 \\ 1 \end{bmatrix} \qquad \epsilon_\mu^q < \lambda^q \tag{1.53a}$$

$$\begin{bmatrix} u_\mu^{q\,2} \\ v_\mu^{q\,2} \end{bmatrix} = \begin{bmatrix} 1 \\ 0 \end{bmatrix} \qquad \epsilon_\mu^q > \lambda^q\,, \tag{1.53b}$$

that is, the quasiparticle basis is defined as (i) $\hat{\beta}_\mu^q = \hat{a}_\mu^{q\,\dagger}$ for a hole state, and (ii) $\hat{\beta}_\mu^q = \hat{a}_\mu^q$ for a particle state. In addition, the HFB equations reduce to $[h'^q, \rho^q] = 0$. That is, there exists a set of single-particle states that solves the one-body equation

$$h^q\,\phi_i^q = \epsilon_i^q\,\phi_i^q\,, \tag{1.54}$$

but also diagonalizes the one-body density ρ^q. The HF, canonical and quasiparticle bases coincide. Note that there is a difference between the HF realization and the zero pairing limit of the HFB realization of the SR-EDF formalism, since the latter allows the existence of *at most* one $(j+1)$-degenerated set of single-particle states $\epsilon_{\mu_0}^q = \lambda^q$ such that [131]

$$u_{\mu_0}^{q\,2} = v_{\mu_0}^{q\,2} = \frac{1}{2j+1}\,. \tag{1.55}$$

1.2.8 Spontaneous symmetry breaking and single-particle basis

Spontaneous symmetry breaking lies at the core of the EDF formalism as it allows the inclusion, within a SR formalism, of crucial static collective correlations by optimizing the one-body fields self-consistently [132; 133]. That is, SR-EDF constitutes the optimal approximation of the dynamics of a system with a single auxiliary product state. MR-EDF calculations restore, in a second step, all symmetries that are spontaneously broken at the SR-EDF level. Spontaneous symmetry breaking can relate to time-reversal symmetry, symmetries associated with the shape of the nucleus or the particle number. For instance, a static closed-shell nucleus is well described in spherical symmetry, while open-shell nuclei spontaneously break rotational invariance, thus inducing a deformation of the single-particle field h. A nucleus whose ground state is spontaneously deformed at the SR-EDF level will present rotational collective excitations, which can be obtained through a MR configuration mixing. At the same time, quantum numbers of single-particle states φ_μ will reflect the symmetries that are either imposed or broken.

At the most general level for parity-conserving systems[4], single-particle states are characterized by $\mu \equiv [n, \pi, \zeta, q]$ where (i) n is the principal quantum number, (ii) $\pi = \pm 1$ is the parity,

[4] In the case of parity- and signature-breaking systems the definition of the conjugated states by the Bogoliubov transformation is less trivial. In most cases one assumes that at least the z-signature is conserved.

(iii) ζ is the z-signature, and (iv) $q = \pm\frac{1}{2}$ is the isospin projection. For time-reversal invariance, degenerated states $\mu/\tilde{\mu}$ have opposite signatures, and are defined by convention as

$$\mu \equiv [n, \pi, +1, q] \qquad \tilde{\mu} \equiv [n, \pi, -1, q]\,. \tag{1.56}$$

For nuclei restricted to an axial symmetry along the z axis, and for which parity is conserved, single-particle states are expressed as linear combinations of states with angular momentum ℓ of same parity. The z-signature relates in this case to the projection of the orbital momentum m_ℓ and spin σ on the z-axis according to

ζ_μ	m_ℓ	σ
$+1$	even	$+1/2$
$+1$	odd	$-1/2$
-1	even	$-1/2$
-1	odd	$+1/2$

and single-particle states can be labeled by $\mu \equiv [n, \pi, m, q]$, where $m = m_\ell + \sigma$ is the projection of the total angular momentum on the z axis.

For spherical symmetry, different phase conventions are possible to define single-particle states. The spinors are written here as

$$\langle\, \vec{r}\,|\, \mu\rangle = \varphi_\mu(\vec{r}\, q) = \frac{u_{n\ell j}(r\, q)}{r} \sum_{m_\ell \sigma} Y_\ell^{m_\ell}(\hat{r})\, \langle \ell\, m_\ell\, \frac{1}{2}\, \sigma | j\, m\rangle\, |\sigma\rangle \equiv \frac{u_{n\ell j}(rq)}{r}\, \Omega_{\ell j m}(\hat{r})\,, \tag{1.57}$$

where $\mu \equiv [n, \ell, j, m, q]$. The $\Omega_{j\ell m}(\hat{r})$ are spherical spinors that couple the angular part of the wave function to spinors associated with spin 1/2. The quantum numbers of a spinor are given by (i) the principal quantum number n, (ii) the total angular momentum j (iii) the projection of the angular momentum m along the z axis, (iv) the value of the orbital angular momentum ℓ, and (v) the isospin q. For a given j, only $\ell = j \pm \frac{1}{2}$ are possible values. The total spin quantum number s is a good quantum number but is the same $\left(s = \frac{1}{2}\right)$ for all nucleons. The spin projection is *not* a good quantum number since single-particle states mix $\sigma = \pm\frac{1}{2}$. For states defined by Eq. (1.57), parity and z-signature are given by $\pi_\mu = (-1)^\ell$ and $\zeta_\mu = -i^{2m+1} = (-1)^{m-\frac{1}{2}}$, respectively. In a time-independent calculation, a system that sustains a self-consistent spherical symmetry is necessarily time-reversal invariant. In these conditions, one finds $\tilde{\mu} \equiv [n, \ell, j, -m, q]$ and $\eta_\mu \equiv (-1)^{\ell-j-m} = (-1)^{\ell-j-\frac{1}{2}}\, \zeta_\mu$.

The quantum number ζ_μ is the one used to differentiate the two halves of the basis ($\zeta_\mu > 0$ and $\zeta_\mu < 0$). The real number η_μ is the phase connecting a state with its time-reversed partner of opposite signature when the system is time-reversal invariant. Here are typical values of η_μ and ζ_μ for a selection of spherical shells

$p_{3/2}$	$j = 3/2$	$\ell = 1$		$d_{3/2}$	$j = 3/2$	$\ell = 2$
m	ζ_μ	η_μ	—	m	ζ_μ	η_μ
$+3/2$	-	-		$+3/2$	-	+
$+1/2$	+	+		$+1/2$	+	-
$-1/2$	-	-		$-1/2$	-	+
$-3/2$	+	+		$-3/2$	+	-

which shows that η_μ has opposite signs for states belonging to the two different halves of the basis and that it is *never* equal to ζ_μ.

1.2.9 Constrained HFB calculations

In addition to constraints on proton and neutron numbers and the idempotence of $\mathcal{R}^q$ in the minimization process, additional constraints on the average value of an operator $\hat{Q}$ can be enforced at the level of Eq. (1.23), through the addition of an extra term $-\lambda_Q \langle\Phi|\hat{Q}|\Phi\rangle$ with an associated Lagrange multiplier λ_Q. The latter is fixed such that the expectation of $\hat{Q}$ in the state $|\Phi\rangle$ corresponds to a given value q. A minimum of SR-EDF corresponding to a non-zero value q_0 of $\langle\Phi|\hat{Q}|\Phi\rangle$ in an unconstrained calculation will be the signature of a spontaneously broken symmetry associated with the collective variable q. On the other hand, constrained calculations repeated for a range of values $q \neq q_0$ provide energy surfaces that probe the response of the N-body system with respect to the breaking of the broken symmetry in the direction of q.

The most common constraints relate to the geometrical shape of the many-body system [122], through the use of multipolar moments of the one-body density, e.g. by considering axial quadrupolar $\hat{Q}_{20}$ (associated with a deformation parameter β_2), octupolar $\hat{Q}_{30}$ (β_3) and hexadecapolar $\hat{Q}_{40}$ (β_4) operators, or the triaxial quadrupolar moment $\hat{Q}_{22}$... This is the starting point of calculations of fission properties of heavy elements [134; 135], or MR-EDF calculations of collective excitations, using technique such as the GCM or the five-dimension collective Bohr Hamiltonian [136]. Other constraints can be envisioned, such as on the radial moments $\langle\hat{r}^m\rangle$ of the one-body density for the calculation of breathing modes.

1.3 Existing empirical models

An accepted way to write the nuclear EDF $\mathcal{E}[\rho,\kappa,\kappa^*]$ is to make explicit its **minimal bilinear form** in ρ and κ, constrained by the fundamental symmetries of the problem, under the form

$$\mathcal{E}[\rho,\kappa,\kappa^*] \equiv \mathcal{E}_{\rm kin}[\rho] + \mathcal{E}_{\rm ph}[\rho,\kappa,\kappa^*] + \mathcal{E}_{\rm pp}[\rho,\kappa,\kappa^*] \quad , \tag{1.58a}$$

$$= \sum_{ij,q} t^q_{ij}\,\rho^q_{ji} + \frac{1}{2}\sum_{ijkl,qq'} \bar{v}^{\rho\rho}_{ikjl}\,\rho^q_{ji}\,\rho^{q'}_{lk} + \frac{1}{4}\sum_{ijkl,q} \bar{v}^{\kappa\kappa}_{ikjl}\,\kappa^{q\,*}_{ik}\,\kappa^q_{jl}\,, \tag{1.58b}$$

or equivalently

$$\mathcal{E}[\rho,\tilde{\rho},\tilde{\rho}^*] = \sum_{ij,q} t^q_{ij}\,\rho^q_{ji} + \frac{1}{2}\sum_{ijkl,qq'} \bar{v}^{\rho\rho}_{ikjl}\,\rho^q_{ji}\,\rho^{q'}_{lk} + \frac{1}{4}\sum_{ijkl,q} \bar{v}^{\tilde{\rho}\tilde{\rho}}_{ikjl}\,\tilde{\rho}^{q\,*}_{ik}\,\tilde{\rho}^q_{jl}\,, \tag{1.58c}$$

where t^q_{ij} denote the matrix elements of the one-body kinetic operator whereas $\bar{v}^{\rho\rho}$ and $\bar{v}^{\kappa\kappa/\tilde{\rho}\tilde{\rho}}$ are possibly antisymmetrized vertices and contain further dependencies on ρ and κ. The latter constitutes the main difference between the EDF method and a true Hamiltonian-based

mean-field theory. Another difference stems from the fact that $\bar{v}^{\rho\rho}$ and $\bar{v}^{\kappa\kappa/\tilde{\rho}\tilde{\rho}}$ are *a priori* different, and must not be seen as interactions in the real sense. Of course, they are in principle related to the underlying vacuum NN/NNN forces, but in the absence of an ab initio derivation (see Sec. 8.1), this link remains entirely implicit. Existing functionals are such that $\bar{v}^{\rho\rho}$ and $\bar{v}^{\kappa\kappa/\tilde{\rho}\tilde{\rho}}$ may only depend on the local scalar/isoscalar part of ρ. One may note that $\bar{v}^{\rho\rho}$ is not necessarily antisymmetrized. On the other hand, since the pairing tensor κ is skew symmetric, only the antisymmetric part of $\bar{v}^{\kappa\kappa}$ is probed. There is no coupling between nucleons of different isospin from $\bar{v}^{\kappa\kappa/\tilde{\rho}\tilde{\rho}}$, corresponding to the fact that pairing correlations are assumed here to be block-diagonal in q.

Starting from such an EDF, the particle-hole and particle-particle fields can be constructed through Eq. (1.58b) with the chosen independent set of variables for ρ^q and κ^q from Eq. (1.11), and read

$$\begin{aligned} h^q_{ij} =& t^q_{ij} + \frac{1}{2}\sum_{kl,q'}\left(\bar{v}^{\rho\rho}_{jlik} + \bar{v}^{\rho\rho}_{ljki}\right)\rho^{q'}_{kl} \\ &+ \frac{1}{2}\sum_{klmn,q'q''}\frac{\partial\bar{v}^{\rho\rho}_{nlmk}}{\partial\rho^q_{ij}}\rho^{q'}_{mn}\rho^{q''}_{kl} + \frac{1}{4}\sum_{klmn,q'}\frac{\partial\bar{v}^{\kappa\kappa}_{nlmk}}{\partial\rho^q_{ij}}\kappa^{q'\,*}_{mn}\kappa^{q'}_{kl}\,, \end{aligned} \tag{1.59a}$$

$$\Delta^q_{ij} = \frac{1}{2}\sum_{kl}\bar{v}^{\kappa\kappa}_{ijkl}\kappa^q_{kl} + \frac{1}{2}\sum_{klmn,q'q''}\frac{\partial\bar{v}^{\rho\rho}_{nlmk}}{\partial\kappa^{q\,*}_{ij}}\rho^{q'}_{mn}\rho^{q''}_{kl}\,. \tag{1.59b}$$

The so-called *particle-hole* and *particle-particle* channels interactions $v^{ph/pp}$ can then be defined through

$$h^q_{ij} \equiv \sum_{kl,q'}\bar{v}^{ph}_{ikjl}\rho^{q'}_{lk}\,, \tag{1.60a}$$

$$\Delta^q_{ij} \equiv \sum_{kl}\bar{v}^{pp}_{ikjl}\kappa^q_{lk}\,. \tag{1.60b}$$

Two remarks are to be made at this point. Firstly, having $v^{ph} = v^{\rho\rho}$ and $v^{pp} = v^{\kappa\kappa}$ is only possible in the very particular case where $v^{\rho\rho}$ and $v^{\kappa\kappa}$ are independent on ρ^q and κ^q. In general, the separation of the EDF into a particle-hole and a particle-particle part, as it is done in Eq. (1.58b), is a usual but misleading stretch of words, as it is only at the level of the fields that such a definition of channels can be done unambiguously. Both definitions will match if $v^{\rho\rho}$ only depends on ρ and $v^{\kappa\kappa}$ only depends on κ.

For non-relativistic EDF calculations, two families of energy functionals $\mathcal{E}$ will be considered, i.e. the Gogny and the Skyrme ones. Both of these models have a restricted number of free parameters, typically between 10 and 15, that are to be adjusted. They share an empirical nature, that is (i) their expressions are postulated and there is almost no connection with the underlying NN (+NNN...) forces, and (ii) free parameters are adjusted on a selected set of experimental data. This raises the question of their extrapolability towards the limits of stability as it will exemplified in the case of nuclear halos (see Part I). Thus, practitioners have to define a set of observables on which the free parameters of the nuclear EDFs are fitted. So far, most standard procedures consist of using a minimal set of observables containing [77]

- binding energies and charge radii of doubly-magic nuclei, e.g. ^{40,48}Ca, ^{56}Ni, ^{90}Zr, ^{100}Sn, ^{208}Pb...
- the equation of state of pure neutron matter,

- basic properties of symmetric nuclear matter: saturation density $\rho_{\rm sat}$ and energy per particle E/A, bulk compressibility K_∞, isoscalar effective mass $(m^*/m)_s$, Thomas-Reiche-Kuhn enhancement factor κ_v...

Skyrme or Gogny EDFs provide (i) similar good descriptions of bulk properties of nuclei with mass $A \gtrsim 40$, i.e. an overall reproduction of known experimental ground-state masses with a residual at the MeV level [137–140], and (ii) the possibility to make extrapolations for very exotic nuclei beyond the reach of state-of-the-art radioactive isotopes facilities. Obviously, when finer details of low-energy nuclear structure are taken into account, the specificities of the Skyrme and Gogny approaches become more explicit.

1.3.1 Skyrme energy density functionals

In the Skyrme-EDF model [141; 142], the energy density functional $\mathcal{E}$ is given as the sum of kinetic, Skyrme, pairing, Coulomb and center-of-mass correction terms, i.e.

$$\mathcal{E}[\rho,\kappa,\kappa^*] = \mathcal{E}_{\rm kin.}[\rho] + \mathcal{E}_{\rm Skyrme}[\rho] + \mathcal{E}_{\rm pair.}[\rho,\kappa,\kappa^*] + \mathcal{E}_{\rm Coul.}[\rho] + \mathcal{E}_{\rm c.o.m.}[\rho]\,. \tag{1.61}$$

Except for the center-of-mass correction, $\mathcal{E}$ is quasi-local and is expressed as the single integral in coordinate space of a local energy density. The latter is motivated by the short range of the (bare) nuclear interaction compared to the scale over which the density matrix varies. In an ab initio approach, yet to be implemented on a quantitative level, such a quasi-local EDF can be generated through the Density Matrix Expansion (DME) formalism [143–145]. Expressions for $\mathcal{E}_{\rm kin.}$, $\mathcal{E}_{\rm Coul.}$, and $\mathcal{E}_{\rm c.o.m.}$ can be found in the litterature [146; 147]. The Coulomb interaction is computed exactly for the direct term, while the exchange part is ususally treated at the Slater approximation [148].

1.3.1.1 Particle-hole functional

The Skyrme functional [77; 141; 149–152] approximates the "particle-hole" part $\mathcal{E}_{\rm ph}$ of the EDF in a coordinate space basis. The latter can be connected with the configuration space representation of Eq. (1.58a) by extracting the appropriate matrix elements $\bar{v}^{\rho\rho}_{ijkl}$ and $\bar{v}^{\kappa\kappa}_{ijkl}$ [153–155]. The Skyrme EDF resembles meta-GGA functionals in a DFT context as it uses explicit dependencies on several local densities and currents, including spin-orbit densities. This is crucial to treat properly finite nuclei. The functional is the most general bilinear combination of all local densities, built from the density matrix up to second order derivatives, in such a way that $\mathcal{E}$ remains invariant under the transformations associated with all symmetries of the nuclear Hamiltonian, i.e. parity, time-reversal, rotation, translation, gauge and isospin transformations [156]. The

Skyrme functional reads

$$
\begin{aligned}
\mathcal{E}_{\rm ph}[\rho] =& \mathcal{E}_{\rm Skyrme}[\rho] \\
=& \sum_q \int \mathrm{d}\vec{r}\, A^{\rho\rho}\, \rho^q\, \rho^q + A^{\rho\Delta\rho}\, \rho^q \Delta\rho^q + A^{\rho\tau} \left(\rho^q \tau^q - \vec{j}^{\,q} \cdot \vec{j}^{\,q}\right) \\
&+ A^{ss}\, \vec{s}^{\,q} \cdot \vec{s}^{\,q} + A^{s\Delta s}\, \vec{s}^{\,q} \cdot \Delta \vec{s}^{\,q} + A^{\rho\nabla J} \left(\rho^q \vec{\nabla} \cdot \vec{J}^{\,q} + \vec{j}^{\,q} \cdot \vec{\nabla} \times \vec{s}^{\,q}\right) \\
&+ A^{\nabla s \nabla s}\, (\nabla \cdot \vec{s}^{\,q})(\nabla \cdot \vec{s}^{\,q}) + A^{JJ} \Big(\sum_{\mu\nu} J^q_{\mu\nu} J^q_{q,\mu\nu} - \vec{s}^{\,q} q \cdot \vec{T}^{\,q} q \Big) \\
&+ A^{J\bar{J}} \Big[\Big(\sum_\mu J^q_{\mu\mu} \Big) \Big(\sum_\mu J^q_{\mu\mu} \Big) + \sum_{\mu\nu} J^q_{\mu\nu} J^q_{\nu\mu} - 2\, \vec{s}^{\,q} \cdot \vec{F}^{\,q} \Big] \\
&+ \sum_{q \neq q'} \int \mathrm{d}\vec{r}\, B^{\rho\rho}\, \rho^q \rho^{q'} + B^{\rho\Delta\rho}\, \rho^q \Delta \rho^{q'} + B^{\rho\tau} \left(\rho^q \tau^{q'} - \vec{j}^{\,q} \cdot \vec{j}^{\,q'}\right) \\
&+ B^{ss}\, \vec{s}^{\,q} \cdot \vec{s}^{\,q'} + B^{s\Delta s}\, \vec{s}^{\,q} \cdot \Delta \vec{s}^{\,q'} + B^{\rho\nabla J} \left(\rho^q \vec{\nabla} \cdot \vec{J}^{\,q'} + \vec{j}^{\,q} \cdot \vec{\nabla} \times \vec{s}^{\,q'}\right) \\
&+ B^{\nabla s \nabla s}\, (\nabla \cdot \vec{s}^{\,q})(\nabla \cdot \vec{s}^{\,q'}) + B^{JJ} \Big(\sum_{\mu\nu} J^q_{\mu\nu} J^{q'}_{\mu\nu} - \vec{s}^{\,q} \cdot \vec{T}^{\,q'} \Big) \\
&+ B^{J\bar{J}} \Big[\Big(\sum_\mu J^q_{\mu\mu} \Big) \Big(\sum_\mu J^{q'}_{\mu\mu} \Big) + \sum_{\mu\nu} J^q_{\mu\nu} J^{q'}_{\nu\mu} - 2\, \vec{s}^{\,q} \cdot \vec{F}^{\,q'} \Big] ,
\end{aligned}
\tag{1.62}
$$

where the coupling constants A^X/B^X refer to the interaction between particles with identical/different isospins, respectively. Scalar and vector density matrices for isospin q are defined as

$$
\rho_0(\vec{r},\vec{r}\,') = \sum_{\sigma q} \rho^{\sigma q}(\vec{r},\vec{r}\,') , \qquad = \sum_i \mathrm{Tr}_{\sigma\, q} \left[\varphi_i^\dagger(\vec{r}\,')\, \varphi_i(\vec{r}) \right] , \tag{1.63a}
$$

$$
\rho_1(\vec{r},\vec{r}\,') = \sum_{\sigma q} \rho^{\sigma q}(\vec{r},\vec{r}\,')\, (-1)^{1/2-q} , \qquad = \sum_i \mathrm{Tr}_{\sigma\, q} \left[\varphi_i^\dagger(\vec{r}\,')\, \tau_z\, \varphi_i(\vec{r}) \right] , \tag{1.63b}
$$

$$
\vec{s}_0(\vec{r},\vec{r}\,') = \sum_{\sigma q} \rho^{\sigma q}(\vec{r},\vec{r}\,')\, (-1)^{1/2-\sigma} , \qquad = \sum_i \mathrm{Tr}_{\sigma\, q} \left[\varphi_i^\dagger(\vec{r}\,')\, \vec{\sigma}\, \varphi_i(\vec{r}) \right] , \tag{1.63c}
$$

$$
\vec{s}_1(\vec{r},\vec{r}\,') = \sum_{\sigma q} \rho^{\sigma q}(\vec{r},\vec{r}\,')\, (-1)^{1/2-\sigma}\, (-1)^{1/2-q} \qquad = \sum_i \mathrm{Tr}_{\sigma\, q} \left[\varphi_i^\dagger(\vec{r}\,')\, \vec{\sigma}\, \tau_z \varphi_i(\vec{r}) \right] , \tag{1.63d}
$$

where vector and isovector densities correspond in fact to the z component of the associated vector in spin and isospin spaces, respectively. The non-local density can thus be decomposed into

$$
\rho(\vec{r},\vec{r}\,') = \frac{1}{4} \left[\rho_0(\vec{r},\vec{r}\,') + \rho_1(\vec{r},\vec{r}\,')\, \tau_z + \vec{s}_0(\vec{r},\vec{r}\,') \cdot \vec{\sigma} + \vec{s}_1(\vec{r},\vec{r}\,') \cdot \vec{\sigma}\, \tau_z \right] . \tag{1.64}
$$

Eqs. (1.63a-1.63d) are used to extract local densities and currents (the $*$ indicates time-odd densities)

$$
\rho^q(\vec{r}) \equiv \rho^q(\vec{r},\vec{r}\,')\big|_{\vec{r}=\vec{r}\,'} \qquad \text{one-body density} , \tag{1.65a}
$$

$$
\vec{s}^{\,q}(\vec{r}) \equiv \vec{s}^{\,q}(\vec{r},\vec{r}\,')\big|_{\vec{r}=\vec{r}\,'} \qquad \text{spin (pseudovector) density } (*) , \tag{1.65b}
$$

$$
\tau_q(\vec{r}) \equiv \vec{\nabla} \cdot \vec{\nabla}\,'\, \rho^q(\vec{r},\vec{r}\,')\big|_{\vec{r}=\vec{r}\,'} \qquad \text{kinetic density} , \tag{1.65c}
$$

$$
T^q_\mu(\vec{r}) \equiv \vec{\nabla} \cdot \vec{\nabla}\,'\, s^q_\mu(\vec{r},\vec{r}\,')\big|_{\vec{r}=\vec{r}\,'} \qquad \text{spin kinetic (pseudovector) density } (*) , \tag{1.65d}
$$

$$
\vec{j}^{\,q}(\vec{r}) \equiv -\frac{i}{2} (\vec{\nabla} - \vec{\nabla}\,')\, \rho^q(\vec{r},\vec{r}\,')\big|_{\vec{r}=\vec{r}\,'} \qquad \text{current (vector) density } (*) , \tag{1.65e}
$$

$$J^q_{\mu\nu}(\vec{r}) \equiv -\frac{i}{2}(\nabla_\mu - \nabla'_\mu)\, s^q_\nu(\vec{r},\vec{r}\,')\big|_{\vec{r}=\vec{r}\,'} \qquad \text{spin-current (pseudotensor) density } (*)\,, \tag{1.65f}$$

$$F^q_\mu(\vec{r}) \equiv \frac{1}{2}\sum_{\nu=x}^{z}\left(\nabla_\mu\nabla'_\nu + \nabla'_\mu\nabla_\nu\right) s^q_\nu(\vec{r},\vec{r}\,')\big|_{\vec{r}=\vec{r}\,'} \quad \text{tensor-kinetic (pseudovector) density}\,. \tag{1.65g}$$

From densities carrying a good isospin quantum number, isoscalar/isovector densities can be defined as

$$X_T(\vec{r}) \equiv X^n(\vec{r}) + (-1)^T X^p(\vec{r}) \qquad X \equiv \rho, \vec{s}\ldots \tag{1.66}$$

The coupling constants A^X/B^X may further depend on densities that do not involve spatial derivatives. In the present work, and because of the form of the functionals used so far, we will only consider that $A^{\rho\rho/ss}/B^{\rho\rho/ss}$ might depend on the scalar-isoscalar density $\rho_0(\vec{r})$. This derives from the usual approximation which consists of deriving $\mathcal{E}_{\rm ph}[\rho]$ from an initial *vertex* which contains zero-range terms plus finite-range corrections (gradient terms), and is a sum of central, spin-orbit and tensor terms, i.e.

$$v^{\rm Skyrme}(\vec{R},\vec{r}) = v^{\rm cent.}(\vec{R},\vec{r}) + v^{\rm LS}(\vec{R},\vec{r}) + v^{\rm tens.}(\vec{R},\vec{r}) \tag{1.67a}$$

$$\begin{aligned} v^{\rm cent}(\vec{R},\vec{r}) =& t_0\,(1+x_0\hat{P}_\sigma)\,\delta(\vec{r}) + \frac{1}{6}\,t_3\,(1+x_3\hat{P}_\sigma) \\ &+ \frac{1}{2}\,t_1\,(1+x_1\hat{P}_\sigma)\big[\hat{\vec{k}}'^2\,\delta(\vec{r}) + \delta(\vec{r})\,\hat{\vec{k}}^{\,2}\big] + t_2\,(1+x_2\hat{P}_\sigma)\,\hat{\vec{k}}'\cdot\delta(\vec{r})\,\hat{\vec{k}} \\ &+ \rho^\alpha(\vec{r})\,\delta(\vec{r}) \end{aligned} \tag{1.67b}$$

$$v^{\rm LS}(\vec{r}) = iW_0\,(\hat{\vec{\sigma}}_1 + \hat{\vec{\sigma}}_2)\cdot\hat{\vec{k}}'\times\delta(\vec{r})\,\hat{\vec{k}} \tag{1.67c}$$

$$\begin{aligned} v^{\rm tens.}(\vec{r}) =& \frac{1}{2}\,t_e\Big\{\big[3\,(\vec{\sigma}_1\cdot\vec{k}\,')\,(\vec{\sigma}_2\cdot\vec{k}\,') - (\vec{\sigma}_1\cdot\vec{\sigma}_2)\,\vec{k}'^2\,\big]\,\delta(\vec{r}) \\ &\qquad + \delta(\vec{r})\,\big[3\,(\vec{\sigma}_1\cdot\vec{k})\,(\vec{\sigma}_2\cdot\vec{k}) - (\vec{\sigma}_1\cdot\vec{\sigma}_2)\,\vec{k}^{\,2}\big]\Big\} \\ &+ t_o\Big[3\,(\vec{\sigma}_1\cdot\vec{k}\,')\,\delta(\vec{r})\,(\vec{\sigma}_2\cdot\vec{k}) - (\vec{\sigma}_1\cdot\vec{\sigma}_2)\,\vec{k}\,'\cdot\,\delta(\vec{r})\,\vec{k}\Big]\,, \end{aligned} \tag{1.67d}$$

that is $\mathcal{E}_{\rm ph}[\rho]$ is constructed from a zero-range phenomenological Skyrme vertex. In this context, the time-even and time-odd terms of the coupling constants of the Skyrme energy functional, which can in principle be decorrelated except for those that are constructed through local gauge invariance, are related through the underlying parameters of the Skyrme interaction [152].

In the HFB realization of the SR-EDF method local densities and currents can be expressed from single-particle wave functions of any arbitrary basis through

$$\rho^q(\vec{r}) = \sum_{ij}\varphi^\dagger_j(\vec{r}\,q)\,\varphi_i(\vec{r}\,q)\,\rho^q_{ij}\,, \tag{1.68a}$$

$$\tau^q(\vec{r}) = \sum_{ij}\left[\vec{\nabla}\varphi^\dagger_j(\vec{r}\,q)\right]\cdot\left[\vec{\nabla}\varphi_i(\vec{r}\,q)\right]\rho^q_{ij}\,, \tag{1.68b}$$

$$J^q_{\mu\nu}(\vec{r}) = -\frac{i}{2}\sum_{ij}\Big\{\varphi^\dagger_j(\vec{r}\,q)\,\sigma_\nu\left[\nabla_\mu\varphi_i(\vec{r}\,q)\right] - \left[\nabla_\mu\varphi^\dagger_j(\vec{r}\,q)\right]\sigma_\nu\,\varphi_i(\vec{r}\,q)\Big\}\,\rho^q_{ij}\,, \tag{1.68c}$$

$$s^q_\mu(\vec{r}) = \sum_{ij}\varphi^\dagger_j(\vec{r}\,q)\,\sigma_\mu\,\varphi_i(\vec{r}\,q)\,\rho^q_{ij}\,, \tag{1.68d}$$

$$T^q_\mu(\vec{r}) = \sum_{ij}\vec{\nabla}\varphi^\dagger_j(\vec{r}\,q)\,\sigma_\mu\cdot\vec{\nabla}\varphi_i(\vec{r}\,q)\,\rho^q_{ij}\,, \tag{1.68e}$$

	ρ_{sat} [fm^{-3}]	K_∞ [MeV]	$(m^*/m)_s$	κ_v	E/A [MeV]	Ref.
SLy4	0.160	229.9	0.70	0.25	−15.97	[147; 160]
SIII	0.145	355.4	0.76	0.53	−15.85	[161]
m^*1	0.162	230.0	1.00	0.25	−16.07	[162]
ρ^1_{sat}	0.145	230.0	0.70	0.25	−15.69	[162]
ρ^2_{sat}	0.160	230.0	0.70	0.25	−15.99	[162]
ρ^3_{sat}	0.175	230.0	0.70	0.25	−16.22	[162]
T6	0.161	235.6	1.00	0.00	−15.93	[163]
SKa	0.155	263.1	0.61	0.94	−15.99	[164]
T21-T26	0.161	230.0	0.70	0.25	−16.00	[158]

Table 1.2: Infinite matter properties of Skyrme functionals used in the present study: saturation density ρ_{sat}, bulk compressibility K_∞, isoscalar effective mass $(m^*/m)_s$, Thomas-Reiche-Kuhn enhancement factor κ_v and energy per particle at saturation E/A.

$$j^q_\mu(\vec{r}) = -\frac{i}{2}\sum_{ij}\left\{\varphi^\dagger_j(\vec{r}q)\left[\nabla_\mu\varphi_i(\vec{r}q)\right] - \left[\nabla_\mu\varphi^\dagger_j(\vec{r}q)\right]\varphi_i(\vec{r}q)\right\}\rho^q_{ij}\,, \tag{1.68f}$$

$$F^q_\mu(\vec{r}) = \frac{1}{2}\sum_{ij}\left\{\left[\vec{\nabla}\cdot\vec{\sigma}\varphi_j(\vec{r}q)\right]^\dagger\left[\nabla_\mu\varphi_i(\vec{r}q)\right] + \left[\nabla_\mu\varphi^\dagger_j(\vec{r}q)\right]\left[\vec{\nabla}\cdot\vec{\sigma}\varphi_i(\vec{r}q)\right]\right\}\rho^q_{ij}\,, \tag{1.68g}$$

1.3.1.2 Existing parametrizations

About 150 parametrizations of the Skyrme EDF have been defined so far and adjusted for various purposes (see Ref. [157] and references therein for the most common parametrizations). To study the effect of specific features of the particle-hole functional on nuclear structure, a set of Skyrme functionals characterized by different properties (infinite matter properties are defined in Sec. 7.4.6) will be considered, i.e. (i) SLy4 will stand as reference point, (ii) SIII displays a different density dependence ($\alpha = 1$) which leads to a too high infinite matter compressibility K_∞, (iii) T6 has an isoscalar effective nucleon mass $(m^*/m)_s = 1$, providing a denser single-particle spectrum, (iv) SKa has a different isoscalar effective mass, but also a different density dependence (density-dependent term with an exponent of 1/3 instead of 1/6), (v) the functional "m^*1" has been specifically adjusted for the present work with the same procedure as for SLy4 but with the constraint $(m^*/m)_s = 1$, (vi) the parameterizations "$\rho^{1/2/3}_{\text{sat}}$" have also been adjusted specifically, with different nuclear matter saturation densities ρ_{sat}, (vii) T21 to T26 incorporate tensor terms that differ by their neutron-neutron couplings [158]. The parameterizations "m^*1" and "$\rho^{1/2/3}_{\text{sat}}$" have been adjusted using the procedure of Ref. [158]. Infinite matter properties of all used parameterizations are summarized in Tab. {1.2}. The isovector effective mass (related to the Thomas-Reiche-Kuhn enhancement factor κ_v) is significantly different for these parameterizations but its effect on static properties of nuclei is rather small [159].

1.3.1.3 Particle-particle functional

Neutron-neutron and proton-proton pairing acts mostly in the spin singlet channel $S = 0$ of the nuclear interaction, as shown by the properties of the bare NN force [110]. At the same time, it occurs mainly in the s wave, that is a local pairing functional. This justifies the expression of

the "particle-particle" functional $\mathcal{E}_{\rm pp}$ as[5]

$$\mathcal{E}_{\rm pp}[\rho,\kappa,\kappa^*] = \int \mathrm{d}\vec{r}\, A^{\tilde{\rho}\tilde{\rho}} \sum_q |\tilde{\rho}^q|^2 \,, \tag{1.69}$$

where usually

$$A^{\tilde{\rho}\tilde{\rho}} \equiv \frac{\tilde{t}_0}{4}\left[1-\eta\left(\frac{\rho_0}{\rho_{\rm sat}}\right)^{\alpha}\right] . \tag{1.70}$$

The latter expression derives from a density-dependent delta interaction (DDDI) [165–169]

$$v^{\tilde{\rho}\tilde{\rho}}(\vec{r},\vec{R}\,) \equiv v^{\tilde{\rho}\tilde{\rho}}(\vec{R}\,)\,\delta(\vec{r}\,) \equiv \tilde{t}_0\left(\frac{1-P_\sigma}{2}\right)\left[1-\eta\left(\frac{\rho_0(\vec{R}\,)}{\rho_{\rm sat}}\right)^{\alpha}\right]\delta(\vec{r}\,) . \tag{1.71}$$

It is bilinear in the pair density $\tilde{\rho}^q$ whereas the strength $\tilde{t}_0$ is taken to be the same for neutron-neutron and proton-proton pairing. $\mathcal{E}_{\rm pp}[\rho,\tilde{\rho},\tilde{\rho}^*]$ enforces pairing correlations only in the $T=1$ channel, as proton-neutron pairing is usually neglected. The introduction of $T=0$ pairing requires a more involved formalism, since pairing correlations can now couple between superblocks of different signature in the HFB equations [170; 171].

Two parameters η and α control the spatial dependence of the coupling constant through the overall isoscalar density-dependent coupling. A zero value of η corresponds to a pairing strength that is uniform over the nuclear volume ("volume pairing") while $\eta=1$ corresponds to pairing strength which is stronger in the vicinity of the nuclear surface ("surface pairing"). A value $\eta=1/2$ corresponds to an intermediate situation ("mixed-type pairing"), as seen in Fig. 1.3. The parameter α is usually set to one. Values $\alpha<1$ correspond to stronger pairing correlations at low density. In the present work, we are interested in varying those empirical parameters over a large interval of values to quantify how much the characteristics of the pairing functional impact many-body systems. Note finally that the strength $\tilde{t}_0$ is usually chosen so that the neutron spectral gap $\langle\Delta^n_\kappa\rangle$, defined as

$$\langle\Delta^q_\kappa\rangle = \frac{\sum_{i>0}\Delta^q_{i\bar{i}}\,\kappa^q_{i\bar{i}}}{\sum_{i>0}\kappa^q_{i\bar{i}}} , \tag{1.72}$$

equals 1.250 MeV for ^{120}Sn [172], which provides reasonable gaps in Ca, Sn and Pb regions. Of course such an adjustment of $\tilde{t}_0$ depends on the Skyrme parametrization it is coupled to. Finally, the quasi-local expression for $\mathcal{E}_{\rm pp}[\rho,\tilde{\rho},\tilde{\rho}^*]$ induces divergences of the anomalous density $\tilde{\rho}$, which need to be properly handled and become critical for weakly bound systems, e.g. exotic nuclei. This will be the topic of Sec. 1.4.

1.3.1.4 Nuclear structure with Skyrme functionals

Since Skyrme EDFs are quasi-local, exchange terms in the fields h^q and $\Delta^q/\tilde{h}^q$ have the same structure as the direct ones, which reduces the number of integrations during a calculation and renders these functionals very well suited for calculations using a cartesian basis. Various methods have been used to perform calculations with Skyrme functionals, on cartesian/spherical meshes [77; 173–175], deformed harmonic oscillator (HO) or transformed HO bases [176–179].

[5] The Russian representation is used in the following, since it simplifies the HFB problem for time-reversal invariant systems (Sec. 1.2.5.1).

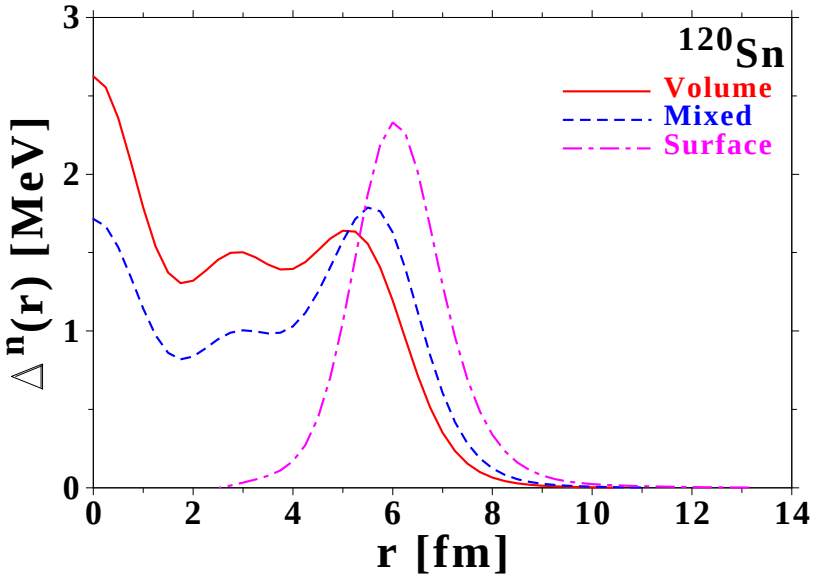

Figure 1.3: Neutron pairing field in ^{120}Sn obtained from the Skyrme SLy4 EDF and different pairing functionals.

In any case, 3D deformed calculations remain tedious, and can only be performed routinely on supercomputers. One ususally needs to discretize the energy continuum by putting the system in a finite box, and to include enough states in the calculations to have properly converged results. The latter is a demanding task as the disk space needed to store individual wave functions increases exponentially with the energy cut in the continuum.

One will focus here on spherical calculations, where the complexity of the equations to be solved can be reduced analytically, and numerical calculations can be safely performed with very large bases on standard computers [175]. In the following, spin/isospin indices are sometimes omitted for simplicity. Calculations are performed using a code [180] that takes advantage of the so called "two-bases method" to solve the HFB equations [181]. The basic idea is to build first the eigenbasis $\{\psi_{n\ell jq}\}$ of the one-body field h^q. Thanks to the spherical symmetry, this reduces to a one-dimensional Schrödinger equation of the form [124]

$$(h^q\,\psi)_{n\ell jq}\,(r) = \epsilon^q_{n\ell j}\,\psi_{n\ell jq}(r)\,. \tag{1.73}$$

In the second step of the calculation, one solves the Hartree-Fock-Bogoliubov problem of Eq. (1.30) in the basis $\{\psi_{n\ell jq}\}$, i.e. expanding the HFB spinors in a given (ℓ, j) block as

$$\begin{bmatrix} U^q_{n\ell j}(r) \\ V^q_{n\ell j}(r) \end{bmatrix} = \sum_k \begin{bmatrix} \tilde{U}^q_{kn\ell j}\,\psi_{n\ell jq}(r) \\ \tilde{V}^q_{kn\ell j}\,\psi_{n\ell jq}(r) \end{bmatrix}\,. \tag{1.74}$$

In spherical symmetry, the HFB equation are solved for each (ℓ, j) block separately. The two-bases method authorizes to perform calculations in very large boxes. It is at variance with an integration of the HFB equations in coordinate representation where the large difference of amplitudes between the upper and lower parts of the Bogoliubov spinors can make the solutions inaccurate at large distances [175]. The latter method has other advantages and shortcomings that will not be discussed here. The nucleus is put in a spherical box and all wave functions are computed up to a radial distance $R_{\rm box}$, with vanishing boundary conditions (Dirichlet) imposed.

The value of $R_{\rm box}$ has to be chosen to ensure convergence of the calculations, with typical values of about 40 fm when dealing with very diffuse (halo) nuclei. The differential equation (1.73) is solved on a discrete mesh of step size $h = 0.25$ fm using the Numerov algorithm [175; 182]. The calculation of matrix elements of one-body fields are not too time-consuming since h^q is by construction diagonal in the representation $\{\psi_{n\ell jq}\}$. Furthermore, a significant part of the pairing field matrix elements can be zero if the active space in which pairing acts around the Fermi energy (see Sec. 1.4) is narrow.

In Eq. (1.74) the upper bound of the sum over k is not specified. In an actual calculation, the sum is truncated by keeping states $\{\psi_{n\ell jq}\}$ up to a certain maximum energy $E_{\rm max}$. Its actual value ranges from several MeV up to hundreds of MeVs depending on the method used to regularize the quasi-local pairing functional. In addition to the energy cut, a truncation j^q_{cut} on the angular momentum of partial waves kept in the basis $\{\psi_{n\ell jq}\}$ is also implemented. In principle, all wave functions below $E_{\rm max}$ should be kept, but this makes the computation time rather long considering that wave functions with very high angular momenta will not contribute to the nuclear density. Nonetheless, a truncation on angular momenta cannot be too drastic, in particular when treating loosely bound nuclei. Checks of convergence of all observables of interest with respect to $R_{\rm box}$, $E_{\rm max}$ and $j^q_{\rm cut}$ are therefore mandatory.

1.3.2 Gogny energy density functional

The Gogny strategy consists of parametrizing $v^{\rho\rho}$ and $v^{\kappa\kappa}$ with the same phenomenological finite-range two-body interaction, and thus to work at the vertex level. This is at variance with the Skyrme phenomenology for which the meaninful mapping occurs at the functional level *after* a DME-like approximation. The initial expression of the usual Gogny finite-range local effective vertex reads [183–186]

$$v(\vec{r}_i) = \delta(\vec{r}_1 - \vec{r}_3)\delta(\vec{r}_2 - \vec{r}_4)\, v_{\rm D1X}(\vec{r}, \vec{R}, \overleftarrow{k}', \overrightarrow{k}), \tag{1.75}$$

where

$$v_{\rm D1X}(\vec{r}, \vec{R}) = \sum_{i=1}^{2} [W_i + B_i\, P_\sigma - H_i\, P_\tau - M_i\, P_\sigma\, P_\tau]\, e^{-\frac{r^2}{\mu_i^2}} \tag{1.76a}$$

$$+ t_0(1 + x_0 P_\sigma)\rho^\alpha(\vec{R})\delta(\vec{r}) \tag{1.76b}$$

$$+ i\, W_{LS}\, (\vec{\sigma}_1 + \vec{\sigma}_2)\, \overleftarrow{k}' \wedge \delta(\vec{r})\, \overrightarrow{k}\,, \tag{1.76c}$$

that is, the Gogny vertex consists of a finite-range central force plus zero-range spin-orbit and density-dependent terms. In the particle-particle channel, chosen parametrizations ($x_0 = 1$) make the zero-range density-dependent term vanish[6], whereas the remaining finite-range central term contains an implicit cutoff in momentum space which prevents the apparition of ultraviolet divergences (see Sec. 1.4.1). Recently, improved parametrizations have been proposed that

[6] The spin-orbit part of the vertex is usually omitted in the pairing channel, except in specific implementations [187].

	i	μ_i [fm]	W_i [MeV]	B_i [MeV]	H_i [MeV]	M_i [MeV]	W_{LS} [MeV.fm^5]
D1S	1	0.700	−1720.3	1300.0	−1813.6	1397.6	130.0
	2	1.200	103.63	−163.48	162.81	−223.92	
					x_0	α	t_0 [MeV.fm$^{3\alpha+3}$]
					1	1/3	1390.6
D1N	1	0.800	−2047.6	1700.0	−2414.9	1519.4	115.0
	2	1.200	293.01	−300.78	414.59	−316.84	
					x_0	α	t_0 [MeV.fm$^{3\alpha+3}$]
					1	1/3	1609.5
D2	1	0.800	−1176.440	800.000	−927.366	1115.573	130.0
	2	1.300	93.741	−162.161	122.414	−223.859	
	3	0.600	1800.000	600.000	400.000	−600.000	
						α	1/3

Table 1.3: Existing parametrizations for the Gogny forces.

contain finite-range density-dependent terms, leading to the D2 parametrization [188]. It reads

$$v_{\mathrm{D2}}(\vec{r},\vec{R}\,) = \sum_{i=1}^{2} \left[W_i + B_i\,P_\sigma - H_i\,P_\tau - M_i\,P_\sigma\,P_\tau\right] e^{-\frac{r^2}{\mu_i^2}} \tag{1.77a}$$

$$+ \left[W_3 + B_3\,P_\sigma - H_3\,P_\tau - M_3\,P_\sigma\,P_\tau\right] e^{-\frac{r^2}{\mu_3^2}} \left(\frac{\rho^\alpha(\vec{r}_1\,) + \rho^\alpha(\vec{r}_2\,)}{2}\right) \tag{1.77b}$$

$$+ i\,W_{LS}\,(\vec{\sigma}_1 + \vec{\sigma}_2)\,\overleftarrow{k}'\wedge\delta(\vec{r}\,)\,\overrightarrow{k}\,, \tag{1.77c}$$

where μ_3 is usually equal to the smallest range of the central terms (μ_1). This constitutes a first step towards a full finite-range effective force which will be primordial for the description of RPA/QRPA correlations [185].

The finite-range interaction can be converted into a non-local EDF. In comparison with Skyrme EDFs, the HFB problem with the non-local Gogny EDF involves complex integro-differential equations. This affects the single-particle structure of the many-body system and might play a role in long-range correlations responsible for nuclear deformation.

1.3.2.1 Existing parametrizations

The adjustement procedure of the empirical Gogny functional is similar to the one for Skyrme EDFs, as it makes use of a set of experimental data and ab initio calculations of nuclear matter. The free parameters $\{\mu_i, W_i, B_i, H_i, M_i, \alpha, W_{LS}\}$ are adjusted by a sequence of matrix inversions and functional interpolations [188]. Two major parametrizations called D1S and D1N are commonly used, that will be commonly referred to as D1X, and the corresponding values for the parameters are found in Tab. {1.3}. D1N consists of a recent re-parametrization of D1S where the neutron matter equation of state is used as a constraint [189]. A set of parameters for the force D2 including finite-range density dependencies can also be found in Tab. {1.3}.

1.3.2.2 Nuclear structure calculations with Gogny forces

The gaussian structure of the Gogny force makes it very well suited for calculations in an harmonic oscillator basis [186], while there have been some recent attempts to perform such calculations in coordinate space in a Woods-Saxon basis [190]. Indeed, most matrix elements are then analytical, or reduce to one-dimension integrals. Single-particle wave functions are expanded on HO solutions. For the general triaxial case, these basis states are characterized by their quantum numbers $\{n_x, n_y, n_z\}$ in each direction. Simpler versions of EDF codes have also been designed, in particular in axial symmetry where the degrees of freedom are quantum numbers along the z axis $n_{//}$ and perpendicular to it $n_\perp$ [191]. The basis size is characterized by the number of oscillator shells included in the calculations, typically between 8 and 20, and by a truncation scheme depending on the deformation of the basis.

One inconvenience of calculations in a HO basis is that single-particle states behave asymptotically as HO wave functions, i.e. $\sim \frac{e^{-\kappa^2 r^2}}{r}$, while the correct behavior for bound states is $\sim \frac{e^{-\kappa r}}{r}$ (see Eq. (3.24)). In particular, any quantitative study involving long-range properties of the single-particle wave functions is hazardous at best, as it will be the case for the study of halo systems. To illustrate this, Fig. 1.4 compares the neutron one-body densities in (semi-magical) ^{74}Cr obtained from spherical calculations with Skyrme and Gogny EDFs. By no means the density obtained by Skyrme EDF calculations corresponds to the result of a somewhat "exact" many-body result (in particular since no experimental data for neutron densities is available in this mass region). However it has the proper asymptotic behavior and thus serves as a reference point for a comparison with results obtained with the Gogny force. The overall agreement in the small-r region and the large discrepancies for large distances, where the inadequate asymptotic behavior of HO wave functions becomes apparent, are clearly seen, whatever the (already demanding) number of HO shells $N_{\hbar\omega}$ included in the calculations.

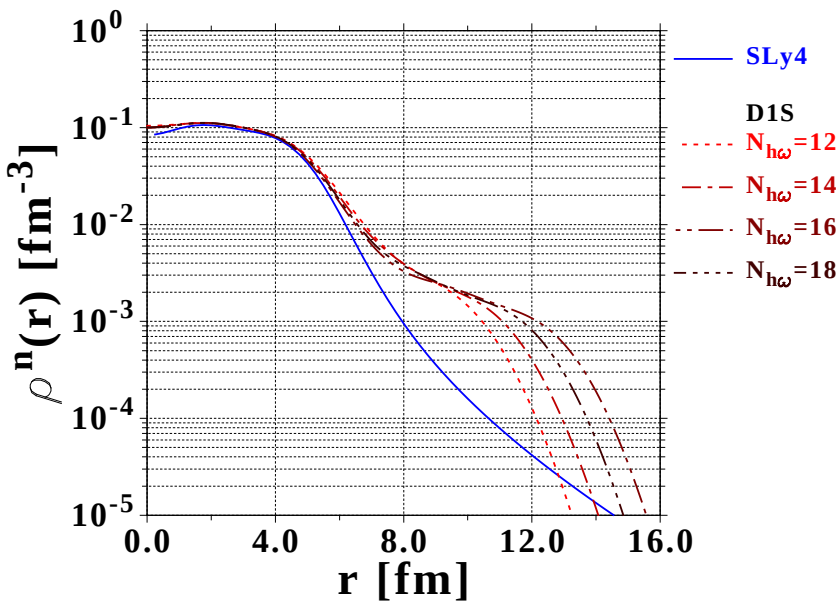

Figure 1.4: One-body neutron densities for ^{74}Cr computed with the Skyrme EDF SLy4 in a spherical cartesian basis and the Gogny EDF D1S in a spherical HO basis for various number of oscillator shells $N_{\hbar\omega}$.

1.3.3 Successes and limitations of existing empirical EDF models

As already stated, state-of-the-art empirical EDF models have been sucessfully used for a broad range of nuclear structure applications. Recently, the growth of available computational power has allowed large-scale projects, such as deformed calculations of ground-state properties over the nuclear chart. Systematic calculations of ground-state properties [140; 192; 193], as well as some collective excitations [194; 195], for all known and theoretically predicted nuclei, are now available. Mass residuals over about two thousand known nuclei obtained at the SR-EDF level are of the order of one MeV, that is an accuracy which is good enough for a direct comparison with experimental data [137–139]. Such calculations provide a reasonably good description of static properties beyond the ground-state energy, e.g. shell structure, pairing gaps, charge radii, individual excitations or deformation. Likewise, MR-EDF calculations [196; 197] have already met a lot of success, in particular for the description of dynamical correlation energies, vibrational/rotational excitations and superdeformed bands or shape transitions [136; 198–206]. Among other challenging areas of interest, extensive studies have for instance been dedicated to (i) (asymmetric) fission properties of heavy elements [134; 135], (ii) the formation of superheavy nuclei [207; 208], (iii) the application of dynamical approaches based on the time-dependent HF/HFB formalism to describe nuclear fission/fusion [209–211], or (iv) collective motions through the self-consistent (quasiparticle) random phase approximation ((Q)RPA) [195; 212–214]...

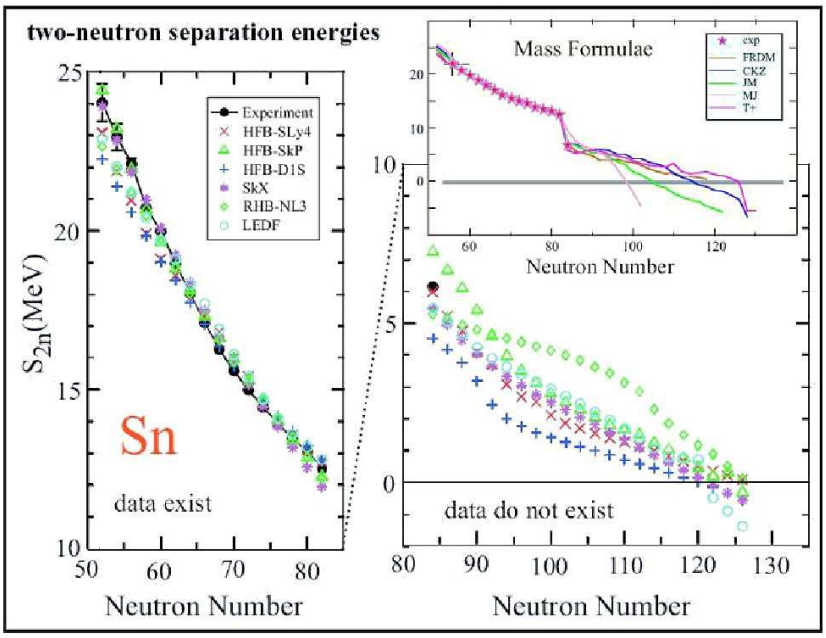

Figure 1.5: Illustration of the asymptotic freedom of phenomenological EDF models in the case of two-neutron separation energies. In the major shell where empirical EDFs are adjusted on experimental data, the agreement between all relativistic and non-relativistic calculations is clearly seen. In the next major shell where no data exist, discrepancies between these models become more apparent (from J. Dobaczewski *et al.* [215]).

However, many challenges are still ahead in order to (i) further increase the overall precision of EDF-based methods, e.g. decrease mass residuals, (ii) describe excited states with spectroscopic accuracy (of the order of 300 keVs), as it is achieved for *sd*-shell nuclei using the Shell Model [216–218], and (iii) improve the predictive power of used EDFs in the unknown region of

the nuclear chart. Indeed, while all empirical models constrained by experimental data agree with each other within the major shell they are adjusted in, extrapolations towards the nucleon drip-line do not agree with each other. This divergence in the next major shell ("asymptotic freedom") is seen for most standard observables such as the two-nucleon separation energy or the pairing gap and is exemplified on Fig. 1.5. Two complementary approaches are currently undertaken towards this improvement, and will benefit from each other as they unfold.

Firstly, improving the existing phenomenology via focusing [219; 220] on (a) the amelioration of existing empirical models, i.e. the enrichment of the functional itself through trial and error, (b) a better understanding of adjustement procedures, in particular through a better use of existing data in fits (fission barriers, superdeformed states, single-particle energies), and the development of improved fitting algorithms and post-analysis methods, and (c) numerical improvements for the resolution of HFB equations, in particular when no symmetry is a priori assumed for the systems, e.g. full three-dimensional calculations. Theoretical efforts along those lines have been dedicated in the past years to (i) understanding the flaws of the empirical anzätze used for the EDF that may lead to spin [221] or finite-size instabilities [159; 222], (ii) adjusting Skyrme EDFs within a functional framework, that is liberating the unnecessary constraints between couplings originating from the derivation of $\mathcal{E}_{\text{Skyrme}}$ from v^{Skyrme} [223], (iii) characterizing the results of the adjustment procedure in terms of theoretical error bars, minimal set of observables to eliminate under-constrained systems, error correlation analysis [224]... or (iv) studying in details the impact of so far overlooked contributions such as tensor terms [158; 225; 226]...

Second, microscopic constraints associated with the derivation of the SR-EDF from vacuum interactions are being envisioned. For instance, the construction of Skyrme-like functionals directly from χ-EFT will provide a missing link and explicit non-trivial density dependencies of the coupling constants arising from long-range pion exchange physics. The aim of the present work is precisely to make progress along those lines with the practical difference that the extra step necessary to produce a quasi-local Skyrme-like functional is avoided by working with a non-local EDF based on the construction of a non-empirical Gogny-like effective vertex (see Chap. 8).

On a longer term, a better understanding of the connection between EDF and DFT methods is required. Indeed, "raw" DFT (i) cannot be applied to self-bound systems, thus, an extension of the Hohenberg-Kohn theorem is needed [227–229], (ii) does not give a coherent framework for the description of both ground- and excited-states properties, (iii) does not provide a meaningful interpretation of single-particle properties, e.g. single-nucleon energies or occupations. Also, and as already discussed, the EDF method is a two-step procedure, i.e. the SR-EDF implementation which exploits broken symmetries, and the MR-EDF which restores them. Such an approach does not fit with existing Hohenberg-Kohn-like theorems. On the practical side, the use of naive empirical EDF models gives birth to spurious effects. For instance, the particle-hole effective vertex extracted from typical empirical functionals is rarely fully antisymmetric (e.g. fractional density-dependencies). This leads to a series of difficulties in single-reference (self-interaction and self-pairing) and multi-reference (poles and spurious steps) EDF calculations [200; 230; 231]. Some of these issues have been identified and practical cures have been proposed [153–155]. However further developments are required in order to develop a fully satisfactory theory.

1.4 Pairing correlations for zero-range EDFs

A concrete use of EDF-based methods to quantitatively characterize an exotic phenomenon, i.e. the formation of nuclear halos, is discussed in details in Part I, where both successes and

limitations of empirical functionals are exemplified. For this study however, the treatment of pairing correlations through the use of quasi-local functionals need to be commented on, and is the topic of the present section, which constitutes an original and published work [43].

1.4.1 UV divergences for contact pairing functionals

For Skyrme EDF calculations, the use of a quasi-local pairing functional (Eq. (1.69)) causes the apparition of an ultraviolet divergence corresponding to the equiprobable scattering of nucleon pairs at very high energy/small relative distance [232; 233]. Indeed, the pair density matrix for isospin q reads from Eq. (1.31) as

$$\tilde{\rho}^q(\vec{r}_1\,\sigma_1,\vec{r}_2\,\sigma_2) \equiv -\sum_{E_i>0} \mathcal{V}_i^{[\tilde{\rho}]}(\vec{r}_1\,\sigma_1\,q)\,\mathcal{U}_i^{[\tilde{\rho}]^*}(\vec{r}_1\,\sigma_2\,q)\,, \tag{1.78}$$

where $(\mathcal{U}_i^{[\tilde{\rho}]},\,\mathcal{V}_i^{[\tilde{\rho}]})$ are solutions of Eq. (1.34) in the Russian representation with energy $E_i>0$. When a local functional is used in the particle-particle channel, nucleon pairs can scatter up to infinite excitation energy with constant amplitude. This corresponds to an ultraviolet divergence of the non-local pairing density which can be characterized in uniform nuclear matter where quasiparticle states take the form

$$\begin{pmatrix} \mathcal{U}_{\vec{k}}^{[\tilde{\rho}]}(\vec{r}\,q) \\ \mathcal{V}_{\vec{k}}^{[\tilde{\rho}]}(\vec{r}\,q) \end{pmatrix} = \begin{pmatrix} u_k^q \\ -v_k^q \end{pmatrix} e^{i\,\vec{k}\cdot\vec{r}}\,, \tag{1.79}$$

and are characterized by the momentum $\vec{k}$. The BCS-like coefficients u_k^q and v_k^q satisfy

$$\begin{pmatrix} u_k^{q\,2} \\ v_k^{q\,2} \end{pmatrix} = \frac{1}{2}\left[1 \pm \frac{\epsilon_k^q - \lambda^q}{\sqrt{(\epsilon_k^q-\lambda^q)^2+\Delta_k^{q\,2}}}\right]\,, \tag{1.80}$$

where single-particle energies are typically approximated by

$$\epsilon_k^q = \frac{\hbar^2\,k^2}{2\,m_q^*}\,. \tag{1.81}$$

In the case of the Skyrme local (momentum-independent) pairing functional, the gap equation restricted to $^1\mathrm{S}_0$ pairing correlations can be recast into (see Sec. 7.5)

$$1 = -A^{\tilde{\rho}\tilde{\rho}} \int \frac{k'^2\,\mathrm{d}k'}{(2\pi)^2}\,\frac{1}{\sqrt{\left(\epsilon_k^q-\mu^q\right)^2+\Delta^{q\,2}(k_F^q)}}\,. \tag{1.82}$$

Indeed, the pairing gap is in this case independent of the wave vector $\vec{k}$. This leads to a pair density matrix $\tilde{\rho}$ in the spin singlet channel of the form

$$\tilde{\rho}^q(\vec{r}_1,\vec{r}_2\,) = \int \frac{\mathrm{d}\vec{k}}{(2\pi)^3}\,\frac{\Delta^q}{2}\,\frac{e^{i\,\vec{k}\cdot(\vec{r}_1-\vec{r}_2)}}{\sqrt{(\epsilon_k^q-\lambda^q)^2+\Delta^{q\,2}}} = \frac{\Delta^q}{(2\pi)^2}\int \frac{k^2\,\mathrm{d}k}{\sqrt{(\epsilon_k^q-\lambda^q)^2+\Delta^{q\,2}}}\,\frac{\sin(k\,r)}{k\,r}\,. \tag{1.83}$$

The remaining integral over k can be split into two parts. Considering an arbitrary large momentum Λ such that

$$k^2\,u_k^q\,v_k^q \underset{k>\Lambda}{\sim} \frac{\Delta^q\,m_q^*}{\hbar^2}\,, \tag{1.84}$$

one can write

$$\tilde{\rho}^q(\vec{r}_1,\vec{r}_2\,) = \frac{\Delta^q}{(2\pi)^2}\int_0^{\Lambda}\frac{k^2\,\mathrm{d}k}{\sqrt{(\epsilon_k^q-\lambda^q)^2+\Delta^{q\,2}}}\,\frac{\sin(k\,r)}{k\,r} + \frac{\Delta\,m_q^*}{4\pi^2\,\hbar^2}\int_{\Lambda}^{+\infty}\mathrm{d}k\,\frac{\sin(k\,r)}{k\,r}$$
$$\equiv \mathcal{A}(r,\Lambda)+\mathcal{B}(r,\Lambda)\,. \tag{1.85}$$

The inner integral $\mathcal{A}(r,\Lambda)$ remains finite when $r\to 0$, whereas one finds

$$\mathcal{B}(r,\Lambda)\underset{r\to 0}{\longrightarrow}\frac{\Delta^q\,m_q^*}{4\,\pi\,\hbar^2}\,\frac{1}{|\vec{r}_1-\vec{r}_2|}\,, \tag{1.86}$$

that is [234]

$$\tilde{\rho}^q(\vec{r}_1,\vec{r}_2\,)\equiv\sum_{\sigma}\tilde{\rho}^q(\vec{r}_1\,\sigma,\vec{r}_2\,\sigma)\underset{r\to 0}{\sim}\frac{\Delta^q(\vec{R}\,)\,m_q^*(\vec{R}\,)}{4\pi\,\hbar^2}\,\frac{1}{r}\,. \tag{1.87}$$

As a result, the local part of the pairing density $\tilde{\rho}^q(\vec{r}\,)\equiv\tilde{\rho}^q(\vec{r},\vec{r}\,)$ cannot be defined. Thus a local pairing functional leads to a diverging anomalous local density when high-energy pair scattering is taken into account. A calculation similar to the one presented above shows that the normal one-body density matrix $\rho^q(\vec{r}_1,\vec{r}_2)$ is well defined in the limit $r\to 0$, whereas $\tau^q(\vec{r}_1,\vec{r}_2)$ diverges in the same way as $\tilde{\rho}^q(\vec{r}_1,\vec{r}_2)$.

1.4.2 Regularization scheme

To compensate for the ultraviolet divergence of the pairing density, a common procedure consists of *regularizing* all integrals through the use of a high-energy energy cutoff [124], for example on quasiparticle energies $E_i < E_{\mathrm{cut}}$ at the level of Eq. (1.78). Pairing functionals using such a regularization scheme are referred to as "REG" in the following. In particular REG-S, REG-M and REG-V will denote regularized surface-, mixed- and volume-type pairing functionals, respectively. If the parameter η differs from 0, 1/2 and 1, or if α differs from 1 the functional will be noted REG-X. Using such a method, the pairing strength $\tilde{t}_0^{\mathrm{reg}}$ depends on E_{cut} and is adjusted for each cutoff, eventually taken large enough for observables to be insensitive to its precise value. A widely used value is $E_{\mathrm{cut}}=60$ MeV [124; 172; 235].

As the density dependence of the pairing functional is made more surface-peaked, the strength $|\tilde{t}_0^{\mathrm{reg}}|$ increases for a fixed value of E_{cut}, as is exemplified in Fig. 1.6 for the functional REG-X. This is a consequence of the fitting procedure that uses a single nucleus to adjust the overall strength. Indeed, if the pairing strength is peaked at the nuclear surface, individual gaps decrease, especially for well-bound orbitals residing in the nuclear interior. To compensate for this effect and maintain the same value of the average gap $\langle\Delta_\kappa^n\rangle$, the overall pairing strength has to be increased.

1.4.3 Vacuum and in-medium renormalization schemes

Another possibility is to renormalize the pairing density and the pairing field through the substraction of a physical quantity that diverges in the same way. In this case, the cutoff energy E_{cut} is taken equal to the basis cutoff E_{max} for consistency. One example, hereafter referred to as *vacuum renormalization*, consists of using the vacuum scattering length a_0 in the ${}^1S_0$ channel [236–238] that fulfills

$$-\frac{m\,\tilde{t}_0}{4\,\pi\,\hbar^2\,a_0}+1=-\tilde{t}_0\int_0^{k_c^q}\mathrm{d}k\,\frac{k^2}{2\pi^2}\,\frac{1}{\hbar^2\,k^2/m}\,, \tag{1.88}$$

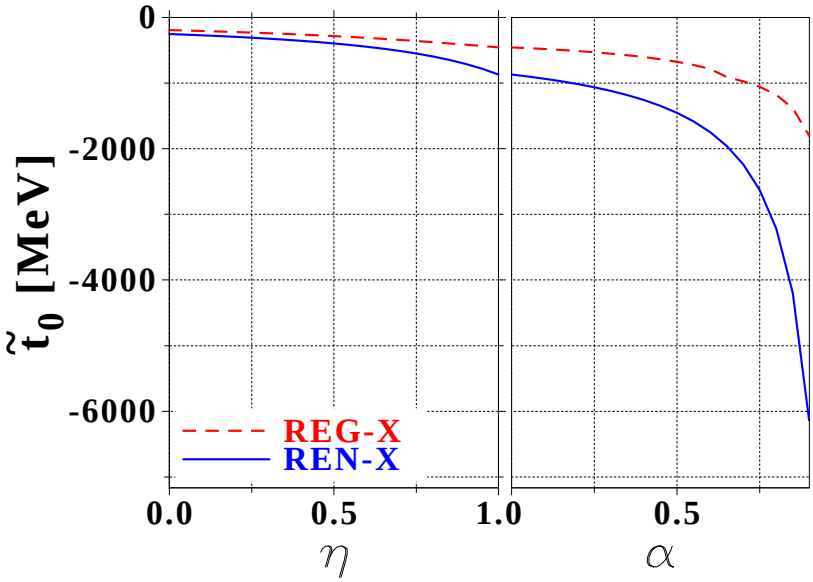

Figure 1.6: Pairing strength $\tilde{t}_0$ as a function of η and α for regularized REG-X and in-medium renormalized REN-X pairing functionals.

where k_c^q is defined through

$$E_{\rm cut} \equiv \frac{\hbar^2\, k_c^{q\,2}}{2\,m}. \tag{1.89}$$

It is clear that the scattering length displays the same ultraviolet divergence as the local pairing gap if the boundary of the integral is taken to infinity. Posing $\tilde{t}_0^{\rm ref} \equiv 4\pi\,\hbar^2\,a_0/m$ and subtracting Eq. (1.88) from the gap equation (Eq. (1.82)) to obtain

$$\tilde{t}_0 \int_0^{k_c^q} {\rm d}k\, \frac{k^2}{4\pi^2}\, \frac{1}{\sqrt{(\epsilon_k^q - \lambda^q)^2 + \Delta^{q\,2}}} = -1\,, \tag{1.90}$$

one sees that the coupling $\tilde{t}_0^{\rm vac}$ which replaces $\tilde{t}_0$ in the expression of $A^{\tilde{\rho}\tilde{\rho}}$ to define the *renormalized* gap equation, which is now well behaved as $E_{\rm cut}$ increases, is given by

$$\frac{1}{\tilde{t}_0^{\rm vac}(\rho^q, E_{\rm cut})} \equiv \frac{1}{\tilde{t}_0^{\rm ref}} - \frac{m}{4\pi\,\hbar^2}\,\frac{2\,k_c^q}{\pi}\,. \tag{1.91}$$

Such a vacuum renormalization scheme has been put forward in different contexts [236–238]. It was found that, although the prescription does remove the unwanted divergence, its convergence as a function of $E_{\rm cut}$ is very slow. Note finally that, while conserving the mathematical ingredients of the method, one is not forced to set a_0 to its physical value and one can use $\tilde{t}_0^{\rm ref}$ as a free parameter to be adjusted on experimental data. Taking such an empirical point of view to construct the pairing functional to be used in connection with finite nuclei is along the line of what has been mostly done so far.

To accelerate the convergence, the renormalization scheme can evolve with the density of the system. This will be referred to as the in-medium renormalization scheme. We follow here the procedure introduced in Refs. [232–234; 239–241]. To do so, one first rewrites the spin singlet

part of the non-local pair density matrix as

$$\tilde{\rho}^q(\vec{r}_1,\vec{r}_2) = -\sum_{0<E_i\leq E_{\rm cut},\sigma} \mathcal{V}_i^{[\tilde{\rho}]}(\vec{r}_1\sigma q)\,\mathcal{U}_i^{[\tilde{\rho}]\,*}(\vec{r}_2\sigma q) \tag{1.92a}$$

$$-\frac{1}{2}\,\Delta^q(\vec{R}\,)\sum_{\epsilon_i^q-\lambda^q\leq E_{\rm cut},\sigma}\frac{\phi_i(\vec{r}_1\sigma q)\,\phi_i^*(\vec{r}_2\sigma q)}{\epsilon_i^q-\lambda^q} \tag{1.92b}$$

$$+\sum_{E_i>E_{\rm cut},\sigma}\left[-\mathcal{V}_i^{[\tilde{\rho}]}(\vec{r}_1\sigma q)\,\mathcal{U}_i^{[\tilde{\rho}]\,*}(\vec{r}_2\sigma q)-\frac{1}{2}\,\Delta^q(\vec{R}\,)\,\frac{\phi_i(\vec{r}_1\sigma q)\,\phi_i^*(\vec{r}_2\sigma q)}{\epsilon_i^q-\lambda^q}\right] \tag{1.92c}$$

$$+\frac{1}{2}\,\Delta^q(\vec{R}\,)\sum_{\epsilon_i^q,\sigma}\frac{\phi_i(\vec{r}_1\sigma q)\,\phi_i^*(\vec{r}_2\sigma q)}{\epsilon_i^q-\lambda^q}\,. \tag{1.92d}$$

For large values of $E_{\rm cut}$ the two terms in Eq. (1.92c) cancel each other. Calculating the two terms from Eqs. (1.92b,1.92d) in the Thomas-Fermi approximation [233], throwing away the diverging part of Eq. (1.92d) in the limit $r\to 0$, one obtains the renormalized local pair density under the form

$$\tilde{\rho}^q_{\rm ren}(\vec{R}\,)\equiv\tilde{\rho}^q_{\rm reg}(\vec{R}\,)-\frac{\Delta^q(\vec{R}\,)\,m_q^*(\vec{R}\,)\,k_c^q(\vec{R}\,)}{2\pi^2\,\hbar^2}\left[1-\frac{k_F^q(\vec{R}\,)}{2\,k_c^q(\vec{R}\,)}\,\ln\left(\frac{k_c^q(\vec{R}\,)+k_F^q(\vec{R}\,)}{k_c^q(\vec{R}\,)-k_F^q(\vec{R}\,)}\right)\right] \tag{1.93}$$

where $\tilde{\rho}^q_{\rm reg}(\vec{r}\,)$, $k_F^q(\vec{r}\,)$ and $k_c^q(\vec{r}\,)$ are defined by

$$\tilde{\rho}^q_{\rm reg}(\vec{r}\,)\equiv-\sum_{E_i\leq E_{\rm cut},\sigma}V_i(\vec{r}\sigma q)\,U_i^*(\vec{r}\sigma q)\,, \tag{1.94a}$$

$$\lambda^q\equiv\frac{\hbar^2\,{k_F^q}^2(\vec{r}\,)}{2\,m_q^*}+U_q(\vec{r}\,)\,, \tag{1.94b}$$

$$E_{\rm cut}\equiv\frac{\hbar^2\,k_c^{q2}(\vec{r}\,)}{2\,m_q^*}+U_q(\vec{r}\,)\,, \tag{1.94c}$$

$U_q(\vec{r}\,)$ being the (central) potential field of the normal self-energy for a particle of isospin q. The use of the renormalized density $\tilde{\rho}^q_{\rm ren}(\vec{r}\,)$ in the calculation of the pairing field can be recast into the use of the regularized one $\tilde{\rho}^q_{\rm reg}(\vec{r}\,)$ together with a position/density-dependent renormalized coupling constant [233]

$$\frac{1}{\tilde{t}_0^{\rm med}(\rho^q,E_{\rm cut})}\equiv\frac{1}{\tilde{t}_0^{\rm ref}}-\frac{m_q^*}{4\pi\,\hbar^2}\,\frac{2\,k_c^q}{\pi}\left[1-\frac{k_F^q}{2\,k_c^q}\,\ln\left(\frac{k_c^q+k_F^q}{k_c^q-k_F^q}\right)\right]\,. \tag{1.95}$$

The in-medium renormalization converges much faster than the vacuum one thanks to the action of the second term in the bracket in Eq. (1.95). Whereas values of $E_{\rm cut}$ of the order of a few tens of MeVs are necessary to reach convergence using in-medium renormalization, $E_{\rm cut}$ of the order of several GeVs are necessary to do so when using the vacuum renormalization scheme [234]. Pairing functionals combined with the in-medium renormalization scheme will be referred to as "REN" in the following. In particular REN-S, REN-M and REN-V will denote renormalized surface-, mixed- and volume-type functionals, respectively.

In the following, a new analysis of the consequences of using empirical local pairing functionals for EDF calculations with the REG and REG procedures is carried on. In particular, an emphasis on spurious effects appearing for weakly bound nuclei is done and connected to the more general notion of BCS-BEC phase transition.

1.4.4 Gap in symmetric nuclear matter

As said above, using a local pairing functional the regularized/renormalized gap is a solution of Eq. (1.82) where the original density-dependent coupling $A^{\tilde{\rho}\tilde{\rho}}$ has been replaced by the regularized/renormalized one $A_x^{\tilde{\rho}\tilde{\rho}}(\rho^q, E_{\rm cut})$, where $x =$ "reg", "vac" or "med". The chemical potential λ^q entering the gap equation is adjusted self-consistently for a given density through

$$\rho^q = \frac{\rho_0}{2} = \int \frac{\mathrm{d}\vec{k}}{(2\pi)^3}\, v_k^{q2}\,, \tag{1.96}$$

where ρ_0 is the demanded (isoscalar) density of infinite nuclear matter (Eqs. (7.56a,7.56b)). The gap equation can be solved for different values of the parameters (η, α) entering the pairing functional, using both the regularization and in-medium renormalization schemes. Corresponding results are presented in Figs. (1.7a,1.7b). In all cases (i) single-particle energies are taken as free kinetic energies $\epsilon_k^q = \hbar^2 k^2/2m$, which implies that $U_q = 0$ and $m_q^* = m$ in all formulæ of Sec. 1.4.3, (ii) we use a cutoff of $E_{\rm cut} = 60/200$ MeV for regularized/renormalized functionals, and (iii) the reference pairing strength is systematically adjusted using the standard procedure defined in Sec. 1.3.1.3. Results are compared with those obtained from a microscopic nucleon-nucleon interaction [242] that provides identical pairing gaps to AV18 [3] in the $^1S_0$ channel when free kinetic energies are used in the gap equation.

For both regularization and in-medium renormalization schemes, the gap profile as a function of the Fermi momentum k_F^q is significantly modified as the values of (η, α) are varied. In both cases, a pairing strength peaked at the nuclear surface translates into stronger pairing correlations at low k_F^q. For a given set (η, α), the amplitude of the gap in the REG-X and REN-X cases is almost the same, but their shapes differ, as REN-X gaps are more asymmetric. REN-X gaps are suppressed at very low densities for all values of (η, α), whereas REG-X ones become larger and larger as the functional becomes more intense at low density. One may notice that they become systematically larger than microscopic gaps in the low-k region for $\alpha \ll 1$. Such a feature of REG-X gaps leads to unphysical behaviors, as is explained in the next section.

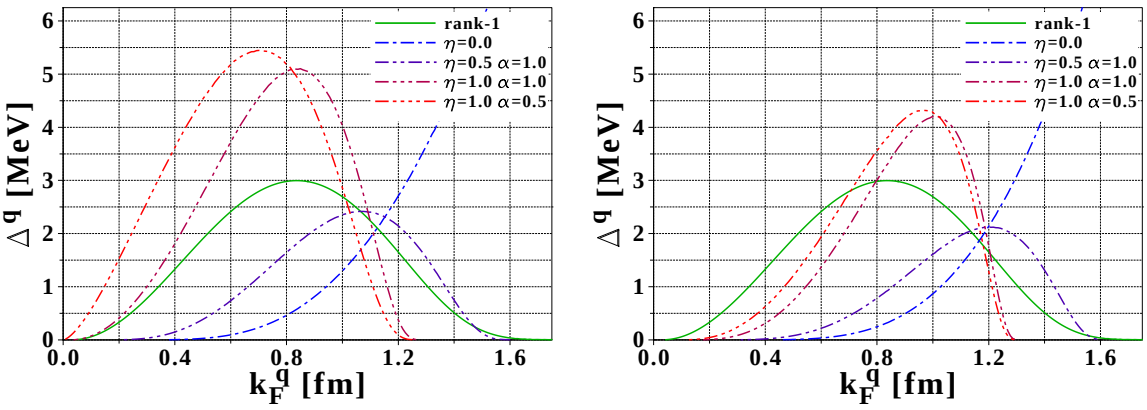

(a) Standard regularization scheme

(b) In-medium renormalization scheme

Figure 1.7: Pairing gap in symmetric nuclear matter obtained using free kinetic energies and plotted as a function of the Fermi momentum $k_F = k_F^q$. Results are compared with those obtained in the $^1S_0$ channel using a (rank-1 separable) microscopic nucleon-nucleon interaction [242].

1.4.5 Low-density behaviors and BCS-BEC crossover

For extreme surface pairing functionals ($\eta = 1$, $\alpha \ll 1$), the self-consistent procedure to solve the gap equation converges at small densities k_F^q for negative values of the chemical potential λ^q when regularized REG-X functionals are used. This indicates the presence of a bound di-nucleon state in the $^1\mathrm{S}_0$ channel, which is unphysical as it is known that the nuclear interaction cannot bind a di-neutron/di-proton in the $T = 1/S = 0$ channel. To illustrate this point, Results obtained for the diagram $\mu^q = f(k_F^q \xi^q)$ usually used to represent Bardeen-Cooper-Schrieffer/Bose-Einstein-Condensate (BCS/BEC) crossovers in superconducting systems [238; 243] is presented in Fig. 1.8. In this expression, the coherence length ξ^q is evaluated through [244]

$$\xi^q = \theta^q \frac{\hbar^2}{2\, m_q^*} \frac{k_F^q}{\Delta^q}\,, \tag{1.97}$$

where θ is a free parameter close to one, which varies with the interaction used, and sets the phase transition point at $k_F^q\, \xi^q = 1$. The scaled chemical potential μ^q is defined as [245]

$$\mu^q \equiv \frac{\lambda^q}{\epsilon_F^q} \qquad \text{when } \lambda^q > 0\,, \tag{1.98a}$$

$$\mu^q \equiv \frac{2\lambda^q}{\epsilon_0} \qquad \text{when } \lambda^q < 0\,, \tag{1.98b}$$

$\epsilon_F^q \equiv \hbar^2\, {k_F^q}^2/(2\, m_q^*)$ being the Fermi energy, and ϵ_0 the binding energy of the di-nucleon state in the vacuum. Note that how much μ^q differs from 1 indicates to which extent the chemical potential must be calculated from the number conservation condition Eq. (1.96), and not equated to the non-interacting Fermi energy ϵ_F^q. Such a situation occurs typically when one leaves the weak-coupling BCS regime to enter the BCS/BEC crossover as discussed below. The binding energy ϵ_0 of the di-nucleon state in the vacuum is the lowest eigenvalue of the Schrödinger equation for the relative motion in the $^1S_0$ channel, to which the BCS gap equation reduces at zero density [246]. In the present case, it reads

$$\frac{\hbar^2\, k^2}{m}\, \Psi_k^q + \int \frac{\mathrm{d}p\, p^2}{2\pi^2}\, v_x^{\tilde{\rho}\tilde{\rho}}\, \Psi_p^q = \epsilon_0\, \Psi_k^q\,. \tag{1.99}$$

In Eq. (1.99), the di-nucleon wave function Ψ_k in the vacuum corresponds to the zero-density limit of the Cooper pair wave function $u_k^q\, v_k^q$.

The different regimes of interest, as obtained from a finite-range interaction, are usually defined as [245] (i) BCS phase for $k_F^q\, \xi^q > 2\pi$, (ii) BEC phase for $k_F^q\, \xi^q < \pi^{-1}$, and (iii) BCS/BEC crossover region in-between. In the present case, the fact that a density-dependent coupling is active in the gap equation, but not in the computation of the di-nucleon binding energy in the vacuum, modifies the scaling of $\mu^q < 0$ as a function of $k_F^q\, \xi^q$ and will make the crossover diagrams given below look different from what is shown in Ref. [245]. In particular, the actual BEC regime ($\mu^q \approx -1$) is reached at values of $k_F^q\, \xi^q$ much lower than π^{-1}. The crossover diagram is displayed in Fig. 1.8 for several REG-X pairing functionals and compared to the one obtained with the low-momentum NN interaction [242]. The penetration into the BCS/BEC crossover regime with the latter NN force is not as pronounced as it should be because the neutron-neutron scattering length it generates is equal to $a_{nn}^{^1\mathrm{S}_0} = -14.9$ fm, which is slightly larger than the experimental one $a_{nn}^{^1\mathrm{S}_0} = -18.7 \pm 0.6$ fm [247]. For standard surface REG-X pairing functionals ($\eta = 1$, $\alpha = 1$), the nuclear matter barely enters the BCS/BEC crossover region and results are close to those obtained with the microscopic interaction. It is important to understand the behavior of the curves in Figs. (1.8,1.9). As k_F^q decreases, the coherence length ξ^q first decreases.

If the interaction sustains a bound state in the vacuum, ξ^q continues to decrease and the curve proceeds to the bottom left of the plot. If the interaction is not attractive enough to generate a bound state, ξ^q increases again faster than k_F^q decreases and the curve displays a turning point before overlapping itself in the upper right corner of the plot. As a matter of fact, the BEC transition is completed at low densities for extreme-surface REG-X functionals corresponding to $\alpha \leq 0.85$ which indeed sustain an unphysical bound di-nucleon state in the vacuum. On the contrary, no such behavior is observed using renormalized REN-X pairing functionals. In particular, the chemical potential always remains positive, even for extreme surface pairing functionals, as seen in Fig. 1.9.

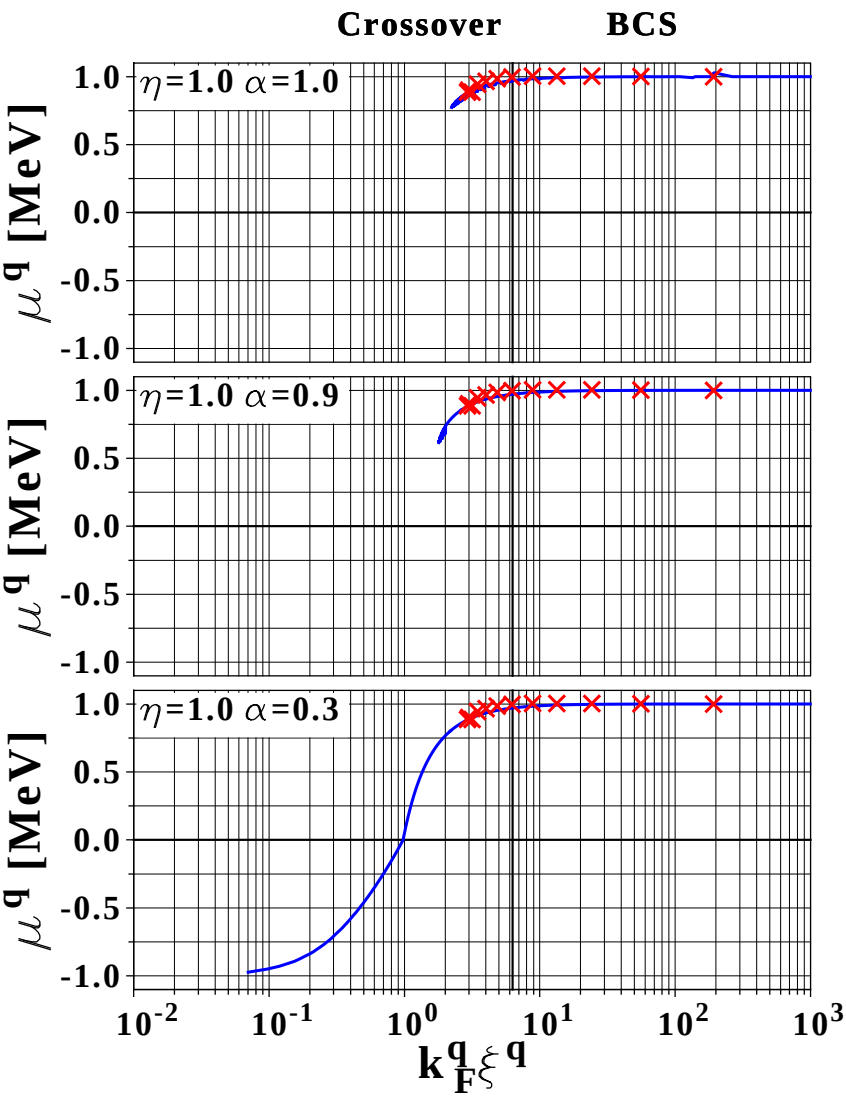

Figure 1.8: BCS-BEC Crossover diagram in infinite nuclear matter for three different surface-type regularized REG-X pairing functionals. The value $k_F^q\,\xi^q = 2\pi$ separating the BCS and BCS/BEC crossover phases is represented by a vertical line. The red crosses provide results obtained using the $^1S_0$ part of a realistic low-momentum interaction [242].

A comparison of both treatments of the ultraviolet divergence allows one to understand how the standard regularization scheme authorizes a spurious BCS/BEC phase transition whereas

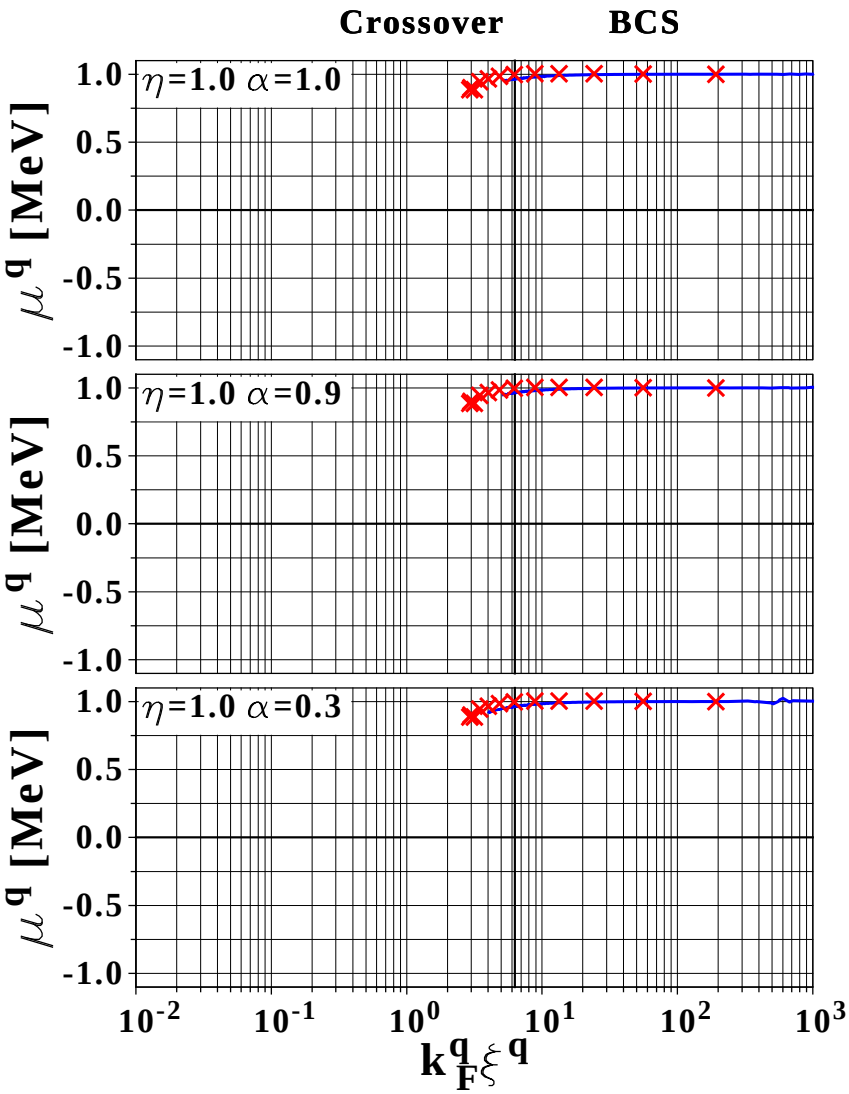

Figure 1.9: Same as in Fig. 1.8 with renormalized REN-X pairing functionals.

the in-medium renormalization does not. On the one hand, the density dependence of the local pairing functional makes it possible to generate a BCS-BEC crossover through a variation of the density of the system, which is not possible for a density-independent contact vertex [248]. On the other hand, the vacuum and in-medium renormalization procedures generate a counter-term (see Eqs. (1.91,1.95)) which prevents this from happening. Given that the overall strength is fixed once and for all on an unique system which does not probe low density behaviors (^{120}Sn), the counter term reduces significantly the effective coupling strength $\tilde{t}_0^{\rm vac/med}$ as compared to $\tilde{t}_o^{\rm reg}$, especially for large $E_{\rm cut}$ and small k_F^q, even though $\tilde{t}_0^{\rm ref}$ is larger for the renormalized functional than for the regularized one (see Fig. 1.6). Care is required when comparing those values as cutoffs are different for the regularization ($E_{\rm cut}$ = 60 MeV) and renormalization ($E_{\rm cut}$ = 200 MeV) schemes. Such a reduction of the effective coupling strength is sufficient to prevent the di-nucleon to be bound in the vacuum when using the in-medium renormalization scheme.

To characterize more precisely the occurrence of such a spurious transition for REG-X functionals, BCS and crossover regions are represented in Figs. (1.10a,1.10b) as a function of the parameters (η, α) on one axis and of the particle density on the other. We separate the

BCS/BEC crossover region into two subparts associated with a positive (BCS crossover) and a negative (BEC crossover) chemical potential, respectively. For REG-X functionals, a region where $\lambda^q < 0$ appears for $(\eta = 1, \alpha < 1)$. The region for which the chemical potential is negative relates to small densities but, as α decreases, its extension grows up to the point where such a spurious pattern may affect finite nuclei, as is discussed in the next section. Such a region is not found when the in-medium renormalization scheme is employed.

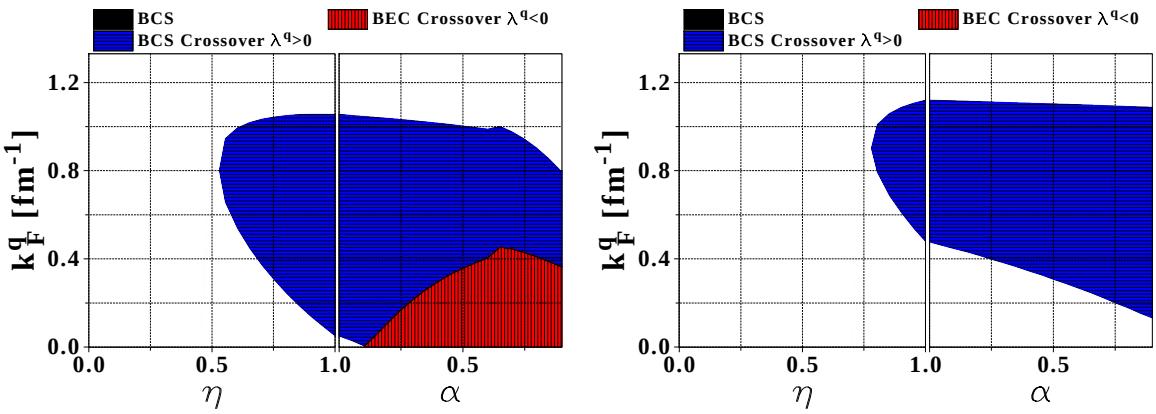

(a) Regularization scheme

(b) In-medium renormalization scheme

Figure 1.10: BCS and crossover phases as a function of (i) particle density $k_F^q \equiv (3\pi^2\rho^q)^{1/3}$ of isospin q, and (ii) parameters (η, α) of the pairing functional, with different methods to tackle the ultraviolet divergence.

1.4.6 Consequences for finite nuclei

The consequences of such a spurious BCS/BEC phase transition of infinite matter on finite nuclei can now be addressed. For extreme surface REG-X functionals, the range on k_F^q over which nuclear matter resides in the BEC crossover regime ($\lambda^q < 0$) becomes compatible with densities probed by very neutron-rich nuclei. Thus, the combination of extreme surface pairing and standard regularization may lead to meaningless results and misinterpretations. To evaluate to which extent this is the case, properties of the last bound Cr isotopes are calculated using different pairing functionals (i) $(\eta \leq 1, \alpha = 1)$, which covers from volume to standard surface pairing functionals, and (ii) $(\eta = 1, \alpha \leq 1)$, which correspond to extreme surface pairing functionals.

When the regularization scheme is used, one first observes that the position of the drip-line seems to change drastically for extreme surface pairing functionals. For instance, ^{84}Cr is predicted to be bound against neutron emission ($\lambda^q < 0$) for $\alpha = 0.5$, whereas ^{80}Cr remains the last bound nucleus using more standard $\alpha = 1$ functionals. However, the situation is more subtle than it looks at first. As exemplified by Fig. 1.11 for ^{80}Cr, nuclei bound against the emission of a single nucleon are in fact no longer bound as a gas of low-density superfluid neutron matter develops. The latter is illustrated by Fig. 1.12 where the single-particle energy spectrum for weakly bound chromium isotopes is represented, and the anomalously large occupation of the continuum (gas-like states) for ^{84}Cr is highlighted. Normal and pairing (neutron) densities grow at long distances and become uniform beyond a radius $r \approx 9$ fm for $\alpha \lesssim 0.5$. For a box of radius $R_{\rm box} = 40$ fm and $(\eta, \alpha) = (1.0, 0.2)$, the system composed of 24 protons and 56 neutrons displays a uniform gas of density $\rho^n \approx 1.10^{-4}$ fm$^{-3} \Leftrightarrow k_F^n \approx 0.14$ fm^{-1} beyond $r \approx 9$ fm. As shown by Fig. 1.10a, such a density belongs to the BEC crossover regime, which demonstrates

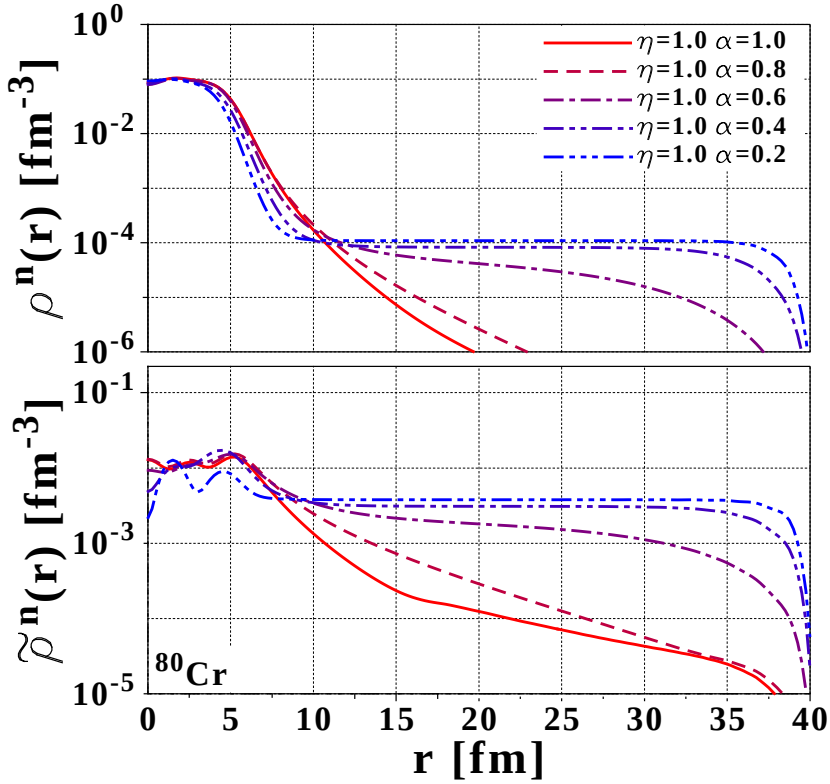

Figure 1.11: Neutron normal $\rho^n(r)$ and pairing $\tilde{\rho}^n(r)$ densities plotted in logarithmic scale for ^{80}Cr and several regularized REG-X pairing functionals. Calculations are done in a box of 40 fm and using all partial waves up to $j^n_{\rm cut} = j^p_{\rm cut} = J_{\rm max} = 151/2$.

that it is energetically favorable for the system to expell a gas of bound di-neutrons rather than staying bound. Of course, the energetics and the density of the uniform gas depend on the size of the box. Also, it is important to use enough partial waves in the single particle basis to describe the gas properly. Here, calculations are performed including all partial waves up to $j^n_{\rm cut} = j^p_{\rm cut} = J_{\rm max} = 151/2$. This is of course an extreme situation. To describe a gas accurately, one should also switch from Dirichlet to mixed boundary conditions. As we are not presently interested in extracting detailed information about the gas, this refinement is not needed here.

The appearance of a uniform gas of bound di-neutrons is driven by the neutron-neutron pairing interaction but not by the proximity of the continuum. The system displays a position-dependent BCS-BEC transition as one goes from its center to the outside which favors the dripping of bound pairs outside the system. The latter is still bound against single-nucleon emission. In such a situation, even a stable nucleus will take advantage of creating such a gas of bound di-neutrons.

On the other hand, using REN functionals such a spurious phase transition is not seen. For instance, the drip-line position remains very stable regardless of the choice of (η, α). That is, ^{80}Cr remains the last bound nucleus. At the same time, the apparition of a spurious gas is not observed on one-body densities, as seen in Fig. 1.13. Likewise, the particle continuum is not as populated as it was in the REG case (see Fig. 1.14).

Finally, one concludes that using a functional which wrongly predicts the existence of a bound di-nucleon state in the $^1S_0$ channel in the vacuum translates into creating a spurious low-density

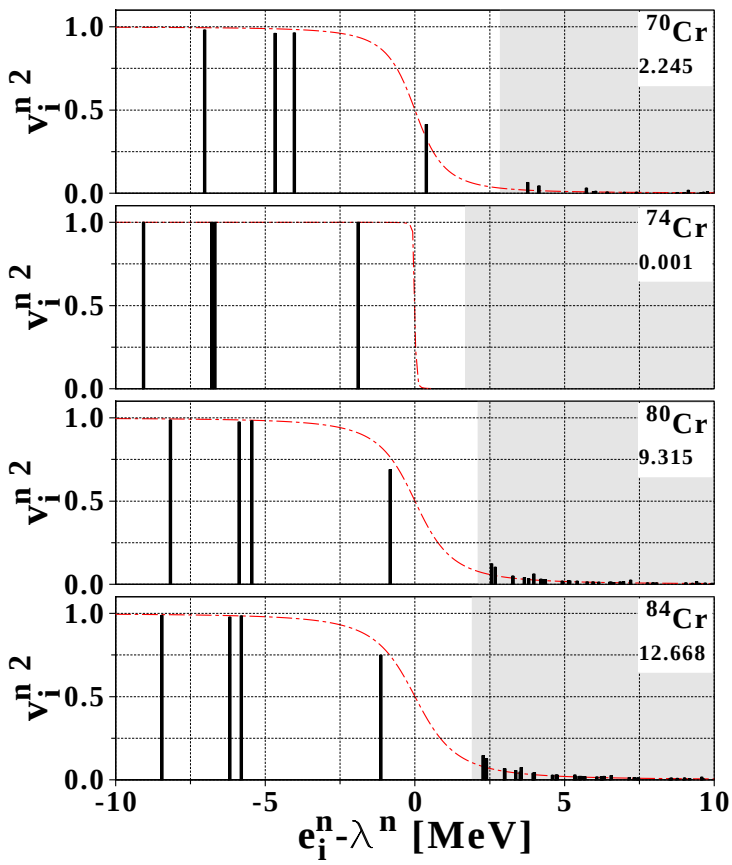

Figure 1.12: Neutron canonical occupations v_i^{q2} as a function of $(e_i^q - \lambda^q)$ for several drip-line Cr isotopes and a REG-X functional corresponding to extreme surface pairing correlations ($\eta = 1, \alpha = 0.5$). The positive energy spectrum is highlighted in grey shading, and the dashed-dotted curve represents a BCS-type approximation of those occupations using the neutron spectral gap of the nucleus. The number under the nucleus name represents the number of nucleons which belong to the positive canonical energy spectrum $e_i > 0$.

di-neutron gas surrounding finite nuclei that should be bound. Obviously, this is of importance regarding the analysis of very exotic systems such as nuclear halos. Indeed, it signals that the use of strongly surface-peaked pairing functionals, combined with the regularization scheme, might lead to unphysical predictions. The danger resides in particular in the use of pairing functionals for which such a phase transition is not that explicit, i.e. for which the di-neutron gas is not yet fully developed.

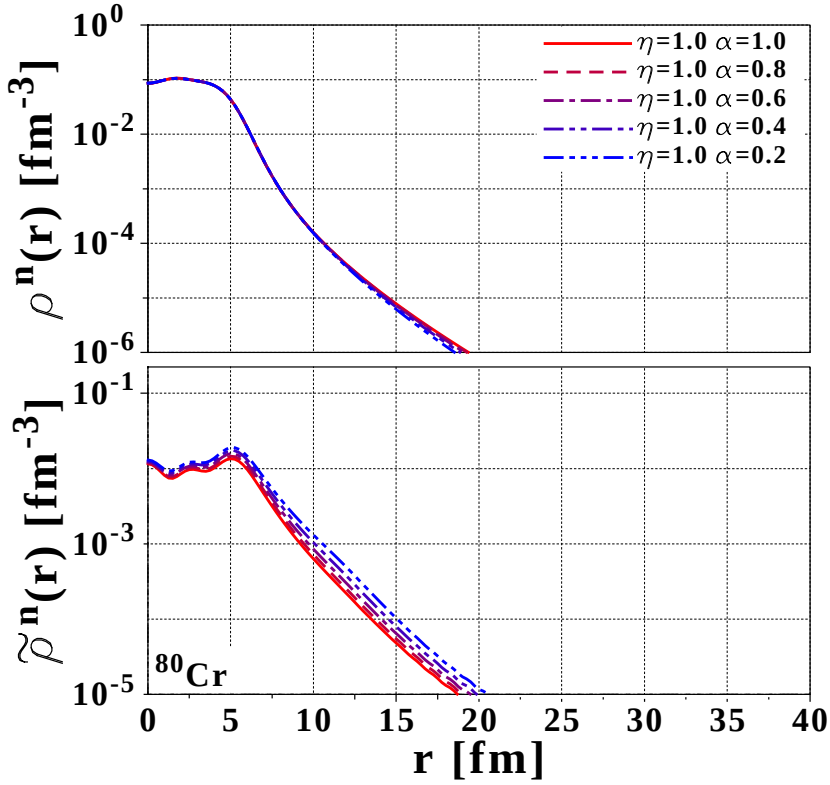

Figure 1.13: Same as in Fig. 1.11 for REN-X pairing functionals.

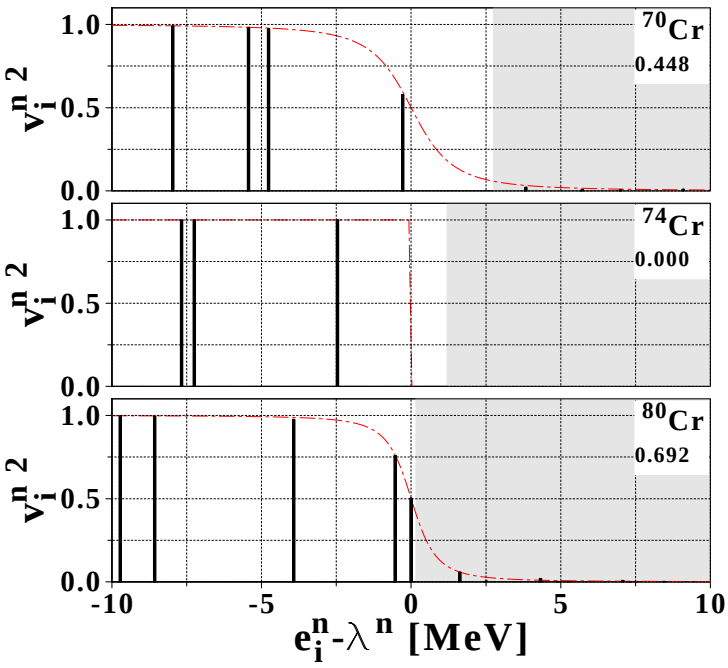

Figure 1.14: Same as in Fig. 1.14 for a REN-X functional corresponding to extreme surface pairing correlations ($\eta = 1, \alpha = 0.5$).

1.4.7 Discussion

The previous analysis demonstrates the danger of treating the ultraviolet divergence of the local pairing functional in a way that is incompatible with the density-dependent profile of that functional. In particular, the regularization scheme cannot handle pairing functionals that are extremely strong at low densities. This was already observed empirically in Ref. [249]. Here, we outline that the fundamental problem stems from the fact that such a combination leads, considering the (standard) fitting procedure used for the pairing strength, to a spurious BCS-BEC transition of nuclear matter in the $^1S_0$ channel that eventually relates to the unphysical existence of a bound di-nucleon in the vacuum. Contrarily, the in-medium renormalization method can handle such extreme surface pairing functionals as infinite nuclear matter never transitions into the BEC regime.

We underline that only a regularization scheme can be used with a strongly surface-enhanced pairing functional if the low-density part of the latter is physically constrained. For instance, Fig. 1.15 shows density-dependent couplings extracted to reproduce the pairing gaps in infinite matter provided by a bare nucleon-nucleon interaction using free kinetic energies [242]. Such a procedure represents an indirect way to prevent the functional from providing a spurious bound di-nucleon in the vacuum. Results are presented for both the regularization and the in-medium renormalization schemes. As a result of the physical constraint, the ratio $\tilde{t}_0^{\rm reg}/\tilde{t}_0^{\rm med}$ (extracted from Fig. 1.15 at $k_F^q = 0$) is much smaller than the one extracted from Fig. 1.6 for small α and neither the renormalized functional nor the regularized one sustain a bound di-nucleon in the vacuum or a BCS-BEC crossover of nuclear matter at low densities.

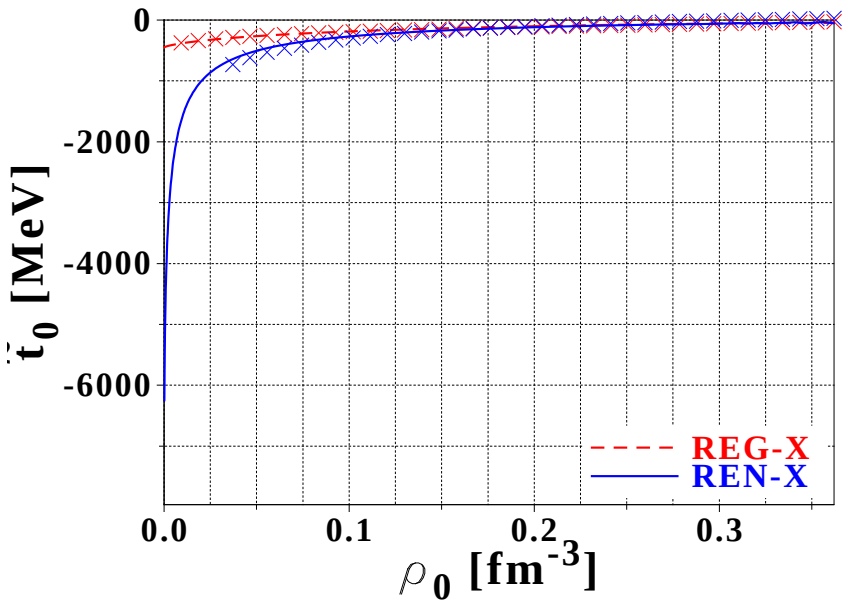

Figure 1.15: Density-dependent coupling strengths of regularized and in-medium renormalized local pairing functionals extracted by quadrature to reproduce pairing gaps provided in infinite nuclear matter by the bare nucleon-nucleon interaction using free kinetic energies [242]. Rough least-square fits of such dependencies are displayed in symbols (× / see text).

For practical calculations of finite nuclei, one may extract DDDI-like parameters (η, α) that reproduce best density-dependent coupling strengths displayed in Fig. 1.15 [238; 250]. The

analytical density dependence of the pairing functional needed to reproduce the microscopic gap evolution is evaluated here with a rough fit, and results are found in Tab. {1.4}. For REG functionals, a good agreement is found for a surface-enhanced density dependence, which was already pointed out [249]. For REN functionals the pairing strength is much larger at low density, since a hyperbolic representation with a negative critical exponent ($\alpha < 0$) is required to achieve a good description of the pairing strength $A^{\tilde{\rho}\tilde{\rho}}(\rho_0)$.

	$\tilde{t}_0$ [MeV]	η	α
REG-X	-562.2	0.75	0.287
REN-X	423.1	1.37	-0.470

Table 1.4: Fit of DDDI parameters to reproduce microscopic results for the pairing gap in symmetric nuclear matter.

This calculation only illustrates our point. Indeed, one should be aware that pairing effects mediated by the exchange of surface vibrations, although not yet under control, might renormalize pairing gaps in finite nuclei beyond the direct bare interaction term [251; 252], in a way that is different from infinite nuclear matter [253–256]. That is, there is no strong motivation as of today in adjusting a "universal" DDDI pairing functional directly at the level of infinite nuclear matter.

Part I

Halo phenomenon in medium- and heavy-mass nuclei

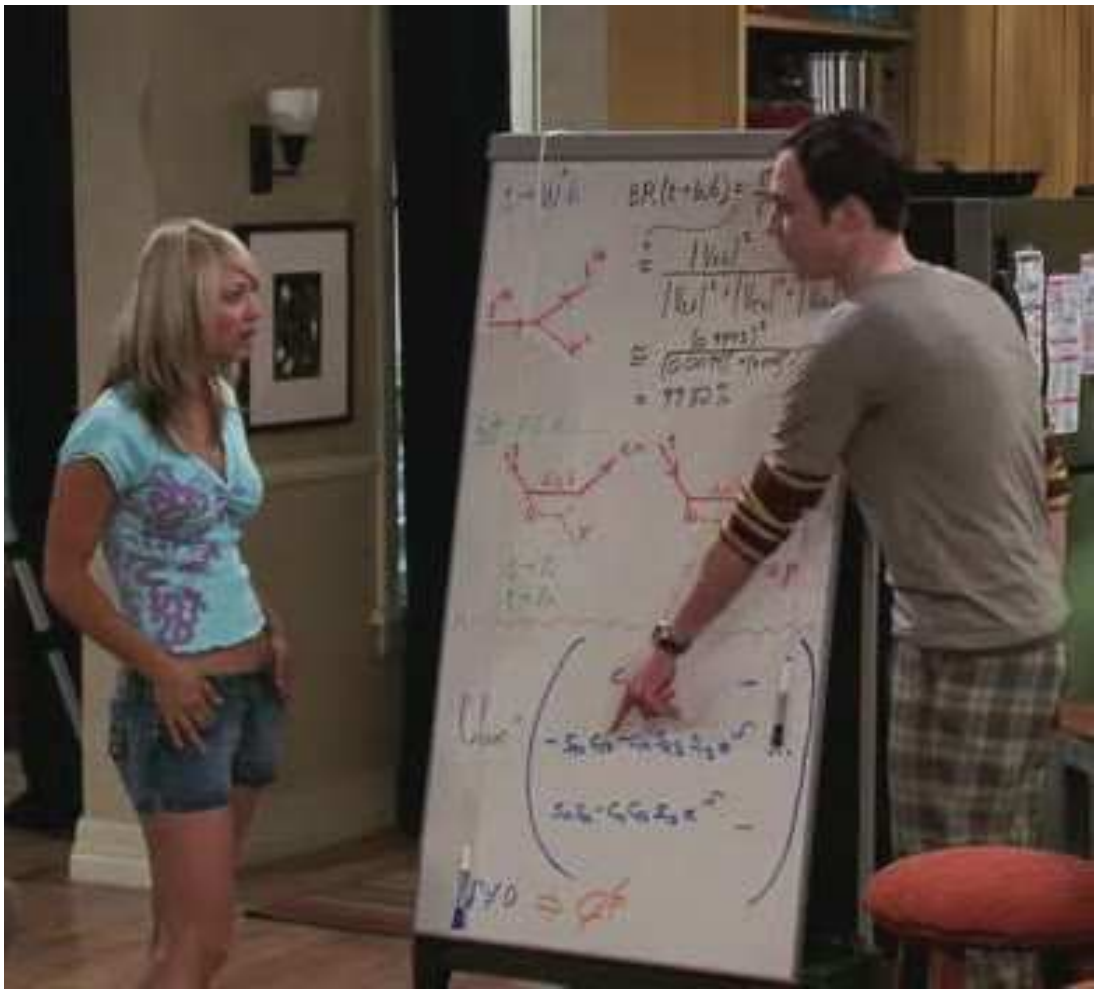

- [Penny] This looks like some serious stuff.

- [Sheldon] Yeah. Well, it's just some quantum mechanics with a little string theory doodling around the edges. That part there, that's just a joke.

Introduction

The study of light nuclei at the limit of stability has been possible in the last two decades thanks to the first generations of radioactive ion beam facilities. One of the interesting phenomena observed close to the nucleon drip-line is the formation of nuclear halos. In such systems, either the proton or the neutron density displays an unusually extended tail due to the presence of weakly-bound nucleons [36]. Since the first experimental observation of such an exotic structure in ^{11}Li [40; 41], other light neutron halo systems have been identified, e.g. ^{6}He [257], ^{11}Be [38; 39; 258], ^{14}Be [38; 259], ^{17}B [38] or ^{19}C [260; 261]. On the proton-rich side, theoretical works demonstrated the existence of halo structures in spite of the presence of the Coulomb barrier [262], as was seen experimentally for ^{8}B [263–266] and ^{17}Ne [267; 268]. Halos in excited states have been observed for ^{17}F [269; 270], ^{12}B [271] or ^{13}B [272], and several others are predicted [273].

The theoretical description of light halo systems is rather well under control. It usually relies on a cluster vision where one (^{11}Be, ^{19}C...) or two (^{11}Li, ^{6}He...) loosely bound nucleons define a low-density region surrounding a core. Assuming that core and halo degrees of freedom can be decoupled, essentially exact solutions of the simplified many-body problem are obtained by solving the Schrödinger equation for two-body systems [274; 275], or Faddeev equations for three-body ones [257; 274; 276; 277]. However, the boundary between halo and non-halo nuclei is blurred by the presence of core excitations. Indeed, the inert decoupling of the loosely bound nucleons from the core is only an approximation. Nevertheless it has been assessed that halo systems arise when [278; 279] (i) the probability of nucleons to be in the forbidden region outside the classical turning point is greater than 50%, and (ii) the cluster structure is dominant and accounts for at least 50% of the ground-state configuration. Such conditions have been thoroughly studied [280; 281] and found to be fulfilled when (a) the separation energy of the nucleus is very small, of the order of 2 MeV$/A^{2/3}$, (b) the loosely bound nucleons occupy low angular-momentum states ($\ell = 0$ or $\ell = 1$) for two-body clusters, or low hyperangular momentum states ($K = 0$ or $K = 1$) for three-body ones, to limit the effect of the centrifugal barrier preventing the nucleons from spreading out [282], and (c) the charge of the core remains small for proton halos. The latter requirement need to be softened because of a potential Coulomb-induced rearrangement of the single-particle states [283].

When going to heavier nuclei, SR-EDF methods become the tool of choice for low-energy nuclear structure. However, as recalled in Sec. 1.3, state-of-the-art EDFs are adjusted empirically, and their properties are not yet under control in extreme conditions, where low-density configurations, isospin or surface effects come strongly into play. Thus, the capacity of existing functionals to predict properties of exotic nuclei, such as their limits of stability, remains rather weak [215]. In that respect, the input from the coming generation of radioactive beam facilities will help to further constrain models and to design a universal EDF. Halo structures can contribute to such a quest as they emphasize low-density configurations and surface/finite-size effects. Their study in medium-mass nuclei might provide important information regarding isovector density dependencies and gradient/finite-size corrections to the nuclear EDF. The pairing strength in

low-density regimes and the evolution of shell structures at the limit of stability might also be further constrained. However, two questions arise as we discuss potential medium-mass halos. Indeed, medium-mass nuclei are (i) large enough that the cluster picture at play in light nuclei needs to be revisited, in such a way that the standard understanding of the halo phenomenon developed in light nuclei might change significantly, and (ii) light enough that explicit correlations associated with symmetry restorations and shape fluctuations are important and may impact halo properties. Tackling the latter problem would require to use MR-EDF approaches.

In the following, we introduce a new method to identify and characterize halo structures in medium-mass nuclei [42; 43]. Robust theoretical considerations allow to extract model-independent criteria, which are used to perform a large-scale analysis of halo properties in medium-mass nuclei predicted by self-consistent HFB calculations. Given the new analysis method, important questions can also be addressed, e.g. the influence of (i) the low-density character of the pairing functional, (ii) the angular-momentum cutoff in the single-particle basis, (iii) the isoscalar effective mass, (iv) saturation density of nuclear matter, or (v) tensor terms in the particle-hole part of the energy functional [158]... on the properties of halo nuclei. More generally, the different ways pairing correlations impact halo nuclei are studied, such as the anti-halo effect [284; 285], the decorrelation of $\ell = 0$ orbitals from the pairing field [286–288], as well as the impact of the regularization/renormalization scheme used [234; 240]. We focus on spherical even-even nuclei. Further extensions of the method to odd and deformed systems can be envisioned. The charge restriction for proton halos identified in light nuclei is such that we do not expect proton halos in medium-mass systems. As a result, the present work focuses on exotic structures at the neutron drip-line.

Sec. 2.1 provides a quick overview of the ingredients that are crucial to the formation of halos. In Sec. 2.2, the limitations of existing tools used to characterize skins and halos, such as the Helm model [289], are highlighted. A new method to properly identify and characterize halo features of weakly-bound systems in a model-independent fashion is introduced in Chap. 3. We validate the method using a selection of toy models before applying it to the results obtained from self-consistent spherical HFB calculations of Cr and Sn isotopes in Sec. 4.2. As a second step, systematic results of halo properties for all (predicted) spherical nuclei are presented in Sec. 4.4, alongside with the sensibility of halo properties to the characteristics of the particle-hole part of the EDF. Sec. 4.5 is then devoted to discussing the effect of pairing correlations on the formation of halos. Finally, the model-independence of the method is proven, as it is applied to other quantum many-body systems and the universality of the halo formation is highlighted in Sec. 4.6.

Chapter 2

Phenomenology of halo systems

Abstract: The goal of the present section is to outline some of the elements that are crucial to the formation of halos. This will serve as an introduction to the more quantitative discussion proposed later on as we develop our new analysis method. For convenience, the discussion is conducted within the EDF framework. However, the features discussed are not specific to a particular many-body method or approximation but constitute generic aspects of halos. Then, observables and analysis tools that are usually used to identify and quantify halo signatures in nuclear systems are discussed. The purpose is to introduce general features which turn out to be useful later on, but above all to demonstrate the limitations of existing analysis tools.

Contents

2.1 Basic features **63**
2.1.1 Importance of low angular-momentum orbits 63
2.1.2 Role of pairing correlations 64
2.2 Existing investigations and analysis methods **65**
2.2.1 First characterizations 65
2.2.1.1 Chromium isotopes 65
2.2.1.2 Tin isotopes 66
2.2.2 The Helm model 69
2.2.2.1 Presentation 69
2.2.2.2 Limitations 70

2.1 Basic features

2.1.1 Importance of low angular-momentum orbits

We first discuss the impact of low-angular momentum orbitals[(1)] on the density profile of halo nuclei. To discuss this specific aspect, we use the realization of the EDF method in which the reference state is taken as a Slater determinant, i.e. the Hartree-Fock realization. Within such a realization of the EDF method, the HFB equations reduce to a standard one-body eigenvalue problem that provides the canonical orbitals $\varphi_\nu(\vec{r})$ from which the Slater determinant $|\Phi\rangle$ is constructed. Restricting the description to spherical systems, considering for simplicity a

[1] Although the notion of *orbital* often refers to an independent-particle picture or a Hartree-Fock approximation, it is important to note that the EDF method includes correlations beyond such approximations. In fact, and as discussed in Sec. 3.1, the notion of *orbital* should rather be replaced by the one of *overlap function* in the present discussion.

multiplicative local potential $U(r)$ and forgetting about the spin degree of freedom, it can be proven [290] that the density $\rho(r)$ behaves asymptotically as $e^{-2\kappa_0 r}/(\kappa_0 r)^2$, where the decay constant $\kappa_0 = \sqrt{-2m\epsilon_0/\hbar^2}$ is related to the single-particle energy of the least bound occupied orbital in the reference Slater determinant. As the density used in the SR-EDF method is meant to reproduce the exact local density, an analogue of Koopmans' theorem [291] holds, that is ϵ_0 is equal to minus the one-nucleon separation energy $S_n = E_0^{N-1} - E_0^N$, where E_0^N (resp. E_0^{N-1}) is the ground-state internal energy of the N-body (resp. $(N-1)$-body) system. As a result, long density tails arise for weakly-bound systems; i.e. in the limit $S_n \to 0$.

A more quantitative characterization of the density is provided by its radial moments $\langle r^n \rangle$. Such moments are of special interest in the case of halo systems. At long distances, the dominant contribution to $\langle r^n \rangle$ comes from φ_0. In the limit of weak binding one has $\epsilon_0 \to 0$, that is $\langle r^n \rangle_0$ (i) diverges as $\epsilon_0^{\frac{2\ell-1-n}{2}}$ for $n > 2\ell - 1$, (ii) diverges as $\ln(\epsilon_0)$ for $n = 2\ell - 1$, and (iii) remains finite for $n < 2\ell - 1$ [290]. In particular, one finds that the wave function normalization $\langle r^0 \rangle_0$ diverges for s waves, whereas the second moment $\langle r^2 \rangle_0$ diverges for both s and p waves. As a result, the root-mean-square (r.m.s.) radius, defined as

$$R_{\text{r.m.s.}} \equiv \sqrt{\frac{\langle r^2 \rangle}{\langle r^0 \rangle}}\,, \tag{2.1}$$

diverges as $\epsilon \to 0$ when φ_0 corresponds to a s or a p wave. It diverges as $1/\sqrt{\epsilon_0}$ in the case of a s wave, and as $\epsilon_0^{-\frac{1}{4}}$ for a p wave. The centrifugal barrier confines wave functions with higher orbital angular momenta, in such a way that $R_{\text{r.m.s.}}$ remains finite as $\epsilon_0 \to 0$ if φ_0 has an angular momentum $\ell \geq 2$. Equivalent arguments are found in the case of three-body systems [282].

According to the above analysis, only low-lying s or p waves near the threshold are able to extend significantly outside the classically forbidden region. The consequences of those specific patterns are that (i) one usually focuses on the evolution of the neutron r.m.s radius as a function of neutron number to characterize the presence of halos, (ii) the presence and occupation of low-lying s or p waves are often seen as a prerequisite for the formation of neutron halos, and (iii) orbitals with $\ell \geq 2$ are not believed to contribute to halos. However, it is important to notice that $\langle r^2 \rangle$ is only the (next-to) leading moment in the representation of the density. The complete expansion of $\rho(r)$ involves moments of higher orders which probe the nuclear density at increasing distances. Even if those higher-order moments weight usually little in the expansion, one cannot rule out $\ell \geq$2-type halo structures, as $\langle r^n \rangle_0$ with $n \geq 2$ diverges in the limit $\epsilon_0 \to 0$ for such angular momenta: $\langle r^4 \rangle$ diverges for $\ell = 0, 1, 2$, $\langle r^6 \rangle$ diverges for $\ell = 0, 1, 2, 3...$ and so on [37].

2.1.2 Role of pairing correlations

The explicit treatment of pairing correlations through dependencies of the nuclear EDF on the anomalous density changes qualitatively the density profile in loosely bound systems. By studying the asymptotic form of the quasiparticle wave functions, it is easy to show that the decay constant κ_0 at play becomes $\kappa_0 = \sqrt{-2m\epsilon_0/\hbar^2}$, with $|\epsilon_0| = E_0 - \lambda$ whereas $E_0 = \min_\nu[E_\nu]$ is the lowest positive quasiparticle energy solution of Eq. (1.34). Considering the most extreme case of a canonical state lying at the Fermi level at the drip-line ($e_0 \approx \lambda \approx 0$), one sees that $E_0 \approx \Delta_0 \geq 0$. Therefore, everything else being equal, paired densities decrease faster than unpaired ones at long distances. Because the decay constant does not go to zero, the second moment of the density cannot diverge, whatever the angular momentum of the least bound quasiparticle. In other words, the effect of pairing correlations is to induce a generic *anti-halo effect* by localizing the

density [284; 285].

Two additional effects may however blur such a picture. First, recent HFB calculations performed in terms of a fixed one-body Wood-Saxon potential have shown that such a pairing anti-halo effect could be ineffective under extreme conditions [286; 287]. Indeed, very weakly bound $s_{1/2}$ states (bound by a few keVs) tend to decouple from the pairing field because of their abnormal extension. As a consequence, $E_0 = \min_\nu[E_\nu]$ tends towards zero again as $e_0 \approx \lambda \approx 0$ and the r.m.s. radius of such an unpaired orbital may diverge, contributing strongly to the formation of a halo. Although this possibility should be considered in principle, the depicted situation of a $\ell = 0$ orbit bound by a few keVs right at the drip-line is rather improbable and would be highly accidental in realistic nuclei. Second, pair scattering distributes particles over several natural orbitals located around the Fermi level. As compared to the implementation of the EDF based on a Slater determinant, this might lead to the promotion of particles from low/high angular-momentum states to high/low angular momentum orbitals [292]. Depending on the situation, this will favor or inhibit the formation of halos. The way this process impacts halos depends on the system and on the particular distribution of orbitals around the Fermi energy at the drip-line. These issues will be discussed more extensively in Sec. 4.5.

2.2 Existing investigations and analysis methods

Halo properties of medium-mass drip-line nuclei have been studied for various isotopic chains using relativistic or non-relativistic EDF methods [289; 292–299]. Owing to the discussion provided above, the evolution of the r.m.s. radii along isotopic chains is often used to characterize halos in a qualitative manner. One needs however more quantitative characterizations of the halo itself. For example, the concept of *giant halo* was recently introduced on the basis of summing up the occupations of low-lying orbitals with large r.m.s. radii [293]. Such halo structures, supposedly composed of six to eight neutrons, have been characterized through relativistic and non-relativistic methods [292; 296–299], mainly for Zr and Ca isotopes, and were related to the presence of $\ell = 1$ states close to the Fermi level at the drip-line. These results are intuitively surprising. Indeed, spatially decorrelated neutrons seem less likely to appear as the mass of the system increases and their behavior tends to become more collective. We will come back to this point.

Chromium and tin isotopic chains are chosen as testing cases for now. Calculations are performed using the Skyrme SLy4 functional in the particle-hole channel, while a mixed-type pairing functional REG-M is used in the pairing channel. The HFB problem being solved self-consistently, the shape of the central potential cannot be manually adjusted to tune the binding energy of weakly-bound orbitals. Thus, potential nuclear halos candidates have to be identified a posteriori, the elementary criterion being the presence of low-lying low-ℓ orbitals near the Fermi energy at the neutron drip-line, by analogy with the situation in lighter systems.

2.2.1 First characterizations

2.2.1.1 Chromium isotopes

Chromium isotopes ($Z = 24$) at the neutron drip-line are good halo candidates among all predicted spherical medium-mass nuclei [140; 300]. In Fig. 2.1, the least bound neutron canonical energies e_i^n are plotted along the isotopic chain, ^{80}Cr being the predicted drip-line nucleus. The presence of low-lying $3s_{1/2}$ and $2d_{5/2}$ states at the drip-line provides ideal conditions for the formation of halo structures.

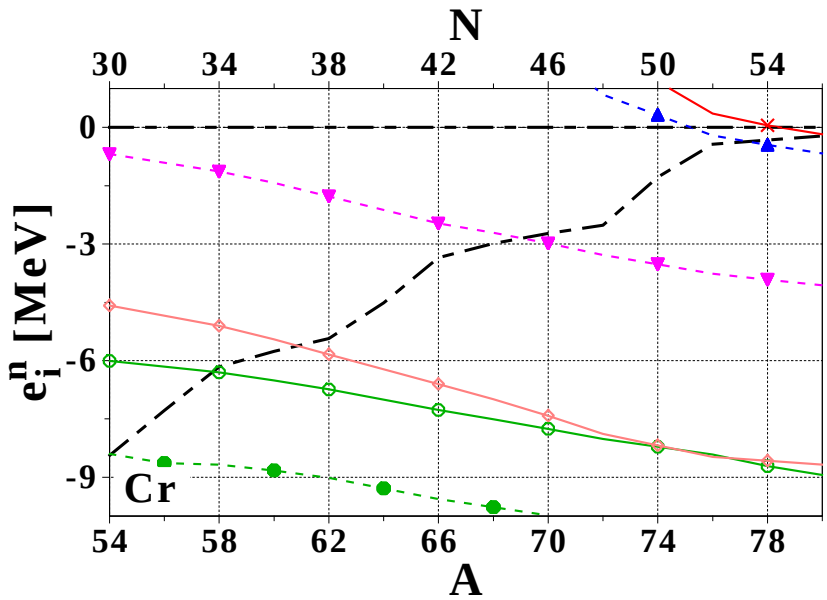

Figure 2.1: Neutron canonical energies e_i^n along the Cr isotopic chain, obtained through spherical HFB calculations with the {SLy4+REG-M} functional. Conventions for the labeling of single-particle states are given at the beginning of the manuscript (Fig. 8).

As discussed in Sec. 2.1.1, the abnormal extension of the one-body neutron density is usually characterized through the evolution of the neutron r.m.s. radius as one approaches the drip-line, which is presented in Fig. 2.2. A significant kink in the neutron r.m.s. radius is seen at the $N = 50$ shell closure. Such a kink is usually interpreted as the emergence of a neutron halo [289; 293]. However, this could equally be due to a simple shell effect. Indeed, as the $N = 50$ gap is crossed, the two-neutron separation energy S_{2n} drops, as seen in Fig. 2.3. As a result, the decay constant κ_0 of the one-body density is largely reduced. A genuine halo phenomenon relates more specifically to the presence of nucleons which are spatially decorrelated from a core. Even though the case of drip-line Cr isotopes seems favorable, the occurrence of a halo cannot be thoroughly addressed by looking only at the evolution of the neutron r.m.s. radius.

2.2.1.2 Tin isotopes

Sn isotopes ($Z = 50$) have always been considered as a milestone for EDF methods. Because of the magic proton number, they are rather easy to produce in radioactive beam facilities. Properties of nuclei between the two doubly-magic tin isotopes, ^{100}Sn and ^{132}Sn, are known with a good experimental precision and may enter the fitting procedure of Skyrme or Gogny functionals [77; 188]. Finally, it is a long isotopic chain convenient for systematic studies. At the neutron drip-line, which corresponds to ^{174}Sn for the {SLy4+REG-M} EDF, the least-bound orbitals are mostly odd-parity states, among which the $3p_{3/2}$ and $3p_{1/2}$ states that might form a halo (Fig. 2.4). However, (i) these $\ell = 1$ states are relatively well bound, and (ii) the least bound orbital is the $1i_{13/2}$ ($\ell = 6$) intruder state, which is strongly affected by the confining centrifugal barrier. Nevertheless, the neutron r.m.s. radius (Fig. 2.5) exhibits a weak kink at the $N = 82$ shell closure, which has been interpreted as a halo signature [289]. As pointed out previously, an analysis based only on r.m.s. radii is somewhat incomplete/misleading. Indeed, although shell effects at the $N = 82$ magic number generate a sudden decrease of S_{2n}, the latter does not drop to zero at this point, as seen in Fig. 2.6. A direct connection between the kink of

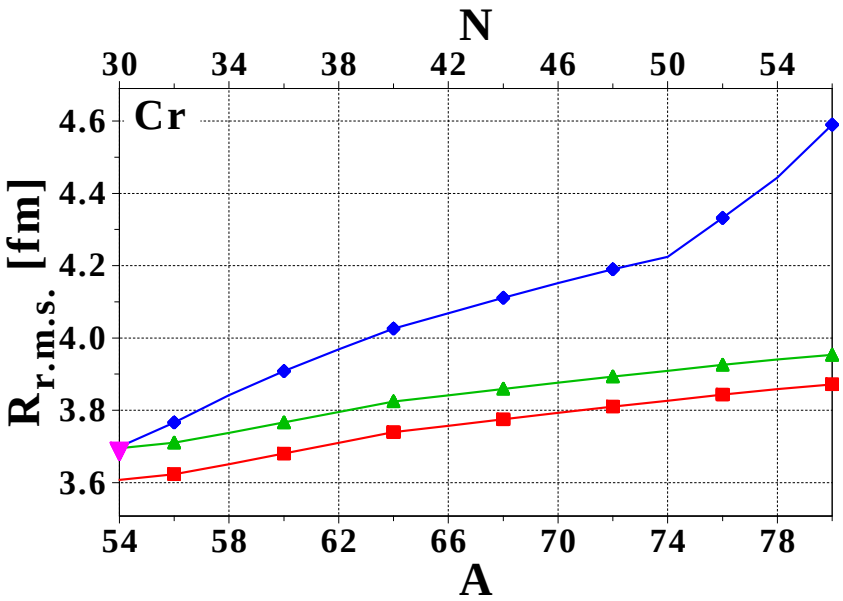

Figure 2.2: Same as FIG. 2.1 for proton (■), neutron (♦) and charge (▲) r.m.s. radii. Experimental values for charge r.m.s. radii are indicated when available (▼), along with experimental error bars [301].

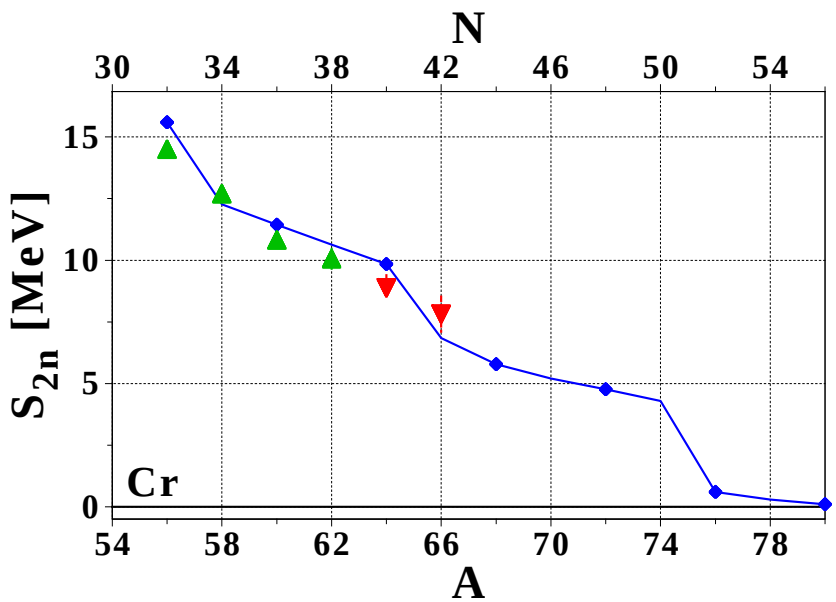

Figure 2.3: Same as FIG. 2.1 for two-neutron separation energies S_{2n} (♦). Experimental values are indicated when available [302; 303] (▲ when both masses are known, ▼ when at least one comes from mass extrapolation), along with experimental error bars.

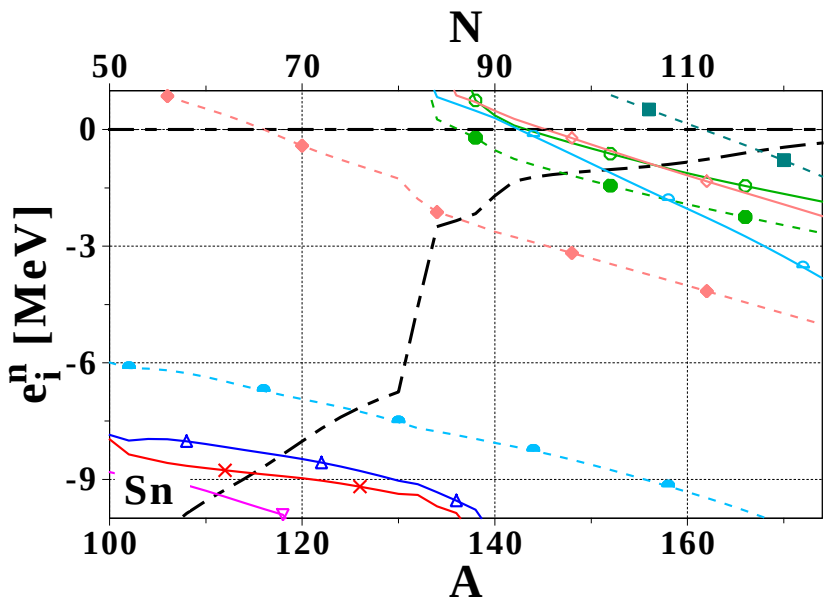

Figure 2.4: Same as FIG. 2.1 for Sn isotopes.

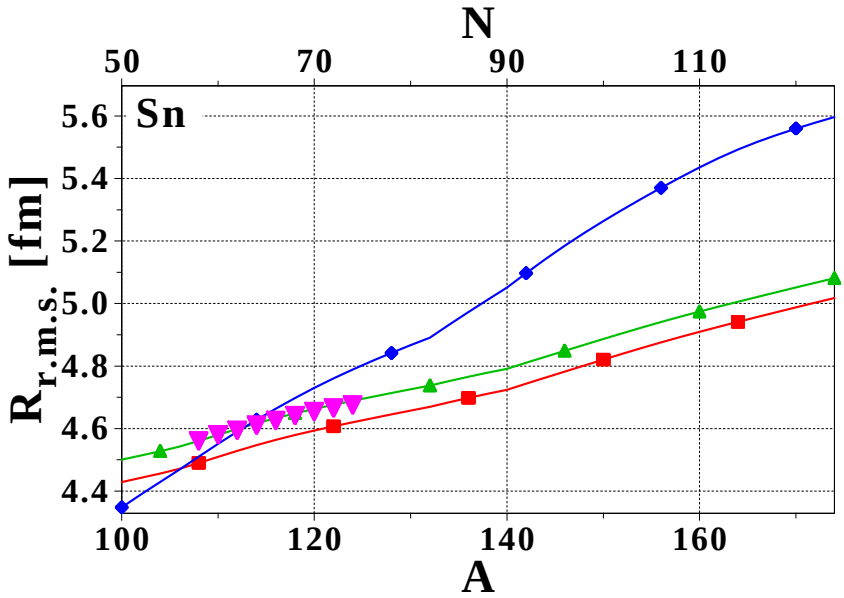

Figure 2.5: Same as FIG. 2.2 for Sn isotopes.

the r.m.s. radius and the formation of a neutron halo is very dubious. This point will be further discussed below.

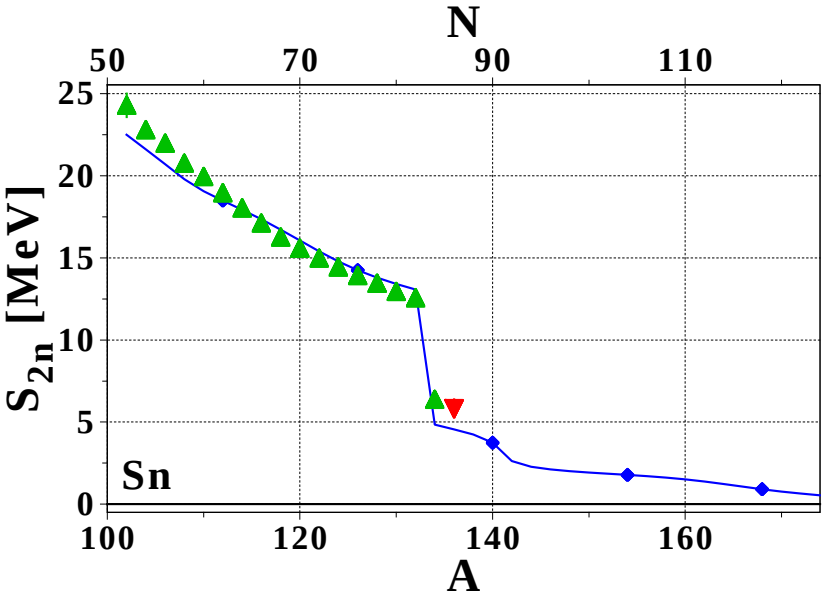

Figure 2.6: Same as Fig. 2.3 for Sn isotopes.

As already mentioned, the previous analysis is useful but insufficient to characterize a halo in a quantitative manner that would allow one to use such systems to extract information useful to nuclear structure and theoretical models. The characterization of halos through the definition of the neutron matter thickness and the one-neutron region thickness is possible [295] but remains arbitrary and correlated to a one-neutron halo hypothesis. Another possible way is to extract so-called "halo factors" from the individual spectrum through antiproton annihilation probing the nuclear density extension [294; 304]. However, such tools do not allow the extraction of quantitative properties, such as the actual number of nucleons participating in the halo. They also define the halo as the region where the neutron density dominates the proton one, which is an admixture of the neutron skin and the (potential) halo. Another method, which is expected to allow a more quantitative analysis, is now reviewed in more details.

2.2.2 The Helm model

2.2.2.1 Presentation

The original purpose of the Helm model, introduced in Refs. [305–307] for the analysis of electron scattering on even-even nuclei, is to fit the experimental charge density using a few-parameter anzatz. The normalized nuclear charge density is approximated by the convolution of a sharp-sphere density of radius R_0 defining the nuclear extension, and a gaussian smoothing profile of width σ describing the surface thickness, i.e.

$$\rho_H(\vec{r}) = \rho_0 \int f_g(\vec{r}-\vec{r}\,')\,\Theta\left(R_0 - |\vec{r}\,'|\right)\,\mathrm{d}\vec{r}\,' \,, \tag{2.2}$$

where Θ is the Heaviside function, and

$$f_g(\vec{r}) = \frac{1}{(2\pi)^{3/2}\sigma^3} e^{-\frac{r^2}{2\sigma^2}} \,, \qquad \rho_0 = \frac{3}{4\pi R_0^3} \,. \tag{2.3}$$

The invariance of Eq. (2.2) under an arbitrary rotation ensures that the Helm density ρ_H is spherical. Its Fourier transform, the form factor $F_H(\vec{k}) = F_H(k)$, is analytical and reads as

$$F_H(k) = \int \rho_H(\vec{r})\, e^{i\,\vec{k}\cdot\vec{r}}\, \mathrm{d}\vec{r} = \frac{3}{R_0 k}\, j_1(kR_0)\, e^{-\frac{\sigma^2 k^2}{2}} \,. \tag{2.4}$$

The r.m.s. radius of the Helm density only depends on R_0 and σ, i.e.

$$R^H_{\text{r.m.s.}} = \sqrt{\frac{\int \rho_H(r)\, r^4\, \mathrm{d}r}{\int \rho_H(r)\, r^2\, \mathrm{d}r}} = \sqrt{\frac{3}{5}\left(R_0^2 + 5\sigma^2\right)} \,. \tag{2.5}$$

This model has been used to study neutron skins and halos in medium-mass nuclei close to the neutron drip-line [289]. Proton and neutron densities were defined as a superposition of a core density ρ^q_{core} plus a tail density ρ^q_{tail} describing, when necessary, the halo. The idea was to reproduce the core part ρ^q_{core} using the Helm anzatz ρ^q_H, normalized to the nucleon number N^q ($N^q = N$ or Z). The two free parameters (R^q_0, σ^q) were adjusted on the high-momentum part of the realistic form factor

$$F^q(k) = 4\pi \int \rho^q(r)\, r^2\, j_0(k\,r)\, \mathrm{d}r \,, \tag{2.6}$$

where $\rho^q(r)$ is the density coming out of the actual calculations. It was suggested in Ref. [289] to evaluate (i) R^q_0 through the first zero k^q_1 of the realistic form factor: $R^q_0 = z^1_1/k^q_1$, where z^1_1 is the first zero of the Bessel function j_1 ($z^1_1 \approx 4.49341$), and (ii) σ^q by comparing the model and realistic form factors at their first extremum k^q_M (a minimum in the present case). Then, the following radii are defined

- $R_{\text{geom}}(q) = \sqrt{5/3}\, R_{\text{r.m.s.}}(q)$ (geometric radius) for realistic densities,
- $R_{\text{Helm}}(q) = \sqrt{5/3}\, R^H_{\text{r.m.s.}}(q) = \sqrt{R_0^{q\,2} + 5\,\sigma^{q\,2}}$ (Helm radius) for model densities.

Adjusting the Helm parameters to the high momentum part of the realistic form factor was meant to make the fitting procedure as independent of the asymptotic tail of $\rho^q(r)$ as possible. Constructed in this way, $R_{\text{Helm}}(n)$ should not incorporate the growth of $R_{\text{geom}}(n)$ when the neutron separation energy drops to zero and the spatial extension of weakly-bound neutrons increases dramatically. In addition, it was checked that the difference between $R_{\text{Helm}}(p)$ and $R_{\text{geom}}(p)$ was negligible near the neutron drip-line. From these observations, the neutron skin and neutron halo contributions to the geometric radius were defined as[2]

$$\Delta R_{\text{skin}} = R_{\text{Helm}}(n) - R_{\text{Helm}}(p) \,, \qquad \Delta R_{\text{halo}} = R_{\text{geom}}(n) - R_{\text{Helm}}(n) \,. \tag{2.7}$$

2.2.2.2 Limitations

Proton and neutron Helm radii are compared to the geometric ones on Fig. 2.7 for chromium and tin isotopes. The behavior of $R_{\text{geom}}(q)$ and $R_{\text{Helm}}(q)$ for Sn isotopes is the same as in Ref. [289][3]. For both isotopic chains, the sudden increase of the neutron geometric radius beyond the last neutron shell closure might be interpreted as a signature of a halo formation. However, ΔR_{halo} is non-zero along the entire Cr isotopic chain, even on the proton-rich side. The latter result is problematic since no neutron halo is expected at the proton drip-line. Such non-zero values for ΔR_{halo} can be understood as a direct consequence of the gaussian folding

[2] Similar definitions could be applied to nuclei close to the proton drip-line, where a proton halo is expected instead of a neutron one.

[3] Results differ slightly from Ref. [289] because of the different pairing functional and regularization scheme used, as well as the larger number of j-shells taken into account in the present calculations. The influence of limiting the number of j shells in the calculations will be discussed in Sec. 4.2.2.2.

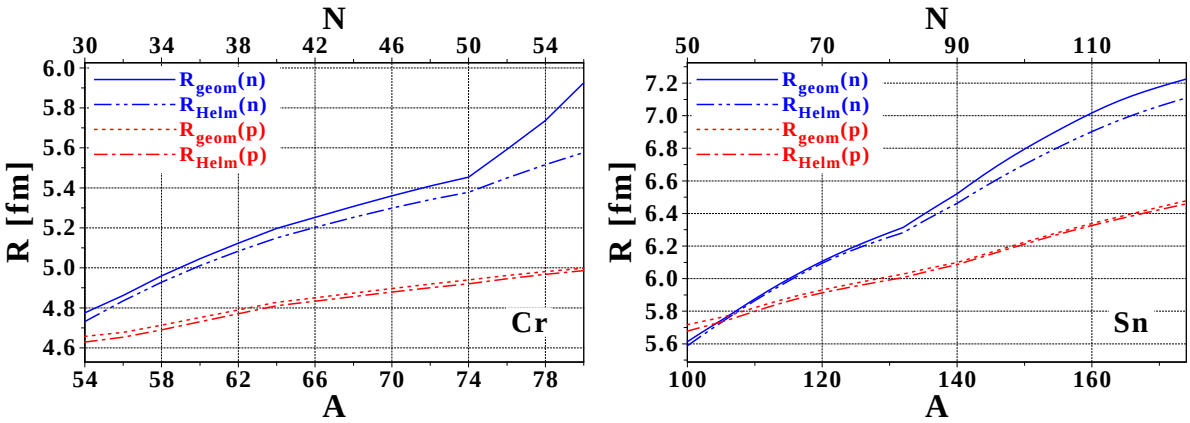

Figure 2.7: Geometric and Helm radii for Cr and Sn isotopes calculated in the spherical HFB approach with the {SLy4+REG-M} functional.

in the definition of the Helm density. The asymptotic decay of the Helm density is roughly quadratic in logarithmic scale, whereas a linear decay is expected [124; 172; 174]. To illustrate this point, Fig. 2.9 displays the realistic and Helm densities of ^{54}Cr (in the valley of stability) and ^{80}Cr (drip-line nucleus). The difference in asymptotic behaviors is obvious, while at the same time the adjusted form factors, presented in Fig. 2.8 do not seem that much different. In particular, Helm densities are unable to reproduce the correct long-range part of the non-halo proton density, or the neutron density of nuclei in the valley of stability.

Such features lead to unsafe predictions for the halo parameter ΔR_{halo} because the neutron skin and the potential halo cannot be properly separated with this method. These problems, as well as a lack of flexibility to account for finer details of the nuclear density, had already been pointed out [308].

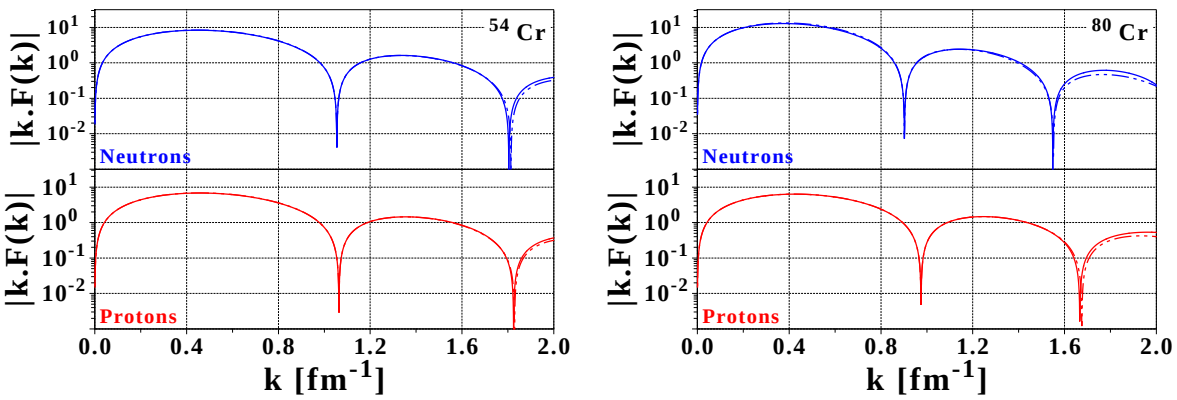

Figure 2.8: Realistic (solid lines) and Helm (dashed-dotted lines) form factors of ^{54}Cr and ^{80}Cr.

One might thus question the fitting procedure introduced in Ref. [289]. The method naturally requires R_0^q and σ^q to be adjusted on the form factor at sufficiently large k for the Helm density to relate to the core part of the density only. For these reasons, the procedure proposed in Ref. [289] seems appropriate. Having said that, some flexibility remains, e.g. using the second zero k_2^q of $F^q(k)$ to adjust R_0^q. Following such arguments, four slightly different adjustments, all

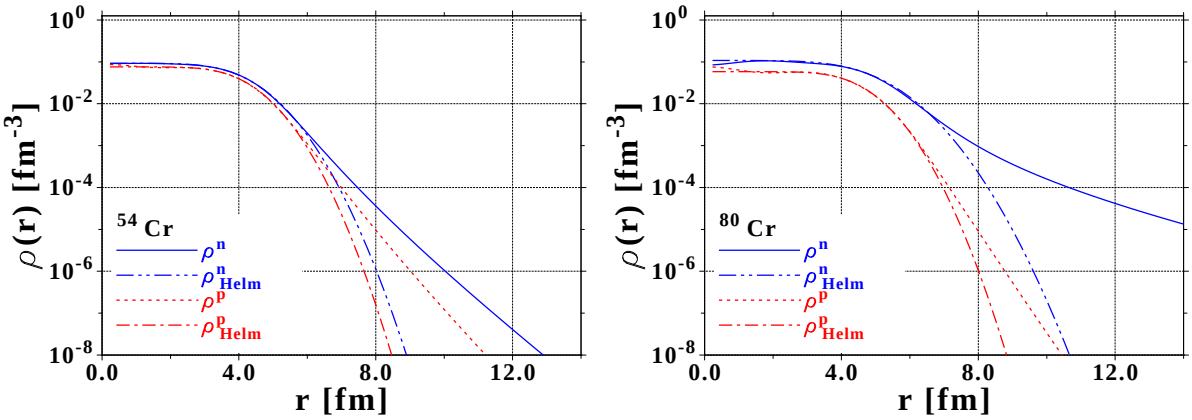

Figure 2.9: Same as in FIG. 2.8 for realistic and Helm one-body densities.

consistent with the general requirement exposed above, have been tested to check the stability of the Helm model, e.g.

A_1 : (i) $F^q_H(k^q_1) = F(k^q_1)$, and (ii) $F^q_H(k^q_M) = F^q(k^q_M)$,

A_2 : (i) $F^q_H(k^q_1) = F^q(k^q_1)$, and (ii) $F^{q\,\prime}_H(k^q_1) = F^{q\prime}(k^q_1)$,

A_3 : (i) $F^q_H(k^q_2) = F^q(k^q_2)$, and (ii) $F^{q\,\prime}_H(k^q_2) = F^{q\prime}(k^q_2)$,

A_4 : (i) $F^q_H(k^q_1) = F^q(k^q_1)$, and (ii) $F^{q\,\prime}_H(0.4\,k^q_1) = F^{q\prime}(0.4\,k^q_1)$.

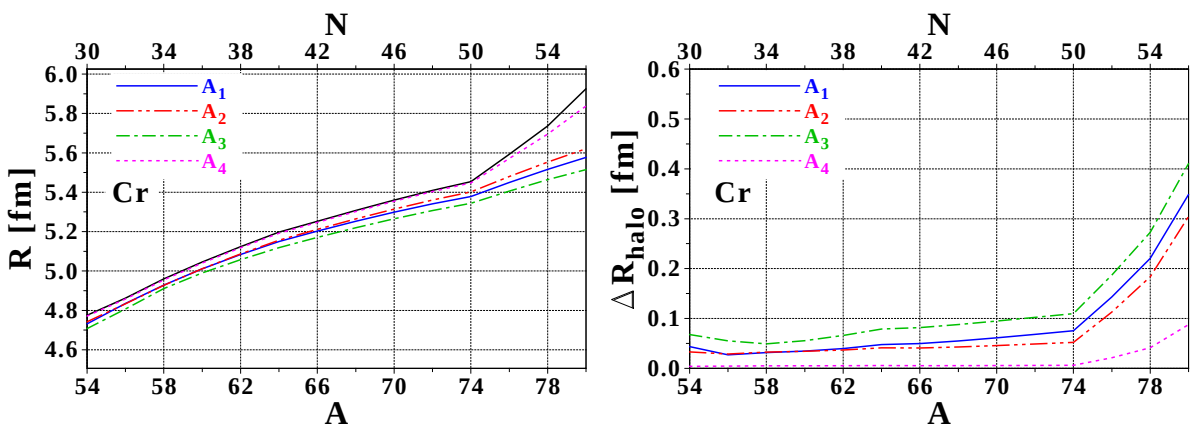

Figure 2.10: Neutron Helm r.m.s. radius $R^H_{\text{r.m.s.}}(n)$ and halo parameter ΔR_{halo} for Cr isotopes using different fitting procedures for the Helm parameters (R^q_0, σ^q) (see text).

FIG. 2.10 shows the halo parameter ΔR_{halo} obtained for Cr isotopes using protocols A_1 to A_4. Note that protocol A_1 is the one proposed in REF. [289] and used earlier on whereas protocol A_4 includes on purpose more of the long distance part of the realistic density. Although the general pattern remains unchanged, the halo parameter significantly depends on the fitting procedure used to determine (R^q_0, σ^q). Because of the wrong asymptotic behavior of the Helm density discussed above, one cannot make ΔR_{halo} to be zero for magic and proton-rich nuclei (see protocol A_4), keeping unchanged its values for halo candidates at the neutron drip-line. Helm densities obtained with the A_4 protocol still do not match realistic ones, even for protons, as

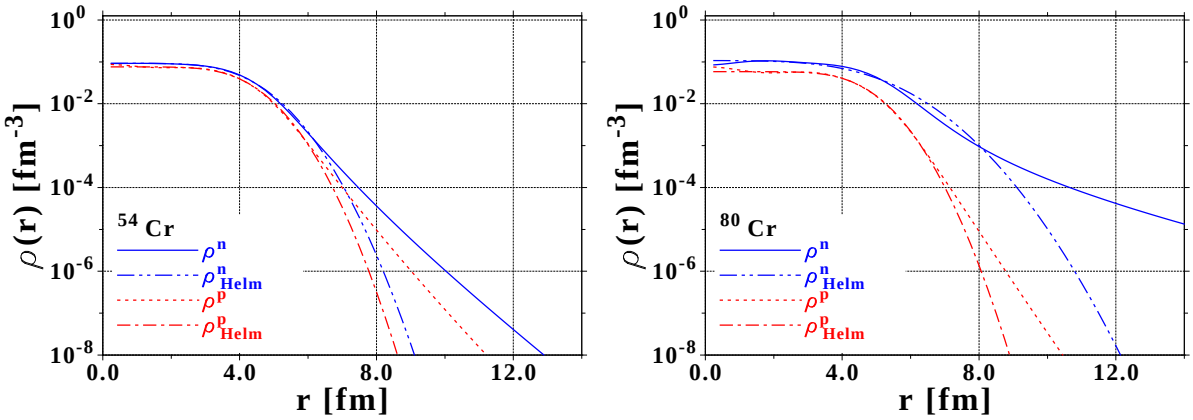

Figure 2.11: Same as in Fig. 2.9 with the fit protocol A_4 for the Helm parameters.

shown in Fig. 2.11. Such a fine tuning of the fitting procedure that would make use of an a priori knowledge of non-halo nuclei is impractical and unsatisfactory.

As a next step, we tried to use other trial densities to improve the standard Helm model. However, a key ingredient is to have an analytical expression for the associated form factor, as the parameters can then be easily adjusted on the realistic form factor. We could not find any expression of the density leading to analytical expressions of F_H^q and good asymptotics at the same time, with only two free parameters[4]. Finally, adjusting the model density on the realistic one in coordinate space to capture those missing asymptotics would rely on an arbitrary *a priori* separation of the density into core and halo contributions.

Although the Helm model looked promising at first, we have shown the versatility of its predictions. The inability of the model to describe the correct asymptotics of the nuclear density in the valley of stability, as well as the too large freedom in the fitting procedure, limit very much its predictive power. Therefore a more robust analysis method is needed to characterize medium-mass halo nuclei.

[4]Using model densities depending on three parameters would make the Helm model even more dependent on the fitting procedure.

Chapter 3

New criteria for a quantitative analysis of halo properties

Abstract: A useful method to study halos must be able to characterize a *spatially* decorrelated component in the nucleon density in a model-independent fashion. We propose in the following a method which allows the identification of such a contribution. Our starting point is a thorough analysis of the one-body density. The latter needs first to be defined very precisely, since one deals with so-called internal degrees of freedom, which is a critical point for self-bound systems. Asymptotic properties of the internal one-body density allow then to relate the existence of a spatially decorrelated region in the nuclear density profile to the existence of typical energy scales in the excitation spectrum of the $(N-1)$-body system. From these specific patterns, new quantitative criteria to characterize halos can then be defined.

Contents

3.1 Properties of the one-body density **76**
3.1.1 Definitions and notations 76
3.1.2 Decomposition of the N-body wave function 77
3.1.3 Asymptotics of overlap functions 77
3.1.4 Internal density 78
3.2 Crossing pattern in $\rho^{\infty}_{[1]}(r)$ **80**
3.3 Halo characterization **81**
3.3.1 Spatial definition 81
3.3.2 Relevant energy scales 81
3.3.3 Definition of the halo region 82
3.3.4 Quantitative halo criteria 87

3.1 Properties of the one-body density

3.1.1 Definitions and notations

Let us start from the exact non-relativistic N-body Hamiltonian[1]

$$H^N = \sum_{i=1}^{N} \frac{p_i^2}{2m} + \sum_{\substack{i,j=1 \\ i<j}}^{N} v(r_{ij}) \,, \tag{3.1}$$

where p_i is the single-particle momentum, $r_{ij} = |\vec{r}_i - \vec{r}_j\,|$ and v denotes the bare nucleon-nucleon interaction. H^N is invariant under translation and can be decomposed into a center-of-mass $H^N_{\text{c.o.m.}}$ and a so-called internal part H^N_{int}

$$\begin{cases} H^N_{\text{c.o.m.}} = & -\dfrac{\hbar^2}{2mN}\left(\displaystyle\sum_{i=1}^{N} \nabla_i\right)^2 \,, \\[2ex] H^N_{\text{int}} = & \displaystyle\sum_{\substack{i,j=1 \\ i<j}}^{N} \left[-\frac{\hbar^2}{2m_{red}}\left(\nabla_i - \nabla_j\right)^2 + v(r_{ij})\right] \,, \end{cases} \tag{3.2}$$

where $m_{red} \equiv m(N-1)/N$. This allows the factorization of $\Psi^N_{i,\vec{K}}(\vec{r}_1 \ldots \vec{r}_N)$ into a center-of-mass (plane wave) and an internal part, i.e.

$$\Psi^N_{i,\vec{K}}(\vec{r}_1 \ldots \vec{r}_N) = e^{i\,\vec{K}\cdot\vec{R}_N}\, \Phi^N_i(\vec{r}_1 \ldots \vec{r}_N) \,. \tag{3.3}$$

"Internal" relates to a wave function Φ^N_i expressed in terms of relative coordinate systems, such as the Jacobi variables

$$\vec{\xi}_i = \vec{r}_{i+1} - \frac{1}{i}\sum_{j=1}^{i} \vec{r}_j \,, \tag{3.4}$$

which are invariant under translation. Thus $\Phi^N_i(\vec{r}_1 \ldots \vec{r}_N) \equiv \tilde{\Phi}^N_i(\vec{\xi}_1 \ldots \vec{\xi}_{N-1})$ behaves for any vector $\vec{a}$ as

$$\Phi^N_i(\vec{r}_1 + \vec{a} \ldots \vec{r}_N + \vec{a}\,) = \Phi^N_i(\vec{r}_1 \ldots \vec{r}_N) \,. \tag{3.5}$$

Orthogonality and completeness relationships of the set $\{\Phi^N_i\}$ are obtained in the sense of [309]

$$\int \mathrm{d}\vec{r}_1 \ldots d\vec{r}_N\, \Phi^{N*}_i(\vec{r}_1 \ldots \vec{r}_N)\, \delta(\vec{R}_N)\, \Phi^N_j(\vec{r}_1 \ldots \vec{r}_N) = \delta_{ij} \,, \tag{3.6}$$

and

$$\sum_{i=1}^{+\infty} \Phi^{N*}_i(\vec{r}_1 \ldots \vec{r}_N)\, \Phi^N_i(\vec{r}\,'_1 \ldots \vec{r}\,'_N) = \int \mathrm{d}\vec{r}\, \frac{1}{N!} \det_{i,j=1..N} \left[\delta(\vec{r}_i - \vec{r}\,'_j + \vec{r}\,)\right] \,, \tag{3.7}$$

where the extra integral over $\vec{r}$ expresses the equivalence of translated configurations.

[1] The Coulomb interaction is omitted here, as the focus is on neutron halos. Spin degrees of freedom are also not explicitly included, but their introduction would not change the final results. Finally, the Hamiltonian is restricted to a two-body interaction. The conclusions would not change either with the introduction of the missing three-body force, because of its short range.

3.1.2 Decomposition of the N-body wave function

The ground-state internal wave function Φ_0^N can be expanded in terms of the complete orthonormal set of internal $(N-1)$-body wave functions Φ_ν^{N-1}, which are eigenstates of the $(N-1)$-body internal Hamiltonian [309–312], such that[2,3]

$$\Phi_0^N(\vec{r}_1 \dots \vec{r}_N) = \frac{1}{\sqrt{N}} \sum_\nu \Phi_\nu^{N-1}(\vec{r}_1 \dots \vec{r}_{N-1})\, \varphi_\nu(\vec{r}_N - \vec{R}_{N-1})\,. \tag{3.8}$$

The states Φ_ν^{N-1} are ordered by increasing energy, $\nu = 0$ corresponding to the ground state of the $(N-1)$-body system. Overlap functions [313] $\varphi_\nu(\vec{r})$ represent the probability amplitudes to find a particle at position $\vec{r}$ with respect to the center-of-mass of the $(N-1)$-body system in the internal state Φ_ν^{N-1}, considering that the initial system is in its ground state with zero momentum, that is

$$\varphi_\nu(\vec{r}) = \sqrt{N} \int \mathrm{d}\vec{r}_1 \dots \vec{r}_{N-1} \Phi_\nu^{N-1^*}(\vec{r}_1 \dots \vec{r}_{N-1})\, \delta(\vec{R}_{N-1})\, \Phi_0^N(\vec{r}_1 \dots \vec{r}_{N-1}, \vec{r})\,. \tag{3.9}$$

The latter quantity is of direct relevance for knockout reactions [314–316]. Spectroscopic amplitudes φ_ν are not canonical overlaps of the N-body system defined in the laboratory frame. Indeed, they relate to the center-of-mass of the $(N-1)$-body system fixed at the origin. The normalization of the overlap functions are the so-called spectroscopic factors [314; 315]

$$S_\nu = \int \mathrm{d}\vec{r}\, |\varphi_\nu(\vec{r})|^2\,. \tag{3.10}$$

3.1.3 Asymptotics of overlap functions

The asymptotic properties of overlap functions are important, as the internal one-body density at large distances is completely determined by those. The asymptotic equation satisfied by φ_ν is obtained from a further decomposition of the internal N-body Hamiltonian into

$$H_{\mathrm{int}}^N = H_{\mathrm{int}}^{N-1} - \frac{\hbar^2}{2m_{\mathrm{red}}} \left(\nabla_N - \frac{1}{N-1} \sum_{i=1}^{N-1} \nabla_i \right)^2 + \sum_{i=1}^{N} v(r_{iN})\,. \tag{3.11}$$

The trivial identity

$$\int \mathrm{d}\vec{r}_1 \dots \mathrm{d}\vec{r}_{N-1}\, \Phi_\nu^{N-1^*}(\vec{r}_1 \dots \vec{r}_{N-1})\, \delta(\vec{R}_{N-1}) \left[H_{\mathrm{int}}^N - E_0^N \right] \Phi_0^N(\vec{r}_1 \dots \vec{r}_N) = 0 \tag{3.12}$$

gives a system of coupled channel equations for the overlap functions:

$$\begin{aligned} -\frac{\hbar^2}{2m_{red}} \Delta_N\, \varphi_\nu(\vec{r}_N) - (E_0^N - E_\nu^{N-1}) \varphi_\nu(\vec{r}_N) \\ + (N-1)\sqrt{N} \int \mathrm{d}\vec{r}_1 \dots \mathrm{d}\vec{r}_{N-1}\, \Phi_\nu^{N-1^*}(\vec{r}_1 \dots \vec{r}_{N-1}) \\ \times \delta(\vec{R}_{N-1})\, v(|\vec{r}_N - \vec{r}_{N-1}|)\, \Phi_0^N(\vec{r}_1 \dots \vec{r}_N) = 0\,. \end{aligned} \tag{3.13}$$

[2] The sum over ν in Eq. (3.8) corresponds to a discrete sum over bound states of the $(N-1)$-body system and an integral over unbound resonant scattering channels.

[3] Antisymmetry is properly handled in Eq. (3.8), but is hidden in the overlap functions φ_ν. It is carried out in the same way as when a (antisymmetrized) Slater determinant is expanded according to its first column. In that case, one has

$$\det_{i,j=1..N} [\varphi_i(\vec{r}_j)] = \sum_{k=1}^{N} (-1)^{k+1}\, \varphi_k(\vec{r}_1) \det_{\substack{i,j=1..N \\ i\neq k, j\neq 1}} [\varphi_i(\vec{r}_j)]\,.$$

In the previous sum, each of the individual terms are not antisymmetric under the exchange of particle coordinates but the total sum is. For a more complete discussion on this subject we refer the reader to Ref. [312].

For large distances, the nuclear interaction vanishes and the radial part $\bar{\varphi}_\nu$ of the overlap function become solution of the free Schrödinger equation

$$\left[\left(\frac{d^2}{dr^2}+\frac{2}{r}\frac{d}{dr}-\frac{\ell_\nu(\ell_\nu+1)}{r^2}\right)-\kappa_\nu^2\right]\bar{\varphi}_\nu^\infty(r)=0\,, \tag{3.14}$$

with $\kappa_\nu=\sqrt{-2m_{\rm red}\epsilon_\nu/\hbar^2}$, whereas $\epsilon_\nu=\left(E_0^N-E_\nu^{N-1}\right)$ is minus the nucleon separation energy to reach the state Φ_ν^{N-1}. Solutions of the asymptotic free Schrödinger equation take the form

$$\varphi_\nu^\infty(\vec{r})=B_\nu\,h_{\ell_\nu}(i\,\kappa_\nu\,r)\,Y_{\ell_\nu}^{m_\nu}(\theta,\varphi)\,. \tag{3.15}$$

3.1.4 Internal density

In the laboratory frame, the one-body density is the expectation value of the operator

$$\hat{\rho}(\vec{r})=\sum_{i=1}^N\delta(\vec{r}-\hat{\vec{r}}_i)\,, \tag{3.16}$$

which leads for the N-body ground state to

$$\begin{aligned}\rho(\vec{r})=&N\int{\rm d}\vec{r}_1\ldots{\rm d}\vec{r}_{N-1}\,|\Psi_0^N(\vec{r}_1\ldots\vec{r}_{N-1},\vec{r})|^2\\ =&N\int{\rm d}\vec{\xi}_1\ldots{\rm d}\vec{\xi}_{N-2}\,{\rm d}\vec{R}_{N-1}\,|\tilde{\Phi}_0^N(\vec{\xi}_1\ldots\vec{\xi}_{N-2},\vec{r}-\vec{R}_{N-1})|^2\,.\end{aligned} \tag{3.17}$$

Using Eq. (3.5), one easily proves that the one-body density in the laboratory frame is translationally invariant, $\rho(\vec{r}+\vec{a})=\rho(\vec{r})$, and thus is uniform. This is a general property of translationally invariant systems which underlines that the density in the laboratory frame is not the proper tool to study self-bound systems. The relevant object for self-bound systems is the internal one-body density matrix, defined as the expectation value of the operator

$$\hat{\rho}_{[1]}(\vec{r},\vec{r}\,')=\delta(\vec{R}_N)\sum_{i=1}^N\delta(\vec{r}-\hat{\vec{r}}_i+\hat{\vec{R}}_{N-1}^i)\delta(\vec{R}_N')\sum_{j=1}^N\delta(\vec{r}\,'-\hat{\vec{r}}_j'+\hat{\vec{R}}_{N-1}^{j'})\prod_{\substack{k,l=1..N\\k,l\neq i,j}}\delta(\hat{\vec{r}}_k-\hat{\vec{r}}_l)\,, \tag{3.18}$$

where

$$\hat{\vec{R}}_{N-1}^i=\frac{1}{N-1}\sum_{\substack{j=1\\j\neq i}}^N\hat{\vec{r}}_j\,. \tag{3.19}$$

Defining the internal density with respect to the center-of-mass of the remaining $(N-1)$-body is the relevant choice[4]. Using Eqs. (3.6,3.8), one obtains [311; 317; 318]

$$\begin{aligned}\rho_{[1]}(\vec{r},\vec{r}\,')=&N\int{\rm d}\vec{r}_1\ldots{\rm d}\vec{r}_{N-1}\,\Phi_0^{N*}(\vec{r}_1\ldots\vec{r}_{N-1},\vec{r}\,')\,\delta(\vec{R}_{N-1})\Phi_0^N(\vec{r}_1\ldots\vec{r}_{N-1},\vec{r})\\ =&\sum_\nu\varphi_\nu^*(\vec{r}\,')\varphi_\nu(\vec{r})\,,\end{aligned} \tag{3.20}$$

which shows that the internal one-body density matrix is completely determined by the overlap functions [317]. The internal one-body density $\rho_{[1]}(\vec{r})$ is the local part of the internal density matrix, and is the expectation value of the operator

$$\hat{\rho}_{[1]}(\vec{r})=\delta(\vec{R}_N)\sum_{i=1}^N\delta(\vec{r}-\hat{\vec{r}}_i+\hat{\vec{R}}_{N-1}^i)\,. \tag{3.21}$$

[4]One could define another internal one-body density taking another pivot point, e.g. the center-of-mass of the N-body system. However, this leads to complications since the internal density obtained is no more definite positive. This point is discussed in Appendix C.

According to Eq. (3.20), one has

$$\rho_{[1]}(\vec{r}) = \sum_{\nu} |\varphi_\nu(\vec{r})|^2 = \sum_{\nu} \frac{2\ell_\nu + 1}{4\pi} |\bar{\varphi}_\nu(r)|^2 \,, \tag{3.22}$$

where the energy degeneracy associated with the orbital momentum has been resolved through the summation over spherical harmonics. Note that Eqs. (3.15,3.22) are exactly the expressions that one would have found in the case of independent particles bound by a central non-self-consistent potential (e.g. electrons in a central Coulomb field), where second quantization can be used. That is, from this point and since all further derivations only use Eqs. (3.15,3.22), everything will be model-independent, in the sense that these results can be applied to both self-bound and confined many-body systems.

From Eqs. (3.15,3.22), the internal one-body density behaves asymptotically as[5]

$$\rho^{\infty}_{[1]}(r) = \sum_{\nu} \frac{B_\nu^2}{4\pi} (2\ell_\nu + 1) |h_{\ell_\nu}(i\,\kappa_\nu r)|^2 \,. \tag{3.23}$$

The internal one-body density at large distances is a superposition of energy- and ℓ-dependent individual components. For very large arguments, the squared modulus of a Hankel function behaves as $e^{-2\kappa_i r}/(\kappa_i r)^2$ [320]. Thus the $\nu = 0$ component dominates and provides the usual asymptotic behavior [124; 172; 174][6]

$$\rho^{\infty}_{[1]}(r) \underset{r\to+\infty}{\longrightarrow} \frac{B_0^2}{4\pi} (2\ell_0 + 1) \frac{e^{-2\kappa_0\, r}}{(\kappa_0\, r)^2} \,. \tag{3.24}$$

The asymptotic form of the Hankel function is independent of the angular momentum[7]. As a result, contributions from the overlap functions to $\rho^{\infty}_{[1]}$ at very large distances are ordered according to their corresponding separation energies $|\epsilon_\nu|$, independently of ℓ_ν. Of course, corrections to this ordering at smaller distances come from (i) the ℓ-dependence of the Hankel functions due to the centrifugal barrier, which favors low angular momentum states, and (ii) the $(2\ell + 1)$ degeneracy factor which favors high angular momentum states. Again, for extremely large distances the least bound component will always prevail, although this may happen very far out[8]. To characterize the net effect of corrections (i) and (ii), contributions $(2\ell_\nu + 1)|\bar{\varphi}_\nu(r)|^2$, for a fixed energy but different angular momenta, are compared in Fig. 3.1 for the solutions of a simple finite spherical well. Outside the well, Hankel functions are exact solutions of the problem. The potential depth is adjusted to obtain identical eigenenergies for all ℓ_ν. Although the $(2\ell_\nu + 1)$ factor reduces the gap between s and p components, the effect of the centrifugal barrier is always the strongest at large r, where states are clearly ordered according to ℓ_ν, favoring low angular momenta. In any case, the separation energy remains the leading factor as far as the ordering of overlap functions at long distances is concerned.

[5] Rigorously, this is true only if the convergence of the overlap functions to their asymptotic regime is uniform in the mathematical sense, i.e. if they reach the asymptotic regime at a common distance R [317]. This is not actually proven in nuclear physics, but has already been shown in atomic physics [99; 319] for the electron charge density.

[6] Note that the asymptotics of ρ^p and ρ^n are different because of the charge factor (Hankel functions for neutrons, Whittaker functions for protons).

[7] This explains why high-order moments $\langle r^n \rangle$ of the density diverge when high-ℓ states are loosely bound, as it was observed in Sec. 2.1.1.

[8] For instance, if a $\ell = 6$ component is less bound than a $\ell = 0$ one by only a very few keVs, the former will only become the leading component in the asymptotic density at very large distance.

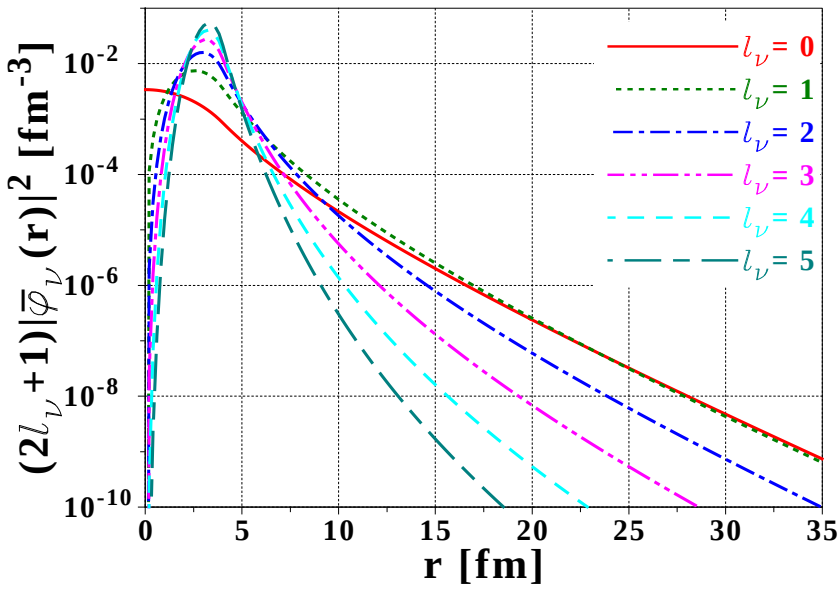

Figure 3.1: Squared components of the solutions of a finite spherical well of fixed radius $a = 4$ fm, multiplied by the degeneracy factor $(2\ell_\nu + 1)$, for various angular momenta and fixed energy $\epsilon_\nu = -100$ keV. The first state for each ℓ_ν (nodeless component corresponding to a primary quantum number equal to zero) is represented.

3.2 Crossing pattern in $\rho^{\infty}_{[1]}(r)$

The (model-independent) ordering of the individual components in $\rho^{\infty}_{[1]}$ at long distances has interesting consequences on the properties of the density as a whole. As discussed below, this ordering induces a typical crossing pattern between the individual components which is going to be used to characterize halo nuclei. Introducing normalized overlap functions $\psi_\nu(\vec{r})$, Eq. (3.22) becomes

$$\rho_{[1]}(r) = \sum_\nu \frac{2\ell_\nu + 1}{4\pi} S_\nu \left|\bar{\psi}_\nu(r)\right|^2 \equiv \sum_\nu C_\nu(r)\,. \tag{3.25}$$

Let us take all spectroscopic factors equal to one for now. The $\nu = 0$ component, corresponding to the smallest separation energy, dominates at large distances. Because of continuity ($r\,\bar{\psi}_\nu(r) \in \mathcal{L}^2(\mathbb{R}^+)$) and normalization conditions, this implies that $\bar{\psi}_0(r)$ has to cross all the other overlap functions as r goes inward from $+\infty$ to zero. The position at which ψ_0 crosses each ψ_ν depends on the difference of separation energies and on angular momenta. In particular, there will exist a crossing between $\bar{\psi}_0(r)$ and the remaining density $\sum_{\nu\geq 1} C_\nu(r)$. The same is true about $\bar{\psi}_1(r)$: it must cross the remaining density $\left[\rho^{[1]}(r) - C_0(r)\right]$ and so on... As a result, a given individual component always crosses all more bound ones. Of course, the centrifugal barrier will influence the position of such crossings but not their occurrence because of the universality of the asymptotic ordering pattern discussed in the previous section.

Let us now incorporate the role of spectroscopic factors. In practice, S_ν is known to increase with the excitation energy of the corresponding eigenstate of the $(N-1)$-body system. Thus, the norm of φ_0 is smaller than those of the excited components φ_ν, which mechanically ensures the existence of the crossings discussed previously. A similar reasoning holds when going from

φ_0 to φ_1 etc...

One should finally pay attention to the number of nodes of overlaps $\bar{\varphi}_\nu$. This feature actually favors low angular momentum states as far as the asymptotic positioning is concerned. If two components have the same energy but different angular momenta, the one with the lowest ℓ will have a greater number of nodes, according to Hund's rule. This will reduce the normalization of the wave function in the nuclear interior. That is, the weight of the asymptotic tail is increased, which favors its dominance at long distance. However, this effect is expected to have a small impact in comparison with other corrections. As a result, the occurrence of crossings between components of the density is not jeopardized by the existence of nodes in the overlap functions.

3.3 Halo characterization

The discussion of Sec. 3.2 shows how individual contributions to the one-body density (i) are positioned with respect to each other, and (ii) display a very typical crossing pattern. Such features are now used to characterize halo systems.

3.3.1 Spatial definition

As pointed out earlier, a general and model-independent definition of a halo relates to the existence of nucleons which are spatially decorrelated from others constituting the core. This can only be achieved if some contributions to the internal density exhibit very long tails. Also, the delocalization from the core requires the latter to exist and remain well localized. To achieve such a spatial decorrelation between a core and a tail part, it is necessary to have a crossing between two well-identified groups of orbitals with significantly different asymptotic slopes, which reduces their spatial overlap. This will necessarily translate into a sharp crossing between those two groups of orbitals and to a pronounced curvature in the density. The previous observation is key and will be used in the following to design model-independent criteria to characterize halo systems. Such a pronounced crossing is illustrated in Fig. 3.2 for a simple model where the halo is due to a single state. Of course, more complex situations have to be considered where multiple states contribute to the core and the halo. Indeed, the presence of collective motions in medium-mass systems implies that one hardly expects a single state to be well separated from the others.

3.3.2 Relevant energy scales

The need for an abrupt change of slope in the density provides critical conditions for the existence of a halo. This translates eventually into specific patterns in the excitation energy spectrum of the $(N-1)$-body system, that is (i) the least bound component φ_0 must have a very small separation energy to extend far out, (ii) several components $\varphi_1, \varphi_2 \ldots \varphi_m$ may contribute significantly to the density tail if, and only if, they all have separation energies of the same order as that of φ_0, and (iii) for this tail to be spatially decorrelated, in a sense that is further specified below, from the rest of the density (the "core"), components $\nu > \nu_m$ have to be much more localized than those with $\nu \leq \nu_m$. This third condition is fulfilled when the crossing between the mth and $(m+1)^{th}$ components in the density is sharp, which corresponds to significantly different decay constants $\kappa_m \ll \kappa_{m+1}$ at the crossing point. The latter observations suggest that a halo appears when (i) the one-neutron separation energy $S_n = |\epsilon_0|$ is close to zero, (ii) one or a bunch of low energy states in the $(N-1)$-body system have separation energies $|\epsilon_\nu|$ close to zero, and (iii) a significant gap in the spectrum of the $(N-1)$-body system exists, which separates the latter bunch of states φ_ν from higher excitations.

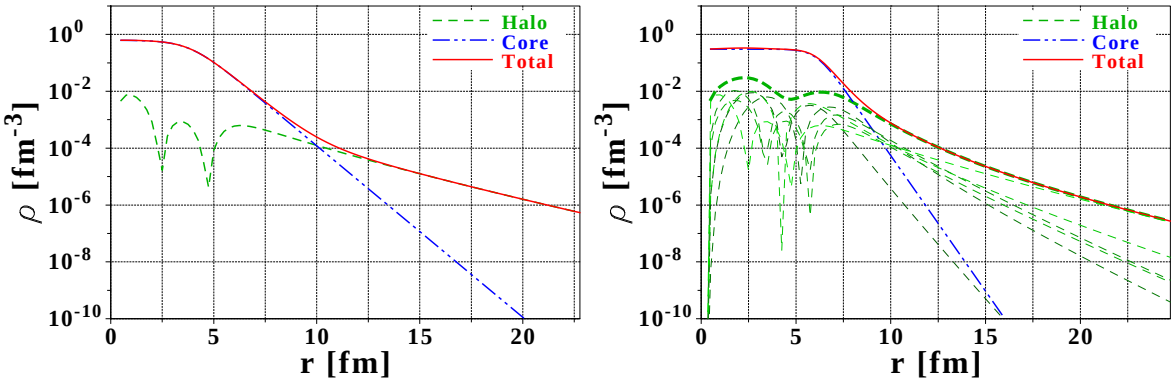

(a) One component in the halo ($3s_{1/2}$ realistic state from ^{80}Cr)

(b) Multiple components in the halo

Figure 3.2: "Core+tail" simplified models. The total density is the superposition of a well-bound component and loosely-bound ones. A semi-phenomenological density (Eq. (3.31)) is used for the core density, whereas the halo part is composed of realistic states obtained from spherical HFB calculations with the {SLy4+REG-M} functional.

A similar discussion naturally appeared in the context of designing an effective field theory (EFT) for weakly-bound nuclei [321], where two energy scales (E, E') were found to be relevant, i.e. (i) the nucleon separation energy $E = S_n$ which drives the asymptotic behavior of the one-body density, and (ii) the core excitation energy $E' = |\epsilon_{m+1}|$ which needs to be such as $E' \gg E$, in order for the tail orbitals to be well decorrelated from the remaining core. The additional energy scale that we presently identify is the energy spread ΔE of low-lying states in the $(N-1)$-body system, which becomes relevant when more than one component is involved in the halo. To obtain a coherent picture, dynamical properties of such low-lying excitations should be explainable through a model making use of a few degrees of freedom outside a (almost) frozen core. The corresponding picture is displayed in the bottom panel of Fig. 3.3 and is also translated in terms of canonical energies e_i in the upper panel of the same figure. More quantitatively, the ideal situation for the formation of a halo is obtained for (i) a very small separation energy, in orders of a few hundred keVs. The empirical value of 2 MeV/$A^{2/3}$ from Refs. [280; 281] gives a good approximation of expected values, (ii) a narrow bunch of low-lying states, whose spread ΔE should not exceed about one MeV, and (iii) a large gap E' with the remaining states, at least four or five times the separation energy E. Those are only indicative values, knowing that there is no sharp limit between halo and non-halo domains.

3.3.3 Definition of the halo region

As discussed in the previous section, a halo will be characterized by a pronounced ankle in the density, due to the sharp crossing between aggregated low-lying components and upper-lying ones. Such a curvature translates into a peak in the second derivative of the (base-10) logarithmic profile ($\log_{10}$) of the one-body density, as seen in Fig. 3.4 for a schematic calculation. At the radius $r = r_{\max}$ corresponding to the maximum of that peak, core and tail contributions cross; i.e. they contribute equally to the total density. At larger radii, the halo, if it exists, dominates. Therefore, **we define the spatially decorrelated region as the region beyond the radius r_0 where the core density is one order of magnitude smaller than the halo one**. In practice, the previous definition poses two problems. First, in realistic calculations, one

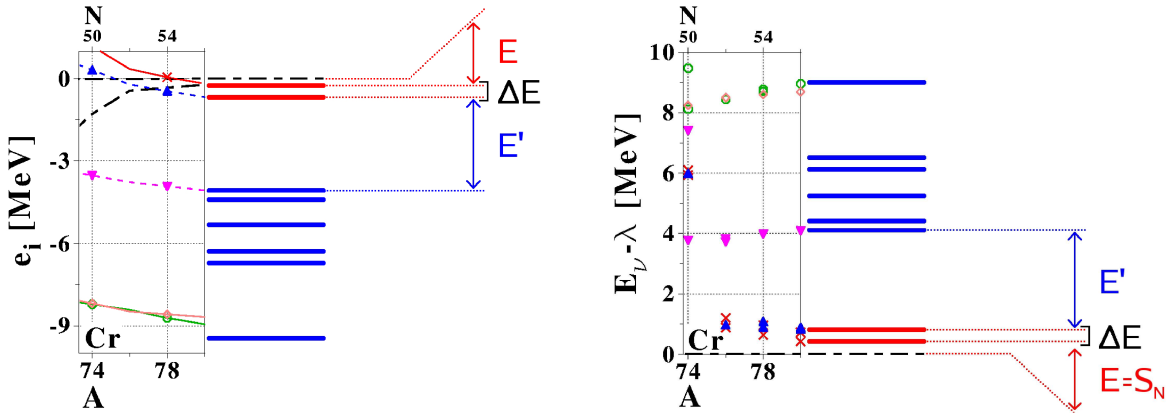

(a) Canonical neutron energy spectrum e_i.

(b) Separation energy spectrum $|\epsilon_\nu|$ for the $(N-1)$-body system.

Figure 3.3: Schematic display of energy scales relevant for the appearance of halos (right-hand side). The realistic spectra obtained through HFB calculations of the four last bound chromium isotopes are shown on the left-hand sides.

only accesses the total density. Second, the choice of one order of magnitude is somewhat arbitrary.

Simulations can be performed to characterize r_0 unambiguously. Let us start with a very crude toy model, where everything is analytical. The total density ρ is assumed to be a superposition of a core ρ_c and a tail ρ_h, both taking the form

$$\rho_i(r) = A_i\,\kappa_i\,e^{-\kappa_i\,r}\,. \tag{3.26}$$

This amounts to considering that the asymptotic regime is reached in the region of the crossing between ρ_c and ρ_h, and neglecting for now the r^{-2} factor. In this model the second-order (base-10) log-derivative of the total density is analytical, as well as the exact positions of (i) its maximum $r_{\max}$, and (ii) the point r_0 where the halo density is exactly equal to ten times the core one. Then, the ratio $\mathcal{R}(r_0) = \log''_{10}\,\rho(r_0)/\log''_{10}\,\rho(r_{\max})$ can be evaluated and becomes in the weak binding limit of interest $\kappa_h/\kappa_c \to 0$

$$\mathcal{R}(r_0) \underset{\kappa_h/\kappa_c\to 0}{\longrightarrow} \frac{40}{121} + \mathcal{O}\left[\left(\frac{\kappa_h}{\kappa_c}\right)^2\right]\,. \tag{3.27}$$

This shows that the position where there is a factor of ten between ρ_c and ρ_h is equivalently obtained by finding the position where there is a given ratio between the value of the second-order log-derivative of the density and its maximal value. The critical value $40/121 \approx 0.33$ found in the toy model is not believed to be accurate for complex nuclei, as (i) the asymptotic regime is not reached at the crossing point and is more complicated because of the r^{-2} factor, and (ii) the total density is a superposition of more than two components. However, we expect the one-to-one correspondence between ratios on the densities and ratios on $\log''_{10}\,\rho$ to hold in realistic cases. Thus, *the position where the halo dominates the core by one order of magnitude can be found using* $\log''_{10}\,\rho$ *as the only input.*

More realistic model calculations have been used to characterize the position of r_0. The total density is taken as a linear combination of core and halo contributions. Their relative normalizations are free parameters in this simulation, allowing to artificially change the fraction

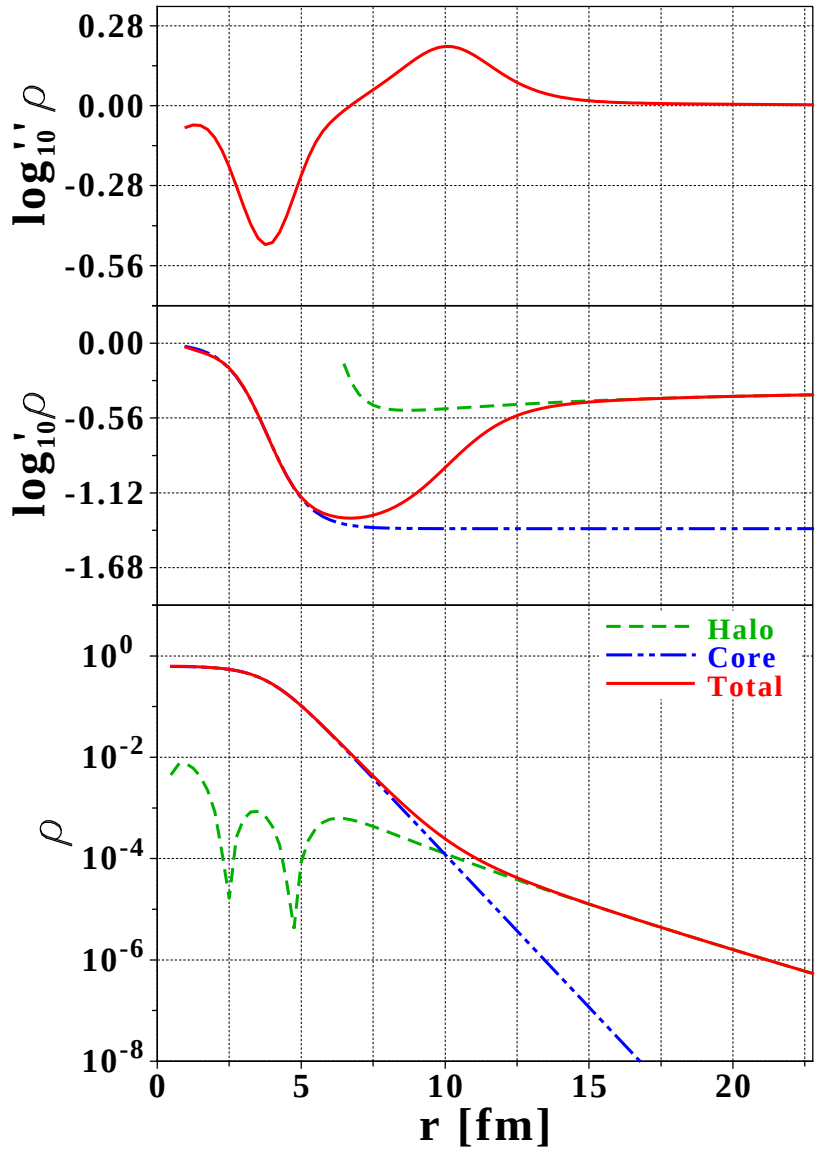

Figure 3.4: Ankle in the (base-10) log-density due to the presence of a low-lying state well separated from remaining ones: log-density (bottom panel), first (middle panel) and second (top panel) log-derivatives. Conventions are the same as in Fig. 3.2.

of halo in the total density, i.e.

$$\rho_{\rm tot}(r) = N_c\,\rho_c(r) + \sum_{\nu=1}^{m} N_\nu\,\rho_\nu(r)\,, \tag{3.28}$$

where N_c and $N_h = \sum_{\nu=1}^{m} N_\nu$ are the number of nucleons in the core part and in the halo part, respectively. Densities ρ_c and ρ_ν are normalized to one. We considered (i) simple models, where core and each halo components are defined as

$$\begin{cases} \rho_i(r) = \dfrac{1}{\mathcal{N}_i} & r < R_0\,, \\[2ex] \rho_i(r) = \dfrac{1}{\mathcal{N}_i} e^{\frac{R_0 - r}{a_i}} & r > R_0\,, \end{cases} \tag{3.29}$$

$\mathcal{N}_i$ standing for a normalization constant. This model only accounts for the basic features of the nuclear density, namely a uniform core of radius R_0 and a spatial extension becoming larger as $a_i \to 0$, (ii) double Fermi models, where the unphysical sharp edge in the logarithmic representation of the previous density is smoothened out using

$$\rho_i(r) = \frac{\rho_0}{1 + e^{\frac{r - R_0}{a_i}}}\,, \tag{3.30}$$

(iii) semi-phenomenological models, which fulfill the asymptotic behavior of Eq. (3.24). Core and tail densities vanish at $r = 0$, as well as their derivatives with respect to x, y and z, in order to avoid singularities at the nucleus center [322]. Such densities can be adjusted on experimental data [323–325]. The core part was defined as

$$\rho_c(r) = \frac{\rho_{0,c}}{1 + \frac{1}{2^\alpha}\left[1 + \left(\frac{r}{R_{0,c}}\right)^2\right]^\alpha \left[e^{\frac{r - R_{0,c}}{a_c}} + e^{\frac{-r - R_{0,c}}{a_c}}\right]}\,, \tag{3.31}$$

where $\alpha = 1$ for neutrons, and the halo density as

$$\rho_h(r) = \rho_{0,t}\left[\frac{r^2}{\left(r^2 + R_{0,t}^2\right)}\right] e^{-\frac{r}{a_t}}\,, \tag{3.32}$$

and (iv) more realistic models, where the core density is still defined as in Eq. (3.31), but halo contributions are realistic wave functions taken from self-consistent EDF calculations of Cr and Sn isotopes.

Results from a wide panel of test cases, using either one or several contributions to the halo density, and covering large energy ranges for E, E' and ΔE, are presented in Fig. 3.5. We recall that r_0 is defined as the radius for which $\rho_h(r_0) = 10\rho_c(r_0)$. The goal is to determine such a radius through the value of another ratio: $\mathcal{R}(r_0)$. For each simulation, the position r_0 and the ratio $\mathcal{R}(r_0)$ are computed. The main panel of Fig. 3.5 shows the distribution of $\mathcal{R}(r_0)$ which is peaked around 0.4. This value is greater than in the toy model case for the reasons detailed above. The distribution of $\mathcal{R}(r_0)$ is asymmetric, but the tail towards high values corresponds precisely to non-halo systems. In any case, we are going to reflect such an asymmetry into the choice of theoretical uncertainties in the determination of r_0. Inserts of Fig. 3.5 display the distribution of ratio r/r_0 corresponding to a given value of $\mathcal{R}(r)$. The ratio $\mathcal{R}(r) = 2/5$

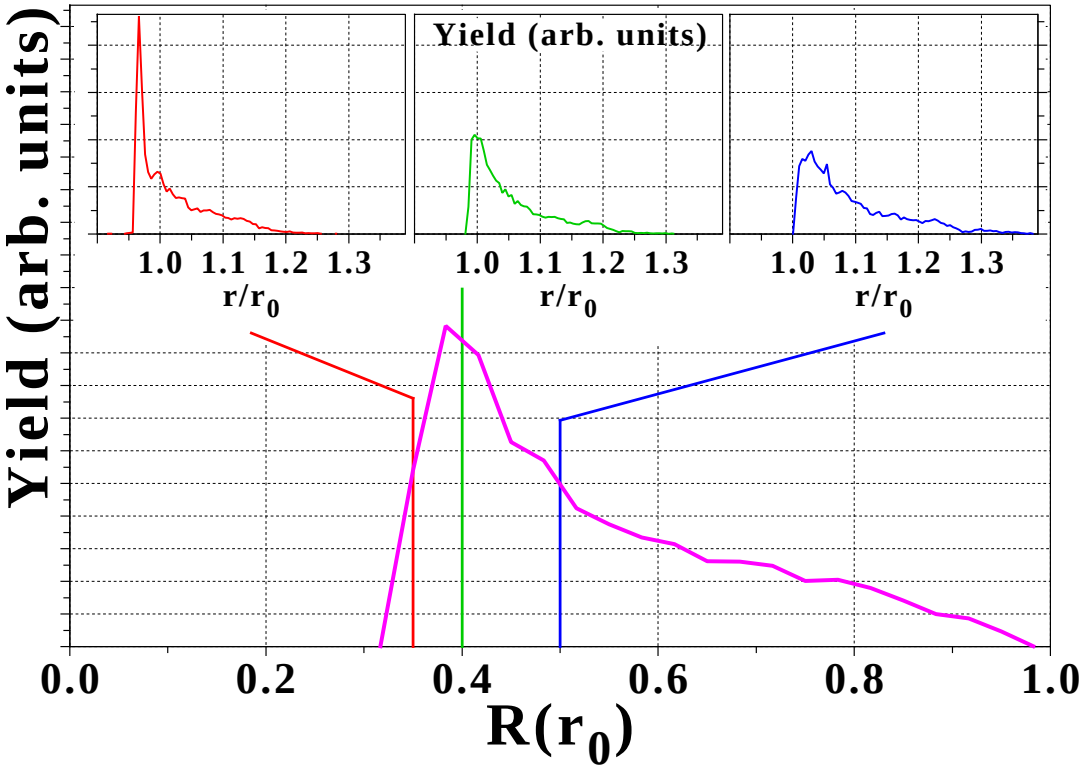

Figure 3.5: [Main panel] Ratio between the second-order log-density at r_0 and its peak value $\log''_{10}\,\rho(r_{\max})$ [Top panels] Distribution of r/r_0 for which $\mathcal{R}(r)$ is equal to a given value (left panel: $\mathcal{R}(r) = 0.35$, middle panel: $\mathcal{R}(r) = 0.4$, right panel: $\mathcal{R}(r) = 0.5$), and r_0.

(top-center panel) indeed picks out quite consistently the radius r_0. For $\mathcal{R}(r) = 40/121$ (top-left panel), the position r is in most cases below r_0. As a consequence, the average ratio between tail and core components in the density will be consistently below ten in this case. On the contrary for $\mathcal{R}(r) = 1/2$ (top-right panel), r is systematically larger than r_0, meaning that the ρ_h/ρ_c larger than ten on the average. In the end, it appears that r_0 is indeed well picked out through the condition

$$\mathcal{R}(r_0) = \frac{2}{5}\,. \tag{3.33}$$

We also use $\mathcal{R}(r)$ to evaluate error bars on the determination of r_0. Of course, we need to account for the fact that a difference by one order of magnitude between core and halo densities to define the halo region is somewhat arbitrary and that the corresponding radius r_0 cannot be perfectly picked out in all cases through Eq. (3.33). As a result, we add a tolerance margin to the definition of r_0 by allowing $\mathcal{R}(r_0)$ to vary between 0.35 and 1/2. The upper margin is greater than the lower one to account for the asymmetry of the peak in Fig. 3.5. Note that the procedure chosen to determine r_0 combined with that asymmetry puts us on the safe side, i.e. the radius found through that procedure, if not perfect, is likely to be too large, leading to a slight underestimation of the halo factors N_{halo} and δR_{halo} that we are defining in the following.

Given $r_{\max}$, which can be extracted from the total density, r_0 can then be reliably defined through

$$\begin{cases} r_0 > r_{\max}\,, \\ \left.\dfrac{\partial^2 \log_{10}\rho(r)}{\partial r^2}\right|_{r\,=\,r_0} \equiv \dfrac{2}{5}\left.\dfrac{\partial^2 \log_{10}\rho(r)}{\partial r^2}\right|_{r\,=\,r_{\max}}\,, \end{cases} \tag{3.34}$$

as exemplified in FIG. 3.6. Theoretical uncertainties on the determination of r_0 are introduced, such that

$$0.35 \leq \frac{\log''_{10}(\rho(r_0))}{\log''_{10}(\rho(r_{\max}))} \leq 0.50\,, \tag{3.35}$$

where $'$ is the compact notation for $\partial/\partial r$.

Once validated by simulations, the method to isolate the halo region only relies on the density as an input, and does not require an *a priori* separation of the one-body density into core and halo parts. Finally, one may note that our definition of the halo region does not a priori exclude contributions from components with angular momenta greater than one.

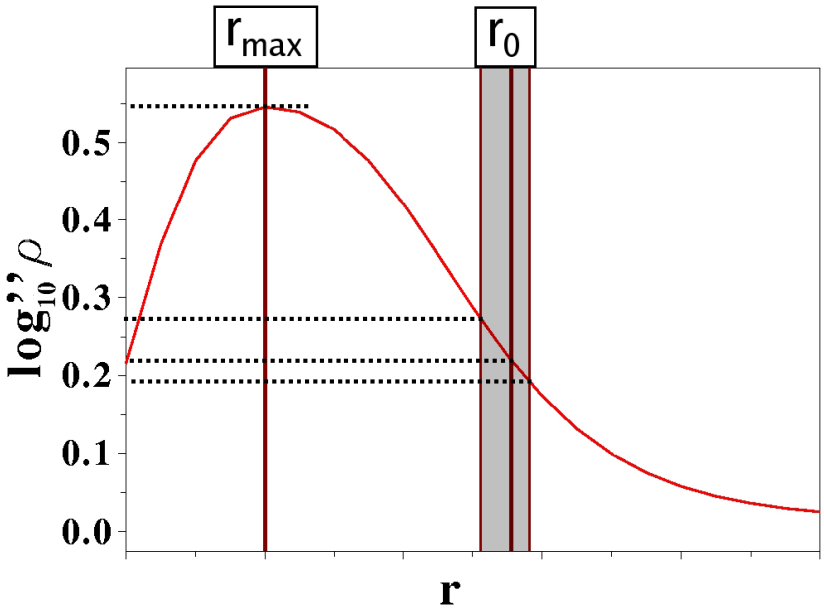

Figure 3.6: Definition of r_0 through the second derivative of the log-density. r_0 is represented by the central vertical line. The shaded area corresponds to the tolerance margin on r_0 (see text).

3.3.4 Quantitative halo criteria

We now introduce several criteria to characterize the halo in a quantitative way, by applying the previous analysis to the neutron one-body density[9]. First, the average number of nucleons in the halo region can be extracted through

$$N_{\text{halo}} \equiv 4\pi \int_{r_0}^{+\infty} \rho^n(r)\, r^2\, \mathrm{d}r\,. \tag{3.36}$$

[9]For neutron-rich medium-mass nuclei, protons are well confined in the nuclear interior, thus do not participate in the long-range part of the total density ρ. The two densities ρ and ρ^n can be used regardless to evaluate N_{halo} and δR_{halo}.

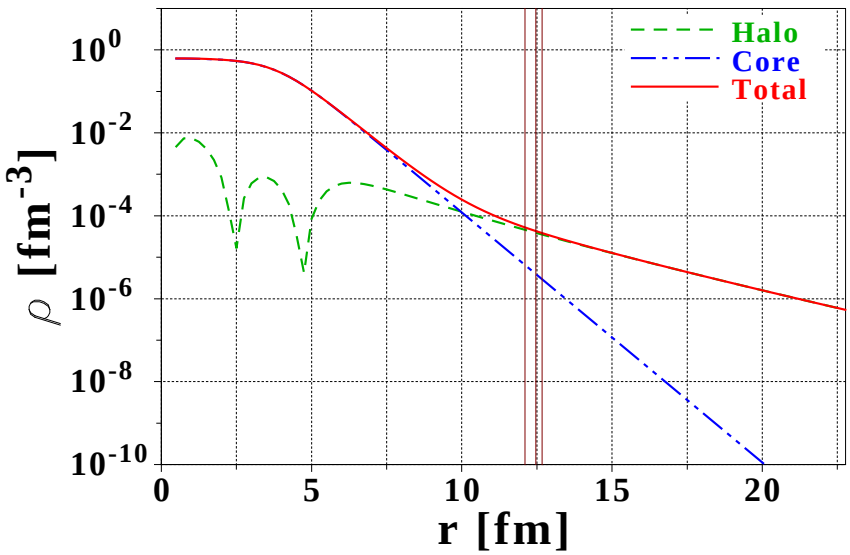

Figure 3.7: Consequences of the definition of r_0 (vertical lines for the values of r_0 and the tolerance margin - see text) in the same model as in FIG. 3.4. The halo density dominates the core part by around one order of magnitude.

An important information is the effect of the halo region on the radial moments of the density. By definition, the contribution of the core to any moment $\langle r^n \rangle$ is negligible for $r \geq r_0$[10]. Thus, one can evaluate the effect of the decorrelated region on the nuclear extension through

$$\delta R_{\text{halo}} \equiv R^n_{\text{r.m.s.,tot}} - R^n_{\text{r.m.s.,inner}} = \sqrt{\frac{\int_0^{+\infty} \rho^n(r) r^4 \, \mathrm{d}r}{\int_0^{+\infty} \rho^n(r) r^2 \, \mathrm{d}r}} - \sqrt{\frac{\int_0^{r_0} \rho^n(r) r^4 \, \mathrm{d}r}{\int_0^{r_0} \rho^n(r) r^2 \, \mathrm{d}r}} \, . \tag{3.37}$$

The quantity δR_{halo} is similar to ΔR_{halo} defined within the Helm model (EQ. (2.7)). However, the former does not rely on any a priori decomposition of the density into core and halo components. That is of critical importance. Extensions to all radial moments of the density can be envisioned[11]. The quantities N_{halo} and δR_{halo} are of course correlated, but they do not carry exactly the same information. The latter feature will strongly manifest itself when dealing with systematic calculations over the nuclear landscape (see SEC. 4.4). Note that tolerance margins on r_0 from EQ. (3.35) propagate into theoretical uncertainties on N_{halo} and δR_{halo}. In the case of stable/non-halo nuclei, both quantities will be extremely small. There is still a slight curvature in the density profile that provides a radius r_0 but the computed criteria will be consistent with zero. In the particular case of magic neutron number, the curvature becomes particularly weak and translates into a very broad peak in the second log-derivative. As a result, the radius r_0 value is large and defines a region where the density is particularly low. This is illustrated by FIG. 3.8, where r_0 is plotted for chromium isotopes as a function of A. The maximum of r_0 is attained for the magic shell $N = 50$.

[10] It has been checked in the case of the r.m.s. radius, and is all the more true as n increases.

[11] However, numerical issues appear when going to high order moments. Indeed, $\langle r^n \rangle$ is more and more sensitive to the upper limit of integration as n increases. Thus, the result may significantly depend on the box size used to discretize the continuum or on the size of the basis used to expand quasiparticle wave functions in HFB calculations.

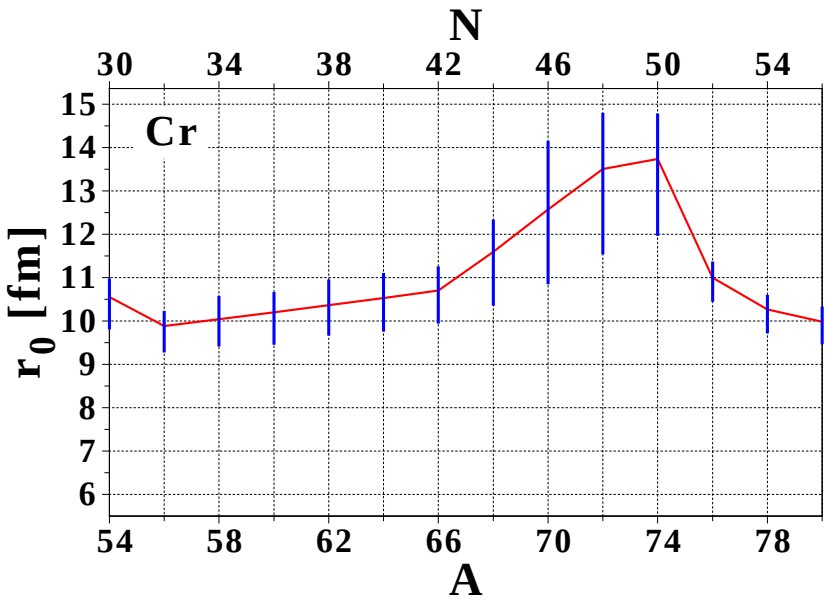

Figure 3.8: Evolution of r_0 along the Cr isotopic chain, obtained through spherical HFB calculations with the {SLy4+REG-M} functional.

Finally, further characterization of the halo can be achieved by looking at individual contributions of each overlap function, i.e.

$$N_{\text{halo},\nu} \equiv 4\pi\,(2j_\nu^n + 1) \int_{r_0}^{+\infty} |\bar{\varphi}_\nu^n(r)|^2\, r^2\, \mathrm{d}r\,. \tag{3.38}$$

$N_{\text{halo},\nu}$ provides a decomposition of the halo in terms of single-particle-like states. Note that the $r < r_0$ part of each overlap function naturally does not contribute to halo observables. By analogy with the criterion used for light halo systems, the probability of each individual overlap function φ_ν to be in the $r \geq r_0$ region can also be defined through

$$P_\nu \equiv \frac{\displaystyle\int_{r_0}^{+\infty} |\bar{\varphi}_\nu(r)|^2\, r^2\, \mathrm{d}r}{\displaystyle\int_{0}^{+\infty} |\bar{\varphi}_\nu(r)|^2\, r^2\, \mathrm{d}r}\,. \tag{3.39}$$

Chapter 4

Results

Abstract: The new analysis method that we have devised for the analysis of halo properties is now applied to nuclear many-body systems. Although some precautions are needed to properly define internal degrees of freedom for SR-EDF calculations, the formation of halos can be precisely quantified for specific isotopic series, before large-scale calculations over the whole nuclear chart are performed, and allow one to identify several spherical halo candidates. However, the sensibility of these properties to the ingredients of the EDF need to be carefully studied, in particular the influence of pairing correlations on the formation of halos. Eventually, the model-independence of the analysis method is highlighted on other quantum many-body systems.

Contents

4.1 Implementation of the method **92**
4.1.1 Intrinsic overlaps in EDF calculations 92
4.1.1.1 Slater determinant as an auxiliary state 92
4.1.1.2 Quasiparticle vacuum as an auxiliary state 92
4.1.2 Numerical implementation of halo criteria 94
4.2 Formation of halos in medium-mass nuclei **94**
4.2.1 Results for specific isotopic series 94
4.2.1.1 Cr isotopes 94
4.2.1.2 Sn isotopes 98
4.2.2 Convergence of the calculations 105
4.2.2.1 Box radius 106
4.2.2.2 Angular-momentum truncation 106
4.2.2.3 Energy cutoff 107
4.3 Impact of the Skyrme EDF **110**
4.4 Large-scale calculations **111**
4.5 Role of pairing correlations **116**
4.5.1 Pairing anti-halo effect 116
4.5.2 Decorrelation from pairing field 119
4.5.3 Importance of low densities 120
4.6 Model-independence of the method **124**
4.6.1 Light nuclei 124
4.6.2 Atom-positron/ion-positronium complexes 126
4.6.3 Universality of the phenomenon 127

4.1 Implementation of the method

4.1.1 Intrinsic overlaps in EDF calculations

In Chap. 3, the energies ϵ_ν^q that characterize internal overlap functions denote exact nucleon separation energies. No approximation to the nuclear many-body problem was involved in the analysis. Thus, patterns extracted from the internal one-body density are fully general and model-independent. In practice of course, one uses an approximate treatment of the N-body problem. This raises some issues for the specific case of EDF calculations.

First, an important clarification regarding the physical interpretation of the quantities at play in the calculations must be carried out. In single-reference realizations of EDF, one deals with a so-called "intrinsic" one-body density, in the sense that it is built from an *auxiliary* state that explicitly breaks intrinsic symmetries of the Hamiltonian, e.g. translational, rotational and gauge invariances. This intrinsic density is associated with a wave packet from which true eigenstates, and their laboratory and internal densities, can be recovered by restoring broken symmetries through multi-reference EDF calculations [77]. Still, the intrinsic density at play in SR-EDF calculations and the internal density associated with the true eigenstate of interest are different[(1)] [326]. However, it is customary in SR-EDF calculations to use the intrinsic density as if it were the true internal one; e.g. when analyzing electron scattering data. It is motivated by the fact that asymptotic equations (Eq. (3.14)) verified by internal overlap functions are also satisfied by HFB quasiparticle wave functions. Therefore the latter obey the same type of (crossing) patterns as exact internal overlap functions.

The identification between internal and intrinsic quantities acts at the one-body density level. Then, it translates into mapping HF/HFB wave functions with internal overlap functions. As a result, the smallest energy $|\epsilon_0^q|$ relates to the exact separation energy. This is an analogue to Koopmans' theorem derived originally in the case of the Hartree-Fock approximation. On the other hand, rearrangement terms come into play to be able to match energies extracted from Eq. (1.30) with exact separation energies. Considering the customary identification of intrinsic and internal densities, we apply in the present work our new analysis method to the intrinsic density whenever results from SR-EDF calculations are used. Of course, such an identification is not rigourously justified and formulations of EDF methods directly in terms of the internal density are currently being considered[(2)] [227].

4.1.1.1 Slater determinant as an auxiliary state

In the implementation of the EDF method based on a Slater determinant, *explicit* spectroscopic factors are either zero or one, and behave according to a step function, that is $S_\nu^q = \Theta(\epsilon_F^q - e_\nu^q)$. Single-particle orbitals φ_ν^q play the role of overlap functions and the density takes the form given by Eq. (3.21).

4.1.1.2 Quasiparticle vacuum as an auxiliary state

In the implementation of the EDF method based on a quasiparticle vacuum, the one-body density can be evaluated using either canonical states ϕ_i^q or lower components V_ν^q of the quasiparticle

[1] In the shell model, the internal wave function is explicitly computed when the center-of-mass part of the N body wave function can be mapped onto a $0s$ state.

[2] The SR-EDF method, as it is applied to self-bound nuclei, might be not related to an existence theorem *à la* Hohenberg-Kohn.

states, i.e.

$$\rho^q(r) = \sum_i \frac{2j_i^q+1}{4\pi}\, {v_i^q}^2\, |\bar{\phi}_i^q(r)|^2 = \sum_\nu \frac{2j_\nu^q+1}{4\pi}\, |\bar{V}_\nu^q(r)|^2 \,. \tag{4.1}$$

Within such a scheme, the lower component of each quasiparticle eigenstate extracted through Eq. (1.30) approximates the exact internal overlap functions leading from the ground state of the N-body system to the corresponding excited state of the $(N-1)$-body system [(3)]. Also, spectroscopic factors S_ν^n identify with quasiparticle occupations N_ν^n as defined by Eq. (1.47). This underlines that the implementation of the EDF approach based on a quasiparticle vacuum incorporates *explicitly* parts of the spreading of the single-particle strength [328].

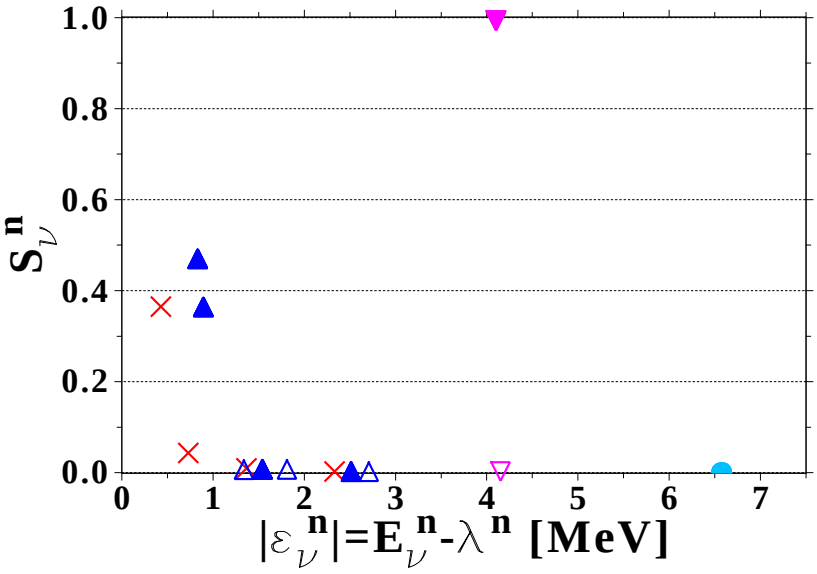

Figure 4.1: Neutron quasiparticle occupation as a function of the separation energy in ^{80}Cr, calculated with the {SLy4+REG-M} functional. Conventions from Fig. 8 are used to label individual quasiparticle states. Only quasiparticles with occupations N_ν^n greater than 10^{-3} are displayed.

The function $S_\nu^n = f(|\epsilon_\nu^n|)$, whose typical behavior is presented in Fig. 4.1 for ^{80}Cr, takes values between zero and one. The difference between hole-like quasiparticle excitations and particle-like ones is visible. Indeed, S_ν^n increases with excitation energy $|\epsilon_\nu^n|$ for hole-like excitations. This constitutes the main branch which tends towards a step function when correlations are not explicitly included into the auxiliary state; i.e. for the EDF approach based on an auxiliary Slater determinant. On the other hand, spectroscopic factors of particle-like quasiparticle excitations remain small and go to zero for high-lying excitations.

[3]It can be shown that the perturbative one-quasiparticle state ${\beta_i}^\dagger|\Phi\rangle$ contains $N + {u_i}^2 - {v_i}^2$ particles on the average if $|\Phi\rangle$ is constrained to N particles on the average. It is only for deep-hole quasiparticle excitations ($v_i^2 \approx 1$) that the final state will be a good approximation of the $(N-1)$-body system. The correct procedure, that also contains some of the rearrangement terms alluded to above, consists of (i) constructing each one-quasiparticle state self-consistently by breaking time-reversal invariance and requiring $(N-1)$ particles in average, or (ii) creating the quasiparticle excitation on top of a fully paired vacuum designed such that the final state has the right average particle number [131; 327]. Overlap functions and spectroscopic factors would have to be computed explicitly in such a context.

4.1.2 Numerical implementation of halo criteria

The HFB problem is solved in a spherical box, that is all densities are computed up to a distance R_{box} from the center of the nucleus, on a radial mesh of step size $\Delta r = 0.25$ fm. For $R_{\text{box}} = 40$ fm, the mesh has 160 points in the radial direction, for both individual wave functions and densities. To obtain a satisfactory precision, the second order log-derivative is computed using a five-points difference formula [320]. The precision of the formula is then the same as the intrinsic precision of the Numerov algorithm used for the integration of second-order differential equations (which is $\mathcal{O}\left(\Delta r^6\right)$) [175; 182]. Approximate positions of the maximum of the second order log-derivative of $\rho^n(r)$ and of r_0 are first determined with a simple comparison algorithm. To increase the precision, a 11-points polynomial spline approximation to the density and its second log-derivative around the two points of interest is performed. Because the functions involved are regular enough, a spline approximation provides the radii r_{max} and r_0 with a good precision, as they are obtained using a dichotomy procedure up to a (arbitrary) precision of 10^{-5}. Finally, integrations necessary to compute N_{halo} and δR_{halo} are performed with six-points quadrature rules.

In the definition of δR_{halo}, the core contribution to the total r.m.s. radius is approximated as the root-mean-square radius of the density distribution truncated to $r < r_0$. To check the influence of this cut, the core density was extrapolated beyond the point where the second order log-derivative crosses zero[4] using Eq. (3.24) and enforcing continuity of ρ^n and $\rho^{n\prime}$. No difference was seen for δR_{halo}. Individual contributions $N_{\text{halo,i}}$, as well as the individual probabilities P_i, are evaluated in the canonical basis. Equivalently, $N_{\text{halo},\nu}$ and P_ν can be calculated in the quasiparticle basis. Quasiparticle states are the best approximation to the overlap functions, but canonical and quasiparticle bases really constitute two equivalent pictures. Indeed, each canonical state is, roughly speaking, split into quasiparticle solutions of similar energies. A summation of quasiparticle contributions having the same quantum numbers in a given energy range would allow to recover the single-particle canonical approximation. The latter is preferred here, as it is more intuitive to work in the natural basis.

4.2 Formation of halos in medium-mass nuclei: first examples

4.2.1 Results for specific isotopic series

4.2.1.1 Cr isotopes

According to the qualitative analysis of Sec. 3.3.1, drip-line chromium isotopes appear to be ideal halo candidates. The separation energy spectrum $|\epsilon_\nu^n| = E_\nu^n - \lambda^n$ to the states in the $(N-1)$-body system is shown in Fig. 4.2. Tab. {4.1} displays the canonical and quasiparticle spectra for the drip-line nucleus ^{80}Cr. In the canonical basis, $|e_0^n|$ is associated with a $3s_{1/2}$ state and is about 180 keV. The next low-lying state ($2d_{5/2}$) is within an energy interval of $\Delta E \approx 500$ keV. Those two states are separated from a core of orbitals by $E' \approx 3.5$ MeV. Equivalently, the separation energy in the quasiparticle basis is $|\epsilon_0^n| \approx 430$ keV, whereas four quasiparticle states (two $s_{1/2}$ and $d_{5/2}$) are present with an energy spread of $\Delta E \approx 470$ keV, and are further separated from higher-excited states by $E' \approx 3.2$ MeV. The separation energy S_n for ^{80}Cr is compatible with the phenomenological binding energy suggested for light halo nuclei, namely 2 MeV$/A^{2/3} \approx 137$ keV. According to the discussion of Sec. 3.3.2, energy scales at play in the three last bound Cr isotopes correspond to ideal halo candidates.

[4] This is the point where the halo contribution effect becomes significant.

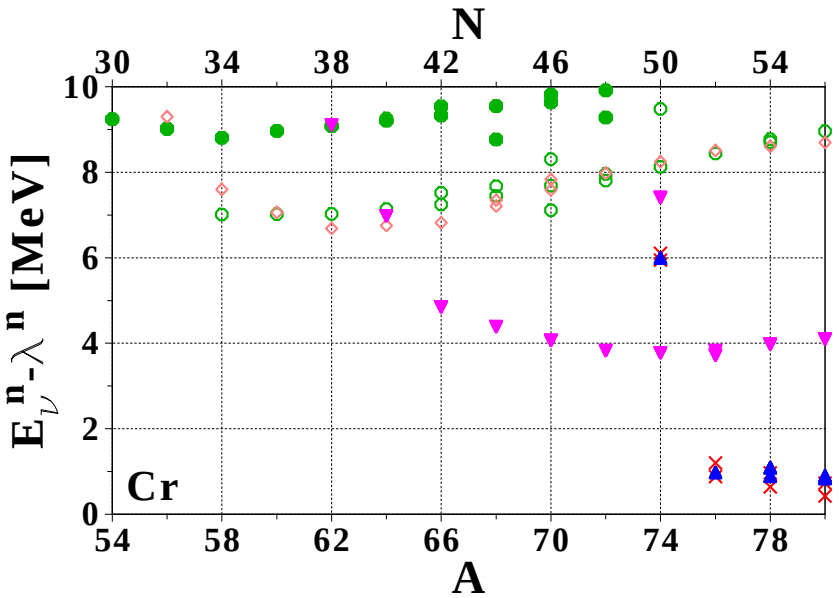

Figure 4.2: Neutron separation energies $|\epsilon_\nu^n| = E_\nu^n - \lambda^n$ along the Cr isotopic chain, obtained through spherical HFB calculations with the {SLy4+REG-M} functional. Only relevant quasiparticle energies ($N_\nu^n > 0.01$) are displayed. Conventions for labeling individual states are found in FIG. 8.

Can. spectrum ^{80}Cr		Exc. spectrum ^{79}Cr	
	e_i^n [MeV]		$E_\nu^n - \lambda^n$ [MeV]
———	> 0		> 10
$E \updownarrow$		$f_{5/2}$	8.694
ΔE $3s_{1/2}$	-0.178	$p_{1/2}$	8.960
$2d_{5/2}$	-0.670	$g_{9/2}$	4.103
E'		E'	
		$d_{5/2}$	0.893
$1g_{9/2}$	-4.062	ΔE $d_{5/2}$	0.832
$1f_{5/2}$	-8.676	$s_{1/2}$	0.728
$1f_{5/2}$	-8.676	$s_{1/2}$	0.427
$2p_{1/2}$	-8.942	$E \updownarrow$	
	< -10	———	0

Table 4.1: Neutron canonical energies e_i^n in ^{80}Cr and separation energies $|\epsilon_\nu^n| = E_\nu^n - \lambda^n$, using the {SLy4+REG-M} EDF. Quasiparticle states with a spectroscopic factor smaller than 10^{-2} are not included.

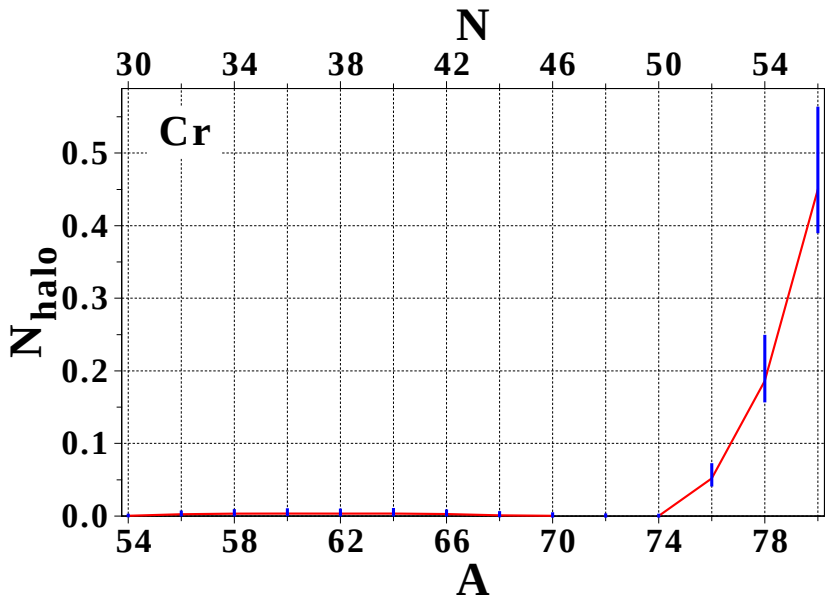

Figure 4.3: Average number of nucleons participating in the halo along the Cr isotopic chain, as a function of the nuclear mass, as predicted by the {SLy4+REG-M} functional. Theoretical uncertainties are included (see text).

The criteria introduced in Sec. 3.3.1 are now calculated. Fig. 4.3 shows the average number of nucleons participating in the potential halo. Whereas N_{halo} is consistent with zero for $N \leq 50$, a sudden increase is seen beyond the $N = 50$ shell closure. The appearance of a decorrelated region in the density of the last three Cr isotopes can be seen in the evolution of the neutron densities along the isotopic chain in Fig. 4.4. For $N > 50$, such a behavior translates into a non-zero value of N_{halo}. Numbers remains small for N_{halo}, as the decorrelated region is populated by ~ 0.45 nucleons on the average in ^{80}Cr, in comparison with the total neutron number. In absolute value however, N_{halo} is comparable to what is found in light s-wave halo nuclei like ^{11}Be, where roughly 0.3 nucleons constitute the decorrelated part of the density (see Sec. 4.6.1) [329]. The halo factor δR_{halo} is shown in Fig. 4.5 as a function of A. The halo contributes significantly to the total neutron r.m.s. radius (up to ~ 0.13 fm) beyond the $N = 50$ shell closure. The latter result can be recast as a splitting of the total r.m.s. radius into core and halo contributions, as displayed in Fig. 4.6. In comparison with the Helm model, shell effects are here properly separated from halo effects, e.g. the core r.m.s. radius includes a kink at $N = 50$ which is due to the filling of least bound states after a major shell closure and not to the halo *per se*. Only the physics related to the existence of truly decorrelated neutrons is extracted by N_{halo} and δR_{halo}. One may observe that the kink of the neutron r.m.s radius (i) was not assumed as a halo signature *a priori* [293; 330] but recovered *a posteriori*, and (ii) must be corroborated using finer tools such as N_{halo} and δR_{halo} to extract quantitatively the contribution of the halo to that kink.

To characterize further this halo region, individual contributions $N_{\text{halo,i}}$ are evaluated. Results are summarized in Tab. {4.2} and Fig. 4.7. As expected, the main contributions to the halo come from the most weakly-bound states, while for non-halo nuclei, like ^{74}Cr, all contributions are consistent with zero. At the neutron drip-line, important contributions are found from both $3s_{1/2}$ and $2d_{5/2}$ states. The latter $\ell = 2$ states contribute for almost 50% of the total number of nucleons in the decorrelated region, although this state is more localized than the $3s_{1/2}$ because of its binding energy and of the effect of the centrifugal barrier. Such hindrance effects are compensated by the larger canonical occupation of the $d_{5/2}$ states and the larger intrinsic

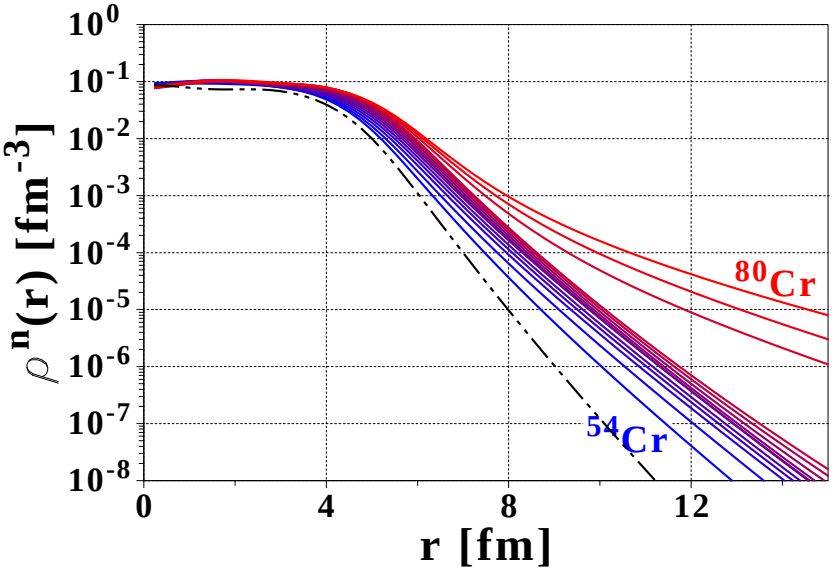

Figure 4.4: Neutron densities for even-even Cr isotopes, from ^{54}Cr to ^{80}Cr. The proton density of ^{54}Cr is given (dashed-dotted line) as a reference for the neutron skin.

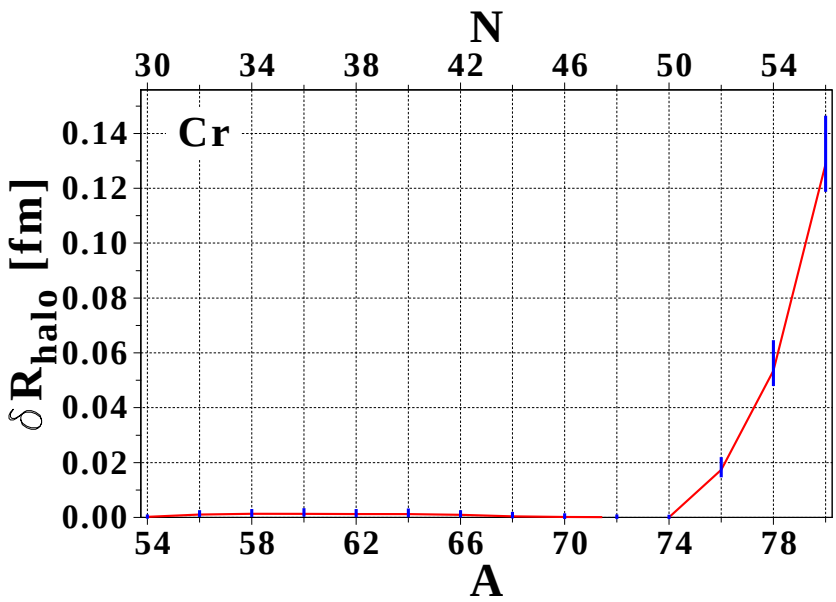

Figure 4.5: Halo factor parameter δR_{halo} in the Cr isotopic chain.

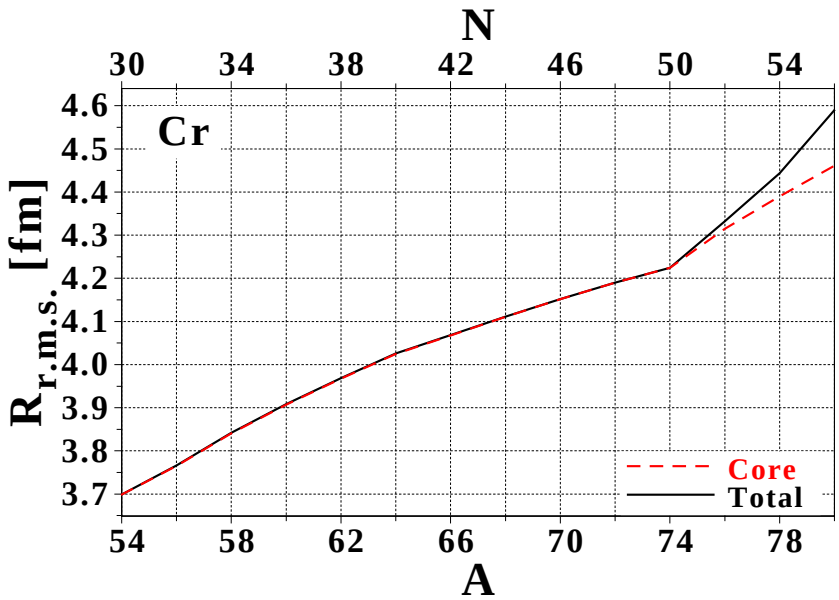

Figure 4.6: Total neutron root-mean-square radius (solid line) and core contribution (dashed line) for chromium isotopes, as predicted by the {SLy4+REG-M} functional.

degeneracy of the shell. The significant contribution of the $\ell = 2$ states could not be expected from the standard qualitative analysis presented in Sec. 2.1.1 or, with a few exceptions [261], from the experience acquired in light nuclei. Finally, the probability P_i for nucleons occupying the canonical state ϕ_i^n to be in the outer region $r \geq r_0$ in ^{80}Cr is typical of $s-$wave halo systems; i.e. 49% for the $3s_{1/2}$ state and a little bit lower for the $2d_{5/2}$ state, around 26%.

The analysis method applied to neutron-rich Cr isotopes demonstrates unambiguously that a halo is predicted for the last three bound isotopes. We have indeed been able to characterize the apparition of a decorrelated region in the density profile for isotopes beyond the $N = 50$ shell closure. Such a region contains a small fraction of neutrons which impact significantly the extension of the nucleus. It is generated by an admixture of $s_{1/2}$ and $d_{5/2}$ states, whose probability to be in that outer region $r \geq r_0$ are both compatible with what is seen in light halo nuclei. **This provides the picture of a rather *collective* halo building up at the neutron drip-line for Cr isotopes, in the sense that several single-particle orbitals contribute to it**.

4.2.1.2 Sn isotopes

So far, halo predictions in tin isotopes beyond the $N = 82$ shell closure [289] have been based on the Helm model, whose limitations have been pointed out in Sec. 2.2.2.2. The robust analysis tools introduced in the present work are expected to give more reliable results. Neutron densities of Sn isotopes do exhibit a qualitative change for $N > 82$, as seen in Fig. 4.8. However, the transition is smoother than in the case of chromium isotopes (Fig. 4.4). This is partly due the increase of collectivity associated with the higher mass. There are also specific elements of structure that will explain the absence of halo in drip-line Sn isotopes, as highlighted below. Tab. {4.3} displays the canonical and quasiparticle spectra for the drip-line nucleus ^{174}Sn. Energy scales at play are not compliant with the definition of a halo, as can also be seen from Fig. 4.9. In the canonical basis, the separation energy E is roughly 1.2 MeV, whereas six states with an energy spread $\Delta E \approx 3.8$ MeV are separated from a core of orbitals by a gap

	^{74}Cr			
	N_{halo}		$1.7.10^{-4}$	
	e_i^n [MeV]	$v_i^{n\,2}$	$N_{\text{halo,i}}$	P_i
$3s_{1/2}$	$+0.036$	0.000	0.000	0.0%
$2d_{5/2}$	-0.024	0.000	0.000	0.0%
$1g_{9/2}$	-3.618	1.000	0.001	0.1%
$2p_{1/2}$	-8.100	1.000	0.000	0.0%
$1f_{5/2}$	-8.400	1.000	0.000	0.0%
Other	< -10.0	—	$\sim 1.7.10^{-4}$	—
	^{76}Cr			
	N_{halo}		$5.2.10^{-2}$	
	e_i^n [MeV]	$v_i^{n\,2}$	$N_{\text{halo,i}}$	P_i
$3s_{1/2}$	$+0.356$	0.050	0.007	14.8%
$2d_{5/2}$	-0.209	0.311	0.039	12.6%
$1g_{9/2}$	-3.764	0.991	0.002	0.2%
$2p_{1/2}$	-8.416	0.998	0.000	0.0%
$1f_{5/2}$	-8.477	0.998	0.000	0.0%
Other	< -10.0	—	$\sim 2.2.10^{-3}$	—
	^{78}Cr			
	N_{halo}		0.186	
	e_i^n [MeV]	$v_i^{n\,2}$	$N_{\text{halo,i}}$	P_i
$3s_{1/2}$	$+0.052$	0.147	0.045	30.4%
$2d_{5/2}$	**-0.450**	**0.604**	**0.128**	**21.2%**
$1g_{9/2}$	-3.919	0.991	0.005	0.5%
$1f_{5/2}$	-8.576	0.998	0.001	0.1%
$2p_{1/2}$	-8.714	0.998	0.001	0.1%
Other	< -10.0	—	$\sim 6.2.10^{-3}$	—
	^{80}Cr			
	N_{halo}		0.450	
	e_i^n [MeV]	$v_i^{n\,2}$	$N_{\text{halo,i}}$	P_i
$3s_{1/2}$	**-0.178**	**0.421**	**0.207**	**49.3%**
$2d_{5/2}$	**-0.670**	**0.843**	**0.223**	**26.4%**
$1g_{9/2}$	-4.062	0.995	0.008	0.8%
$1f_{5/2}$	-8.676	0.999	0.001	0.1%
$2p_{1/2}$	-8.942	0.999	0.002	0.2%
Other	< -10.0	—	$\sim 9.4.10^{-2}$	—

Table 4.2: Contributions of the least bound canonical orbitals to the number of nucleons in the decorrelated region, and probabilities for those states to be in the outer region $r \geq r_0$. The data are provided for the four last (predicted) bound Cr isotopes.

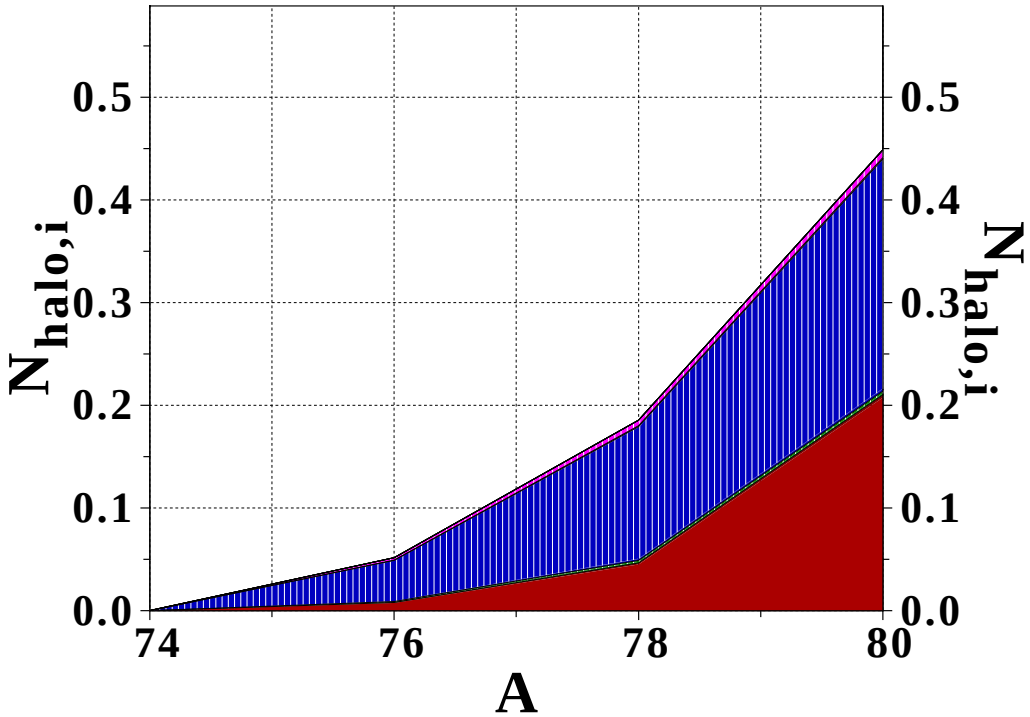

Figure 4.7: Decomposition of the halo region for chromium isotopes, as predicted by the {SLy4+REG-M} functional. Single-particle shading conventions are found in FIG. 8.

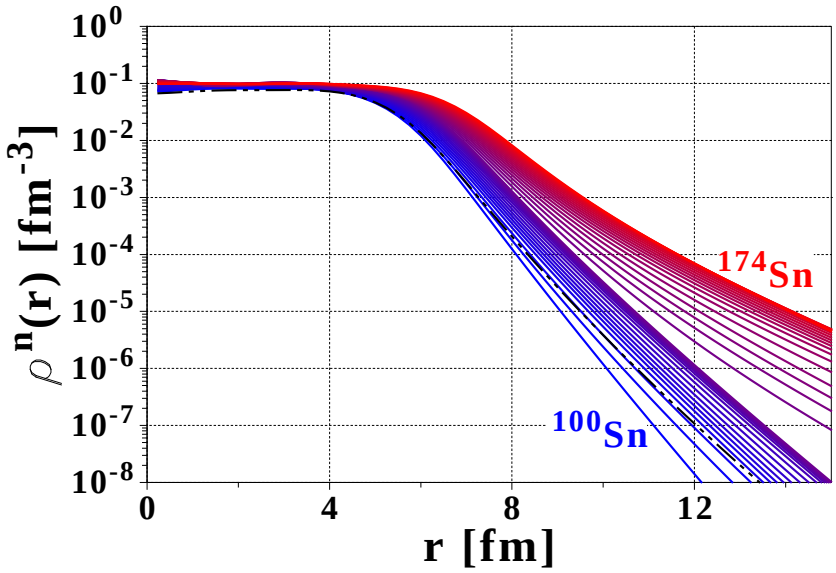

Figure 4.8: Same as FIG. 4.4 for Sn isotopes. The "separation" between the two groups of neutron densities occurs for $N = 82$. Proton density of ^{100}Sn is given as a reference in dashed-dotted line.

Can. spectrum ^{174}		Exc. spectrum ^{173}Sn	
	e_i^n [MeV]		$E_\nu^n - \lambda^n$ [MeV]
	> 0		> 15
		$d_{5/2}$	14.169
E		$d_{3/2}$	12.026
		$s_{1/2}$	11.967
$1i_{13/2}$	-1.208	$1h_{11/2}$	10.603
$3p_{1/2}$	-1.855		
$2d_{5/2}$	-2.227	E'	
ΔE $3p_{3/2}$	-2.665		
$1h_{9/2}$	-3.823		
$2f_{7/2}$	-5.014	$f_{7/2}$	4.937
		$f_{7/2}$	4.463
		$h_{9/2}$	3.890
		$p_{3/2}$	2.722
E'		$p_{1/2}$	2.648
		ΔE $p_{3/2}$	2.559
		$f_{5/2}$	2.290
		$f_{5/2}$	2.082
		$p_{1/2}$	1.905
$1h_{11/2}$	-10.575	$p_{1/2}$	1.610
$2d_{3/2}$	-12.581	$i_{13/2}$	1.502
$3s_{1/2}$	-12.747	E	
$2d_{5/2}$	-14.944		
	< -15		0

Table 4.3: Same as Tab. {4.1} for the neutron canonical energies of ^{174}Sn, and associated separation energies $|\epsilon_\nu^n|$ of ^{173}Sn.

$E' \approx 5.5$ MeV. Equivalently, in the quasiparticle basis one has (i) $S_n = E \approx 1.5$ MeV, (ii) four low-lying quasiparticles with a spread $\Delta E \approx 3.4$ MeV, and (iii) separated from higher excitations by $E' \approx 5.6$ MeV. In particular, the energy spread of low-lying states ΔE is too large to permit the formation of a halo. Also, according to the phenomenological criterion for light halo nuclei, the separation energy of ^{174}Sn should have been of the order of 2 MeV$/A^{2/3} \approx 64$ keV for a halo to emerge.

The N_{halo} parameter is displayed in Fig. 4.11. The maximum value of N_{halo}, around 0.18, is very small compared to the total number of nucleons. Absolute numbers are also smaller than the ones obtained in (lighter) Cr halos. We may add that the value of N_{halo} found here is of the same order of magnitude as that one encounters for a non-halo/one-neutron p-wave nucleus such as ^{13}Ne, where around 0.12 neutron out of six reside in average in the classically forbidden region [329]. An interesting feature is the decrease of N_{halo} for $N > 166$. This is a consequence of the filling of the highly degenerate $1i_{13/2}$ state right at the drip-line (see Fig. 2.4). As the number of neutrons occupying this $1i_{13/2}$ shell increases, the depth of the one-body potential also increases through self-consistency and shells become more bound, thus more localized. As this happens over a significant number of neutrons, the effect on N_{halo} is visible. This constitutes an additional

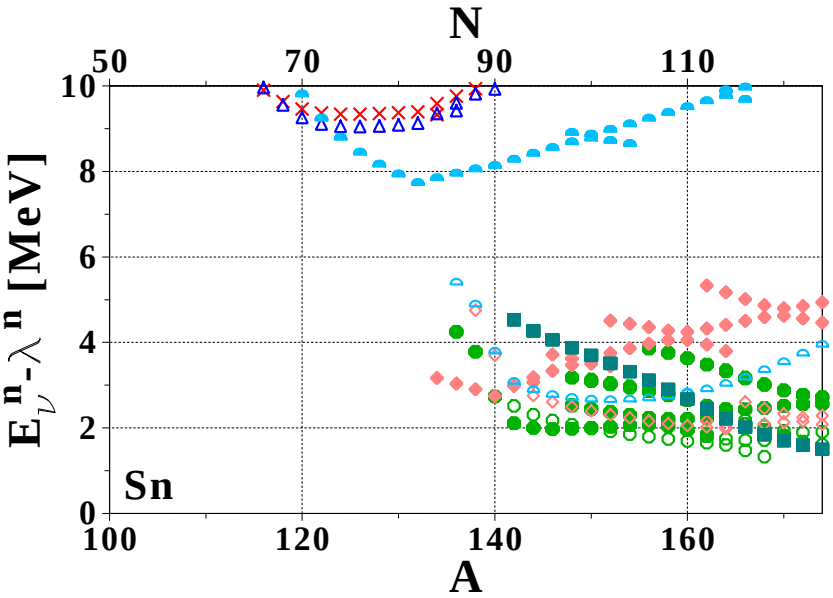

Figure 4.9: Same as Fig. 4.2 for neutron separation energies of Sn isotopes.

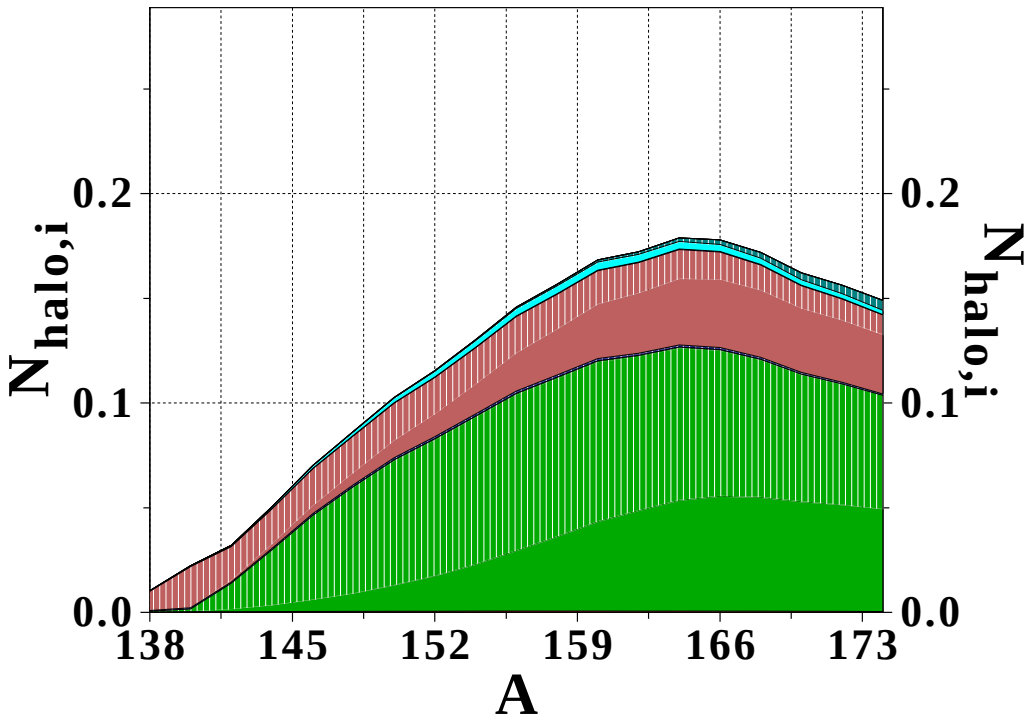

Figure 4.10: Same as in Fig. 4.7 for tin isotopes.

	^{132}Sn			
	N_{halo}		$0.13.10^{-2}$	
	e_i^n [MeV]	$v_i^{n\,2}$	$N_{\text{halo,i}}$	P_i
$1i_{13/2}$	+2.648	0.000	0.000	0.0%
$3p_{1/2}$	+2.489	0.000	0.000	0.0%
$2f_{5/2}$	+1.661	0.000	0.000	0.0%
$3p_{3/2}$	+1.240	0.000	0.000	0.0%
$1h_{9/2}$	+1.141	0.000	0.000	0.0%
$2f_{7/2}$	−1.785	0.000	0.000	0.0%
Other	< -7.0	—	$\sim 0.13.10^{-2}$	—
	^{146}Sn			
	N_{halo}		$0.71.10^{-1}$	
	e_i^n [MeV]	$v_i^{n\,2}$	$N_{\text{halo,i}}$	P_i
$1i_{13/2}$	+1.435	0.064	0.000	0.2%
$2f_{5/2}$	−0.056	0.155	0.004	2.4%
$3p_{1/2}$	−0.202	0.143	0.005	3.8%
$1h_{9/2}$	−0.401	0.262	0.001	0.3%
$3p_{3/2}$	−1.050	0.442	0.040	9.0%
$2f_{7/2}$	−3.037	0.923	0.017	1.9%
Other	< -7.0	—	$\sim 3.1.10^{-3}$	—
	^{164}Sn			
	N_{halo}		0.179	
	e_i^n [MeV]	$v_i^{n\,2}$	$N_{\text{halo,i}}$	P_i
$1i_{13/2}$	−0.216	0.349	0.002	0.5%
$3p_{1/2}$	−1.347	0.804	0.052	6.6%
$2f_{5/2}$	−1.481	0.155	0.032	4.0%
$3p_{3/2}$	−2.143	0.923	0.072	7.8%
$1h_{9/2}$	−2.503	0.894	0.003	0.4%
$2f_{7/2}$	−4.301	0.975	0.014	1.4%
Other	< -7.0	—	$\sim 4.7.10^{-3}$	—
	^{174}Sn			
	N_{halo}		0.149	
	e_i^n [MeV]	$v_i^{n\,2}$	$N_{\text{halo,i}}$	P_i
$1i_{13/2}$	−1.208	0.872	0.005	0.5%
$3p_{1/2}$	−1.854	0.979	0.049	5.0%
$2f_{5/2}$	−2.227	0.977	0.028	2.9%
$3p_{3/2}$	−2.665	0.989	0.054	5.5%
$1h_{9/2}$	−3.823	0.989	0.002	0.2%
$2f_{7/2}$	−5.014	0.996	0.009	0.9%
Other	< -7.0	—	$\sim 2.3.10^{-3}$	—

Table 4.4: Same as TAB. {4.2} for Sn isotopes.

hindrance to the formation of halos from low-lying high angular momentum states at the drip-line. The second halo parameter δR_{halo} displayed in Fig. 4.12 shows that the decorrelated region has

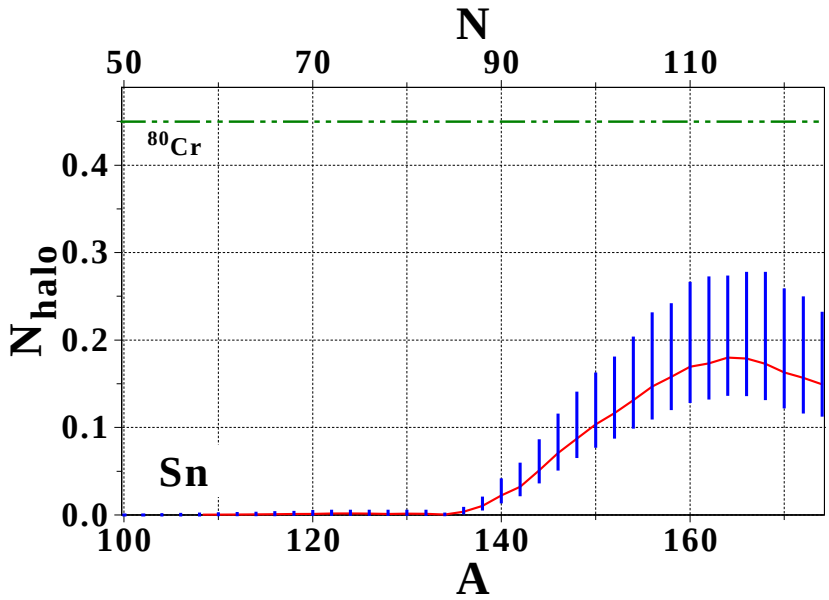

Figure 4.11: Average number of nucleons in the spatially decorrelated region for Sn isotopes. For comparison, $N_{\text{halo}}(^{80}\text{Cr})$ is shown as a horizontal dashed-dotted line.

little influence on the nuclear extension, of the order of 0.02 fm. Its contribution is found to be much less than predicted by the Helm model. The heavy mass of tin isotopes hinders the possibility of a sharp separation of core and tail contributions in the total density and thus, of the formation of a halo. The analysis of single-particle contributions, summarized in Tab. {4.4} and

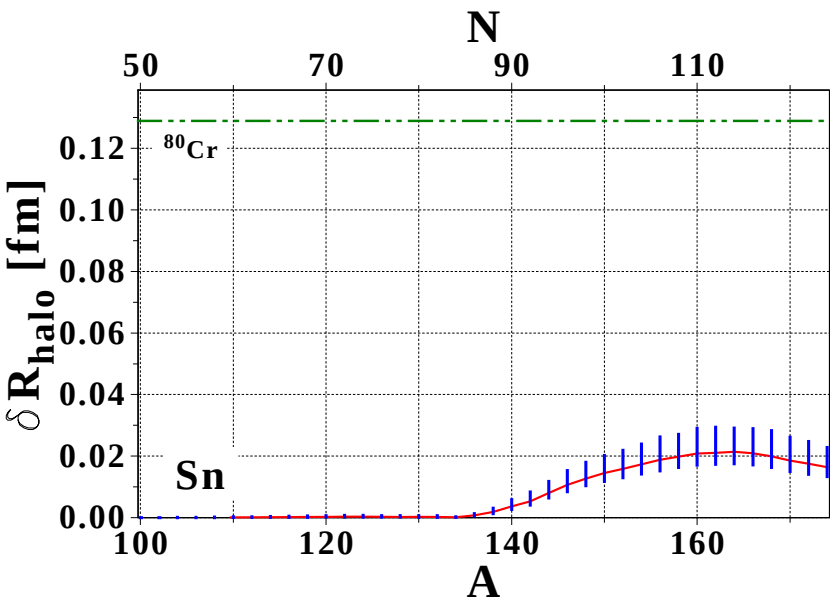

Figure 4.12: Halo factor parameter δR_{halo} in the Sn isotopic chain. For comparison purposes, $\delta R_{\text{halo}}(^{80}\text{Cr})$ is represented as a horizontal dashed-dotted line.

Fig. 4.10, confirms the latter analysis. Firstly, $3p_{1/2}$, $3p_{3/2}$ and $2f_{7/2}$ ($\ell = 3$) states contribute

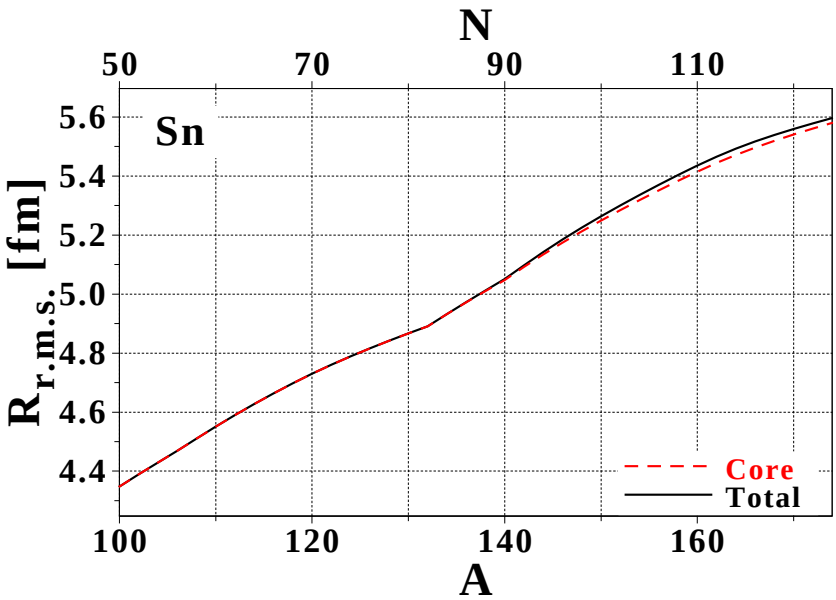

Figure 4.13: Same as FIG. 4.6 for Sn isotopes.

roughly the same to $N_{\rm halo}$. For higher angular-momentum orbitals, the effect of the centrifugal barrier is seen, i.e. $1h_{9/2}$ and $1i_{13/2}$ orbitals, the latter being the least bound orbital, do not contribute significantly to the decorrelated region. Finally, individual probabilities P_i remain very small, and do not exceed a few percents.

For all the reasons exposed above, only an extended neutron skin effect is seen in tin isotopes, and no significant halo formation is envisioned. Of course, these results have been obtained with a particular EDF. The sensitivity of the predictions to the different ingredients of the EDF need to be evaluated (see SECS. 4.3&4.5). In any case, the two previous examples already provide a coherent picture regarding properties of halo or non-halo medium-mass nuclei. In particular, it is rather obvious that the notion of *giant halo* [292; 293; 296–299] constituted of six to eight neutrons is misleading. Indeed, such a picture was obtained by summing up *total* occupations of loosely bound orbitals. Our analysis relies on a physically motivated picture and the decomposition of the halo into single-particle components comes only *a posteriori* when the former has been extracted. Although loosely bound orbits are indeed those responsible for the formation of the halo, nucleons occupying them reside mostly inside the nuclear volume. The present identification of the halo region allowed us to define the meaningful quantity $N_{\rm halo}$.

4.2.2 Convergence of the calculations

EDF calculations have been performed in coordinate representation with spherical symmetry. Several basis truncations are introduced under the form of (i) a box of finite radius $R_{\rm box}$, (ii) an angular-momentum cutoff $j^q_{\rm cut}$ for each isospin, and (iii) a continuum energy cutoff $E_{\rm max}$, to accelerate the convergence of the calculations (see SEC. 1.3.1.4). Such truncations are physically motivated but their values have to be carefully chosen not to exclude meaningful physics. As a result, the convergence of observables of interest has to be checked. In the present case, the dependence of (i) global properties, e.g. the ground state binding energy E^N, pairing gaps $\langle\Delta^q_\kappa\rangle$ and r.m.s. radii $R^q_{\rm r.m.s.}$... (ii) individual canonical energies e^q_i and pairing gaps Δ^q_i, and (iii) halo observables such as the values of r_0, $N_{\rm halo}$ and $\delta R_{\rm halo}$, on the parameters $R_{\rm box}$, $j^q_{\rm cut}$ and $E_{\rm max}$ is

investigated separately. All tests are performed for chromium isotopes using the {SLy4+REN-M} functional.

4.2.2.1 Box radius

The evolution of several observables related to halo properties for ^{80}Cr as a function of $R_{\rm box}$ is represented in FIGS. (4.14,4.15) for angular-momentum truncations $j^n_{\rm cut} = 65/2$ and $j^p_{\rm cut} = 61/2$, and an energy cutoff $E_{\rm max} = 200$ MeV. The pairing strength is not refitted for each bin, since the overall effect is found to be negligible. For very small box sizes, those observables are not fully

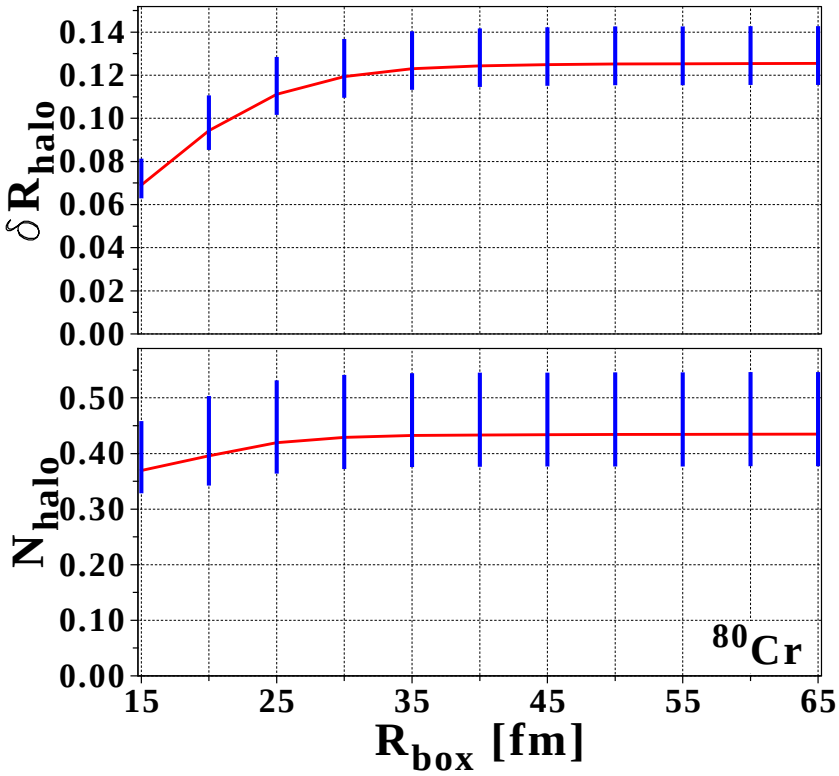

Figure 4.14: Evolution of $N_{\rm halo}$ and $\delta R_{\rm halo}$ as a function of the box radius for ^{80}Cr.

converged, and evolve as $R_{\rm box}$ is increased. The most sensitive observable is naturally $\delta R_{\rm halo}$. A box radius $R_{\rm box} = 40$ fm, for which convergence is achieved for all observables of interest, is used in the following.

4.2.2.2 Angular-momentum truncation

The choice of $j^n_{\rm cut}$ and $j^p_{\rm cut}$ is critical because the partial-wave truncation impacts the way the continuum is represented in the calculations. Indeed, high-ℓ orbitals can still contribute to nuclear properties of interest such as pairing gaps. To quantify such an effect we calculate, in the canonical basis, the probability distribution of particle $P^q_{v^2}(j)$ and pair $P^q_{uv}(j)$ occupations as a function of the single-particle angular momentum j, defined as

$$P^q_{v^2}(j) = \frac{(2j+1)\sum_{n\ell|j=\ell\pm1/2} {v^q_{nj\ell}}^2}{\sum_{n'j'\ell'}(2j'+1)\,{v^q_{n'j'\ell'}}^2}\,, \qquad P^q_{uv}(j) = \frac{(2j+1)\sum_{n\ell|j=\ell\pm1/2} u^q_{nj\ell}\,v^q_{nj\ell}}{\sum_{n'j'\ell'}(2j'+1)\,u^q_{n'j'\ell'}\,v^q_{n'j'\ell'}}\,. \tag{4.2}$$

The neutron distribution $P^n_{v^2}(j)$ is shown in FIG. 4.16a for the halo nucleus ^{80}Cr and different angular momentum truncations $j^n_{\rm cut} = j^p_{\rm cut} = J_{\rm max}$. It is found that the $v^{n\,2}$ strength is mostly

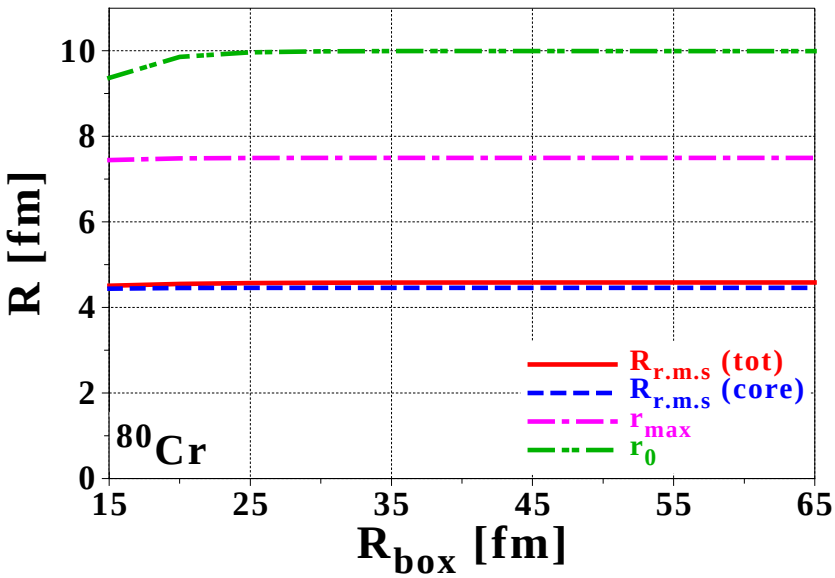

Figure 4.15: Halo region limit r_0, radius $r_{\max}$ at the maximum of the second order log-derivative of the neutron density, and neutron total and core root-mean-square radii for ^{80}Cr, as a function of the box radius R_{box}.

distributed over states with $j \leq 9/2$. As a result, such an occupation distribution is converged, at least to first approximation, for $j^n_{\text{cut}} = j^p_{\text{cut}} = J_{\max} = 15/2$. The corresponding $P^n_{uv}(j)$ distribution (Fig. 4.16b) extends much further towards high j values. This could be expected since $v^{q\,2}$ is maximum for deeply bound canonical states whereas $u^q\,v^q$ is peaked around the Fermi level and decays slower as the canonical energy increases above λ^q. Correspondingly, the local pair density $\tilde{\rho}^q(r)$ extends further out in space than the normal density $\rho^q(r)$ [124]. As one goes to drip-line (halo) nuclei in particular, $\tilde{\rho}^q(r)$ extends very far out and requires many partial waves to be well represented [331]. It is clear from Fig. 4.16b that a minimal cutoff of $J_{\max} = 31/2$ is needed to achieve a reliable description of the pair distribution. One sees in particular that for $J_{\max} = 15/2$ (i) the missing $u^n\,v^n$ strength at high j is wrongly redistributed over $j = 1/2$ and $j = 5/2$, making those states more paired and thus more localized, whereas (ii) some of the $v^{n\,2}$ strength of the $j = 1/2$ states is transferred to $j = 5/2$ states. There is no qualitative difference between results obtained with REG and REN pairing functionals, as seen in Fig. 4.17.

Considering that $3s_{1/2}$ and $2d_{5/2}$ states are precisely those building up the halo in ^{80}Cr, the latter effects associated with using a too small angular momentum cutoff artificially inhibit the formation of the halo. Rather high values of $J_{\max}$ are thus needed to properly describe the continuum, as seen in Fig. 4.18 where N_{halo} and δR_{halo} are given for ^{80}Cr as a function of $J_{\max}$. Both quantities reach a plateau around $j^q_{\text{cut}} = 35/2$. The previous analysis shows that HFB calculations with too small values of j^n_{cut} and j^p_{cut} cannot be trusted at the limits of stability if one is interested in detailed information about potential halos. Of course, considering the ultimate experimental accuracy achievable for matter r.m.s. radii, one should not be too extreme as far as the required convergence is concerned. From a theoretical perspective, and considering theoretical error bars on the determination of N_{halo} and δR_{halo}, it is necessary to include partial waves up to $j^n_{\text{cut}} = j^p_{\text{cut}} = J_{\max} \approx 31/2$.

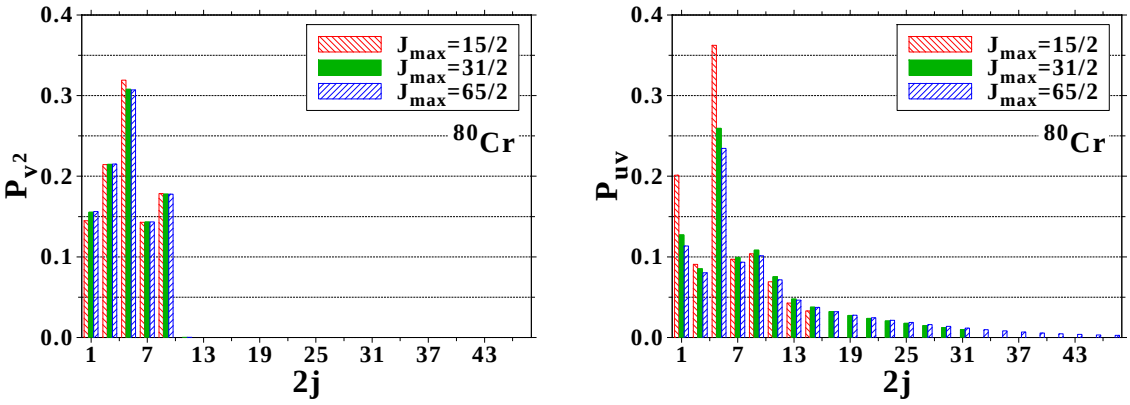

(a) Occupations $v^{n\,2}$ (b) Distribution of $u^n\,v^n$

Figure 4.16: Distribution of neutron canonical states as fractions of the total strength for ^{80}Cr computed with {SLy4+REN-M} functionals and different angular momentum truncations $j^n_{\rm cut} = j^p_{\rm cut} = J_{\rm max}$.

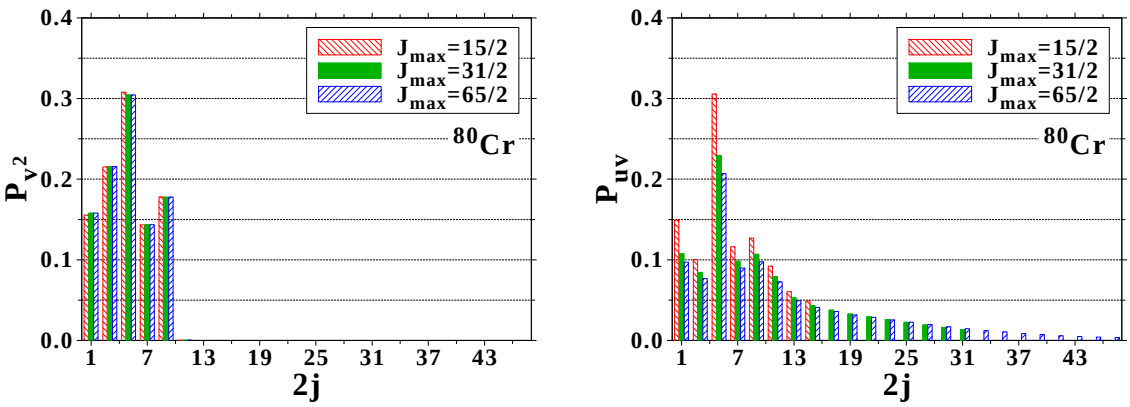

(a) Occupations $v^{n\,2}$ (b) Distribution of $u^n\,v^n$

Figure 4.17: Same as in Fig. 4.16 for the REG-M pairing functional.

4.2.2.3 Energy cutoff

The value of the energy cutoff $E_{\rm max}$ in the quasiparticle continuum is an important parameter of the calculation. For regularized pairing functionals, values of $J_{\rm max}$ and $E_{\rm max}$ must be taken large enough that, including a re-fitting of the coupling strength, observables of interest are independent with respect to $E_{\rm max}$. It was found that smaller basis truncations could be used for the REG case than for the REN case, since convergence is reached faster, as exemplified in Figs. (4.19a,4.19b). For the REG case, convergence for the ground-state energy as well as for the neutron pairing gap is almost achieved for $J_{\rm max} = 21/2$ and $E_{\rm max} = 200$ MeV. For in-medium renormalized functionals, the situation is more subtle. First, $E_{\rm max}$ must be large enough for the result to be independent of its value [233]. However, it must be remembered that the field theory renormalization scheme subtracts a diverging part on the basis where all partial waves below a certain energy cutoff have been included. Thus, for a given (high enough) $E_{\rm max}$, the angular momentum truncation must be large enough to prevent the renormalization counter term from removing contributions of states that were not considered in the first place. This is illustrated in Figs. (4.20a,4.20b) displaying the binding energy and neutron spectral gap of ^{80}Cr as a function

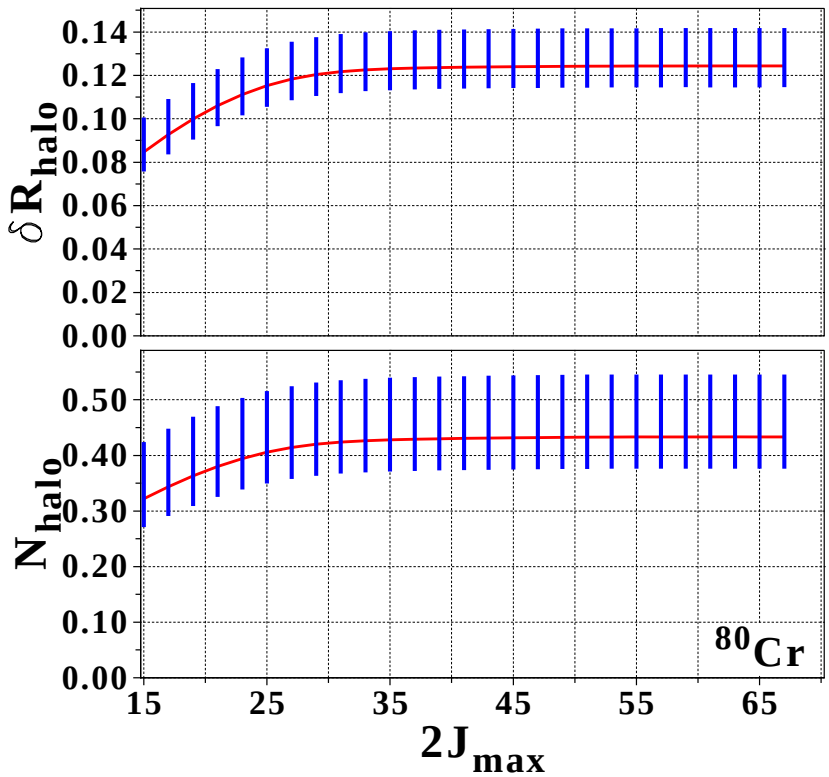

Figure 4.18: Evolution of N_{halo} and δR_{halo} in ^{80}Cr and {SLy4+REN-M} functionals for different angular momentum truncations $j^n_{\text{cut}} = j^p_{\text{cut}} = J_{\text{max}}$.

of the angular momentum cutoff J_{max}, for fixed values of E_{max}. Note that all values considered for E_{max} are large enough to obtain converged observables. However, one sees that increasing the energy cutoff necessitates a larger number of partial waves to reach converged values for both the energy and the gap. Consequently, it can be counter-productive to use a safe but unnecessarily large energy cut E_{max} as it results in the necessity to also increase J_{max}. On the other hand, the proper description of certain physical phenomena such as halos intrinsically requires a large number of partial waves. In such a case, one first fixes J_{max} and makes sure to use a coherent energy cutoff. In the present work, we use $E_{\text{max}} = 200$ MeV and $J_{\text{max}} = 65/2$. This corresponds to an conservative choice as $E_{\text{max}} = 70$ MeV and $J_{\text{max}} = 41/2$ would be sufficient for Cr isotopes.

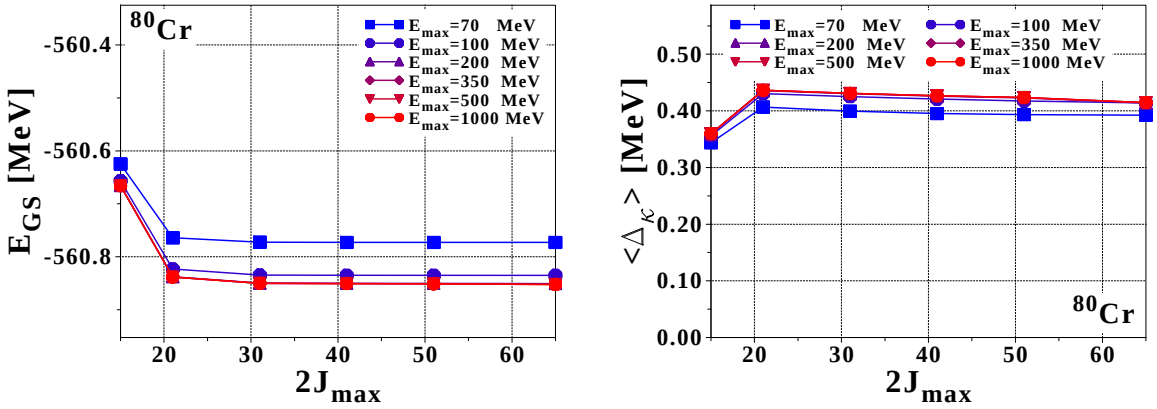

(a) Binding energy (b) Neutron spectral gap

Figure 4.19: Ground-state properties of ^{80}Cr as a function of the angular momentum cutoff $J_{\max}$ for fixed values of $E_{\max}$ as obtained from the {SLy4+REG-M} functional.

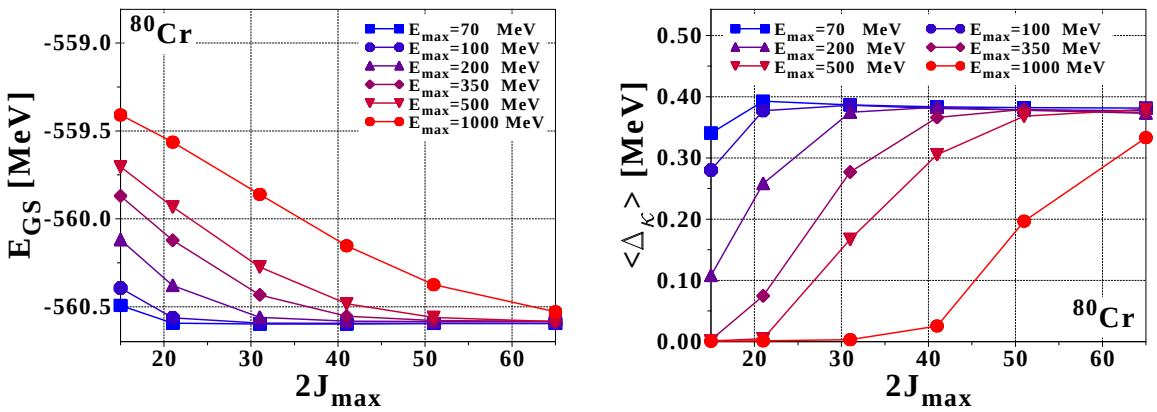

(a) Binding energy (b) Neutron spectral gap

Figure 4.20: Same as in Fig. 4.19 for the in-medium renormalized {SLy4+REG-M} functional.

4.3 Impact of the Skyrme EDF

To study the impact of the particle-hole functional characteristics on the formation of halos, N_{halo} and δR_{halo} have been computed for Cr isotopes using the set of particle-hole functionals presented in Sec. 1.3.1.1 combined with a mixed-type REG-M pairing functional. Results previously obtained with SLy4 will act as a reference point. Halo parameters N_{halo} and δR_{halo} as well as neutron canonical single-particle energies are displayed in Fig. 4.21 for ^{80}Cr. One finds that

- Skyrme functionals with an isoscalar effective mass of one (m^*1 and T6) predict denser single-particle spectra around the Fermi level. As a consequence, the $2d_{5/2} - 1g_{9/2}$ energy gap corresponding to the core excitation energy scale E' is reduced. Additionally, the Fermi level is shifted down, which enhances the separation energy E. Both effects contribute to hindering the halo formation.
- The modification of K_∞ affects collective properties, such as the breathing mode energy [332]. It also impacts the canonical spectrum. As a result, ^{80}Cr is predicted to be unbound

with the {SIII+REG-M} parametrization which has a particularly large compressibility $K_\infty = 355$ MeV.

- As the nuclear matter saturation density increases (from $\rho^1_{\rm sat}$ to $\rho^3_{\rm sat}$), the nuclear interior becomes denser, as shown in FIG. 4.22. Through self-consistency, a denser nuclear interior generates a sharper surface, that ultimately makes weakly bound orbitals to be less coupled to the nuclear potential and thus even less bound. As a result, the density extends further out asymptotically. While the $2d_{5/2} - 1g_{9/2}$ energy gap remains the same, the tail excitation energy E decreases with $\rho_{\rm sat}$ and halo factors increase.
- Tensor couplings may also impact the formation of halos; as it was found for light systems [333]. For medium-mass nuclei, a series of recent studies have assessed the impact of tensor couplings on the evolution of spherical single-particle shells [158; 225; 334–336]. To study the impact on halos, the newly available Skyrme T21-T26 functionals have been used [158]. This particular series of parametrizations is characterized by a varying tensor coupling between particles of same isospin. The like-particle coupling constant is (i) negative for T21, which corresponds to a repulsion between particles of identical isospin, (ii) zero for the functional T22, which makes it similar to SLy4, and (iii) increasingly positive from T23 to T26. All TXX functionals display otherwise the same infinite matter properties, as seen in TAB. {1.2}, i.e. variations single-particle properties are solely due to the tensor interaction. As the like-particle interaction becomes attractive, both $3s_{1/2} - 2d_{5/2}$ and $2d_{5/2} - 1g_{9/2}$ energy gaps involving neutron states of the same parity are found to decrease. The Fermi level is pushed up at the same time. Even though the core excitation energy scale E' is slightly decreased, the overall effect favors the formation of the halo in the present case.

By no means SLy4 or any other existing Skyrme parametrization of the nuclear EDF is to be seen as universal. As exemplified above, it is found that the choice of the particle-hole Skyrme parametrization can affect significantly the neutron canonical spectrum close to the Fermi energy. As a result, the drip-line position and halo energy scales are modified, hence values of $N_{\rm halo}$ and $\delta R_{\rm halo}$. Scanning the set of parameterizations used in the present study, $N_{\rm halo}$ and $\delta R_{\rm halo}$ can change by as much as 100 %. Thus, solid experimental data on medium-mass halo nuclei might be useful in constraining some characteristics of the particle-hole part of the EDF. Eventually, (reasonable) variations in the characteristics of currently used EDFs translate into rather large uncertainties in the prediction of halo properties. For instance, no halo nucleus would be predicted at the drip-line of Cr isotopes using the Skyrme SkM* parametrization, as the semi-magic nucleus ^{74}Cr is predicted to be the last bound Cr isotope in this case. The same precautions have to be taken when considering large-scale predictions of spherical halo candidates over the nuclear chart presented in the next section.

4.4 Large-scale calculations

Systematic predictions of halo properties with the {SLy4+REG-V} EDF are now presented. We restrict ourselves to even-even spherical nuclei, as predicted by the Gogny D1S interaction [140]. Among all even-even nuclei, we define the sub-set of "spherical" nuclei as those fulfilling the condition

$$-0.1 < \beta_2 < 0.1\,, \tag{4.3}$$

where β_2 characterizes the axial mass quadrupole deformation. The rather large interval allowed on β_2 is arbitrary and also does not distinguish between soft and rigid ground states. Such a condition provides a list of about 500 nuclei, in agreement with similar predictions obtained using Skyrme functionals [300], although drip-line positions slightly differ between the two models. Results for $N_{\rm halo}$ are shown in FIG. 4.23. We observe that (i) several isotopic chains display

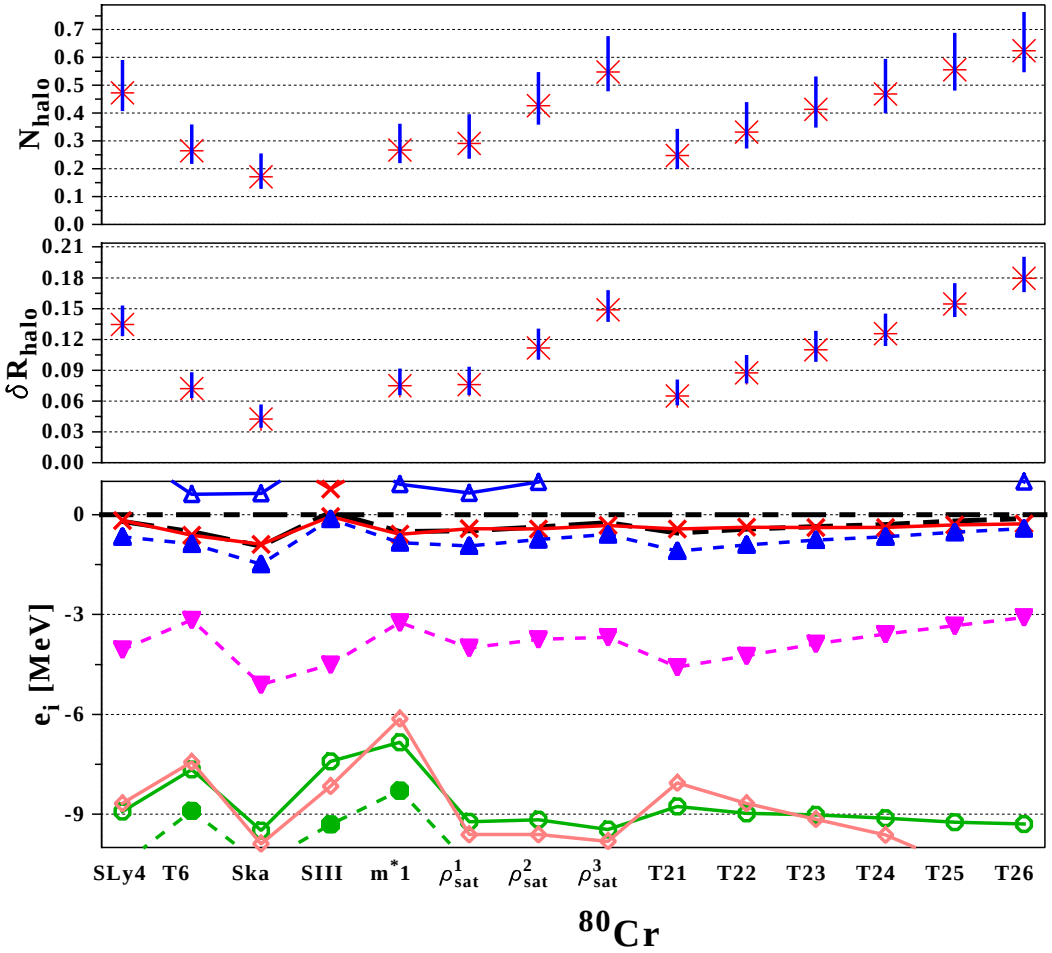

Figure 4.21: Single-particle spectrum and halo properties for ^{80}Cr, computed with different particle-hole (see text) and mixed-type pairing functionals.

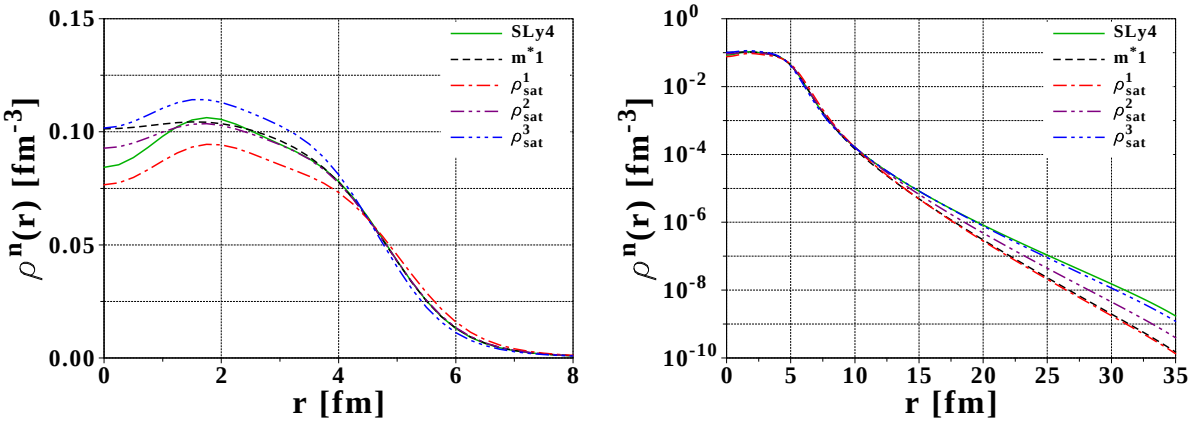

Figure 4.22: Neutron densities for ^{80}Cr (left: linear scale, right: logarithmic scale) with the {SLy4+REG-M} functional and refits of the Skyrme parameters corresponding to (i) a different isoscalar effective mass $m^* = 0.70 \rightarrow 1.00$, and (ii) different nuclear saturation densities: $\rho_{\rm sat}^{1/2/3} = 0.145\,/\,0.160\,/\,0.175$ fm^{-3}.

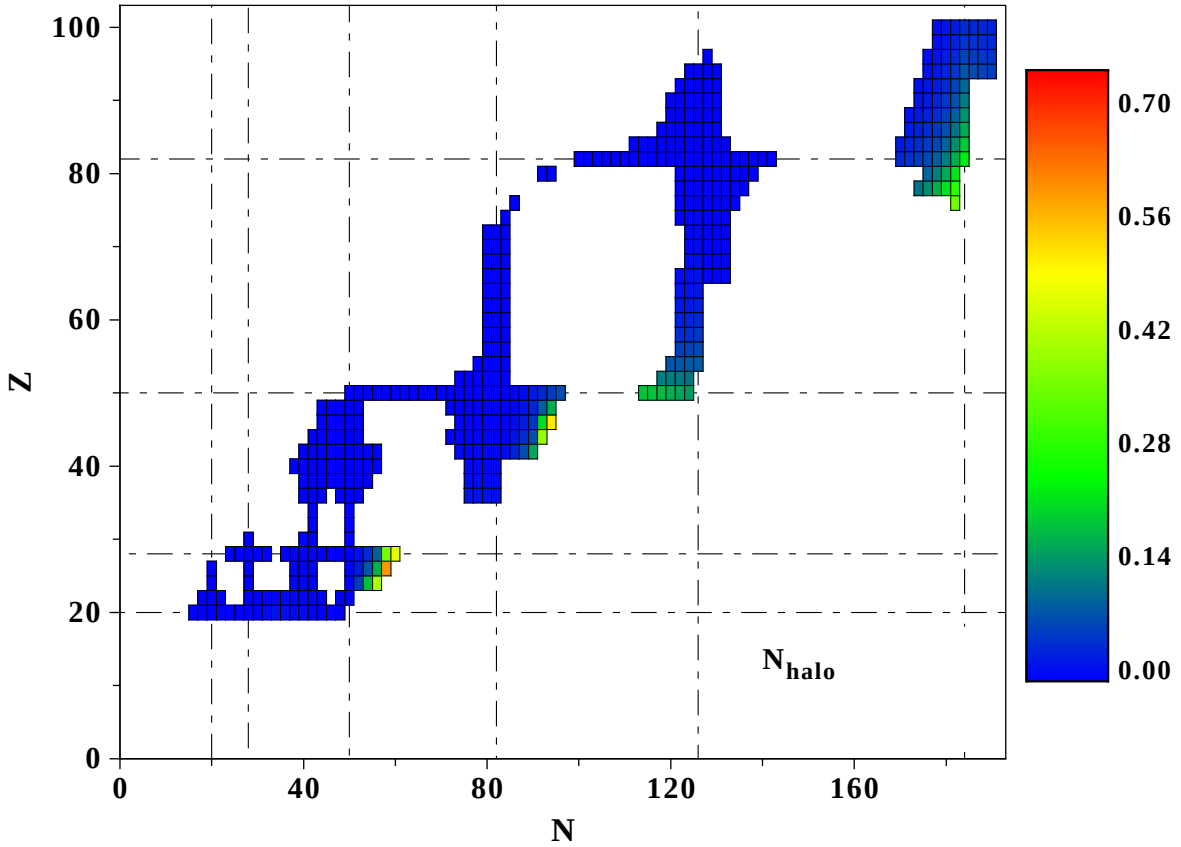

Figure 4.23: N_{halo} parameter predicted by the {SLy4+REG-V} EDF for about 500 spherical nuclei.

neutrons halos, (ii) halos only appear at the very limit of neutron stability, (iii) the maximum value of N_{halo} is about ~ 0.7, (iv) very few heavy elements in the (Pt, Hg, Tl...) region are found to have a non-zero halo parameter N_{halo}, (v) on the large scale, the halo phenomenon is very rare and almost accidental, and (vi) looking at the best cases between $Z = 20$ to $Z = 100$, absolute and relative values of N_{halo} decrease with the nuclear mass.

Results for δR_{halo} are presented in Fig. 4.24 and confirm the above analysis on N_{halo}. In particular, it is seen that the fraction of decorrelated nucleons has almost no influence on the nuclear extension of very massive nuclei. Only two very localized regions where the predicted halo significantly affects the neutron r.m.s. radius are found, e.g. for (i) Cr, Fe and Ni nuclei, and (ii) Pd and Ru isotopes. Drip-line isotopes of these elements are predicted as the best halo candidates for the {SLy4+REG-V} EDF. An analysis of single-particle properties of the best halo candidates is found in Fig. 4.26. These nuclei have in common the presence of very weakly bound s or p states. Although states with larger angular momentum contribute to the nuclear halo the presence of weakly bound $\ell = 0, 1$ orbitals remains mandatory for a halo to develop significantly. That being said, no pure s-wave or p-wave halo has been found, which demonstrates the collectivity of the phenomenon in medium-mass systems.

The complementarity between the two criteria N_{halo} and δR_{halo} appears more clearly through the large-scale analysis. Fig. 4.25 shows that (i) the two observables are correlated within a given isotopic chains and the information carried by both quantities is somewhat redundant, but (ii) the correlation pattern changes as the proton number increases (between Cr and Pd isotopes

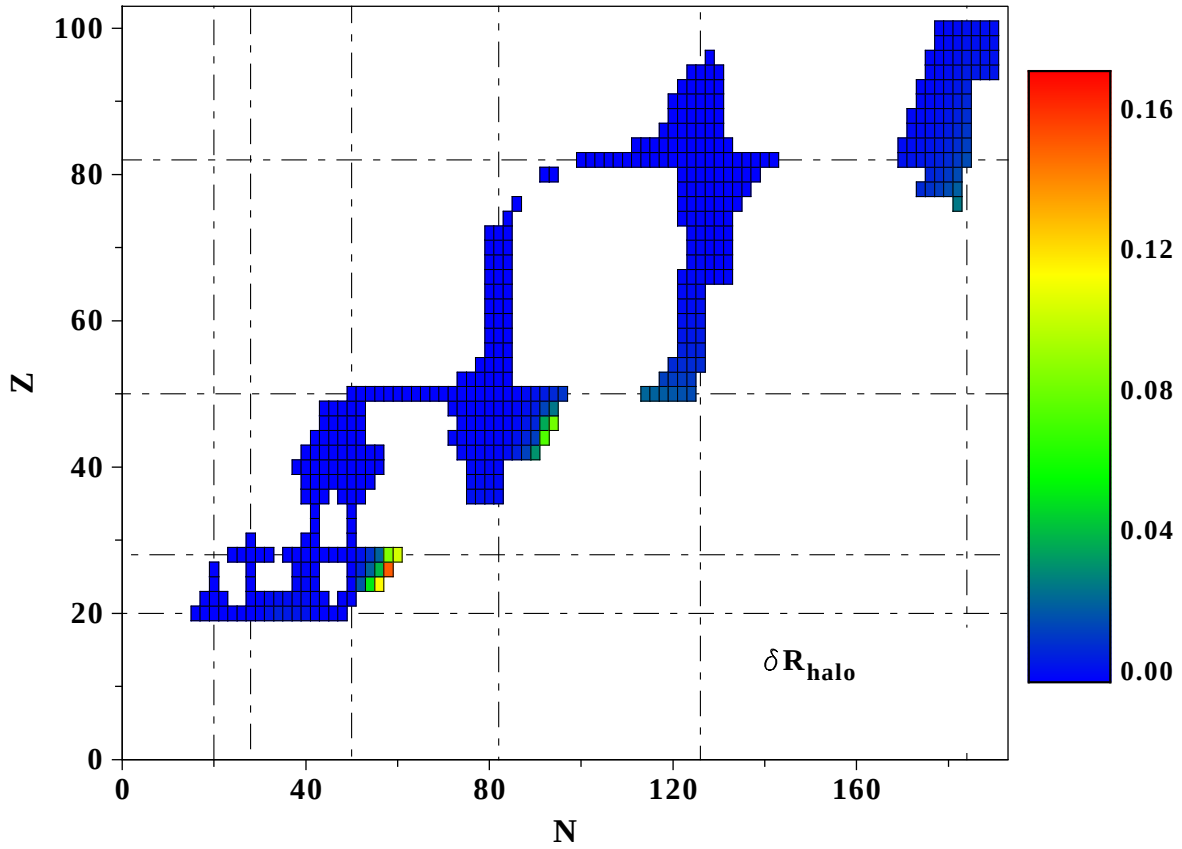

Figure 4.24: Same as in FIG. 4.23 for δR_{halo}.

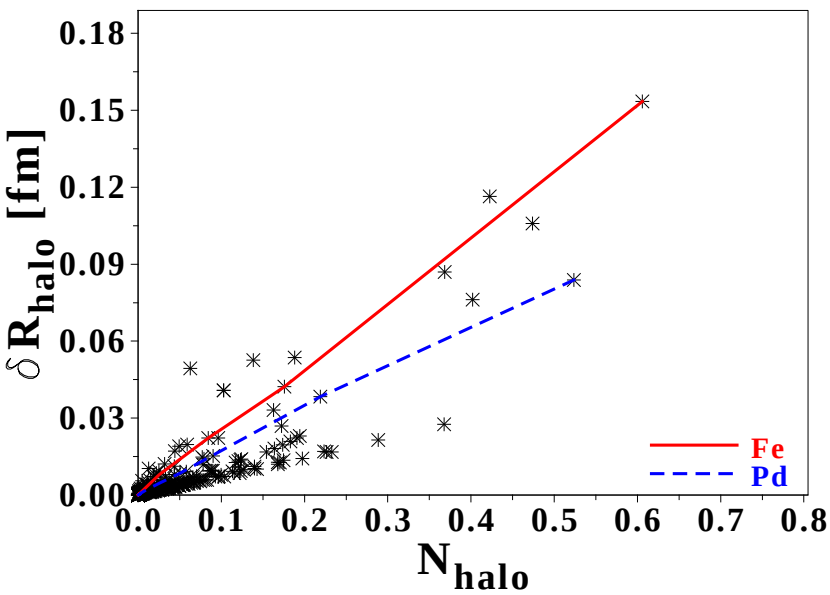

Figure 4.25: Correlation between N_{halo} and δR_{halo} for all spherical nuclei computed with the {SLy4+REG-V} functional. The evolution of δR_{halo} as a function of N_{halo} for Fe and Pd isotopes are highlighted.

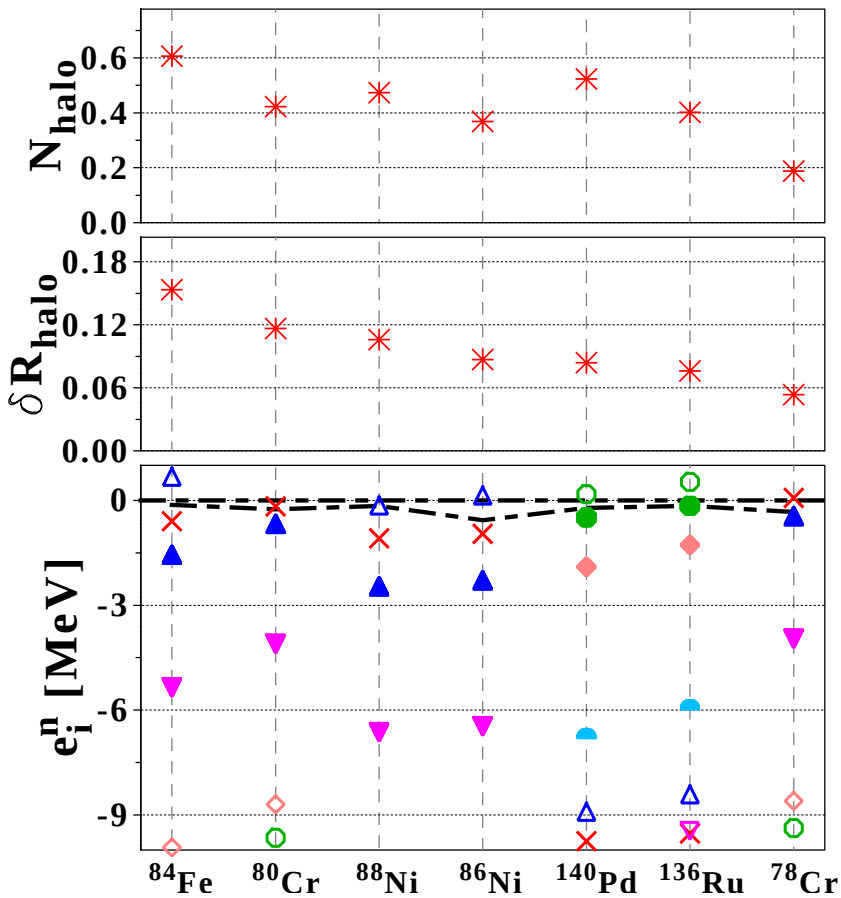

Figure 4.26: Canonical spectrum and halo factors of the best halo candidates, as predicted with the {SLy4+REG-V} functional.

for instance). In particular, for heavier masses $\delta R_{\rm halo}$ increases much less with $N_{\rm halo}$.

Finally, one can turn to the particular case of Zr and Ca isotopes which have been predicted to be giant halo nuclei [292; 293; 296–299]. In the present study, values of $N_{\rm halo}$ and $\delta R_{\rm halo}$ do not lead to such a conclusion. The first reason resides in the different single-particle spectra predicted by the functionals used in the present study. Considering that relativistic models (TM1 [337], NLSH [338], NL3 [296]...) or non-relativistic ones (SkI4 [339]...) predict weakly bound p states [292; 296–299] at the neutron drip-line of those elements, it is likely that the application of our criteria on those results would lead to predicting the existence of halos. However, we put into question the very notion of "giant halo" that comes from summing up occupations of weakly bound orbitals. Such a counting procedure is qualitatively incorrect as nucleons occupying weakly bound orbitals are mostly located within the nuclear volume. Although several single-particle states do contribute to the halo, the notion of giant halo implies that a cluster picture involving several decorrelated neutrons is at play which is not the case. Such an unjustified counting is a reminiscence of the denomination of "1(2)-neutron" halo used for light systems. However, the latter relates to the fact that these light nuclei are well described by a "core+1(2) neutrons" cluster model whereas practitioners are well aware that only a fraction of nucleon resides in average beyond the classical turning point. Similarly, we prove in the present work that the average number of neutrons in the halo does not scale with A and remains of

the same order as in light nuclei. The notion of spatial decorrelation is key to the meaningful definition of the halo region and the halo parameters N_{halo} and δR_{halo}.

4.5 Role of pairing correlations

4.5.1 Pairing anti-halo effect

In the presence of pairing correlations, the asymptotics of the one-body neutron density takes a different form from the one it has in the EDF treatment based on an auxiliary Slater determinant. In first approximation, paired densities decrease faster than unpaired ones (see Sec. 2.1.2) and pairing correlations induce an *anti-halo effect* by localizing the one-body density [284; 285; 340]. To evaluate the quantitative impact of this effect, drip-line Cr isotopes have been calculating with and without explicit treatment of pairing correlations. In the latter case, a "filling approximation" is used for incomplete spherical shells. In both cases, the SLy4 Skyrme functional is used. When including pairing, a mixed-type pairing is added. A comparison between neutrons single-particle levels is represented in Fig. 4.27 for the last bound nuclei, ^{82}Cr being predicted to be bound when pairing correlations are excluded from the treatment. This is interesting in itself as it shows that pairing correlations can change the position of the drip-line and modify the number of halo candidates over the nuclear chart. There is only little difference between canonical energies e_i^n in the two cases. However, values of halo criteria N_{halo} and δR_{halo} are significantly different, i.e. the neutron halo is significantly quenched in ^{80}Cr when pairing is included whereas the situation is reversed in the lighter isotopes, as seen in Fig. 4.28.

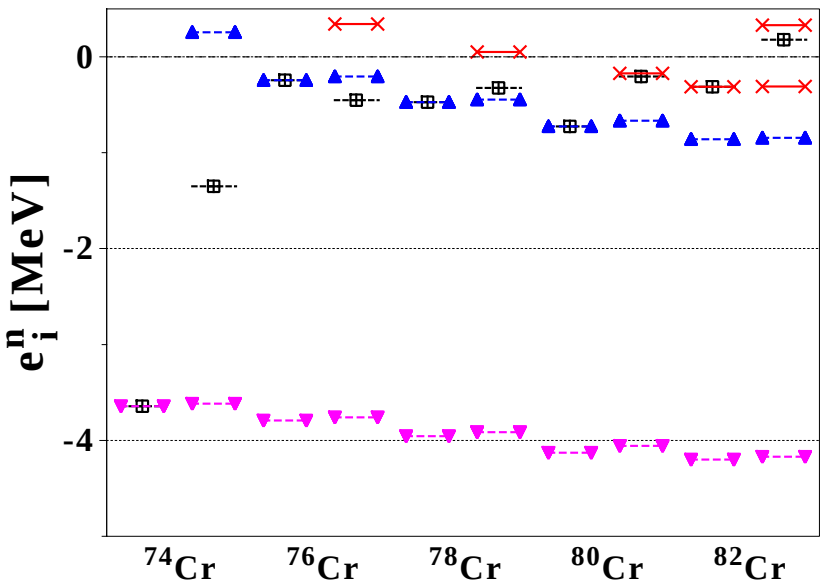

Figure 4.27: Neutron canonical energies e_i^n along the Cr isotopic chain, obtained without (left) and with (right) pairing correlations. The Skyrme SLy4 functional is used in both cases. When including pairing correlations, a mixed-type REG-M functional is added. The Fermi level (⊞) is set to the last filled orbital for the EDF treatment based on an auxiliary Slater determinant.

Such results underline that pairing correlations affect halos in two opposite ways. Pairing (i) inhibits the formation of halos through the anti-halo effect, but also (ii) enhances the formation of halos by scattering nucleons to bound states with smaller decay constants. For example, the

anti-halo effect dominates in ^{76}Cr and ^{78}Cr whereas the promotion of neutrons into the weakly bound $3s_{1/2}$ makes the halo to be more pronounced in ^{80}Cr when pairing is included. When pairing is ommited, the number of nucleons in the $2d_{5/2}$ orbital increases linearly as one goes from ^{76}Cr to ^{80}Cr. At the same time, the $2d_{5/2}$ shell becomes more bound as a result of self-consistency. This explains the negative curvature of $\delta R_{\rm halo}$ as one goes from ^{76}Cr to ^{80}Cr, while $N_{\rm halo}$ is indeed almost linear. In ^{82}Cr, two effects contribute to the very pronounced halo that is predicted in the absence of pairing correlations, that is (i) the $3s_{1/2}$ gets fully occupied, whereas (ii) the pairing anti-halo effect is inoperative. Results discussed above are further illustrated in Fig. 4.29 where the contributions of different single-particle states to the halo are shown.

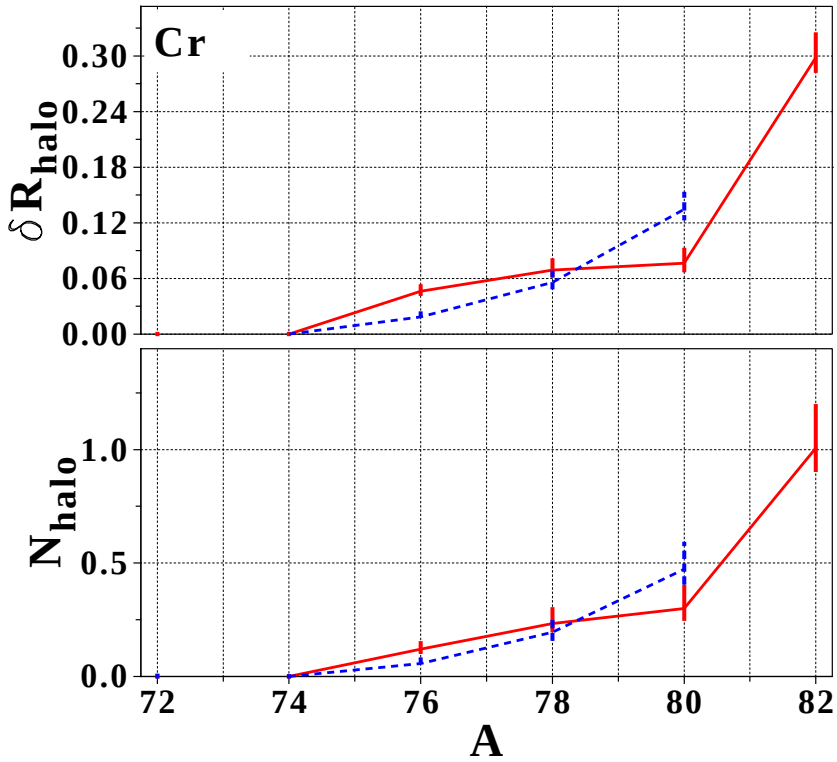

Figure 4.28: Halo criteria $N_{\rm halo}$ and $\delta R_{\rm halo}$ for Cr isotopes, obtained through spherical HF (solid lines) and HFB (dashed lines) calculations with the Skyrme SLy4 functional. For HFB calculations, mixed-type REG-M pairing is used.

To specifically extract the contribution from the pairing anti-halo effect, we now perform a toy model calculation of a fictitious "^{80}Cr*" nucleus. Providing the single-particle wave functions obtained from the calculation of ^{82}Cr without pairing correlations with the canonical occupations of the same states obtained from the calculation of ^{80}Cr with pairing, we extract $N_{\rm halo,i}$ from each of those orbitals[(5)]. Such a procedure allows to isolate, in a semi-quantitative manner, the net change of $N_{\rm halo}$ due to the difference in the asymptotics of the paired orbitals but not to their change in occupation when pairing is explicitly treated. Doing so, it is found that the contribution of the $3s_{1/2}$ state to the halo is smaller in ^{80}Cr than in ^{80}Cr* by about 26 %. For the $2d_{5/2}$ orbital the suppression of $N_{\rm halo,i}$ is about 15 %[(6)]. As a result, one sees that if the

[5]Single-particle states extracted from the calculation of ^{80}Cr without pairing cannot be used because the essential $3s_{1/2}$ orbital belongs to the continuum and has plane wave asymptotics in this case.

[6]The value of r_0 is also different for ^{80}Cr and ^{80}Cr*, but this does not affect the results significantly.

	^{80}Cr (pairing)		
N_{halo}	0.473		
	e_i^n [MeV]	$v_{i\,2}^n$	$N_{\text{halo,i}}$
	> 0.0	—	$\sim 1.3.10^{-2}$
$3s_{1/2}$	-0.173	0.451	0.225
$2d_{5/2}$	-0.665	0.828	0.222
$1g_{9/2}$	-4.056	0.993	0.008
$1f_{5/2}$	-8.673	0.999	0.001
$2p_{1/2}$	-8.920	0.999	0.002
Other	< -10.0	—	$\sim 2.8.10^{-4}$
	^{82}Cr (no pairing)		
N_{halo}	1.007		
	e_i^n [MeV]	$v_{i\,2}^n$	$N_{\text{halo,i}}$
	> 0.0	—	0.000
$3s_{1/2}$	-0.312	1.000	0.675
$2d_{5/2}$	-0.858	1.000	0.314
$1g_{9/2}$	-4.200	1.000	0.010
$1f_{5/2}$	-8.783	1.000	0.001
$2p_{1/2}$	-9.078	1.000	0.002
Other	< -10.0	—	$\sim 2.7.10^{-3}$
	^{80}Cr* (pairing)		
N_{halo}	0.582		
	e_i^n [MeV]	$v_{i\,2}^n$	$N_{\text{halo,i}}$
	> 0.0	—	??????
$3s_{1/2}$	-0.312	0.451	0.305
$2d_{5/2}$	-0.858	0.828	0.260
$1g_{9/2}$	-4.200	0.993	0.010
$1f_{5/2}$	-8.784	0.999	0.002
$2p_{1/2}$	-9.078	0.999	0.002
Other	< -10.0	—	$\sim 2.7.10^{-3}$

Table 4.5: N_{halo}, individual contributions to the halo $N_{\text{halo,i}}$, single-particle canonical energies e_i^n and occupations $v_i^{n\,2}$ for (i) ^{80}Cr with pairing, (ii) ^{82}Cr without pairing, and (iii) ^{80}Cr* with pairing but using single-particle states calculated in the absence of pairing.

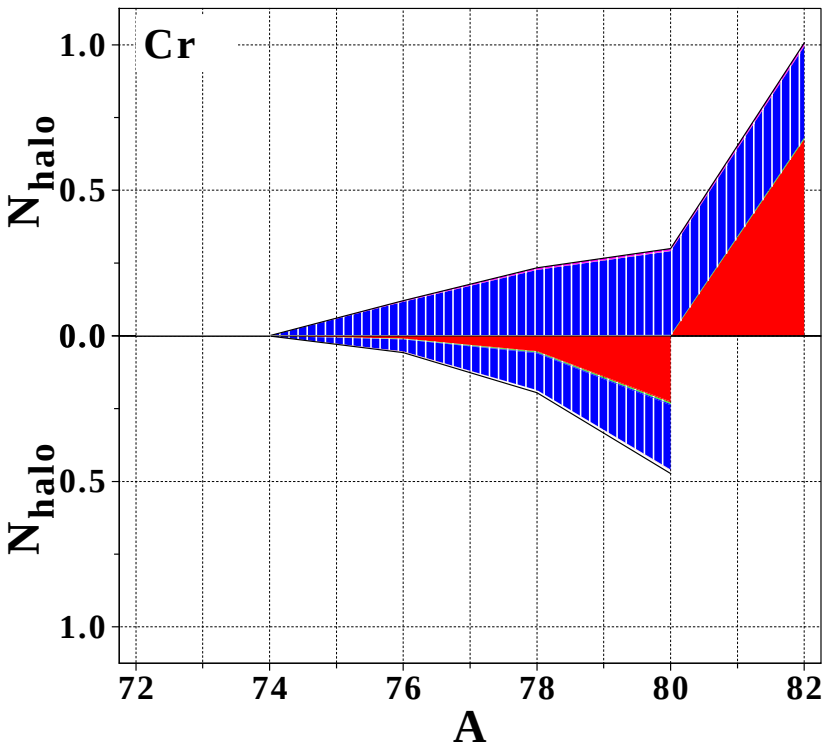

Figure 4.29: Contributions of individual orbitals to the halo: EDF calculation of the least bound Cr isotopes with (bottom) and without (top) pairing.

anti-halo effect were ineffective, the scattering of particles into higher-lying orbitals would bring $N_{\rm halo}$ from 0.300 to 0.582. Instead, $N_{\rm halo}$ is only increased to 0.473 in the full fledged calculation of ^{80}Cr with pairing correlations, i.e. the anti-halo effect reduces the potential increase by 40 %.

There is no simple answer as to whether pairing correlations enhance or hinder the formation of halos. The net result depends on structure details of the particular nucleus of interest [292; 341].

4.5.2 Decorrelation from pairing field

An additional effect might come into play as far as the role of pairing in the formation of halos is concerned. Very weakly bound $\ell = 0$ orbitals are expected to decouple from the pairing field as the neutron separation energy goes to zero [286–288]. As a result, such an orbital would not be subject to the anti-halo effect and may develop a very long tail. The signature of this effect can be seen in the single-particle occupation profile. Canonical occupations of all neutron single-particle states in Cr isotopes are gathered in Fig. 4.30 and plotted as a function of $(e_i^n - \lambda^n)$. Those occupations are compared to the BCS formula

$$v_i^{n\,2} = \frac{1}{2}\left(1 - \frac{e_i^n - \lambda^n}{\sqrt{(e_i^n - \lambda^n)^2 + \langle\Delta_\kappa^n\rangle^2}}\right) , \tag{4.4}$$

calculated using the maximum/minimum neutron spectral gap $\langle\Delta_\kappa^n\rangle$ found among all non-magic drip-line Cr isotopes, using the {SLY4+REG-M} functional. The s-wave occupation probability follows closely the BCS-type profile calculated using the minimal spectral gap, whereas high-ℓ orbitals follow well the BCS-type profile computed with the maximal one. This corroborates the trend discussed in Refs. [286–288] and underlines that $\ell = 0$ orbitals with $e_i^n \approx \lambda^n \approx 0$ are less

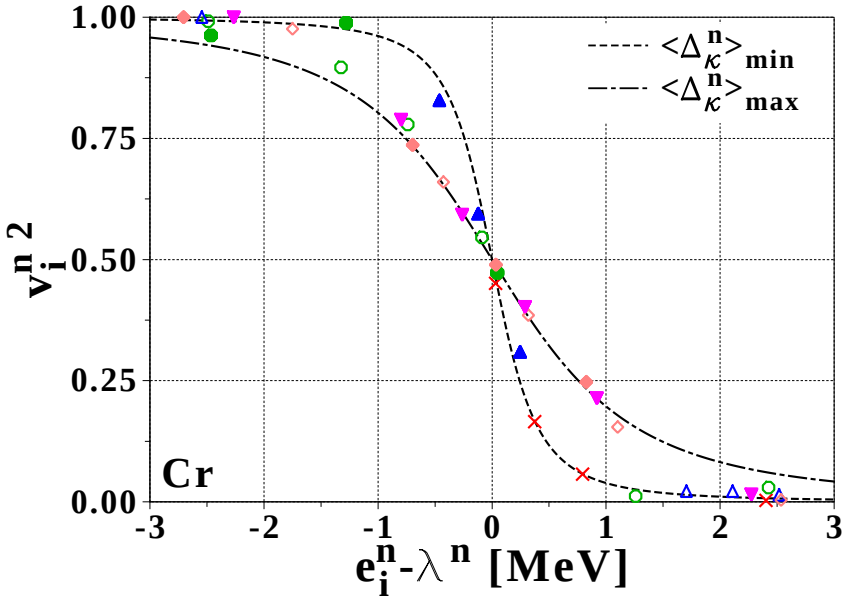

Figure 4.30: Neutron canonical occupations $v_i^{n\,2}$ as a function of $(e_i^n - \lambda^n)$ for all drip-line Cr isotopes, from ^{50}Cr to ^{80}Cr, with the {SLY4+REG-M} EDF. Profiles computed from BCS-type formulæ using the minimum (dashed line) and maximum (dashed-dotted line) spectral neutron gaps $\langle\Delta_\kappa^n\rangle$ among all those isotopes are shown for reference.

paired than high-ℓ ones. This is also confirmed by looking at individual gaps given in Fig. 4.31. The $3s_{1/2}$ state displays a smaller gap than other orbitals as it approaches the Fermi level (from above), the latter reaching the continuum threshold. On the other hand, the canonical gap of the $3s_{1/2}$ state remains significant as it crosses the Fermi level and the anti-halo effect is still in effect for that orbital. In fact, the critical decoupling of s orbitals from the pairing field, discussed in Refs. [286–288] through schematic HFB calculations, becomes fully effective only when the Fermi level and the s state energy are both of the order of a few keVs. Such extreme situations (i) are not reached in realistic systems [342], and (ii) would require an accuracy on the predicted value of the separation energy which is far beyond the present capacity of EDF calculations.

4.5.3 Importance of low densities

Values of η and α entering the pairing functional (Eq. (1.70)) strongly affect the spatial localization of the pairing field, as exemplified in Fig. 1.3. As a result, individual gaps of weakly-bound orbitals lying at the nuclear surface are affected. Considering the discussion of Sec. 1.4.6, such a change in the characteristics of the pairing functional could significantly impact halo properties. In previous studies [249], it was found that the size of a neutron halo could change by one order of magnitude when the pairing functional evolves from a volume to a extreme-surface type. However (i) the evaluation of the halo size was performed through the Helm model, and (ii) the standard regularization scheme was used with extreme-surface pairing functionals which, as discussed in Sec. 1.4.5, could have led to unsafe predictions.

The renormalization scheme is used in the present section since it prevents any unphysical feature from appearing with extreme surface pairing functionals. Properties of the last bound Cr isotopes are evaluated for different pairing functionals. Overall, neutron canonical energies evolve very little with (η, α), as seen in Fig. 4.32b. The change of canonical pairing gaps Δ_i^n is presented in Fig. 4.32a. For surface-enhanced pairing functionals, well-bound orbitals residing

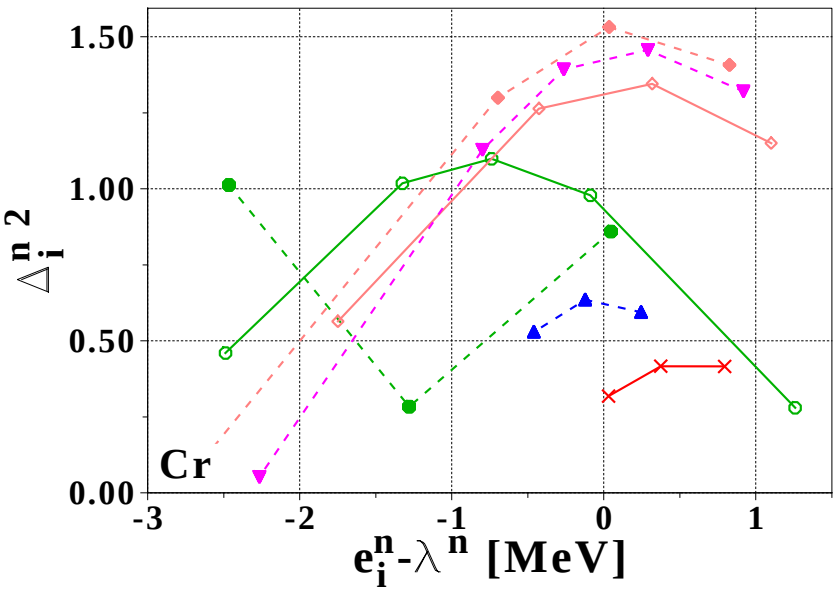

Figure 4.31: Individual neutron canonical gaps Δ_i^n computed for drip-line Cr isotopes with the {SLY4+REG-M} functional and plotted as a function of $(e_i^n - \lambda^n)$.

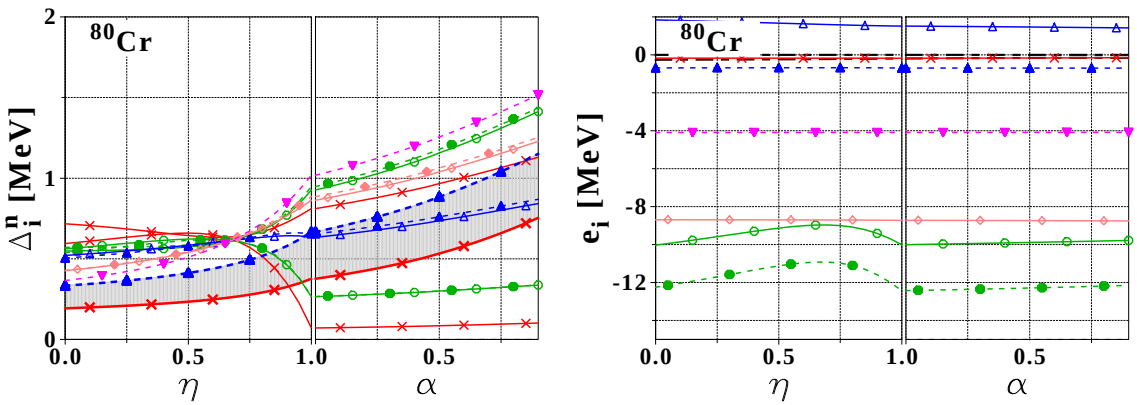

(a) Pairing gaps (b) Canonical energies

Figure 4.32: Neutron single-particle properties for ^{80}Cr and different REN-X pairing functionals.

in the center of the nucleus become less paired. On the other hand, pairing gaps of states close to the Fermi level increase as the effective pairing strength becomes more important at the nuclear surface[7]. Considering theoretical error bars, the values of $N_{\rm halo}$ and $\delta R_{\rm halo}$ presented in FIGS. (4.34,4.35) can be considered to be almost independent of the density-dependent form factor of the pairing functional, although the anti-halo effect becomes more effective as α decreases. In the latter figures, one parameter is varied at a time, while the other one is fixed at one, i.e. $\alpha = 1$ when η goes from zero ("volume" pairing) to one ("surface" pairing), whereas $\eta = 1$ when α goes from one to zero. $N_{\rm halo}$ and $\delta R_{\rm halo}$ are maximal for the standard surface pairing functional $\eta = \alpha = 1$, for which the occupation of the $3s_{1/2}$ state and its localization due to an increased coupling to the pairing field presents the best compromise for the halo to develop. This reflects

[7]The pairing strength is readjusted to produce a fixed value of the neutron spectral gap in ^{120}Sn. As some orbitals become less paired, others display larger individual gaps to maintain the same total neutron spectral gap.

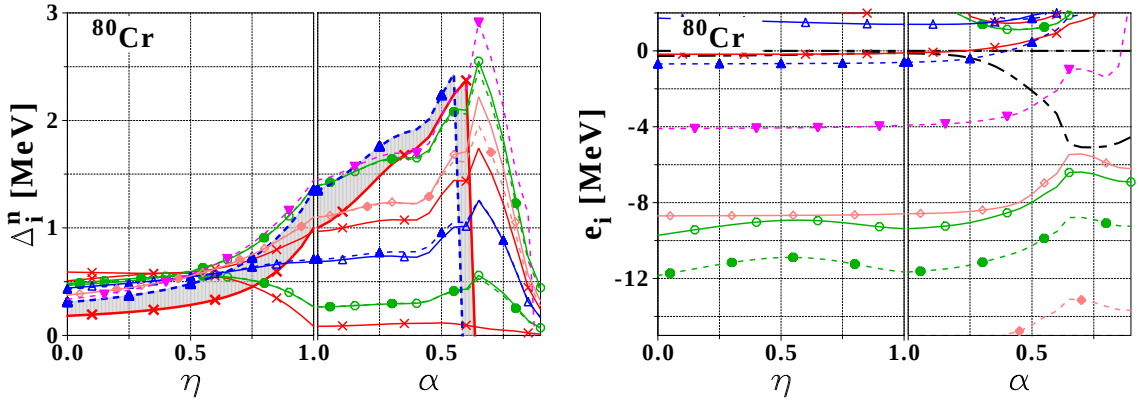

(a) Pairing gaps (b) Canonical energies

Figure 4.33: Same as FIG. 4.32 for REG-X pairing functionals.

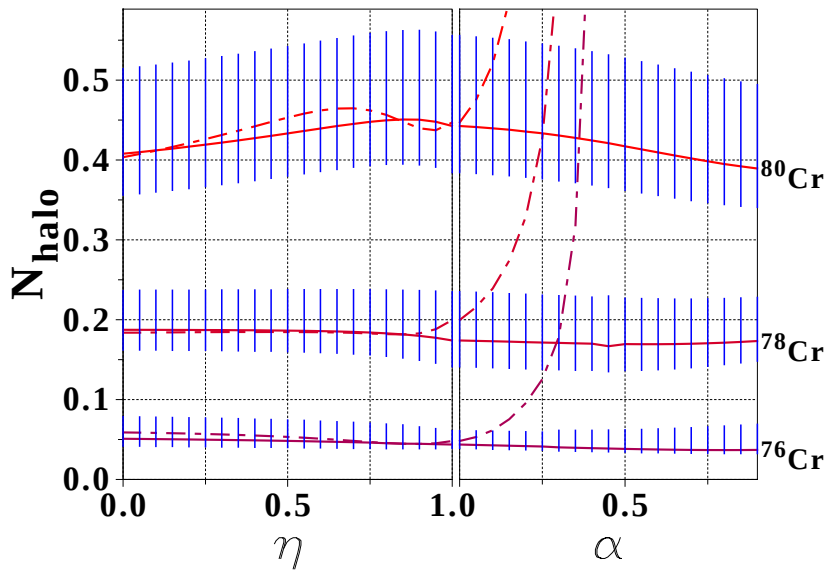

Figure 4.34: N_{halo} parameter for Cr isotopes calculated using renormalized REN-X pairing functionals with different form factors (see text). Results for regularized REG-X functionals diverge for very strong surface pairing correlations and are represented in dashed lines. One parameter is varied at a time, while the other one is fixed at one, i.e. $\alpha = 1$ when η goes from zero ("volume" pairing) to one ("surface" pairing), whereas $\eta = 1$ when α goes from one to zero.

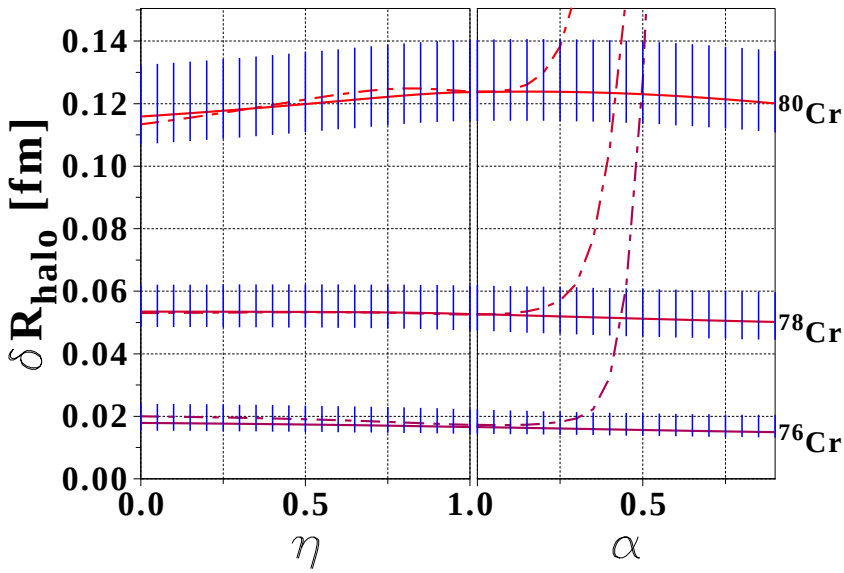

Figure 4.35: Same as FIG. 4.34 for δR_{halo}.

on the composition of the neutron halo in ^{80}Cr displayed in FIG. 4.36. As a comparison, the situation with REG-X pairing functional is very different, since single-particle energies change drastically as the pairing strength at the nuclear surface is enchanced, as shown in FIG. 4.33b. In that respect, individual gaps also change drastically, and ^{84}Cr becomes bound beacuse of the formation of the unphysical di-nucleon gas. Suddden variations of e_i^n and Δ_i^n for $\alpha < 1$ REG-X functionals indicates that they cannot be safely used, as it was already predicted looking at the diverging evolutions of N_{halo} and δR_{halo}. Finally, one notes that, as long as $\alpha = 1$, N_{halo} and δR_{halo} are almost identical for the regularization and renormalization schemes. This shows that results using the regularized scheme are valid and that both REG-X or REN-X functionals can be used with "standard" density dependencies. As a conclusion, the impact of low-density characteristics of the the pairing functional on halo properties is found to be small, as long as the adequate renormalization scheme is used to prevent the formation of the unphysical gas of bound di-neutrons. Consequently, experimental constraints of the pairing localization and strength based solely on halo properties are unlikely.

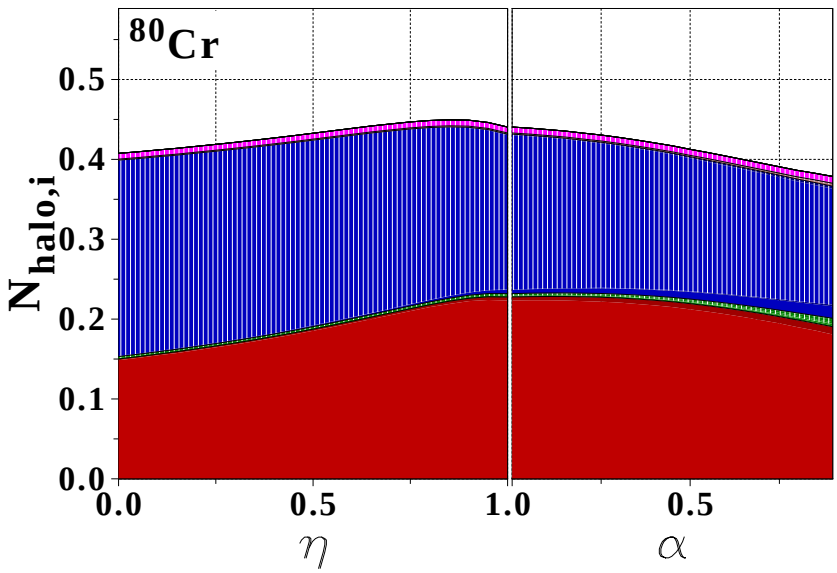

Figure 4.36: Individual neutron contributions $N_{\text{halo,i}}$ for ^{80}Cr and different renormalized REN-X pairing functionals.

4.6 Model-independence of the method

In order to illustrate the model-independence of the new analysis method, we show how it can be applied to other quantum many-body systems, e.g. to results of many-body ab initio calculations of light nuclei nuclei as well as of atom-positron complexes. The purpose is to illustrate the fact that the formation of a halo is a generic quantum phenomenon caused by the possibility for non-classical systems to expand through a potential barrier, i.e. it is related to an universality class in terms of dimensionless quantities.

4.6.1 Light nuclei

To check the consistency of the method in a situation where core and halo densities are explicitly computed, values of N_{halo} and δR_{halo} have been extracted from coupled-channels calculations of light nuclei. The latter are performed for a core+neutron system for which the internal dynamics of the core is taken into account [275; 276] and the total Hamiltonian reads as

$$H_{\text{tot}} = H_{\text{core}} + T_{\text{rel}} + v_{\text{n-core}} \,, \tag{4.5}$$

where T_{rel} is the kinetic energy of the loose nucleon with respect to the core fragment, described by the Hamiltonian H_{core}, and $v_{\text{n-core}}$ denotes the residual core-nucleon interaction. To provide adequate nuclear quadrupole couplings, a deformed Woods-Saxon potential in the core rest frame is considered, i.e.

$$v_{\text{WS}}(r,\theta) = \left[1 + e^{\frac{r-R(\theta)}{a_{\text{WS}}}}\right]^{-1} , \qquad R(\theta) = R_{\text{WS}}\left(1 + \beta\, Y_2^0(\theta)\right) , \tag{4.6}$$

where β is the core quadrupole deformation. The total wave-function is expanded in a basis of eigenstates of the total angular momentum using a separation of the core internal motion, with eigenstates associated to the energies ϵ_i, from the core-neutron relative motion. Resulting coupled-channels equations for the loosely bound nucleon wave function Ψ_i read then

$$\left(T_{\text{rel}} + \epsilon_i - E\right)\, \Psi_i + \sum_j v_{ij}^{n-c}\, \Psi_j = 0 \,, \tag{4.7}$$

	Core		Total		
	N_{halo}	δR_{halo} [fm]	N_{halo}	δR_{halo} [fm]	$R_{\text{r.m.s.}}$ [fm]
^{13}C	0.000	0.000	$0.66.10^{-3}$	$0.74.10^{-3}$	2.487
^{11}Be	0.000	0.000	0.270	0.394	2.908

Table 4.6: Values of N_{halo} and δR_{halo} for ^{13}C (non-halo) and ^{11}Be (one-neutron halo). Criteria are applied to results obtained through coupled-channels calculations [275; 276].

and are solved in a Sturmian basis[8], that is a basis which maintains proper asymptotics [343].

Calculations have been performed for two nuclei: the well-established one-neutron halo ^{11}Be, whose total density and core+halo decomposition are plotted in FIG. 4.37a, and the stable nucleus ^{13}C as a control case for non-hao nuclei in FIG. 4.37b. Results are summarized in TAB. {4.6}, where the two criteria are evaluated for core and total densities. For ^{11}Be, r_0 is

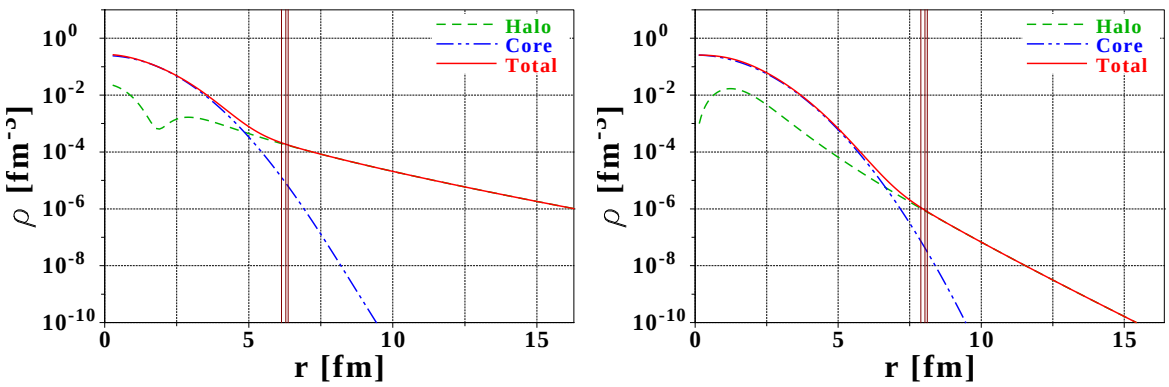

(a) ^{11}Be (b) ^{13}C

Figure 4.37: Core, halo and total neutron densities obtained from coupled-channels calculations [275; 276]. The value of r_0 and the tolerance margin are indicted by vertical lines.

found to be compatible with the condition to have one order of magnitude difference between core and halo densities at that radius. The tail-to-core ratio is slightly different from ten, partly because the core is represented by a gaussian profile with the wrong asymptotics. In any case, the ideal value of r_0 still lies within the allowed theoretical error. This validates the method on a realistic system. The halo parameter N_{halo} shows that around 0.3 neutron reside in the decorrelated region in average. The reason why one only finds a fraction of a neutron within the halo region is because the wave function of the "halo nucleon" lies partly inside the volume of the core. The denomination of one-neutron halo is somewhat misleading from that point of view. The influence δR_{halo} of the halo on the nuclear extension is large, of about 0.4 fm out of a total root-mean-square (r.m.s.) radius of 2.90 fm. Note that such a value is very close to the value extracted experimentally when going from ^{11}Be to ^{10}Be [344]. Last but not least, N_{halo} and δR_{halo} are found to be negligible for the two control cases considered, i.e. ^{13}C and the core density of ^{11}Be. This illustrates the ability of the method to discriminate between halo and non-halo systems.

[8]The latter is also defined as Weinberg states.

Atom	Asympt.	N_{e^-}	N_{halo}	$R_{\text{r.m.s.}}$	δR_{halo}	P_{e^+}	P_{e^-}	E_{gs} [a.u.]	ϵ [a.u.]	Ref.
Be	e^++Be	4	0.624	5.66	3.19	98.1	01.9	−1.0151	0.0032	[353]
Mg	e^++Mg	12	0.669	2.30	0.83	80.3	19.7	−0.8477	0.0156	[354]
Cu	e^++Cu	29	0.754	1.78	0.98	88.6	11.4	−0.2891	0.0051	[351]
He	Ps+He$^+$	2	1.982	15.47	14.57	50.3	49.7	−2.2506	0.0006	[355]
Li	Ps+Li$^+$	3	1.972	7.78	7.09	50.8	49.2	−7.5324	0.0024	[356]

Table 4.7: Results of the halo analysis for various atom-positron systems evaluated with the fixed-core stochastic variational method. Fron left to right: neutral atom symbol, asymptotic form, total number of electrons N_{e^-}, halo factors N_{halo} and δR_{halo}, total matter r.m.s. radius $R_{\text{r.m.s.}}$, relative proportions P_{e^+} and P_{e^-} of electrons and positrons in the halo region (in %), ground-state energy E_{gs} of the e^++A complex, and binding energy ϵ with respect to the corresponding dissociation threshold. All length units are normalized to the Bohr radius a_0, and energy values are in atomic units (1 a.u. = 27.21162 eV).

4.6.2 Atom-positron/ion-positronium complexes

In atomic physics, valence electrons of neutral atoms can be located at a large distance from the core. Because of the very long range of the Coulomb interaction, the penetration of the wave-function into the classically forbidden part of the potential as the separation energy of the system becomes small cannot be interpreted as a halo formation [37]. However, a positron can be attached to a neutral atom by the polarization potential, which can be parametrized as

$$v_{\text{pol},1}(\vec{r}) = -\frac{\alpha_D\, g^2(r)}{2r^4} \underset{r\to+\infty}{\longrightarrow} -\frac{\alpha_D}{2r^4}\,, \qquad g^2(r) = 1 - e^{-\frac{r^6}{\beta^6}}\,, \tag{4.8}$$

where α_D is the core polarization constant and β a cutoff distance. In this case, the r^{-4} decay of the potential at large distances does not ensure that particles are able to tunnel through the potential barrier. It was found that several atom-positron complexes can exist [345–352], some of which having halo characteristics [353]. To quantify such an observation, values of N_{halo} and δR_{halo} are evaluated. The Hamiltonian of the atom-positron system with N_{val} valence electrons reads with normalized units ($m_e = e = 1$) [346; 347]

$$\begin{aligned}\hat{H} = &\sum_{i=1}^{N_{\text{val}}}\left(-\frac{1}{2}\vec{\nabla}_i^2 + v_{\text{dir}}(\vec{r}_i) + v_{\text{ex}}(\vec{r}_i) + v_{\text{pol},1}(\vec{r}_i)\right) + \sum_{\substack{i,j=1\\ i<j}}^{N_{\text{val}}}\left(\frac{1}{r_{ij}} - v_{\text{pol},2}(\vec{r}_i,\vec{r}_j)\right)\\ &-\frac{1}{2}\vec{\nabla}_0^2 - v_{\text{dir}}(\vec{r}_p) + v_{\text{pol},1}(\vec{r}_p) - \sum_{i=1}^{N_{\text{val}}}\left(\frac{1}{|\vec{r}_i - \vec{r}_p|} - v_{\text{pol},2}(\vec{r}_i,\vec{r}_p)\right)\,,\end{aligned} \tag{4.9}$$

where $\vec{r}_p$ is the positron position, $\vec{r}_{ij} = \vec{r}_i - \vec{r}_j$ is the relative position of two valence electrons, whereas direct v_{dir} and exchange v_{ex} potentials between valence electrons and the core are computed exactly in the Hartee-Fock approximation. The two-body polarization potential is defined as

$$v_{\text{pol},2}(\vec{r}_i,\vec{r}_j) = \frac{\alpha_d}{r_i^3\, r_j^3}(\vec{r}_i\cdot\vec{r}_j)\, g(r_i)\, g(r_j)\,. \tag{4.10}$$

When the e^++A system is bound, its asymptotic behavior can correspond to (i) a neutral core A plus a positron e^+, or (ii) a charged core A^+ and a neutral positronium complex Ps,

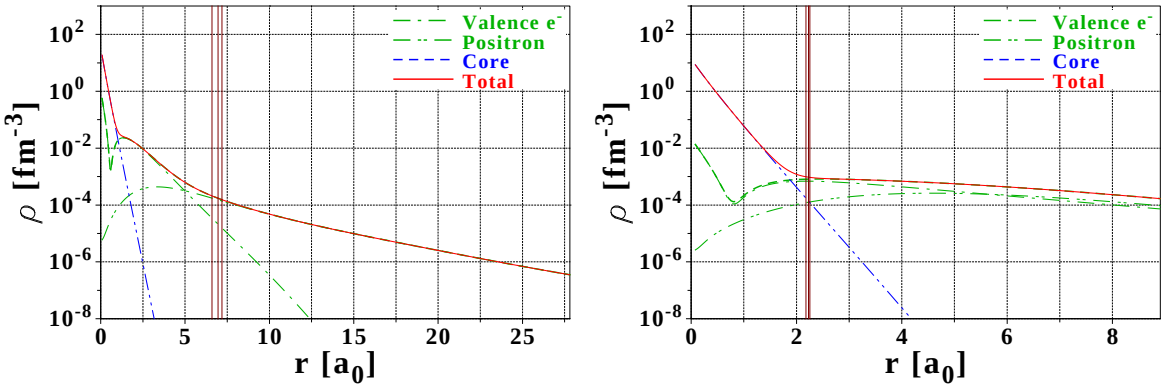

(a) e^++Be (b) e^++Li

Figure 4.38: Valence electron, positron, core and total density for e^++A complexes evaluated with the fixed-core stochastic variational method. All length units are normalized to the Bohr radius a_0. The value of r_0 and the tolerance margin are indicated by vertical lines.

depending on the relative binding energies of those configurations. Calculations are performed with the fixed-core stochastic variational method (FCSVM) [347; 354; 357–359], in a basis of explicitly correlated gaussians for the individual wave functions. The basis is taken large enough to correctly reproduce the asymptotic behavior of the e^++A or Ps+A$^+$ systems. Results of such calculations for e^++Be, corresponding to the e^+Be complex, are presented in Fig. 4.38a, where the separation at large distances between a weakly bound positron and a core composed of the electrons is visible. As a result, a positron extended tail appears. In Fig. 4.38b are also displayed the results for the e^++Li system, which corresponds to a PsLi$^+$ complex. Indeed, one clearly observes that the density tail is composed of almost identical e^+ and e^- components.

Results of our analysis, performed for several atom-positron complexes, are presented in Tab. {4.7}. The separation energy ϵ in the appropriate channel (e^++A or Ps+A$^+$) is small compared to the ground-state energy $E_{\rm gs}$ of the complex. The situation regarding the energy scales at play is very favorable as far as the formation of halos is concerned. It is also possible to evaluate the composition of the halo region in terms of the proportion of electrons P_{e^-} and of positrons P_{e^+}. Values of $N_{\rm halo}$ and $\delta R_{\rm halo}$ demonstrate the existence of halos in e^++Be, e^++Mg and e^++Cu which strongly affect the system extension. For example, the spatially decorrelated part of the density accounts for about half of the total r.m.s. radius in e^++Be, although it contains only ~ 0.7 particle in average. In those cases, a positron halo is predicted given that the halo region is almost exclusively built from the positron wave-function ($P_{e^+} \gg P_{e^-}$). In the cases of e^++Li and e^++He, very large values for $N_{\rm halo}$ and $\delta R_{\rm halo}$ are also extracted. It corresponds to ion-positronium halos with $P_{e^+} \approx P_{e^-}$. Considering the values of $N_{\rm halo}$ and $\delta R_{\rm halo}$, one realizes that atom-positron and ion-positronium complexes display more extreme halo structures than nuclei. This is of course due to the nature of the interaction at play in such systems.

4.6.3 Universality of the phenomenon

Even if the analysis method that we have developes intended to provide quantitative criteria for halos in medium-mass nuclei, the previous section demonstrated that it can be applied successfully to other finite quantum systems. Our method actually relies on a model-independent analysis of the intrinsic one-body density $\rho_{[1]}(\vec{r})$. In all cases, a fraction of constituents extends

far out from the core and influences strongly the size of the system.

Halo systems display scaling properties which do not depend on their dimension and constituency. This can be characterized by the extension of the halo wave-function $\langle r_h^2 \rangle$ as a function of the separation energy E, and those quantities can be made dimensionless using as a scale the classical turning point R_q for the interaction potential of interest and the reduced mass of the systems μ [37; 274; 278; 280]. Generic asymptotic scaling laws for the two-body domain are extracted using a finite spherical well, and depend on the angular momentum of the weakly-bound overlap function [280], as seen in Fig. 4.39. Results for light nuclei obey rather well such universal scaling laws. For few-body nuclei, it is commonly admitted that halos appear when $\langle r_h^2 \rangle / R_q^2 > 2$, which corresponds to a probability greater than 50 % for the weakly-bound nucleon to be in the forbidden region [37].

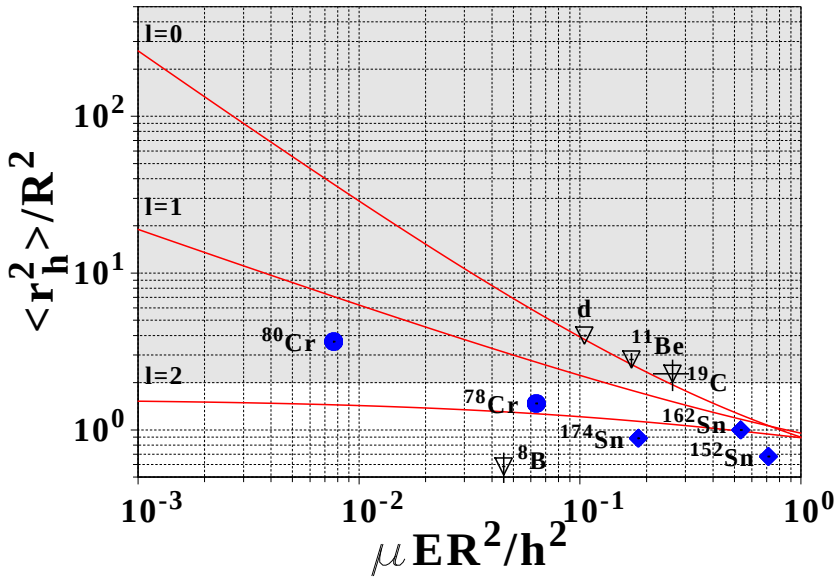

Figure 4.39: Universality of halos features. The dimensionless extension of the halo is plotted against the dimensionless separation energy for EDF calculations of medium-mass nuclei (filled symbols) and experimental results for few-body systems (open symbols). Generic scaling relationships obtained from a finite spherical well are given in solid lines, while the gray-shaded area corresponds to the halo are, as defined by the commonly-used criterion for few-body halo nuclei $\langle r_h^2 \rangle / R^2 > 2$.

Results obtained for medium-mass nuclei can also be displayed in Fig. 4.39 and compared with generic scaling laws. However, dimensionless quantities have to be redefined. For medium-mass systems the halo r.m.s. radius is evaluated, by analogy with Ref. [278], through

$$\langle r_h^2 \rangle = \frac{N}{\mu} \langle r_{\text{tot}}^2 \rangle - \frac{N - N_{\text{halo}}}{\mu} \langle r_{\text{core}}^2 \rangle \,, \tag{4.11}$$

where $\langle r_{\text{tot}}^2 \rangle$ is the total neutron r.m.s. radius, and the core r.m.s. radius is approximated by $R_{\text{r.m.s.,inner}}$ (see Eq. (3.37)). The reduced mass is taken as the effective isoscalar nucleon mass m^*, while the classical turning point R^n of the central part $U^n(r)$ of the one-body potential is

evaluated, by analogy with the finite-well potential, as [280]

$$\frac{\int \mathrm{d}r\, r^3\, U^n(r)}{\int \mathrm{d}r\, r\, U^n(r)} = \frac{R^{n2}}{2}\,. \tag{4.12}$$

Last bound Cr isotopes are located in-between the $\ell = 0$ and $\ell = 2$ scaling curves, ^{78}Cr being closer to the $\ell = 2$ curve than ^{80}Cr. This is consistent with the admixture of orbitals that builds the corresponding halos. The neutron density of most medium-mass halo nuclei does not extend as much as those of few-body systems such as ^{11}Be. Still, ^{78}Cr and ^{80}Cr display few-body-like halo properties and the ratio $\langle r_h^2 \rangle / R_n^2$ does exceed 2 for ^{80}Cr. On the contrary, the extension of neutron-rich tin isotopes is not significant enough in regard with their separation energy to be characterized as halo systems. This is consistent with the findings of Sec. 4.2.1.2.

It would be of interest to place atom-positron complexes in Fig. 4.39. However, the many-body method used to compute their properties does not allow an easy extraction of the corresponding classical turning point. As a result, corresponding values do not appear in Fig. 4.39.

Conclusions

The existence of halos at the neutron drip-line of medium-mass nuclei is still an open question. Several attempts to characterize their properties have already been made using relativistic or non-relativistic energy density functional methods [289; 294; 295]. However, those analysis were based on a limited set of observables, such as the root-mean-square radius, and remain rather qualitative.

In the present work, a quantitative analysis method is developed to characterize halos in a completely model-independent fashion. It is based on the decomposition of the internal one-body density in terms of overlap functions. The definition of the halo, as a region where nucleons are spatially decorrelated from the others, is connected to specific patterns of the internal one-body density and of the energy spectrum of the $(N-1)$-body system. Indeed, specific scales appearing in that excitation energy spectrum translate into the existence of more or less sharp crossings between overlaps functions contributing to the internal density of the N-body system. We highlight the possibility to characterize the halo in terms of three energy scales: the small nucleon separation energy E, the small energy spread ΔE of low-lying excitations, and the large excitation energy E' of the upper-lying states (the "core") with respect to low-lying ones. The method to identify the radius beyond which the halo density dominates over the core has been defined and validated by simulations. It is important to stress that the method does not rely on an *a priori* separation of the density into core and halo components. The latter are extracted from the analysis, using the total matter density as the only input. Several quantitative observables are then introduced, namely (i) the average number of nucleons participating in the halo region, (ii) the influence of the halo region on the total nuclear extension, and (iii) the contributions from individual overlap functions to the total halo. In comparison with other methods [292; 293; 296–299], all properties related to the formation of halos, such as the kink of the neutron r.m.s. radius or the core/halo decomposition, come only as *outputs* of the method, which is solely based on model-independent properties of $\rho(r)$ and a generic definition of the halo.

The new analysis method has been applied to the results obtained from energy density functional calculations of chromium and tin isotopes. Drip-line Cr isotopes appear as ideal halo candidates whereas tin isotopes do not. For drip-line Cr isotopes, the average number of nucleons participating in the halo is of the order of ~ 0.5. Such a value is compliant with the ones found for light halo systems. The halo region is also found to influence significantly the nuclear extension. Contributions from several individual states, including $\ell = 2$ ones, are identified, which is not expected in the standard picture that arises from few-body models. **The notion of collective halos in medium-mass nuclei is introduced**. In the case of Sn isotopes, the average number of nucleons participating in the halo is very small nd has no influence on the nuclear extension. Thus, the drip-line phenomenon previously discussed for tin isotopes [289] is rather a pronounced neutron skin effect. Such skin effects are of course of great interest as they emphasize the isovector dependence of the energy density functionals. However, they should not

be confused with halo systems which display an additional long tail of low-density matter.

The impact of pairing correlations on halo systems is further studied according to different directions. First, it is shown that the pairing anti-halo effect might be counter-balanced by pair scattering to less-bound orbitals, possibly with small orbital angular momenta. The net effect on the formation of halos greatly depends on the details of the single-particle spectrum of the nucleus under study. Second, low-ℓ orbitals are found to be less paired than high-ℓ ones, but not enough to really decorrelate from the pairing field, as it is the case in (non-realistic) extreme conditions [286; 287]. Third, the low-density-dependence of the pairing functional is shown to have almost no effect on the formation of halos, as long as it is combined with the proper renormalization scheme.

On the contrary, halo properties significantly depend on the characteristics of the particle-hole part of the nuclear EDF. This shows that medium-mass halo systems might be more useful to constrain the particle-hole part of the functional than its particle-particle counterpart. Unfortunately, such experimental data are not likely to become available any time soon, even with the next generation of radioactive beam facilities. Indeed, although the neutron density becomes accessible through several experimental techniques [304; 360–364], extracting it in medium-mass drip-line nuclei is more than a challenge for the decade(s) to come. In addition, the neutron r.m.s. radius is not sufficient to study halos quantitatively, and other probes have to be envisioned [37]. Of course, a precise determination of the neutron r.m.s. radius and associated neutron skin in non-halo systems is already crucial as it provides constraints on the physics of neutron stars [365; 366] and on the nuclear symmetry energy [367; 368], for instance. As a result, one should focus at first on the study of neutron skins in non-halo systems to constrain the isovector nature of the nuclear EDF. The fine tuning provided by extreme exotic systems such as medium-mass halo nuclei should only come as a second step. One will see in the following that other constraints based on microscopy look more promising in that respect.

Still, it is of theoretical interest to understand the structure of halo nuclei and to assess their occurrence over the nuclear chart. With that in mind, we performed large-scale calculations over all (predicted) spherical even-even nuclei. It was concluded that (i) several isotopic chains may display neutron halos, (ii) halos can only exist at the *very* limit of neutron stability, (iii) very few heavy elements, in the (Pt, Hg, Tl...) region, are found as possible halo candidates, (iv) on the large scale, the halo phenomenon is very rare, almost accidental and requires the presence of a low-lying state with an orbital angular momentum $\ell \leq 1$, (vi) medium-mass halos are more collective than in light nuclei, with non-negligeable contributions from several low-lying states, and (vi) as expected, the impact of the halo on the nuclear extension decreases with the total mass.

Let us now turn to potential further works and developments. First, several extensions of the newly proposed method can be envisioned. For instance, the extraction of halo properties in deformed systems, which represent the majority of known or predicted nuclei, requires additional formal developments, starting from a decomposition of the nuclear density in multipoles, i.e.

$$\rho(\vec{r}\,) = \sum_{\ell,m_\ell} \rho_\ell^{m_\ell}(r)\, Y_\ell^{m_\ell}(\hat{r}\,)\,. \tag{4.13}$$

The analysis regarding the relative asymptotic positioning of spectroscopic amplitudes should then be adapted to multipoles $\rho_\ell^{m_\ell}(r)$. Effects such as the increased contamination of weakly-bound deformed orbitals by $\ell = 0$ components at the limit of stability, favoring the formation of halos in deformed systems [288; 369–371], could be investigated. In addition to deformed systems, the method should be extended to odd-even and odd-odd nuclei. This would require to

formulate the method for non-zero spin states. Also, effects of an explicit treatment of long-range correlations, e.g. symmetry restorations and large-amplitude collective motion, on medium-mass halo nuclei should be studied in connection with the analysis method proposed in the present work. Then, the explicit inclusion of such correlations would allow a more reliable extraction of N_{halo} and δR_{halo} in light systems through EDF calculations. For instance, the study of ^{22}C, which is predicted to be a halo system by few-body calculations [372], could provide a bridge between few- and many-body techniques. Restoration of cluster correlations could also play a significant role, since they are believed to hinder the halo formation in heavy systems [37]. Pionic fusion reactions might allow the extraction of such correlations [373].

Finally, it would be of interest to conduct the same study using the Gogny effective interaction to further probe the dependence of the results on the characteristics of the energy density functional, e.g. finite-range effects. Such a study is not feasible using traditional codes making use of a harmonic oscillator basis because the asymptotics of the one-body density is not described correctly enough to extract N_{halo} and δR_{halo} reliably. However, a newly developed code expanding the quasiparticle states on the eigenstates of a a Woods-Saxon potential should allow one to do so [190].

Part II

Ab-initio approach to the nuclear many-body problem

- [Bart] I was so bored I cut the pony tail off the guy in front of us. Look at me, I'm a grad student. I'm 30 years old and I made $600 last year.

- [Marge] Bart, don't make fun of grad students. They've just made a terrible life choice.

Introduction

Although a description of nuclear forces starting from non-perturbative high-energy QCD calculations is beyond reach, at least for the next decade, the construction of high-quality nucleon-nucleon (NN) models has met a lot of successes so far [79; 80; 83; 374]. "High quality" means that large sets of available experimental data for two-body observables are reproduced with statistical precision. These observables include scattering [375] (amplitudes, phase shifts, scattering lengths...) and bound state [376–379] (binding energy, quadrupolar moments, charge radii...) properties of two-nucleon systems. While different models based on operatorial expansions or one-boson exchange potentials (OBEPs) reach the same level of accuracy on low-energy data, they also share a description of the short-range interaction as a complex process incorporating a hard-core repulsion associated with the inter-penetration of the two nucleons. Such interactions are therefore intrinsically non-perturbative, which raises the question of their practical use for many-nucleons systems, where many-body effects come into play. In a diagrammatic formalism, the relevant object becomes the nuclear G-matrix which derives from the initial bare NN force but adds non-trivial in-medium effects to all orders in the vacuum interaction. The equation of state of infinite nuclear matter can be predicted via hierarchized G-matrix calculations whereas GFMC or NCSM techniques can be applied to very light nuclei. Unfortunately calculations of medium- to heavy-mass nuclei in terms of non-perturbative (NN) potentials are sparse and restricted to doubly-magic nuclei [380].

Likewise, the construction of three-body models that reproduce three-body observables is possible [59; 381–383], while some issues remain. Based on mesons exchanges ($2\pi/3\pi$, $\pi\rho$, $\rho\rho$...) plus empirical short range components, they are adjusted on binding energies and scattering observables of three- (and four-) body systems [384–386]. Ab initio calculations using vacuum two- and three-body forces gives then essentially exact results for very light nuclei.

Regarding the previous discussion, the derivation of vacuum low-momentum potentials $V_{\mathrm{low}\,k}$ using the renormalization group (RG) formalism constitutes a new paradigm for nuclear interactions [87]. Indeed, it allows a coherent construction of low-momentum potentials, i.e. soft-core forces, explicitly connected to hard-core ones through flow equations that keep low-energy two-body scattering and bound state observables unchanged. In that respect, finite nuclei calculations can be envisioned with reduced basis sets which unveils new possibilities for low-energy nuclear structure studies. Indeed, low-momentum interactions are by essence perturbative, in the sense that MBPT calculations are possible and fastly converging. For instance, nuclear matter calculations with low-momentum NN and NNN forces already give good saturation properties at second order in MBPT [387]. This proves that $V_{\mathrm{low}\,k}$ stands as an ideal practical starting point for finite nuclei calculations.

As a first step towards the construction of non-empirical EDFs, a study of existing nuclear forces and the standard benchmarks used to characterize them is needed. Thus, Chap. 5 briefly presents available high-precision NN models including $V_{\mathrm{low}\,k}$, as well as the construction of NNN

forces. Several observables which will be of interest later on are also specified, e.g. scattering phase shifts, deuteron properties or Weinberg eigenvalues. Then, the treatment of the nuclear many-body problem via diagrammatic techniques is briefly introduced in Chap. 6. Finally, the infinite nuclear matter system, which is used as a reference laboratory for nucleon-nucleon interactions, is introduced in Chap. 7. In particular, discussions regarding (i) the framework for constructing effective density-dependent two-body forces from bare NN ones, and (ii) a quantitative characterization of the perturbative nature of different nucleon-nuclon interactions are carried out. Other preliminary results that are essential regarding the construction of non-empirical nuclear EDFs are also given. Complete derivations of the used nuclear observables can be found in Appendix D alongside with all necessary definitions and conventions, whereas only the main results are presented here.

Chapter 5

Vacuum nuclear interactions

Abstract: This chapter presents the status of the theoretical description of nuclear forces. While several accurate models exist for the description of the bare nucleon-nucleon interaction, an emphasis is put on a new paradigm constituted by so-called low-momentum interactions $V_{\text{low}\,k}$ based on the application of the renormalization group (RG). Indeed, such interactions possess important properties that makes them ideal starting points for low-energy nuclear structure calculations. Standard benchmarks used to taylor bare NN forces such as scattering phase shifts, deuteron properties or Weinberg eigenvalues, are introduced. Finally, the description of bare three-body forces in the context of chiral effective field theory ($\chi-$EFT) is also discussed.

Contents

5.1 Bare nucleon-nucleon forces **142**
5.1.1 General expression from fundamental symmetries 142
5.1.2 High-precision parametrizations 143
5.2 Three-nucleon interaction **147**
5.3 Properties of bare nucleon-nucleon forces **151**
5.3.1 Momentum space 152
5.3.2 Partial wave decomposition 153
5.3.3 Scattering phase shifts 154
5.3.3.1 Lippmann-Schwinger equation 154
5.3.3.2 Definitions and conventions 156
5.3.3.3 Coulomb corrections for proton-proton phase shifts 159
5.3.3.4 Scattering parameters 160
5.3.4 Deuteron properties 161
5.3.5 Weinberg eigenvalues 162
5.4 Vacuum NN forces from renormalization group techniques **164**
5.4.1 Low-momentum nucleon-nucleon forces 165
5.4.2 Properties of $V_{\text{low}\,k}$ 170

5.1 Bare nucleon-nucleon forces

5.1.1 General expression from fundamental symmetries

While obtaining an exact expression of the vacuum nucleon-nucleon interaction from first principle is not possible, a general form for the strong nuclear force[(1)]

$$v_S^{\mathrm{NN}}(\mathbf{1},\mathbf{2}) \equiv v_S^{\mathrm{NN}}(\vec{r}_1\,\vec{k}_1\,\sigma_1\,q_1\,;\vec{r}_2\,\vec{k}_2\,\sigma_2\,q_2)\,, \tag{5.1}$$

can be further constrained by considering its fundamental symmetries. Indeed, it is [122]

- hermitean,
- invariant under nucleon exchange
$$v_S^{\mathrm{NN}}(\mathbf{1},\mathbf{2}) = v_S^{\mathrm{NN}}(\mathbf{2},\mathbf{1}),$$
- translationally invariant
$$v_S^{\mathrm{NN}}(\mathbf{1},\mathbf{2}) \equiv v_S^{\mathrm{NN}}(\vec{r};\vec{k}_1\,\sigma_1\,q_1\,;\vec{k}_2\,\sigma_2\,q_2),$$
- Galilean invariant
$$v_S^{\mathrm{NN}}(\mathbf{1},\mathbf{2}) \equiv v_S^{\mathrm{NN}}(\vec{r};\vec{k}\,;\sigma_1\,q_1\,;\sigma_2\,q_2),$$
- invariant under space reflection (no parity violation)
$$v_S^{\mathrm{NN}}(\vec{r};\vec{k}\,;\sigma_1\,q_1\,;\sigma_2\,q_2) = v_S^{\mathrm{NN}}(-\vec{r};-\vec{k}\,;\sigma_1\,q_1\,;\sigma_2\,q_2),$$
- invariant under time-reversal symmetry
$$v_S^{\mathrm{NN}}(\vec{r};\vec{k}\,;\sigma_1\,q_1\,;\sigma_2\,q_2) = v_S^{\mathrm{NN}}(\vec{r};-\vec{k}\,;-\sigma_1\,q_1\,;-\sigma_2\,q_2),$$
- invariant under rotations in cordinate space, that is v_S^{NN} is a scalar and
$$v_S^{\mathrm{NN}}(\vec{r};\vec{k}\,;\sigma_1\,q_1\,;\sigma_2\,q_2) = v_S^{\mathrm{NN}}(\vec{r};\vec{k}\,;\sigma_2\,q_1\,;\sigma_1\,q_2).$$

At the same time, isospin dependencies are more complex. Indeed experimental evidences of NN data [388; 389], such as the $^1\mathrm{S}_0$ scattering lengths, imply that the nucleon-nucleon interaction slightly breaks the charge symmetry [390] (different force between pp and nn), and the charge independence [391; 392] (different force between np and nn/pp in the same isospin T state). In that respect, the bare NN force can be separated according to a classification according to of isospin operators [393], i.e.

- Class I forces have only dependencies on $[\mathbb{I},(\tau_1\cdot\tau_2)]$, and do not break either charge symmetry or independence,
- Class II forces maintain charge symmetry but are charge-independence-breaking (CIB). They are characterized by the isotensor T_{12} defined by analogy to the usual tensor S_{12}, and vanish for $T_z=\pm1$ (nn or pp) systems,
- Class III forces are both charge-symmetry-breaking (CSB) and CIB, but remain invariant under the exchange of the two nucleons, and are thus proportional to $(\tau_{z1}+\tau_{z2})$. They do not cause isospin mixing since T_z commutes with T^2, and vanish for $T_z=0$ (np) systems,
- Class IV forces are both CSB and CIB, and are antisymetric under the exchange of the two nucleons, which causes isospin mixing. They are proportional to $(\tau_{z1}-\tau_{z2})$ or $(\tau_1\times\tau_2)_z$, and vanish for $T_z=\pm1$ systems.

Modern NN potential include CSB/CIB effects [83; 394], through meson/nucleon mass differences (e.g. m_n/m_p mass difference for CSI, $\pi^0/\pi^\pm$ for CIB), meson mixing or isospin-violating couplings ("triangle" and "football" diagrams)...

[1] The dependence on the impulsions of the incoming nucleons is a convenient way to treat the non-locality of the potential as well as taking into account relativistic effects.

The most general class-I two-body potential invariant under the fundamental symmetries recalled above can be decoupled into [395]

$$v_{12}^{\mathrm{NN}} = \sum_p v_p^{\mathrm{NN}}(r) \begin{pmatrix} \mathbb{I}\begin{bmatrix} \mathbb{I} \\ (\sigma_1 \cdot \sigma_2) \end{bmatrix} \\ \mathsf{S}_{12} \\ (\mathbf{L} \cdot \mathbf{S}) \\ \mathsf{Q}_{12} \\ (\sigma_1 \cdot \mathbf{k})(\sigma_2 \cdot \mathbf{k}) \end{pmatrix} \begin{pmatrix} \mathbb{I} \\ (\tau_1 \cdot \tau_2) \end{pmatrix}, \tag{5.2}$$

where appear the so-called central $\mathbb{I}$, tensor S_{12}, spin-orbit $(\vec{\mathbf{L}} \cdot \vec{\mathbf{S}})$, quadratic spin-orbit Q_{12}, and second tensor $[(\sigma_1 \cdot \mathbf{k})(\sigma_2 \cdot \mathbf{k})]$ components, where

$$\mathsf{S}_{12} = \frac{3}{r^2}(\sigma_1 \cdot \mathbf{r})(\sigma_2 \cdot \mathbf{r}) - \sigma_1 \cdot \sigma_2 \tag{5.3a}$$

$$\mathsf{Q}_{12} = \frac{1}{2}\left[(\sigma_1 \cdot \mathbf{L})(\sigma_2 \cdot \mathbf{L}) + (\sigma_2 \cdot \mathbf{L})(\sigma_1 \cdot \mathbf{L})\right] \tag{5.3b}$$

All operators in Eq. (5.2) have radial prefactors that can be constrained from microscopy or experimental data. The strong interaction is complemented by electromagnetic contributions [396–398], e.g. one- and two-photon Coulomb terms, Darwin-Foldy term, vacuum polarization diagrams, magnetic moment interaction... These corrections include short-range functions which represent the finite size of charge distibutions. These are crucial for the proton-proton force but are also present in the neutron-neutron and neutron-proton potentials because of the internal nucleon structure. Fine effects such as vacuum polarization or 2γ Coulomb are necessary for high-precision potentials.

5.1.2 High-precision parametrizations

The construction of modern high-accuracy NN interactions consists of parametrizing the form factors $v_p^{\mathrm{NN}}(r)$. They are all given by the One-Pion Exchange (OPE) at large distances, while the treatment of the intermediate- and short-range parts differs, and can correspond to either realistic/approximate meson exchanges or phenomenological expressions, such as Yukawa potentials, usually complemented by empirical regularizations (sharp/exponential cutoffs) at very small distances (typ. $r \sim 0.8$ fm). For instance the Paris potential [374] includes the ω meson as part of the three-π exchange (3PE) for the short-range repulsion plus a repulsive hard core. A complete interpretation in terms of meson exchanges provides however an approximate picture for the full NN force, as exemplified by Fig. 5.1, where only mesons with masses lower than the nucleon one $M \approx m_n, m_p$ are considered. So-called *phenomenological* potentials are constructed using the operator structure from Eq. (5.2), although variations may include extra or missing terms. Let us review briefly the main models available.

- The Argonne V18 force [3] complements fourteen charge-independent operators from Eq. (5.2)[2], already used in the V14 [400] or Urbana [401] models, by four Class II and III CIB ones, i.e.

$$v_{12}^{\mathrm{NN}} = \sum_{p=1}^{14} v_p^{\mathrm{NN}}(r)\, O_{12}^p + \sum_{p=15}^{18} v_p^{\mathrm{NN,CIB}}(r)\, O_{12}^p\,, \tag{5.4}$$

[2] In this case, the representation chosen involves $\mathbf{L}^2$ and $(\mathbf{L} \cdot \mathbf{S})^2$ operators instead of Q_{12} and the second tensor.

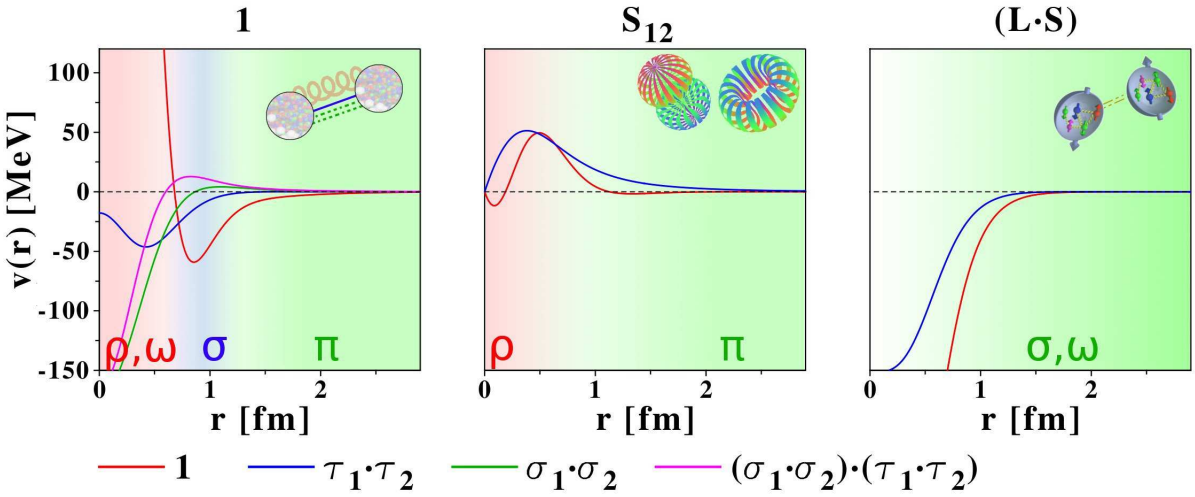

	Mass [MeV] [399]	Range	Type	Contributions		
π	140	Long	Pseudo-scalar	Central	Attractive	$(\sigma_1 \cdot \sigma_2)(\tau_1 \cdot \tau_2)$
				Tensor	Attractive	$\mathsf{S}_{12}\,(\tau_1 \cdot \tau_2)$
σ	600	Int.	Scalar	Central	Attractive	$\mathbb{I}$
				Spin-orbit	Attractive	$\mathbf{L} \cdot \mathbf{S}$
ρ	770	Short	Vector	Central	Attractive	$(\sigma_1 \cdot \sigma_2)(\tau_1 \cdot \tau_2)$
				Tensor	Repulsive	$\mathsf{S}_{12}\,(\tau_1 \cdot \tau_2)$
ω	782	Short	Vector	Central	Repulsive	$\mathbb{I}$
				Spin-orbit	Attractive	$\mathbf{L} \cdot \mathbf{S}$

Figure 5.1: Approximate structure of the bare NN force in terms of meson exchanges. Matrix elements of AV18 in coordinate space are shown in a different representation from FIG. 1.

where

$$O_{12}^{p=1,14} = \begin{pmatrix} \mathbb{I} \\ \mathbf{L}^2 \end{pmatrix} \begin{pmatrix} \mathbb{I} \\ (\sigma_1 \cdot \sigma_2) \end{pmatrix} \begin{pmatrix} \mathbb{I} \\ (\tau_1 \cdot \tau_2) \end{pmatrix}, \begin{pmatrix} \mathbf{L} \cdot \mathbf{S} \\ (\mathbf{L} \cdot \mathbf{S})^2 \end{pmatrix} \begin{pmatrix} \mathbb{I} \\ (\tau_1 \cdot \tau_2) \end{pmatrix}, \tag{5.5a}$$

$$O_{12}^{p=15,18} = \begin{pmatrix} \mathsf{T}_{12} \\ (\sigma_1 \cdot \sigma_2)\,\mathsf{T}_{12} \\ \mathsf{S}_{12}\,\mathsf{T}_{12} \\ (\tau_{z1} + \tau_{z2}) \end{pmatrix}. \tag{5.5b}$$

In this model, only the long-range part is explicitly calculated from one-pion exchange (OPE), while the short- and intermediate-range components are fully phenomenological.

- Relativistic momentum-space one-boson exchange potentials (OBEPs) [402] constructed by the "Bonn group" (Bonn-A/B/C [403], CD-Bonn [79]...) consists of calculating exactly the form factors from exchanged mesons, that is considering scalar, pseudo-scalar and vector

couplings for a transfer momentum $Q = |\vec{q}|$ of the form

$$v_\pi = \frac{f_\pi^2}{3\,m_\pi^2}\,\frac{Q^2}{Q^2+m_\pi^2}\,[-\sigma_1\cdot\sigma_2 - \mathsf{S}_{12}(\hat{q}\,)]\;(\tau_1\cdot\tau_2) \tag{5.6a}$$

$$v_\sigma \approx \frac{g_\sigma^2}{Q^2+m_\pi^2}\left[-1-\frac{\mathbf{L}\cdot\mathbf{S}}{2\,M^2}\right] \tag{5.6b}$$

$$v_\rho = \frac{f_\rho^2}{12\,M^2}\,\frac{Q^2}{Q^2+m_\rho^2}\,[-2\,\sigma_1\cdot\sigma_2 + \mathsf{S}_{12}(\hat{q}\,)]\;(\tau_1\cdot\tau_2) \tag{5.6c}$$

$$v_\omega \approx \frac{g_\omega^2}{Q^2+m_\pi^2}\left[1-3\,\frac{\mathbf{L}\cdot\mathbf{S}}{2\,M^2}\right] \tag{5.6d}$$

Generally, two additional mesons are added within this framework, such that

$$v_{\text{OBEP}} = \sum_{\alpha=\pi,\sigma,\rho,\omega,\eta,a_0\ldots} v_\alpha\,. \tag{5.7}$$

The $\eta(548)$ meson is a pseudo-scalar meson which carries no isospin, i.e. it has the same expression as v_π without the $(\tau_1\cdot\tau_2)$ factor. Likewise, $a_0/\delta(980)$ is a scalar meson with $I=1$, i.e. it has the same expression as v_σ with an extra $(\tau_1\cdot\tau_2)$ factor. Finally, one may note that σ and ω only constitute phenomenological approximations to the correlated two- and three-π exchanges, respectively, and short-range terms are truncated using an exponential regulator. On the other hand, since the σ approximates more than the two-pion exchange (2PE - e.g. $\pi\rho$ exchange...) and it has a very broad mass, its parameters may be refitted in each partial wave to include more physics than a single meson would.

- Another approach consists in representing directly the OBEP in coordinate space, that is involving an extra Fourier transform. Since expressions of the form factors are only analytical in k space, this involves numerical approximations, i.e. expansions up to first order in Q^2/M^2, after which the Fourier transform can be treated. This approach is undertaken by the Nijmegen group for its high-accuracy potentials such as Nijm I& II [80], where heavier mesons also depend on the partial wave. Note that OBEP approaches only contain *iterative* diagrams, that is simple ladders (see Fig. 5.2). On the other hand, several diagrams coming from non-iterative meson exchange contributions are usually omitted, except from more involved models such as the "Bonn Full Model" [404] or the Paris [374] potential, which include these effects, explicitly or implicitly. Nevertheless, these contributions are found to be rather small, and their omission does not drastically reduce the overall precision.

- Potentials based on Chiral Effective Field Theory (χ-EFT) [405] are based on the separation of scale between the chiral symmetry-breaking scale ("hard scale" $\Lambda_\chi \approx 1$ GeV) and typical momenta of low-energy processes (Q usually of the order of the pion mass $m_\pi \approx 150$ MeV) [406–409]. In that respect, few-nucleon processes can be treated using only nucleons and pions as degrees of freedom, the $\pi - N$ interaction being governed by the spontaneously broken chiral symmetry of QCD. All other heavy mesons and nucleon resonances are integrated out of the theory, and their effects are contained inside a renormalized pion exchange and scale-dependent couplings [410]. The effective Lagrangian only depends in this approximation on a finite number of low-energy constants (LECs), and can be classified using a systematic expansion based on a power counting in terms of $(Q/\Lambda_\chi)^\nu$, where ν is called the chiral order. At a given accuracy $(Q/\Lambda_\chi)^\nu$, only a finite number of terms in the Lagrangian are needed in the low-momentum regime. The leading order interaction corresponding to $\nu = 0$ is noted LO. There is no contribution for $\nu = 1$, and following

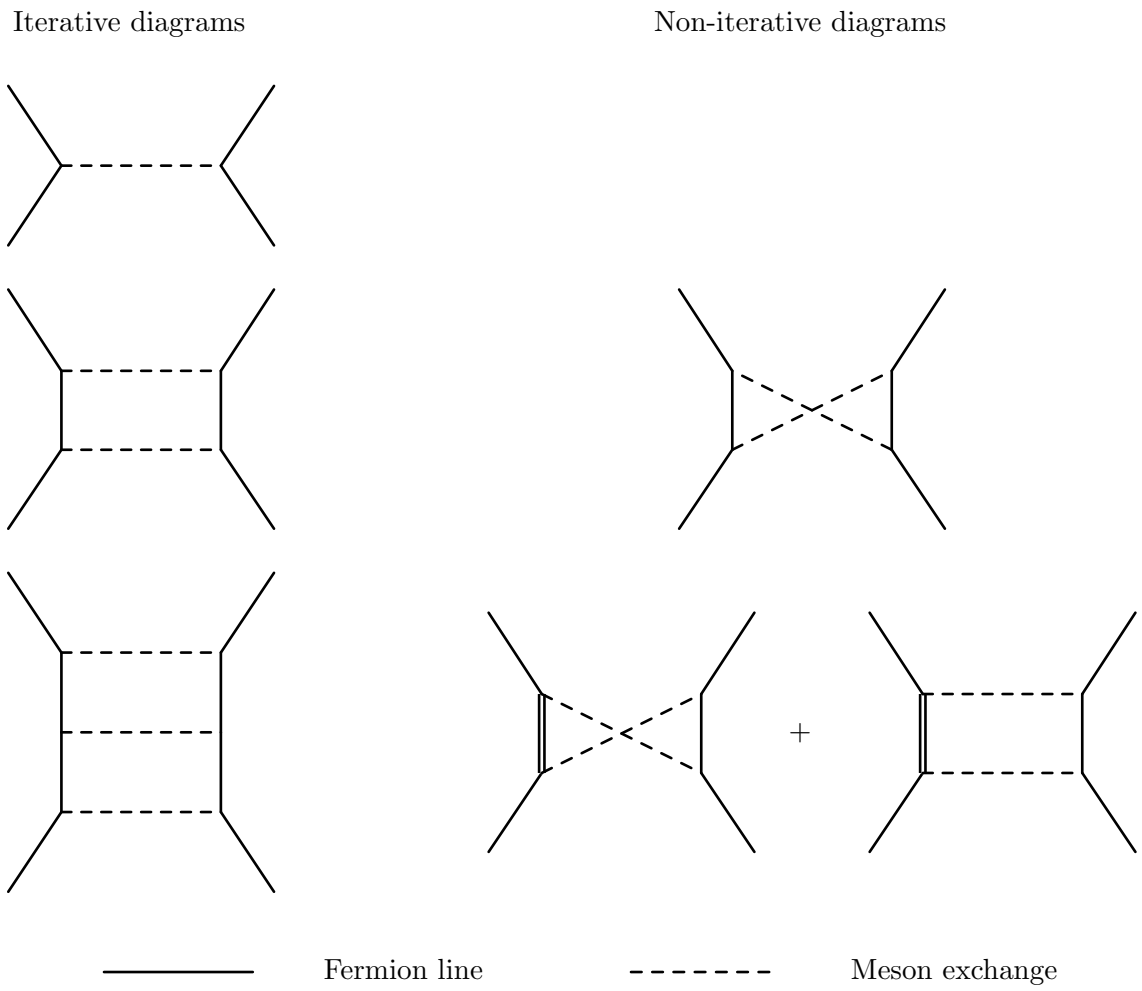

Figure 5.2: (Non-exhaustive examples) Iterative and non-iterative (usually non included in OBEP potentials) diagrams for meson exchanges.

terms $\nu > 1$ are called (next-to-)$^{\nu-1}$ leading-orders ($\mathrm{N}^{\nu-1}\mathrm{LO}$). This framework includes effects beyond the bare NN force, since three-, four-... body effects appear naturally in the perturbative expansion, and the hierarchy $v^{\mathrm{NN}} \gg v^{\mathrm{NNN}} \gg v^{\mathrm{NNNN}} \ldots$ is a natural consequence of the power counting, as shown in Fig. 5.3. For instance, three-body forces do not contribute for $\nu \leq 1$ [405; 411], and appear at next-to-next-to-leading order [411; 412] as the combination of a 2π exchange [2π] process, a 1π exchange between a NN contact force [D], and a pure three-nucleon contact force [E]. Note that LECs associated with NNN forces at $\mathrm{N}^2\mathrm{LO}$ are partly constrained by the two-body domain, such that only the two coupling constants of the contact terms in [D] and [E] are to be adjusted (see Sec. 5.2). At this point, chiral forces exist up to $\mathrm{N}^3\mathrm{LO}$ [83; 409], where most of the NN and OPE/2PE/3PE diagrams have been computed using various approaches such as dimensional [413–417] or spectral function [83; 418; 419] regularization. Improvements of such models may consist in (i) increasing the chiral order ν of the perturbative expansion, although power counting implies that higher contributions will be substantially smaller, as already observed in the case of OPE/2PE [417], (ii) the introduction of four-nucleon forces arising naturally at $\mathrm{N}^3\mathrm{LO}$ [420], (iii) adding extra degrees of freedom, such as nucleon Δ excitations that play a role in three-body forces [10; 83; 421; 422] and isospin breaking NN forces [422], or (iv) refining the short range phenomenological cutoff schemes. Finally,

since χ-PT is a low-momentum expansion, its predictions are by essence only valid for momenta $Q \ll \Lambda_\chi$. Several families of chiral forces are defined depending on the values of the intrinsic high-momentum cutoff up to which they are defined, whose values typically range between 450 and 750 MeVs, that is rather small cuts, such that there is no strong hard core in these potentials.

The two-nucleon part of all previous models are adjusted on low-energy nucleon-nucleon scattering, that is neutron-proton or proton-proton data. In that respect, large sets of experimental data are available [375; 423] for various scattering observables, e.g. angular distributions, scattered and recoil particle polarizations or spin correlations in the final state, for polarized/unpolarized beams/targets at different energies [424]. These amplitudes can be converted into scattering phase shifts, which constitute a standard benchmark to test the accuracy of a given NN force. The standard reference is the partial wave analysis of PWA93 [375]. Some models, like χ-EFT of Paris potentials, are directly adjusted on these phase shifts, but in most cases the fitting occurs at the scattering amplitude level (polarizations and spin correlations...). Thousands of experimental data are available, and make possible the construction of very high-precision form factors, such that most modern forces now have reached statistical accuracy [425; 426], that is a reproduction of experiments with a chi square per degree of freedom $\chi^2/N_{\rm data}$ close to one, as shown in Tab. {5.1}. While χ-EFT forces do not reach yet the accuracy of phenomenological models, the improvement of χ^2 as the order in χ-PT increases is clearly seen, and justifies a posteriori the need to go at least up to N^{3}LO, where the number of free parameters ($N_{\rm data}$) is of the order of phenomenological models, to reach a precision suitable for a direct comparison to experimental data [417; 427].

5.2 Three-nucleon interaction

The need to include many-body forces has been suggested by discrepancies between low-energy properties computed with only two-body forces and experimental data, such as differential nucleon-deuteron cross-sections [4–6], triton and other light nuclei binding energies [7] or the violation of the Koltun sum rule [9]. For instance, the binding energy of ^{3}H versus the one of ^{4}He computed with all available NN models align on a so-called Tjon line that exclude the experimental point [8], as represented in Fig. 5.4. This is seen as a necessity to use consistent NNN forces to sneak away from this Tjon line. Likewise, the Coester line on which lie the saturation point of symmetric nuclear matter computed with NN forces only [12–18], is another indication that NNN forces are essential to reproduce bulk properties of finite nuclei [10; 11].

Phenomenological NNN potentials are available [59; 381–383], based on mesons exchanges ($2\pi/3\pi$, $\pi\rho$, $\rho\rho$...) plus empirical short range components. Using the same philosophy as phenomenological two-nucleon forces, they are adjusted on binding energies and scattering observables of three- (and four-) body systems such as proton/nucleon-deuteron diffusion data [384–386]. In the following, the contribution from three-body forces is discussed in the context of χ-EFT, where they appear naturally at next-to-next-to-leading order in the (Q/Λ_χ) power counting [412]. Note that NNN forces cannot be constructed at this point from RG flow starting from phenomenological models, since the corresponding formalism has not been derived yet. Therefore, there is no consistent low-momentum NN+NNN model available, and three-body effects are added on top of the low-momentum NN force [387].

It is common to decompose the three-body potential as a sum of three terms

$$v^{\rm NNN} = v^{\rm NNN(1)} + v^{\rm NNN(2)} + v^{\rm NNN(3)} \,, \tag{5.8}$$

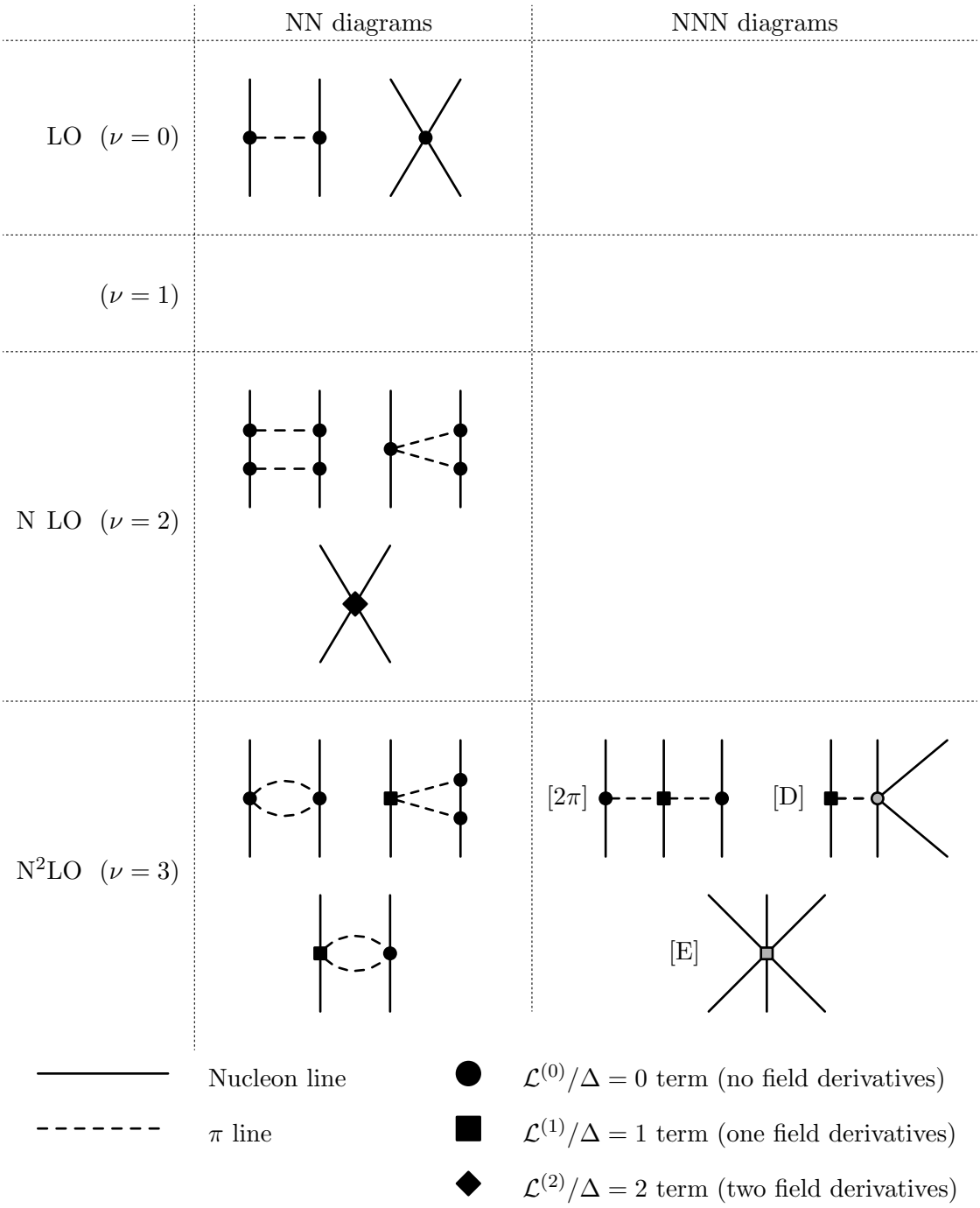

Figure 5.3: Hierarchy of nuclear forces from Chiral Perturbation Theory, classified according to a power counting $(Q/\Lambda_\chi)^\nu$, and restricted to $\nu \leq 3$ for simplicity. Three-body forces appears at next-to-next-to-leading order, but some of the associated low-energy constants are already constrained by the two-body domain (black symbols) while others (gray symbols) are to be adjusted on three-body observables.

	N_{par}	Database		N_{data}	χ^2/N_{data}
PWA93 [375]	39	1992 0 – 350 MeV	np	2514	0.99
			pp	1787	1.00
			np+pp	4301	0.99
		1999 0 – 350 MeV	np	2932	0.99
			pp	1787	1.09
			np+pp	4301	1.04
Argonne V18 [3]	40	1992 0 – 350 MeV	np	2514	1.08
			pp	1787	1.10
			np+pp	4301	1.09
		1999 0 – 350 MeV	np	2932	1.07
			pp	1787	1.35
			np+pp	4301	1.21
CD-Bonn [79]	43	1992 0 – 350 MeV	np	2514	1.03
			pp	1787	1.00
			np+pp	4301	1.02
		1999 0 – 350 MeV	np	2932	1.02
			pp	1787	1.01
			np+pp	4301	1.02
Nijm I [80]	41	1992 0 – 350 MeV	np	2514	1.05
			pp	1787	1.00
			np+pp	4301	1.03
Nijm II [80]	47	1992 0 – 350 MeV	np	2514	1.05
			pp	1787	1.00
			np+pp	4301	1.03
NLO Jülich [428]	2	1999 0 – 290 MeV	np	2402	67 – 105
N^2LO Jülich [428]	9	1999 0 – 290 MeV	np	2402	12 – 27
N^3LO Jülich [83]	26	1999 0 – 290 MeV	np	2402	1.7 – 7.9
		1999 0 – 290 MeV	pp	2057	2.9 – 22.3
N^3LO Idaho [409]	26	1999 0 – 290 MeV	np	2402	1.1 – 1.3
		1999 0 – 290 MeV	pp	2057	1.5 – 2.1

Table 5.1: Accuracy of modern NN models versus experimental scattering data. N_{par} is the number of free parameters. Since pp data are much more precise, the associated χ^2 is systematically higher than for the np case. Two different database for scattering observables have been used, i.e. the 1992 database [375], and an updated version from 1999 [79]. For χ-EFT potential, different families of momentum cutoffs Λ_χ have been used, providing intervals for χ^2/N_{data}.

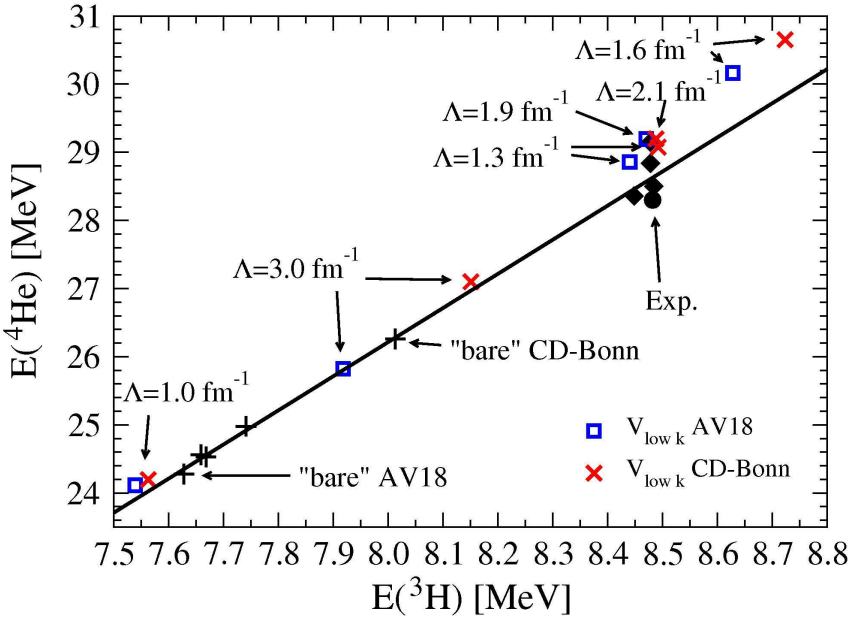

Figure 5.4: The Tjon line for two-body forces, corresponding to the correlation between the binding energies of ^{3}H and ^{4}He for different phenomenological two-body models and $V_{\text{low}\,k}$ (from A. Nogga *et al.* [8]).

where $v^{\text{NNN}(i)}$ is symmetric under the exchange $j \leftrightarrow k$. Specializing to momentum-space representation, in the case of local 3N forces (such as chiral 3NFs), one can show that momentum-space matrix elements have the following structure [429]

$$\langle \vec{k}_1 \vec{k}_2 \vec{k}_3 | v^{\text{NNN}(1)} | \vec{k}'_1 \vec{k}'_2 \vec{k}'_3 \rangle \equiv \left(\frac{2\pi}{\mathcal{V}} \right)^3 \delta(\vec{q}_1 + \vec{q}_2 + \vec{q}_3)\, \tilde{v}^{(1)}(\vec{q}_2, \vec{q}_3)\,, \tag{5.9}$$

where $\mathcal{V}$ is the volume (which drops out of all final expressions) and $\vec{q}_i = \vec{k}_i - \vec{k}'_i$ is the momentum transfer. Similarly, coordinate space matrix elements are given by

$$\langle \vec{r}_1 \vec{r}_2 \vec{r}_3 | v^{\text{NNN}(1)} | \vec{r}'_1 \vec{r}'_2 \vec{r}'_3 \rangle \equiv \delta(\vec{r}_1 - \vec{r}'_1)\, \delta(\vec{r}_2 - \vec{r}'_2)\, \delta(\vec{r}_3 - \vec{r}'_3)\, v^{\text{NNN}(1)}(\vec{r}_2 - \vec{r}_1, \vec{r}_3 - \vec{r}_1)\,, \tag{5.10a}$$

$$v^{\text{NNN}(1)}(\vec{r}_2 - \vec{r}_1, \vec{r}_3 - \vec{r}_1) = \frac{1}{(2\pi)^6} \int \mathrm{d}\vec{q}_2\, \mathrm{d}\vec{q}_3\, e^{i\vec{q}_2 \cdot (\vec{r}_2 - \vec{r}_1)}\, e^{i\vec{q}_3 \cdot (\vec{r}_3 - \vec{r}_1)}\, \tilde{v}^{(1)}(\vec{q}_2, \vec{q}_3)\,. \tag{5.10b}$$

The three-body interaction is obtained from the EFT organization scheme at next-to-next-to-leading order (N^{2}LO) (see Sec. 5.1.2), and includes the following diagrams

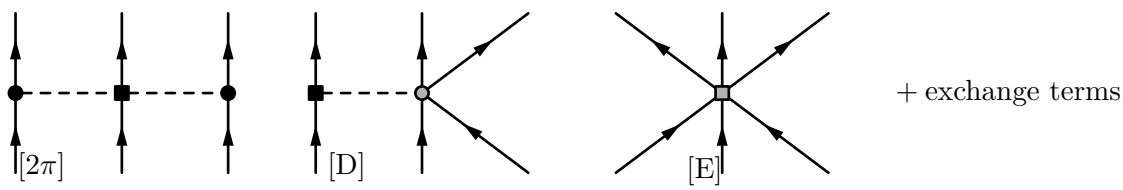

Figure 5.5: Three-body force diagrams from chiral EFT at N^{2}LO.

That is, the vacuum NNN force is constructed as the leading-order chiral NNN force which is comprised of a long-range 2π-exchange part v_c, an intermediate-range 1π-exchange part v_D and

a short-range contact interaction v_E. The 2π-exchange interaction, which provides the dominant contribution in symmetric nuclear matter, is given by [387]

$$\tilde{v}_c^{(k)}(\vec{q}_i,\vec{q}_j) = \sum_{\alpha\beta}\left(\frac{g_A}{2f_\pi}\right)^2 \frac{(\vec{\sigma}_i\cdot\vec{q}_i)(\vec{\sigma}_j\cdot\vec{q}_j)}{(q_i^2+m_\pi^2)(q_j^2+m_\pi^2)}\, F_{ijk}^{\alpha\beta}\,\tau_i^\alpha\,\tau_j^\beta\,, \tag{5.11}$$

where $F_{ijk}^{\alpha\beta}$ reads

$$F_{ijk}^{\alpha\beta} = \delta^{\alpha\beta}\left[-\frac{4c_1 m_\pi^2}{f_\pi^2} + \frac{2c_3}{f_\pi^2}\,\vec{q}_i\cdot\vec{q}_j\right] + \sum_\gamma \frac{c_4}{f_\pi^2}\,\epsilon^{\alpha\beta\gamma}\,\tau_k^\gamma\,\vec{\sigma}_k\cdot(\vec{q}_i\times\vec{q}_j)\,, \tag{5.12}$$

while the 1π-exchange and contact interactions are given respectively by

$$\tilde{v}_D^{(k)}(\vec{q}_i,\vec{q}_j) = -\frac{g_A}{4f_\pi^2}\,\frac{c_D}{f_\pi^2\Lambda_\chi}\,\frac{\vec{\sigma}_j\cdot\vec{q}_j}{q_j^2+m_\pi^2}\,(\vec{\tau}_i\cdot\vec{\tau}_j)\,(\vec{\sigma}_i\cdot\vec{q}_j)\,, \qquad \tilde{v}_E^{(k)}(\vec{q}_i,\vec{q}_j) = \frac{c_E}{f_\pi^4\Lambda_\chi}\,(\vec{\tau}_i\cdot\vec{\tau}_j)\,. \tag{5.13}$$

g_A	1.29
f_π [MeV]	92.4
m_π [MeV]	138.04
c_1 [GeV^{-1}]	-0.76
c_3 [GeV^{-1}]	-4.78
c_4 [GeV^{-1}]	-3.96

Table 5.2: Parameters for the bare three-nucleon force from chiral perturbation theory.

Values of the various coupling constants appearing in Eqs. (5.11-5.13) can be found in Tab. {5.2}. We use $g_A = 1.29$, $f_\pi = 92.4$ MeV and $m_\pi = 138.04$ MeV and the c_i constants extracted by the Nijmegen group in a partial wave analysis with chiral 2π-exchange [430]. Values for the c_D and c_E low-energy constants are typically adjusted such that the binding energies of ^{3}H and ^{4}He from ab initio calculations with $v^{\rm NN+NNN}$ match experimental values. In particular values of c_D and c_E depend on the vacuum two-nucleon force associated with $v^{\rm NNN}$. For instance, for the sharp cutoff $V_{{\rm low}\,k}$ from Argonne AV18, tabulated values are found in Ref. [8] for a range of Λ values. A procedure that adjusts the three-body coupling constants c_D and c_E in order to reproduce the r.m.s. radii of ^{3}H and ^{3}He has been used in the following, that is a different method than the standard one based on the binding energies of the same nuclei. It is found that better nuclear matter properties are obtained with this approach.

Finally, one notes that discussions concerning the potential role of four-body forces are ongoing [431]. In any case, associated effects are expected to be even smaller than NNN ones in the context of χ-PT since four-nucleon interactions only appear at N^{4}LO [420].

5.3 Properties of bare nucleon-nucleon forces

We now turn to the common benchmarks that are used to characterize a generic NN force noted v for simplicity. The former are introduced in details, as they will provide guidelines for constructing and evaluating the accuracy of non-empirical effective forces. In particular, scattering phase shifts and deuteron properties constitute basic experimental observables that are crucial for vacuum two-body models. They can be possibly extended to the case of effective forces using the in-medium T-matrix formalism [432; 433]. The study of Weinberg eigenvalues will lead later

on to critical discussions concerning the perturbative behavior of a given nucleon-nucleon force. One has however to start with preliminary remarks concerning momentum-space expressions and partial wave decompositions. All notations and conventions are properly defined in Appendix A. Detailed calculations and additional comments can also be found there.

A comment can be added at this point. The computation of several quantities such as scattering parameters or deuteron properties requires complex numerical techniques to obtain highly precise results. In the present work, approximate numerical treatments are used, as they provide values with a reasonable numerical cost and a precision suitable for the scope of this work, that is a global check of the properties of the forces we intend to construct. Consistency checks between these values and the ones from experiments or high-precision NN models are thus meaningless beyond the first few digits.

5.3.1 Momentum space

Some models for NN forces are given in momentum space, i.e. under the form $v(\vec{k}_1, \vec{k}_2, \vec{k}_3, \vec{k}_4)$, some other in coordinate space, that is $v(\vec{r}_1, \vec{r}_2, \vec{r}_3, \vec{r}_4)$, dropping for now spin and isospin indices. Since most of the following derivations will be performed in momentum space, conversion rules are recalled here. In momentum space the plane wave basis is the natural basis of interest. The single-particle basis is composed of plane waves with good spin and isospin projection, i.e.

$$\langle \vec{r}\,|\vec{k}\,\sigma\,q\rangle = \varphi_{\vec{k}}(\vec{r}\sigma q) = e^{i\vec{k}\cdot\vec{r}}\,\chi^{\sigma}\,\chi^{q}\,, \tag{5.14}$$

whose scalar product is given by

$$\langle \vec{k}\,\sigma\,q|\vec{k}\,'\,\sigma'\,q'\rangle \;=\; (2\pi)^3\,\delta(\vec{k}-\vec{k}\,')\,\delta_{\sigma\sigma'}\,\delta_{qq'}\,. \tag{5.15}$$

Because of the convention used to define plane waves, integrals in momentum space are characterized by $\int \mathrm{d}\vec{k}\,/\,(2\pi)^3$, such that [(3)]

$$\langle \vec{r}\,|\vec{r}\,'\rangle = \int \frac{\mathrm{d}\vec{k}}{(2\pi)^3}\,e^{i\,\vec{k}\cdot(\vec{r}-\vec{r}\,')} = \delta(\vec{r}-\vec{r}\,')\,. \tag{5.17}$$

One has then

$$v(\vec{k}_{1234}) = \int \mathrm{d}\vec{r}_{1234}\,e^{-i[+\vec{k}_1\cdot\vec{r}_1+\vec{k}_2\cdot\vec{r}_2-\vec{k}_3\cdot\vec{r}_3-\vec{k}_4\cdot\vec{r}_4]}\,v(\vec{r}_{1234})\,, \tag{5.18a}$$

$$v(\vec{k}_{1234}) = \frac{1}{(2\pi)^{12}}\int \mathrm{d}\vec{k}_{1234}\,e^{-i[-\vec{k}_1\cdot\vec{r}_1-\vec{k}_2\cdot\vec{r}_2+\vec{k}_3\cdot\vec{r}_3+\vec{k}_4\cdot\vec{r}_4]}\,v(\vec{k}_{1234})\,. \tag{5.18b}$$

In momentum space it is convenient to introduce relative and transfer momenta for direct and exchange terms according to conventions recalled in Eqs. (2a,2b). Most interactions that will be considered do not depend on $[\vec{R}/\vec{R}\,']$, that is vacuum NN forces or effective interactions in infinite nuclear matter[(4)], thus can be written as

$$v(\vec{k}_{1234}) \equiv v(\vec{k},\vec{k}\,'[,\vec{K}\,])\,\delta(\vec{K}-\vec{K}\,')\,, \tag{5.19}$$

where the Dirac delta function expresses the total momentum conservation and is usually removed.

[3]That is, we are using non-unitary Fourier transforms:

$$\tilde{f}(k) = \int_{-\infty}^{+\infty} f(r)\,e^{-i\,k\,r}\,\mathrm{d}r\,, \tag{5.16a}$$

$$f(r) = \frac{1}{2\pi}\int_{-\infty}^{+\infty} \tilde{f}(k)\,e^{+i\,k\,r}\,\mathrm{d}k\,. \tag{5.16b}$$

[4]In this case the potential depends on the total momentum $\vec{K}$.

5.3.2 Partial wave decomposition

The standard expansion of a plane wave in terms of spherical harmonics reads [1]

$$e^{i\,\vec{k}\cdot\vec{r}} \equiv \langle \vec{r}|\vec{k}\,\rangle = 4\pi \sum_{\ell\, m_\ell} i^\ell\, Y_\ell^{m_\ell *}(\hat{k})\, Y_\ell^{m_\ell}(\hat{r})\, j_\ell(k\,r) = \sum_\ell i^\ell\, [\ell\,]\, P_\ell(\hat{k}\cdot\hat{r})\, j_\ell(k\,r)\,, \tag{5.20}$$

using spherical Bessel functions of the first kind j_ℓ, Legendre polynomials P_ℓ, and with $[\ell] \equiv 2\ell+1$. Thus a given state $|\,\vec{k}\,\rangle$ is expanded into

$$|\,\vec{k}\,\rangle \equiv 4\pi \sum_{\ell\, m_\ell} i^\ell\, |\,k\,\ell\, m_\ell\,\rangle\, Y_\ell^{m_\ell *}(\hat{k})\,. \tag{5.21}$$

The latter expression is of interest in the case of the scattering of a plane wave $\varphi_{\vec{k}}(\vec{r})$ by a central (spin-independent) potential, where a partial wave expansion decomposes the scattering amplitude into angular components (see FIG. 5.6) that are solutions of Schrödinger equations with partial wave components $u_\ell(r)$ of the original potential $u(\vec{r})$, i.e.

$$u(\vec{r}) \equiv \sum_\ell u_\ell(r)\, P_\ell(\hat{k}\cdot\hat{r})\,. \tag{5.22}$$

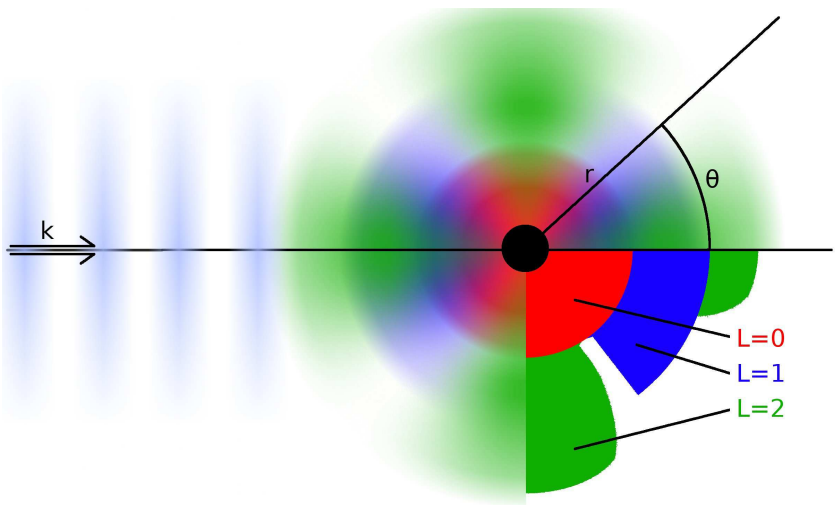

Figure 5.6: Illustration of the principle of a partial wave expansion in terms of the scattered amplitudes from an incident plane wave. Angular distributions for different ℓ come from the Legendre polynomials.

For two-nucleon scattering, the relative orbital angular momentum L couples to the total spin S of the nucleon pair to give a total two-body angular momentum J, which complexifies the problem. Still, a partial wave expansion of the nuclear potential $v(\vec{k},\vec{k}\,)$ can be given. Indeed, by analogy with EQ. (5.20), one can expand the spinor $|\vec{k}\,SS_z\,TT_z\rangle$ describing the two-body relative motion[(5)] into

$$|\vec{k}\,SS_z\,TT_z\rangle \equiv 4\pi \sum_L \sum_{JJ_z} i^L\, \mathcal{Y}^{J_z\,*}_{(LS)J}(\hat{k})\, \sqrt{\frac{\pi}{2}}\, |k\,(LS)JJ_zS_z\,TT_z\rangle\,, \tag{5.23}$$

[5] We choose here to use the spin/isospin projections S_z/T_z rather that projections of spin/isospin angular momenta M_S/M_T. This constitutes a fully equivalent convention.

in terms of spin 0 or 1 tensor spherical harmonics $\mathcal{Y}^{J_z}_{(LS)J}(\hat{k})$ [434], and with

$$\langle \vec{r}\,|k\,(LS)JJ_zS_z\,TT_z\rangle \equiv \sqrt{\frac{2}{\pi}}\,\mathcal{Y}^{J_z}_{(LS)J}(\hat{r})\,j_L(k\,r)\,|TT_z\rangle\,|S_z\rangle\,. \tag{5.24}$$

One has then

$$\langle\,\vec{r}\,|\vec{k}\,SS_z\,TT_z\rangle = 4\pi\sum_{LJJ_z} i^L\,\mathcal{Y}^{J_z}_{(LS)J}{}^{*}(\hat{k})\,\mathcal{Y}^{J_z}_{(LS)J}(\hat{r})\,j_L(kr)\,|TT_z\rangle\,|S_z\rangle\,, \tag{5.25}$$

such that Eq. (5.20) can be easily recovered for both $S=0$ and $S=1$ spinors (Appendix D.2). One cannot couple states with different spins S/S' since the bra and kets would correspond to different $L+S$ coupling schemes. Using a representation where nucleons have a good isospin, and from the fundamental symmetries of the nuclear interaction[6] the dependence of partial waves on T is trivial and no recoupling is needed. The partial wave expansion of potential matrix elements $v(\vec{k},\vec{k}\,')$ reads in a coupled scheme as

$$\langle\vec{k}\,SS_z\,TT_z|v|\vec{k}\,'\,SS_z\,TT_z\rangle = \frac{\pi}{2}\,(4\pi)^2\sum_{LL'}\sum_{JJ'}\sum_{J_zJ'_z} i^{L'-L}\,\mathcal{Y}^{J'_z}_{(L'S)J'}{}^{*}(\hat{k}')\,\mathcal{Y}^{J_z}_{(LS)J}(\hat{k})$$
$$\times\,\langle k\,(LS)JJ_zS_z\,TT_z|v|k'\,(L'S)J'J'_zS_z\,TT_z\rangle\,. \tag{5.26}$$

The latter expression can be further simplified for realistic nuclear interactions using that (i) v is invariant under the rotation of two particles, i.e. it does not depend on J_z/J'_z, (ii) the total angular momentum J is conserved, (iii) the spin/isospin and their projections are conserved, and (iv) in the absence of tensor force or for $S=0$ states, the orbital momentum L is also conserved. If a tensor interaction is present it only couples states such that $|L-L'|=0,2$ and $L,L'>0$. One has then

$$\langle\vec{k}\,SS_z\,TT_z|v|\vec{k}\,'\,SS_z\,TT_z\rangle = \frac{\pi}{2}\,(4\pi)^2\sum_{LL'}\sum_{JJ_z} i^{L'-L}\,\mathcal{Y}^{J_z}_{(L'S)J}{}^{*}(\hat{k}')\,\mathcal{Y}^{J_z}_{(LS)J}(\hat{k})\,v^{JSS_zTT_z}_{LL'}(k,k')\,, \tag{5.27}$$

where the short notation from Eq. (3a) is used. In most case one will not consider CIB/CSB forces, or the isospin projection will be specified, that is the superscripts S_z/T_z can be dropped. One is left with partial wave matrix elements of the kind $v^{JST}_{LL'}(k,k')$, with conventions from Eqs. (3b,3c), that are called matrix elements of the interaction in a given partial wave. General prescriptions for such a decomposition can be found in the litterature [83; 435; 436]. As we are considering the interaction of two fermions, only specific partial waves have to be considered, as indicated by Tab. {5.3}. If one uses common spectroscopic notations $^{[S]}\mathrm{L}_J$, coupled channels only appear because of a tensor interaction, and the coupling $^3(J-1)_J$-$^3(J+1)_J$ is usually noted ϵ_J. As a summary, the possible partial waves for a nuclear interaction are summarized in Tab. {5.4}.

5.3.3 Scattering phase shifts

The most usual benchmark of a bare nucleon-nucleon interaction is performed by comparing its scattering phase shifts in different partial waves with experimental data [375], defined by analogy to hard sphere scattering.

[6] That is, it only couples between states of same spin S and isospin T.

		J	0	1			...	J			
		S	0	0	1		...	0	1		
J	S	L	0	1	1	0 2	...	J	J	$J-1$	$J+1$
0	0	0	■								
1	0	1		■							
	1	1			■						
		0				■					
		2									
...	...	...									
J	0	J						■			
	1	J							■		
		$J-1$								■	
		$J+1$									■

Table 5.3: Block representation of the two-body nuclear interaction. Non-zero matrix elements are shaded, and ϵ_J couplings are zero if no tensor force is considered.

$T_z = \pm 1$ (nn-pp)							$T_z = 0$ (np)						
$^1S_0$							$^1S_0$		$^3S_1$				ϵ_1
	$^3P_0$	$^3P_1$	$^3P_2$			ϵ_2	$^1P_1$	$^3P_0$	$^3P_1$	$^3P_2$			ϵ_2
$^1D_2$							$^1D_2$		$^3D_1$	$^3D_2$	$^3D_3$		ϵ_3
			$^3F_2$	$^3F_3$	$^3F_4$	ϵ_4	$^1F_3$			$^3F_2$	$^3F_3$	$^3F_4$	ϵ_4

Table 5.4: Non-zero partial waves for a nuclear interaction with tensor correlations and $L \leq 3$.

5.3.3.1 Lippmann-Schwinger equation

A convenient way to treat the scattering problem is to introduce the solution $\varphi_{\vec{k}}$ of the free Schrödinger equation and $\Psi_{\vec{k}}$ the solution of the interacting problem with the potential v. The integral equation for $\Psi_{\vec{k}}$ reads then formally [437; 438]

$$\Psi_{\vec{k}} = \varphi_{\vec{k}} + G_0(E)\, v\, \Psi_{\vec{k}}\,, \tag{5.28}$$

where G_0 is the free-particle Green function with energy $E = \frac{\hbar^2 k^2}{2m}$, m being the reduced mass of the two-nucleon system. The scattering T-matrix is defined as

$$T(E)\, \varphi_{\vec{k}} \equiv v\, \Psi_{\vec{k}}\,, \tag{5.29}$$

and relates the solutions of the interacting and non-interacting problems. It is the solution of the self-consistent Lippmann-Schwinger equation

$$T = v + v\, G_0\, T\,. \tag{5.30}$$

The latter is best expressed in momentum space, where G_0 is diagonal, and leads to[7,8]

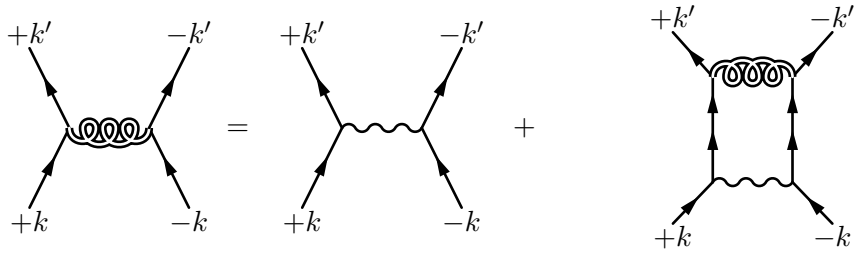

$$\langle \vec{k}\,|T(E)|\vec{k}\,'\rangle \quad = \quad \frac{m}{\hbar^2}\langle \vec{k}\,|v|\vec{k}\,'\rangle \quad + \mathcal{P}\int \frac{\mathrm{d}\vec{k}\,''}{(2\pi)^3}\frac{\langle \vec{k}\,|v|\vec{k}\,''\rangle\,\langle \vec{k}\,''\,|T(E)|\vec{k}\,'\rangle}{E-E(k'')}\,, \tag{5.31}$$

where $\mathcal{P}$ denotes a principal value integration. The T-matrix is directly related to the scattering matrix S through

$$T = -\frac{1}{i\,k}\,\frac{S-\mathbb{I}}{S+\mathbb{I}}\,, \tag{5.32}$$

with the normalization of plane waves chosen here. By analogy with Eq. (5.27), the T-matrix can be expanded into partial waves and has the same block structure as the initial nuclear force (see Tab. {5.3}). The projected Lippmann-Schwinger equation reads then

$$T^{JST}_{LL'}(k,k';E) = \frac{m}{\hbar^2}\,v^{JST}_{LL'}(k,k') + \sum_{L''}\frac{2}{\pi}\mathcal{P}\int k''^2\,\mathrm{d}k\,\frac{v^{JST}_{L''L'}(k,k')\,T^{JST}_{LL''}(E,k,k')}{E-E(k'')}\,. \tag{5.33}$$

In the case of uncoupled channels, it reduces to

$$T^{JST}_{L}(k,k';E) = \frac{m}{\hbar^2}\,v^{JST}_{L}(k,k') + \frac{2}{\pi}\mathcal{P}\int k''^2\,\mathrm{d}k''\,\frac{v^{JST}_{L}(k,k')\,T^{JST}_{L}(k,k';E)}{E-E(k'')}\,. \tag{5.34}$$

For coupled channels Eq. (5.33) reads with the notation $J^{\pm} \equiv J \pm 1$

$$T^{JST}_{L_1=J\pm1\,L_2=J\pm1}(k,k';E) = \frac{m}{\hbar^2}v^{JST}_{L_1L_2}(k,k') + \frac{2}{\pi}\sum_{L_3=J\pm1}\mathcal{P}\int k''^2\,\mathrm{d}k''\,\frac{v^{JST}_{L_1L_3}(k,k')\,T^{JST}_{L_3L_2}(k,k';E)}{E-E(k'')}\,. \tag{5.35}$$

Finally, the T-matrix is called

- "Half on-shell" when $E = \hbar^2\,k^2/m$. Note that fully off-shell matrix elements are not related to any physical observables,
- "Fully on-shell" when $k = k'$ and $E = \hbar^2\,k^2/m$.

5.3.3.2 Definitions and conventions

Scattering phases shifts are defined from a parametrization of the S-matrix which drives the asymptotic behavior of the scattered wave function expanded into partial waves $\Psi^{JST}_{L,k}(r)$.

[7] Using a principal value prescription instead of a $\pm i\,\delta$ scheme to regularize G_0 has important consequences. The choice adopted here corresponds to a stationary state formalism, in which the T-matrix is called reactance matrix [437], reaction matrix or Heitler's matrix, and is related to an hermitian representation of the scattering matrix. Other representations of the T-matrix can be defined corresponding for instance to a time-independent formulation of the scattering problem [439].

[8] In Eq. (5.31) the T-matrix is, as usual, expressed in fm units, while interaction matrix elements are in MeVs.

Uncoupled channels

The restriction S_L^{JST} of the scattering matrix to an uncoupled channel ${}^{[S]}L_J$ is a scalar, and the scattered wave can be written as

$$\Psi_{L,k}^{JST}(r) \underset{r\to+\infty}{\longrightarrow} j_L(kr) + \tan(\delta_L^{JST}(E))\, n_l(kr) \tag{5.36a}$$

$$\underset{r\to+\infty}{\longrightarrow} \mathcal{A}\,\frac{-1}{2i\,kr}\left[e^{-i(kr-L\pi/2)} - S_L^{JST}(E)\, e^{+i(kr-L\pi/2)}\right], \tag{5.36b}$$

where $\mathcal{A}$ stands as a normalization constant. The flux conservation ensures that $|S_L^{JST}|^2 = 1$, thus

$$S_L^{JST}(E) \equiv e^{2i\,\delta_L^{JST}(E)}, \tag{5.37}$$

where $\delta_L^{JST}(E)$ is the scattering phase shift at a given energy E. Using Eq. (5.32), one obtains the usual expression

$$T_L^{JST}\left(k, k; \frac{\hbar^2\,k^2}{m}\right) = -\frac{\tan\left(\delta_L^{JST}(k)\right)}{k}, \tag{5.38}$$

where the T-matrix is fully on-shell. Other methods [1; 440] lead to the same standard expression, with caution needed regarding normalization conventions.

Coupled channels

For channels coupled by the tensor force (hence $S = 1$), each channel ${}^3(J^\pm)_J$ is not an eigenstate of the scattering matrix, and the 2×2 restriction S^{J1T} of the S-matrix between states $L, L' = J \pm 1$ is introduced. The wave function for a state with total angular momentum J reads in this case

$$\begin{pmatrix} \tilde{\Psi}_{J^-,k}^{J1T}(r) \\ \tilde{\Psi}_{J^+,k}^{J1T}(r) \end{pmatrix} \underset{r\to+\infty}{\longrightarrow} \frac{1}{2i\,kr}\left[\begin{pmatrix} \mathcal{A}_1 \\ \mathcal{A}_2 \end{pmatrix}\begin{pmatrix} e^{-i(kr-J^-\pi/2)} \\ e^{-i(kr-J^+\pi/2)} \end{pmatrix} - S^{J1T}\begin{pmatrix} \mathcal{A}_1 \\ \mathcal{A}_2 \end{pmatrix}\begin{pmatrix} e^{+i(kr-J^-\pi/2)} \\ e^{+i(kr-J^+\pi/2)} \end{pmatrix}\right], \tag{5.39}$$

Two parametrizations of the scattering matrix, leading to different definitions for the phase shifts, are commonly used.

1. The eigenphase shifts convention [441] where

$$S^{J1T} \equiv U^{J1T\,-1}\,\exp(2i\,\Delta^{J1T})\,U^{J1T}, \tag{5.40a}$$

$$U^{J1T} = \begin{pmatrix} \cos(\epsilon_J) & \sin(\epsilon_J) \\ -\sin(\epsilon_J) & \cos(\epsilon_J) \end{pmatrix}, \tag{5.40b}$$

$$\Delta^{J1T} = \begin{pmatrix} \delta_{J\alpha} & 0 \\ 0 & \delta_{J\beta} \end{pmatrix} \equiv \begin{pmatrix} \delta_\alpha & 0 \\ 0 & \delta_\beta \end{pmatrix}, \tag{5.40c}$$

$$S^{J1T} = \begin{pmatrix} \cos^2(\epsilon_J)\,e^{2i\,\delta_\alpha} + \sin^2(\epsilon_J)\,e^{2i\,\delta_\beta} & \cos(\epsilon_J)\,\sin(\epsilon_J)\left[e^{2i\,\delta_\alpha} - e^{2i\,\delta_\beta}\right] \\ \cos(\epsilon_J)\,\sin(\epsilon_J)\left[e^{2i\,\delta_\alpha} - e^{2i\,\delta_\beta}\right] & \cos^2(\epsilon_J)\,e^{2i\,\delta_\beta} + \sin^2(\epsilon_J)\,e^{2i\,\delta_\alpha} \end{pmatrix}. \tag{5.40d}$$

The latter corresponds, in first approximation, to writing the two eigenstates $\tilde{\Psi}_\alpha$ and $\tilde{\Psi}_\beta$ of the T-matrix as a superposition of uncoupled solutions in the $J^\pm$ states, with a mixture

parameter ϵ_J. One obtains from Eq. (5.32) [1]

$$\tan\left[2\,\epsilon_J\,(E)\right] = \frac{T^{J1T}_{J^-J^+}\left(k,k;\frac{\hbar^2\,k^2}{m}\right) + T^{J1T}_{J^+J^-}\left(k,k;\frac{\hbar^2\,k^2}{m}\right)}{T^{J1T}_{J^-J^-}\left(k,k;\frac{\hbar^2\,k^2}{m}\right) - T^{J1T}_{J^+J^+}\left(k,k;\frac{\hbar^2\,k^2}{m}\right)}\,, \tag{5.41a}$$

$$\tan\left[\delta^{J1T}_{J^-}\,(E)\right] = -\,\frac{k}{2}\Bigg[T^{J1T}_{J^-J^-}\left(k,k;\frac{\hbar^2\,k^2}{m}\right) + T^{J1T}_{J^+J^+}\left(k,k;\frac{\hbar^2\,k^2}{m}\right) + \frac{T^{J1T}_{J^-J^-}\left(k,k;\frac{\hbar^2\,k^2}{m}\right) - T^{J1T}_{J^+J^+}\left(k,k;\frac{\hbar^2\,k^2}{m}\right)}{\cos(2\,\epsilon_J)}\Bigg]\,, \tag{5.41b}$$

$$\tan\left[\delta^{J1T}_{J^+}\,(E)\right] = -\,\frac{k}{2}\Bigg[T^{J1T}_{J^-J^-}\left(k,k;\frac{\hbar^2\,k^2}{m}\right) + T^{J1T}_{J^+J^+}\left(k,k;\frac{\hbar^2\,k^2}{m}\right) - \frac{T^{J1T}_{J^-J^-}\left(k,k;\frac{\hbar^2\,k^2}{m}\right) - T^{J1T}_{J^+J^+}\left(k,k;\frac{\hbar^2\,k^2}{m}\right)}{\cos(2\,\epsilon_J)}\Bigg]\,, \tag{5.41c}$$

where one does the usual (wrong) approximation, coming from the zero coupling limit $\epsilon_j \to 0$ where the identification $\alpha \equiv J^-$ and $\beta \equiv J^+$ is exact, i.e.

$$\delta_\alpha \equiv \delta^{J1T}_{J^-}\,(E)\;, \qquad \delta_\beta \equiv \delta^{J1T}_{J^+}\,(E)\;. \tag{5.42}$$

2. The bar-phaseshifts [442], where the scattering matrix is now defined as

$$S^{J1T} \equiv \exp(i\,\bar\delta)\,\exp(2i\,\bar\epsilon)\,\exp(i\,\bar\delta)\,, \tag{5.43a}$$

$$S^{J1T} = \begin{pmatrix} \exp(i\,\bar\delta^{J1T}_{J^-}) & 0 \\ 0 & \exp(i\,\bar\delta^{J1T}_{J^+}) \end{pmatrix} \begin{pmatrix} \cos(2\,\bar\epsilon_J) & i\,\sin(2\,\bar\epsilon_J) \\ i\,\sin(2\,\bar\epsilon_J) & \cos(2\,\bar\epsilon_J) \end{pmatrix} \times \begin{pmatrix} \exp(i\,\bar\delta^{J1T}_{J^-}) & 0 \\ 0 & \exp(i\,\bar\delta^{J1T}_{J^+}) \end{pmatrix}. \tag{5.43b}$$

In this case $\bar\epsilon_J$ provides the proportions into which an incoming beam of a given channel divides between the two outgoing channels. Bar- and eigen-phaseshifts are related through

$$\delta^{J1T}_{J^+} + \delta^{J1T}_{J^-} = \bar\delta^{J1T}_{J^+} + \bar\delta^{J1T}_{J^-}\,, \tag{5.44a}$$

$$\sin(\bar\delta^{J1T}_{J^-} - \bar\delta^{J1T}_{J^+}) = \frac{\tan 2\,\bar\epsilon_J}{\tan(2\,\epsilon_J)}\,, \tag{5.44b}$$

$$\sin(\delta^{J1T}_{J^-} - \delta^{J1T}_{J^+}) = \frac{\sin 2\,\bar\epsilon_J}{\sin(2\,\epsilon_J)}\,. \tag{5.44c}$$

Both of these conventions are equivalent for uncoupled channels. In the present work one will use the bar-phaseshift convention, as it is done for the reference PWA93, and will remove the overbar on the notations δ and ϵ. Scattering phase shifts can be given either as a function of the relative momentum k or the energy in the laboratory frame $E_{\rm lab}$, which reads

$$E_{\rm lab} = 4\,\frac{\hbar^2\,k^2}{m}\,. \tag{5.45}$$

5.3.3.3 Coulomb corrections for proton-proton phase shifts

In the case of proton-proton scattering, the long-range Coulomb interaction modifies the previous picture. Indeed, the scattering matrix has to be formulated in terms of electromagnetic states, since plane waves are not good asymptotic solutions any more. Different formulations of the phase shifts in the presence of the electromagnetic interaction are possible corresponding to the type of functions that are used to match asymptotically the interacting and non-interacting scattering solutions. They correspond to the notation δ_X^Y, denoting the phase shift solution with potential X with respect to the asymptotic solution of the potential Y. For instance for neutron-neutron scattering if the nuclear strong interaction is noted N, scattering phase shifts defined at the level of Eq. (5.38) and Eqs. (5.40a-5.40d) correspond to δ_N^0, since the plane waves used for the matching are solutions of the free Schrödinger equation. In the presence of long-range electromagnetic interactions, proton-proton scattering phase shifts are usually defined as nuclear-electromagnetic phase shifts δ_{N+EM}^{EM}, that is with respect to electromagnetic wave functions. The easiest way to compute them is to use as an intermediate step the phase shifts δ_{N+C1}^{C1} of the Coulomb+nuclear interaction with respect to Coulomb wave functions [83]. For uncoupled channels, the asymptotic wave function can be written as

$$\Psi_{L,k}^{JST}(r) \underset{r\to+\infty}{\longrightarrow} F_L^c(r) + \tan(\delta_L^{JST})\, G_L^c(r)\,, \tag{5.46}$$

where F_L^c and G_L^c are regular and irregular Coulomb wave functions [443; 444]. Likewise, for a short-range vanishing potential one has

$$\tilde{\Psi}_{L,k}^{JST}(r) \underset{r\to+\infty}{\longrightarrow} F_L^0(r) + \tan(\tilde{\delta}_L^{JST})\, G_L^0(r)\,, \tag{5.47}$$

where F_L^0 and G_L^0 are so-called solutions of the Coulomb problem with zero charge, and usually expressed in terms of Bessel and Neumann functions (Eq. (5.36a)). Now the two solutions can be matched at an arbitrary distance R where $\tilde{\delta}_L^{JST}$ has been calculated with a Fourier-transformed Coulomb potential integrated up to the radius R [445]. Indeed, the two wave functions $\Psi_{L,k}^{JST}$ and $\tilde{\Psi}_{L,k}^{JST}$ describe the same system on the sphere with radius $R+\varepsilon$. By matching logarithmic derivatives, the phase shift δ_L^{JST}, corresponding to δ_{N+C}^{C}, can then be obtained from $\tilde{\delta}_L^{JST}$ in a Wronskian form by

$$\tan(\delta_L^{JST}) = \frac{\tan(\tilde{\delta}_L^{JST})\,[F_L, G_L^0] + [F_L, F_L^0]}{[F_L^0, G_L] + \tan(\tilde{\delta}_L^{JST})\,[G_L^0, G_L]}\,, \tag{5.48}$$

where

$$[X_L, Y_L] \equiv \left(Y_L \frac{d\,X_L}{d\,r} - X_L \frac{d\,Y_L}{d\,r} \right)_{r=R}\,. \tag{5.49}$$

For instance, for vacuum NN forces such as AV18 that are expressed in momentum space through a Fourier transform, phase shifts δ_L^{JST} are easily obtained by setting the value of R and computing accordingly the values of $\tilde{\delta}_L^{JST}$. The radius R is determined such that the short-range nuclear interaction vanishes beyond this value. At the same time, the truncated Fourier transform of the Coulomb potential will have rapid oscillations for too large values of R. For these reasons, a value $R \approx 10$ fm is usually used [446]. For coupled channels, e.g. $^3\mathrm{P}_2$-$^3\mathrm{F}_2$, the same prescription can be applied in the 2×2 subspace of the scattering matrix [83].

Since electromagnetic corrections beyond the Coulomb potential are small, phase shifts δ_{N+EM}^{EM} can then be expanded into [83; 398]

$$\delta_{N+EM}^{EM} \equiv \delta_{N+C1}^{C1} + \rho + \phi + \tau - \tilde{\Delta}\,, \tag{5.50}$$

where ρ is the improved Coulomb phase shift [447], ϕ the magnetic moment phase shift [398], τ the vacuum polarization phase shift [448] and $\tilde{\Delta}$ the improved Coulomb-Foldy correction [447], and are usually computed using a distorted-wave Born approximation. Now all $L \geq 1$ partial waves are only weakly affected by eletromagnetic corrections, and one has in first approximation

$$\delta^{EM}_{N+EM} \approx \delta^{C1}_{N+C1} \,. \tag{5.51}$$

On the other hand, phase shifts ρ, ϕ, τ and $\tilde{\Delta}$ have to be explicitly computed for $L = 0$ partial waves, that is the $^1\mathrm{S}_0$ channel (there is no proton-proton interaction in the coupled $^3\mathrm{S}_1$-$^3\mathrm{D}_1$ channel corresponding to $T = 0$). However (i) the first three corrections are independent of the nuclear strong interaction, and (ii) the improved Coulomb-Foldy correction $\tilde{\Delta}_0$ is found to be independent of it with a reasonable precision [447]. For these reasons, tabulated values at low energy can be used [447] instead of exact computations with a suitable precision for the scope of this work.

5.3.3.4 Scattering parameters

In the case of a short-range two-body potential, it can be shown that phase shifts behave like

$$\delta^{JST}_L \underset{k\to 0}{\sim} k^{2L+1}, \tag{5.52}$$

which implies that s-wave scattering dominates at low-energy limit[9]. One can then expand the s-wave effective range function $F_0(k)$ in powers of k^2 [449] under the form

$$F_0(k) \equiv A_0\, k \cot\left[\delta_0^{JST}\right] + B_0 = -\frac{1}{a_S} + \frac{1}{2}\, r_S\, k^2 + v_2\, k^4 + v_3\, k^6 + v_4\, k^8 + \dots \tag{5.53}$$

where the s-wave scattering length a_S, effective range r_S and shape parameters $v_{2/3/4}$ have been introduced.

For uncharged particles, the effective range function correspond to $A_0 = 1$ and $B_0 = 0$, that is [450]

$$F_0(k) = k \cot\left[\left(\delta^0_N\right)^{JST}_0\right] . \tag{5.54}$$

In the case of proton-proton scattering, the effective range function has to be modified to take into account electromagnetic corrections. The effective range function using the Coulomb potential for the long-range part of the interaction [451; 452] will be considered here, since electromagnetic corrections will impact scattering parameters at a level of precision beyond the scope of this work. It reads

$$F_C(k) = C_0(\eta')\, k \cot\left[\left(\delta^{C1}_{N+C1}\right)^{JST}_0\right] + 2\, k\, \eta'\, h(\eta') \,, \tag{5.55}$$

where η' is the relativistic Coulomb parameter [453]

$$\eta' = \frac{\alpha\, m_p}{2k} \frac{1 + 2\frac{k^2}{m_p^2}}{\sqrt{1 + \frac{k^2}{m_p^2}}} \,, \tag{5.56}$$

and

$$C_0^2(\eta') = \frac{2\pi\, \eta'}{e^{2\pi\, \eta'} - 1} \,, \qquad h(\eta') = \mathrm{Re}[\Psi(1 + i\, \eta')] - \ln(\eta') \,, \tag{5.57}$$

Ψ being the digamma function [320].

[9] As long as the nucleons are not identical, in which case p-wave scattering dominates instead, but this is not the case here.

5.3.4 Deuteron properties

Bound state properties of bare NN forces in the coupled $^3S_1$-$^3D_1$ channels, i.e. the deuteron channel, are important observables. The internal deuteron wave function Ψ_d is a spinor

$$\Psi_d \equiv \begin{pmatrix} \Psi_d^S \\ \Psi_d^D \end{pmatrix} , \tag{5.58}$$

corresponding to $L = 0$ and $L = 2$ components, and is the solution of the non-relativistic[10] coupled Shrödinger equation

$$\left[\frac{\hbar^2}{2\,m^r} \Delta + \begin{pmatrix} v_{00}^{110} & v_{02}^{110} \\ v_{20}^{110} & v_{22}^{110} \end{pmatrix} \right] \begin{pmatrix} \Psi_d^S \\ \Psi_d^D \end{pmatrix} = E_d \begin{pmatrix} \Psi_d^S \\ \Psi_d^D \end{pmatrix} , \tag{5.59}$$

where E_d is the deuteron binding energy and m^r the reduced mass. Usually, one denotes by $u(r)$ and $w(r)$ the radial part of the wave functions Ψ_d^S and Ψ_d^D, respectively, while $u(k)$ and $w(k)$ are momentum-space representations of $u(r)/r$ and $w(r)/r$, i.e.

$$u(k) = \frac{2}{\pi} \int_0^{+\infty} r\,\mathrm{d}r\, u(r)\, j_0(k\,r)\,, \qquad w(k) = \frac{2}{\pi} \int_0^{+\infty} r\,\mathrm{d}r\, w(r)\, j_2(k\,r)\,. \tag{5.60}$$

These wave functions are normalized to

$$\int_0^{+\infty} k^2\,\mathrm{d}k\,[u^2(k) + v^2(k)] = \int_0^{+\infty} \mathrm{d}r\,[u^2(r) + v^2(r)] = 1\,. \tag{5.61}$$

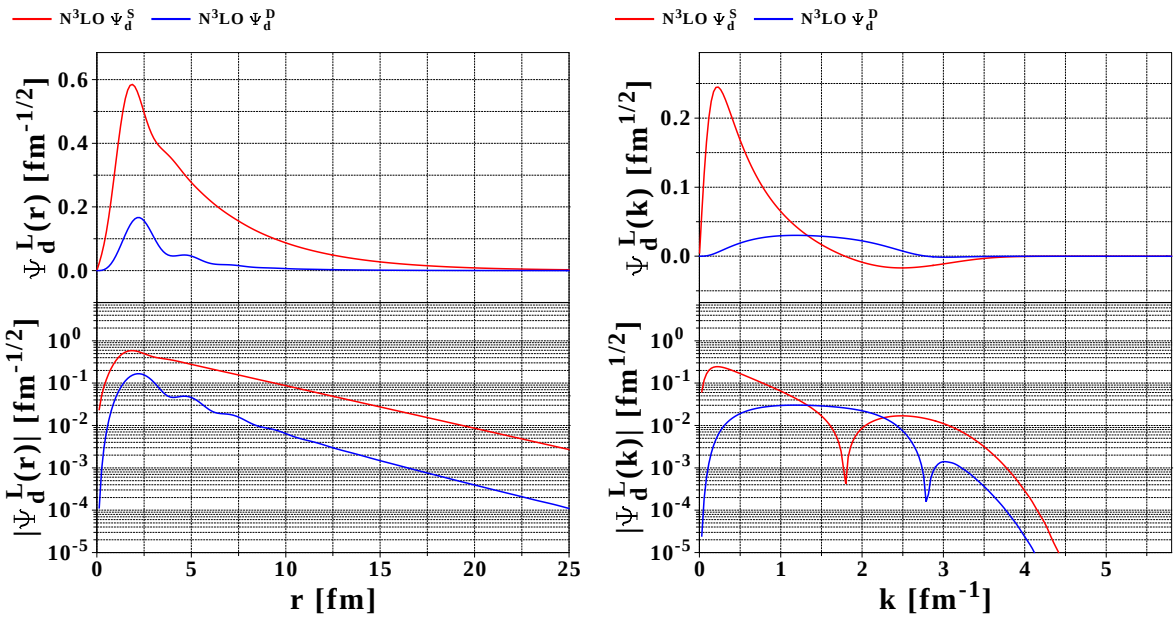

Figure 5.7: Deuteron wave functions in coordinate and momentum space u and w for the N^{3}LO [409] bare nucleon-nucleon interaction.

One then defines the s- and d-wave probabilities as

$$P_S = \int_0^{+\infty} k^2\,\mathrm{d}k\,u^2(k) = \int_0^{+\infty} \mathrm{d}r\,u^2(r)\,, \qquad P_D = \int_0^{+\infty} k^2\,\mathrm{d}k\,w^2(k) = \int_0^{+\infty} \mathrm{d}r\,w^2(r)\,. \tag{5.62}$$

[10] Similar definitions hold in the relativistic case [83].

The deuteron quadrupole moment Q_d and the matter r.m.s. radius $r_d = \sqrt{\langle r^2 \rangle_m^d}$ are also introduced through

$$Q_d = \frac{1}{20} \int_0^{+\infty} r^2 \, \mathrm{d}r \, w(r) \, [\sqrt{8} \, u(r) - w(r)] \tag{5.63a}$$

$$= -\frac{1}{20} \int_0^{+\infty} \mathrm{d}k \left\{ \sqrt{8} \left[k^2 \frac{du(k)}{dk} \frac{dw(k)}{dk} + 3 \, k \, w(k) \frac{du(k)}{dk} \right] + k^2 \left(\frac{dw(k)}{dk} \right)^2 + 6 \, w^2(k) \right\} \tag{5.63b}$$

$$r_d = \frac{1}{4} \int_0^{+\infty} r^2 \, \mathrm{d}r \, [u^2(r) + w^2(r)] \, . \tag{5.63c}$$

Q_d is a physical observable expressed as the expectation value of the quadrupole operator Q_{ij}, but does not take into account relativistic corrections or two-nucleon currents [454]. Likewise, r_d is related to the measured deuteron charge r.m.s. r_d^{ch} radius after taking into account the finite size of the nucleons, i.e.

$$\langle r^2 \rangle_{ch}^d = \langle r^2 \rangle_{pt}^d + \langle r^2 \rangle_{ch}^p + \langle r^2 \rangle_{ch}^n \, , \tag{5.64}$$

where $\sqrt{\langle r^2 \rangle_{ch}^p} = 0.886(11)$ fm [455–457] and $\langle r^2 \rangle_{ch}^n = -0.113(5)$ fm^2 [458] are the proton and neutron charge radii, respectively, whereas the point-like deuteron radius is given by

$$\langle r^2 \rangle_{pt}^d = r_d^2 + \langle r^2 \rangle_B^d \, , \tag{5.65}$$

where $\langle r^2 \rangle_B^d$ corresponds to relativistic corrections or two-nucleon currents which are of the order of 0.016 fm^2 [459].

Additionally, one defines asymptotic normalizations A_S and A_D of the s and d states, respectively, through

$$u(r) \underset{r \to +\infty}{\longrightarrow} A_S e^{-\gamma \, r} \, , \qquad v(r) \underset{r \to +\infty}{\longrightarrow} A_D \, e^{-\gamma \, r} \left(1 + \frac{3}{\gamma \, r} + \frac{3}{(\gamma \, r)^2} \right) \, , \tag{5.66}$$

where $\gamma = \sqrt{|m \, E_d + E_d^2/4|}$. The deuteron normalization N_d and asymptotic d/s ratio are introduced as

$$N_d^2 = A_S^2 + A_D^2 \, , \qquad \eta_d = \frac{A_D}{A_S} \, . \tag{5.67}$$

N_d and η_d are physical observables related to the scattering phase shifts around the S-matrix pole due to the presence of a bound state [460]. Example of deuteron wave functions obtained from the N^{3}LO [409] bare force can be found in Fig. 5.7. One sees there the almost idential asymptotic regimes (Eq. (5.66)) in logarithmic scale.

5.3.5 Weinberg eigenvalues

Weinberg eigenvalues can be used to qualify the perturbativeness of a given NN potential in the vacuum [343; 461], starting from the Born series

$$T(E) = v + v \, \frac{1}{E - H_0} \, v + \ldots = v + v \, G_0(E) \, v + \ldots \tag{5.68}$$

The latter equation can be expanded into partial waves (Eq. (5.33)), e.g.

$$T_{LL'}^{JST}(E) = v_{LL'}^{JST} + \sum_{L''} v_{LL''}^{JST} \, \frac{1}{E - H_0} \, v_{L''L'}^{JST} + \ldots \tag{5.69}$$

Weinberg eigenvalues $\eta_\nu(E)$ are eigenvalues of the operator $G_0(E)\,v$, such that

$$\eta_\nu(E) = \sum_{\substack{LJST \\ \text{uncoupl.}}} \eta_\nu{}_L^{JST}(E) + \sum_{\substack{LJST \\ \text{coupl.}}} \eta'_\nu{}_L^{JST}(E)\,\delta_{LJ^-}\,, \tag{5.70}$$

where

- $\eta_\nu{}_L^{JST}(E)$ are eigenvalues of $G_0(E)\,v$ in uncoupled partial waves with associated eigenvectors $|\Psi_\nu{}_L^{JST}\rangle$, i.e

$$T_L^{JST}(E)\,|\Psi_\nu{}_L^{JST}\rangle = v_L^{JST}\,|\Psi_\nu{}_L^{JST}\rangle\,\left[1 + \eta_\nu{}_L^{JST}(E) + \eta_\nu{}_L^{JST\,2}(E) + \ldots\right]\,, \tag{5.71}$$

  and are computed by solving the integral equation

$$\frac{2}{\pi}\mathcal{P}\int k''^2\,\mathrm{d}k''\,\frac{v_L^{JST}(k,k'')}{E - E(k'')}\langle k''|\Psi_\nu{}_L^{JST}\rangle = \eta_\nu{}_L^{JST}(E)\,\langle k|\Psi_\nu{}_L^{JST}\rangle\,, \tag{5.72}$$

  which can be done in a plane wave basis through a matrix diagonalization, equivalently as the way the Lippmann-Schwinger is solved.
- $\eta'_\nu{}_L^{JST}(E)$ are eigenvalues of $G_0(E)\,v$ in coupled partial waves ${}^3L_1$-${}^3(L+2)_1$ with associated eigenvectors

$$|\Psi_\nu{}_{LL'}^{JST}\rangle \equiv \begin{pmatrix} \Psi_\nu{}_{J^-}^{JST} \\ \Psi_\nu{}_{J^+}^{JST} \end{pmatrix}\,, \tag{5.73}$$

  i.e. they verify

$$\{T^{JST}\}(E)\begin{pmatrix} \Psi_\nu{}_{J^-}^{JST} \\ \Psi_\nu{}_{J^+}^{JST} \end{pmatrix} = \{v^{JST}\}\begin{pmatrix} \Psi_\nu{}_{J^-}^{JST} \\ \Psi_\nu{}_{J^+}^{JST} \end{pmatrix}\left[1 + \eta'_\nu{}_L^{JST}(E) + \eta'_\nu{}_L^{JST\,2}(E) + \ldots\right]\,, \tag{5.74}$$

  where

$$\{X^{JST}\} \equiv \begin{pmatrix} X_{J^-J^-}^{JST} & X_{J^-J^+}^{JST}(E) \\ X_{J^+J^-}^{JST} & X_{J^+J^+}^{JST}(E) \end{pmatrix}\,. \tag{5.75}$$

  Eigenvalues $\eta'_\nu{}_L^{JST}(E)$ are evaluated by solving a coupled eigenvalue equation generalizing Eq. (5.72).

The bottom line of such a computation is that non-perturbative NN potentials are signaled by one or more eigenvalues with $\left|\eta_\nu{}_L^{JST}(E)\right|, \left|\eta'_\nu{}_L^{JST}(E)\right| \geq 1$. In practice these eigenvalues are mostly computed in the ${}^1\mathrm{S}_0$ and ${}^3\mathrm{S}_1$-${}^3\mathrm{D}_1$ channels, since those are the most likely to present non-perturbative characteristics. In the following, one will use the shorthand notations

$$\eta_\nu{}_0^{001}(E) \equiv \eta_\nu^1(E)\,, \qquad \eta'_\nu{}_0^{010}(E) \equiv \eta_\nu^3(E)\,. \tag{5.76}$$

Additional remarks are at play

- In a given uncoupled/coupled partial wave, $\eta_\nu(E)$ can be interpreted as the scaling factor by which v must be multiplied to have a bound state at energy E. That is (i) large negative values for $\eta_\nu(E)$ correspond to bound states of $-v$, thus are caused by the short-range repulsion and sign non-perturbative behaviors, and (ii) positive values for $\eta_\nu(E)$ close to, but lower than, one correspond to (physical) virtual bound states, while values greater than one correspond to physical bound states, such as for the deuteron in the ${}^3\mathrm{S}_1$-${}^3\mathrm{D}_1$ partial waves.

- All eigenvalues are real from the present choice of the principal value regularization of the Lippmann-Schwinger equation. If one uses instead a $\pm i\,\delta$ regularization scheme, $\eta_\nu(E)$ can be complex.
- The eigenvalue spectrum depends on E. As a general principle, the latter will be more unfavorable regarding perturbativeness as $E \to 0$. Thus, we use very small values for E (about 0.0001 MeV) in the following to stay on the safe side. This will be implicit in the notation $\eta_\nu^{1/3}(E) \equiv \eta_\nu^{1/3}$.
- The spectrum depends on the starting bare interaction [461].
- $\eta_0^{1/3}$ will denote, if any, the Weinberg eigenvalue of the virtual/bound state wheras $\eta_\pm^{1/3}$ will characterize extremum values of the *remaining* spectrum.
- It is also possible to compute Weinberg eigenvalues using the in-medium propagator $G_{k_F}(E)$ at a finite density instead of $G_0(E)$ to include Pauli blocking effects. The latter is useful to evaluate non-perturbative behaviors in the nuclear medium [387].

5.4 Vacuum nucleon-nucleon forces from the renormalization group techniques

The phenomenologial short-range repulsion that is a common denominator of all phenomenological NN models is the cause of non-perturbative behaviors. Indeed, the existence of a "minimal approach length" in coordinate space corresponds in momentum space to a possible NN scattering up to very high energies. This is a limiting factor for numerical calculations of finite nuclei, since the basis size needed to achieve convergence is directly related to the energy range for which matrix elements of the nuclear interaction are non-zero. In the case of hard-core potentials this corresponds to very large bases which are numerically difficult to handle and restricted to very light nuclei in practice.

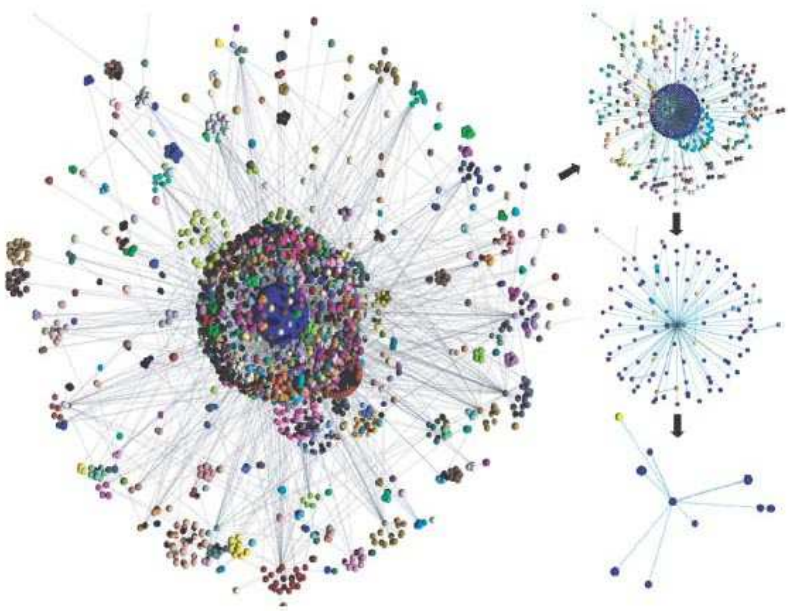

Figure 5.8: Illustration of the renormalization group formalism: a complex interacting system can be reduced at a given resolution scale to a few constituants while preserving the observables of interest.

The construction of energy-independent model space interactions from the renormalization group (RG) formalism provides a consistent way to circumvent this issue. This method is based on the identification of the relevant minimum length necessary in describing a given physical phenomenon. Such a length translates to a relative momentum cutoff Λ for plane waves such that [462–464]

- The length scale characterizing physical phenomena of interest is much larger than Λ^{-1},
- The form of equations and parameters in the equations describing the physical phenomena are defined with respect to Λ^{-1},
- These parameters summarize the relevant information relative to motions over a scale smaller than Λ^{-1}.

That is, the RG reduces a system to its low-energy degrees of freedom that are relevant at a given resolution scale, while (i) preserving low energy observables, and (ii) incorporating missing small-scale physics by integrating out properly high-energy degrees of freedom and incorporating their relevant part into scale-dependent coupling constants, as illustrated by Fig. 5.8. While several approaches can lead to exact RG equations, that is the Wilson [465–467], Polchinski [468–470] or effective average action [471; 472] ones, the formalism has been successfully applied to several systems of very different scales, from sub-microscopic lengths (e.g. quantum electrodynamics [473] or particle physics [474; 475]) to nanotechnology [476], solid state physics (spin physics [477] and description of critical phenomena [467]), fluids mechanics [478], up to mesoscopic applied mathematics such as anti-bubble regimes in finance [479] or the positioning of relay cells in wireless networks [480].

5.4.1 Low-momentum nucleon-nucleon forces

The renormalization group formalism can be applied to the construction of energy-independent model-space two-nucleon forces in the vacuum using the Kuo-Lee-Ratcliff folded diagram theory [481], the similarity transformation method [482] or the half on-shell matrix equivalence [483]. Using the latter prescription corresponds to cutting off all intermediate state summations (loop integrals) over a relative momentum Λ in the Lippmann-Schwinger equation (Eq. (5.31)). At the same time, the conservation of low-energy observables, which are fully on-shell, is enforced by requiring that the half on-shell T-matrix $T\left(\vec{k},\vec{k}\,';\frac{\hbar^2 k^2}{2m}\right)$ is conserved for $k,k' < \Lambda$. This implies that the nucleon-nucleon interaction becomes Λ-dependent. It will be called $V_{\mathrm{low}\,k}$ in the following. One has then

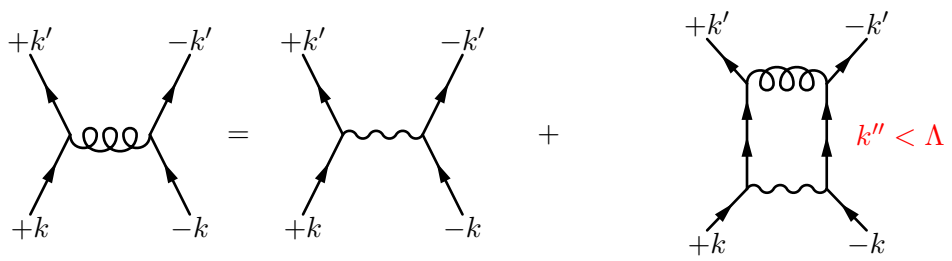

$$T(\vec{k},\vec{k}\,';E) = \frac{m}{\hbar^2}V_{\mathrm{low}\,k}(\vec{k},\vec{k}\,';\Lambda) + \mathcal{P}\int\frac{\mathrm{d}\vec{k}\,''}{(2\pi)^3}\frac{V_{\mathrm{low}\,k}(\vec{k},\vec{k}\,'';\Lambda)\,T(\vec{k}\,'',\vec{k}\,';E)}{E-E(k'')}\,, \quad (5.77)$$

with the condition

$$\frac{\mathrm{d}\,T\left(\vec{k},\vec{k}\,';\frac{\hbar^2 k^2}{2m}\right)}{\mathrm{d}\,\Lambda} = 0\,. \quad (5.78)$$

Regardless of the method applied, the preservation of the half on-shell T-matrix for $k, k' < \Lambda$ (Eq. (5.78)) leads to a flow equation for $V_{\text{low}\,k}$ that reads [87; 483; 484]

$$\frac{\mathrm{d}}{\mathrm{d}\,\Lambda} V_{\text{low}\,k\,LL'}^{JST}(k', k; \Lambda) = \frac{2}{\pi} \frac{V_{\text{low}\,k\,LL'}^{JST}(k', k; \Lambda)\, T_{LL'}^{JST}\left(\Lambda, k; \frac{\hbar^2\,\Lambda^2}{2m}\right)}{1 - \left(\frac{k}{\Lambda}\right)^2}\,, \tag{5.79}$$

following the partial wave decomposition of the Lippmann-Schwinger equation (Eq. (5.33)). Eq. (5.79) can be solved numerically, iteratively when necessary [485], starting from a given phenomenological NN force v^{NN} defined with a higher intrinsic resolution scale (AV18, CD-Bonn, N^{3}LO...) with the initial flow condition

$$V_{\text{low}\,k}(k, k'; \Lambda) \underset{\Lambda \to +\infty}{\longrightarrow} v^{\text{NN}}(k, k')\,. \tag{5.80}$$

The convergence of the flow equation is illustrated by Fig. 5.9 for the $^1\text{S}_0$ matrix elements

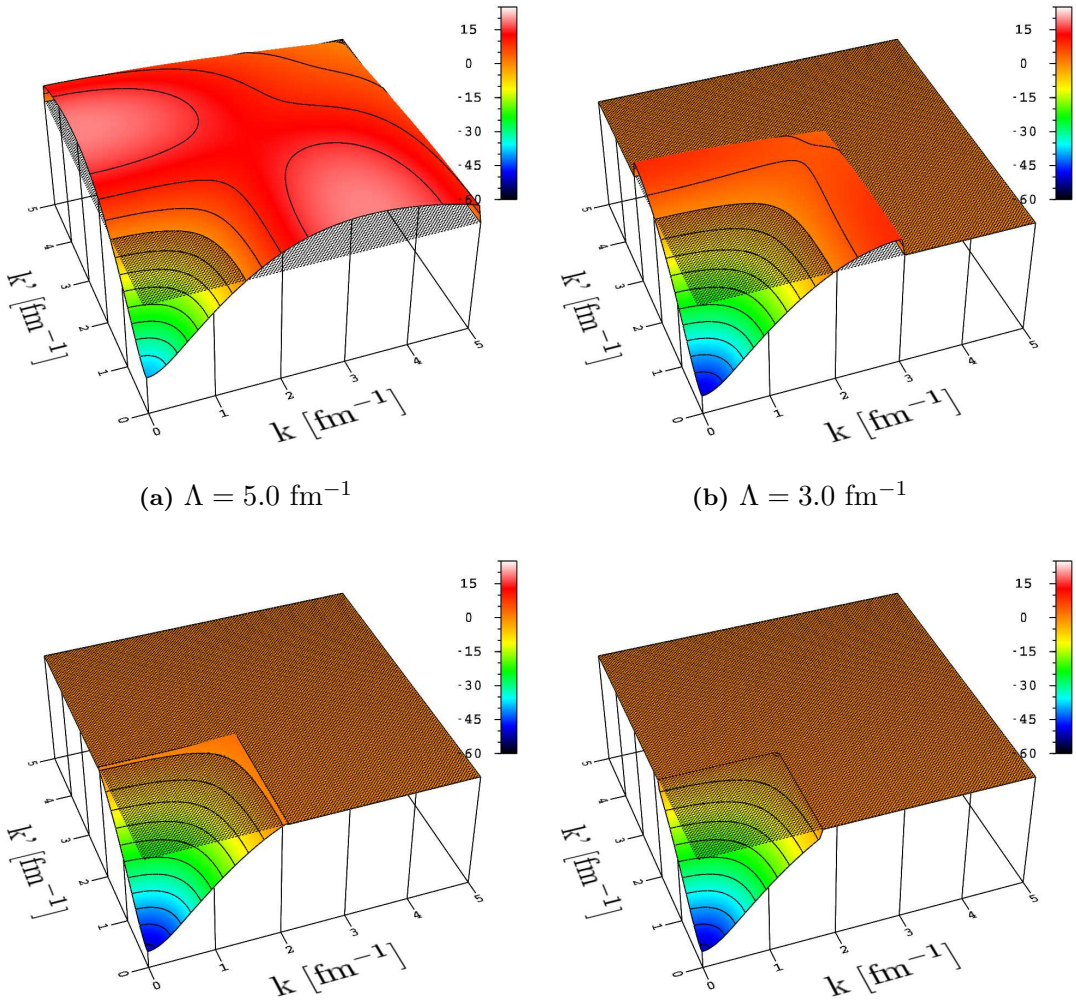

(a) $\Lambda = 5.0$ fm^{-1} (b) $\Lambda = 3.0$ fm^{-1}

(c) $\Lambda = 2.1$ fm^{-1} (d) $\Lambda = 1.8$ fm^{-1}

Figure 5.9: $V_{\text{low}\,k}$ matrix elements in the $^1\text{S}_0$ channel starting from the bare Argonne V18 interation and for different values of the RG cutoff Λ.

of $V_{\text{low}\,k}$ originating from the Argonne V18 potential. While high-momentum components are

integrated out, the depth of the potential for $k \approx k' \approx 0$ also changes, showing the necessary modification of the low-energy part of the NN force in order to preserve the half on-shell T-matrix, that is the application of RG goes beyond simply cutting out high-energy physics. $V_{\text{low}\,k}$ scales properly with the underlying physics [87], e.g. (i) $V_{\text{low}\,k}(0,0;\Lambda)$ flows towards the scattering length for $\Lambda \to 0$, (ii) as long as Λ is large enough to include the relevant degrees of freedom needed to describe the scale one is probing (the pion in the present case), $V_{\text{low}\,k}$ smoothly depends on Λ. For $\Lambda < m_\pi$, the pion is integrated out and rapid changes are observed. For these reasons, one usually never goes below $\Lambda \approx 1.8$ fm^{-1} in view of describing low-energy nuclear structure. Likewise, (iii) $V_{\text{low}\,k}$ preserves two-body scattering and bound states for $k < \Lambda$, such as the deuteron as a pole of the T-matrix in the $^3\text{S}_1$-$^3\text{D}_1$ coupled channels. Matrix elements for all $L \leq 2$ partial waves can be found in Fig. 5.10.

The use of a sharp cutoff Λ implies that $V_{\text{low}\,k}$ is non-hermitian. In the region of interest for Λ, that is from about ~ 1.8 fm^{-1} up to $3 \sim 4$ fm^{-1}, the non-hermicity remains small and can be transformed away [486–488]. However, cusp-like behaviors around Λ lead for small cutoffs to slow convergence or degradation of few-body observables of the order of $10 - 100$ keVs [489]. The solution consists in using smooth cutoff functions in the RG equation instead of sharp one [490; 491] through a three-step approach, that is

1. Construct the energy-dependent interaction and T-matrix by adding momentum cutoff functions $g(k)$, i.e.

$$v_{\text{eff}}(k,k';E) = g(k')\,v(k,k';E)\,g(k)\,, \qquad T_{\text{eff}}(k,k';E) = g(k')\,T(k,k';E)\,g(k)\,, \tag{5.81}$$

   and solve the associated Lippmann-Schwinger equation by preserving the fully off-shell T_{eff}.

2. Convert the energy-dependence of v_{eff} into a momentum-dependence by using a method similar to field redefinition. This leads to a non-hermitian $V_{\text{low}\,k}$ that reproduces matrix elements of the fully off-shell T_{eff}.

3. Hermitize $V_{\text{low}\,k}$ by a similarity transformation.

Smooth cutoff functions f_ϵ are defined with respect to a continuous/integer parameter. Possible choices are[11]

$$g_n(k) = \exp\left[-\left(\frac{k}{\Lambda}\right)^{2n}\right] \qquad \text{exponential regulator}\,, \tag{5.82a}$$

$$g_\epsilon(k) = \frac{1}{1+\exp\left[\frac{k^2-\Lambda^2}{\epsilon^2}\right]} \qquad \text{Fermi-Dirac regulator}\,, \tag{5.82b}$$

$$g_\epsilon(k) = \frac{1}{2}\left[1+\tanh\left(\frac{\Lambda^2-k^2}{\Lambda\,k\,\epsilon}\right)\right] \qquad \text{hyperbolic tangent regulator}\,, \tag{5.82c}$$

and are represented in Fig. 5.12. They all verify

$$g_\epsilon(k) \underset{k\to 0}{\longrightarrow} 1\,, \qquad g_\epsilon(k) \underset{k\to+\infty}{\longrightarrow} 0\,. \tag{5.83}$$

A sharp cutoff $V_{\text{low}\,k}$ corresponds then to $g(k) = \Theta(\Lambda - k)$. In the following, one will always use

[11] One notes that exponential cutoffs might introduce a bias for $k \approx \Lambda$. Indeed, one has

- $f(\Lambda) = 1/2$ for sharp, Fermi-Dirac and hyperbolic tangent regulators,
- $f(\Lambda) = 1/e$ for exponential regulators.

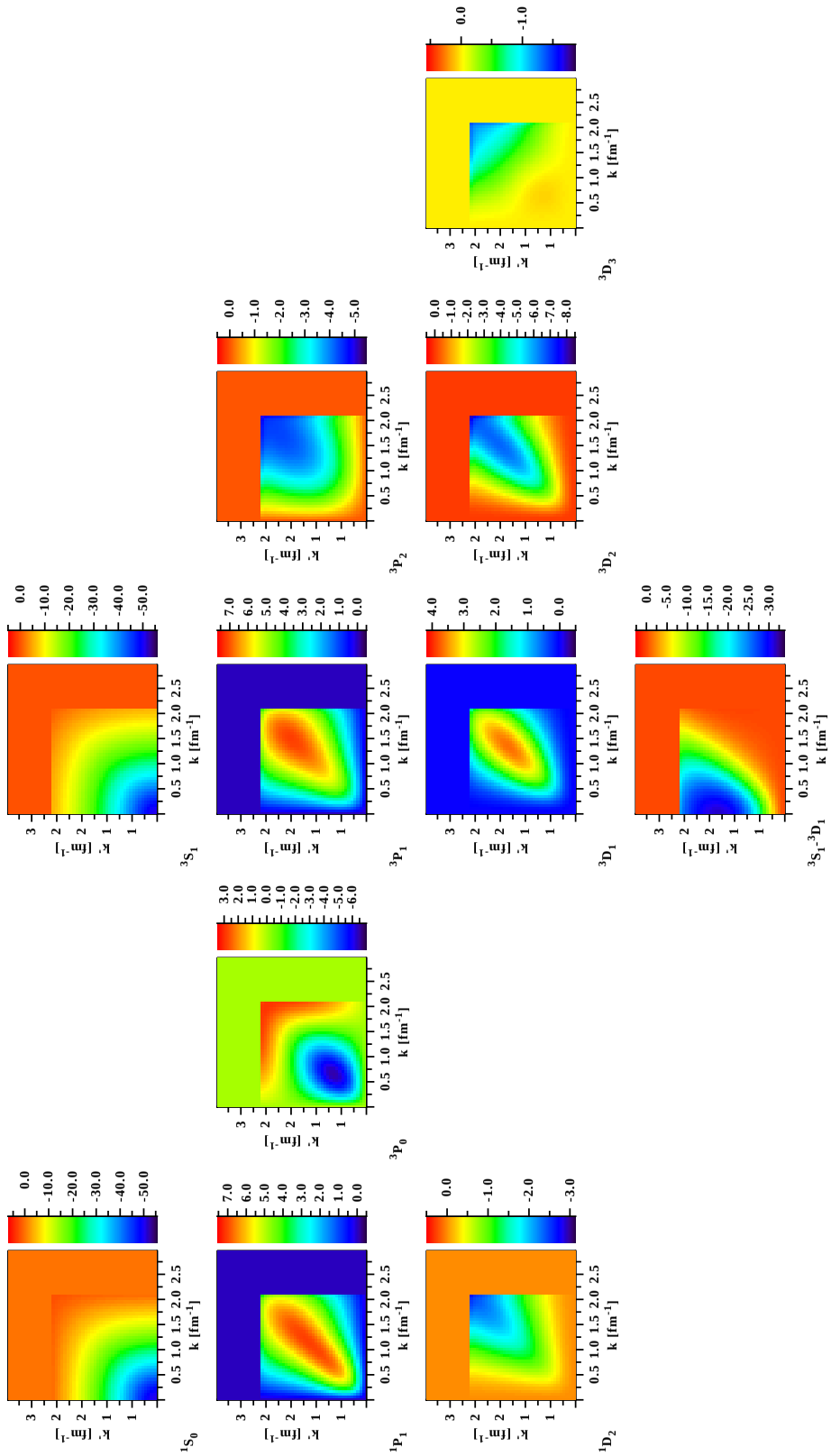

Figure 5.10: $V_{\mathrm{low}\,k}$ matrix elements in all $L \leq 2$ partial waves ($T_z = 0$ if $T = 1$) starting from the bare Argonne V18 interation and $\Lambda = 2.1$ fm^{-1}. A sharp momentum cutoff $k < \Lambda$ is used.

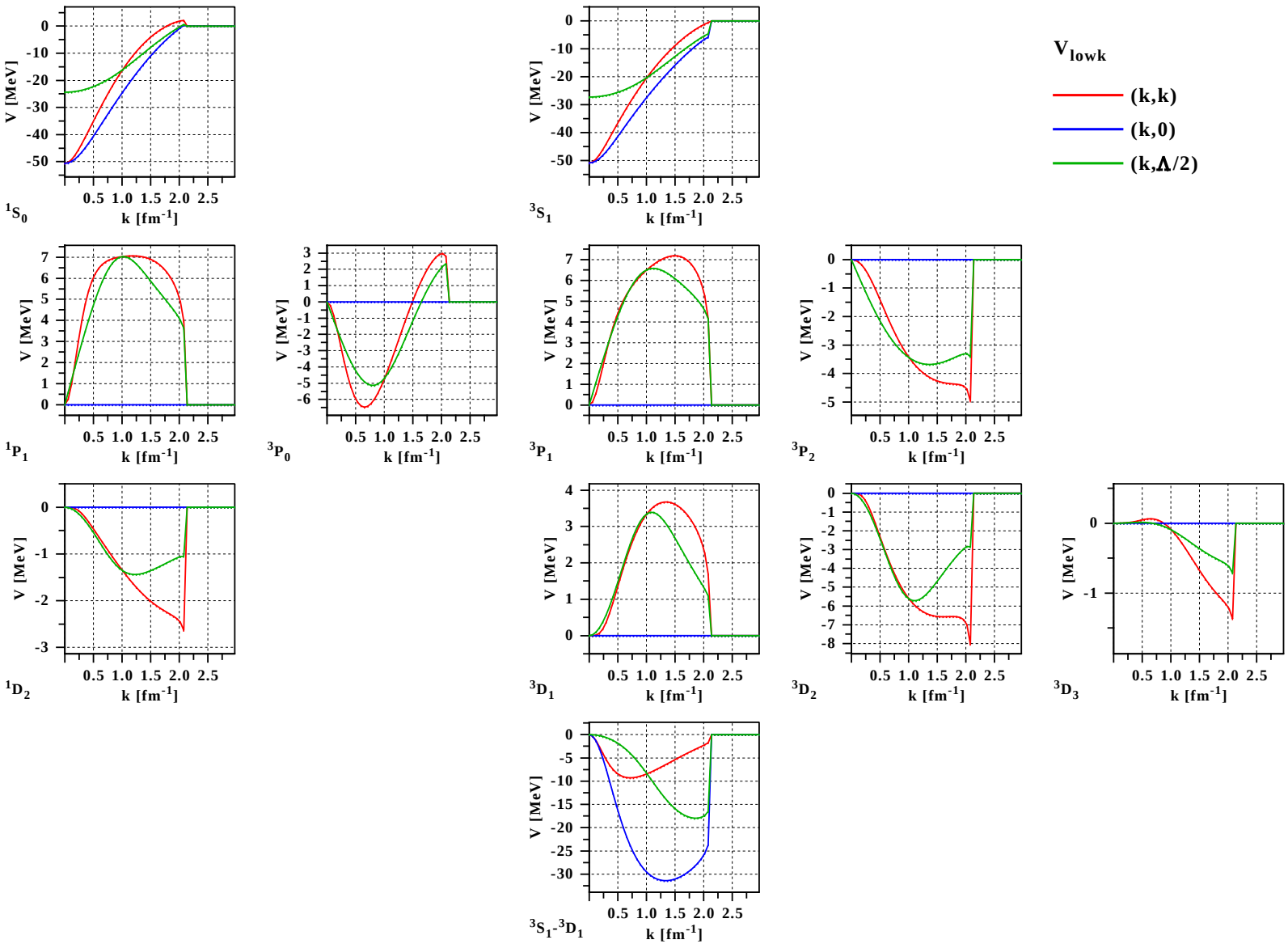

Figure 5.11: Same as in FIG. 5.10 for specific matrix elements of $V_{\text{low}\,k}$.

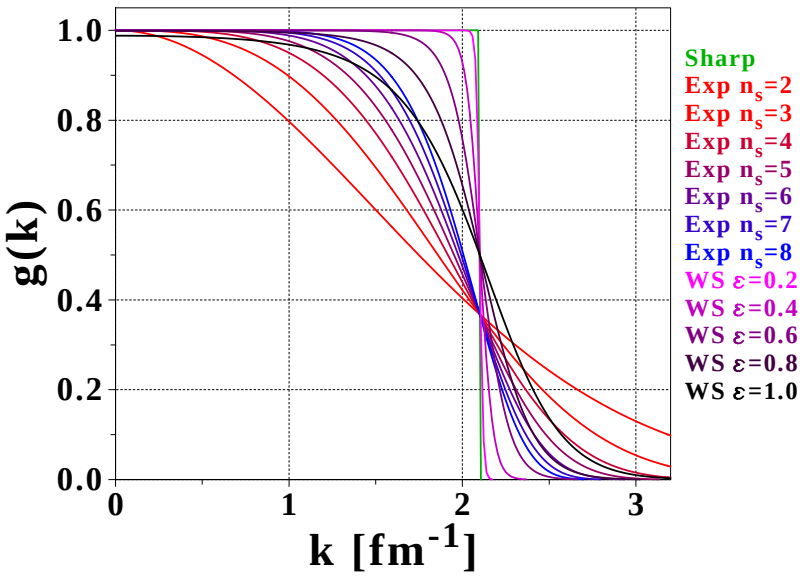

Figure 5.12: Sharp and smooth cutoff functions $f_\epsilon(k)$ for RG flow equations.

$V_{\text{low}\,k}$ with a smooth cutoff. Unless precised, the latter will correspond to an exponential cutoff with $n_S = 8$.

One may also mention a parallel approach to achieve a decoupling between low- and high-energy physics based on the Similarity Renormalization Group (SRG) [492–495], where the same unitary transformation renormalizes all operators at the same time, in opposition to $V_{\text{low}\,k}$ where the RG flow applies to only one operator at a time. While SRG interactions lead to similar low-momentum features as $V_{\text{low}\,k}$, they are based on the suppression of off-diagonal matrix elements and lead to band-diagonal interactions [496]. In particular, they will retain high-momentum diagonal components which makes them not convenient for the purpose of this work. In any case, block diagonalization is possible in the context of SRG [497–499], where high-energy modes are non-zero but decoupled from low-energy matrix elements [500; 501].

5.4.2 Properties of $V_{\text{low}\,k}$

Let us summarize briefly some properties of low-momentum interactions that will turn out to be useful later on.

- The conservation of the low-momentum half on-shell T-matrix implies that phase shifts of $V_{\text{low}\,k}$ are identical to the ones of the phenomenological NN model it is derived from up to the RG cutoff Λ, as seen in Fig. 5.13, that is they reproduce low-energy experimental phase shifts with an accuracy of the same order of high-precision NN potentials.

- Since all state-of-the-art bare NN forces reproduce phase shifts with roughly the same precision, the flow equation for $V_{\text{low}\,k}$ starting from any of them should lead to the same fully on-shell T-matrix. In the low-energy domain $V_{\text{low}\,k}$ is in fact (almost) independent of the bare NN interaction it is derived from [87], as seen in Fig. 5.14, where the RG flow is evolved down for different NN empirical forces. In the end, $V_{\text{low}\,k}$ is to be considered itself as a Λ-dependent NN force in vacuum. Its phase shifts compared to PWA93 results in all $L \leq 2$ partial waves and scattering/deuteron properties can be found in Fig. 5.15 and Tabs. {5.5-5.6}, and are indeed very close to (i) experimental values, and (ii) values found for the phenomenological NN model it is derived from.

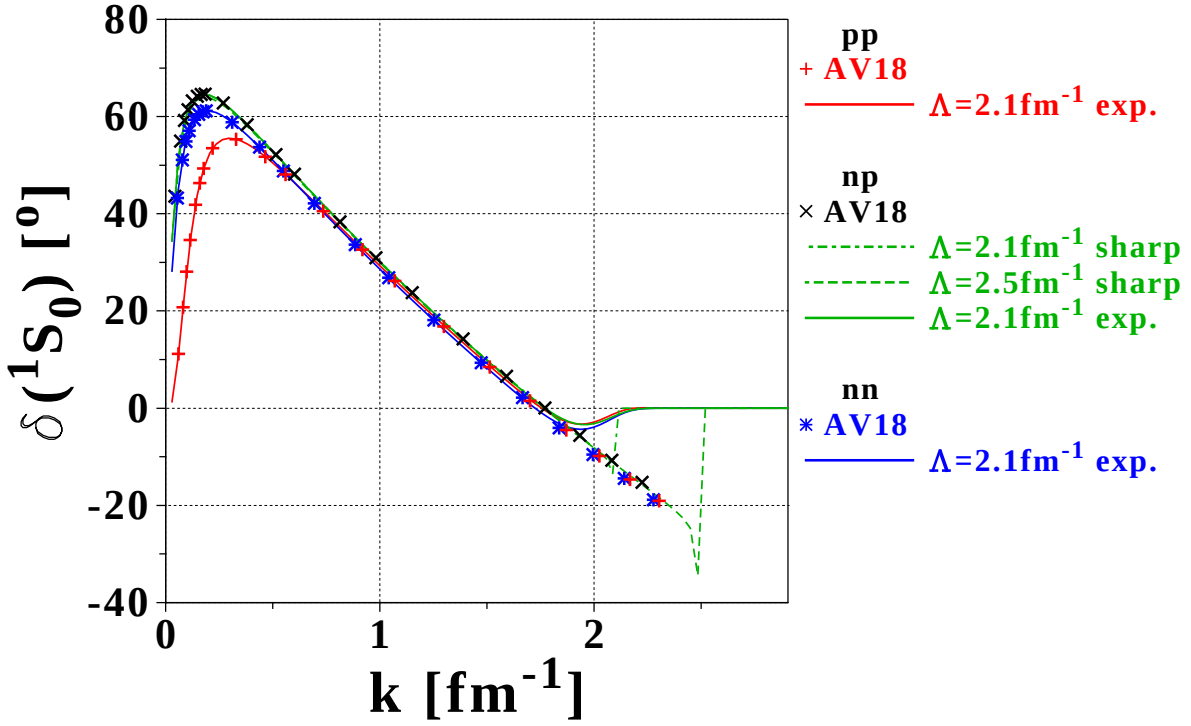

Figure 5.13: $^1S_0$ phase shifts for the Argonne V18 phenomenological potential and $V_{\text{low}\,k}$ using different values of Λ and cutoff functions $g(k)$.

- Since high-momentum matrix elements are integrated out, $V_{\text{low}\,k}$ produced at $\Lambda \approx 2$ fm^{-1} is perturbative, as exemplified by the corresponding Weinberg eigenvalues in the $^1S_0$ and $^3S_1$-$^3D_1$ channels. These eigenvalues for $V_{\text{low}\,k}$ from AV18 at different values of the RG cutoff Λ are represented in Fig. 5.16.

  In the $^1S_0$ channel, the presence of the virtual state is characterized by the Λ-independent eigenvalue $\eta_0^1 \approx 1$. The compression of the rest of the spectrum as the cutoff is running down is visible. In particular $V_{\text{low}\,k}$ becomes perturbative in a strictly mathematical sens (i.e. corresponding to a convergence of the Born series) for approximatively $\Lambda \leq 4.80$ fm^{-1}. When N^{3}LO is used as a starting point for the RG flow[12], the evolution of η_ν^1 proves that the Born series remains perturbative even for cutoffs around 5 fm^{-1}, as seen in Fig. 5.17. This is a consequence of the rather low intrinsic momentum cutoff in χ-EFT potentials, that reduces the effect of the short-range repulsion [505].

  Likewise, in the coupled $^3S_1$-$^3D_1$ channels, the presence of the deuteron bound state is characterized by the almost Λ-independent eigenvalue greater than one. In all rigor, one should have exactly $\eta_0^3 = 1$ for a bound state of the potential, but only when it is computed at the bound state energy, that is the deuteron pole in the present case, as explained in Sec. 5.3.5. Nevertheless, the perturbative behavior of $V_{\text{low}\,k}$ as Λ is lowered is again observed.

  Apart from virtual or bound states, in the low-momentum regime Weinberg eigenvalues are very small and go to zero, which shows that the Born series is (i) converging in the mathematical sense since $|\eta_\nu| < 1$ for all ν, and (ii) rapidly converging since $|\eta_\nu| \ll 1$. The latter can be for instance illustrated by looking at NCSM calculations of light nuclei [506].

[12] One only uses in this case the two-body restriction of chiral forces for the flow equations. This will be implicit in the following

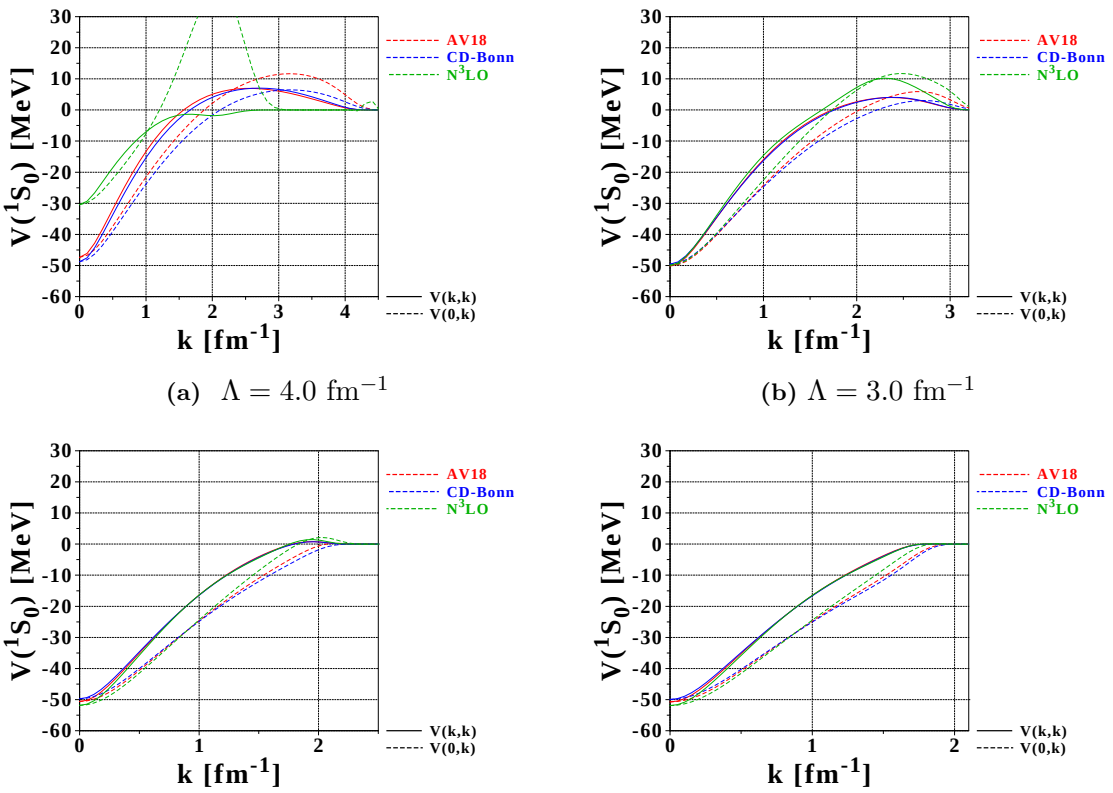

(a) $\Lambda = 4.0$ fm^{-1} (b) $\Lambda = 3.0$ fm^{-1}

(c) $\Lambda = 2.1$ fm^{-1} (d) $\Lambda = 1.8$ fm^{-1}

Figure 5.14: ^{1}S$_0$ ($T_z = 0$) matrix elements of $V_{\text{low}\,k}$ derived from different realistic NN potentials at different values of the RG cutoff. For small values of Λ all models converge to the same limit, which defines $V_{\text{low}\,k}$ as a universal object.

Convergence is rapidly achieved as a function of the number of included HO shells. Likewise, and as discussed in Sec. 7.4.7, convergence of the nuclear G-matrix is almost reached at second order and does not require summing particle-particle ladders to all orders. However, while in-medium virtual/bound states are driven into into the perturbative regime as an effect of Pauli blocking [387], their non-perturbative nature in vacuum still drives superfluid behaviors in INM such as pair condensation, and can be handled by solving the gap equation [507; 508].

Weinberg eigenvalues will be used later on to design a quantitative tool characterizing the perturbativeness of a given bare interaction and applied to the case of v_{BDRS}.

As a conclusion, low-momentum interactions $V_{\text{low}\,k}$ define a new class of two-nucleon forces in the vacuum ("bare"), that can be seen as soft-core potentials which preserve low-energy physical observables.

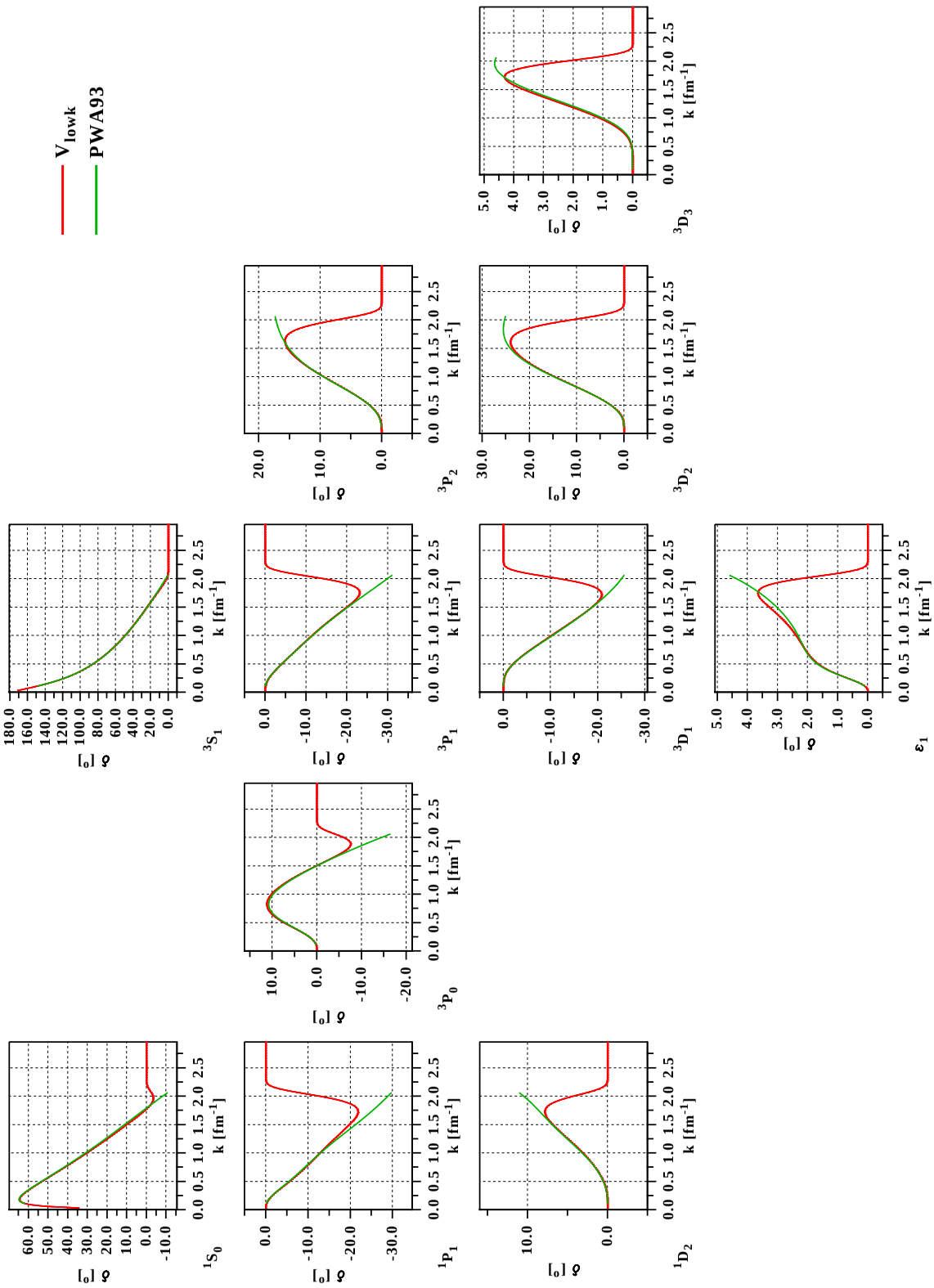

Figure 5.15: $V_{\mathrm{low}\,k}$ scattering phase shifts in all $L \leq 2$ partial waves ($T_z = 0$ if $T = 1$) for $\Lambda = 2.1$ fm^{-1} with a smooth RG cutoff, in comparison with PWA93 [375].

		AV18	Exp.	Ref.	$V_{\text{low}\,k}$
^{1}S$_0$ (pp)	a_0 [fm]	-7.8064	-7.8063 ± 0.0026	[447]	-7.676
	r_0 [fm]	2.788	2.794 ±0.014		2.622
^{1}S$_0$ (nn)	a_0 [fm]	-18.487	-18.5 ±0.5	[502]	-18.472
	r_0 [fm]	2.840	2.8 ±0.1		2.834
^{1}S$_0$ (np)	a_0 [fm]	-23.732	-23.749 ±0.008	[503]	-23.721
	r_0 [fm]	2.697	2.81 ±0.05		2.694
^{3}S$_1$ (np)	a_1 [fm]	5.419	5.424 ±0.003	[447]	5.430
	r_1 [fm]	1.753	1.760 ±0.005		1.754

Table 5.5: s-wave scattering lengths a_S and effective ranges r_S of $V_{\text{low}\,k}$ with a smooth cutoff and $\Lambda = 2.1$ fm^{-1} in comparison with Argonne V18 and experimental data. The agreement between AV18 and $V_{\text{low}\,k}$ obtained with approximate numerical calculations of the scattering parameters is sufficient for the scope of this work. For proton-proton phase shifts the scattering parameters are computed with respect to the Coulomb effective range function instead of the full EM one (see Appendix D.3), which explains most of the (small) discrepancies that are observed.

	AV18	Exp.	Ref.	$V_{\text{low}\,k}$
E_d [MeV]	-2.224575	-2.224575 ± 0.000009	[376]	-2.22459
$\langle r^2\rangle^d_m$ [fm]	1.967	1.9660 ±0.0068	[504]	1.968
Q_d [fm^2]	0.270	0.2859 ±0.0003	[377; 378]	0.264
A_S [fm$^{1/2}$]	0.8850	0.8846 ±0.0008	[378]	0.889
η_d [fm$^{1/2}$]	0.0250	0.0256 ±0.0004	[379]	0.0337
P_d [%]	5.76			3.69

Table 5.6: Same as in Tab. {5.5} for deuteron properties. The agreement between AV18 and $V_{\text{low}\,k}$ obtained with approximate numerical calculations of the deuteron properties is sufficient for the scope of this work.

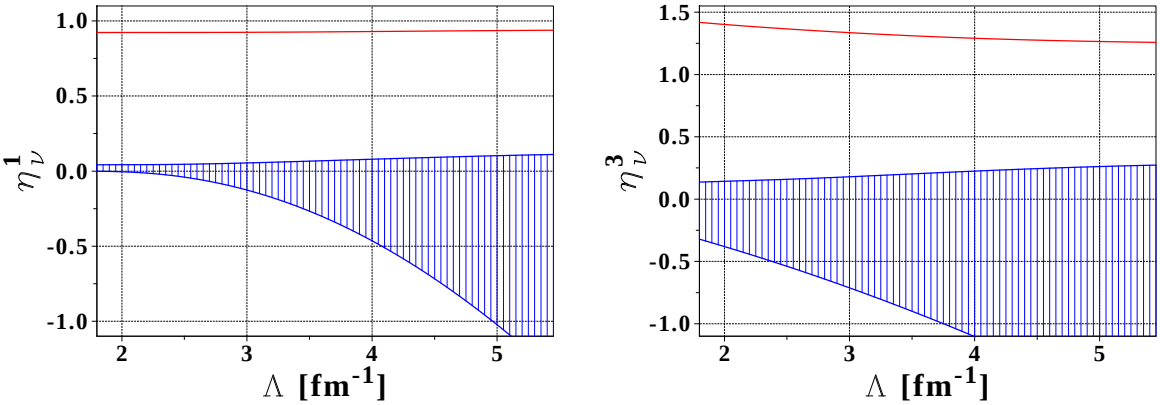

Figure 5.16: Weinberg eigenvalues for $V_{\mathrm{low}\,k}$ as a function of the RG cutoff Λ in the $^1\mathrm{S}_0$ and $^3\mathrm{S}_1$-$^3\mathrm{D}_1$ channels starting from Argonne V18.

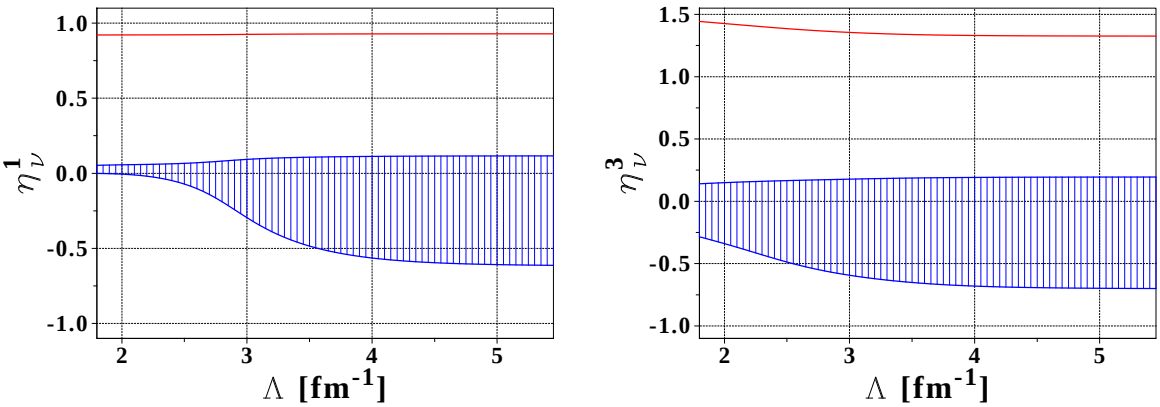

Figure 5.17: Same as in Fig. 5.16 starting from the chiral potential N^{3}LO.

Chapter 6

Many-body problem

Abstract: This chapter very briefly presents many-body techniques in the context of many-body perturbation theory (MBPT). If starting vacuum two- and three-body forces lead to a perturbative diagrammatic expansion of the ground-state wave function and energy, a connection with the EDF used for finite nuclei calculations, together with the one-body fields that derive from it, can be rather easily envisioned.

Contents

6.1 Introduction **177**
6.2 Treatment of in-medium correlations **178**
6.2.1 Goldstone-Brueckner formalism 178
6.2.2 Expansion of the ground-state wave-function and energy 180
6.2.2.1 Hole-line expansion for non-perturbative potentials 180
6.2.2.2 Perturbative expansion 181
6.2.3 Choice of the one-body potential Γ 181
6.3 Pairing correlations within a diagrammatic framework **182**
6.3.1 Conventions 182
6.3.2 Compensation of dangerous diagrams 183

6.1 Introduction

While ab initio treatments of finite nuclei using realistic NN and NNN potentials are in principle possible, the non-perturbative behavior of standard interaction models makes such calculations limited to few-nucleon systems [65–68]. Causes for non-perturbativeness are manyfold [509], i.e. (i) the hard-core repulsion that makes nucleons scatter up to very high energies and requires basis sets way beyond current numerical capabilities, (ii) the tensor force coming from OPE which is singular at short distances [510; 511], and (iii) the presence or virtual (di-neutron) or bound (deuteron) states [512; 513]. On the other hand, bare nuclear interactions are strongly renormalized in the nuclear medium. This suggests that expressing the many-body energy in terms of an unperturbed Slater determinant coupled to an **effective in-medium interaction** that already includes many-body correlations might be possible. That is, the minimal set of in-medium correlations that have to be included to reach a reasonable description of the system, i.e. infinite nuclear matter or finite nuclei, need to be incorporated in the definition of the in-medium interaction. This can be achieved for simple systems in the context of Goldstone-Brueckner theory [514]. The latter consists of an expansion of the many-body wave function, energy and self-energy around a mean-field solution that is yet to be determined, such that the repulsive

short-range interaction of the vacuum force is properly renormalized. If the non-perturbative nature of the vacuum interaction is reduced, this scheme simplifies and might become tractable in view of finite nuclei calculations.

Only general guidelines for the design of such effective interactions are given in the present chapter. Exact diagrammatic calculations can be found in the references that are given in the following. Notations for all diagrams involved are summarized in Tab. {6.1}.

	Fermion line
	π exchange
	vacuum NN force v^{NN}
	vacuum NN + $\overline{\mathrm{NNN}}$ (averaged) force $v^{\mathrm{NN}+\overline{\mathrm{NNN}}}$
	Effective two-body vertex $v^{\mathrm{ph}}_{\mathrm{eff}}$ (particle-hole channel)
	Effective two-body vertex $v^{\mathrm{pp}}_{\mathrm{eff}}$ (particle-particle channel)
	Kinetic energy
	T-matrix $T(\omega)$
	G-matrix $G(\omega)$

Table 6.1: Conventions for the lines and diagrams involved in MBPT calculations. All vertices are supposed to be antisymmetrized, unless specified.

6.2 Treatment of in-medium correlations

6.2.1 Goldstone-Brueckner formalism

As long as pairing is not explicitly included, the Hamiltonian[1] $H = t + v$ can be decomposed in terms of a one-body hamiltonian h_0 that has Slater determinants $|\Phi_i\rangle$ as eigenstates, and a perturbation h_1, i.e.

$$H = h_0 + h_1 \,, \tag{6.1a}$$

$$h_0 \equiv t + \Gamma = \sum_i t_i + \sum_{ij} \Gamma_{ij}\, \hat{a}_i^\dagger\, \hat{a}_j = \sum_n \epsilon_n\, \hat{c}_n^\dagger\, \hat{c}_n \,, \tag{6.1b}$$

$$h_1 = v - \Gamma \,. \tag{6.1c}$$

The quantities ϵ_p are the eigenenergies of h_0 corresponding to single-particle states φ_p, whereas ε_i will denote many-body eigenenergies of h_0 associated with unperturbed Slater determinants, i.e.

$$\varepsilon_i = \sum_{i=p}^{N} \epsilon_p \qquad\qquad |\Phi_i\rangle = \prod_{p=1}^{N} \hat{c}_p^\dagger |0\rangle \,. \tag{6.2}$$

[1] v represents the vacuum two-body nuclear interaction that may contain averaged three-body contributions.

According to Gell-Mann-Low's adiabatic theorem [515], the true ground state $|\Theta_0\rangle$ of H can be obtained from the adiabatic evolution of the ground state of h_0 from $t = -\infty$ to $t = 0$ by plugging in gradually the residual interaction [516; 517], i.e.

$$|\Theta_0\rangle = \lim_{\epsilon\to 0}\left(\frac{U_\epsilon(0,-\infty)|\Phi_0\rangle}{\langle\Phi_0|U_\epsilon(0,-\infty)|\Phi_0\rangle}\right), \tag{6.3}$$

where the adiabatic evolution operator $U_\epsilon(t,t_0)$ from t to t_0 is defined in the interaction representation starting from the Hamiltonian in the Shrödinger representation $H(\epsilon, t-t_0)$ as

$$U(t,t_0) \equiv \exp\left[\frac{i\,h_0\,t}{\hbar}\right] U_\epsilon(t,t_0)\, \exp\left[-\frac{i\,h_0\,t}{\hbar}\right] \tag{6.4a}$$

$$U_\epsilon(t,t_0) \equiv \exp\left[-\frac{i}{\hbar}\int_{t_0}^{t} \mathrm{d}\tau\, H(\epsilon,\tau)\right]. \tag{6.4b}$$

From an expansion of U_ϵ in powers of the residual interaction and integrations over time in Eq. (6.3), a series expansion of the ground state $|\Theta_0\rangle$ is obtained [88], i.e.

$$|\Theta_0\rangle = \sum_n \left(\frac{1}{\varepsilon_0 - h_0} h_1\right)^n |\Phi_0\rangle_{\text{linked}}, \tag{6.5}$$

where the sum runs only over linked diagrams, i.e. where $|\Phi_0\rangle$ does not appear as an intermediate state. The latter is enforced at the level of Eq. (6.3) where the denominator fixes the normalization of $|\Theta_0\rangle$ by eliminating disconnected vacuum-to-vacuum diagrams [89]. Likewise, a similar expansion of the ground-state energy E_0 reads

$$E_0 = \varepsilon_0 + \sum_n \langle\Phi_0|h_1\left(\frac{1}{\varepsilon_0 - h_0} h_1\right)^n |\Phi_0\rangle_{\text{connected}}, \tag{6.6}$$

where the sums now only runs over connected diagrams, thats is vacuum-to-vacuum ones.

However, if the expansions of Eqs. (6.5,6.6) are truncated at a given order, non-converging results arise if the vacuum interaction presents a non-perturbative hard core. On the other hand, it is possible to extract a series of ladder diagrams where a succession of interactions v scatters nucleons into particle states. This series can be replaced by a reaction matrix G which resums those Brueckner's particle-particle ladders and can be represented by the self-consistent Bethe-Goldstone equation [518–521]

$$G(\omega) \quad = \quad v \quad + \quad v\,\frac{Q}{\omega - h_0}\,G(\omega) \tag{6.7a}$$

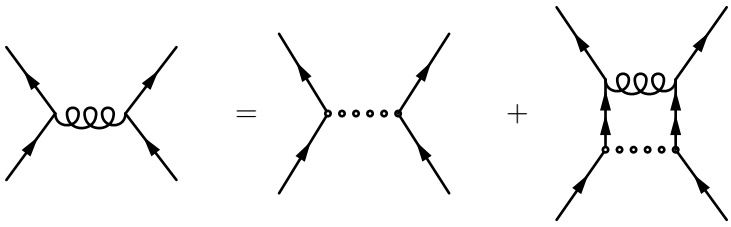

(6.7b)

where ω is the starting energy that corresponds to the in-medium energy of the nucleons at the location where G is inserted, whereas the Pauli operator Q excludes occupied states, i.e. those below the Fermi level ϵ_F associated with the unperturbed vacuum $|\Phi_0\rangle$, that is

$$Q = \sum_{\epsilon_p,\epsilon_{p'}>\epsilon_F} |\,1:p,\,2:p'\,\rangle\langle 1:p,\,2:p'\,|\,. \tag{6.8}$$

The replacement of the initial interaction by the resummed G-matrix modifies the short-range part of the two-body wave function, such that it is strongly suppressed over a distance of the order of the range of the repulsive core, that is the healing distance, or wound [122; 514]. As a result, the interaction energy at a given order in the expansion (see below) is not artificially large any more.

6.2.2 Expansion of the ground-state wave-function and energy

The general idea consists in regrouping, if necessary, clusters of diagrams under G in such a way that a converging series is obtained, i.e. a truncation at a given order provides a result of a given precision [88]. Once the G-matrix has been computed, it replaces all instances of v in diagrams, excluding those where successive G-matrices are connected by a two-particle intermediate state, that is no particle-particle ladder connecting two G-matrices must be written.

6.2.2.1 Hole-line expansion for non-perturbative potentials

While the G-matrix regularizes the hard-core repulsion, an expansion in terms of G for the ground-state and single-particle energies remains non-perturbative, in such a way that the proper expansion parameter is the number of hole lines [522]. At lowest order in the hole-line expansion, the ground-state energy E reads as in Fig. 6.1 [517], where self-energies ϵ_i that enter intermediate propagators are obtained by a functional derivative of the ground-state energy. That is, the lowest order in hole lines for E_0 (two hole lines) leads not only to a term with one line in the self energy but also to a rearrangement term containing two hole lines and coming from the functional derivative of the particle-particle ladder propagator.

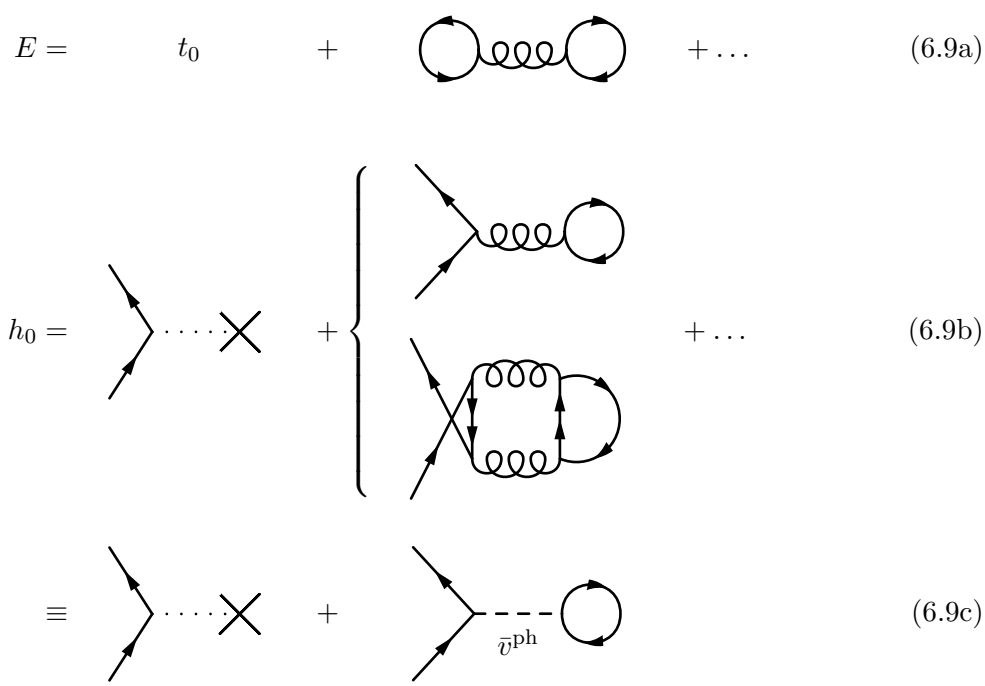

Figure 6.1: Ground-state energy E_0 at lowest order in the hole-line expansion and single-particle ϵ_i energies obtained through a functional derivative. Following this definition, the self-energy contains a so-called rearrangement term.

6.2.2.2 Perturbative expansion

If the starting interaction is in fact perturbative, as it will be the case for low-momentum interactions, in-medium correlations can be treated through converging perturbative series in powers of v for E_0 and ϵ_i. Indeed, the ladder series from Eq. (6.7a) becomes perturbative, such that it can be truncated at a given order in intermediate ladders. For instance, the ladder series for $V_{\text{low}\,k}$ is almost converged at second order in MBPT (see Sec. 7.4.7). One then rephrases the perturbative expansions for E_0 and ϵ_i from Eqs. (6.9a,6.9b) in terms of the original vacuum interaction, as seen in Fig. 6.2.

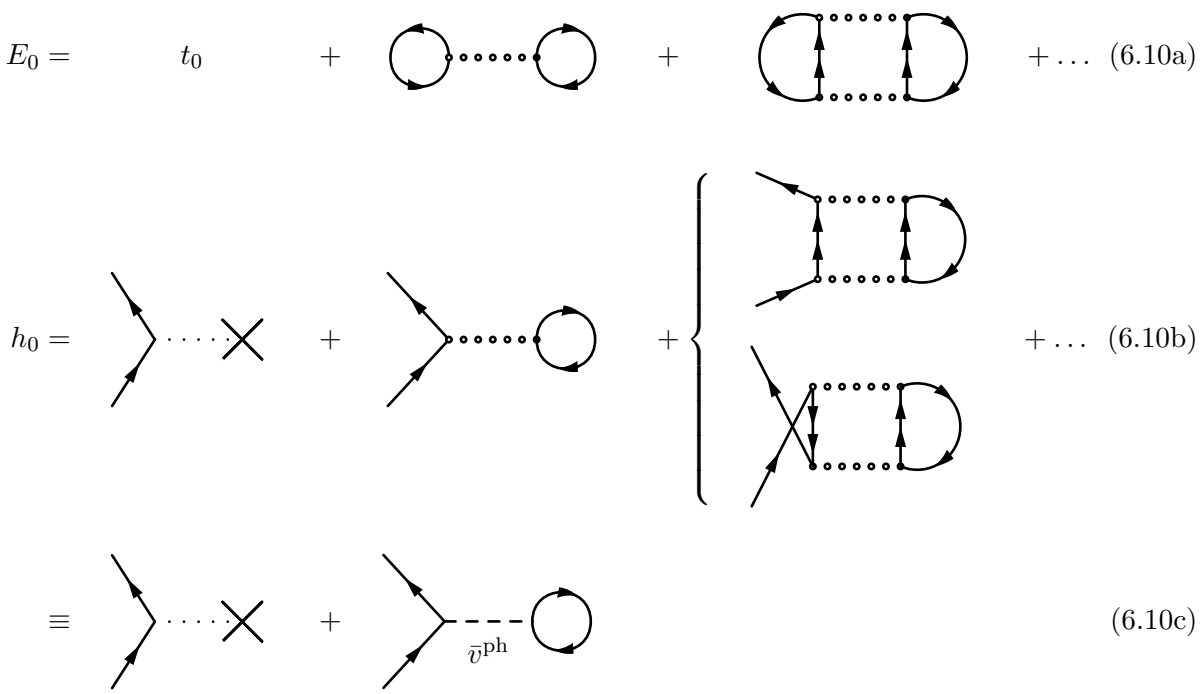

Figure 6.2: Many-body perturbation theory for the ground-state energy E_0 and self-energies ϵ_i at second order in MBPT. The self-energy not only enters intermediate calculations but is also crucial for the study of $N \pm 1$-particle systems. In the present case, rearrangement terms come from the second order diagram in the energy and account for 2p-1h/1p-2h contributions to the self-energy.

6.2.3 Choice of the one-body potential Γ

The proper choice of the unperturbed hamiltonian h_0 is crucial to have a rapidly convergent series [523]. Several choices for the one-body field Γ are possible, among which (i) a phenomenological expression that is fixed a priori, (ii) the Hartree-Fock approximation where ϵ_k are eigenenergies of the Schrödinger equation associated with the vacuum force, or (iii) a more involved approach necessary for non-perturbative potentials, e.g. where the one-body field Γ is constructed at lowest order in the on-shell G-matrix or includes rearragement terms (extended Brueckner-Hartree-Fock calculations) [524–527]. The Brueckner-Hartree-Fock approximation obtained at lowest order in the hole-line expansion is provided by the explicit diagrams of Eq. (6.9b), excluding rearragement terms, and amounts to canceling order by order specific

insertions of G and Γ.

Note that the truncation orders can be different in the series for the energy E_0 and the self-energy ϵ_i, e.g. E_0 can be computed at second order while single-particle energies are derived from a more simple (Woods-Saxon...) potential or only at first order in v. Still, adding more orders in the expansion of the single-particle energies adds extra diagrams in the series for E_0 such that it converges faster. In most cases one tries to preserve a consistency between the two series such that diagrams for ϵ_i can be obtained through functional derivatives of the ones entering the expansion of E_0. This is essential to ensure thermodynamic consistency [528]. A complete discussion of this topic is beyond the scope of the present work but relates to the so-called Φ-derivability of a given truncation scheme [529; 530].

6.3 Pairing correlations within a diagrammatic framework

As explained in Sec. 1.1.2, an explicit account of pairing correlations is needed from the outset to achieve an accurate description of finite nuclei. The latter can be achieved in the context of MBPT by anticipating the infrared divergences brought by energy denominators $(\sum \varepsilon_i - \sum \varepsilon_j)^{-1}$ appearing at the level of Eq. (6.7a). It is well known that a Cooper pair instability is signaled by the occurrence of a pole in the T- or G-matrices [531; 532]. As a matter of fact the pole of the G-matrix has the structure of the gap equation.

6.3.1 Conventions

To capture the physics associated with the Cooper pair condensation, it is necessary to redefine the unperturbed vacuum and the perturbation h_1 (Eqs. (6.1a-6.1c)) by considering a new one-body field Ξ such that

$$H = \tilde{h}_0 + \tilde{h}_1 \,, \tag{6.11a}$$

$$\tilde{h}_0 \equiv t + \Gamma + \Xi = \sum_i t_i + \sum_{ij} \Gamma_{ij}\, \hat{a}_i^\dagger\, \hat{a}_j + \sum_{ij} \Xi_{ij}\, \hat{a}_j^\dagger\, \hat{a}_i^\dagger + \sum_{ij} \Xi_{ij}{}^*\, \hat{a}_i\, \hat{a}_j \,, \tag{6.11b}$$

$$\tilde{h}_1 \equiv v - \Gamma - \Xi \,. \tag{6.11c}$$

In order to simplify the diagrammatics, we consider that a BCS-like transformation performed on the eigenbasis of $t + \Gamma$ is sufficient, rather than a full Bogoliubov one. One can then assign BCS-like coefficients u and v to single-particle operators depending on whether they correspond to particle or hole propagators, respectively. Non-zero contractions corresponding to the density matrices ρ, κ and κ^* can be introduced, as seen in Fig. 6.3, where the convention for Goldstone diagrams is such that time is running upward.

6.3.2 Compensation of dangerous diagrams

As mentioned above, energy denominators appearing in the perturbative expansion of the many-body ground-state wave function and energy expressed in terms of normal contractions ρ only may vanish when propagator lines have pair-wise equal and opposite momenta and lie on the Fermi surface. In this case, the singularities at each order are integrable but infinite sums of these diagrams lead to logarithmic divergences. The general idea of Bogoliubov is to properly cancel such poles by only conserving quasiparticle states that are not associated to these singularities [533; 534]. This "compensation of dangerous diagrams" consists of equating to zero the sum of all diagrams leading from the vacuum to an isolated pair of quasiparticles, such that resulting quasiparticle energies are always greater than some minimum value (the "gap").

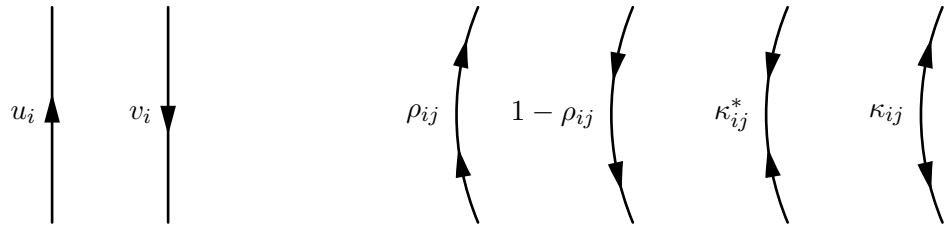

(a) Operators (b) Propagators

Figure 6.3: Propagators and contractions involved in MBPT when pairing correlations are added. In the BCS approximation one has $\rho_{ij} \equiv v_i^2 \delta_{ij}$ and $\kappa_{ij} \equiv u_i v_i \delta_{j\bar{\imath}}$.

The purpose of the Bogoliubov transformation, performed prior to any truncation, is therefore to achieve this compensation as exemplified in Fig. 6.4[2]. At lowest order, this condition leads to the usual BCS gap equation [535]. When pairing correlations are not accounted for, i.e.

- $u_k = 0$ and $v_k = 1$ for $\epsilon_k < \epsilon_F$,
- $u_k = 1$ and $v_k = 0$ for $\epsilon_k > \epsilon_F$,

the condition $\mathcal{H}^{20} = 0$ reduces to the cancelation of one-particle-one-hole diagrams. This corresponds to having $[h_0, \rho] = 0$. One is left with an extra unitary transformation such that the single-particle basis of interest diagonalizes h_0 [122]. Note finally that such a procedure cancels only the most dangerous diagrams, but leaves open the possibility to have further divergences, e.g. due to vacuum-to-four-quasiparticle (0-4qp) diagrams.

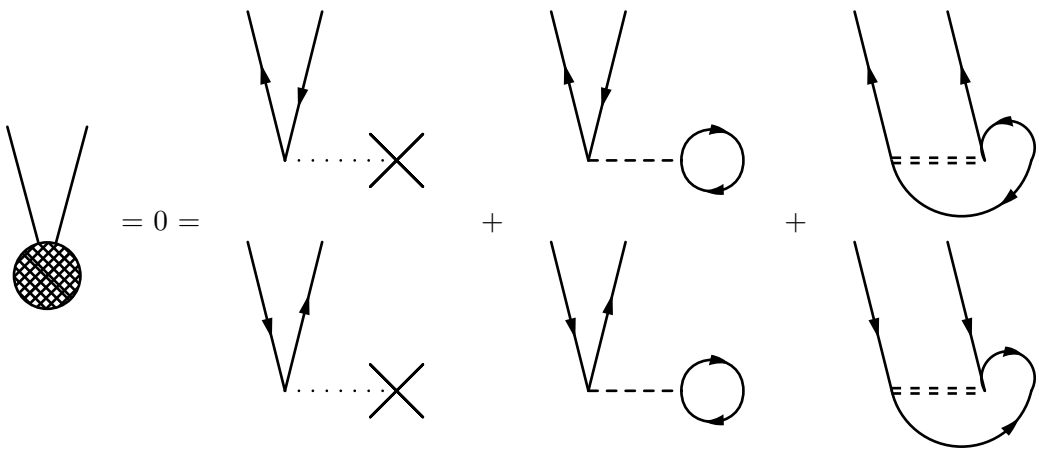

Figure 6.4: Diagrammatic representation of the compensation of dangerous diagrams, that is the cancellation of vacuum-to-two-quasiparticle diagrams. The latter are separated into two categories according to the particle-hole or particle-particle/hole-hole nature of the external lines.

Vacuum-to-pair diagrams appearing in the compensation condition can be separated into two families corresponding to the particle-hole or particle-particle/hole-hole nature of the external lines, as presented in Fig. 6.4. Through consistency requirements, the compensation condition constrains the vertices $\bar{v}^{\mathrm{ph}}$ and $\bar{v}^{\mathrm{pp}}$, defined at the level of the particle-hole (Γ) and particle-particle (Ξ) fields, respectively, to only contain two-particle-irreducible diagrams, as exemplified in Fig. 6.5 at lowest order in two-particle-irreducible vertices. For instance diagrams like

[2] This is equivalent to the condition $\mathcal{H}^{20} = 0$ from Sec. 1.2.5.1.

$\Gamma \equiv$ 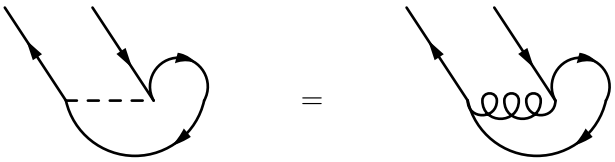 (6.12a)

$\Xi \equiv$ 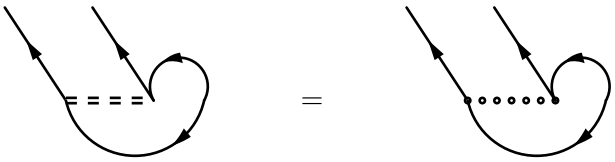 (6.12b)

Figure 6.5: Diagrammatic representation of one-body fields at lowest order in two-particle-irreducible vertices.

come at second order of the expansion. The first one is suppressed with respect to the second one because of an extra uv factor. That is why one can restrict the EDF to be bilinear in κ, while containing more complex ρ-dependencies Such a procedure is justified as long as one is not dealing with the so-called strong coupling regime that appear for instance when going through a BCS-BEC phase transition.

As a result of the allowed topology for the one-body fields stemming from the compensation of dangerous diagrams, one sees that the vertices $\bar{v}^{\mathrm{ph}}$ and $\bar{v}^{\mathrm{pp}}$ have different structures. At lowest order, one obtains the G-matrix in the particle-hole field and the bare vacuum interaction in the particle-particle one. At next orders, one obtains so-called polarization diagrams associated with density, spin and isospin fluctuations.

Chapter 7

Nuclear matter

Abstract: Infinite nuclear matter (INM) properties, e.g. (i) the equation of state (EOS) of symmetric/asymmetric matter and associated saturation properties (saturation density, compressibility, energy per particle...), and (ii) the gap equation, are considered as standard benchmarks for vacuum forces and the many-body method employed. The construction procedure of effective two-body forces from vacuum NNN interactions is discussed. Results obtained for low-momentum interactions show the crucial role played by the NNN interaction in the saturation process [387]. In addition, the perturbative treatment of many-body effects allows a good reproduction of empirical saturation properties of symmetric INM with only a few orders in the expansion. Expressions are given for the EOS associated with a (effective) two-body vertex in the case where the latter is expanded in partial waves.

Contents

7.1 Introduction **186**
7.2 Conventions **187**
7.3 Averaged three-body vacuum interaction **188**
7.3.1 Decomposition of the three-body Hamiltonian 188
7.3.2 Three-body contributions to the effective two-body interaction 189
7.3.3 Expressions for $v^{\overline{\mathrm{NNN}}}$ with low-momentum interactions 191
7.4 Nuclear matter equation of state **191**
7.4.1 Introductory remarks 192
7.4.2 Kinetic energy 192
7.4.3 Correlation energy: generalities 193
7.4.4 Correlation energy: partial wave expansion 194
7.4.5 Correlation energy: MBPT calculations 195
7.4.6 Infinite matter properties 196
7.4.7 Results 197
7.4.7.1 G-matrix calculations 197
7.4.7.2 Nuclear matter equation of state 200
7.5 Pairing gaps **207**
7.6 Quantitative characterization of perturbative behaviors **210**

7.1 Introduction

Infinite nuclear matter is an extrapolation of the conditions in the center of a heavy nucleus. In this idealized homogenous and isotropic medium, that fulfills translational and rotational invariances, the weak isospin breaking of nucleon masses and the Coulomb interaction are neglected (i.e. $m_p = m_n \equiv m$). Although this system is not directly observable, its properties provide an intuitive way to characterize bulk properties of nuclei as well as some parts of the core of a neutron star. Two cases are usually considered, i.e. (i) symmetric nuclear matter (SNM), composed by an equal admixture of protons and neutrons, and (ii) asymmetric nuclear matter where these proportions are not equal and the two Fermi spheres only partly overlap. It is well acknowledged that the equation of state (EOS) of SNM reaches a minimum at a finite density ($k_{\text{sat}} \approx 1.33$ fm^{-1}) corresponding to a negative energy per particle $E/A \approx -16$ MeV called the saturation point, while pure neutron matter (PNM) does not saturate such that its energy per particle always remains positive.

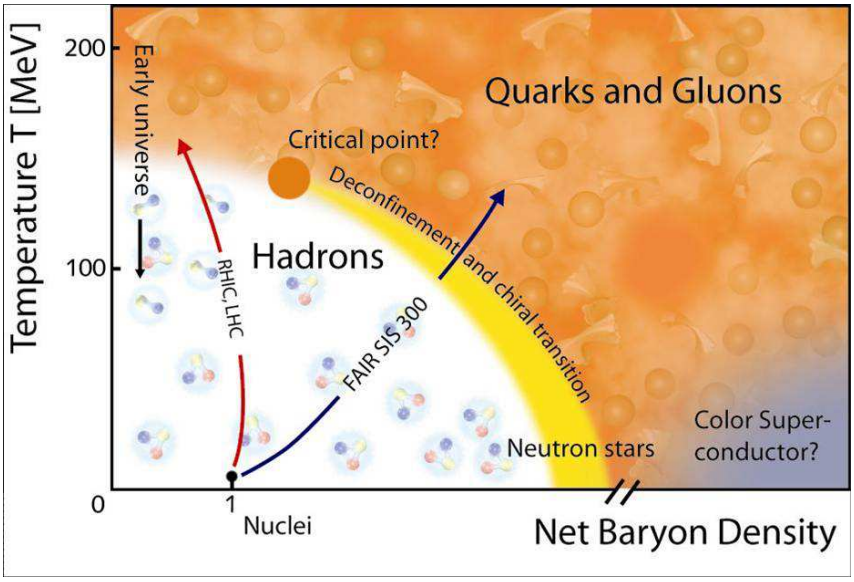

Figure 7.1: Nuclear matter phases. Only the region corresponding to small temperatures and densities up to a few ρ_{sat} can be probed by models based on realistic nuclear forces (from the CBM collaboration [536]).

The nuclear matter phase diagram is complex and several phases are beyond the scope of the present dissertation, e.g. (i) very high temperatures where quark-gluon deconfinement is expected [537; 538], or (ii) very high baryonic densities where color superconductivity might exist [539; 540]. The study of nuclear matter from realistic vacuum interactions at low/zero temperature and (rather) small densities is nevertheless of great interest for low-energy nuclear structure and astrophysics. Indeed

- the saturation point of SNM corresponds to a density ρ_{sat} reached in the center of a nucleus, that is it drives bulk properties of nuclei (regardless of fine structure effects), such as (i) the average energy per nucleon, (ii) the r.m.s. radii that can be extrapolated from the energy per particle and density at saturation, respectively, as well as (iii) the energy of the isoscalar monopolar giant resonance in nuclei which, in a non-trivial way, relates to the INM compressibility at saturation [541]. In that respect, specific nuclear matter properties computed using ab initio techniques based on realistic vacuum interactions are

usually included in the fitting protocol of empirical EDFs [147; 160; 188]. Additionally, the response of infinite nuclear matter to perturbations of various wave lengths allows the isolation of spinodals [542–544] or spurious phase transitions, e.g. spin flips or finite-size isovector instabilities [159]. Finally, isovector properties of nuclear matter at low density are of interest for the study of neutron skins in neutron-rich nuclei [545].

- nuclear matter properties in a broad range of density ($0.1 - 9\rho_{\rm sat}$) are crucial for the understanding of nuclear astrophysics. Indeed, the nuclear matter equation of state drives the behavior of β-equilibrium matter, e.g. in cold neutron stars or in mergers of compact objects such as neutron stars or black holes. The density dependence of the symmetry energy is the key quantity for stability criteria in neutron star matter, and controls the position of crust-core transition and cooling scenarii [546]. Likewise the description of the collapse of type-II supernovæ is partly constrained by the EOS at sub-nuclear densities [365; 547]. Nuclear astrophysics can provide interesting laboratories for low-energy nuclear structure, since the validity of realistic NN forces or empirical EDFs adjusted for finite nuclei, that is densities of the order of $\rho_{\rm sat}$, can be put to the test at two or three times the saturation density [548; 549].

- nuclear matter properties are also of interest for heavy-ion collisions. The latest RIB facilities allow to probe high-density and momentum regions and might put constraints on realistic NN models [550; 551].

7.2 Conventions

In infinite nuclear matter, the system is characterized by its spin, isospin and density composition. In the most general case of spin/isospin polarized matter, one faces four different Fermi momenta $k_F^{\sigma q}$ associated to the four different spin-isospin components. For each species, one can associate to the Fermi momentum $k_F^{\sigma q}$ a density $\rho^{\sigma q}$ and a Fermi energy $E_F^{\sigma q}$ according to

$$\rho^{\sigma q} \equiv \frac{1}{6\pi^2} k_F^{\sigma q\,3}\,, \qquad\qquad E_F^{\sigma q} \equiv \frac{\hbar^2 k_F^{\sigma q\,2}}{2m}\,. \tag{7.1}$$

One can define an overall (scalar-isoscalar) Fermi momentum k_F through

$$k_F \equiv \left[\frac{1}{4}\sum_{\sigma q} k_F^{\sigma q\,3}\right]^{1/3} \equiv \left[\frac{1}{2}\sum_{q} k_F^{q\,3}\right]^{1/3}\,, \tag{7.2}$$

where the spin-averaged Fermi momentum k_F^q has also been introduced. Instead of the densities associated with the four spin/isospin species, one may prefer to use scalar/vector-isoscalar/isovector densities $(\rho_0, \rho_1, \vec{s}_0, \vec{s}_1)$ (Eqs. (1.63a-1.63d)) to characterize the system. The scalar-isoscalar particle density ρ_0 is the only non-zero component in spin-unpolarized symmetric nuclear matter. It reads

$$\rho_0 = \frac{2}{3\,\pi^2}\,k_F^3 \qquad \text{in symmetric matter,} \tag{7.3a}$$

$$\rho_0 = \frac{1}{3\,\pi^2}\,k_F^3 = \frac{1}{6\,\pi^2}\,k_F^{n\,3} \qquad \text{in neutron matter.} \tag{7.3b}$$

Eventually, spin/isospin "polarizations" are sometimes preferred. In such a case, the set of four variables used to characterize the system is

$$\left\{\rho_0, \beta \equiv \frac{\rho_1}{\rho_0}, \vec{\delta}_0 \equiv \frac{\vec{s}_0}{\rho_0}, \vec{\delta}_1 \equiv \frac{\vec{s}_1}{\rho_0}\right\}, \tag{7.4}$$

where the neutron-proton asymmetry is introduced as

$$\beta \equiv \frac{\rho^n - \rho^p}{\rho^n + \rho^p} = \frac{\rho^n - \rho^p}{\rho_0}\,, \tag{7.5}$$

in a way that INM and PNM correspond to $\beta = 0$ and $\beta = 1$, respectively, and that

$$\rho^n = \frac{1+\beta}{2}\,\rho_0\,, \qquad \rho^p = \frac{1-\beta}{2}\,\rho_0\,. \tag{7.6}$$

7.3 Averaged three-body vacuum interaction

While an exact treatment of the three-body interaction in either INM or light nuclei is possible but remains difficult, its approximation in terms of an **effective**, that is density-dependent, two-body vertex already provides results with a good precision [72; 73; 552]. We follow this approach for treating three-nucleon forces. Note that the resulting vertex will be referred to as "vacuum" $\mathrm{NN} + \overline{\mathrm{NNN}}$ interaction although the averaging procedure over the third nucleon implies the presence of an underlying system, that is a Fermi sea, i.e. symmetric infinite nuclear matter in the present case.

7.3.1 Decomposition of the three-body Hamiltonian

The nuclear Hamiltonian in second quantized form, restricted to two- and three-body forces is given as

$$H = \sum_{ij} t_{ij} \hat{a}_i^\dagger\, \hat{a}_j + \frac{1}{2!^2} \sum_{ijkl} \bar{v}^{\mathrm{NN}}_{ijkl}\, \hat{a}_i^\dagger\, \hat{a}_j^\dagger\, \hat{a}_l\, \hat{a}_k + \frac{1}{3!^2} \sum_{ijklmn} \bar{v}^{\mathrm{NNN}}_{ijklmn}\, \hat{a}_i^\dagger\, \hat{a}_j^\dagger\, \hat{a}_k^\dagger\, \hat{a}_n\, \hat{a}_m\, \hat{a}_l + \cdots\,. \tag{7.7}$$

Physically, one hopes to include most of the NNN force effects in the form of density-dependent zero-, one-, and two-body forces obtained by averaging three, two, or one of the ingoing and outgoing single-particle states over the Fermi sea. Mathematically, this is accomplished by writing H in normal-ordered form with respect to that non-interacting Fermi sea.

The normal ordering is performed using Wick's theorem [553] (normal phase) for strings of operators. Let A_i represent either $\hat{a}_i^\dagger$ or $\hat{a}_i$. Wick's theorem states that

$$\begin{aligned} A_i A_j A_k A_l \cdots A_m =& \mathcal{N}(A_i A_j A_k A_l \cdots A_m) \\ &+ \mathcal{N}\Big((\overbracket{A_i A_j} A_k A_l \cdots A_m) + \text{all other single contractions} \Big) \\ &+ \mathcal{N}\Big((\overbracket{A_i A_j} \overbracket{A_k A_l} \cdots A_m) + \text{all other double contractions} \Big) \\ &\vdots \\ &+ \mathcal{N}\Big(\text{all fully contracted terms} \Big)\,, \end{aligned} \tag{7.8}$$

where $\mathcal{N}$ denotes normal-ordering and the contraction is defined by $A_i A_j = \mathcal{N}(A_i A_j) + \overbracket{A_i A_j}$. There are two non-vanishing contractions in the natural basis of the Slater determinant describing the unperturbed Fermi sea, i.e.

$$\overbracket{\hat{a}_i\, \hat{a}_j^\dagger} = \delta_{ij}\, \theta(\epsilon_i - \epsilon_F) = (1 - \rho_{ii})\,, \qquad \overbracket{\hat{a}_i^\dagger\, \hat{a}_j} = \delta_{ij}\, \theta(\epsilon_F - \epsilon_i) = \rho_{ii}\,. \tag{7.9}$$

The many-body Hamiltonian can be then recast into

$$H = \langle H\rangle_0 + \sum_{kp} f_{kp}\,\mathcal{N}(\hat{a}^\dagger_k\,\hat{a}_p) + \frac{1}{2!^2}\sum_{kpqr}\bar{v}^{\mathrm{NN}+\overline{\mathrm{NNN}}}_{kpqr}\,\mathcal{N}(\hat{a}^\dagger_k\,\hat{a}^\dagger_p\,\hat{a}_r\,\hat{a}_q) + \frac{1}{3!^2}\sum_{kpqrst}\bar{v}^{\mathrm{NNN}}_{kpqrst}\,\mathcal{N}(\hat{a}^\dagger_k\,\hat{a}^\dagger_p\,\hat{a}^\dagger_q\,\hat{a}_t\,\hat{a}_s\,\hat{a}_r)\,, \tag{7.10}$$

where the various terms are given by

$$\langle H\rangle_0 = \sum_i t_{ii}\,\rho_{ii} + \frac{1}{2}\sum_{ij}\bar{v}^{\mathrm{NN}}_{ijij}\,\rho_{ii}\,\rho_{jj} + \frac{1}{6}\sum_{ijk}\bar{v}^{\mathrm{NNN}}_{ijkijk}\,\rho_{ii}\,\rho_{jj}\,\rho_{kk}\,, \tag{7.11a}$$

$$f_{ij} \equiv t_{ij} + \sum_k \bar{v}^{\mathrm{NN}}_{ikjk}\,\rho_{kk} + \frac{1}{2}\sum_{kl}\bar{v}^{\mathrm{NNN}}_{iklikl}\,\rho_{kk}\,\rho_{ll}\,, \tag{7.11b}$$

$$\bar{v}^{\mathrm{NN}+\overline{\mathrm{NNN}}}_{kpqr} \equiv \bar{v}^{\mathrm{NN}}_{kpqr} + \frac{1}{4}\sum_i \bar{v}^{\mathrm{NNN}}_{kpiqri}\,\rho_{ii} \equiv \bar{v}^{\mathrm{NN}} + \bar{v}^{\overline{\mathrm{NNN}}}\,. \tag{7.11c}$$

If the above equations are written for an infinite homogenous system, the plane wave single-particle basis is used. From momentum conservation, one can then show that the so-called Fock operator ("f") is diagonal in this representation and provides HF single-particle energies ϵ_i including the three-body force effects.

The previous equations suggest an obvious approximation where the "residual" NNN force involving a normal-ordered product of six creation/annihilation operators is dropped from H. In this case, the bulk of NNN force effects is explicitly included by calculating the NNN contribution to $v^{\mathrm{NN}+\overline{\mathrm{NNN}}}$ (as well as to $\langle H\rangle_0$ and f)[1].

7.3.2 Three-body contributions to the effective two-body interaction

The antisymmetrized effective normal-ordered two-body contribution (to $v^{\mathrm{NN}+\overline{\mathrm{NNN}}}$) from the three-body force in nuclear matter is given from Eq. (7.11c) by

$$\langle\vec{k}_1\,\vec{k}_2|v^{\mathrm{NNN}}\,(1-P_{12})|\vec{k}'_1\,\vec{k}'_2\rangle = \sum_3\langle\vec{k}_1\,\vec{k}_2\,\vec{k}_3|v^{\mathrm{NNN}}\big(1+P_{13}P_{12}+P_{23}P_{12}\big)\big(1-P_{12}\big)|\vec{k}'_1\,\vec{k}'_2\,\vec{k}'_3\rangle\,\rho_{\vec{k}_3\vec{k}_3}\,, \tag{7.13}$$

from which we obtain the unsymmetrized vertex

$$(\vec{k}_1\,\vec{k}_2|v^{\mathrm{NNN}}|\vec{k}'_1\,\vec{k}'_2) = \frac{1}{\mathcal{V}}\delta_{\vec{k}_1+\vec{k}_2,\vec{k}'_1+\vec{k}'_2}(\vec{k}_1\,\vec{k}_2|v^{\mathrm{NNN}}|\vec{k}'_1\,\vec{k}'_2)\,, \tag{7.14a}$$

$$(\vec{k}_1\,\vec{k}_2|v^{\mathrm{NNN}}|\vec{k}'_1\,\vec{k}'_2) = \mathrm{Tr}_3\int\frac{d\vec{k}_3}{(2\pi)^3}(\vec{k}_1\,\vec{k}_2\,\vec{k}_3|v^{\mathrm{NNN}}(1+\Pi)|\vec{k}'_1\,\vec{k}'_2\,\vec{k}_3)\,\rho_{\vec{k}_3\vec{k}_3}\,, \tag{7.14b}$$

where the curved bras/kets remind that the overall delta function has been pulled off, whereas and $\Pi = P_{13}P_{12} + P_{23}P_{12}$.

[1] When plugged into many-body calculations, this translates into performing MBPT calculations with $v^{\mathrm{NN}+\overline{\mathrm{NNN}}}$ replacing v^{NN} everywhere, i.e. by expliciting Eq. (6.10a) at second order in $v^{\mathrm{NN}+\overline{\mathrm{NNN}}}$ such that

$$E_0 = t_0 + \frac{1}{2}\sum_{hh}\rho_{hh}\,\rho_{h'h'}\,\bar{v}^{\mathrm{NN}+\overline{\mathrm{NNN}}}_{hh'hh'} + \frac{1}{4}\sum_{hh'pp'}\rho_{hh}\,\rho_{h'h'}\,(1-\rho_{pp})\,(1-\rho_{p'p'})\,\frac{|\bar{v}^{\mathrm{NN}+\overline{\mathrm{NNN}}}_{hh'pp'}|^2}{f_{hh}+f_{h'h'}-f_{pp}-f_{p'p'}} + \cdots\,. \tag{7.12}$$

However, the evaluation of $\mathrm{Tr}_3\langle v^{\mathrm{NNN}}\Pi\rangle$ is very difficult. First of all, the exchange operators imply that the momentum transfers in $v^{\mathrm{NNN}}(\vec{q}_2,\vec{q}_3)$ are no longer just $\vec{q}_i = \vec{k}_i - \vec{k}'_i$, which translates into very complicated integrals over the Fermi sea. Moreover, spin/isospin structures that result from $\mathrm{Tr}_3\{v^{\mathrm{NNN}}\Pi\}$ create spin-violating operator structures (e.g., $\vec{\sigma}_1 - \vec{\sigma}_2$) that are very complicated to include in standard infinite matter calculations based on decoupled partial waves.

To simplify further the calculations, the standard approximation [73; 554; 555] consists in removing the so-called "double-exchange" terms, that is to keep only

$$(\vec{k}_1\,\vec{k}_2|v^{\overline{\mathrm{NNN}}}|\vec{k}'_1\,\vec{k}'_2) = \mathrm{Tr}_3 \int \frac{d\vec{k}_3}{(2\pi)^3}(\vec{k}_1\,\vec{k}_2\,\vec{k}_3|v^{\mathrm{NNN}}|\vec{k}'_1\,\vec{k}'_2\,\vec{k}_3)\,\rho_{\vec{k}_3\vec{k}_3}\,. \tag{7.15}$$

This approximation is based on the fact that short-range three-body contributions are suppressed by the "wounds" in the pair wave functions resulting from the NN hard core. In our case neglecting double-exchanges is not as unfounded as it seems. For example, at the HF level, one finds that double-exchange terms only contribute about 1/3 of the total three-body contribution.

To summarize, the above procedure amounts to defining the effective $\overline{\mathrm{NNN}}$ contribution from NNN diagrams averaged on the third particle. This provides a two-body density-dependent diagram for the $\mathrm{NN} + \overline{\mathrm{NNN}}$ force in vacuum of the form given in Fig. 7.2, which implicitly contains direct and exchange terms relative to the two outgoing lines. The remaining part of "triples" contributions, that is diagram that cannot be approximated by effective two-body terms, is found to be negligible in benchmark nuclei [73].

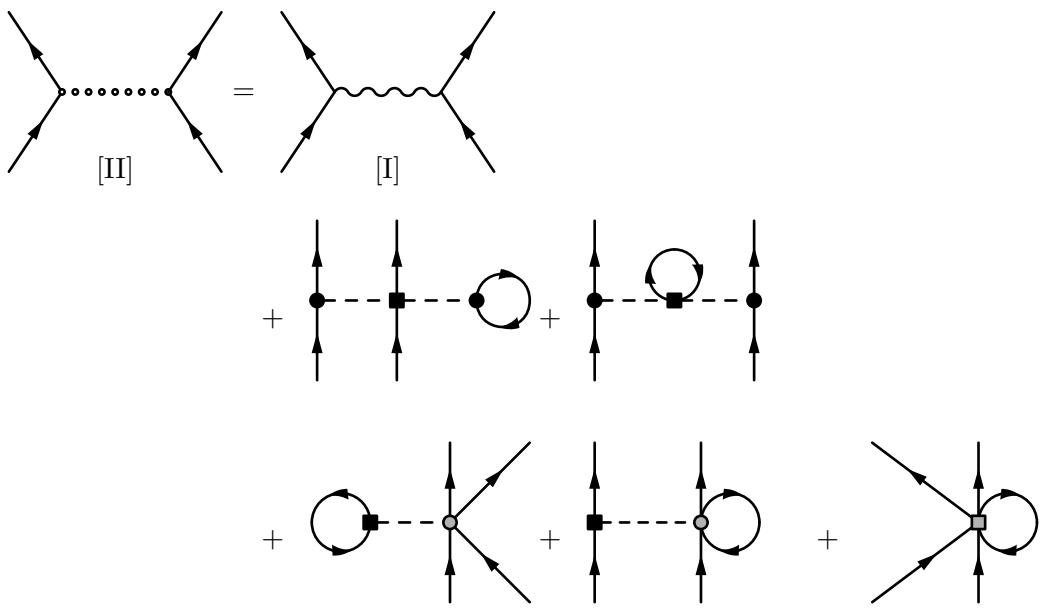

Figure 7.2: Diagrammatic definition of the bare $\mathrm{NN} + \overline{\mathrm{NNN}}$ force from chiral-EFT diagrams at $\mathrm{N^2LO}$, which is assumed to contain both direct and exchange terms.

7.3.3 Expressions for $v^{\overline{\text{NNN}}}$ with low-momentum interactions

The construction of three-body low-momentum interactions involves the use of a (smooth) three-body regulator with an associated momentum cutoff Λ_{NNN} that reads

$$g_{\text{NNN}}|\vec{k}_1\,\vec{k}_2\,\vec{k}_3\rangle = |\vec{k}_1\,\vec{k}_2\,\vec{k}_3\rangle \times \exp\left[-\left(\frac{(\varepsilon_{k_1}+\varepsilon_{k_2}+\varepsilon_{k_3})-E_P}{\Lambda^2_{\text{NNN}}}\right)^{n_S}\right], \tag{7.16}$$

where $\varepsilon_k = \hbar^2k^2/2m$, $E_P = \hbar^2(\vec{k}_1+\vec{k}_2+\vec{k}_3)^2/6m$ and n_S defines the sharpness of the RG cutoff. The NNN regulator can be ignored for HF calculations where $k_F \ll \Lambda_{\text{NNN}}$. In this case the integrals over $\vec{k}_3$ are trivial and one finds for the χ-EFT two-body effective contributions from the vacuum chiral NNN force

$$(\vec{k}_1\,\vec{k}_2|v_E^{\overline{\text{NNN}}}|\vec{k}'_1\,\vec{k}'_2) = \rho\frac{c_E}{f_\pi^4\Lambda_\chi}\,\vec{\tau}_1\cdot\vec{\tau}_2\,, \tag{7.17a}$$

$$(\vec{k}_1\,\vec{k}_2|v_D^{\overline{\text{NNN}}}|\vec{k}'_1\,\vec{k}'_2) = -\rho\frac{g_A}{4f_\pi^2}\frac{c_D}{f_\pi^2\Lambda_\chi}\frac{(\vec{\sigma}_1\cdot\vec{q}_1)(\vec{\sigma}_2\cdot\vec{q}_1)}{q_1^2+m_\pi^2}\vec{\tau}_1\cdot\vec{\tau}_2\,, \tag{7.17b}$$

$$(\vec{k}_1\,\vec{k}_2|v_c^{\overline{\text{NNN}}}|\vec{k}'_1\,\vec{k}'_2) = -\rho\frac{g_A^2}{4f_\pi^2}\frac{(\vec{\sigma}\cdot\vec{q}_1)(\vec{\sigma}_2\cdot\vec{q}_1)}{(\vec{q}_1^{\,2}+m_\pi^2)^2}\vec{\tau}_1\cdot\vec{\tau}_2\left[\frac{4c_1m_\pi^2}{f_\pi^2}+\frac{2c_3}{f_\pi^2}q_1^2\right]. \tag{7.17c}$$

On the other hand, to iterate the effective vertex to higher orders, one needs to properly account for the three-body regulator. In current calculations, its only effect is to replace

$$\int\frac{d\vec{k}_3}{(2\pi)^3}\theta(k_F-|\vec{k}_3|) \longrightarrow \int\frac{d\vec{k}_3}{(2\pi)^3}\theta(k_F-|\vec{k}_3|)\,g_{\text{NNN}}(\vec{k}_1,\vec{k}_2,\vec{k}_3)\,g_{\text{NNN}}(\vec{k}'_1,\vec{k}'_2,\vec{k}_3)\,, \tag{7.18}$$

in the definition of the effective vertex (Eq. (7.15)). This amounts to multiplying the above expressions for $v_c^{\overline{\text{NNN}}}$, $v_D^{\overline{\text{NNN}}}$ and $v_E^{\overline{\text{NNN}}}$, by a correction factor

$$\zeta = \frac{4}{\rho}\int\frac{d\vec{k}_3}{(2\pi)^3}\theta(k_F-|\vec{k}_3|)\,g_{\text{NNN}}(\vec{k}_1,\vec{k}_2,\vec{k}_3)\,g_{\text{NNN}}(\vec{k}'_1,\vec{k}'_2,\vec{k}_3)\,. \tag{7.19}$$

Note that this correction factor has no angular dependence and so does not complicate the partial wave decomposition of $v^{\text{NN}+\overline{\text{NNN}}}$.

7.4 Nuclear matter equation of state

Several methods can be used to evaluate the equation of state of nuclear matter [552; 556]. For instance, the Variational Monte-Carlo (VMC) formalism [557; 558] constructs an approximation of the many-body wave function in nuclear matter by minimizing the average value of the vacuum Hamiltonian in a set of trial functions $|\Psi\rangle$. The latter are obtained from the wave function of the non-interacting free Fermi gas $|\Phi\rangle$ by adding explicitly two-body correlations through a correlation operator, i.e. $|\Psi\rangle = \mathcal{F}\,|\Phi\rangle$ where $\mathcal{F}$ is a product of two-body correlations functions

$$\mathcal{F} = \prod_{i<j} f(r_{ij})\,. \tag{7.20}$$

The variational principle consists then in minimizing the expectation value of the correlated Hamiltonian

$$E = \frac{\langle\Phi|\,\mathcal{F}^\dagger\,H\,\mathcal{F}\,|\Phi\rangle}{\langle\Phi|\,\mathcal{F}^\dagger\,\mathcal{F}\,|\Phi\rangle}\,, \tag{7.21}$$

with respect to the free parameters entering the correlator $\mathcal{F}$, and has been succesfully applied to realistic nucleon-nucleon interactions [559–561]. Another approach briefly in Chap. 6 is to

perform Brueckner calculations at lowest or next order in the hole-line expansion [400; 562; 563]. The nuclear matter equation of state can be computed using the partial wave expansion of the G-matrix expressed in momentum space. One can also mention other methods such as the S-matrix approach [564], self-consistent spectral calculations [565], or the self-consistent Green's functions formalism [566]. Here, we focus on MBPT and Brueckner calculations.

7.4.1 Introductory remarks

The total energy per particle of spin-unpolarized infinite matter calculated via MBPT can be decomposed into an uncorrelated kinetic energy term and a correlation part as

$$\frac{E}{A}(k_F^n, k_F^p) = \frac{E^K}{A}(k_F^n, k_F^p) + \frac{E^V}{A}(k_F^n, k_F^p). \tag{7.22}$$

The kinetic part can be evaluated exactly, while the calculation of the correlation energy at lowest (HF) order using a two-body interaction expanded in partial waves is given below in Sec. 7.4.4. Such a derivation uses a partial wave expansion of the vertex, and thus consists in a converging series. Those formulæ are then adapted to calculations at second order in MBPT or resumming particle-particle ladders to all orders by (i) replacing the vacuum interaction with an effective one, and (ii) incorporating the additional dependencies of the latter on the total momentum $\vec{K}$ and the G-matrix starting energy ω (see below).

The system is put in a box of arbitrary volume $\mathcal{V}$, in which case the transformation from discrete sums to continuous integrals reads

$$\sum_{\vec{k}} \longrightarrow \frac{\mathcal{V}}{(2\pi)^3} \int d\vec{k}\,. \tag{7.23}$$

Obviously dependencies on the volume should disappear in the final expression with the introduction of the total particle number $A = \rho\,\mathcal{V}$.

In the case where the Fermi sea is unique (PNM) or identical for protons and neutrons (SNM), one will note $E(k_F^n, k_F^q) \equiv E(k_F)$. However, keep in mind that, from Eq. (7.2)

- for symmetric matter $k_F = k_F^n = k_F^p$,
- for neutron matter $k_F = 2^{-1/3}\,k_F^n$.

In the following, one assumes that the effect of superfluidity can be neglected for the EOS[(2)] and pairing properties are treated separately by solving the gap equation without any feedback on occupations numbers nor the binding energy.

7.4.2 Kinetic energy

The uncorrelated kinetic energy is immediately

$$E^K(k_F^n, k_F^p) \equiv$$

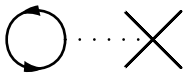

$$= \sum_{\sigma\,q} \frac{\mathcal{V}}{(2\pi)^3} \int_{k<k_F^q} d\vec{k}\,\frac{\hbar^2\,k^2}{2\,m} = \sum_q \frac{3}{5}\frac{\hbar^2\,(k_F^q)^2}{2\,m}\,\rho^q\,\mathcal{V}\,. \tag{7.24}$$

[2]This is incorrect for low-density neutron matter where one approaches a BCS-BEC phase transition.

The kinetic energy per nucleon is thus

$$\frac{E^K}{A}(k_F^n, k_F^p) = \sum_q \frac{3}{5}\frac{\hbar^2\,(k_F^q)^2}{2\,m}\,\frac{\rho^q}{\rho_0}\,. \tag{7.25}$$

Symetric matter

For symmetric matter, one has $\beta = 0$, that is

$$\frac{E^K}{A}(k_F) = \frac{3}{10}\frac{\hbar^2\,k_F^2}{m}\,. \tag{7.26}$$

Neutron matter

For neutron matter, one has $\beta = 1$, that is

$$\frac{E^K}{A}(k_F^n) = \frac{3}{5}\frac{\hbar^2\,k_F^{n\,2}}{2m} = 2^{2/3}\,\frac{3}{5}\frac{\hbar^2\,k_F^2}{2m}\,. \tag{7.27}$$

7.4.3 Correlation energy: generalities

The correlation energy of spin-unpolarized INM reads at the Hartree-Fock level as a double trace over the closed loops of the two-body potential v, i.e.

$E^V(k_F^n, k_F^p) \equiv$

$$= \frac{1}{2}\sum_{ijkl}\langle\, i\,j\,|\,v\,(1-P_{12})\,|\,k\,l\,\rangle\,\rho_{ki}\,\rho_{lj} \tag{7.28a}$$

$$= \frac{1}{2}\sum_{q_1\,q_2}\int_{|\vec{k}_1|<k_F^{q_1}}\int_{|\vec{k}_2|<k_F^{q_2}}\frac{\mathcal{V}\,\mathrm{d}\vec{k}_1}{(2\pi)^3}\,\frac{\mathcal{V}\,\mathrm{d}\vec{k}_2}{(2\pi)^3}\sum_{S\,S_z}\sum_{T\,T_z}\langle\tfrac{1}{2}\tfrac{1}{2}\,q_1 q_2|T\,T_z\rangle^2\,\rho^{q_1}_{\vec{k}_1\vec{k}_1}\,\rho^{q_2}_{\vec{k}_2\vec{k}_2}$$
$$\times\,\langle\,\vec{k}_1\,\vec{k}_2\,S\,S_z\,T\,T_z\,|\,v\,(1-P_{\vec{k}}\,P_\sigma\,P_\tau)\,|\,\vec{k}_1\,\vec{k}_2\,S\,S_z\,T\,T_z\,\rangle\,. \tag{7.28b}$$

The summations over $\vec{k}_i$ run over occupied states $k_i < k_F^{q_i}$, and thus implicitly depend on the associated isospin q_i, which explains why the sum over q_1 and q_2 cannot be resolved yet, contrary to the one over σ_1 and σ_2.

Using the decomposition of the density matrix from Eq. (1.64), it is easy to prove that spin-orbit and tensor components of the two-body interaction will not contribute to the potential energy although they are still present at the vertex level[3]. For instance, given the expression of the tensor operator S_{12} (Eq. (5.3a)), the direct contribution from a pure tensor force $v(r)\,\mathsf{S}_{12}$ can be recast into

$$\langle v\rangle_d = \frac{1}{2}\int \mathrm{d}\vec{r}_1\int \mathrm{d}\vec{r}_2\,v(r)\,\left[\frac{3}{r^2}\big(\vec{r}\cdot\vec{s}_0(\vec{r}_1)\big)\big(\vec{r}\cdot\vec{s}_0(\vec{r}_2)\big) - \vec{s}_0(\vec{r}_1)\cdot\vec{s}_0(\vec{r}_2)\right]\,, \tag{7.29}$$

where only the local vector-isoscalar part of the density matrix is picked out. The exchange term is evaluated using $\mathsf{S}_{12}\,P_{12} = \mathsf{S}_{12}\,P_\tau\,P_{\vec{r}}$, that is

$$\langle v\rangle_e = -\frac{1}{4}\int \mathrm{d}\vec{r}_1\int \mathrm{d}\vec{r}_2\,v(r)\,\left[\frac{3}{r^2}\big(\vec{r}\cdot\vec{s}_0(\vec{r}_1,\vec{r}_2)\big)\big(\vec{r}\cdot\vec{s}_0(\vec{r}_2,\vec{r}_1)\big) - \vec{s}_0(\vec{r}_1,\vec{r}_2)\cdot\vec{s}_0(\vec{r}_2,\vec{r}_1)\right]\,. \tag{7.30}$$

[3] This will be important in the following.

Using the expression of the spin density in INM, i.e.

$$\vec{s}^{\,q}(\vec{r},\vec{r}\,') = \sum_{\sigma} (-1)^{\frac{1}{2}-\sigma} \frac{k_F^{\sigma q\,3}}{2\pi^2} \frac{j_1(k_F^{\sigma q}\,|\vec{r}-\vec{r}\,'|)}{k_F^{\sigma q}\,|\vec{r}-\vec{r}\,'|}\,\vec{e}_z\,, \tag{7.31}$$

one sees that both direct and exchange term vanish in spin-unpolarized INM (where $k_F^{\uparrow q} = k_F^{\downarrow q}$). Likewise, for a pure spin-orbit coupling one gets the same result by decomposing the kinetic density into its scalar-vector/isoscalar-isovector components. Thus one is left only with the pure central terms of a given nucleon-nucleon interaction.

7.4.4 Correlation energy: partial wave expansion

The following derivation allows to evaluate potential energy contributions to nuclear matter equation of state for a generic vertex v. However it will be only valid when the Fermi sea is unique (PNM) or identical for protons and neutrons (INM). In this case one has

$$\begin{aligned} E^V(k_F^n,k_F^p) =& \frac{1}{2}\int_{|\vec{k}_1|<k_F}\int_{|\vec{k}_2|<k_F} \frac{\mathcal{V}\,\mathrm{d}\vec{k}_1}{(2\pi)^3}\frac{\mathcal{V}\,\mathrm{d}\vec{k}_2}{(2\pi)^3} \sum_{S\,S_z}\sum_{T\,T_z} \rho_{\vec{k}_1\vec{k}_1}\,\rho_{\vec{k}_2\vec{k}_2} \\ & \times \langle\, \vec{k}_1\,\vec{k}_2\,S\,S_z\,T\,T_z\,|\,v\,(1-P_{\vec{k}}\,P_\sigma\,P_\tau)\,|\,\vec{k}_1\,\vec{k}_2\,S\,S_z\,T\,T_z\,\rangle \qquad (7.32) \\ =& \frac{(2\pi)^3\,\mathcal{V}}{2}\int \frac{\mathrm{d}\vec{k}}{(2\pi)^3}\frac{\mathrm{d}\vec{K}}{(2\pi)^3}\sum_{S\,S_z}\sum_{T\,T_z}\theta\left(k_F-\left|\vec{K}/2+\vec{k}\right|\right)\,\theta\left(k_F-\left|\vec{K}/2-\vec{k}\right|\right) \\ & \times \langle \vec{k}\,SS_z\,TT_z|v\,(1-P_{\vec{k}}\,P_\sigma\,P_\tau)|\vec{k}\,SS_z\,TT_z\rangle\,. \qquad (7.33) \end{aligned}$$

Now from a partial wave expansion one gets

$$\begin{aligned} E^V(k_F^n,k_F^p) =& \frac{(4\pi)^2\,\mathcal{V}}{2}\int\frac{d\vec{k}}{(2\pi)^3}\int\frac{d\vec{K}}{(2\pi)^3}\,\theta\left(k_F-\left|\vec{K}/2+\vec{k}\right|\right)\,\theta\left(k_F-\left|\vec{K}/2-\vec{k}\right|\right) \\ & \times \sum_{\substack{S\,S_z\\T\,T_z\\L\,L_z\\L'\,L'_z\\J\,J_z}} Y_L^{L_z}(\hat{k})\,Y_{L'}^{L'_z\,*}(\hat{k})\,C^{L'\,S\,J}_{L'_z\,S_z\,J_z}\,C^{L\,S\,J}_{L_z\,S_z\,J_z}\,\left(1-(-1)^{L+S+T}\right)\,v_{LL'}^{JSS_zTT_z}(k,k)\,. \end{aligned} \tag{7.34}$$

After some manipulations (see Appendix D.4), the final result can be explicited for SNM and PNM.

Symmetric matter

One finds for symmetric matter $E^V(k_F,k_F)\equiv E^V(k_F)$, where

$$E^V(k_F) = (4\pi)^2\,\rho\,\mathcal{V}\int_0^{k_F}\frac{k^2\,dk}{(2\pi)^3}\sum_{\substack{L\,S\,J\\T\,T_z}}\left(1-(-1)^{L+S+T}\right)[J]v_{LL'}^{JSTT_z}(k,k)\left(1-\frac{3}{2}\frac{k}{k_F}+\frac{1}{2}\left[\frac{k}{k_F}\right]^3\right)\,, \tag{7.35}$$

where one recalls that $[J]\equiv J+1$. Thus, assuming charge-independence of the potential and summing over T_z[4]

$$\frac{E^V}{A}(k_F) = \frac{4}{\pi}\int_0^{k_F} k^2\,dk\,{\sum_{L\,S\,J\,T}}'\,[J][T]\,v_L^{JST}(k,k)\left(1-\frac{3}{2}\frac{k}{k_F}+\frac{1}{2}\left[\frac{k}{k_F}\right]^3\right)\,, \tag{7.36}$$

[4]This implies that one assumes that the vacuum interaction is charge-independent. In practical calculations, one takes usually $T_z=0$ for CIB forces.

where $\sum'$ denotes that the sum runs only on odd values of $L+S+T$.

Neutron matter

For neutron matter one has equivalently

$$\frac{E^V}{A}(k_F^n,0) \equiv \frac{E^V}{A}(k_F^n) = \frac{48}{\pi}\int_0^{k_F^n} k^2\,dk \sum_{L\,S\,J}{}' [J]\, v_L^{JS1}(k,k)\left(1-\frac{3}{2}\frac{k}{k_F^n}+\frac{1}{2}\left[\frac{k}{k_F^n}\right]^3\right). \tag{7.37}$$

7.4.5 Correlation energy: MBPT calculations

To compute the EOS including the averaged three-nucleon force or the effect of particle-particle ladders, identical formulæ may be applied by replacing the vacuum NN force with the corresponding vertex computed in INM. However, the additional dependencies of the effective vertices must be properly handled.

Using $v^{\mathrm{NN}+\overline{\mathrm{NNN}}}$ at the HF level, the vertex simply carries a dependency on the Fermi level stemming from the average procedure on the third nucleon in INM. Thus Eqs. (7.36,7.37) can be applied directly while the three-body contribution is reevaluated for each density bin.

One can also carry out full Brueckner-Hartree-Fock calculations starting from $v^{\mathrm{NN}+\overline{\mathrm{NNN}}}$, before investigating perturbative approximations at finite orders in particle-particle ladders. The G-matrix calculated in INM in a plane wave basis carries dependencies on the total momentum $\vec{K}$ and on the starting energy ω. It satisfies the self-consistent Bethe-Goldstone equation (Eq. (6.7a))

$$\begin{aligned}\langle\vec{k}\,'|G^{TTz}(\vec{K},\omega)|\vec{k}\rangle = \langle\vec{k}\,'|v^{\mathrm{NN}+\overline{\mathrm{NNN}}}|\vec{k}\rangle + \int\frac{\mathrm{d}\vec{k}\,''}{(2\pi)^3}\langle\vec{k}\,'|v^{\mathrm{NN}+\overline{\mathrm{NNN}}}|\vec{k}\,''\rangle \\ \times\frac{Q^{TT_z}(\vec{K},\vec{k}\,'')}{\omega-\left[\epsilon^q_{\vec{K}/2+\vec{k}\,''}+\epsilon^{q'}_{\vec{K}/2-\vec{k}\,''}\right]+i\,\delta}\langle\vec{k}\,''|G^{TT_z}(\vec{K},\omega)|\vec{k}\rangle\,,\end{aligned} \tag{7.38}$$

where (i) a $\pm i\,\delta$ regularization scheme is used to avoid poles when $\omega \le \epsilon^q_{\vec{K}/2+\vec{k}\,''}+\epsilon^{q'}_{\vec{K}/2-\vec{k}\,''}$, (ii) an isospin dependence must be made explicit when the proton and neutron Fermi seas are different, which disappears for symmetric matter, and (iii) superfluidity is neglected, i.e.

$$\rho^q_{\vec{k}\,\vec{k}} \equiv \Theta(k_F^q-k)\,, \qquad \left(1-\rho^q_{\vec{k}\,\vec{k}}\right) \equiv \Theta(k-k_F^q)\,. \tag{7.39}$$

For all calculations displayed in the present document, single-particle energies are computed in the Hartree-Fock approximation, i.e.

$$\epsilon^q_k(k_f^n,k_F^p) = \frac{\hbar^2\,k^2}{2\,m_q}+\frac{1}{2\pi^2}\sum_{LSJT\,q'}[J]\int_0^{k_F^q}\mathrm{d}k'\,v_L^{JSTT_z}(k,k')\,, \tag{7.40}$$

where $T_z = q+q'$.

A convenient way to solve Eq. (7.38) consists in treating first the Pauli blocking operator (Eq. (6.7a))

$$Q^{TT_z}(\vec{K},\vec{k}) \equiv \left[1-\rho^q_{(\vec{K}/2+\vec{k})(\vec{K}/2+\vec{k})}\right]\left[1-\rho^{q'}_{(\vec{K}/2-\vec{k})(\vec{K}/2-\vec{k})}\right]\,, \tag{7.41}$$

through an angular averaging procedure over $\vec{K}$ [562; 567; 568], which leads in symmetric infinite matter to

$$\tilde{Q}(K,k) \equiv \begin{cases} 0 & \text{for} \quad k \leq \sqrt{k_F^2 - K^2}\,, \\ 1 & \text{for} \quad k_F + K \leq k\,, \\ \dfrac{K^2 + k^2 - k_F^2}{2\,k\,K} & \text{for} \quad k_F + K > k > \sqrt{k_F^2 - K^2}\,. \end{cases} \tag{7.42}$$

The averaging procedure gives a very good approximation, for instance, for the effect of J-coupling on the binding energies [569], and a treatment of the full angular dependency of the Pauli operator is found to be negligible for the scope of this study [429].

Then, the starting energy ω is taken on-shell at the level of Eq. (7.33), that is

$$\omega = \epsilon^{q}_{\vec{K}/2+\vec{k}} + \epsilon^{q'}_{\vec{K}/2-\vec{k}}\,, \tag{7.43}$$

such that the energy denominator of Eq. (7.38) can be separated in hole-hole- and particle-particle contributions, i.e.

$$\varepsilon^{\mathrm{pp}}(\vec{K},\vec{k}\,'') \equiv \epsilon_{\vec{K}/2+\vec{k}\,''} + \epsilon_{\vec{K}/2-\vec{k}\,''}\,, \qquad \varepsilon^{\mathrm{hh}}(\vec{K},\vec{k}\,) \equiv \epsilon_{\vec{K}/2+\vec{k}} + \epsilon_{\vec{K}/2-\vec{k}}\,. \tag{7.44}$$

The latter can be averaged over the relative angle between the total and relative momenta, i.e.

$$\tilde{\varepsilon}^{\mathrm{pp}}(K,k'') = \frac{1}{2}\int \mathrm{d}\cos(\theta)\frac{\varepsilon^{\mathrm{pp}}(\vec{K},\vec{k}\,'')\,Q(\vec{K},\vec{k}\,'')}{\tilde{Q}(K,k'')} \qquad \theta = \hat{K}\cdot\hat{k}\,''\,, \tag{7.45a}$$

$$\tilde{\varepsilon}^{\mathrm{hh}}(K,k) = \frac{1}{2}\int \mathrm{d}\cos(\theta)\frac{\varepsilon^{\mathrm{hh}}(\vec{K},\vec{k}\,)\,H(\vec{K},\vec{k}\,)}{\tilde{H}(K,k)} \qquad \theta = \hat{K}\cdot\hat{k}\,, \tag{7.45b}$$

where $H(\vec{K},\vec{k}\,)$ is the exact two-hole projector and $\tilde{H}(K,k)$ its angular-averaged value, defined in analogy with the Pauli blocking operator.

Given such a procedure, the intermediate two-body propagator entering the Goldstone equation is simplified in such a way that a partial wave decomposition of the G-matrix in symmetric matter can be done into $G^{JSTT_z}_{LL'}(k,k';K,\omega=\tilde{\varepsilon}^{\mathrm{hh}})$. The coupling between partial waves that is carried out at the level of the G-matrix computation, before the EOS is evaluated using only L-diagonal matrix elements, allows to include indirectly the tensor interaction.

Matrix elements of the effective interaction still carry a dependence on the magnitude of the total impulsion K. The latter can be handled by two different approaches, i.e.

- taking an average value of $K = \sqrt{\frac{6}{5}}\,k_F$, such that the integration over the hole-hole phase space $\theta\left(k_F - \left|\vec{K}/2+\vec{k}\right|\right)\,\theta\left(k_F - \left|\vec{K}/2-\vec{k}\right|\right)$ remains identical and Eqs. (7.36,7.37) can be directly applied,
- computing exactly the remaining integral over $K \in [0, 2k_F]$ at the level of Eq. (7.34).

We will use the second approach in the following, given that an accurate treatment of the center-of-mass (c.o.m.) matters for the EOS at the 1 MeV level [429].

7.4.6 Infinite matter properties

From the isospin-symmetric and asymmetric matter equations of state, several quantities of interest can be defined. Empirical values for these quantities have been determined using different aproaches, and are summarized in TAB. {7.1}.

- the SNM saturation point characterized by the density $\rho_{\rm sat}$ (or Fermi momentum $k_F^{\rm sat}$) and energy per particle $E_{\rm sat}/A$. $\rho_{\rm sat}$ can be evaluated from charge distributions in heavy nuclei including Coulomb and surface corrections [570; 571], whereas the saturation energy per particle $E_{\rm sat}/A$ (bulk energy a_V) and symmetry energy a_τ can be evaluated from liquid drop formulæ adjusted on experimental masses [572–576],
- the bulk compressibility K_∞ which characterizes the response of symmetric nuclear matter against compression around $\rho = \rho_{\rm sat}$, provided the saturation point exists, i.e.

$$K_\infty \equiv 9\,\rho_{\rm sat}^2\,\frac{\partial^2\,E/A}{\partial\rho^2}\bigg|_{\substack{\rho=\rho_{\rm sat}\\ \beta=0}} = k_F^{\rm sat\,2}\,\frac{\partial^2\,E/A}{\partial k_F^2}\bigg|_{\substack{k_F=k_F^{\rm sat}\\ \beta=0}}\,. \tag{7.46}$$

  K_∞ can be extracted from Gogny EDF calculations[332] or microscopic calculations of the giant isoscalar monopole resonance [541],
- the symmetry energy a_τ which characterizes the response of symmetric matter in the presence of a fluctuation of the isospin composition, that is

$$a_\tau \equiv \frac{1}{2}\,\frac{\partial^2\,E/A}{\partial\beta^2}\bigg|_{\substack{\rho=\rho_{\rm sat}\\ \beta=0}}\,. \tag{7.47}$$

  a_τ is also evaluated from liquid drop formulæ [572–576],
- the effective mass $m^*(k)$ defined as the momentum-dependent mass corresponding to single-particle energies dressed by the nuclear interaction, i.e.[5]

$$\frac{m_q^*(k,k_F^n,k_F^p)}{m_q} \equiv \left[1+\frac{m_q}{k}\,\frac{{\rm d}\epsilon^q(p,k_F^n,k_F^p)}{{\rm d}p}\bigg|_{p=k}\right]^{-1}\,. \tag{7.49}$$

  The effective mass is obtained in finite nuclei from nucleus-nucleon scattering using an optical potential [577], or from isoscalar giant quadrupole resonance studies.

$\rho_{\rm sat}$ [fm^{-3}]	0.17± 0.02
$E_{\rm sat}/A$ [MeV]	−16.0 ± 1.0
a_τ [MeV]	30.0 ± 2.0
K_∞ [MeV]	215.0 ±15.0
$(m^*/m)_s$	0.70± 0.05

Table 7.1: Empirical values for infinite nuclear matter properties (see text).

[5] From this point one can make an additional effective mass approximation consisting in a parabolic approximation of the dressed single-particle energies around the Fermi level, that is

$$\epsilon_k^q \approx \frac{\hbar^2\,k^2}{2\,m^*(k_F^q)} + \epsilon_0^q\,. \tag{7.48}$$

7.4.7 Results

Part of the results presented in this section come from unpublished work [387], whereas other calculations and analysis useful for later are originally produced within the frame of this work through modifications of the tools provided by S. K. Bogner.

7.4.7.1 G-matrix calculations

The matrix elements of the vacuum NN and NN + $\overline{\text{NNN}}$ interactions are compared to those of the in-medium nuclear interaction at second order in MBPT or including particle-particle ladders to all orders in Figs. (7.3,7.4) for the $^1\text{S}_0$ and $^3\text{S}_1$-$^3\text{D}_1$ channels and at different densities. Using the perturbative $V_{\text{low}\,k}$ as the starting vacuum interaction, the rapid convergence of the G-matrix series is observed at the level of matrix elements and suggests that MBPT calculations with $V_{\text{low}\,k}$ are almost converged at second order in particle-particle ladders. This convergence is very rapid in the singlet channel and matrix elements of NN and (averaged) NNN forces are already very close to those of the in-medium G-matrix for $k_F = 1.33$ fm^{-1}. The latter is not observed at $k_F = 0.9$ fm^{-1} where at least the third order in particle-particle ladders is needed. Since MBPT calculations are close to the results obtained with $v^{\text{NN}+\overline{\text{NNN}}}$, which are intrinsically K-independent, one sees that the K-dependence of the second order MBPT and the full G-matrix remains small. On the other hand, the same level of convergence is reached in the triplet channel only when second order diagrams are included in the effective vertex. This proves that the convergence of matrix elements, in addition to the one of the equation of state must be properly checked when working at the vertex level (see Sec. 8.2) and that different channels might require different MBPT orders. The K-dependence is more significant in the $^3\text{S}_1$ channel, while matrix elements of $v^{\text{NN}+\overline{\text{NNN}}}$ are (i) almost independent of K, and (ii) very close to the G-matrix.

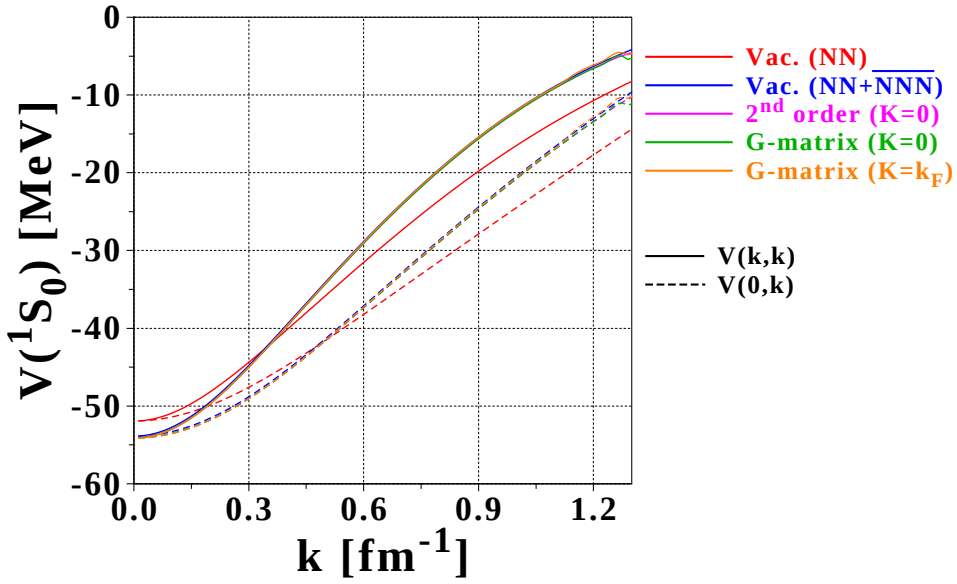

(a) Density $k_F = 1.33$ fm^{-1}

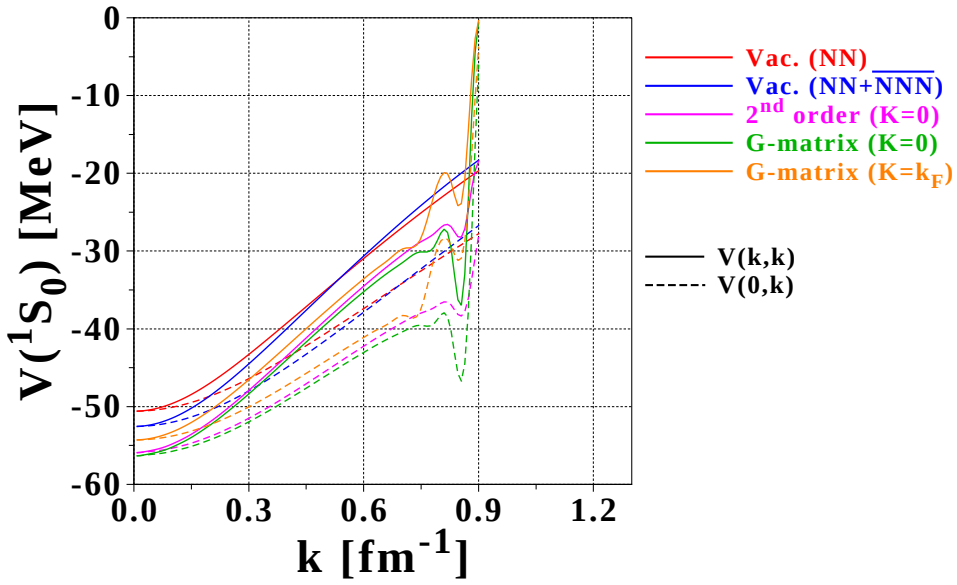

(b) Density $k_F = 0.9$ fm^{-1}

Figure 7.3: Matrix elements of the (effective) two-body vertices at various levels of MBPT in the $^1\mathrm{S}_0$ channel, that is the vacuum $V_{\mathrm{low}\,k}$ computed at $\Lambda = 2.1$ fm^{-1} from N^{3}LO, $V_{\mathrm{low}\,k}$ complemented by the averaged three-body force, the deduced second-order vertex and the fully on-shell G-matrix. Three-body averaging and MBPT calculations are performed in symmetric nuclear matter for two different densities, and only matrix elements relevant for the INM EOS calculations up to the Fermi level are computed. Note that numerical wiggles around k_F are irrelevant for the nuclear matter EOS since they are smeared out by the form factor $\left(1 - \frac{3}{2}\frac{k}{k_F} + \frac{1}{2}\left[\frac{k}{k_F}\right]^3\right)$ in Eq. (7.36). When the full c.o.m. dependence is treated such oscillations also are suppressed around k_F.

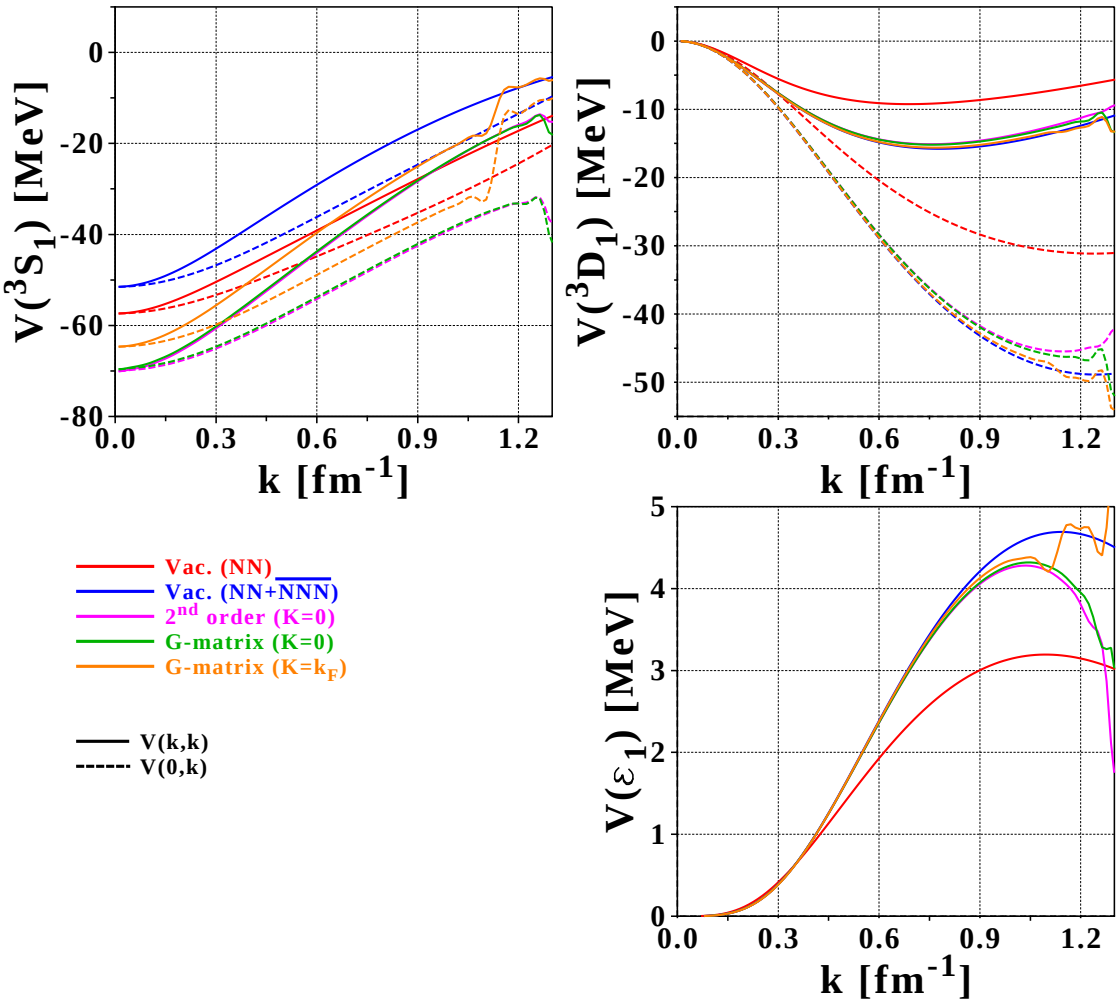

Figure 7.4: Same as in FIG. 7.3 for the $^3S_1$-$^3D_1$ channel at $k_F = 1.33$ fm^{-1}.

7.4.7.2 Nuclear matter equation of state

When using only bare NN forces at the Hartree-Fock level, the nuclear matter equation of state is far from any satisfactory results. Indeed, as shown in FIG. 7.5 for different values of the RG cutoff Λ, SNM equation of state does not even saturate at the Hartree-Fock level when omitting three-body forces [12–15; 578]. Still, low-momentum interactions bind INM at the HF level, in opposition to standard nucleon-nucleon models possessing hard-core repulsion. When the averaged three-nucleon interaction is added, the saturation is obtained, but is far from (i) the empirical point, and (ii) results from calculations performed using VMC or BBG methods.

The EOS can then be computed at higher orders in MBPT. While particle-particle ladders are non-perturbative for standard NN forces characterized by large intrinsic resolution scales, e.g. Argonne V18 [387], the ladder series is rapidly converging with $V_{\text{low}\,k}$, since

- non-perturbative behaviors caused by the hard core and tensor couplings have been suppressed. Indeed, Weinberg eigenvalues associated to the short-range repulsion correspond to perturbative regimes of the Born series when the RG cutoff Λ is lowered enough [505], as discussed in SEC. 5.3.5.
- in-medium effects also drive positive Weinberg eigenvalues corresponding to virtual or bound states into the perturbative regime as a result of Pauli blocking effects [387].

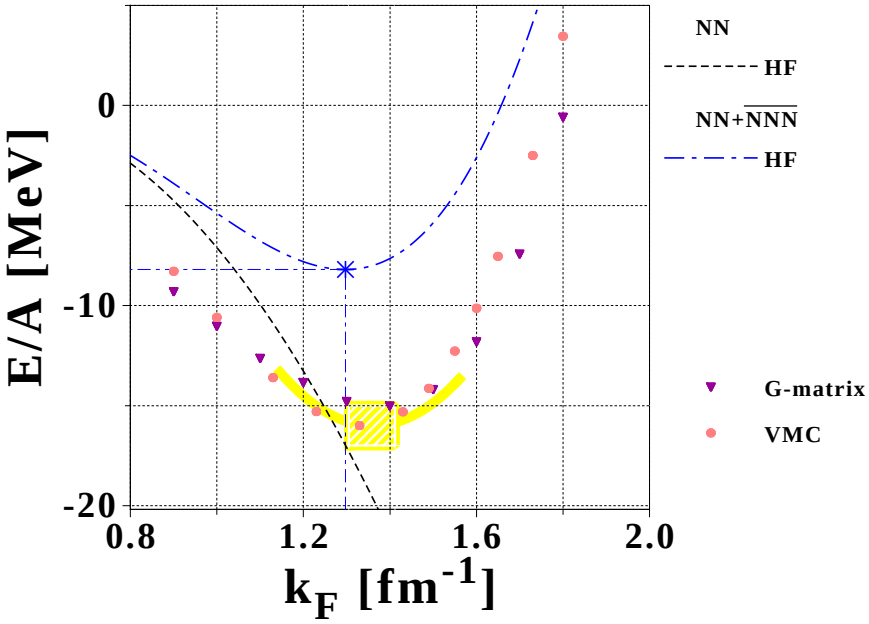

(a) $\Lambda = 2.0$ fm^{-1}

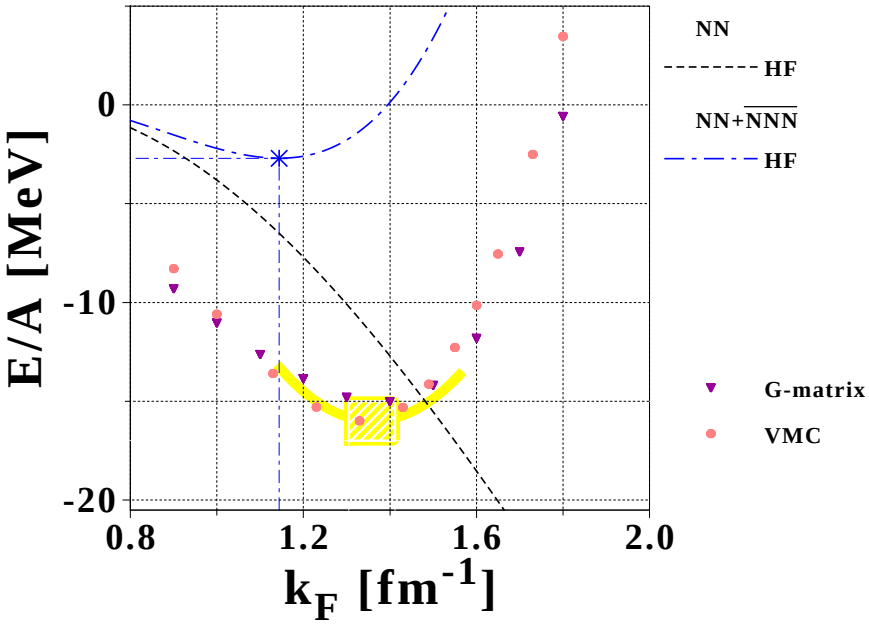

(b) $\Lambda = 2.8$ fm^{-1}

Figure 7.5: Symmetric nuclear matter equation of state computed at the HF level using $V_{\text{low}\,k}$ from N^{3}LO for two RG cutoffs Λ plus a complementary $\overline{\text{NNN}}$ interaction. The three-body bare interaction coming from chiral perturbation theory is refitted at each Λ. The empirical region for the saturation point and the empirical EOS are represented in yellow. Ab initio results from variational Monte-Carlo [559] and Bethe-Brueckner-Goldstone [563] (BBG) calculations with realistic NN (AV14) and NNN (Urbana) forces are presented as filled symbols.

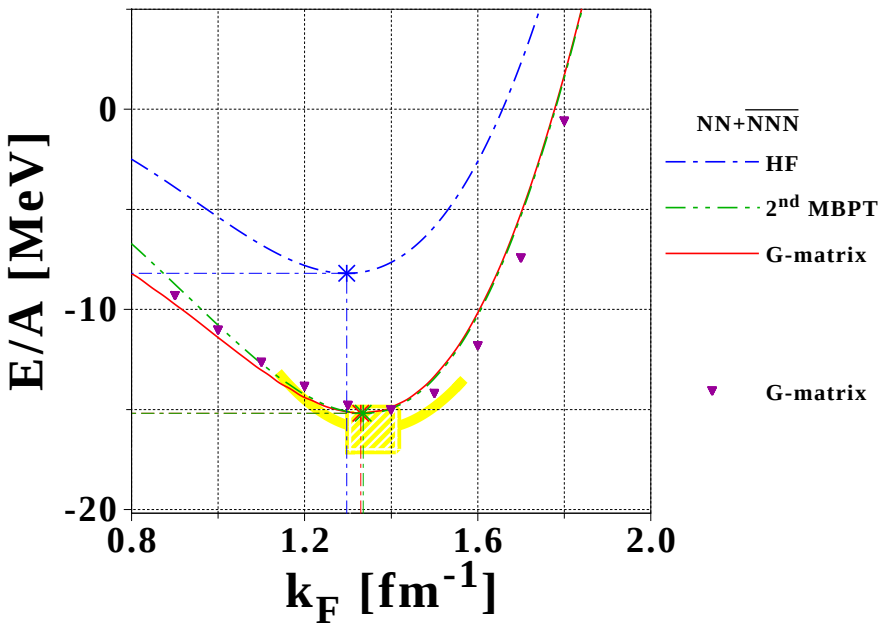

(a) $\Lambda = 2.0$ fm^{-1}

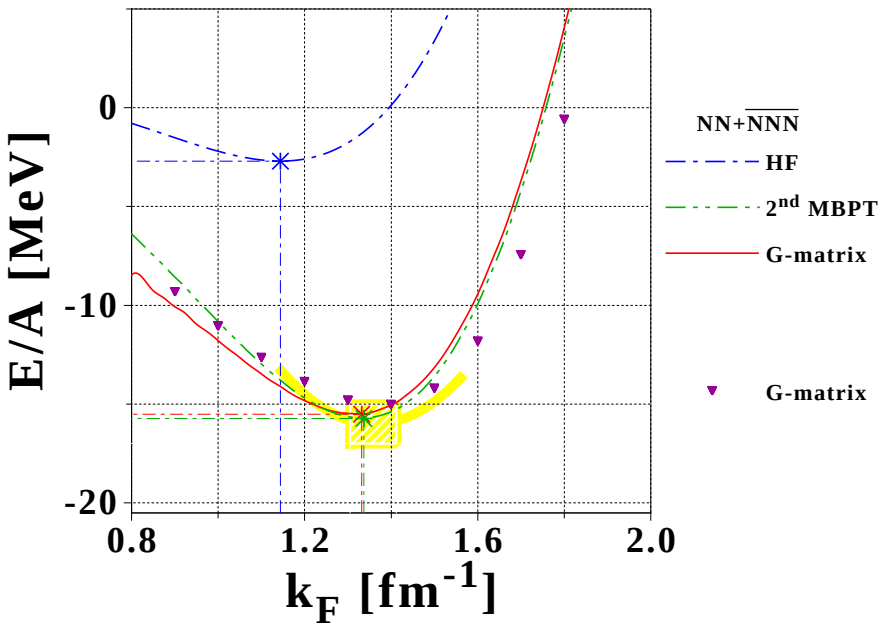

(b) $\Lambda = 2.8$ fm^{-1}

Figure 7.6: Symmetric nuclear matter equation of state computed at different levels of many-body complexity. Conventions and ingredients given for Fig. 7.5 still hold.

The symmetric nuclear matter equations of state corresponding to the different orders of interest are presented in Fig. 7.6 for two values of the RG cutoff Λ. While HF calculations with the vacuum NN + $\overline{\text{NNN}}$ force saturated with non-satisfactory properties, adding the second order in MBPT drives the saturation point in perfect agreement with empirical estimates, as indicted in Tab. {7.2}. The compressibility found by these calculations are smaller than empirical values extracted from EDf calculations using empirical functionals. In addition, calculations are essentially converged at second order, as seen from the comparison with G-matrix calculations,

		$k_F^{\rm sat}$ [fm^{-1}]	$\rho_{\rm sat}$ [fm^{-3}]	$E_{\rm sat}/A$ [MeV]	K_∞ [MeV]
$\Lambda = 2.0$ fm^{-1}	HF	1.297	0.147	−8.20	156.7
	2nd order	1.335	0.161	−15.19	203.0
	G-matrix	1.330	0.159	−15.17	190.1
$\Lambda = 2.4$ fm^{-1}	HF	1.216	0.122	−5.01	114.9
	2nd order	1.321	0.156	−15.33	211.6
	G-matrix	1.311	0.152	−15.20	189.8
$\Lambda = 2.8$ fm^{-1}	HF	1.144	0.101	−2.70	81.1
	2nd order	1.337	0.161	−15.70	235.7
	G-matrix	1.331	0.160	−15.48	215.2

Table 7.2: Saturation properties of symmetric infinite nuclear matter at various levels of many-body complexity and for three different RG cutoffs Λ for the vacuum NN $V_{{\rm low}\,k}$ plus averaged three-body force. The three-body force is always included in the calculations.

except slight differences in the low-density regime. This might indicate that bulk properties of finite nuclei calculated from low-momentum NN + $\overline{\rm NNN}$ interactions could be restricted to the second order in MBPT. In all cases, calculations with the full G-matrix tend to slightly decrease the energy per particle and compressibility at saturation. Meanwhile, almost no Λ-dependence of the results is seen for the EOS at second order and beyond. The saturation density remains almost unchanged while the energy per particle and the compressibility increase slightly with Λ. This constitutes an important result since a Λ-independence of the many-body result indicates that the corresponding calculation is likely to be converged.

Same conclusions hold for the potential energy separated into (S,T) channels, presented in Fig. 7.7, where one notes an excellent convergence of the calculations at second order in MBPT. Having such detailed information from ab initio calculations is of importance as empirical EDFs reproducing SNM/PNM equations of state display large discrepancies when separated into (S,T) channels [159; 188]. The strongest impact of the three-body force is seen in spin-triplet channels. Indeed, when the EOS is computed at the HF level with $v^{\rm NN+\overline{NNN}}$ instead of $v^{\rm NN}$ the correlation energy (i) changes sign in the $S=1,T=1$ channel, (ii) is largely reduced at large k_F in the $S=1,T=0$ channel, and (iii) the correlation energy is enhanced in the $S=0,T=0$ channel in the presence of three-body forces. Secondly, the effect of MBPT is negligible in spin-singlet channels, while it is most important in the $S=1,T=0$ channel. We note that in-medium effects always increase the binding energy in (S,T) channels. Meanwhile, the effect of the RG cutoff Λ is mostly seen in the $S=1,T=0$ channel where the three-body contribution is largely reduced at the HF level when Λ increase, while the final EOS including MBPT remains almost Λ-independent. Likewise, while the present results obtained using low-momentum interactions provide an EOS similar to BBG calculations performed using more conventional nuclear forces, discrepancies are observed in (S,T) channels, in particular for isospin-triplet ones, where differences of ± 10 MeV that compensate each other in the total EOS are observed in Fig. 7.7. This would call for (i) studying the variations of the EOS when starting from different NN models, and (ii) improving the single-particle energies that enter MBPT calculation at large Λ where the HF approximations becomes unappropriate.

Finally, Fig. 7.8 presents the further decomposition of the correlation energy into partial waves. One sees that in the singlet ^{1}S$_0$ channel MBPT only slightly corrects the lowest order,

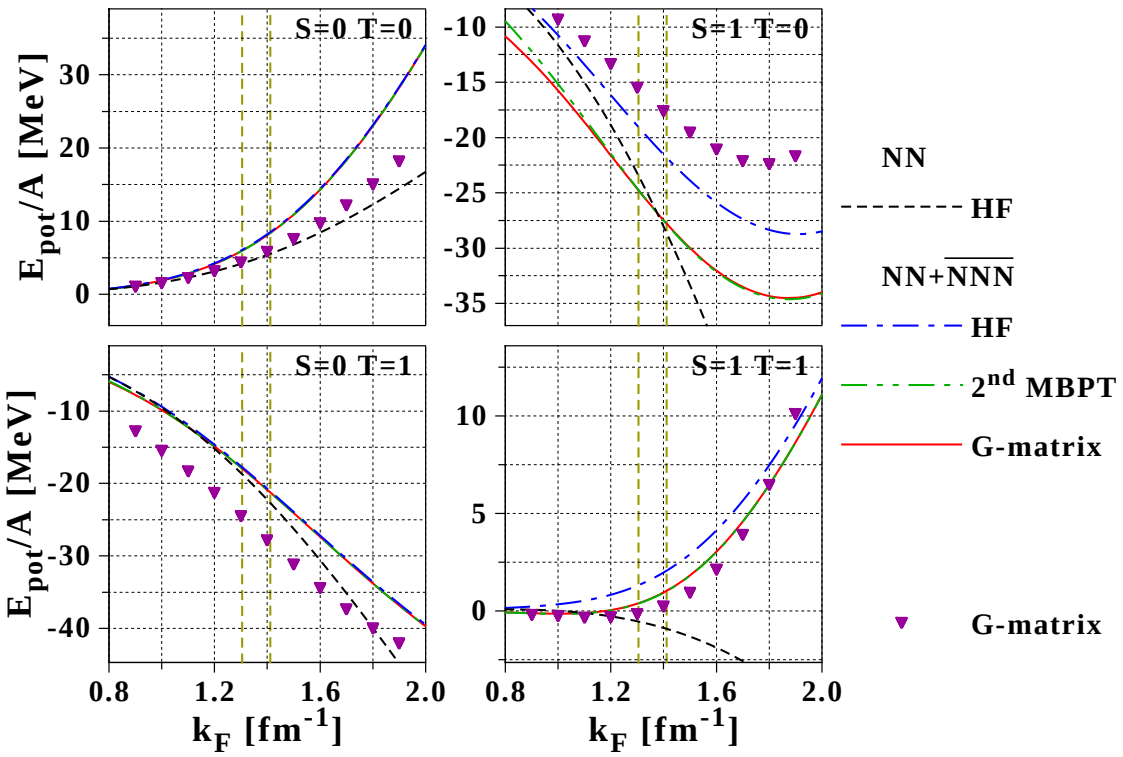

(a) $\Lambda = 2.0$ fm^{-1}

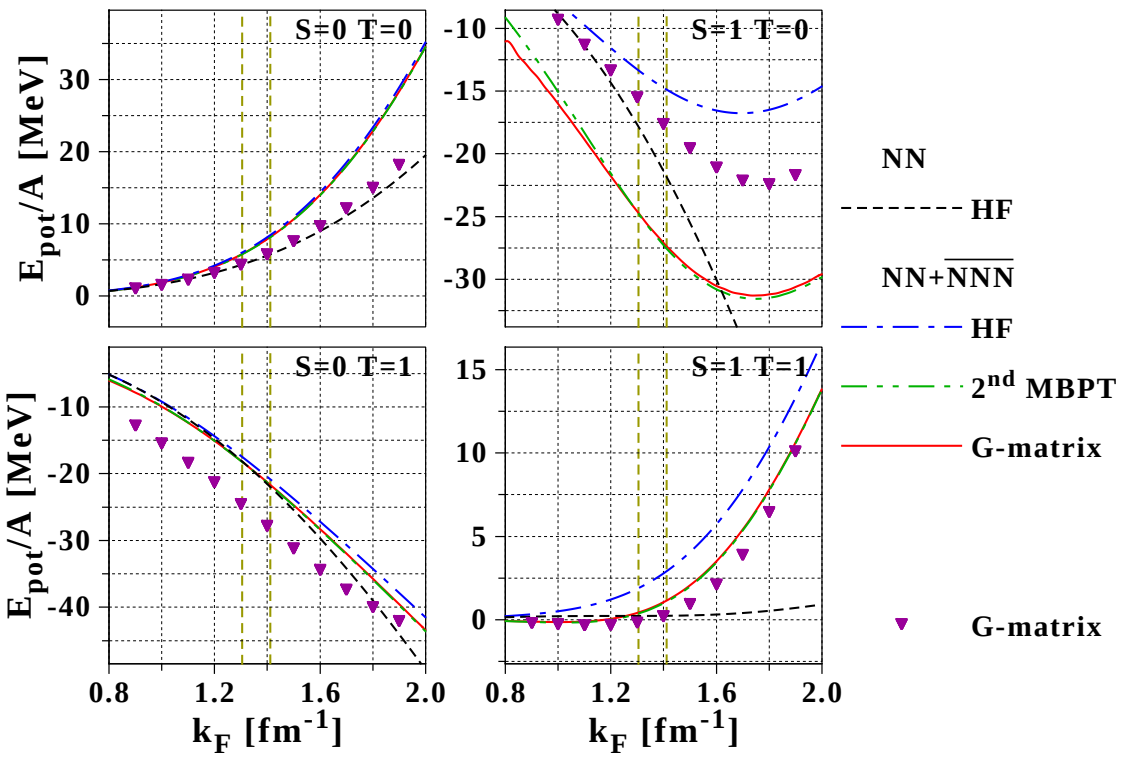

(b) $\Lambda = 2.8$ fm^{-1}

Figure 7.7: Decomposition of the symmetric nuclear matter equation of state from Fig. 7.6a into (S, T) channels. The range of admitted empirical values for the saturation density is represented by vertical yellow lines.

while in the triplet $^3S_1$-$^3D_1$ channel at least the first order in particle-particle ladders is needed (see also Fig. 7.9), as was already noticed at the level of matrix elements. Generally speaking, MBPT effects are significant in coupled channels/at small densities, whereas the (average) three-body force that comes from N^{2}LO is good enough to provide an accurate correlation energy in all other partial waves/at large k_F. Furthermore, one notices that the effect of the (averaged) NNN force in each individual p wave enhances the effect of the vacuum two-body force. This suggests that, as far as the binding energy is concerned, the averaged three-body forces acts as an effective spin-orbit interaction [579]. This corroborates what has already been observed on the level of spectroscopy. Meanwhile, $v^{\overline{\mathrm{NNN}}}$ counteracts v^{NN} in the $^3S_1$ channel. Nevertheless, while some approximations remain, such as the treatment of double-exchange terms in the averaged three-body force, the computation of nuclear matter using many-body perturbation theory is possible with low-momentum vacuum forces and provides very satisfactory results.

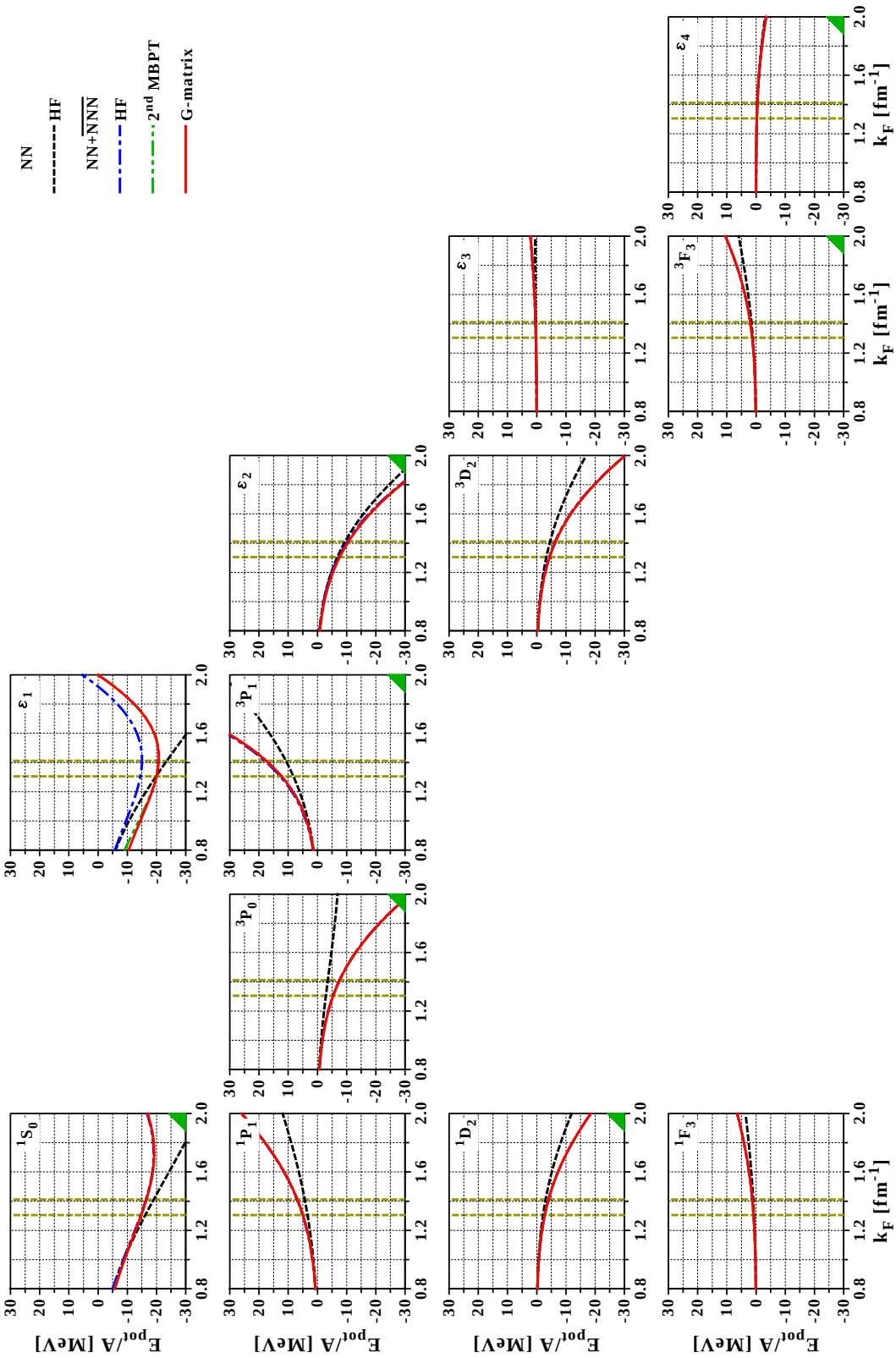

Figure 7.8: Decomposition of the symmetric nuclear matter equation of state from FIG. 7.6a into partial waves for a RG cutoff $\Lambda = 2.0$ fm^{-1}. $S = 0$ channels are put on the left-hand side, while $T = 1$ can be identified by the green triangles. For coupled channels, the summed contribution from $L = J \pm 1$ partial waves is represented. The range of accepted empirical values for the saturation density is represented by vertical yellow lines.

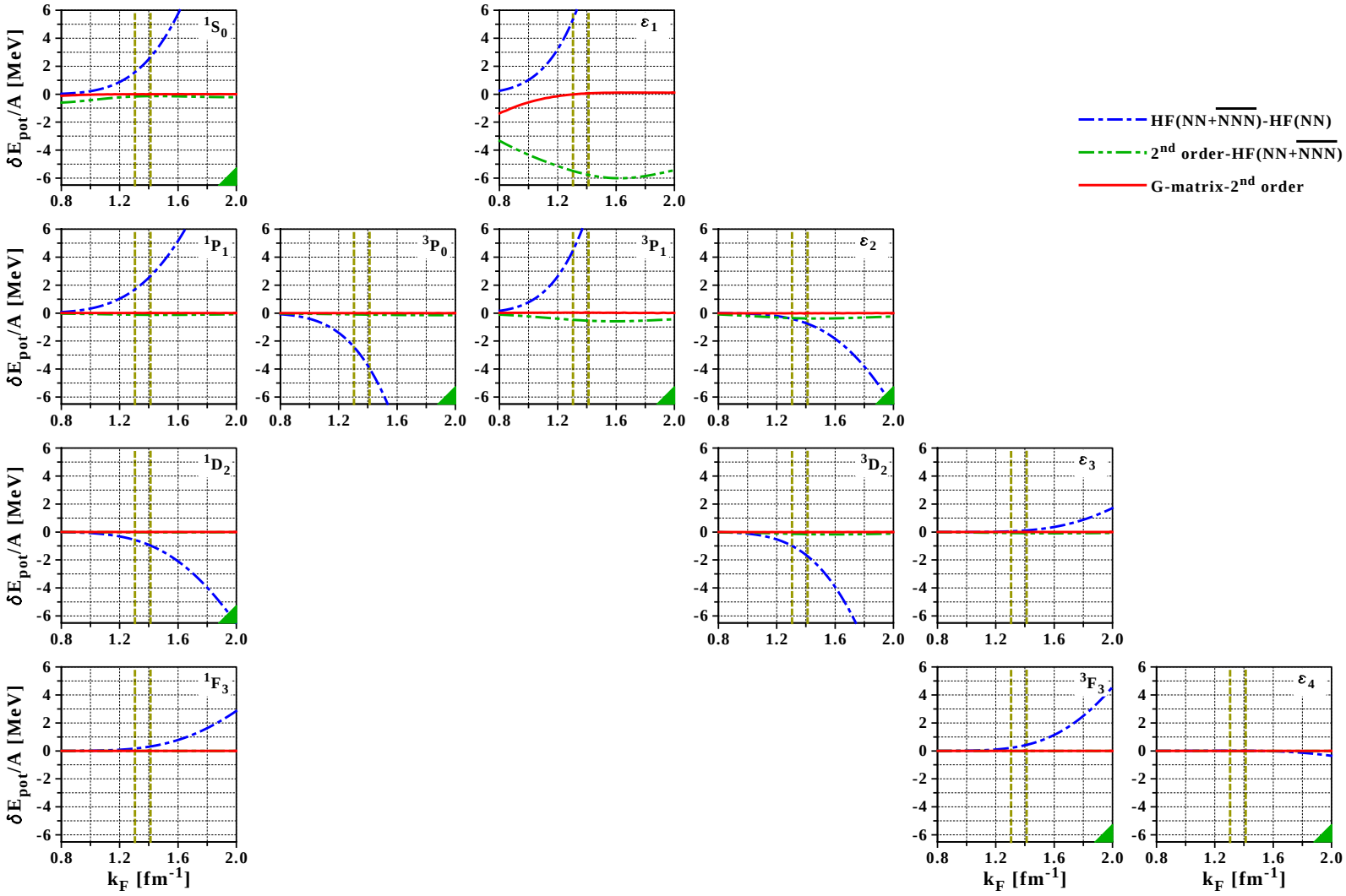

Figure 7.9: Convergence of MBPT calculations of symmetric nuclear matter equation of state decomposed into partial waves for a RG cutoff $\Lambda = 2.0$ fm^{-1}. Conventions from FIG. 7.8 still hold.

7.5 Pairing gaps

We are now interested in computing the pairing gap in the $S = 0, T = 1$ channel[6] in infinite nuclear matter [581]. Given that (i) there is a renormalization of the pairing gap in infinite matter due to higher-order effects associated with couplings to density, spin and isospin fluctuations [251; 252], and that (ii) such a renormalization might be different in finite nuclei and infinite nuclear matter [253–256], we restrict ourselves to studying pairing gaps at lowest order in $v^{\rm NN}$. In addition, recent calculations seem to indicate that gaps provided in semi-magic nuclei at lowest order in the vacuum NN interaction are already close to experimental data [582].

The gap equation [581] reads in INM at lowest order in the vacuum two-body interaction (see Fig. 6.5)

$$\Delta^q(\vec{k}\,, k_F^q) = -\int \frac{{\rm d}\vec{k}\,'}{(2\pi)^3}\, v^{\rm NN}(\vec{k}, \vec{k}\,')\, \frac{\Delta^q(\vec{k}\,', k_F^q)}{2\, E^q_{\vec{k}\,'}}\,, \tag{7.50}$$

where $E^q_{\vec{k}}$ is the quasiparticle energy associated with momentum $\vec{k}$

$$E^q_{\vec{k}} = \sqrt{(\epsilon^q_{\vec{k}} - \mu^q)^2 + \Delta^q(\vec{k}\,, k_F^q)^2}\,, \tag{7.51}$$

$\epsilon^q_{\vec{k}}$ being single-particle energies, and μ^q the chemical potential for isospin q. Eq. (7.50) can be expanded using a partial wave decomposition of the gap (Eq. (5.20)) into [110]

$$\Delta^q(\vec{k}\,, k_F^q) \equiv \sum_{L\,L_z} \sqrt{\frac{4\pi}{[L]}}\, Y_L^{L_z}(\hat{k})\, \Delta^q_{LL_z}(k, k_F^q)\,. \tag{7.52}$$

Performing an angular averaging of the gap, i.e.

$$\Delta^{q\,2}(\vec{k}\,, k_F^q) \equiv \frac{1}{4\pi}\int {\rm d}\hat{k} \sum_{L\,L_z} \frac{4\pi}{[L]}\, Y_L^{L_z\,*}(\hat{k})\, Y_L^{L_z}(\hat{k})\, \Delta^q_{LL_z}{}^2(k, k_F^q) \equiv \sum_L \Delta^q_L{}^2(k, k_F^q)\,, \tag{7.53}$$

Eq. (7.50) becomes in each uncoupled partial wave

$$\Delta^q_L(k, k_F^q) = -\int \frac{{\rm d}k'}{2\pi^2}\, v_L^{JST}(k, k')\, \frac{\Delta^q_L(k', k_F^q)}{2\sqrt{\left(\epsilon^q_{\vec{k}\,'} - \mu^q\right)^2 + \sum_L \Delta^q_L{}^2(k', k_F^q)}}\,. \tag{7.54}$$

Finally, one assumes that the coupling between partial waves coming from the denominator in Eq. (7.54) can be neglected. Corresponding equations can be obtained for coupled partial waves, such as the ^{3}P$_2$-^{3}F$_2$ channels, which are of interest for the study of neutron stars [116]. We only consider here the dominant component of pairing for finite nuclei, that is the ^{1}S$_0$ channel, for which the gap equation reads

$$\Delta^q_0(k, k_F^q) \equiv \Delta^q(k, k_F^q) = -\int \frac{k'^2\, {\rm d}k'}{(2\pi)^2}\, v_0^{010}(k, k')\, \frac{\Delta^q(k', k_F^q)}{\sqrt{\left(\epsilon^q_{\vec{k}\,'} - \mu^q\right)^2 + \Delta^q{}^2(k', k_F^q)}}\,. \tag{7.55}$$

[6] Only pairing between particles of same isospin is considered. Indeed, there is little empirical evidence for static neutron-proton pair correlations in nuclei [580], although $T = 0$ pairing might appear for $N = Z$ nuclei and explain partly the Wigner energy.

Eq. (7.55) must be solved self-consistently together with the associated equation for the chemical potential μ[7]

$$\rho_0 = 2\,\rho_q = 4\int \frac{\mathrm{d}\vec{k}}{(2\pi)^3}\,\frac{1}{2}\left[1-\frac{\epsilon_{\vec{k}}-\mu}{E_{\vec{k}}}\right] = \int \frac{k^2\,\mathrm{d}k}{\pi^2}\left[1-\frac{\epsilon_k-\mu}{E_k}\right], \qquad \text{in symmetric matter,} \tag{7.56a}$$

$$\rho_0 = \rho_n = 2\int \frac{\mathrm{d}\vec{k}}{(2\pi)^3}\,\frac{1}{2}\left[1-\frac{\epsilon^n_{\vec{k}}-\mu^n}{E^n_{\vec{k}}}\right] = \int \frac{k^2\,\mathrm{d}k}{2\,\pi^2}\left[1-\frac{\epsilon^n_k-\mu^n}{E^n_k}\right], \qquad \text{in neutron matter}\,. \tag{7.56b}$$

In most cases we compute gaps using free kinetic single-particle energies $\epsilon^q_k = \hbar^2\,k^2/2m$[8]. For standard interactions, the chemical potential μ can be well approximated by the Fermi energy of the free Fermi gas $\hbar^2\,k_F^2/2m$. However in extreme situations, this is not true any more [43], and the set of coupled self-consistent equations (Eqs. (7.55,7.56a)) has to be solved. Since the pairing gap carries a momentum dependence, these equations are solved using the damping method, i.e. for a given Fermi momentum k_F

1. start from an initial guess for $\Delta^q_0(k,k^q_F)$, noted $\Delta^{q\,[0]}_0(k,k^q_F)$ (typically a constant gap equal to the Fermi energy),
2. compute from Eqs. (7.56a,7.56b) the Fermi momentum (dichotomy),
3. compute the iterated gap

$$\Delta^{q\,[1/2]}_0(k,k^q_F) = -\int \frac{k'^2\,\mathrm{d}k'}{(2\pi)^2}\,v^{010}_0(k,k')\,\frac{\Delta^{q\,[0]}_0(k',k^q_F)}{\sqrt{\left(\frac{\hbar^2\,k'^2}{2\,m_q}-\mu^q\right)^2+\Delta^{q\,[0]\,2}_0(k',k^q_F)}}\,, \tag{7.57}$$

4. if the difference between $\Delta^{q\,[0]}_0(k,k^q_F)$ and $\Delta^{q\,[1/2]}_0(k,k^q_F)$ is small, then exit, else define a new starting point

$$\Delta^{q\,[1]}_0(k,k^q_F) = \kappa\,\Delta^{q\,[0]}_0(k,k^q_F) + (1-\kappa)\,\Delta^{q\,[1/2]}_0(k,k^q_F)\,, \tag{7.58}$$

   where κ is a damping factor (typ. $\kappa \approx 0.25$), and start again from step 2.

The latter method allows a good convergence for standard nuclear interactions, while more involved approaches are sometimes necessary [583]. The final gap function $\Delta^q(k,k^q_F)$ has both a density (k^q_F) and a momentum (k) dependence, but one often refers to the quantity $\Delta^q(k^q_F,k^q_F)$ as the pairing gap.

Results for DDDI pairing functionals have already been presented in Sec. 1.4. The neutron gap calculated using $V_{\mathrm{low}\,k}$ derived from AV18 at different RG cutoffs Λ is presented in Fig. 7.10. The pairing gap computed at lowest order in v^{NN} and using free kinetic energies is independent on the RG cutoff [584], which reflects the strong connection between such a gap and the scattering phase shifts [585] that are equally well reproduced for all Λ. Using dressed particles, in-medium effects affect the magnitude of the pairing gap and the Λ-independence might be lost [586–590]. An example of such an influence is presented in Fig. 7.11, where neutron pairing gaps in pure neutron matter are computed using both free kinetic and Hartree-Fock single-particle energies [591]. In-medium effects in the self-energy at lowest order reduce the pairing gap significantly. At the same level, the reduction would be even larger in symmetric nuclear matter. One observes though that the cutoff dependence remains negligible.

[7] A factor 4 comes from spin and isospin multiplicity in symmetric matter.

[8] In this approximation, when the gap is given as a function of k^q_F, it is not affected by the isospin composition of the nuclear matter.

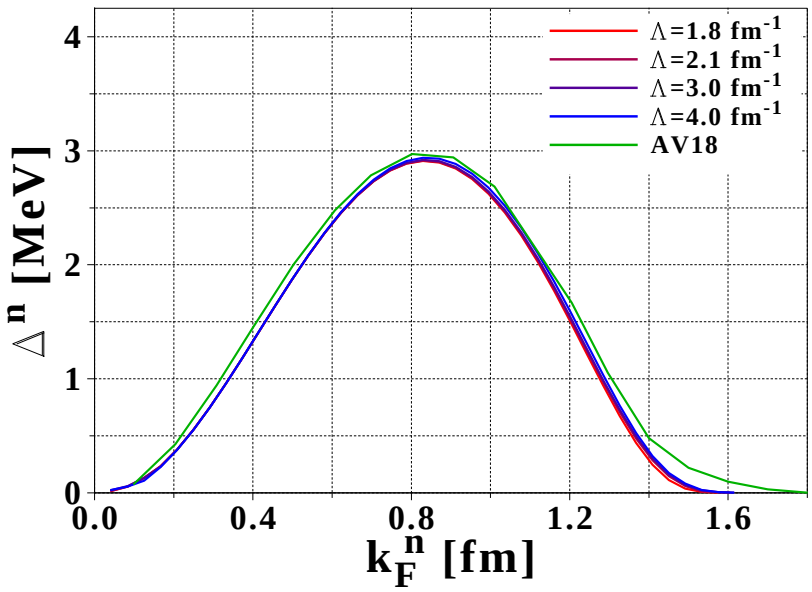

Figure 7.10: Neutron gap obtained from $V_{\mathrm{low}\,k}$ starting from Argonne V18 and for different RG cutoffs Λ. Free kinetic energies are used as single-particle energies.

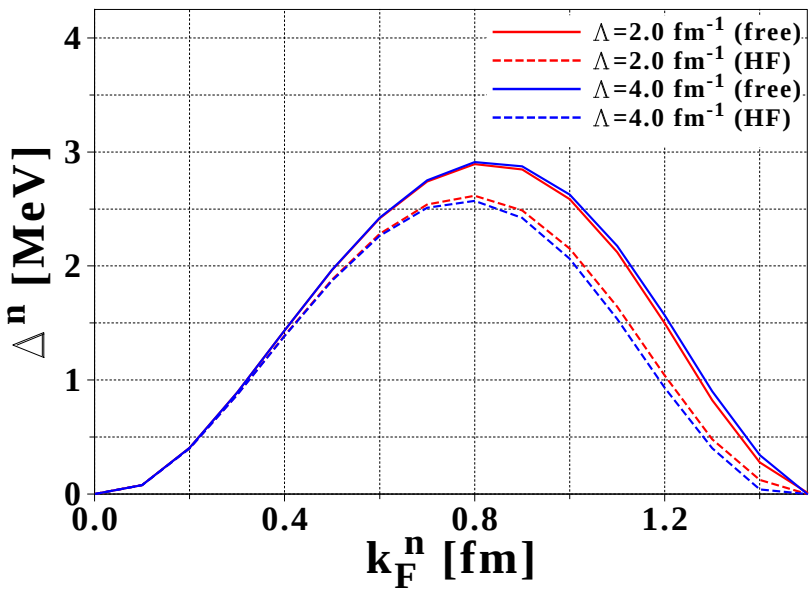

Figure 7.11: Neutron gap calculated in neutorn matter from $V_{\mathrm{low}\,k}$ using free and HF self-energies.

7.6 Quantitative characterization of perturbative behaviors

In the following we attempt to define safeguards that will be used in the construction of analytical non-empirical effective vertices later on, in order to ensure that the fitted interactions are essentially perturbative, and can be treated with reasonable basis sets in SR- and MR-EDF calculations (e.g. (Q)RPA calculations). Indeed, it is crucial for further calculations that the perturbative behavior identified in Sec. 7.4.7 at $\Lambda \approx 2.0$ fm^{-1} is maintained. As a guideline, we will try to quantitatively relate convergence properties of the Born/ladder series of the vacuum interaction to properties of its matrix elements, in particular the possible existence of large positive off-diagonal matrix elements in momentum space, which usually translate into hard-core-like non-perturbative behaviors. In that respect, simple rules can be exhibited from the study of Weinberg eigenvalues. We will use vacuum Weinberg eigenvalues, i.e. defined with respect to the Born series without Pauli blocking effects. This might be questionable as the purpose is to provide guidelines for finite nuclei/nuclear matter where a treatment of in-medium effects is crucial. In fact, it has been proven that the effect of Pauli blocking is to drive all η_ν towards zero as the medium density increases [505]. Thus, using vacuum eigenvalues corresponds to a worst case scenario. Likewise, we focus on the $^1\mathrm{S}_0$ channel, since it is the most unfavorable channel regarding Weinberg eigenvalues ($\eta^1 > \eta^3$ in most cases).

The general idea is to relate (i) the "perturbativeness" of a given potential, evaluated through the cutoff-dependent Weinberg eigenvalue η^1_-, (ii) the presence of positive off-diagonal matrix elements, i.e. the quantity

$$V^{\mathrm{od}}_{\mathrm{max}}(\Lambda) = \max_k [v^{\mathrm{NN}}(0,k;\Lambda)]\,, \tag{7.59}$$

and (iii) the "momentum coupling range" k_{max}, that is the maximum relative momentum with which a two-body state at zero relative momentum is non-negligibly coupled through v^{NN}. We propose several definitions for the latter coupling range

1. $k^{[1]}_{\mathrm{max}} \equiv \Lambda$ as a zeroth-order approximation,
2. $v^{\mathrm{NN}}(0, k^{[2]}_{\mathrm{max}}; \Lambda) = 1$ MeV, where one assumes that matrix elements lower than (arbitrary) 1 MeV will not contribute to INM or finite nuclei binding energies. $k^{[2]}_{\mathrm{max}}$ will not be evaluated if off-diagonal matrix elements never exceed 1 MeV,
3. $v^{\mathrm{NN}}(0, k^{[3]}_{\mathrm{max}}; \Lambda) = V^{\mathrm{od}}_{\mathrm{max}}(\Lambda)$,
4. $v^{\mathrm{NN}}(0, k^{[4]}_{\mathrm{max}}; \Lambda) = V^{\mathrm{od}}_{\mathrm{max}}(\Lambda)/100$, which corresponds to the most defavorable case,

To be of practical use, the coupling ranges $k^{[i]}_{\mathrm{max}}$ will be converted into

1. the equivalent energy cut $E^{[i]}_{\mathrm{max}}$ in the single-particle continuum which would be necessary to consider in spherical HFB calculations to include all matrix elements with relative momenta $k < k^{[i]}_{\mathrm{max}}$. $E^{[i]}_{\mathrm{max}}$ is thus approximated by a scattering energy with respect to an "average" potential whose depth is approximatively taken as $E_0 \approx 55$ MeV[9], i.e.

$$E^{[i]}_{\mathrm{max}} \approx \frac{\hbar^2\, {k^{[i]}_{\mathrm{max}}}^2}{2\,m} - E_0\,. \tag{7.60}$$

2. the equivalent number $N^{[i]}_{\mathrm{max}}$ of shells necessary to consider for spherical calculations performed in a harmonic oscillator basis. The latter is evaluated through

$$N^{[i]}_{\mathrm{max}} \approx \frac{1}{\hbar\Omega}\,\frac{\hbar^2\, {k^{[i]}_{\mathrm{max}}}^2}{2\,m} - 3/2\,. \tag{7.61}$$

[9] This corresponds to the usual depth of Woods-Saxon potential used in macroscopic models.

An average value for the oscillator parameter $\hbar\Omega \approx 10$ MeV is considered, as a typical value used for Gogny-EDF calculations.

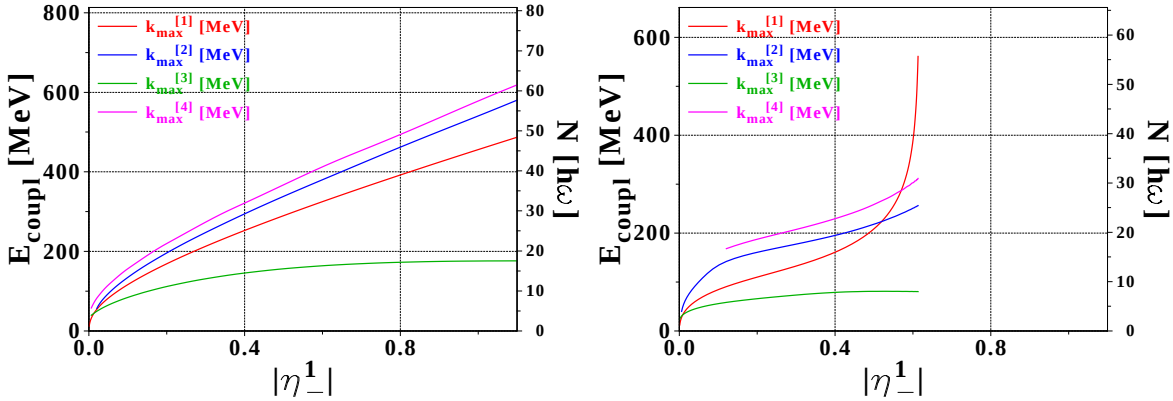

(a) $V_{\text{low}\,k}$ from AV18 (b) $V_{\text{low}\,k}$ from N^{3}LO

Figure 7.12: Correlation between different coupling ranges $E_{\max}^{[i]}/N_{\max}^{[i]}$ (see text) and the lowest negative Weinberg eingenvalue η_-^1 in the ^{1}S$_0$ channel for different values of the RG cutoff Λ.

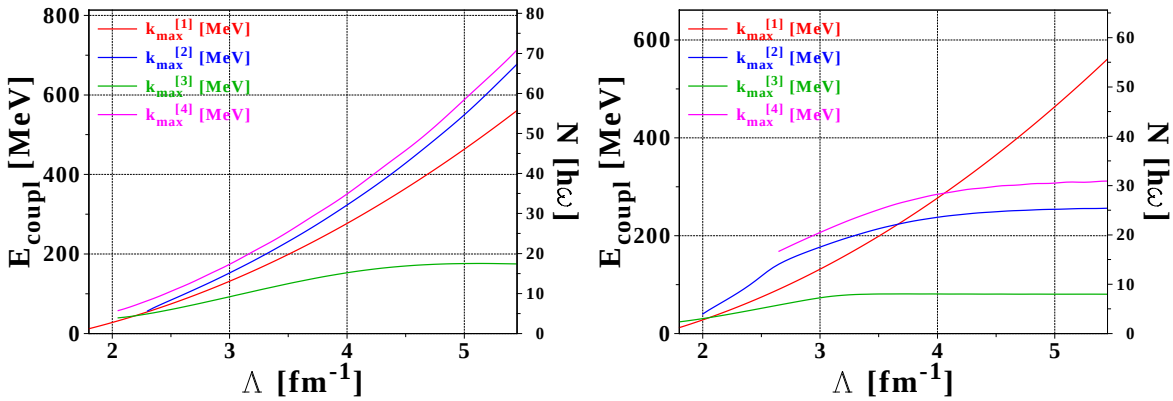

(a) $V_{\text{low}\,k}$ from AV18 (b) $V_{\text{low}\,k}$ from N^{3}LO

Figure 7.13: Correlation between different coupling ranges $E_{\max}^{[i]}/N_{\max}^{[i]}$ (see text) and the RG cutoff Λ in the ^{1}S$_0$ channel

The correlation between $E_{\max}^{[i]}/N_{\max}^{[i]}$ and η_-^1 is presented in FIG. 7.12 for two different starting potentials, e.g. Argonne V18 and chiral N^{3}LO, while the correlation between $E_{\max}^{[i]}/N_{\max}^{[i]}$ and Λ is presented in FIG. 7.13. First of all, one sees that the position of the greatest off-diagonal matrix element ($i = 3$) is not a valid criterion since it does not vary much with Λ whereas one knows that the (non-)perturbative character of the interaction does evolve with Λ.

On the other hand, values of $E_{\max}^{[i]}/N_{\max}^{[i]}$ for other choices of $k_{\max}$ display very similar behaviors. One finds as expected that the energy cutoff/number of HO shells that is needed to include all non-vanishing matrix elements in a given calculation increases with Λ/η_-^1. This corresponds to the need for larger bases as the interaction becomes less perturbative. The difference between AV18 and N^{3}LO is clearly seen when Λ reaches the intrinsic resolution scale

of chiral potentials which is of the order of $4.0 - 5.0$ fm^{-1}. Thus, values of $E^{[i]}_{\max}/N^{[i]}_{\max}$ keep growing for AV18-based potentials as Λ increases while they saturate for chiral forces. Finally, one can evaluate that, in order to keep the required basis size below around the typical value of 20 oscillator shells, the lowest negative Weinberg eigenvalue should be kept below about 0.4[10], or Λ below 3.0 fm^{-1}. As seen in Fig. 7.14, where the correlation between $V^{\rm od}_{\max}$ and η^1_- is presented, this indicates that nuclear forces exhibiting off-diagonal positive matrix elements of the order of 5 MeV do not necessarily manifest non-perturbative behaviors.

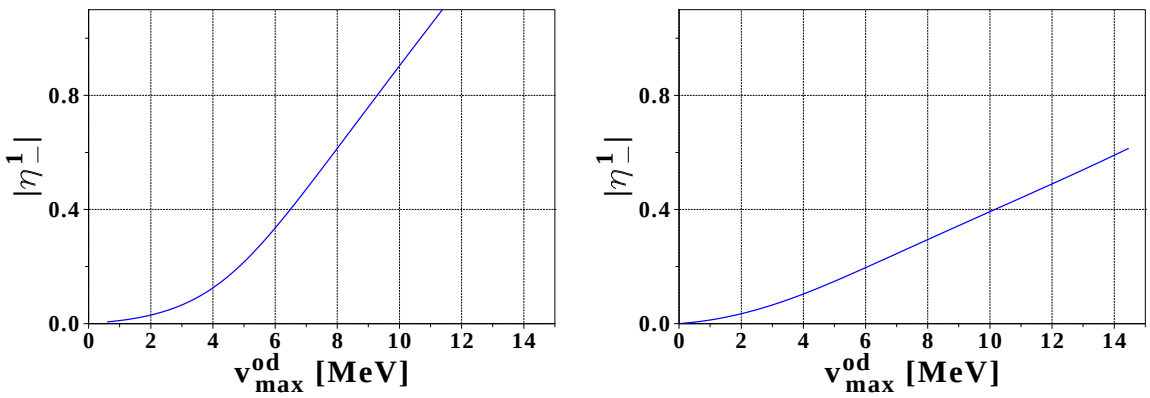

(a) $V_{\mathrm{low}\,k}$ from Argonne V18

(b) $V_{\mathrm{low}\,k}$ from N^{3}LO

Figure 7.14: Correlation between the maximum off-diagonal matrix elements and the lowest negative Weinberg eingenvalue in the ^{1}S$_0$ channel η^1_- for $V_{\mathrm{low}\,k}$ at different RG cutoffs Λ.

[10] This corresponds to a worst case scenario, and in finite nuclei or nuclear matter more freedom might be allowed.

Part III

Non-empirical effective forces

- [Stewie] How you uh, how you comin' on that novel you're working on? Huh? Gotta a big, uh, big stack of papers there? Gotta, gotta nice litte story you're working on there? Your big novel you've been working on for 3 years? Huh? Gotta, gotta compelling protaganist? Yeah? Gotta obstacle for him to overcome? Huh? Gotta story brewing there? Working on, working on that for quite some time? Huh? [...] Yeah? Yeah? No, no, you deserve some time off.

Introduction

In the previous part, we have presented modern approaches to vacuum nuclear interactions and in-medium many-body calculations. While standard potential models such as Argonne V18, CD-Bonn or nuclear forces derived from chiral effective field theory provide a very accurate description of bare NN/NNN forces, the recent advent of vacuum interactions based on the renormalization group constitutes a new paradigm opening new paths for low-energy nuclear structure calculations of medium- and heavy-mass nuclei. Indeed, low-momentum interactions preserve low-energy physical observables such as scattering phase shifts and bound state properties with the same precision as phenomenological models but, in contrary to the latter, are by essence soft-core perturbative forces, as proven for the two-body part through convergence properties of the associated Born series. Moreover, and after recasting the three-body force as an effective density-dependent two-body vertex, many-body correlations become treatable within the context of many-body perturbation theory. As a consequence, low-momentum interactions constitute an appealing starting point to construct effective vertices entering the EDF employed in finite nuclei calculations.

The drawback of low-momentum potentials in that respect is that RG flow equations are solved numerically in such a way that $V_{\mathrm{low}\,k}$ is given as arrays of discretized values on a momentum-space mesh. On the contrary, systematic EDF calculations require convenient analytical expressions of the effective vertices in order to pre-calculate as many integrals as possible. For instance, matrix elements of the Gogny effective force can be computed analytically in a harmonic oscillator basis. If these were to be computed numerically, six-dimensional integrals would have to be performed in such a way that large-scale calculations would not be feasible at all.

To improve on the limits of empirical Skyrme/Gogny EDFs, the last part of this dissertation presents a first step towards an explicit connection between microscopic vacuum/in-medium nuclear forces and EDF models. In that respect, the objectives of the construction of the non-empirical vertex v_{BDRS} can be summarized as follows.

- v_{BDRS} will be defined analytically with an expression that can be used directly, or with limited modifications, in existing nuclear structure codes using so far the Gogny effective interaction. One will thus profit from the experience previously acquired in performing such EDF calculations.
- The free parameters of v_{BDRS} will not be adjusted (at first) on experimental data, but on microscopic models of bare/in-medium nuclear forces. In that respect, one of the aims is to improve the predictive power of calculations targeting so far unknown nuclei.
- To extract as much physics as possible in the process, several realizations of v_{BDRS} will be constructed, corresponding to different levels of many-body complexity and/or envisioned long-term strategies.
- Starting from the vacuum interaction implies that v_{BDRS} contains, among others, finite-range spin-orbit and tensor components. This already corresponds to going beyond existing

EDFs which only account for a simplistic zero-range spin-orbit force and usually omit tensor terms.

The construction of v_{BDRS} is now carried out in a pedestrian way. Firstly, Chap. 8 presents all formal ingredients from the analytical retained expression for v_{BDRS}, which is justified and commented on for all of its envisioned implementations, to its partial wave expansion. The fitting strategy is then discussed, Chap. 9 being a mandatory digression introducing the numerical framework that will be used to perform the adjustement, i.e. evolutionary techniques based on a hybridation of simplex and genetic algorithms, as well as post-fit analysis methods (covariance analysis, theoretical error bars...). Finally, Chap. 10 presents the very first results of the adjustement procedure. Precise analytical representations of $V_{\mathrm{low}\,k}$ are constructed and present very good physical properties, which opens new perspectives for non-empirical EDF calculations.

Part of this work has therefore been dedicated to establishing a long-term strategy that extends beyond the scope of this thesis. We have established several possible ways that are worth being pursued. These complementary approaches will allow to perform cross-checks and comparisons as well as to evaluate the loss of precision inherent to (more and more) effective approaches. This third tier of the dissertation reflects one year and a half of work in this direction, which explains why only the first few steps have been undertaken. Still, we have chosen to provide a complete discussion concerning long-term strategies and guidelines.

Chapter 8

Defining non-empirical vertices

Abstract: The definition of non-empirical effective vertices is obtained through a mapping of the EDF formalism onto MBPT. The guidelines to proceed to such a mapping at lowest order in two-particle-irreducible vertices are given. Then, the expression of the microscopic vertex v_{BDRS} used to construct those effective vertices is presented and discussed in all of its envisioned realizations. The partial wave expansion of v_{BDRS} is performed and the nuclear matter equation of state is derived using such a generalized gaussian vertex including finite-range spin-orbit and tensor terms. Finally, the adjustment procedure of the free parameters of v_{BDRS} is discussed, in particular for the features that do not depend on the details of the scenario chosen to build it (i.e. levels of MBPT complexity).

Contents

8.1 Non-empirical effective vertices for the EDF formalism **219**
8.2 Long-term strategies **222**
8.2.1 Strategy 1: representation of the vacuum NN interaction 222
8.2.2 Strategy 2: representation of the vacuum NN + $\overline{\mathrm{NNN}}$ interaction 223
8.2.3 Strategy 3: representation of the in-medium effective vertices 223
8.3 Expression and key features **224**
8.3.1 Analytical operatorial form 226
8.3.2 Tensor interaction 228
8.3.3 Various remarks 229
8.4 Useful expressions for $v^{[\mathrm{X}]}_{\mathrm{BDRS}}$ **230**
8.4.1 Momentum space 230
8.4.2 Infinite matter: vertices 231
8.4.3 Infinite matter: correlation energy 232
8.4.4 Partial wave decomposition 233
8.4.4.1 D1X/D2 interactions 234
8.4.4.2 BDRS vertex 235
8.5 Adjustment procedure **237**

8.1 Non-empirical effective vertices for the EDF formalism

The definition of non-empirical effective vertices proceeds through a matching of the two formalisms so far introduced, i.e. the SR-EDF method presented in Chap. 1 and many-body perturbation theory from which in-medium effective vertices can be explicitly constructed using

	Effective two-body vertex $v^{\rho\rho}_{\text{eff}}$
	Effective two-body vertex $v^{\kappa\kappa}_{\text{eff}}$

Table 8.1: Additional conventions for the effective vertices that appear in non-empirical EDF calculations

vacuum low-momentum interactions as a starting point. We explicit now general guidelines to perform such a matching.

On the one hand, and as discussed in Chap. 6, we consider in the present work the many-body energy calculated at lowest order in two-particle-irreducible vertices. The associated binding energy, expressed in the natural basis of the unperturbed vacuum, reads

$$E_0 = \sum_{i,q} t^q_{ii}\,\rho^q_{ii} + \frac{1}{2}\sum_{ij,qq'} \bar{\mathcal{G}}^{\text{NN}+\overline{\text{NNN}}}_{ijij}(E^q_i + E^{q'}_j)\,\rho^q_{ii}\,\rho^{q'}_{jj} + \frac{1}{4}\sum_{ij,q} \bar{v}^{\text{NN}+\overline{\text{NNN}}}_{i\bar{i}j\bar{j}}\,\kappa^q_{i\bar{i}}\,\kappa^{q\,*}_{j\bar{j}}\,, \tag{8.1}$$

where $\mathcal{G}^{\text{NN}+\overline{\text{NNN}}}$ (possibly reduced to second order for a perturbative vacuum force) and $v^{\text{NN}+\overline{\text{NNN}}}$ denote the Brueckner matrix and the vacuum interaction, respectively. The binding energy is of course complemented with the appropriate definitions of the normal and anomalous self-energies (see Fig. 6.5).

On the other hand, the binding energy in the HFB realization of the SR-EDF formalism (Sec. 1.3), expressed in the canonical basis of the reference product state, reads

$$\mathcal{E}[\rho,\kappa,\kappa^*] \equiv \sum_{i,q} t^q_{ii}\,\rho^q_{ii} + \frac{1}{2}\sum_{ij,qq'} \bar{v}^{\rho\rho}_{ijij}\,\rho^q_{ii}\,\rho^{q'}_{jj} + \frac{1}{4}\sum_{ij,q} \bar{v}^{\kappa\kappa}_{i\bar{i}j\bar{j}}\,\kappa^q_{i\bar{i}}\,\kappa^{q\,*}_{j\bar{j}}\,. \tag{8.2}$$

The expressions given in Eqs. (8.1,8.2) display obvious similarities, meaning that the SR-EDF should be constructible from MBPT. In that context, the symmetry-breaking reference state of the SR-EDF formalism is nothing but the unperturbed product state of MBPT. However, the mapping of the standard SR-EDF formalism onto MBPT is not as straightforward at it may seem at this point and necessitates some words of caution.

Firstly, the historical separation of the correlation energy entering the SR-EDF into a so-called *particle-hole* channel that only depends on the normal density matrix and a *particle-particle* channel that is bilinear in κ, with $\bar{v}^{\kappa\kappa}$ possibly further depending on ρ, does not fit in general with MBPT as the latter generates diagrams which a priori mixes normal and anomalous propagators, i.e. dependencies on ρ and κ. As a matter of fact, the proper definition of particle-hole and particle-particle channels can only be accomplished at the level of the one-body-fields through

$$h^q_{ji} \equiv \frac{\delta\mathcal{E}}{\delta\rho^q_{ij}} \equiv \sum_{kl,q'} \bar{v}^{\text{ph}}_{ikjl}\,\rho^{q'}_{lk}\,, \qquad \Delta^q_{ij} \equiv \frac{\delta\mathcal{E}}{\delta\kappa^{q\,*}_{ij}} \equiv \sum_{kl} \bar{v}^{\text{pp}}_{ikjl}\,\kappa^q_{lk}\,, \tag{8.3}$$

where the corresponding effective vertices $\bar{v}^{\text{ph}}$ and $\bar{v}^{\text{pp}}$ can be defined. This suggests to perform the mapping of the EDF onto MBPT at the level of the one-body fields. In the present study however (i) the Brueckner matrix is computed as if the system were not superfluid[1], i.e. $\mathcal{G} = G$, so that it does not depend on the pairing tensor, and (ii) the vacuum interaction enters the

[1] It is expected to be a good approximation except for systems in the strong BCS coupling regime, e.g. low-density neutron matter.

lowest-order anomalous diagram, so that the latter is bilinear in κ and depends linearly on ρ through the averaged three-body force. As a result, the correlation energy in Eq. (8.1) does split into two terms whose structures fit those usually considered in standard nuclear EDFs (Eq. (8.2)). Such a situation makes it easy to perform the mapping at the level of the binding energy, i.e. defining $v^{\rho\rho} \equiv \mathcal{G}^{\mathrm{NN}+\overline{\mathrm{NNN}}}$ and $v^{\kappa\kappa} \equiv v^{\mathrm{NN}+\overline{\mathrm{NNN}}}$ (see Figs. (8.1,8.2)), still fulfilling the topological constraints on v^{ph} and $v^{\mathrm{pp}(2)}$ [535] (see Fig. 6.1). Again, such a mapping is easily realized thanks to the restrictive set of diagrams incorporated in our MBPT scheme[3].

Secondly, the G-matrix depends on single-particle energies. Such dependencies do not appear in the standard formulation of the SR-EDF method where the energy is postulated to be a functional of the normal and anomalous density matrices only. From that point of view, the matching advocated above does not fit with the current EDF formalism. To proceed further, it is necessary (i) to recast such energy dependencies in terms of more appropriate variables, or (ii) to provide an energy-dependent formulation of the SR-EDF formalism in analogy to orbital-dependent DFT [592] and possibly design approximation schemes that simplify the treatment of energy dependencies [593].

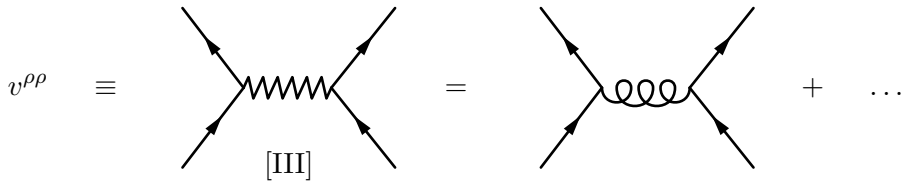

(8.4)

Figure 8.1: Identification of the "particle-hole" effective EDF vertex $v^{\rho\rho}$ with the G-matrix calculated from $v^{\mathrm{NN}+\overline{\mathrm{NNN}}}$.

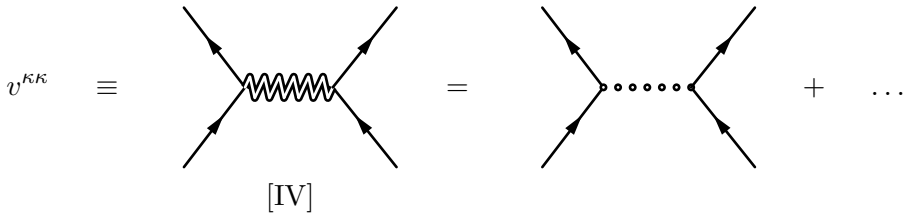

Figure 8.2: Same as in Fig. 8.1 for the "particle-particle" effective EDF vertex Fig. 8.2. At lowest order in two-particle irreducible vertices, $v^{\kappa\kappa}$ is mapped onto $v^{\mathrm{NN}+\overline{\mathrm{NNN}}}$.

Working at the level of the effective vertices $v^{\rho\rho}$ and $v^{\kappa\kappa}$, the binding energy of Eqs. (8.1,8.2) is simply obtained by closing the external legs onto the Fermi sea of interest and adding the kinetic energy. The result is shown diagrammatically in Fig. 8.3.

[2]In Fig. 6.1, the rearrangement terms in v^{ph} coming from $v^{\kappa\kappa}$, and related to the contribution of the three-body force to the anomalous diagram, are not displayed. This is because the latter will not be considered in the course of the present work. When it is computed in the future, the associated rearrangement term will have to be incorporated.

[3]This relates to our aim to only resum "bulk" correlations into the SR-EDF and leaves room for incorporating dynamical correlations in finite nuclei associated with spin, isospin and density fluctuations, as well as with symmetry restorations, through MR-EDF calculations.

$\mathcal{E}[\rho,\kappa,\kappa^*] =$ 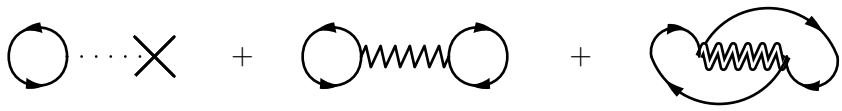 (8.5a)

$=$ 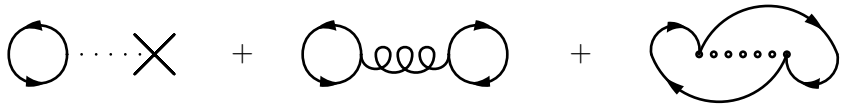 (8.5b)

Figure 8.3: Diagrammatic representation of the SR-EDF (top) in terms of the effective vertices $v^{\rho\rho}$ and $v^{\kappa\kappa}$, and (bottom) from MBPT at lowest order in two-particle-irreducible vertices.

8.2 Long-term strategies

In the previous section, the many-body content of the effective vertices $v^{\rho\rho}$ and $v^{\kappa\kappa}$ has been stated from the general viewpoint. Starting from there, our goal is to design a microscopic vertex v_{BDRS} of gaussian structure from which $v^{\rho\rho}$ and $v^{\kappa\kappa}$ can be computed, in such a way that they can be handled through modifications of existing codes using HO basis sets to make systematic EDF calculations of finite nuclei tractable. Within such an approach, the physical content of v_{BDRS} and its relationship with $v^{\rho\rho}$ and $v^{\kappa\kappa}$ will vary, i.e. several realizations $v_{\text{BDRS}}^{[\text{X}]}$ will be considered, as explained in details below. If the general operator structure is common to all realizations, the adjustment procedure of its free parameters, generically denoted by $Y_i^{[\text{X}]}$, will differ in agreement with the physics incorporated into $v_{\text{BDRS}}^{[\text{X}]}$. Such a strategy is inspired from previous studies in that direction [594], but benefits from (i) the new paradigm constituted by low-momentum interactions, (ii) breakthroughs in the construction of modern three-body forces, and (iii) the possible connection between EDF and MBPT. Let us now explicit the different strategies that we envision to follow[(4)].

8.2.1 Strategy 1: representation of the vacuum NN interaction

The microscopic vertex $v_{\text{BDRS}}^{[\text{bare}(2)]}$ is constructed to represent the vacuum nucleon-nucleon interaction, at the level of diagram [I] (Fig. 7.2), i.e.

$v_{\text{BDRS}}^{[\text{bare}(2)]} =$ 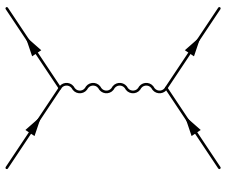 . (8.6)

The free parameters $Y_i^{[\text{bare}(2)]}$ of $v_{\text{BDRS}}^{[\text{bare}(2)]}$ are adjusted to reproduce $V_{\text{low}\,k}$ in momentum space. There is no in-medium dependence of the vertex as the vacuum nucleon-nucleon force only depends on incoming $\vec{k}$ and outgoing $\vec{k}'$ relative momenta. Thus, the couplings $Y_i^{[\text{bare}(2)]}$ are density-independent. In a second step, the effective vertices $v^{\rho\rho/\kappa\kappa}$ are constructed (i) by adding to $v_{\text{BDRS}}^{[\text{bare}(2)]}$ the averaged three-body averaged force $v^{\overline{\text{NNN}}}$ as given by Fig. 7.2, and (ii) by evaluating explicitly the appropriate diagrams from $v_{\text{BDRS}}^{[\text{bare}(2)]} + v^{\overline{\text{NNN}}}$. To compute finite nuclei,

[4]Due to time constraints not all of them are touched on in the present dissertation.

we envision in this case to approximate the diagrammatic calculation of $v^{\rho\rho}$ in terms of products of energy-dependent one-body densities, from which a quasi-local functional can be derived by applying the DME [593]. Indeed, performing exact second-order MBPT calculations of heavy open-shell nuclei in a systematic manner is still largely out of reach, in particular given that we have in mind to produce non-empirical EDFs that are eventually tractable in MR-EDF calculations.

8.2.2 Strategy 2: representation of the vacuum $\mathrm{NN} + \overline{\mathrm{NNN}}$ interaction

The microscopic vertex $v^{[\mathrm{bare}(3)]}_{\mathrm{BDRS}}$ is constructed to represent the sum of the bare nucleon-nucleon and averaged NNN force, at the level of diagram [II] (Fig. 7.2), i.e.

$v^{[\mathrm{bare}(3)]}_{\mathrm{BDRS}} =$ 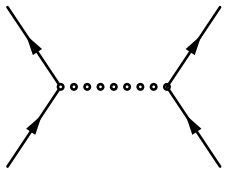 . (8.7)

The adjustment procedure takes as an input INM calculations of $v^{\mathrm{NN}+\overline{\mathrm{NNN}}}$ [429]. Since the three-body force is approximated by a density-dependent two-body one through closing the third leg over the INM Fermi sea(s) (see Sec. 7.3), $v^{[\mathrm{bare}(3)]}_{\mathrm{BDRS}}$ carries dependencies on $\vec{k}$, $\vec{k}\,'$ and on the medium density possibly characterized by the densities $(\rho_0, \rho_1, \vec{s}_0, \vec{s}_1)$. Thus, free parameters $Y_i^{[\mathrm{bare}(3)]}$ will already depend on such densities[5]. In a second step, the construction of $v^{\rho\rho/\kappa\kappa}$ proceeds in the exact same way as in **strategy 1**.

8.2.3 Strategy 3: representation of the in-medium effective vertices

The microscopic vertices $v^{[\rho\rho]/[\kappa\kappa]}_{\mathrm{BDRS}}$ are defined to reproduce directly $v^{\rho\rho/\kappa\kappa}$ computed in SNM from $v^{\mathrm{NN}+\overline{\mathrm{NNN}}}$, at the level of diagrams [III-IV], i.e.

$v^{[\rho\rho]}_{\mathrm{BDRS}} =$ 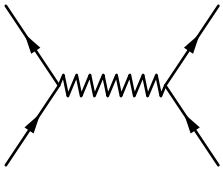 $v^{[\kappa\kappa]}_{\mathrm{BDRS}} =$ 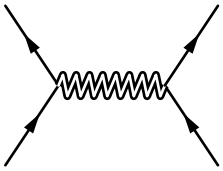 (8.8)

The adjustment procedure takes as an input MBPT calculations of $v^{\rho\rho/\kappa\kappa}$ computed in INM [429]. The vertex $v^{[\kappa\kappa]}_{\mathrm{BDRS}}$ carries in principal dependencies on $\vec{k}$, $\vec{k}\,'$ and in-medium densities[6]. The vertex $v^{[\rho\rho]}_{\mathrm{BDRS}}$ carries additional dependencies on the magnitude of the total momentum $\vec{K}$ and on the starting energy ω. The latter (i) is taken on-shell when calculating the INM equation of state, i.e. $\omega = \epsilon_{\vec{K}/2+\vec{k}} + \epsilon_{\vec{K}/2-\vec{k}}$, where the two single-particle states involved are hole states, and (ii) is eventually averaged over the angle between $\vec{K}$ and $\vec{k}$. The starting energy is thus recast into an extra dependence of $v^{[\rho\rho]}_{\mathrm{BDRS}}$ on K, k and on $(\rho_0, \rho_1, \vec{s}_0, \vec{s}_1)$. The overall K dependence is averaged over the Fermi sea such that diagram [III] only depends on $\vec{k}$, $\vec{k}\,'$ and $(\rho_0, \rho_1, \vec{s}_0, \vec{s}_1)$ in the end. As for $Y_i^{[\mathrm{bare}(3)]}$, coupling constants $Y_i^{[\rho\rho]/[\kappa\kappa]}$ are medium-dependent, where density

[5] The first step will be to compute in-medium dependencies in symmetric nuclear matter, thus only dependencies on ρ_0 will be considered, as explained later on.

[6] Dependencies of $v^{[\kappa\kappa]}_{\mathrm{BDRS}}$ on $(\rho_0, \rho_1, \vec{s}_0, \vec{s}_1)$ will not be touched on in the present work since the contribution from the three-body force to $v^{\kappa\kappa}$ will not be studied.

dependencies of $Y_i^{[\rho\rho]}$ not only account for the three-body force effects but also for many-body correlations. Finally, in-medium dependencies of $v_{\rm BDRS}^{[\rho\rho]/[\kappa\kappa]}$ will be approximated through a local density approximation in order to compute finite nuclei. The treatment of the starting energy dependence of the effective vertex at the level of INM, and its recast into a momentum dependence, removes the difficulty to consider an energy-dependent EDF formalism when proceeding to finite nuclei calculations.

Our ultimate goal is to perform finite nuclei calculations. Still, one sees that more and more in-medium effects are directly resummed into $v_{\rm BDRS}^{[\rm X]}$ at the level of infinite nuclear matter as one goes from **strategy 1** to **strategy 3**. This corresponds to averaging the corresponding correlations in a homogenous system and simplifying accordingly finite nuclei calculations. Still, it is crucial to realize that in all envisioned strategies, the matching is done at the vertex level rather than at the binding energy level, as always done so far to build (empirical) EDFs, in which the momentum dependence of the effective vertices is averaged out while the contribution of its residual spin-orbit and tensor components cancels out [147; 160; 595; 596]. **Strategy 3** for instance amounts to constructing the effective vertices in homogeneous matter but keeping a full account of the momentum dependence of all their components, and "closing the external legs" only when calculating the finite system.

The three complementary approaches outlined above and summarized in Fig. 8.4 will allow one to perform cross-checks and comparisons as well as to evaluate the loss of precision inherent to (more and more) effective approaches, i.e. going from **strategy 1** to **strategy 3**. Considering the quality of the SR-EDF calculations thus obtained, one can envision as a last step to perform a linear refit of $Y_i^{[\rm X]}$ through finite nuclei calculations within a given parameter space that is yet to be determined and provided by the first adjustment. This corresponds to incorporating additional many-body effects into $v_{\rm BDRS}^{[\rm X]}$, while keeping an explicit connection with underlying vacuum two- and three-body forces.

8.3 Expression and key features

The operator structure of the effective vertex $v_{\rm BDRS}^{[\rm X]}$ is written below in its full generality, that is in an appropriate form for finite nuclei, possibly asymmetric in spin and isospin. Thus, we somehow start from the end and provide simpler forms to be used in infinite nuclear matter, in particular for spin and isospin symmetric matter. When necessary, the specificities of the different realizations $v_{\rm BDRS}^{[\rm X]}$ are discussed in framed boxes, i.e.

[bare(2)] level

[bare(2)] accounts for the strict NN vacuum interaction. Its coupling constants $Y_i^{[\rm bare(2)]}$ do not relate to any Fermi sea and are medium-independent.

[bare(3)/$\rho\rho$/$\kappa\kappa$] levels

[bare(3)/$\rho\rho$/$\kappa\kappa$] cases. Coupling constants $Y_i^{[\rm X]}$ are medium-/density-dependent and relate to a reference unperturbed Fermi sea.

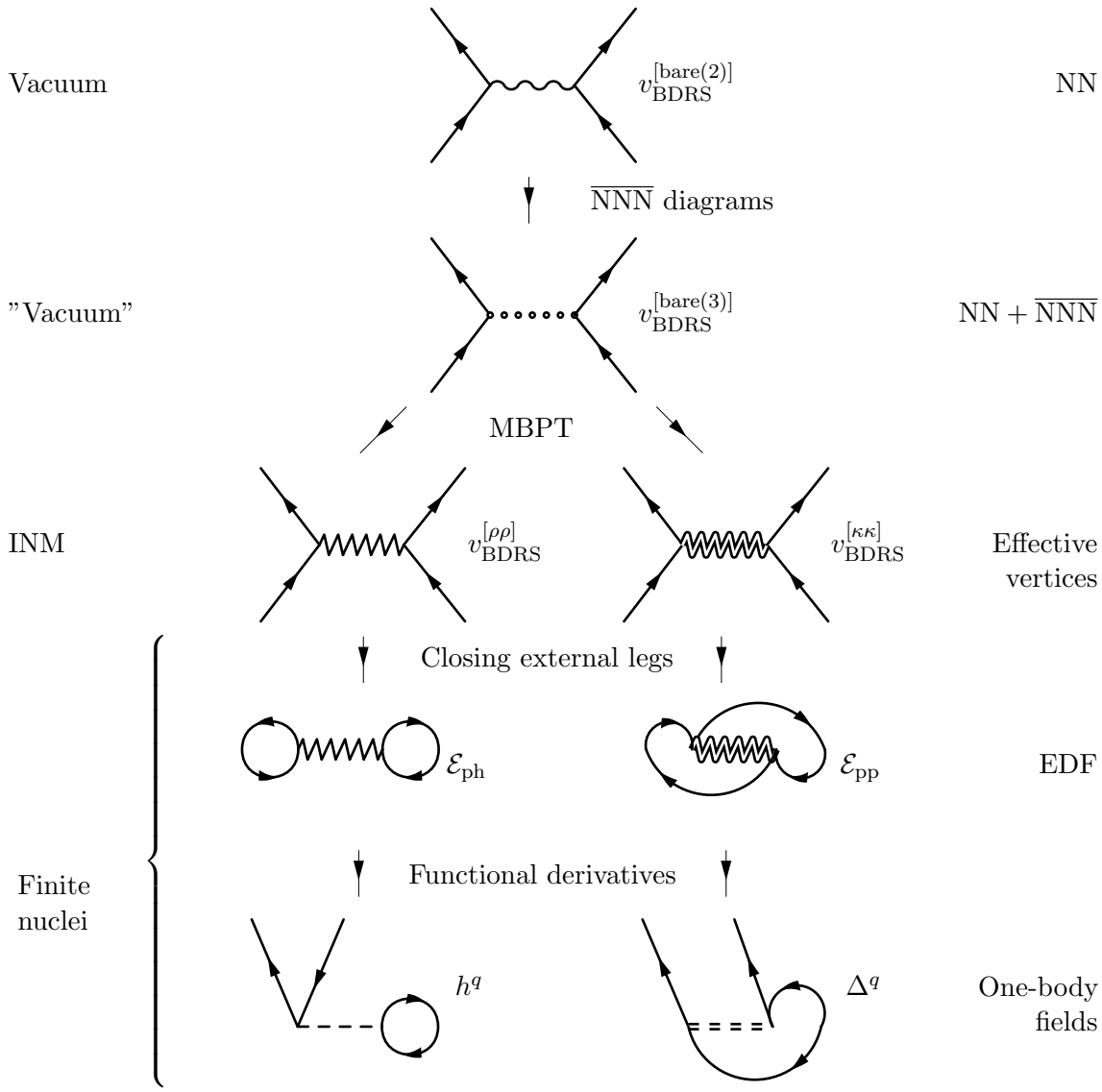

Figure 8.4: Summary of the long-term strategy to construct microscopic bare/effective vertices v_{BDRS} and the steps required starting from each realization of $v_{\mathrm{BDRS}}^{[\mathrm{X}]}$ to compute finite nuclei through EDF calculations. We are constructing non-antisymmetrized vertices, that is exchange terms are explicitly computed at the level of the EDF calculations. This implies that diagrammatic definitions given here are valid as long as one assumes that the involved vertices are not antisymmetrized.

8.3.1 Analytical operatorial form

The vertex $v^{[\mathrm{X}]}_{\mathrm{BDRS}}$ is expressed using a gaussian-based structure similar to the Gogny effective vertex[7], where finite-range spin-orbit and tensor forces are introduced. The latter typically couples $^3\mathrm{S}_1$ to $^3\mathrm{D}_1$ ("even" tensor) and $^3\mathrm{P}_2$ to $^3\mathrm{F}_2$ ("odd" tensor) partial waves. The generic expression reads

$$v^{[\mathrm{X}]}_{\mathrm{BDRS}}(\vec{r},\vec{R},\Lambda) = \sum_{i=1}^{N}\left[\sum_{SS_zTT_z} f^{SS_zTT_z}_{c,i}([\mathrm{X}],\vec{r},\vec{R},\mu_i,\Lambda)\prod_{SS_z}\prod_{TT_z}\right] \tag{8.9a}$$

$$+\sum_{S_zTT_z} f^{1S_zTT_z}_{so}([\mathrm{X}],\vec{r},\vec{R},\mu_{so},\Lambda)\,(\vec{\sigma}_1+\vec{\sigma}_2)\cdot\vec{r}\wedge\overrightarrow{k}\prod_{S=1}\prod_{S_z}\prod_{TT_z} \tag{8.9b}$$

$$+\sum_{S_zTT_z} f^{1S_zTT_z}_{t}([\mathrm{X}],\vec{r},\vec{R},\mu_t,\Lambda)\,\mathsf{S}_{12}\prod_{S=1}\prod_{S_z}\prod_{TT_z}, \tag{8.9c}$$

where [X]=[bare(2)/bare(3)/$\rho\rho/\kappa\kappa$]. The form factors $f^{SS_zTT_z}_x([\mathrm{X}],\vec{r},\vec{R},\mu_x)$ are different for the [bare(2)] and [bare(3)/$\rho\rho/\kappa\kappa$] levels but are defined in both cases as gaussian-type factors of ranges μ_x. The projector on $S=1$ waves in the spin-orbit and tensor terms is unnecessary as can be seen from the partial wave expansion (Appendix E.2.2), but we keep it nevertheless. Subscripts $x=c;so;t$ denote respectively central, spin-orbit and tensor parts of the vertex. Note that the form factor is slightly different for the tensor part. Indeed:

[bare(2)] level

The form factors $f^{SS_zTT_z}_x([\mathrm{bare}(2)],[...])$ read

$$f^{SS_zTT_z}_x([\mathrm{bare}(2)],\vec{r},\vec{R},\mu_x,\Lambda) \equiv C^{SS_zTT_z}_x[\Lambda]\,e^{-\frac{r^2}{\mu_x^2}} \qquad x=c;so\,, \tag{8.10a}$$

$$f^{SS_zTT_z}_t([\mathrm{bare}(2)],\vec{r},\vec{R},\mu_t,\Lambda) \equiv C^{SS_zTT_z}_t[\Lambda]\,r^2\,e^{-\frac{r^2}{\mu_t^2}}\,. \tag{8.10b}$$

The functions $C^{SS_zTT_z}_x$ are Λ-dependent coupling constants.

[7] One cannot call $v^{[\mathrm{X}]}_{\mathrm{BDRS}}$ a *generalization* of Gogny D1X/D2 in the general case, as different realizations of $v^{[\mathrm{X}]}_{\mathrm{BDRS}}$ account for different levels of many-body physics. At the [bare(2)/bare(3)] levels, a direct comparison between $v^{[\mathrm{X}]}_{\mathrm{BDRS}}$ (bare) and Gogny (effective) is non-sense. At the [$\rho\rho/\kappa\kappa$] level v_{BDRS} does represent a non-empirical extension of the Gogny empirical effective vertex.

[bare(3)/$\rho\rho/\kappa\kappa$] levels

The form factors $f_x^{SS_zTT_z}([\mathrm{X}],[...])$ read

$$f_x^{SS_zTT_z}([\mathrm{X}],\vec{r},\vec{R},\mu_x,\Lambda) \equiv C_x^{SS_zTT_z}[\rho_0(\vec{R}),\rho_1(\vec{R}),\vec{s}_0(\vec{R}),\vec{s}_1(\vec{R}),\Lambda]\, e^{-\frac{r^2}{\mu_x^2}} \qquad x=c;so\,, \tag{8.11a}$$

$$f_t^{SS_zTT_z}([\mathrm{X}],\vec{r},\vec{R},\mu_t,\Lambda) \equiv C_t^{SS_zTT_z}[\rho_0(\vec{R}),\rho_1(\vec{R}),\vec{s}_0(\vec{R}),\vec{s}_1(\vec{R}),\Lambda]\, r^2\, e^{-\frac{r^2}{\mu_t^2}}\,. \tag{8.11b}$$

The functions $C_x^{SS_zTT_z}$ contain in-medium effects associated with the averaging of the three-body force and the resummation of correlations to second order/of all particle-particle ladders in perturbation theory ([$\rho\rho$]/[$\kappa\kappa$] levels). They are encoded through dependencies on $\rho_T(\vec{R})$ and $\vec{s}_T(\vec{R})$, which refer to isoscalar and isovector densities (Eqs. (1.63a-1.63d)). Such dependencies relate to a local approximation applied to in-medium dependencies resummed in infinite matter. The envisioned density dependence is in principle much richer than for the DX Gogny forces since it appears in all terms of the vertex.

The four densities $\rho_T(\vec{R})$ and $\vec{s}_T(\vec{R})$ characterize completely the (local) spin-isospin content of the system under consideration. Dependencies of the couplings f^{ST} on these originate from the dependence of self-energies on the composition of the system that appear in the denominator of the in-medium propagator (Eq. (6.7a)). When using free kinetic energies, those dependencies disappear. The second source of density dependencies is the dependence of the Pauli operator on the Fermi energies of the interacting nucleons. Finally, the averaging procedure for the three-nucleon force induces additional density dependencies. Obviously, those in-medium effects resummed into the vertex do not only depend on the overall composition of the matter but also on the spin and isospin of the two interacting nucleons in spin/isospin polarized matter[8]. The latter provides v_{BDRS} with a dependence of the effective vertex on T_z and S_z which complements the one brought by charge-symmetry/charge-invariance breaking effects in the vacuum interaction one starts from. If the matter is not polarized in spin for instance, the dependencies on S_z and $\vec{s}_T(\vec{R})$ drop alltogether. If the matter is further symmetric in isospin, the dependencies on T_z and on $\rho_1(\vec{R})$ will drop and one is left with an overall dependence on the scalar-isoscalar density $\rho_0(\vec{R})$.

[bare(3)/$\rho\rho/\kappa\kappa$] levels

At first, $v_{\mathrm{BDRS}}^{[\mathrm{X}]}$ is going to be built in isospin-symmetric spin-unpolarized nuclear matter. Thus, only dependencies on $\rho_0(\vec{R})$ will be considered, which will be the same for all (S,T). Note that, if ground states of even-even nuclei are indeed spin unpolarized, we are mainly dealing with isospin asymmetric (exotic) nuclei which implies in principle a dependence on $\rho_1(\vec{R})$. Such a dependence does not exist in usual Skyrme / Gogny functionals and extracting it along the lines outlined above is one of the long-term motivations of this work.

[8] Since we always consider nucleons with good isospin projection, the projection on T_z in a two body matrix element is trivial since it corresponds to $T_z = q + q'$, where q and q' are the isospin of the interacting nucleons. Thus, it can be read directly from the isospin of the two particles involved. In infinite matter, the same is true for spin as one works in a basis where single-particle states have a good spin projection. Thus, the vertex is naturally separated into $S_z = \sigma + \sigma'$ terms. This is however less trivial in finite nuclei where single-particle states of interest (HF basis for instance) mix the two spin projections as a result of the action of the spin-orbit and tensor components. This is true even for even-even nuclei which have no net spin density. In this case, the projection on S_z must be performed explicitly.

Dependencies on S_z and T_z correspond to charge-symmetry- and charge-independence-breaking interactions that will not be considered in the present dissertation. Thus superscripts S_z and T_z will be dropped and one will use the shorthand notation $f^{SS_zTT_z} \equiv f^{ST}$.

8.3.2 Tensor interaction

A few comments about the tensor part of the effective vertex are in order. It appears that expressing the tensor force using a pure gaussian form factor in coordinate space [334] may not be the most convenient form with respect to the adjustement procedure (see Sec. 8.5) that is performed in momentum space. This point is discussed in Appendix E.1.4.1.

As a consequence, a different form factor f_t^{ST} needs to be introduced (Eqs. (8.10b,8.11b)). One starts from the exact derivation of the tensor force originating from OPE (Appendix D.1). The pseudoscalar meson exchange reads

$$v_\pi(\vec{r}) = (\vec{\tau}_1 \cdot \vec{\tau}_2)\left(\vec{\sigma}_1 \cdot \vec{\nabla}\right)\left(\vec{\sigma}_2 \cdot \vec{\nabla}\right) v_0(\vec{r}), \tag{8.12}$$

where $v_0(\vec{r})$ is a Yukawa potential $\dfrac{e^{-\mu r}}{r}$. One can separate the pure tensor component from the central one to obtain explicitly

$$v_\pi(\vec{r}) = \mu^3 \left(\frac{g_A}{\sqrt{2} f_\pi}\right)^2 (\vec{\tau}_1 \cdot \vec{\tau}_2)\left[\mathsf{S}_{12}\left(1 + \frac{1}{3\mu r} + \frac{1}{(\mu r)^2} + \frac{1}{(\mu r)^3}\right) e^{-\mu r} + \frac{1}{3}(\vec{\sigma}_1 \cdot \vec{\sigma}_2)\left[\frac{e^{-\mu r}}{\mu r} - \frac{4\pi}{3\mu^3}\delta(\vec{r})\right]\right]. \tag{8.13}$$

In momentum space, one finds that

$$v_\pi(\vec{q}) = -4\pi\,(\vec{\tau}_1 \cdot \vec{\tau}_2)\,(\vec{\sigma}_1 \cdot \vec{q})\,(\vec{\sigma}_2 \cdot \vec{q})\,\tilde{v}_0(\vec{q}), \tag{8.14}$$

where $\tilde{v}_0(\vec{q})$ is the Fourier transform of $v_0(\vec{r})$, i.e.

$$v_0(\vec{r}) = \int \frac{\mathrm{d}\vec{q}}{(2\pi)^3} e^{i\,\vec{q}\cdot\vec{r}}\,\tilde{v}_0(\vec{q}). \tag{8.15}$$

The previous arguments allow to find the most convenient form for the tensor force to be included in $v_{\mathrm{BDRS}}^{[\mathrm{X}]}$. If one uses a pure gaussian form factor in coordinate space multiplied by the cartesian tensor operator S_{12}, the associated vertex in momentum space is complicated and the partial wave decoupling that is required in the fitting procedure becomes extremely difficult to perform, if not impossible. Rather, we choose a simple expression in momentum space that remains tractable when transformed back into coordinate space, i.e.

$$\tilde{v}_0(\vec{q}) \equiv (\mu_t\sqrt{\pi})^3\, e^{-\frac{1}{4}\mu_t^2 q^2}, \tag{8.16}$$

such that the tensor force in momentum spaces becomes

$$v_t(\vec{q}) = -(\vec{\tau}_1 \cdot \vec{\tau}_2)\left[(\vec{\sigma}_1 \cdot \vec{q})\,(\vec{\sigma}_2 \cdot \vec{q}) - \frac{1}{3}(\vec{\sigma}_1 \cdot \vec{\sigma}_2)\, q^2\right](\mu_t\sqrt{\pi})^3\, e^{-\frac{1}{4}\mu_t^2 q^2}, \tag{8.17}$$

and transforms in coordinate space into

$$v_t(\vec{r}) = \frac{4}{3\mu_t^4}\,(\vec{\tau}_1 \cdot \vec{\tau}_2)\,\mathsf{S}_{12}\, r^2\, e^{-\frac{r^2}{\mu_t^2}}, \tag{8.18}$$

where the form factor is a gaussian multiplied by r^2, which can be handled in calculations in a HO basis. In the end, the prefactor is reinjected into the coupling constant C_t^{ST}, which leads to the expression of Eq. (8.9c).

One may note that

$$(\vec{\tau}_1 \cdot \vec{\tau}_2\,) = 2T(T+1) - 3\,, \tag{8.19}$$

thus a bare tensor interaction from one-pion exchange is three times stronger in the isospin singlet channel than in the triplet one, and of opposing sign. However, in Eq. (8.9c) the relative strength of the two isospin channels is relaxed in order to allow more freedom in the fit and to account for in-medium effects. In the case where $V_{\text{low}\,k}$ is provided from a NN model that explicitly contains a correlated 2PE exchange part (which is not the case for AV18), such a decoupling allows to account for the corresponding tensor contribution. Note that we only keep here the pure tensor contribution of $\tilde{v}_0(\vec{q}\,)$.

8.3.3 Various remarks

Additional remarks are at play here.

1. The parameters of $v^{[\mathrm{X}]}_{\mathrm{BDRS}}$ depend on the RG cutoff Λ[9]. This dependence will be used to provide "theoretical error bars" on the parameters of the force, thus giving a natural parameter space for a linear refit.

2. Dependencies on spin and isospin projections (S_z, T_z) are dropped and the central term of $v^{[\mathrm{X}]}_{\mathrm{BDRS}}$ can be recast in terms of the standard prefactors appearing in the Gogny effective force (Eq. (1.76a))

$$C^{ST}_{c,i}[(...),\Lambda] = W_i + (-1)^{S+1}\,B_i + (-1)^{T}\,H_i + (-1)^{S+T+1}\,M_i\,, \tag{8.20a}$$

$$W_i \equiv \frac{1}{4}\left[+C^{00}_{c,i}[(...),\Lambda] + C^{10}_{c,i}[(...),\Lambda] + C^{01}_{c,i}[(...),\Lambda] + C^{11}_{c,i}[(...),\Lambda]\right]\,, \tag{8.20b}$$

$$B_i \equiv \frac{1}{4}\left[-C^{00}_{c,i}[(...),\Lambda] + C^{10}_{c,i}[(...),\Lambda] - C^{01}_{c,i}[(...),\Lambda] + C^{11}_{c,i}[(...),\Lambda]\right]\,, \tag{8.20c}$$

$$H_i \equiv \frac{1}{4}\left[+C^{00}_{c,i}[(...),\Lambda] + C^{10}_{c,i}[(...),\Lambda] - C^{01}_{c,i}[(...),\Lambda] - C^{11}_{c,i}[(...),\Lambda]\right]\,, \tag{8.20d}$$

$$M_i \equiv \frac{1}{4}\left[-C^{00}_{c,i}[(...),\Lambda] + C^{10}_{c,i}[(...),\Lambda] + C^{01}_{c,i}[(...),\Lambda] - C^{11}_{c,i}[(...),\Lambda]\right]\,. \tag{8.20e}$$

3. The number N of gaussian terms present in the central part is to be determined. The usual Gogny D1S interaction uses two gaussians with ranges $\mu_1 = 0.7$ fm and $\mu_2 = 1.2$ fm which might qualitatively be related to meson exchanges. In the present work, matrix elements of the vertex will be adjusted for each partial wave. Each gaussian term contributing to all partial waves (s-, p-, d-waves...)[10], it may turn out useful to increase the number of terms in the fitting procedure. However one has to remember that gaussian functions do not form an orthogonal basis of $\mathcal{L}^2(\mathbb{R}^+)$ thus, if many gaussians are used to represent a given function, the coupling constants and ranges can be somewhat arbitrary. This shows that extra care has to be used if variations of N are to be considered.

   The total number of parameters is $5N + 6$, that is 16 and 21 parameters for $N = 2$ and $N = 3$, respectively. This is to be compared with the number of parameters of standard NN interactions which is of the order of 40. This is the approximate number of free parameters

[9] There is an implicit Λ-dependence in the ranges μ_x.

[10] This is easily seen when performing the Taylor expansion around $r = 0$ of those terms.

that are needed for an accurate reproduction of experimental data, as shown by previous studies in the context of chiral effective field theory [597].

[bare(2)] level

A general restriction is to have a representation of $V_{\text{low}\,k}$ *as good as possible* with a number of gaussian terms *as little as possible*, in order to keep a physical interpretation of these terms (meson exchanges).

4. At the [bare(3)]/[$\rho\rho$]/[$\kappa\kappa$] levels, density dependencies are constrained from symmetry considerations. The invariance of the final energy density functional under rotations in real/isospin space requires that the functional is a scalar under those transformations. Thus, while the dependence on the scalar/isoscalar densities is unrestricted, one must form scalar products of vector/isovector densities in the functional[11].

5. As we presently omit the role of $v^{\overline{\text{NNN}}}$ in the pairing channel, the first step is to use $v^{[\text{bare}(2)]}_{\text{BDRS}}$ as the effective vertex $v^{\kappa\kappa}$. The latter will be further restricted to $S = 0, T = 1$ channels, which are responsible for pairing correlations in nuclei. For implementation purposes, one can thus write

$$v^{[\kappa\kappa]}_{\text{BDRS}}(\vec{r}\,) = \frac{1}{4}\sum_{i=1}^{2}\left[C^{10}_{c,i}[\Lambda] - C^{10}_{c,i}[\Lambda]\,P_\sigma - C^{10}_{c,i}[\Lambda]\,P_\tau + C^{10}_{c,i}[\Lambda]\,P_\sigma\,P_\tau\right] e^{-\frac{r^2}{\mu_i^2}}. \tag{8.21}$$

6. The starting vacuum NN and (averaged) NNN interactions are intrinsically non-local. This suggests that a proper representation of such non-locality might be a first step of interest. Indeed, while our final goal is to design a local effective vertex $v^{[\text{X}]}_{\text{BDRS}}$, an intermediate step dedicated to a detailed study of non-local components which provide information concerning parts that are left out in EDF approaches based on effective vertices.

8.4 Useful expressions for $v^{[\text{X}]}_{\text{BDRS}}$

In the following, expressions of $v^{[\text{X}]}_{\text{BDRS}}$ that will be necessary for the adjustment procedure are provided (i) in momentum space, (ii) for infinite nuclear matter, and (iii) expanded into partial waves. Only the results of the calculations that are detailed in appendix (Appendix E) are presented here.

8.4.1 Momentum space

The adjustment of $v^{[\text{X}]}_{\text{BDRS}}$ is done in momentum space where the plane wave basis is the natural basis of interest. We use the conventions outlined in Sec. 5.3.1, and the compact notation[12] for the coupling constants $C^{ST}_x[\rho_0(\vec{R}\,), \rho_1(\vec{R}\,), \vec{S}_0(\vec{R}\,), \vec{S}_1(\vec{R}\,), \Lambda] \equiv C^{ST}_x(\vec{R}, \Lambda)$. The spatial part of the matrix elements of the vertex becomes for the direct term

$$\begin{aligned}\langle \vec{k}_k\ \vec{k}_l|v^{[\text{X}]}_{\text{BDRS}}(\Lambda)|\vec{k}_i\ \vec{k}_j\rangle^{ST}_{\text{dir}} &= \int \mathrm{d}\vec{r}_1\,\mathrm{d}\vec{r}_2\,\mathrm{d}\vec{r}_3\,\mathrm{d}\vec{r}_4\,\langle \vec{k}_k\ \vec{k}_l|\vec{r}_1\ \vec{r}_2\rangle\, v^{[\text{X}]}_{\text{BDRS}}(\vec{r}_i, \vec{k}_i, \Lambda)\,\langle \vec{r}_3\ \vec{r}_4|\vec{k}_i\ \vec{k}_j\rangle\big|_{ST} \\ &= \int \mathrm{d}\vec{r}_1\,\mathrm{d}\vec{r}_2\,\langle \vec{k}_k\ \vec{k}_l|\vec{r}_1\ \vec{r}_2\rangle\, v^{[\text{X}]}_{\text{BDRS}}(\vec{r}, \vec{R}, \overleftarrow{k}\,', \overrightarrow{k}\,, \Lambda)\,\langle \vec{r}_1\ \vec{r}_2|\vec{k}_i\ \vec{k}_j\rangle\big|_{ST}\,,\end{aligned} \tag{8.22}$$

[11] The scalar product in spin/isospin space is defined through the usual cartesian scalar product of spin/isospin Pauli matrices.

[12] For the [bare(2)] implementation there is no $\vec{R}$-dependence of the coupling constants.

where the overlaps are

$$\langle \vec{k}_k\ \vec{k}_l | \vec{r}_1\ \vec{r}_2 \rangle = e^{-i\,\vec{k}_k\cdot\vec{r}_1}\, e^{-i\,\vec{k}_l\cdot\vec{r}_2}\,, \qquad \langle \vec{r}_3\ \vec{r}_4 | \vec{k}_i\ \vec{k}_j \rangle = e^{i\,\vec{k}_i\cdot\vec{r}_3}\, e^{i\,\vec{k}_j\cdot\vec{r}_4}\,. \tag{8.23}$$

Matrix elements for the direct terms of the central, spin-orbit and tensor parts read respectively[13]

$$\langle \vec{k}_k\ \vec{k}_l | v^{[\mathrm{X}]}_{\mathrm{BDRS}}(\Lambda) | \vec{k}_i\ \vec{k}_j \rangle^{ST}_{i,\mathrm{dir}} = (\mu_i\sqrt{\pi})^3 e^{-\frac{1}{4}\mu_i^2 q^2}\, \tilde{C}^{ST}_i(\vec{K}\,' - \vec{K}, \Lambda) \prod_S \prod_T \tag{8.24a}$$

$$\langle \vec{k}_k\ \vec{k}_l | v^{[\mathrm{X}]}_{\mathrm{BDRS}}(\Lambda) | \vec{k}_i\ \vec{k}_j \rangle^{S=1\,T}_{so,\mathrm{dir}} = i\,\frac{\mu_{so}^2\,(\mu_{so}\sqrt{\pi})^3}{2}\, e^{-\frac{1}{4}\mu_{so}^2 q^2}\, \tilde{C}^{ST}_i(\vec{K}\,' - \vec{K}, \Lambda) \times (\vec{\sigma}_1 + \vec{\sigma}_2)\cdot \vec{k}\,' \wedge \vec{k} \prod_{S=1} \prod_T \tag{8.24b}$$

$$\langle \vec{k}_k\ \vec{k}_l | v^{[\mathrm{X}]}_{\mathrm{BDRS}}(\Lambda) | \vec{k}_i\ \vec{k}_j \rangle^{S=1\,T}_{t,\mathrm{dir}} = -\,(\mu_t\sqrt{\pi})^3 \frac{\mu_t^4}{4}\, \tilde{C}^{ST}_t(\vec{K}\,' - \vec{K}, \Lambda) \times \left[3\,(\vec{\sigma}_1\cdot\vec{q})\,(\vec{\sigma}_2\cdot\vec{q}) - (\vec{\sigma}_2\cdot\vec{\sigma}_2)\ q^2\right]\, e^{-\frac{1}{4}\mu_t^2\, q^2} \prod_{S=1} \prod_T, \tag{8.24c}$$

where $\tilde{C}^{ST}_i(\vec{K}\,' - \vec{K}, \Lambda)$ is the Fourier transform of the coupling constant

$$\tilde{C}^{ST}_i(\vec{K}\,' - \vec{K}, \Lambda) = \int \mathrm{d}\vec{R}\, e^{-i\,\vec{R}\cdot(\vec{K}\,' - \vec{K}\,)} C^{ST}_i(\vec{R}, \Lambda)\,. \tag{8.25}$$

In the [bare(2)] case, one has typically

$$\langle \vec{k}_k\ \vec{k}_l | v^{[\mathrm{bare(2)}]}_{\mathrm{BDRS}}(\Lambda) | \vec{k}_i\ \vec{k}_j \rangle^{ST}_{i,dir} = (\mu_i\sqrt{\pi})^3 e^{-\frac{1}{4}\mu_i^2 q^2} C^{ST}_i[\Lambda]\,(2\pi)^3\,\delta(\vec{K}\,' - \vec{K}\,) \prod_S \prod_T, \tag{8.26}$$

since the couplings are independent of $\vec{R}$ in this strategy.

8.4.2 Infinite matter: vertices

In-medium dependencies of $v^{[\mathrm{X}]}_{\mathrm{BDRS}}$ must be appropriately specified. We will directly write the expression of the effective vertex in the case of spin/isospin symmetric nuclear matter, where density-dependent strengths only depend on the scalar-isoscalar density ρ_0. In this case the coupling constants become independent of $\vec{R}$, thus

$$\tilde{C}^{ST}_i(\vec{K}\,' - \vec{K}, \Lambda) = C^{ST}_i[\rho_0, \Lambda]\,(2\pi)^3\,\delta(\vec{K}\,' - \vec{K}\,).$$

The effective vertex can therefore be written in momentum space as

$$\langle \vec{k}_k\ \vec{k}_l | v^{[\mathrm{X}]}_{\mathrm{BDRS}}(\Lambda) | \vec{k}_i\ \vec{k}_j \rangle \equiv \delta(\vec{K} - \vec{K}\,')\, v^{[\mathrm{X}]}_{\mathrm{BDRS}}(\vec{k}\,', \vec{k}, \Lambda), \tag{8.27}$$

[13] Exchange terms are easily computed by changing $\vec{q}$ into $\vec{q}\,'$ in those expressions.

where, writing only the direct term, one has

$$v^{[\mathrm{X}]}_{\mathrm{BDRS}}(\vec{k}\,',\vec{k},\Lambda) = \sum_{i=1}^{N}\left[\sum_{ST}\frac{C_i^{ST}[\rho_0,\Lambda]}{(2\pi)^3}(\mu_i\sqrt{\pi})^3\,e^{-\frac{1}{4}\mu_i^2 q^2}\prod_S\prod_T\right] \tag{8.28a}$$

$$+\sum_T i\,\frac{C_{so}^{1T}[\rho_0,\Lambda]}{(2\pi)^3}\frac{\mu_{so}^2(\mu_{so}\sqrt{\pi})^3}{2}e^{-\frac{1}{4}\mu_{so}^2 q^2}\,(\vec{\sigma}_1+\vec{\sigma}_2)\cdot\vec{k}\,'\wedge\vec{k}\prod_{S=1}\prod_T \tag{8.28b}$$

$$-\sum_T\frac{C_t^{1T}[\rho_0,\Lambda]}{(2\pi)^3}\frac{\mu_t^4(\mu_t\sqrt{\pi})^3}{4}\left[3\,(\vec{\sigma}_1\cdot\vec{q})\,(\vec{\sigma}_2\cdot\vec{q})-(\vec{\sigma}_1\cdot\vec{\sigma}_2)\;q^2\right]\,e^{-\frac{1}{4}\mu_t^2 q^2}\prod_{S=1}\prod_T\,. \tag{8.28c}$$

8.4.3 Infinite matter: correlation energy

With gaussian (effective) vertices, the computation of SNM/PNM equations of state can be done exactly, without a (truncated) partial wave summation. It can be proven that these two methods are rigorously equivalent (see Appendix D). One considers a gaussian vertex restricted to a central term[14]

$$v(\vec{r}\,) = \sum_{ST}\sum_i C_i^{ST}[\rho_0]\,e^{-\frac{r^2}{\mu_i^2}}\prod_S\prod_T \equiv \sum_{ST}\sum_i v_i^{ST}(\vec{r}\,)\prod_S\prod_T, \tag{8.29}$$

containing, if necessary, density-dependent couplings, depending only on ρ_0 in the present work. The potential energy reads after some manipulations

$$\begin{aligned}E^V(k_F^n,k_F^p) =& A\sum_{S\,T}[S]\,C_i^{ST}[\rho_0]\sum_{M_T}\sum_{q_1\,q_2}\sum_i\langle\tfrac{1}{2}\tfrac{1}{2}\,q_1q_2|T\,M_T\rangle^2\\ &\times\left[\frac{1}{48\sqrt{\pi}}\left(\frac{X_i^{q_1}\,X_i^{q_2}}{X_i}\right)^3-(-1)^{S+T}\frac{1}{8\sqrt{\pi}}\frac{F(X_i^{q_1},X_i^{q_2})}{X_i^3}\right]\\ =&\frac{A}{8\sqrt{\pi}}\sum_{S\,T}[S]\sum_i\frac{C_i^{ST}[\rho_0]}{X_i^3}\left[\frac{1}{6}\left(T\,X_i^{n6}+T\,X_i^{p6}+(X_i^n\,X_i^p)^3\right)\right.\\ &\left.-(-1)^{S+T}\left(T\,F(X_i^n,X_i^n)+T\,F(X_i^p,X_i^p)+\frac{F(X_i^n,X_i^p)+F(X_i^p,X_i^n)}{2}\right)\right],\end{aligned} \tag{8.30}$$

where

$$X_i^{q_j} = \mu_i\,k_F^{q_j}\,, \tag{8.31a}$$

$$I(X_i^{q_1},X_i^{q_2}) = \frac{\pi^2}{6}\left(\frac{2}{\mu_i}\right)^6 F(X_i^{q_1},X_i^{q_2})\,, \tag{8.31b}$$

$$\begin{aligned}F(X,Y) =& e^{-\left(\frac{X+Y}{2}\right)^2}(X^2+Y^2-XY-2)-e^{-\left(\frac{X-Y}{2}\right)^2}(X^2+Y^2+XY-2)\,,\\ &+\frac{\sqrt{\pi}}{2}\,\mathrm{erf}\left(\frac{X+Y}{2}\right)(X^3+Y^3)+\frac{\sqrt{\pi}}{2}\,\mathrm{erf}\left(\frac{X-Y}{2}\right)(X^3-Y^3)\end{aligned} \tag{8.31c}$$

$$\mathrm{erf}(X) = \frac{2}{\sqrt{\pi}}\int_0^X \mathrm{d}u\,e^{-u^2}\,. \tag{8.31d}$$

[14] As recalled in Sec. 7.4.3, spin-orbit and tensor do not contribute to the binding energy of spin-saturated INM.

Symmetric matter

One has for symmetric matter $X_i^n = X_i^p = X_i$, and

$$F(X_i, X_i) = e^{-X_i^2}(X_i^2 - 2) - 3\,X_i^2 + 2 + \sqrt{\pi}\,\mathrm{erf}(X_i)\,X_i^3\,. \tag{8.32}$$

The potential energy is then

$$\frac{E^V}{A}(k_F) = \sum_{S\,T} \frac{1}{8\sqrt{\pi}}\,[S]\,[T] \sum_i C_i^{ST}[\rho_0] \left[\frac{X_i^3}{6} - (-1)^{S+T}\frac{F(X_i, X_i)}{X_i^3}\right]. \tag{8.33}$$

for which the (S, T) decomposition is explicit.

Neutron matter

Likewise for neutron matter $X_i^{n3} = 2\,X_i^3$, $X_i^p = 0$, and

$$F(X_i, 0) = F(0, X_i) = F(0, 0) = 0\,. \tag{8.34}$$

The potential energy is then

$$\frac{E^V}{A}(k_F^n) = \sum_S \frac{1}{4\sqrt{\pi}}\,[S] \sum_i C_i^{S1}[\rho_0] \left[\frac{X_i^{n3}}{6} + (-1)^S\frac{F(X_i^n, X_i^n)}{X_i^{n3}}\right]. \tag{8.35}$$

8.4.4 Partial wave decomposition

Since $v_{\rm BDRS}$ has a similar structure to the Gogny effective force, we provide here momentum-space partial-wave decompositions for both of them in the framework of Sec. 5.3.2. This might be useful in the case where one tries to apply the same fitting protocol of $v_{\rm BDRS}$ to directly construct (non-empirical) forces that are strictly restricted to the original Gogny form. As explained, the separation into independent J channels in the case of microscopic effective vertices relies on an angular averaging of the Pauli operator [562; 567; 568] which we suppose to be accurate here.

The following functions are used

$$\frac{\tilde{g}_0^i(k,k')}{4\pi} \equiv \frac{e^{-\frac{1}{4}\mu_i^2\,(k^2+k'^2)}}{\Gamma_i}\,\mathrm{sh}(\Gamma_i) \tag{8.36a}$$

$$\frac{\tilde{g}_1^i(k,k')}{4\pi\sqrt{3}} \equiv -\frac{e^{-\frac{1}{4}\mu_i^2\,(k^2+k'^2)}}{\Gamma_i^2}\big[\Gamma_i\,\mathrm{ch}(\Gamma_i) - \mathrm{sh}(\Gamma_i)\big] \tag{8.36b}$$

$$\frac{\tilde{g}_2^i(k,k')}{4\pi\sqrt{5}} \equiv \frac{e^{-\frac{1}{4}\mu_i^2\,(k^2+k'^2)}}{\Gamma_i^3}\big[-3\Gamma_i\,\mathrm{ch}(\Gamma_i) + (3+\Gamma_i^2)\mathrm{sh}(\Gamma_i)\big] \tag{8.36c}$$

$$\frac{\tilde{g}_3^i(k,k')}{4\pi\sqrt{7}} \equiv -\frac{e^{-\frac{1}{4}\mu_i^2\,(k^2+k'^2)}}{\Gamma_i^4}\big[\Gamma_i\,(15+\Gamma_i^2)\,\mathrm{ch}(\Gamma_i) - 3\,(5+2\Gamma_i^2)\mathrm{sh}(\Gamma_i)\big] \tag{8.36d}$$

$$\frac{\tilde{g}_4^i(k,k')}{4\pi\sqrt{9}} \equiv \frac{e^{-\frac{1}{4}\mu_i^2\,(k^2+k'^2)}}{\Gamma_i^5}\big[-5\Gamma_i\,(21+2\Gamma_i^2)\mathrm{ch}(\Gamma_i) + (105+45\Gamma_i^2+\Gamma_i^4)\mathrm{sh}(\Gamma_i)\big] \tag{8.36e}$$

$$\frac{\tilde{g}_5^i(k,k')}{4\pi\sqrt{11}} \equiv -\frac{e^{-\frac{1}{4}\mu_i^2\,(k^2+k'^2)}}{\Gamma_i^6}\big[\Gamma_i\,(945+105\Gamma_i^2+\Gamma_i^4)\mathrm{ch}(\Gamma_i) - 15(63+28\Gamma_i^2+\Gamma_i^4)\mathrm{sh}(\Gamma_i)\big] \tag{8.36f}$$

$$\Gamma_i \equiv \frac{1}{2}\,\mu_i^2\,kk'. \tag{8.36g}$$

8.4.4.1 D1X/D2 interactions

One finds for the first partial waves

$$v_{\mathrm{D1X/D2}}({}^1S_0,k,k') = \frac{1}{2\pi^2}\sum_{i=1}^{2}(\mu_i\sqrt{\pi})^3\,\frac{\tilde{g}_0^i(k',k)}{4\pi}\,[W_i - B_i - H_i + M_i] + 2\,t_0\,\rho_0^\alpha\,(1-x_0)\,, \tag{8.37a}$$

$$v_{\mathrm{D1X/D2}}({}^3S_1,k,k') = \frac{1}{2\pi^2}\sum_{i=1}^{2}(\mu_i\sqrt{\pi})^3\,\frac{\tilde{g}_0^i(k',k)}{4\pi}\,[W_i + B_i + H_i + M_i] + 2\,t_0\,\rho_0^\alpha\,(1+x_0)\,, \tag{8.37b}$$

$$v_{\mathrm{D1X/D2}}({}^1P_1,k,k') = -\frac{1}{2\pi^2}\sum_{i=1}^{2}(\mu_i\sqrt{\pi})^3\,\frac{\tilde{g}_1^i(k',k)}{4\pi\sqrt{3}}\,[W_i - B_i + H_i - M_i]\,, \tag{8.37c}$$

$$v_{\mathrm{D1X/D2}}({}^3P_0,k,k') = -\frac{1}{2\pi^2}\sum_{i=1}^{2}(\mu_i\sqrt{\pi})^3\,\frac{\tilde{g}_1^i(k',k)}{4\pi\sqrt{3}}\,[W_i + B_i - H_i - M_i] + \frac{8}{3}\,W_{LS}\,kk'\,, \tag{8.37d}$$

$$v_{\mathrm{D1X/D2}}({}^3P_1,k,k') = -\frac{1}{2\pi^2}\sum_{i=1}^{2}(\mu_i\sqrt{\pi})^3\,\frac{\tilde{g}_1^i(k',k)}{4\pi\sqrt{3}}\,[W_i + B_i - H_i - M_i] + \frac{4}{3}\,W_{LS}\,kk'\,, \tag{8.37e}$$

$$v_{\mathrm{D1X/D2}}({}^3P_2,k,k') = -\frac{1}{2\pi^2}\sum_{i=1}^{2}(\mu_i\sqrt{\pi})^3\,\frac{\tilde{g}_1^i(k',k)}{4\pi\sqrt{3}}\,[W_i + B_i - H_i - M_i] - \frac{4}{3}\,W_{LS}\,kk'\,, \tag{8.37f}$$

$$v_{\mathrm{D1X/D2}}({}^1D_2,k,k') = \frac{1}{2\pi^2}\sum_{i=1}^{2}(\mu_i\sqrt{\pi})^3\,\frac{\tilde{g}_2^i(k',k)}{4\pi\sqrt{5}}\,[W_i - B_i - H_i + M_i]\,, \tag{8.37g}$$

$$\begin{aligned} v_{\mathrm{D1X/D2}}({}^3D_1,k,k') &= v_{\mathrm{D1X/D2}}({}^3D_2,k,k') = v_{\mathrm{D1X/D2}}({}^3D_3,k,k') \\ &= \frac{1}{2\pi^2}\sum_{i=1}^{2}(\mu_i\sqrt{\pi})^3\,\frac{\tilde{g}_2^i(k',k)}{4\pi\sqrt{5}}\,[W_i + B_i + H_i - M_i]\,, \end{aligned} \tag{8.37h}$$

Equivalently, for D2

$$v_{\mathrm{D2}}({}^1S_0,k,k') = \frac{1}{2\pi^2}\sum_{i=1}^{3}(\mu_i\sqrt{\pi})^3\,\frac{\tilde{g}_0^i(k',k)}{4\pi}\,[W_i - B_i - H_i + M_i]\,, \tag{8.38a}$$

$$v_{\mathrm{D2}}({}^3S_1,k,k') = \frac{1}{2\pi^2}\sum_{i=1}^{3}(\mu_i\sqrt{\pi})^3\,\frac{\tilde{g}_0^i(k',k)}{4\pi}\,[W_i + B_i + H_i + M_i]\,, \tag{8.38b}$$

$$v_{\mathrm{D2}}({}^1P_1,k,k') = -\frac{1}{2\pi^2}\sum_{i=1}^{3}(\mu_i\sqrt{\pi})^3\,\frac{\tilde{g}_1^i(k',k)}{4\pi\sqrt{3}}\,[W_i - B_i + H_i - M_i]\,, \tag{8.38c}$$

$$v_{\mathrm{D2}}({}^3P_0,k,k') = -\frac{1}{2\pi^2}\sum_{i=1}^{3}(\mu_i\sqrt{\pi})^3\,\frac{\tilde{g}_1^i(k',k)}{4\pi\sqrt{3}}\,[W_i + B_i - H_i - M_i] + \frac{8}{3}\,W_{LS}\,kk'\,, \tag{8.38d}$$

$$v_{\mathrm{D2}}({}^3P_1,k,k') = -\frac{1}{2\pi^2}\sum_{i=1}^{3}(\mu_i\sqrt{\pi})^3\,\frac{\tilde{g}_1^i(k',k)}{4\pi\sqrt{3}}\,[W_i + B_i - H_i - M_i] + \frac{4}{3}\,W_{LS}\,kk'\,, \tag{8.38e}$$

$$v_{\mathrm{D2}}({}^3P_2,k,k') = -\frac{1}{2\pi^2}\sum_{i=1}^{3}(\mu_i\sqrt{\pi})^3\,\frac{\tilde{g}_1^i(k',k)}{4\pi\sqrt{3}}\,[W_i + B_i - H_i - M_i] - \frac{4}{3}\,W_{LS}\,kk'\,, \tag{8.38f}$$

$$v_{\mathrm{D2}}({}^1D_2,k,k') = \sum_{i=1}^{3}(\mu_i\sqrt{\pi})^3\,\frac{\tilde{g}^i_2(k',k)}{4\pi\sqrt{5}}\,[W_i - B_i - H_i + M_i]\,, \tag{8.38g}$$

$$\begin{aligned} v_{\mathrm{D2}}({}^3D_1,k,k') =& v_{\mathrm{D2}}({}^3D_2,k,k') = v_{\mathrm{D2}}({}^3D_3,k,k') \\ =& \frac{1}{2\pi^2}\sum_{i=1}^{3}(\mu_i\sqrt{\pi})^3\,\frac{\tilde{g}^i_2(k',k)}{4\pi\sqrt{5}}\,[W_i + B_i + H_i - M_i]\,, \end{aligned} \tag{8.38h}$$

with the convention that components $\tilde{g}^3_\lambda(k',k)$ include an extra ρ_0^α factor, to simplify the notations.

8.4.4.2 BDRS vertex

We give here all channels needed to evaluate matrix elements and phase shifts up to $L = 2$. Note that evaluating scattering phase shifts in the coupled ${}^3\mathrm{P}_2$ channel requires matrix elements in the ${}^3\mathrm{P}_2$, ${}^3\mathrm{F}_2$ and coupled ${}^3\mathrm{P}_2$-${}^3\mathrm{F}_2 = \epsilon_2$ channels (see Sec. 5.3.3). Equivalently for the ${}^3\mathrm{D}_3$ channel one needs matrix elements in the ${}^3\mathrm{D}_3$, ${}^3\mathrm{G}_3$ and coupled ${}^3\mathrm{D}_3$-${}^3\mathrm{G}_3 = \epsilon_3$ channels.

One finds

$$v^{[\mathrm{X}]}_{\mathrm{BDRS}}({}^1S_0,k,k') = \frac{1}{2\pi^2}\sum_{i=1}^{N} C_i^{01}[\rho_0,\Lambda]\,(\mu_i\sqrt{\pi})^3\,\frac{\tilde{g}^i_0(k',k)}{4\pi}\,, \tag{8.39a}$$

$$v^{[\mathrm{X}]}_{\mathrm{BDRS}}({}^3S_1,k,k') = \frac{1}{2\pi^2}\sum_{i=1}^{N} C_i^{10}[\rho_0,\Lambda]\,(\mu_i\sqrt{\pi})^3\,\frac{\tilde{g}^i_0(k',k)}{4\pi}\,, \tag{8.39b}$$

$$v^{[\mathrm{X}]}_{\mathrm{BDRS}}({}^1P_1,k,k') = \frac{1}{2\pi^2}\sum_{i=1}^{N} C_i^{00}[\rho_0,\Lambda]\,(\mu_i\sqrt{\pi})^3\,\frac{\tilde{g}^i_1(k',k)}{4\pi\sqrt{3}}\,, \tag{8.39c}$$

$$\begin{aligned} v^{[\mathrm{X}]}_{\mathrm{BDRS}}({}^3P_0,k,k') =& \frac{1}{2\pi^2}\sum_{i=1}^{N} C_i^{11}[\rho_0,\Lambda]\,(\mu_i\sqrt{\pi})^3\,\frac{\tilde{g}^i_1(k',k)}{4\pi\sqrt{3}} \\ &+ 4\,\frac{1}{2\pi^2}\,C^{11}_{so}[\rho_0,\Lambda]\,\frac{\mu_{so}^2\,(\mu_{so}\sqrt{\pi})^3}{2}\,kk'\left[\frac{1}{3}\,\frac{\tilde{g}^{so}_0(k',k)}{4\pi} - \frac{1}{3}\,\frac{\tilde{g}^{so}_2(k',k)}{4\pi\sqrt{5}}\right] \\ &- \frac{1}{2\pi^2}\,C^{11}_t[\rho_0,\Lambda]\,\frac{\mu_t^4\,(\mu_t\sqrt{\pi})^3}{4} \\ &\qquad\times\frac{4}{3}\left[5\,\frac{\tilde{g}^t_0(k',k)}{4\pi}\,kk' + 3\,(k^2+k'^2)\,\frac{\tilde{g}^t_1(k',k)}{4\pi\sqrt{3}} + \frac{\tilde{g}^t_2(k',k)}{4\pi\sqrt{5}}\,kk'\right]\,, \end{aligned} \tag{8.39d}$$

$$\begin{aligned} v^{[\mathrm{X}]}_{\mathrm{BDRS}}({}^3P_1,k,k') =& \frac{1}{2\pi^2}\sum_{i=1}^{N} C_i^{11}[\rho_0,\Lambda]\,(\mu_i\sqrt{\pi})^3\,\frac{\tilde{g}^i_1(k',k)}{4\pi\sqrt{3}} \\ &+ 2\,\frac{1}{2\pi^2}\,C^{11}_{so}[\rho_0,\Lambda]\,\frac{\mu_{so}^2\,(\mu_{so}\sqrt{\pi})^3}{2}\,kk'\left[\frac{1}{3}\,\frac{\tilde{g}^{so}_0(k',k)}{4\pi} - \frac{1}{3}\,\frac{\tilde{g}^{so}_2(k',k)}{4\pi\sqrt{5}}\right] \\ &- \frac{1}{2\pi^2}\,C^{11}_t[\rho_0,\Lambda]\,\frac{\mu_t^4\,(\mu_t\sqrt{\pi})^3}{4} \\ &\qquad\times\frac{2}{3}\left[5\,\frac{\tilde{g}^t_0(k',k)}{4\pi}\,kk' + 3\,(k^2+k'^2)\,\frac{\tilde{g}^t_1(k',k)}{4\pi\sqrt{3}} + \frac{\tilde{g}^t_2(k',k)}{4\pi\sqrt{5}}\,kk'\right]\,, \end{aligned} \tag{8.39e}$$

$$
\begin{aligned}
v^{[\mathrm{X}]}_{\mathrm{BDRS}}({}^3P_2,k,k') =& \frac{1}{2\pi^2}\sum_{i=1}^{N} C_i^{11}[\rho_0,\Lambda]\,(\mu_i\sqrt{\pi})^3\,\frac{\tilde{g}_1^i(k',k)}{4\pi\sqrt{3}} \\
&- 2\,\frac{1}{2\pi^2}\,C_{so}^{11}[\rho_0,\Lambda]\,\frac{\mu_{so}^2\,(\mu_{so}\sqrt{\pi})^3}{2}\,kk'\left[\frac{1}{3}\,\frac{\tilde{g}_0^{so}(k',k)}{4\pi}-\frac{1}{3}\,\frac{\tilde{g}_2^{so}(k',k)}{4\pi\sqrt{5}}\right] \\
&- \frac{1}{2\pi^2}\,C_t^{11}[\rho_0,\Lambda]\,\frac{\mu_t^4\,(\mu_t\sqrt{\pi})^3}{4} \\
&\qquad\times\frac{2}{15}\left[5\,\frac{\tilde{g}_0^t(k',k)}{4\pi}\,kk'+3\,(k^2+k'^2)\,\frac{\tilde{g}_1^t(k',k)}{4\pi\sqrt{3}}+\frac{\tilde{g}_2^t(k',k)}{4\pi\sqrt{5}}\,kk'\right],
\end{aligned}
\tag{8.39f}
$$

$$
v^{[\mathrm{X}]}_{\mathrm{BDRS}}({}^1D_2,k,k') = \frac{1}{2\pi^2}\sum_{i=1}^{N} C_i^{01}[\rho_0,\Lambda]\,(\mu_i\sqrt{\pi})^3\,\frac{\tilde{g}_2^i(k',k)}{4\pi\sqrt{5}}\,,
\tag{8.39g}
$$

$$
\begin{aligned}
v^{[\mathrm{X}]}_{\mathrm{BDRS}}({}^3D_1,k,k') =& \frac{1}{2\pi^2}\sum_{i=1}^{N} C_i^{10}[\rho_0,\Lambda]\,(\mu_i\sqrt{\pi})^3\,\frac{\tilde{g}_2^i(k',k)}{4\pi\sqrt{5}} \\
&- 6\,\frac{1}{2\pi^2}\,C_{so}^{10}[\rho_0,\Lambda]\,\frac{\mu_{so}^2\,(\mu_{so}\sqrt{\pi})^3}{2}\,\frac{kk'}{5}\,\left[\frac{\tilde{g}_1^{so}(k',k)}{4\pi\sqrt{3}}-\frac{\tilde{g}_3^{so}(k',k)}{4\pi\sqrt{7}}\right] \\
&+ \frac{1}{2\pi^2}\,C_t^{10}[\rho_0,\Lambda]\,\frac{\mu_t^4\,(\mu_t\sqrt{\pi})^3}{4} \\
&\qquad\times\frac{2}{5}\left[7\,kk'\,\frac{\tilde{g}_1^t(k',k)}{4\pi\sqrt{3}}+5(k^2+k'^2)\frac{\tilde{g}_2^t(k',k)}{4\pi\sqrt{5}}+3\,kk'\,\frac{\tilde{g}_3^t(k',k)}{4\pi\sqrt{7}}\right],
\end{aligned}
\tag{8.39h}
$$

$$
\begin{aligned}
v^{[\mathrm{X}]}_{\mathrm{BDRS}}({}^3D_2,k,k') =& \frac{1}{2\pi^2}\sum_{i=1}^{N} C_i^{10}[\rho_0,\Lambda]\,(\mu_i\sqrt{\pi})^3\,\frac{\tilde{g}_2^i(k',k)}{4\pi\sqrt{5}} \\
&- 2\,\frac{1}{2\pi^2}\,C_{so}^{10}[\rho_0,\Lambda]\,\frac{\mu_{so}^2\,(\mu_{so}\sqrt{\pi})^3}{2}\,\frac{kk'}{5}\,\left[\frac{\tilde{g}_1^{so}(k',k)}{4\pi\sqrt{3}}-\frac{\tilde{g}_3^{so}(k',k)}{4\pi\sqrt{7}}\right] \\
&+ \frac{1}{2\pi^2}\,C_t^{10}[\rho_0,\Lambda]\,\frac{\mu_t^4\,(\mu_t\sqrt{\pi})^3}{4} \\
&\qquad\times\frac{2}{5}\left[7\,kk'\,\frac{\tilde{g}_1^t(k',k)}{4\pi\sqrt{3}}+5(k^2+k'^2)\frac{\tilde{g}_2^t(k',k)}{4\pi\sqrt{5}}+3\,kk'\,\frac{\tilde{g}_3^t(k',k)}{4\pi\sqrt{7}}\right],
\end{aligned}
\tag{8.39i}
$$

$$
\begin{aligned}
v^{[\mathrm{X}]}_{\mathrm{BDRS}}({}^3D_3,k,k') =& \frac{1}{2\pi^2}\sum_{i=1}^{N} C_i^{10}[\rho_0,\Lambda]\,(\mu_i\sqrt{\pi})^3\,\frac{\tilde{g}_2^i(k',k)}{4\pi\sqrt{5}} \\
&+ 4\,\frac{1}{2\pi^2}\,C_{so}^{10}[\rho_0,\Lambda]\,\frac{\mu_{so}^2\,(\mu_{so}\sqrt{\pi})^3}{2}\,\frac{kk'}{5}\,\left[\frac{\tilde{g}_1^{so}(k',k)}{4\pi\sqrt{3}}-\frac{\tilde{g}_3^{so}(k',k)}{4\pi\sqrt{7}}\right] \\
&+ \frac{1}{2\pi^2}\,C_t^{10}[\rho_0,\Lambda]\,\frac{\mu_t^4\,(\mu_t\sqrt{\pi})^3}{4} \\
&\qquad\times\frac{4}{35}\left[7\,kk'\,\frac{\tilde{g}_1^t(k',k)}{4\pi\sqrt{3}}+5(k^2+k'^2)\frac{\tilde{g}_2^t(k',k)}{4\pi\sqrt{5}}+3\,kk'\,\frac{\tilde{g}_3^t(k',k)}{4\pi\sqrt{7}}\right],
\end{aligned}
\tag{8.39j}
$$

$$
\begin{aligned}
v^{[\mathrm{X}]}_{\mathrm{BDRS}}({}^3F_2,k,k') =& \frac{1}{2\pi^2}\sum_{i=1}^{N} C_i^{11}[\rho_0,\Lambda]\,(\mu_i\sqrt{\pi})^3\,\frac{\tilde{g}_3^i(k',k)}{4\pi\sqrt{5}} \\
&+\frac{1}{2\pi^2}\,C_{so}^{11}[\rho_0,\Lambda]\,\frac{\mu_{so}^2\,(\mu_{so}\sqrt{\pi})^3}{2}\,kk'\,\frac{8}{7}\left[\frac{\tilde{g}_2^{so}(k',k)}{4\pi\sqrt{5}}-\frac{\tilde{g}_4^{so}(k',k)}{4\pi\sqrt{9}}\right] \\
&-\frac{1}{2\pi^2}\,C_t^{11}[\rho_0,\Lambda]\,\frac{\mu_t^4\,(\mu_t\sqrt{\pi})^3}{4} \\
&\qquad\times\frac{8}{35}\left[9\,kk'\,\frac{\tilde{g}_2^t(k',k)}{4\pi\sqrt{5}}+7(k^2+k'^2)\frac{\tilde{g}_3^t(k',k)}{4\pi\sqrt{7}}+5\,kk'\,\frac{\tilde{g}_4^t(k',k)}{4\pi\sqrt{9}}\right],
\end{aligned}
\tag{8.39k}
$$

$$
\begin{aligned}
v^{[\mathrm{X}]}_{\mathrm{BDRS}}({}^3G_3,k,k') =& \frac{1}{2\pi^2}\sum_{i=1}^{N} C_i^{10}[\rho_0,\Lambda]\,(\mu_i\sqrt{\pi})^3\,\frac{\tilde{g}_4^i(k',k)}{4\pi\sqrt{5}} \\
&-\frac{1}{2\pi^2}\,C_{so}^{10}[\rho_0,\Lambda]\,\frac{\mu_{so}^2\,(\mu_{so}\sqrt{\pi})^3}{2}\,kk'\,\frac{10}{9}\left[\frac{\tilde{g}_3^{so}(k',k)}{4\pi\sqrt{7}}-\frac{\tilde{g}_5^{so}(k',k)}{4\pi\sqrt{11}}\right] \\
&+\frac{1}{2\pi^2}\,C_t^{10}[\rho_0,\Lambda]\,\frac{\mu_t^4\,(\mu_t\sqrt{\pi})^3}{4} \\
&\qquad\times\frac{10}{63}\left[11\,kk'\,\frac{\tilde{g}_3^t(k',k)}{4\pi\sqrt{7}}+9(k^2+k'^2)\frac{\tilde{g}_4^t(k',k)}{4\pi\sqrt{9}}+7\,kk'\,\frac{\tilde{g}_5^t(k',k)}{4\pi\sqrt{11}}\right],
\end{aligned}
\tag{8.39l}
$$

$$
\begin{aligned}
v^{[\mathrm{X}]}_{\mathrm{BDRS}}(\epsilon_1,k,k') =& -\frac{1}{2\pi^2}\,C_t^{10}[\rho_0,\Lambda]\,\frac{\mu_t^4\,(\mu_t\sqrt{\pi})^3}{4} \\
&\times\;4\sqrt{2}\left[\frac{1}{2}\,k^2\,\frac{\tilde{g}_0^t(k',k)}{4\pi}+kk'\,\frac{\tilde{g}_1^t(k',k)}{4\pi\sqrt{3}}+\frac{1}{2}\,k'^2\,\frac{\tilde{g}_2^t(k',k)}{4\pi\sqrt{5}}\right],
\end{aligned}
\tag{8.39m}
$$

$$
\begin{aligned}
v^{[\mathrm{X}]}_{\mathrm{BDRS}}(\epsilon_2,k,k') =& +\frac{1}{2\pi^2}\,C_t^{11}[\rho_0,\Lambda]\,\frac{\mu_t^4\,(\mu_t\sqrt{\pi})^3}{4} \\
&\times\frac{12\sqrt{6}}{5}\left[\frac{1}{2}\,k^2\,\frac{\tilde{g}_1^t(k',k)}{4\pi\sqrt{3}}+kk'\,\frac{\tilde{g}_2^t(k',k)}{4\pi\sqrt{5}}+\frac{1}{2}\,k'^2\,\frac{\tilde{g}_3^t(k',k)}{4\pi\sqrt{7}}\right],
\end{aligned}
\tag{8.39n}
$$

$$
\begin{aligned}
v^{[\mathrm{X}]}_{\mathrm{BDRS}}(\epsilon_3,k,k') =& -\frac{1}{2\pi^2}\,C_t^{10}[\rho_0,\Lambda]\,\frac{\mu_t^4\,(\mu_t\sqrt{\pi})^3}{4} \\
&\times\frac{24\sqrt{3}}{7}\left[\frac{1}{2}\,k^2\,\frac{\tilde{g}_2^t(k',k)}{4\pi\sqrt{5}}+kk'\,\frac{\tilde{g}_3^t(k',k)}{4\pi\sqrt{7}}+\frac{1}{2}\,k'^2\,\frac{\tilde{g}_4^t(k',k)}{4\pi\sqrt{9}}\right],
\end{aligned}
\tag{8.39o}
$$

where the coupling constants are independent of ρ_0 in the [bare(2)] case.

8.5 Adjustment procedure

We provide now general guidelines concerning the adjustement procedure, remembering that observables of interest are different for the different realizations of $v^{[\mathrm{X}]}_{\mathrm{BDRS}}$.

As already mentioned, the underlying purpose behind the construction of $v^{[\mathrm{X}]}_{\mathrm{BDRS}}$ is to adjust bare/effective vertices on microscopic inputs rather than on experimental data, in order to gain predictive power in unknown regions of the nuclear chart. In that respect, the free parameters $Y_i^{[\mathrm{X}]}$ will be adjusted on specific properties of $V_{\mathrm{low}\,k}$ or effective in-medium interactions computed from $V_{\mathrm{low}\,k}$ in MBPT at various levels of complexity (see Sec. 8.2). Correspondingly, several strategies have to be devised regarding which observables are taken as inputs in the fit procedure.

What is crucial is that the adjustment is done at the **vertex** level in all cases, which allows to adjust at the same time the central, spin-orbit and tensor terms. This is at variance with possible strategies using only non-spin-polarized quantities such as the INM EOS to which tensor and spin-orbit components do not contribute. Typically, all $L \leq 2$ partial waves, corresponding to the main interaction channels, will be kept in the procedure. Indeed, as seen in Sec. 8.4.4, $S = 1$ and $L > 1$ waves are sensitive to both spin-orbit and tensor coupling. One sees here the need to carefully choose the variables of interest in the fitting protocol. If one only uses matrix elements, the parameters $Y_i^{[\mathrm{X}]}$ are chosen to minimize the deviation, or chi-square

$$\chi^2 = \sum_{LL'SJT} \sum_{i,j} \left[\frac{\left(v^{[\mathrm{X}]}\right)_{LL'}^{JST} (k_i, k_j; \Lambda, [...]) - \left(v_{\mathrm{BDRS}}^{[\mathrm{X}]}\right)_{LL'}^{JST} (k_i, k_j; Y_i^{[\mathrm{X}]}, [...])}{\left(\delta v^{[\mathrm{X}]}\right)_{LL'}^{JST} (k_i, k_j; \Lambda, [...])} \right]^2 , \tag{8.40}$$

where the first sum runs over the chosen set of partial waves, and the second one correspond to the discretized mesh $\{k_i\}$ over which $V_{\mathrm{low}\,k}$ is sampled. Likewise $v^{[\mathrm{X}]}$ stands for the two-body vertex at the appropriate level of MBPT complexity, that is (i) $v^{[\mathrm{X}]} = V_{\mathrm{low}\,k}$ for $[\mathrm{X}] = [\mathrm{bare}(2)]$, (ii) $v^{[\mathrm{X}]} = V_{\mathrm{low}\,k} + \overline{\mathrm{NNN}}$ for $[\mathrm{X}] = [\mathrm{bare}(3)]$, and (iii) $v^{[\mathrm{X}]}$ comes from MBPT calculations for $[\mathrm{X}] = [\rho\rho]/[\kappa\kappa]$. Note that the latter are not necessarily restricted to second order in particle-particle ladders as the full sum might also be considered[15]. Additionally, the chi square function is weighted by tolerances margins $\left(\delta v^{[\mathrm{X}]}\right)_{LL'}^{JST}$ that are yet to be explicited. The latter will allow to put constraints on specific regions of the (k, k') space provided by an a priori knowledge of the underlying physics. For instance, adding more weight on diagonal matrix elements will improve the reproduction of fully on-shell quantities such as scattering phase shifts or the nuclear matter equation of state.

As a second step, additional constraints can be put into the total merit function of Eq. (8.40). For instance, in the [bare(2)] case, the cost function can be complemented by a similar chi square on the scattering phase shifts or on deuteron properties (binding energies, radius...). In the present work, we chose to focus on the reproduction of the matrix elements. The next chapter is dedicated to the algorithm that we are using to find optimal values for the effective ranges and coupling constants.

[15] For small values of the RG cutoff Λ the ladder series is converged at second order, whereas it is not the case for larger values where the hard core is not completely renormalized by the RG flow.

Chapter 9

Stochastic model optimization in large dimension space

Abstract: This chapter presents the fitting techniques that are used for the optimization of the free parameters of $v_{\mathrm{BDRS}}^{[\mathrm{X}]}$. The presentation is given in a model-independent framework, that is for a generic merit function. The method is based on an hybridation between a local search algorithm and a stochastic phase space exploration using genetic techniques, which are briefly presented. The corresponding FITPACK library is validated on a few standard test cases. In a second step, scaling properties, in particular with respect to the genetic population size and the dimensionality, suggest that parallelization might be needed for very complex problems, e.g. large number of variables to be optimized. Two different methods are discussed, i.e. simplex parallelization or island-parallel genetic algorithm, implemented in the FITPACK environment, and profiled. Finally, post-analysis techniques that allow to define stochastic error bars are also introduced.

Contents

9.1 Introduction **239**
9.2 Nelder-Mead method **241**
9.3 Canonical genetic algorithms **245**
9.4 Simplex-coded genetic algorithms **247**
9.5 The fitpack fit module **250**
9.5.1 Efficiency benchmarking 250
9.5.2 Performance optimization 252
9.5.2.1 Brute-force parallelization 253
9.5.2.2 Island-parallel genetic algoritm 259
9.6 Confidence intervals **263**
9.6.1 Linear model 263
9.6.2 Non-linear model 265

9.1 Introduction

Data modeling is common in many domains, e.g. applied or theoretical science, or finance. Many algorithms are available to solve such optimization problems, usually recast in terms of minimization of a merit, or cost, function [182; 598–602]. While some of them are specifically taylored to the problem they are applied to, techniques can be generically decomposed into (i)

downhill-based methods which follow local gradients/neighboring values of the merit function to reach its minimum (Powell's, conjugate gradient, quasi-Newton techniques...), and (ii) combinatorial/continuous techniques (e.g. simulated annealing [603–605]), depending on whether the phase space allowed for the parameters to be optimized is discrete or continuous, which make use of random jumps to prevent premature convergence in secondary minima. The latter is one of the most serious problems that arise for model optimization. Indeed, while standard gradient-based algorithms are adequate in the case of simple cost functions, they find their limits when the global optimum of a cost function (i) is hardly distinguishable from many secondary minima, or (ii) corresponds to a very narrow phase space region that is not reached when following local gradients. As exemplified in Fig. 9.1, the result of simple algorithms will then depend on the initialization point, which becomes a limiting factor in high dimensionality[1], even using impulsion-conserving downhill methods, that are able to prevent premature convergence in metastable secondary minima. On the contrary, genetic algorithms [606; 607] (GAs) based on stochastic exploration of the phase space can handle complex merit functions, but at a numerical cost. Their ability to treat very different complex problems makes them ideal candidates for the purpose of this work.

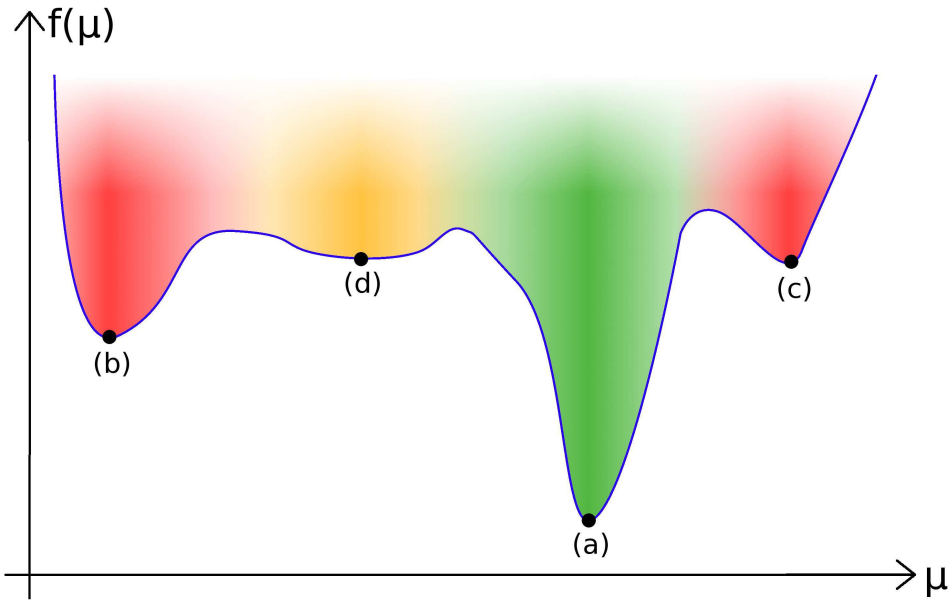

Figure 9.1: Illustration of the limitations of very simple optimization techniques for a 1D cost function f depending on one parameter μ to be adjusted that possesses (i) one global minimum (a), (ii) a metastable minimum (d), and (iii) two stable secondary minima (b-c). Depending on the starting point of a minimization algorithm based on a simple downhill method, the optimal minimum (i) can be found in any case (green region), (ii) might be reached using impulsion-based techniques to overcome the metastable minimum (orange region), or (iii) will never be found, as the algorithm will be stuck in secondary minima (red region).

The solution which has been retained exploits the strengths of both approaches. It consists in combining (i) a stochastic cost-driven exploration of the phase space by means of a genetic

[1] Indeed, the best approach would consist in taking starting points sampling uniformly the phase space, but this is out of question in high dimensionality since the evaluation time would scale exponentially with the number of free parameters.

algorithm, which globally moves the search area, and (ii) a local minimum search based on the simplex/Nelder-Mead algorithm [608] (SA), which locally explores the phase space around the region defined at the level of (i). Both of these approaches are briefly introduced in Sec. 9.2 and Sec. 9.3, before their hybridation is discussed in Sec. 9.4 and results for standard benchmarks are presented.

The optimization problem will be generically reduced to the optimization of a merit function

$$f \equiv f_N^P \equiv f_{\{\mu\}}(X_1 \dots X_N)\,, \tag{9.1}$$

which depends on N variables $\{X_1 \dots X_N\}$ and a set $\{\mu\} = \{\mu_1 \dots \mu_P\}$ of P continuous parameters to be adjusted. When necessary, the global extremum of f will be noted $\hat{\mu}$. One defines a diagrammatic representation of a given algorithm using the following building blocks

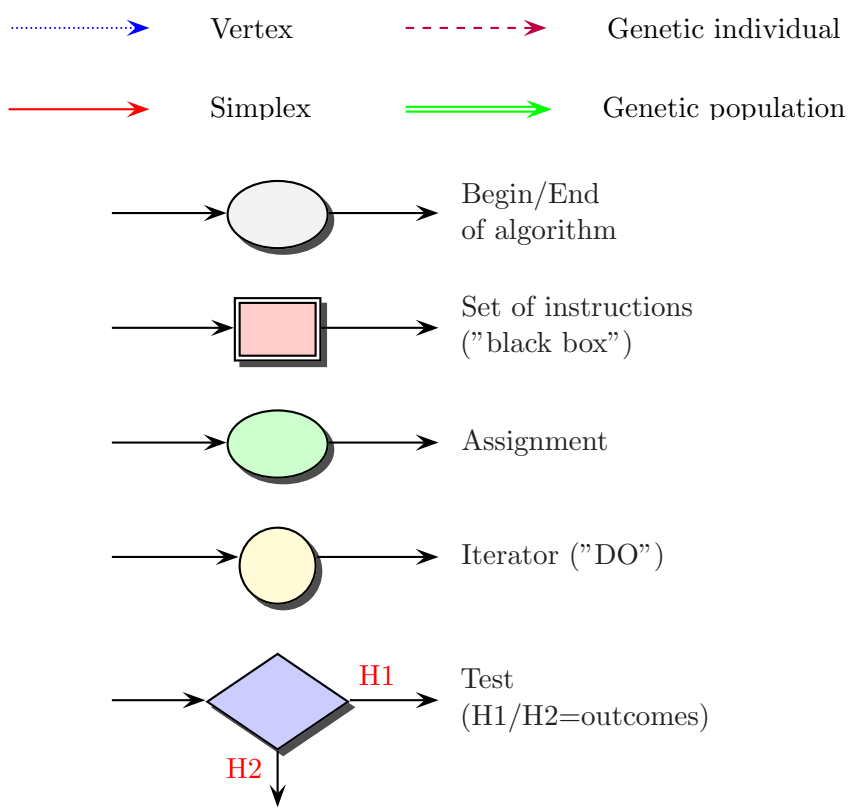

Figure 9.2: Diagrams for a flow representation of an algorithm.

We acknowledge that function optimization constitutes by itself a whole field of study, and the following chapter is obviously non-exhaustive on such a subject. For instance, many variations are possible for a given algorithm, most of the time regarding specific features of the cost function. We only present here general aspects, and we refer the reader to review papers in Ref. [609] for more information.

9.2 Nelder-Mead method

The simplex algorithm (SA) performs a local function optimization by requiring only evaluations of the merit function f, in contrary to other downhill-base approaches that also requires the

computation of derivatives of f, such as Powell's algorithm. Additionally, it allows a continuous optimization up to an arbitrary precision, in contrary to canonical genetic algorithms (see Sec. 9.3). The trade-off is that simplex-based minimization involves a lot of evaluations and might not be the most cost-efficient approach for problems where the evaluation of f is the limiting factor.

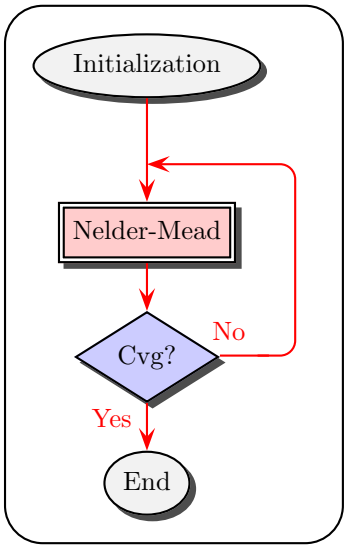

Figure 9.3: Diagramatic representation of the simplex algorithm.

The algorithm defined in Fig. 9.3 consists in evolving a volume, the "simplex", delimited by $P+1$ points $P_i \in \mathbb{R}^{P+1}$ called vertices such that (i) the simplex volume ultimately goes to zero, and (ii) the global optimum of the cost function is maintained within the simplex, such that in the end a high-precision approximation of $\hat{\mu}$ is easily defined from the final vertices. It can be represented as the repeated application of the Nelder-Mead algorithm [608; 610], as in Fig. 9.4. The latter consists in applying elementary steps to a given simplex that define additional points, which are kept or discarded depending on whether they correspond to decreasing or increasing the cost function. It depends on four parameters, i.e. (i) the reflexion coefficient $\rho > 0$ (typ. 1), (ii) the expansion coefficient $\chi > 1$ (typ. 2), (iii) the contraction coefficient $0 < \gamma < 1$ (typ. 0.5), and (iv) the shrinkage coefficient $0 < \sigma < 1$ (typ. 0.5).

More precisely, elementary operations, illustrated in Fig. 9.5 in the two-dimension case[2], are defined as

- **order** consists in sorting the vertices $\{P_1 \dots P_{P+1}\}$ according to the cost function, e.g. $f(P_1) < f(P_2) < \dots < f(P_{P+1})$,
- **reflect** computes the reflected point P_r of the worst vertex with respect to the centroid $\bar{P}$ of the P best ones, i.e.

$$P_r = \bar{P} + \rho(\bar{P} - P_{P+1})\,, \qquad \bar{P} = \frac{1}{P}\sum_{i=1}^{P} P_i\,. \tag{9.2}$$

  The reflected point P_r replaces then P_{P+1} if it corresponds to a better value of f. Otherwise one goes to the next step,

[2]Meaning that two parameters μ_1 and μ_2 must be fitted, and a simplex can be represented as a triangle.

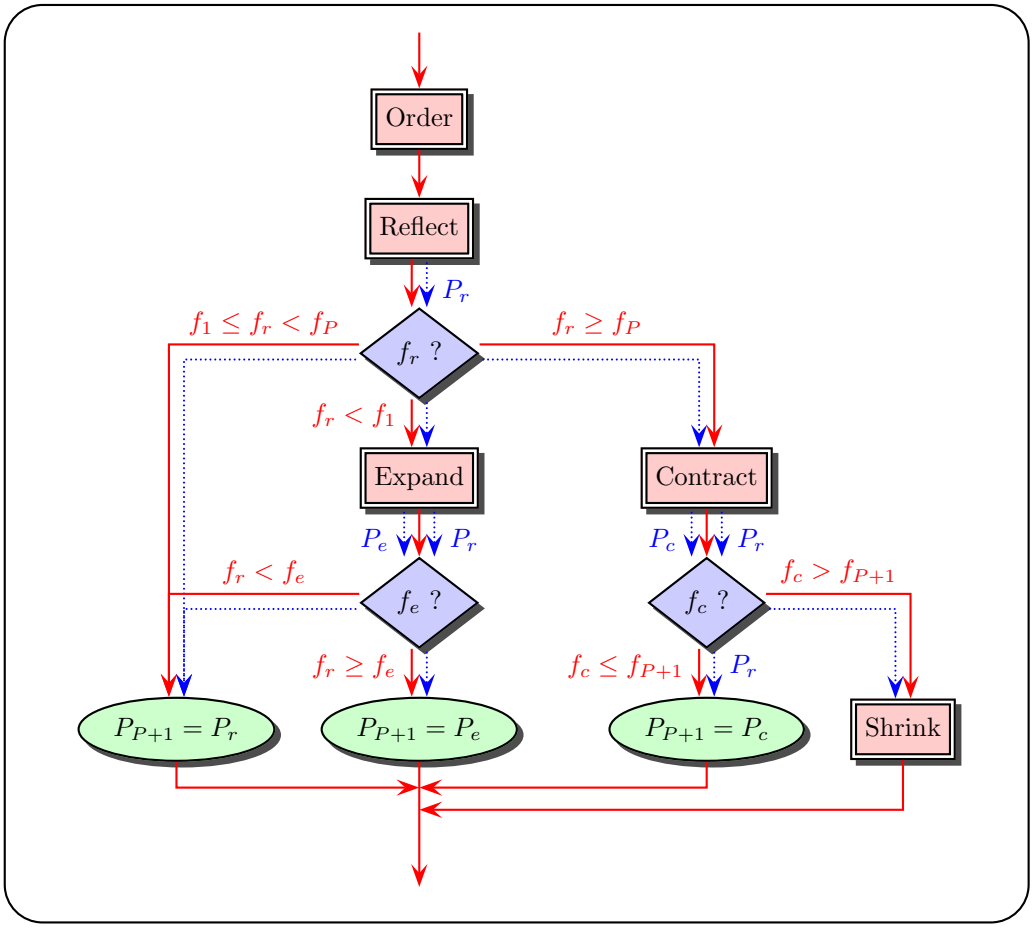

Figure 9.4: Diagramatic representation of the elemetary Nelder-Mead step involved in the simplex algorithm.

- **expand** computes the expansion point P_e from P_r if the reflected point was better than the best vertex P_1 in terms of f, i.e.

$$P_e = \bar{P} + \chi(P_r - \bar{P})\,. \tag{9.3}$$

  The expanded point P_e replaces then P_{P+1} if it corresponds to a better value of f. This corresponds to the situation where the global minimum of f was not included in the initial simplex, in which case one tries to move it towards a more accurate search region. Otherwise one will continue to the next step,

- **contraction** tries to reduce the simplex overall volume, with respect to the best vertex between P_r and P_{P+1}, that it tries to move this vertex towards the centroid $\bar{P}$, by defining the inner or outer contracted points as

$$P_c \equiv P_{oc/ic} = \bar{P} + \gamma(P_{r/P+1} - \bar{P})\,. \tag{9.4}$$

  These points replace P_{P+1}, that is the simplex shrinks with respect to the worst vertex if they correspond to better solutions than P_{P+1},

- if none of the operations presented above have led to an update of the inital simplex, it means that P_1 is already very close to the global minimum of f in comparison with the

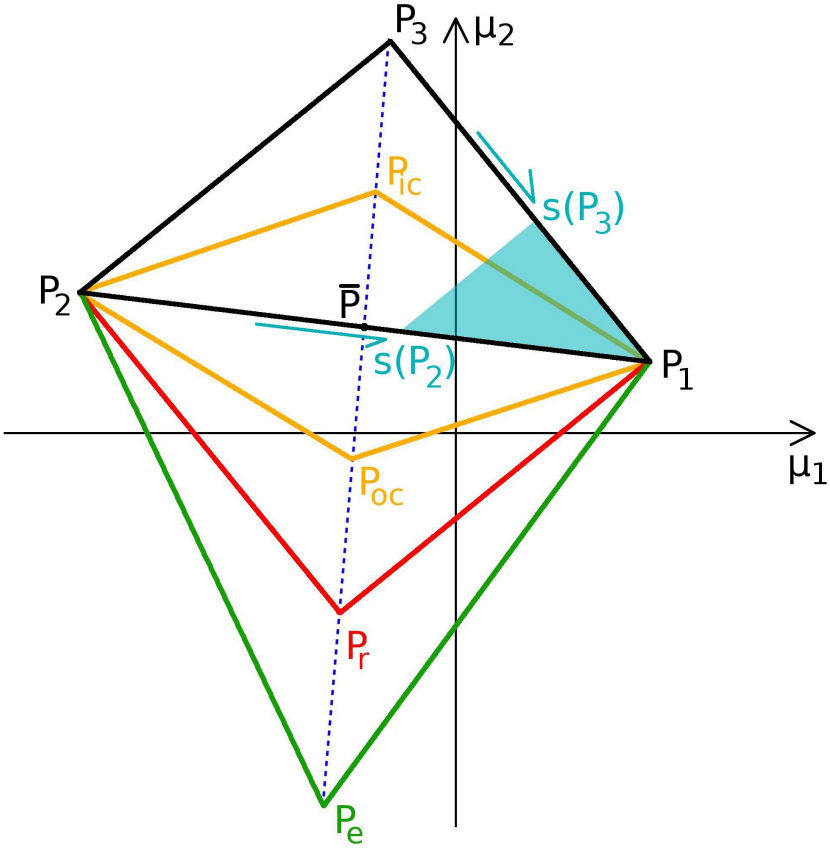

Figure 9.5: Elementary steps of the Nelder-Mead algorithm in two dimensions.

other vertices, in which case the **shrink** step corresponds to reducing the simplex volume by moving each vertex towards P_1, i.e.

$$\forall i = 2 \dots P+1\,, \qquad P_i = s(P_i) = P_1 + \sigma(P_i - P_1)\,. \tag{9.5}$$

Finally, the convergence criteria to end the algorithm is usually taken as a comparison of the distance between the best and worst vertices of the simplex $f(P_{P+1}) - f(P_1)$ with a convergence criterion ϵ.

While the Nelder-Mead algorithm works very well for simple models, in the presence of complex cost functions its convergence becomes very dependent on the simplex initialization, which leads to low success probabilities as the program is easily trapped in secondary minima. The latter is illustrated in Tab. {9.3}, where the probability of success of the latter algorithm is evaluated for common benchmarking cost functions that are recalled in Appendix F.1. They correspond to different classes of problems, i.e. (i) functions with one ($f_1 - f_6$), several ($f_{16} - f_{22}$) or many ($f_7 - f_{15}$) secondary minima (unimodal or multimodal functions), (ii) sharp or smooth cost functions around the global extremum, and (iii) the dimensionality n of the problem. Values that are used for the initial search space are large enough to catch the complexity of the problem, and the simplex algorithm is restarted 250 times with a random initialization of the starting simplex within this space.

The simplex algorihm finds its limits when the merit profile becomes complex and many local traps are present. Even for quite simple problems ($f_4 - f_6$) convergence is only reached for some cases, while for the most difficult problems the global optimum is almost never reached.

The latter illustrates the limits of the simplex algorithm for complex optimization problems, where the probability of success depends on the actual cost function. This constitutes therefore a non-efficient solution for a versatile fitting procedure.

9.3 Canonical genetic algorithms

Genetic algorithms rely on an analogy with natural selection, that is "survival of the fittest" [606; 607]. In this context, it can be summarized as follows:

> A population of several individuals evolves according to a given fitness function. At each generation they reproduce and partly transmit their genome to their offspring. Finally, the offspring can randomly mutate, leading to the apparition of new phenotypes. In all cases, only the best individuals will survive in the next generation, such that the overall fitness of the population increases.

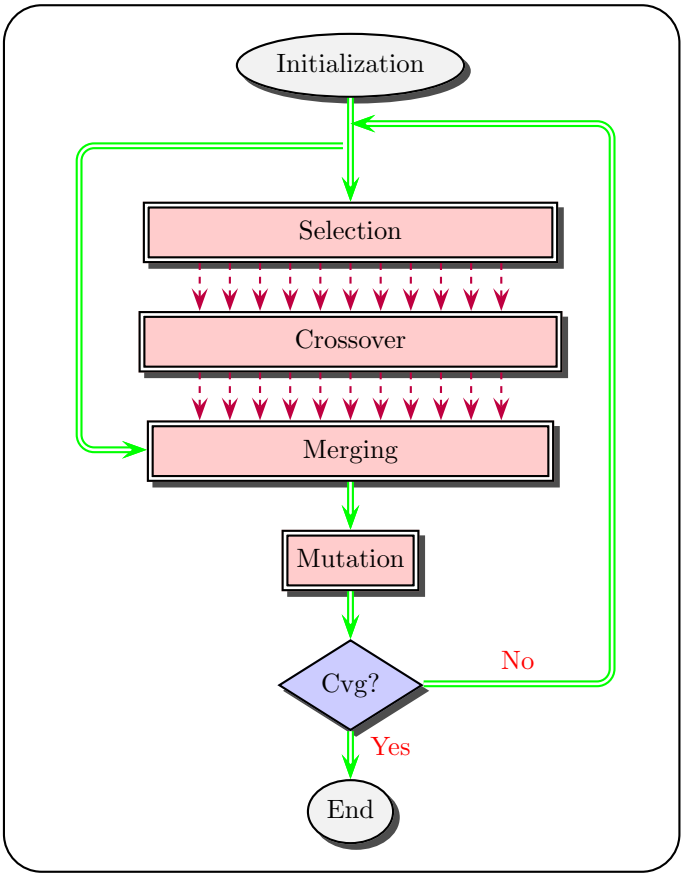

Figure 9.6: Diagramatic representation of a generic algorithm.

Thus genetic algorithms consists in evolving a given population such that only the best phenotypes, coming from reproduction and mutation operations, survive, and can be diagramatically represented as in Fig. 9.6. An implementation of a GA corresponds then to defining the elementary **mutation**, **reproduction** (**selection+crossover**) and **merging** procedures, which are summarized as follows.

- **Reproduction** selects two (or more) individuals based on their fitness (the more fit they are, the more likely they will be selected) that will reproduce with a given probability and generate new offsprings to which they transmit partly their own genotype.

- **Mutation** corresponds to a random change in one or several phenotypes, that will be carried on to the next generation only if they correspond to more fit individuals.
- **Merging** builds the next generation from existing individuals (initial population+offspring) by keeping only the more fit elements, and potentially including several biases, such that the aging of an individual or external migrations...

Function optimization is only one application of genetic techniques, and a whole field of computational science is dedicated to the use of evolutionary methods, such as genetic programming where the program used for solving a given problem is itself evolved towards an "optimal" solution, in terms of speed, efficiency... For fitting purposes, a genetic algorithm makes use of (i) a stochastic exploration of phase space provided by random mutations, in the sense that mutated individuals can constitute attractive points in unexplored areas, (ii) a natural selection of the best characterictics using reproduction phases in which one may build from two individuals a better one.

Canonical GAs correspond to combinatorial optimization problems, such as the traveling salesman[3], where the set of possible solutions is discrete. In this case, and to preserve a biological analogy, an individual is encoded into a binary sequence (a "gene")[4]. The elementary GA building blocks are defined as follows:

- **mutation** corresponds to bit flips at random positions and for randomly selected individuals with a given probability,

1	0	1	1	0	0	1	0	$\longrightarrow$	1	0	0	1	0	0	1	0
Normal Coding							178	$\longrightarrow$	146							
Grey Coding (standard)							210	$\longrightarrow$	227							

Table 9.1: Mutation step in a canonical genetic algorithm with binary encoding: several bits are randomly flipped. For illustration we show results using standard and Gray code embeddings [611].

Note that this justifies the use of Gray code [611–613] for the encoding rather than just a simple binary embedding. Indeed, Grey code has no boundary effect, i.e. any bit flip leads to a random increment in the decoded value, in contrary to canonical binary encoding where the magnitude of the change in the decoded value depends on the significance of the flipped bit, as illustrated by Tab. {9.1}. The latter lead to the phenomenon of *Hamming walls*, where to many simultaneous mutations are necessary to increase slightly the decoded value,

- **reproduction** consists in selecting two individuals in the genetic population, which are mated into two offsprings using binary crossovers, as illustrated in Tab. {9.2}. Several methods exist for the selection of mating individuals [614], e.g. roulette [615], tournament [616] or linear ranking[617; 618] selection, such that the selection process is usualy considered as an independent step of a GA. Likewise, multiple crossover methods can be envisioned (see Tab. {9.2}).

[3]The traveling salesman corresponds to the real-life situation where a salesman has to visit N towns V_i trying to optimize a specific cost function such as the minimal length of its journey, by adding specific requirement, e.g. reducing the number of times he has to cross a given river...

[4]For the traveling salesman problem for instance, this corresponds to encoding the sequence of visited towns.

Uniform single crossover

1	0	1	1	0	0	1	0		1	0	1	1	0	1	1	1
								$\longrightarrow$								
0	0	1	1	0	1	1	1		0	0	1	1	0	0	1	0

Uniform multiple crossover

1	0	1	1	0	0	1	0		0	0	1	1	0	1	1	1
								$\longrightarrow$								
0	0	1	1	0	1	1	1		1	0	1	1	0	0	1	0

Table 9.2: Crossover step in a canonical genetic algorithm with binary encoding: different possible methods.

- **merge** corresponds to building a new population with the same size than the initial one by keeping only the best fit individuals.

In comparison to standard downhill-based fitting methods, it can be proven that genetic algorithms always converge to the absolute minimum of a given merit function [619], given that the population evolves long enough and that *elitism* is enforced, that is the best individual of a given population always carries on to the next generation However, since they rely on a correlated evolution of several individuals, the number of evaluations of the cost function is drastically increased, which can lead to very expensive calculations.

9.4 Simplex-coded genetic algorithms

The application of canonical GAs to continuous optimization problems raises some issues, in particular when high-accuracy fitting is needed. Indeed, binary encoding has an intrinsic precision which depends on the number of bits used which corresponds therefore to the maximum precision to which adjusted parameters can be known ("genetic noise"). Likewise, while they can scan very rapidly large phase space regions, which is of very interest in high dimensionality, local search around a given minimum is quite slow. To bypass this, several solutions based on dynamic ranging of the encoding process can be used, e.g. dynamic parameter encoding [620], adaptive precision coding [621], fuzzy logic encoding [622–624], or stochastic coding [625]. In both cases, the continuous interval in which parameters are coded shrinks as the algorithm evolves. Another approach consists in using directly real-valued GAs, which requires a redefinition of the elementary operations. It is also possible to combine GAs with continuous optimization techniques that work up to an arbitrary precision, that is exploiting both the global search ability of GAs and efficient local search routines given by the complementary algorithm. Different approaches have been pursued so far with various local search techniques, such as Hopfield Neural Networks, dynamic hillclimbing [626], or messy genetic algorithm [627]. In all cases genetic techniques are now used in many domains, e.g. engineering science [628–634], simulation and stratagey in video games [635] or real-life situations [636; 637], scheduling problems [638; 639], stock market trading [640–642]...

Recent studies of nuclear resonances [643; 644] or bound state wave functions [645] by means of genetic algorithms constitute, to our knowledge, the first applications of GAs in theoretical nuclear physics. The solution that we have retained consists in using a local solver based on the simplex algorithm presented in Sec. 9.2, and the algorithm is presented in the following.

Different hybridations schemes between GAs and simplex algorithms are possible [646–650], depending on how the reproduction and mutation phases are defined. A memetic algorithm[5] derived from the simplex-coded genetic algorithm (SCGA) will be used [651]. It consists in exploration(GA)-exploitation(simplex) phases, where individuals and offsprings are improved at each generation to accelerate local convergence by a small number of Nelder-Mead iterations. The elementary GA building blocks are defined as follows.

- The genetic population is composed of M simplexes $\{P_1^j \dots P_{P+1}^j\}$, which act as individuals. At initialization they are randomly distributed within a given hypercube of $\mathbb{R}^P$. The fitness of an individual is then defined as the cost $f(P_1^{j0})$ of the best vertex in the associated simplex.

- Mutation consists in blowing up a simplex, that is spreading out all vertices from the best one with an arbitrary ratio τ

$$\forall i = 2 \dots P\,, j = 1 \dots M\,, \qquad P_i^j = P_1^j + \tau(P_i^j - P_1^j)\,. \tag{9.6}$$

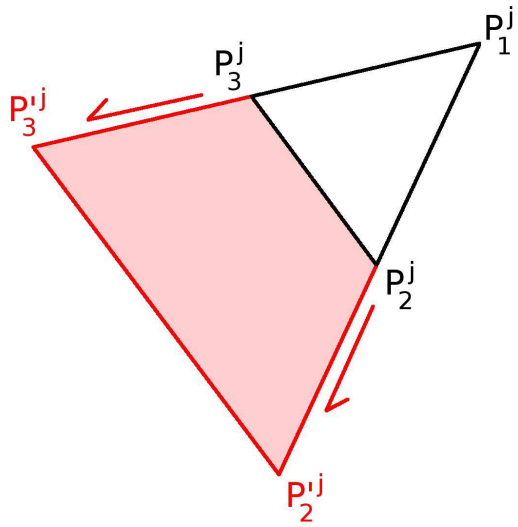

Figure 9.7: Mutation step in a hybrid genetic algorithm (black→red): a given simplex is blown up from its best vertex P_1^j.

- Crossover acts on a random number of simplexes selected by linear ranking up to a maximal value (typ. $2 \sim 6$) and generates new offsprings by creating simplexes within the space spanned by the initial ones. This follows the description of crossover phases in canonical GAs where the phenotypes of offsprings are randomly constructed from the initial ones.

[5] Memetic algorithms correspond to a synergy of evolutionary or any population-based approach with separate individual learning or local improvement procedures.

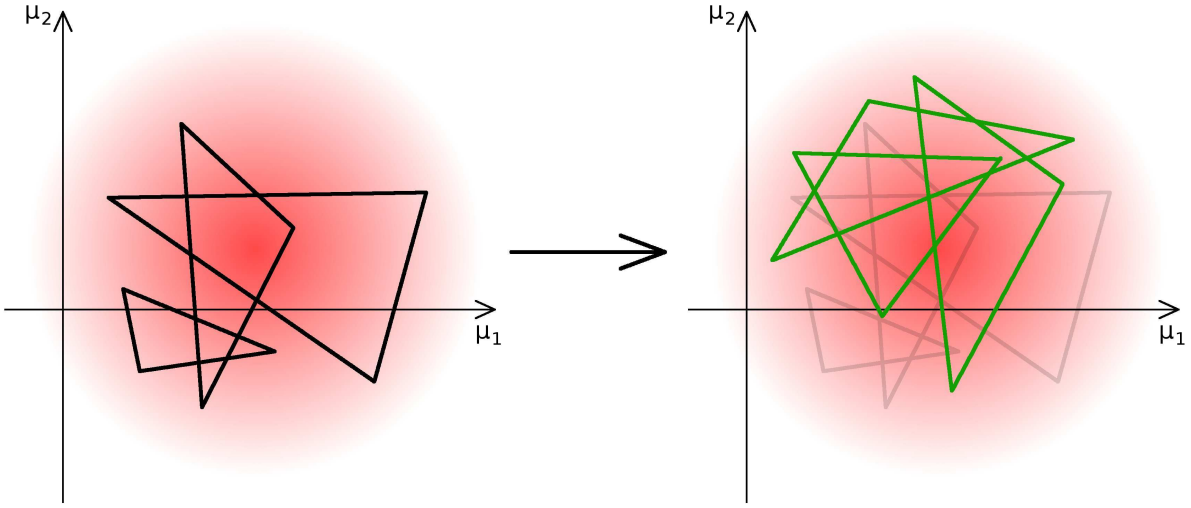

Figure 9.8: Crossover step in a hybrid genetic algorithm: new simplexes (green) are randomly resampled within the phase space (red) spanned by the initial ones (black).

- Convergence criteria are based on (i) the distance between the best and worst vertices of the best simplex $f(P_{P+1}^{j_0} - P_1^{j_0})$, and (ii) the dispersion of the merit among all simplexes.

Note that no binary encoding is used this approach, which prevents the apparition of genetic noise and allows to compute $\hat{\mu}$ up to an arbitrary precision.

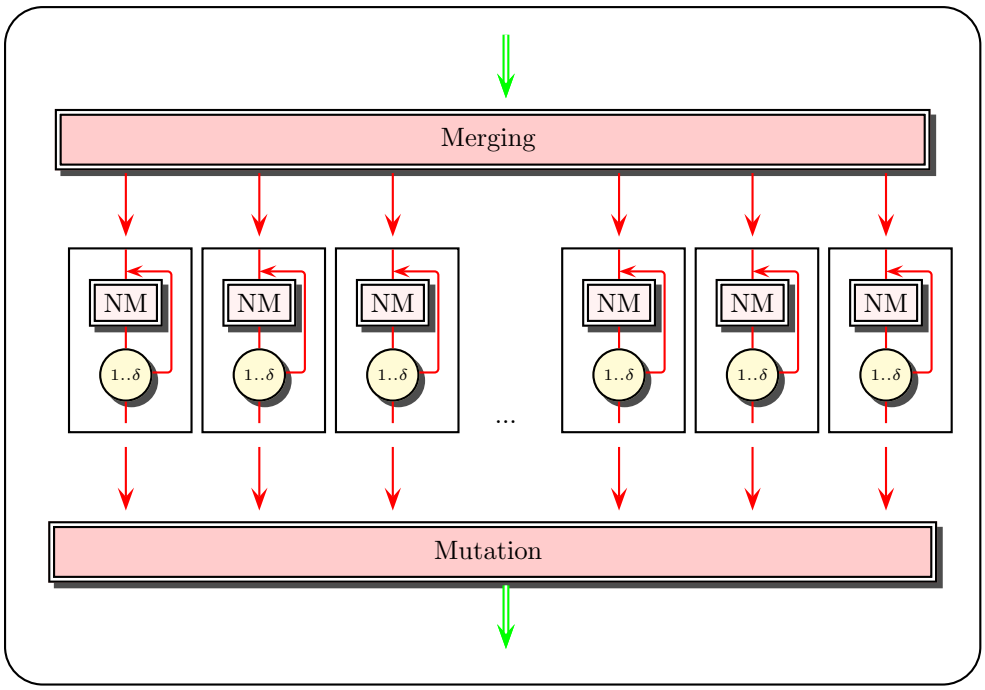

Figure 9.9: Diagramatic representation of the hybrid simplex-genetic algorithm. After the new population is generated from the initial individuals and their offsprings, each surviving simplex undergoes a small number δ of Nelder-Mead iterations to perform a local search.

9.5 The fitpack fit module

In collaboration with T. Lesinski, a complete fitting library called FITPACK has been coded and implements the algorithm previously presented. This program has been written in a model-independent framework, such that it can be applied to any kind of cost function provided in terms of a user-defined module.

Obviously a lot of variations are then possible, e.g. concerning the encoding process, the mutation phase... but we did not enter such details that would require a huge amount of work. Indeed, the results of this algorithm applied to the realistic situations that we will encounter are already very good.

This library has been written such that the core algorithm can be easily applied to different user-implemented situations, beyond the original purpose of fitting $v^{[X]}_{\mathrm{BDRS}}$, such as constrained HF/HFB calculations in multidimensional collective space.

9.5.1 Efficiency benchmarking

	P	SA success rate [%]	M	GA success rate [%]	$\bar{N}_{\mathrm{iters}}$
f_1	4	100.00	500	100.00	11
	10	100.00	500	100.00	17
	20	6.20	2000	100.00	21
f_2	4	100.00	500	100.00	10
	10	99.79	500	100.00	14
	20	15.00	2000	100.00	18
f_3	4	100.00	500	100.00	12
	10	100.00	500	100.00	34
	20	0.00	2000	100.00	71
f_4	4	24.80	500	100.00	25
	10	0.00	500	100.00	42
	20	0.00	2000	100.00	72
f_5	4	82.79	500	100.00	24
	10	48.79	500	100.00	149
	20	0.00	2000	100.00	298
f_6	4	46.20	500	100.00	10
	10	0.00	500	100.00	10
	20	0.00	2000	100.00	10
f_7	4	0.00	500	66.00	37
	10	0.00	500	0.00	16

Table 9.3: Convergence rate for the simplex and genetic algorithms for different optimization problems spanning different classes of cost functions (see text). $\bar{N}_{\mathrm{iters}}$ corresponds to the average number of iterations of FITPACK before convergence (absolute or premature) is reached.

	P	SA success rate [%]	M	GA success rate [%]	$\bar{N}_{\text{iters}}$
f_8	4	0.00	500	100.00	31
	10	0.00	500	0.00	89
f_9	4	0.60	500	100.00	16
	10	0.00	500	0.00	195
f_{10}	4	1.60	500	99.00	30
	10	0.00	500	0.00	330
f_{11}	4	0.00	500	100.00	24
	10	0.00	500	100.00	21
f_{12}	4	52.00	500	100.00	10
	10	12.19	500	100.00	14
f_{13}	4	15.40	500	100.00	11
	10	0.00	500	100.00	19
f_{14}	4	9.00	500	100.00	23
	10	0.00	500	99.20	66
f_{15}	2	0.20	500	100.00	10
f_{16}	2	87.20	500	100.00	10
f_{17}	2	100.00	500	100.00	10
f_{18}	4	38.00	500	100.00	11
f_{19}	4	38.39	500	100.00	11
f_{20}	4	37.00	500	100.00	11
f_{21}	2	2.60	500	100.00	10
f_{22}	4	39.60	500	100.00	16

Table 9.3: (Continued) Convergence rate for the simplex and genetic algorithms for different problems.

The efficiency of FITPACK in comparison with the simplex algorithm can be illustrated by evaluating the probability of success in the optimization of the different merit functions already used for benchmarking the simplex algorithm (SEC. 9.2) presented in Appendix F.1. One again, 250 fits are performed using these different classes of optimization problems, and results are presented in TAB. {9.3}. The population size used in each case is heuristic to keep a rather small computation time, and we can conjecture that increasing the latter size should increase the probability of success. Nevertheless, one sees that

- for quite simple problems ($f_1 - f_6$, $f_{16} - f_{22}$) the success is always guaranteed if the starting population is large enough,
- as the dimensionality of the problem increases, the probability of success decreases while increasing the genetic population size improves the former,
- even with reduced sets of individuals, FITPACK allows to find almost surely the global optimum of the functions $f_7 - f_{15}$ that correspond to a sampling of the most difficult optimization problems. The latter optimization becomes difficult in high dimensionality, as seen by the number of iterations required to achieve convergence, which suggests that large populations might be essential in this case. However (i) increasing the population size

limits the performance of FITPACK, as seen below, which suggest the use of parallelization strategies, and (ii) the cost functions $f_7 - f_{15}$ are much more complex than the realistic situations that we will encounter in the following.

9.5.2 Performance optimization

Disregarding convergence issues inferred in SEC. 9.5.1, FITPACK can find very quickly the optimal solution. However, in real-life situations several sources of inefficiencies must be considered.

- By construction, GAs require a lot of evaluations of the merit function. When the latter involves complex numerical calculations, for instance the computation of scattering phase shifts in our case, this drastically increases computation time.
- For cost functions with a lot of secondary minima and free parameters, the genetic population size has to be rather high, that is (i) combinatorial operations in the GA (selection, crossover...) become more and more limiting factors, since they scale as M^2, and (ii) it further increases the time spend to evaluate the cost function.
- When the number of parameters to be adjusted increases, the computation time increases because of intrinsic numerical combinatorics.

These issues are highlighted by performing benchmark calculations for various situations in which we adjusted (i) the dimensionality P of the problem, (ii) the size of the genetic population M, an (iii) the time Δt necessary for one evaluation of the merit function. In each case we computed the average time δt spent to perform (a) a complete iteration, and (b) the crossover, simplex, mutation and selection steps in FITPACK. The results presented in FIGS. (9.10,9.11,9.12) illustrate some intrinsic features and limitations of the simplex-genetic algorithm for very complex problems, i.e.

- most of the time is always spent performing simplex iterations[6]. The crossover and mutation phases almost do not contribute to the total computation time, which suggests that the optimization is very efficient, since FITPACK focuses on the actual minimization.
- the time spent per iteration scales linearly with the population size (FIG. 9.10) and the dimensionality (FIG. 9.11). The slope only depends on the computation time of the cost function, as it should be expected. When P and M increase, the time spend in genetic processes (crossover, selection and mutation) also increases because of combinatorics, but remains negligible in comparison with the simplex phase.
- on the contrary, the time spent per iteration scales as a power law with Δt, as seen in FIG. 9.12, While the computation time for genetic processes remains unchanged as Δt increases, as it could be expected.

These results suggest that the computation time in FITPACK scales linearly with P and M and exponentially with Δt, thus the latter is the limiting factor. On the other hand, very complex optimization problem correspond to high dimensionality and complex cost functions and require large populations to avoid local traps, which may severely impact the efficency of our algorithm.

This calls for parallelization strategies [652] that make use of high-performance computing facilities with computer grids that can handle thousands of threads in parallel. In the case of FITPACK two different strategies can be considered depending on the situation. We have

[6]The simplex evolution is actually split into two parts. Indeed, Nelder-Mead iterations are applied on (i) the offsprings from the crossover phase, and (ii) the total population after the merging. For simplicity we only represent in FIGS. (9.10,9.11,9.12) the time spent in the latter phase.

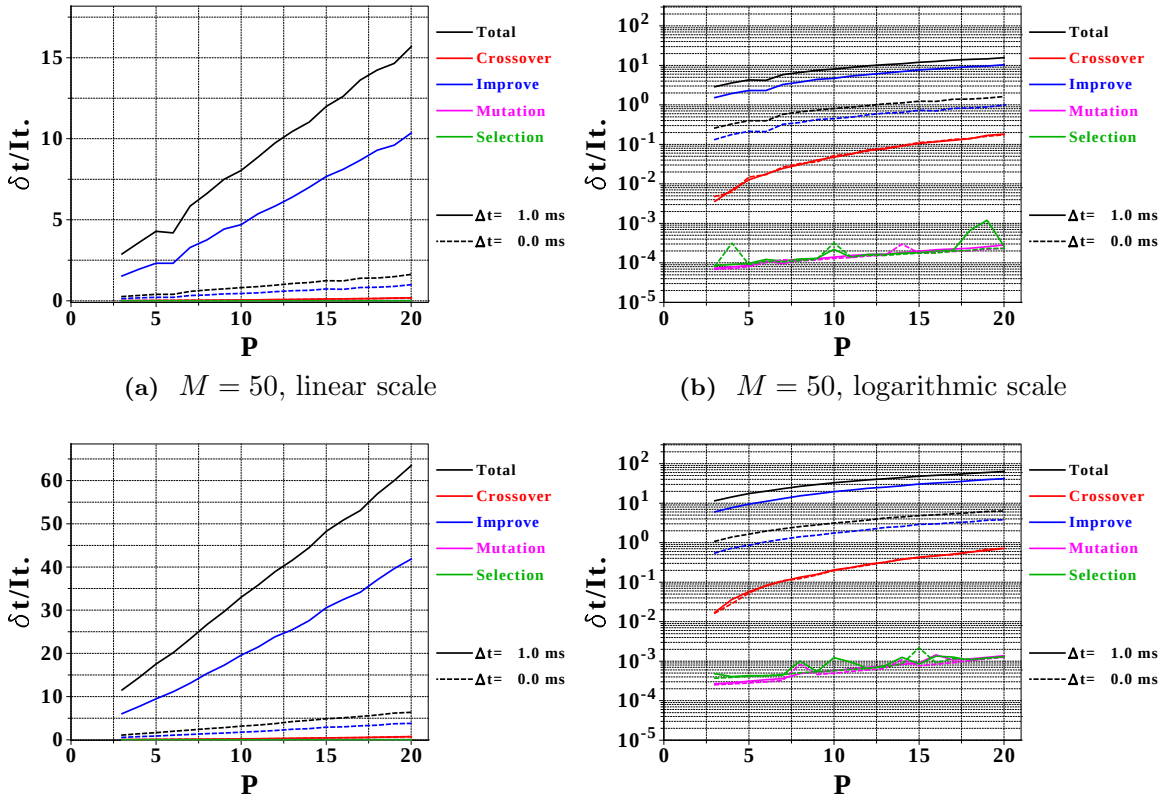

(a) $M = 50$, linear scale (b) $M = 50$, logarithmic scale

(c) $M = 200$, linear scale (d) $M = 200$, logarithmic scale

Figure 9.10: Scaling properties of FITPACK as a function of the dimensionality.

implemented both of them within FITPACK using the Message Passing Interface [653; 654] (MPI) libraries (OpenMPI [655] in the present case). MPI is a language-independent communications protocol which supports both point-to-point and collective communication between threads that evolve independently, that is distributed memory environments[7]. This is the tool of choice for using very large number of simultaneous threads, in comparison with OpenMP threaded shared memory where all threads can access the same memory but their number is limited by hardware architecture (typ. 8 maximum threads). In the following the content of a single thread will be diagramatically represented by a cross-hatched-filled framed box.

9.5.2.1 Brute-force parallelization

The simplest parallelization strategy consists in splitting the simplex evolutions between different CPUs, as illustrated in FIG. 9.13. In this scheme, a main ("father") thread handles the supervision of the whole process and the reproduction/crossover phases, but assigns to the other CPUs the simplex evolutions. The latter is best seen in FIGS. (9.14,9.16) which presents a communication flowchart in FITPACK using MPE profiling libraries and the JUMPSHOT 4.0 performance visualization utility [656], for a very simple cost function. In this case, four processes are used on the CCRT computer grid [657] (supercalculator in Bruyères-Le-Châtel), and one clearly recovers the flow chart from FIG. 9.13, i.e. the main thread assigns simplex evolutions to the remaining ones, but handles the rest of the algorithm (mutation, crossover).

[7]This corresponds to the case where each programs runs on its own private memory allocation and can only access the memory content of other threads by message passing.

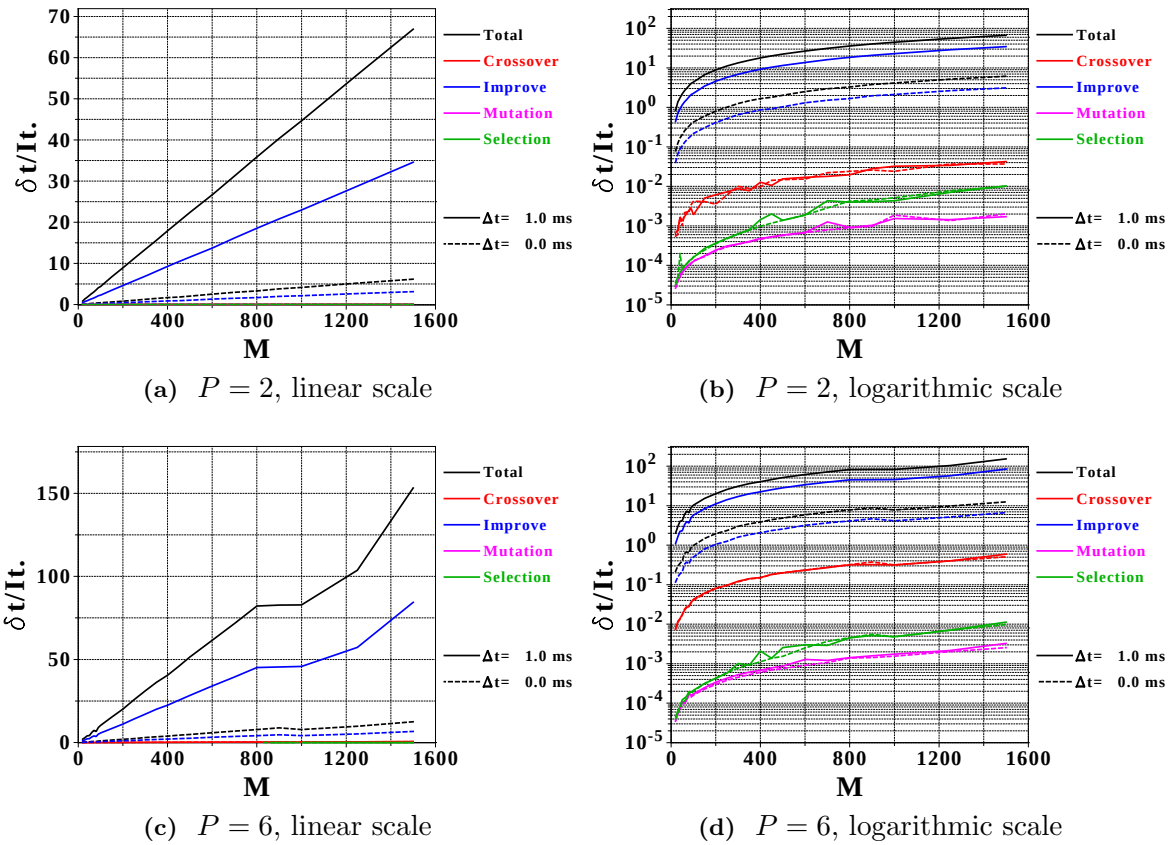

(a) $P = 2$, linear scale

(b) $P = 2$, logarithmic scale

(c) $P = 6$, linear scale

(d) $P = 6$, logarithmic scale

Figure 9.11: Scaling properties of FITPACK as a function of the population size.

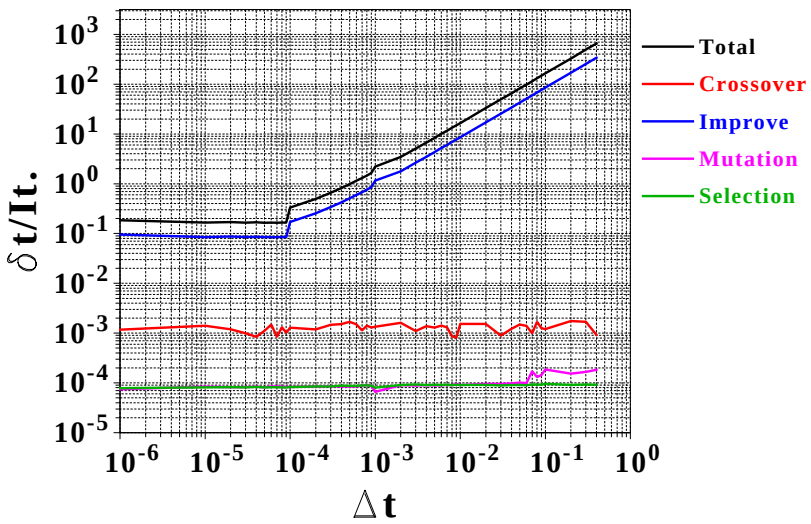

Figure 9.12: Scaling properties of FITPACK as a function of the merit evaluation time.

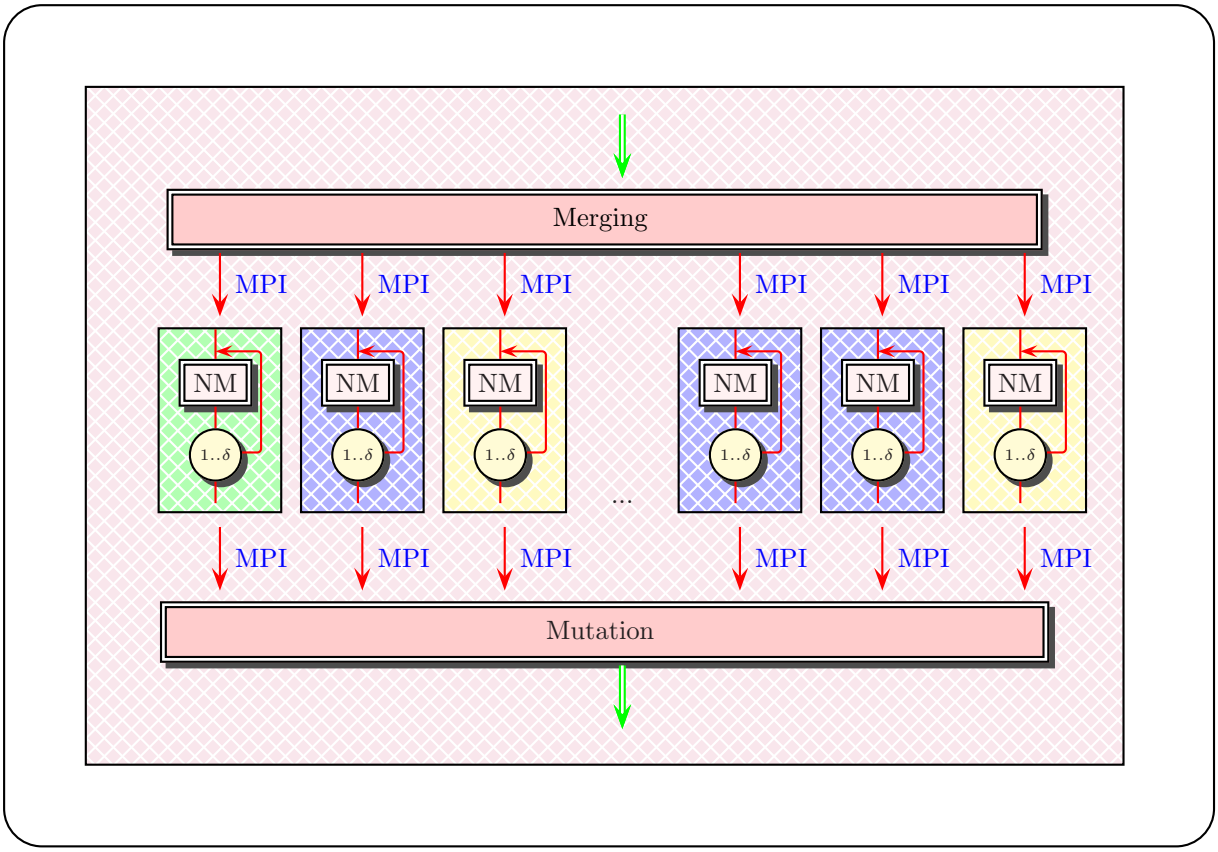

Figure 9.13: First parallelization strategy for FITPACK. A main thread (light purple) assigns Nelder-Mead simplex evolutions to different slave threads (blue, green and yellow levels).

This strategy allows one to handle very large populations which is essential in high dimensionality. On the other hand, since the simplex evolution corresponds only to one elementary step in the whole procedure, this parallel implementation is subject to dead times in the slave threads. As shown in FIG. 9.17, we find indeed that slave threads spend about 80% of the total computation time while waiting for instructions ("RECV" state). The latter picture obviously depends on the evaluation time of the merit function. Dead times are negligible in the case where such an evaluation is very demanding, which will be the case for the fits considered in the present work[8].

[8]For instance fits that involve at each evaluation of the merit function the computation of the scattering phase shifts, the gap equation or the symmetric nuclear matter equation of state.

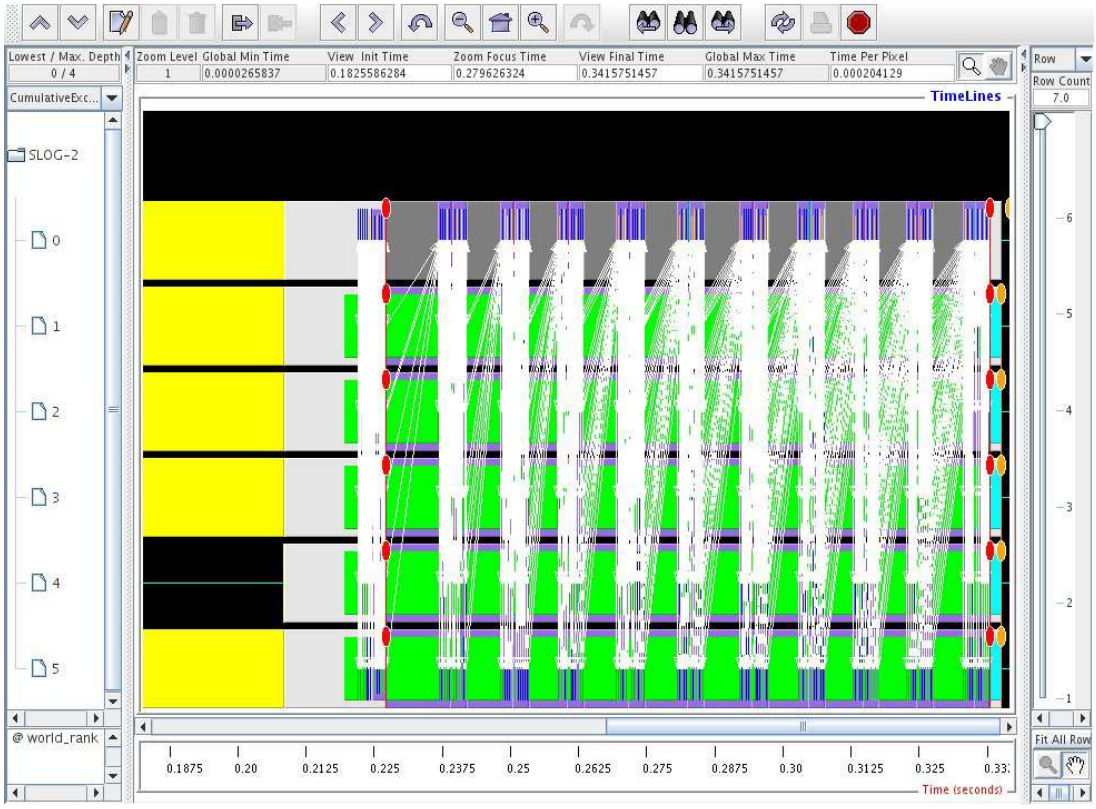

Figure 9.14: Profiling of FITPACK using brute-force parallelization for a simple cost function, 20 simplexes and 4 threads. Color conventions are represented in FIG. 9.15, and arrow represent messages passing between the main thread (Rank 0) and slave ones. On this figure the time scale is too much compressed and many arrows stack into blurry white areas, indicating the periods when communications between threads occur.

Figure 9.15: Conventions for the JUMPSHOT profiling program.

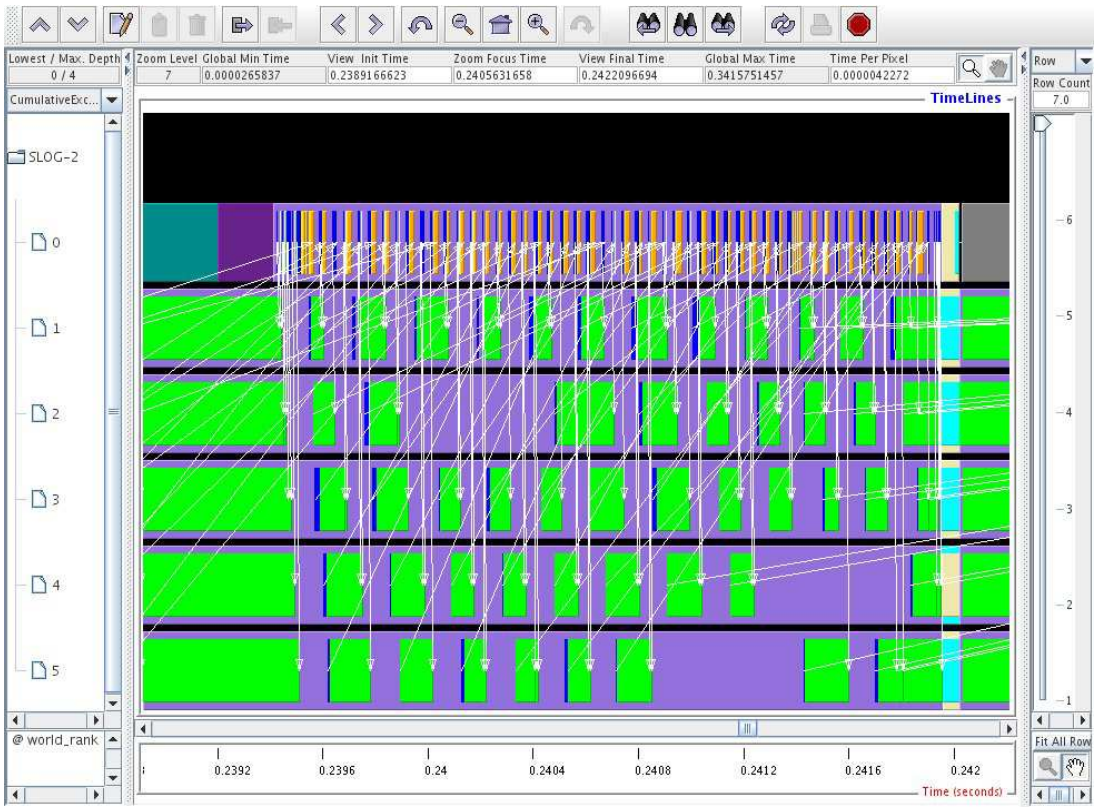

Figure 9.16: Same as in Fig. 9.14 focusing on one evolution phase where the main thread assigns the simplex evolutions.

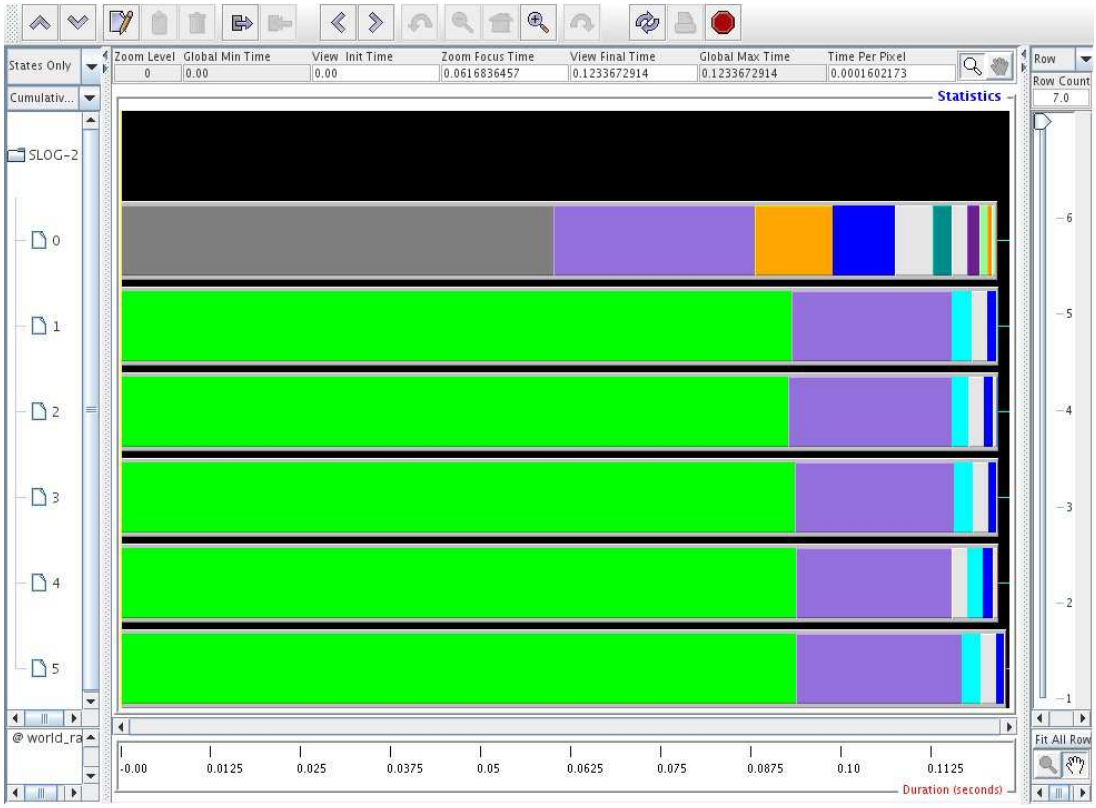

Figure 9.17: Same as in Fig. 9.14 but displaying the aggregated time spend by all threads in each elementary step.

9.5.2.2 Island-parallel genetic algoritm

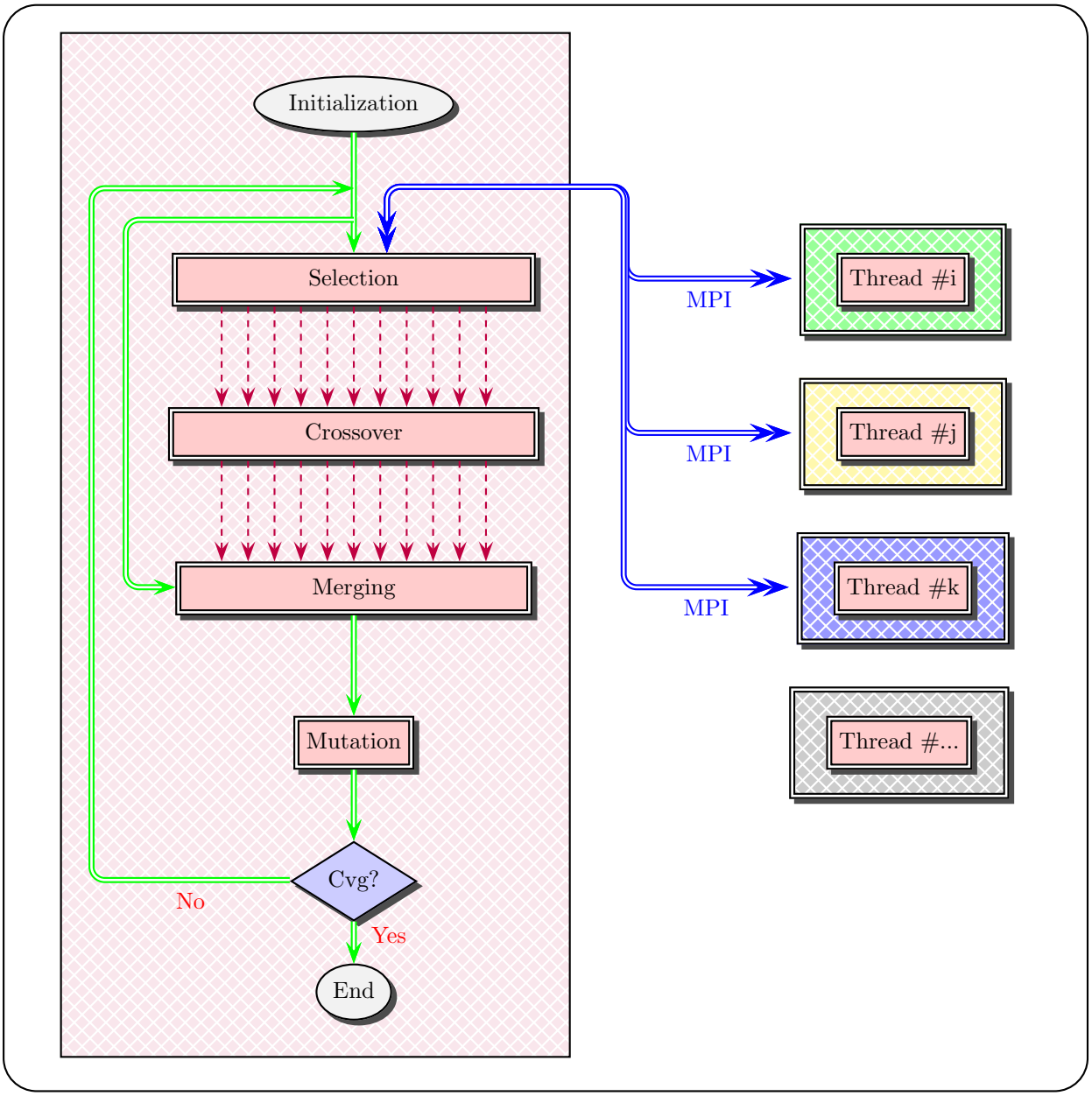

Figure 9.18: Island-parallel strategy for FITPACK. Each thread uses the best specimen from neighboring nodes during the selection process. Neighbors are randomly defined by putting arbitrarily each thread on a uniform grid, as seen in FIG. 9.19. Each node behaves exactly the same.

Another parallelization strategy where dead times are almost suppressed is called island-parallel GA (IPGA) which is a fully symmetric approach. It consists in evolving separately small populations on each thread ("islands"), but at regular intervals allow the best individuals from neighboring islands to participate in the mating process, that is the most fit individuals can "migrate" and diffuse the best phenotypes, as illustrated in FIG. 9.18. If the T is the number of threads available and M the population size on a given island, an IPGA is equivalent to a single GA with a population MT, but where all elementary routines are distributed on all threads.

After a given number of GA iterations on each island (typ. $5 \sim 10$), all threads are randomly put on a grid such that each one has a small number of neighbors α (typ. 4, see Fig. 9.19), the best individuals of which are included in the following reproduction phase. The grid defines a *migration* model, i.e. a given thread sends data to nodes that are different from the ones it gets data from, which needs extra care when implementing the randomized connection matrix.

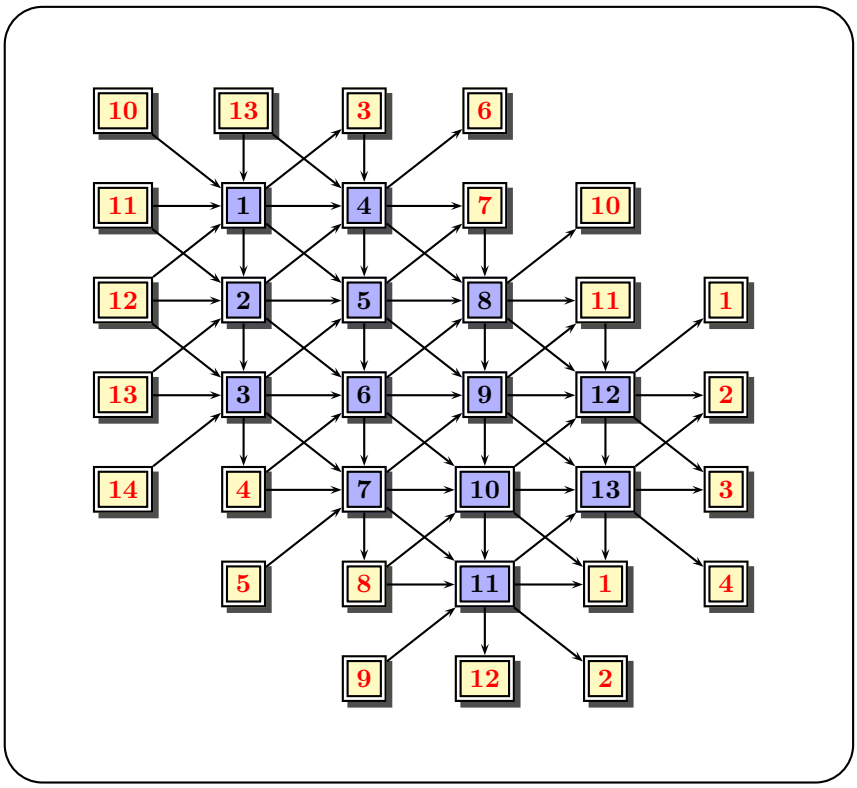

Figure 9.19: Connection grid for threads in the IPGA approach with $\alpha = 4$ and $T = 13$ threads, that is four neighbors for each node. At each generation, a thread is randomly put on a node, which defines its neighbors. Yellow nodes correspond to cyclic connections to not overload the schematics. Note that this defines a migration model, i.e. the nodes a given thread sends data to (black lines) are not the ones it gets data from.

MPE profiling of such an implementation can be found in Figs. (9.20,9.21). One sees that all threads have now a symmetric behavior, and spend most of their time computing evolution and mutation steps, i.e. dead times are greatly reduced, as seen through the aggregated time in Fig. 9.22. This approach is thus very useful to handle a very large population by dividing it between a large number of threads.

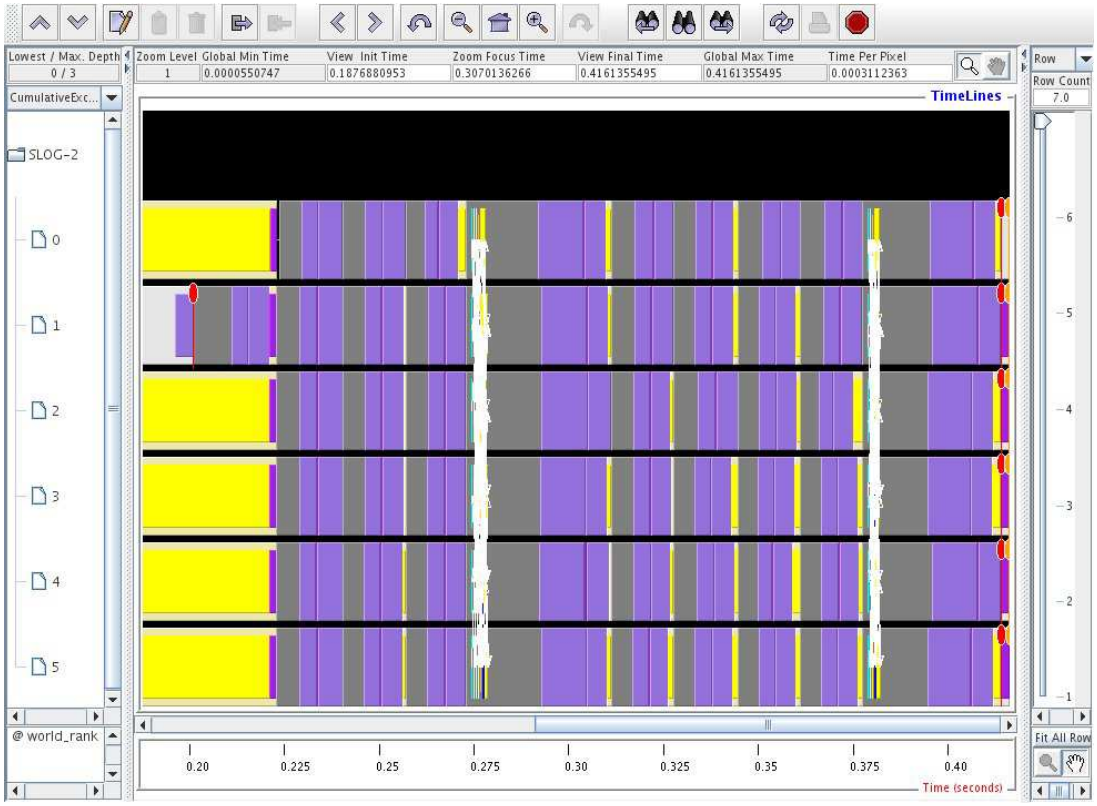

Figure 9.20: Profiling of FITPACK using island parallelization ($\alpha = 4$) for a simple cost function, 20 simplexes and 6 threads. Color conventions are represented in FIG. 9.15. Migration phases occur each five GA steps.

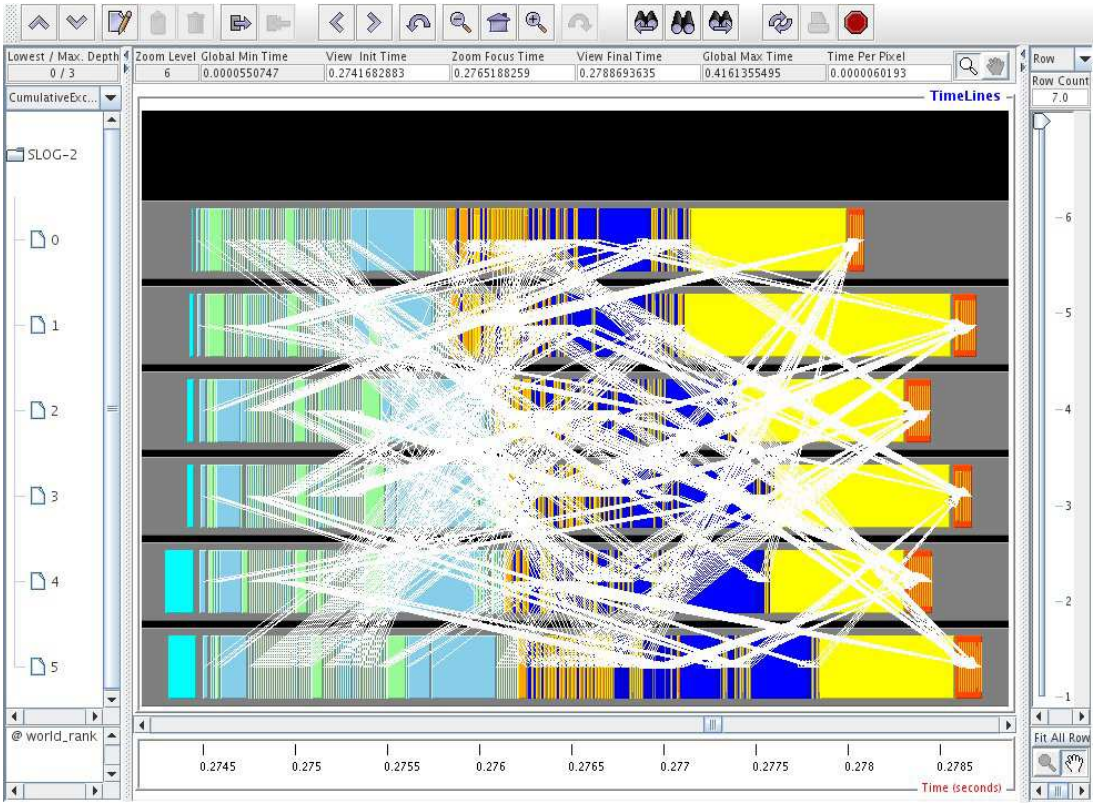

Figure 9.21: Same as in Fig. 9.20 focusing on one migration phase where each thread uses neighboring specimen in the crossover process.

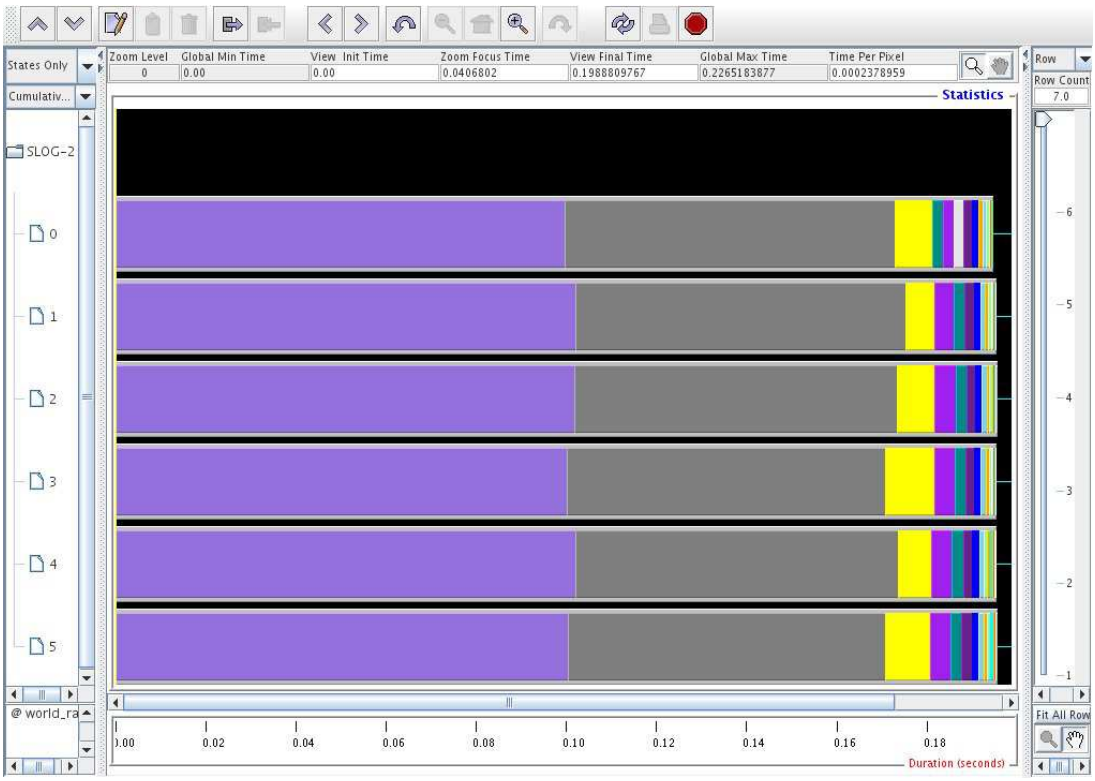

Figure 9.22: Same as in Fig. 9.20 but displaying the aggregated time spend by all threads in each elementary step.

9.6 Confidence intervals

The hybrid genetic-simplex algorithm presented previously allows to evaluate *estimators* of the free parameters of the model which is adjusted. However in realistic situations uncertainties of various origins have to be taken into account. As a consequence, each estimated parameter may be modified around its initial value without modifying the model significance. Thus a coherent framework when adjusting a model should include confidence intervals, i.e. intervals within which belongs the true value of the estimated parameter with a given probability. The construction of such intervals depends on whether the optimization can be recast in terms of a linear or a non-linear problem.

9.6.1 Linear model

A linear model corresponds to the case where the connection between *explanatory variables* $(X_i)_{i=1\ldots N}$[9] and *response, or dependent, variables* $(Y_i)_{i=1\ldots N}$ is linear in terms of the parameters $(\beta_i)_{i=1\ldots P}$ that are adjusted[10] [658; 659], i.e.

$$\forall\, i = 1\ldots N\,, \qquad Y_i = f(X_i, \beta) + \epsilon_i\,, \qquad\qquad \beta \equiv (\beta_1 \ldots \beta_P)^{\mathrm{T}}\,, \tag{9.8}$$

f being β-linear, and $\epsilon \equiv (\epsilon_1 \ldots \epsilon_N)^{\mathrm{T}}$ corresponds to error residuals. One assumes that these errors ϵ_i are independent and their distribution follows a normal law of standard deviation σ_i, i.e.

$$\epsilon = \mathcal{N}(0, \sigma^2\, \mathbb{I})\,, \tag{9.9}$$

$\mathbb{I}$ being the identity matrix. One has then

$$Y = \mathcal{N}(X\,\beta, \sigma^2\, \mathbb{I})\,, \tag{9.10}$$

where $X \equiv (X_1 \ldots X_N)^{\mathrm{T}}$ is a $N \times P$ matrix which depends on the chosen model. For instance, if the model reads

$$\forall\, i = 1\ldots N\,, \qquad Y_i = \beta_1 + \beta_2\, X_i + \beta_3\, X_i^2 + \epsilon_i\,, \tag{9.11}$$

the matrix X is defined as

$$X \equiv \begin{pmatrix} 1 & x_1 & x_1^2 \\ 1 & x_2 & x_2^2 \\ \vdots & \vdots & \vdots \\ 1 & x_N & x_N^2 \end{pmatrix}\,. \tag{9.12}$$

The best estimator $\hat{\beta}$ of β is given by minimizing the model quadratic error, i.e.

$$\hat{\beta} = \min_{\beta} ||\varepsilon||^2 = \min_{\beta} ||Y - X\beta||^2\,, \tag{9.13}$$

which leads to the well-known formula

$$\hat{\beta} = (X^{\mathrm{T}} X)^{-1}\, X^{\mathrm{T}} Y\,, \tag{9.14}$$

called lesser/lower/smaller square estimator of β, assuming that the square matrix $X^{\mathrm{T}} X$ is inversible. β is a random variable with the following properties:

[9] Such variables are also called regressors, exogenous variables, covariates, input variables or predictor variables.

[10] That is a linear model may be non-linear in terms of the exogenous variables, e.g.

$$\forall\, i = 1\ldots N\,, \qquad Y_i = \beta_1 + \beta_2\, X_i + \beta_3\, X_i^2 + \epsilon_i\,, \tag{9.7a}$$

$$\forall\, i = 1\ldots N\,, \qquad Y_i = \beta_1 + \beta_2\, \sin(X_i) + \beta_3\, \tanh(X_i^3) + \epsilon_i\,, \tag{9.7b}$$

correspond both to linear models.

- $\hat{\beta}$ a non-biased estimator of β, i.e $\mathrm{E}\left[\hat{\beta}\right] = \beta$. Indeed

$$\mathrm{E}\left[\hat{\beta}\right] = \mathrm{E}\left[(X^{\mathrm{T}}X)^{-1}X^{\mathrm{T}}Y\right] = (X^{\mathrm{T}}X)^{-1}X^{T}\mathrm{E}\left[Y\right] = (X^{\mathrm{T}}X)^{-1}X^{\mathrm{T}}X\,\beta = \beta\,, \tag{9.15}$$

- The variance of $\hat{\beta}$ is directly related to the variance of the errors σ. Indeed

$$\begin{aligned}\mathrm{Var}\left[\hat{\beta}\right] =&\mathrm{Var}\left[(X^{\mathrm{T}}X)^{-1}X^{\mathrm{T}}Y\right] = (X^{\mathrm{T}}X)^{-1}X^{\mathrm{T}}((X^{\mathrm{T}}X)^{-1}X^{\mathrm{T}})^{\mathrm{T}}\,\mathrm{Var}\left[Y\right]\\ =&(X^{\mathrm{T}}X)^{-1}X^{\mathrm{T}}X\,(X^{\mathrm{T}}X)^{-1}\sigma^2\,\mathbb{I} = \sigma^2\,(X^{\mathrm{T}}X)^{-1} \equiv \sigma^2_{\hat{\beta}}\,.\end{aligned} \tag{9.16}$$

  Matrix elements $(\sigma^2_{\hat{\beta}})_{ij}$ of the square *variance-covariance matrix* $\sigma^2_{\hat{\beta}}$ represent the covariance between $\hat{\beta}_i$ and $\hat{\beta}_j$. In particular its diagonal matrix elements $(\sigma^2_{\hat{\beta}})_{ii}$ correspond to the variance of $\hat{\beta}_i$.

- $\hat{\beta}$ is a linear function of the Gaussian random variable Y, thus one has

$$\hat{\beta} \sim \mathcal{N}\left(\mathrm{E}\left[\hat{\beta}\right], \mathrm{Var}\left[\hat{\beta}\right]\right) \sim \mathcal{N}(\beta, \sigma^2\,(X^{\mathrm{T}}X)^{-1})\,. \tag{9.17}$$

  One gets then

$$\forall j = 1\ldots P\,, \qquad \hat{\beta}_j \sim \mathcal{N}(\beta_j, \sigma^2_{\hat{\beta}_j})\,, \tag{9.18}$$

  where $\sigma^2_{\hat{\beta}_j} \equiv \sigma^2(X^{\mathrm{T}}X)^{-1}_{jj}$. That is

$$\forall j = 1\ldots P\,, \qquad \frac{\hat{\beta}_j - \beta_j}{\sigma_{\hat{\beta}_j}} \sim \mathcal{N}(0,1)\,. \tag{9.19}$$

Eq. (9.19) can be used directly for the construction of confidence intervals in the linear model. The final result depends whether the distribution of initial errors σ is known a priori.

If σ is known, so are the values of $\sigma_{\hat{\beta}_j}$. The confidence interval for the standardized variable associated with $\hat{\beta}_j$ corresponding to a given confidence level is provided by the central limit theorem, i.e.

$$P\left(\left|\frac{\hat{\beta}_j - \beta_j}{\sigma_{\hat{\beta}_j}}\right| \leq a_{\alpha/2}\right) = 1 - \alpha\,, \tag{9.20}$$

where $a_{\alpha/2}$ is the $\alpha/2$-percentile of the standardized normal law table[11], some values of which can be found in Tab. {9.4}. That is the confidence interval for $\hat{\beta}_j$ is associated to a desired confidence level $1-\alpha$ through

$$P\left(\beta_j \in \left[\hat{\beta}_j - \sigma_{\hat{\beta}_j}a_{\alpha/2}, \hat{\beta}_j + \sigma_{\hat{\beta}_j}a_{\alpha/2}\right]\right) = 1 - \alpha\,. \tag{9.23}$$

[11] For any variable X following a known law $\mathcal{L}$ we have

$$P(a'_{(1-\alpha)} \leq X \leq a'_{(\alpha)}) = 1 - 2\alpha\,, \tag{9.21}$$

where the quantiles a'_α depend on $\mathcal{L}$. In particular if the distribution is symmetric one has

$$a'_{(1-\alpha)} = -a'_{(\alpha)}\,, \qquad P(|X| \leq a'_{\alpha/2}) = 1 - \alpha\,. \tag{9.22}$$

α	$\mathcal{N}$	$\chi^2(k)$		$\mathcal{T}(k)$	
		$k=2$	$k=10$	$k=2$	$k=10$
0.2	1.2816	3.2189	13.4420	1.8856	1.3722
0.1	1.6449	4.6052	15.9870	2.9200	1.8125
0.05	1.9600	5.9915	18.3070	4.3027	2.2281
0.02	2.3264	7.8240	21.1608	6.9646	2.7638
0.01	2.5758	9.2103	23.2093	9.9248	3.1693
0.005	2.8070	10.5966	25.1882	14.0890	3.5814
0.002	3.0902	12.4292	27.7216	22.3271	4.1437
0.001	3.2905	13.8155	29.5883	31.5991	4.5869
0.0001	3.8906	18.4207	35.5640	99.9925	6.2111
0.00001	4.4172	23.0259	41.2962	316.2254	8.1503

Table 9.4: Quantiles for normal and Student laws.

On the other hand, when σ, thus $\sigma_{\hat{\beta}_j}$, is not known we have to estimate it, through the estimator of ϵ, i.e.

$$\hat{\epsilon} = ||\hat{Y} - X\hat{\beta}|| \,, \qquad \hat{\sigma}^2 = \frac{1}{n-p}\sum_{i=1}^{n} \hat{\epsilon}_i{}^2 \,, \qquad \hat{\sigma}^2_{\hat{\beta}_j} = \hat{\sigma}^2 \left(X^{\mathrm{T}}X\right)^{-1} . \tag{9.24}$$

According to Cochran's theorem[12] $(n-p)\hat{\sigma}^2_{\hat{\beta}_j}/\sigma^2_{\hat{\beta}_j}$ follows then a χ^2 distribution with $(n-p)$ degrees of freedom. It follows that

$$\frac{\hat{\beta}_j - \beta_j}{\hat{\sigma}_{\hat{\beta}_j}} \sim \mathcal{T}(n-p) \,, \tag{9.26}$$

where $\mathcal{T}(k)$ is a Student law with k degrees of freedom. Indeed, one has for two random variables Z and U

$$\begin{cases} Z \sim \mathcal{N}(0,1) \\ U \sim \chi^2(k) \end{cases} \qquad \Rightarrow \qquad \frac{Z}{\sqrt{U/k}} \sim \mathcal{T}(k) \,. \tag{9.27}$$

Confidence intervals for β can then be evaluated with the same method as in the case where σ is known, i.e.

$$P\left(\beta_j \in \left[\hat{\beta}_j - \hat{\sigma}_{\hat{\beta}_j} t_{\alpha/2}, \hat{\beta}_j + \hat{\sigma}_{\hat{\beta}_j} t_{\alpha/2}\right]\right) = 1 - \alpha \,, \tag{9.28}$$

where $t_{\alpha/2}$ is the $(\alpha/2)$ quantile of the Student law with n degrees of freedom.

9.6.2 Non-linear model

Many realistic optimization problems correspond to non-linear situations, where the relation between explanatory and answer variables is written as

$$Y = \eta(\beta, X) + \epsilon \,, \tag{9.29}$$

[12] If $(U_i)_{i=1\ldots n}$ are independent standard normally distributed random variables, and if one can write

$$\sum_{i=1}^{n} U_i^2 = \sum_{j=1}^{k} Q_j \,, \qquad \sum_{j=1}^{k} r_j = n \,, \tag{9.25}$$

where Q_j is a sum of squares of linear combinations of (U_i) of rank r_j, then the random variables $(Q_j)_{j=1\ldots k}$ are independent and each Q_j follow a χ^2 distribution with r_j degrees of freedom.

such that the best model minimizes the quadratic error, i.e.

$$\min_{\beta} ||\varepsilon||^2 = \min_{\beta} ||Y - \eta(\beta)||^2 \,. \tag{9.30}$$

In contrary to the linear model, no analytic solutions of Eq. (9.30) exist, and iterative methods have to be used to approach the solution (Gauss-Newton, Newton-Raphson or scores methods, simplex or genetic algorithms...). Since the distribution of errors does not follow a priori a given law, one cannot use directly the formulæ from Sec. 9.6.1.

The *linearization method* consists in a possible solution, where $\eta(\beta)$ is approximated by a Taylor expansion at first order around $\hat{\beta}$, i.e.

$$\eta(\beta) \simeq \eta(\hat{\beta}) + \nabla\eta(\hat{\beta})(\beta - \hat{\beta}) + \dots \tag{9.31}$$

The confidence region for β with probability $(1-\alpha)$ is then defined as the interval such that [660]

- if σ^2 is known,

$$(\beta - \hat{\beta})^{\mathrm{T}} \hat{V}^{-1} (\beta - \hat{\beta}) \leqslant \sigma^2 (\chi^2_{P,\alpha/2})^{-1} (1-\alpha) \,, \tag{9.32}$$

- if σ^2 is unknown, using its estimator

$$(\beta - \hat{\beta})^{\mathrm{T}} \hat{V}^{-1} (\beta - \hat{\beta}) \leqslant \hat{\sigma}^2 (\chi^2_{P,\alpha/2})^{-1} (1-\alpha) \,, \tag{9.33}$$

where $\hat{V} = \left(\nabla^{\mathrm{T}}\eta(\hat{\beta})\,\nabla\eta(\hat{\beta})\right)^{-1}$, and $\chi^2_{P,\alpha/2}$ denotes the $\alpha/2$ quantile of the χ^2 distribution with P degrees of freedom.

On the other hand, when (i) the hypotheses of the linear model are not verified, (ii) such a linearization is not possible, or (iii) we only access estimates for β and no estimator $\hat{\beta}$, other methods have to be used. In particular, the quality of the estimated values that are obtained using iterative methods for non-linear problems can be evaluated using the bootstrap method [661–666]. The latter allows a construction of a large sample of estimates whose distribution is not known a priori, but from which confidence intervals are constructed using the same method as in Sec. 9.6.1. Bootstrapping allows then to estimate properties of an estimator by measuring those properties when sampling from an approximating distribution. That is **the fitting algorithm is repeated for slight variations of the input conditions that preserve the model significance, and the values of the estimates are converted into error bars**.

Let us introduce the formalism in the case where resamples are built from of the observed dataset. Suppose that we have a sample $X = (X_1, X_2 \dots X_N)$, and we are interested in a statistic $\theta = \mathcal{S}(X)$, using the studentized bootstrap, or bootstrap-t, method [667; 668], where the distribution of $(\hat{\theta} - \theta)/\hat{\sigma}$ is approximated by an auxiliary distribution $(\hat{\theta}^* - \theta)/\hat{\sigma}^*$. From X one generates B bootstrap samples noted $\{x^{*\,1}, x^{*\,2} \dots x^{*\,B}\}$ of common length N by random sampling with replacement. One evaluates then the quantity

$$Z^*(b) = \frac{\hat{\theta}^*(b) - \hat{\theta}}{\hat{\epsilon}^*(b)} \,, \tag{9.34}$$

where $\hat{\theta}^*(b) = \mathcal{S}(x^{*\,b})$ is the estimation of θ for the sample $x^{*\,b}$ and $\hat{\epsilon}^*(b)$ is the standard error estimation

$$\hat{\epsilon}^*(b) = \sqrt{\mathrm{Var}\left[\hat{\theta}^*(b)\right]} \,. \tag{9.35}$$

The distribution of $Z^*(b)$ constitutes the so-called *bootstrap table*, from which the α-quantiles noted t_α are estimated through

$$\frac{1}{B}\text{card}\left\{Z^*(b) \leq \hat{t}_\alpha\right\} = 1 - \alpha\,. \tag{9.36}$$

The bootstrap-t confident interval reads then

$$\left[\hat{\theta} - \hat{t}_{1-\alpha}\,\hat{\epsilon}, \hat{\theta} - \hat{t}_\alpha\,\hat{\epsilon}\right]\,. \tag{9.37}$$

In practice such intervals are obtained by ordering the values of β_j^* in the bootstrap table noted $(\tilde{\beta}_1^* \ldots \tilde{\beta}_B^*)$, such that

$$\hat{\beta}_j \in \left[\tilde{\beta}_j^{\lceil B\alpha \rceil}, \tilde{\beta}_j^{\lfloor B(1-\alpha) \rfloor}\right]\,. \tag{9.38}$$

Finally, in the case where $\mathcal{S}$ is not know, a similar algorithm based on resampling can be applied to evaluate confidence intervals, which consists in the following steps:

1. the initial parameters β^* are estimated using a given iterative method,
2. the answer variables Y are estimated by $\hat{Y}$ using β^*,
3. we estimate the errors by $\hat{\epsilon} = Y - \hat{Y}$,
4. from the values of $\hat{\epsilon} = (\epsilon_1 \ldots \epsilon_N)$, we construct B bootstrap samples using sampling with replacement noted $(\epsilon^{*\,1} \ldots \epsilon^{*\,B})$,
5. for each $\epsilon^{*\,i}$ one evaluates the new answer variable $\hat{Y}^{*\,i} = \hat{Y} + \epsilon^{*\,i}$,
6. for each $\hat{Y}^{*\,i}$ one estimates the values $\beta_j^{*\,i=1\ldots B}$ of β by the same method used to obtain β^*,
7. the latter values of $\beta_j^{*\,i=1\ldots B}$ are sorted by increasing value for each j into the sequence $\tilde{\beta}_j = (\tilde{\beta}_j^1 \ldots \tilde{\beta}_j^B)$,
8. the confidence intervals with $(1-2\alpha)$ probability are then for each j $\left[\tilde{\beta}_j^{\lceil B\alpha \rceil}, \tilde{\beta}_j^{\lfloor B(1-\alpha) \rfloor}\right]$.

Let us illustrate the method in a linear case where confidence intervals can be evaluated using the method from Sec. 9.6.1 of the bootstrap method that we have just introduced. We consider a model

$$\forall i = 1 \ldots 100\,, \qquad y_i = 15 - 4x_i + 5x_i^2 + 15x_i^3 + \varepsilon_i\,, \qquad x_i \in [-1, 1]\,, \tag{9.39}$$

where a random error $\epsilon_i \sim \mathcal{N}(0, 3)$ is added at each bin. In Fig. 9.23 are represented (i) the data points, (ii) the ideal curve without the errors ϵ, and (iii) the curve corresponding to the adjusted linear model

$$\forall i = 1 \ldots 100\,, \qquad y_i = \beta_0 + \beta_1\,x_i + \beta_2\,x_i^2 + \beta_3\,x_i^3\,. \tag{9.40}$$

Confidence intervals from the Student and bootstrap methods are summarized in Tab. {9.5}, and are found to be very close to each other. Bootstrap intervals are bigger than Student ones, given that for a linear model where the error distribution is known a priori the Student method provides the best possible error bars.

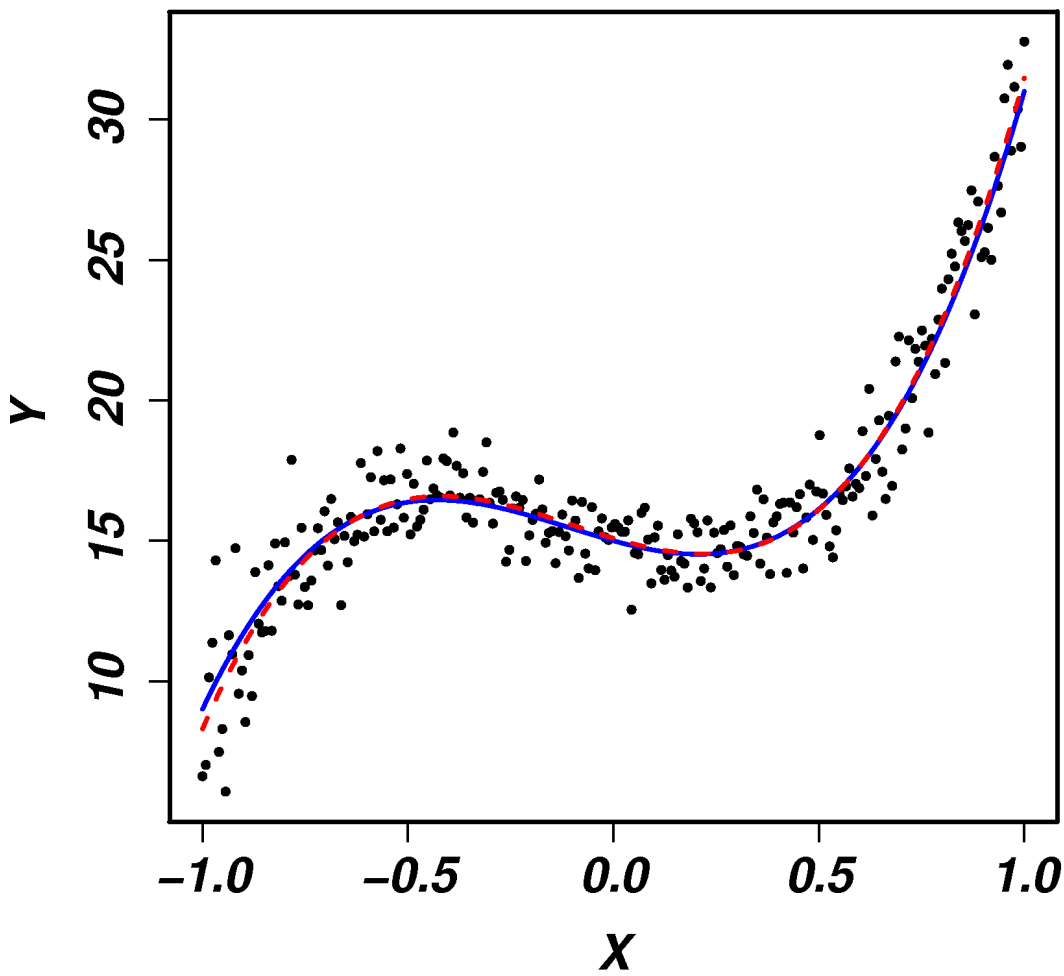

Figure 9.23: Linear model used to illustrate the construction of confidence intervals. The data points are obtained by adding random errors to the ideal curve in red, while the optimized linear model is represented in blue.

	Exact	Estimated	Student		Bootstrap	
			Min	Max	Min	Max
β_0	15.00	14.9946	14.9641	15.0251	14.7870	15.1989
β_1	−4.00	−3.8696	−4.1217	−3.6174	−4.4449	−3.2722
β_2	5.00	5.0560	4.9059	5.2061	4.5965	5.5459
β_3	15.00	14.9727	14.3936	15.5519	14.1148	15.8705

Table 9.5: Confidence intervals obtained for the linear example from Fig. 9.23 with two different methods.

Chapter 10

Results: operatorial representation of the bare nucleon-nucleon force

Abstract: This chapter presents the first results of the adjustment procedure for v_{BDRS}, and several cases of interest are discussed. At first, only the $^1\mathrm{S}_0$ partial wave for $v_{\mathrm{BDRS}}^{[\mathrm{bare}(2)]}$ is adjusted, aiming at a microscopic description of pairing. That is, focus for now is put on **strategy 1**. It is highlighted that including explicitly the RG cutoff function in the momentum space expression of v_{BDRS} allows a very precise description of $V_{\mathrm{low}\,k}$ in that particular channel, with the tradeoff that such representation is unlikely to be used in existing EDF calculations in a harmonic oscillator basis. Nevertheless, several very important features can be extracted within this approach, in particular concerning the decomposition of the potential in terms of zero-/finite-range components. Then, the extraction of the strictly gaussian vertex is performed, firstly restricted to the $^1\mathrm{S}_0$ partial wave, and then extended to all $L \geq 2$ matrix elements, which allows to grab the contributions of spin-orbit and tensor couplings. The addition of theoretical uncertainties provides additional guidelines concerning the long-term strategy which is initiated by this dissertation, that is the construction of non-empirical vertices for finite-range EDF calculations.

Contents

10.1 $^1\mathrm{S}_0$ channel: separable representation 270
10.2 Explicit inclusion of renormalization group cutoffs 270
10.2.1 Motivations 270
10.2.2 One-dimension toy model 276
10.2.2.1 Initial vertex in coordinate space 276
10.2.2.2 RG cutoff function in coordinate space 277
10.2.2.3 RG-induced non-local vertex in coordinate space 277
10.2.3 Applications 278
10.2.4 Realistic RG-induced vertices 284
10.3 Results for $v_{\mathrm{BDRS}}^{[\mathrm{bare}(2)]}$: $^1\mathrm{S}_0$ channel with RG cutoffs 286
10.3.1 Fit setup 286
10.3.2 Convergence issues 287
10.3.3 First results 292
10.3.4 Evolution with the RG cutoff Λ 296
10.3.5 Representation accuracy 298
10.3.6 Impact of the RG cutoff function 299
10.3.7 Evolution with the number of gaussians 303

10.3.8 Isospin-symmetry breaking 304
10.3.9 Comparison with separable interactions 306
10.3.10 Uncertainties analysis 307
10.3.10.1 Fit intrinsic error 308
10.3.10.2 Representation and $V_{\text{low}\,k}$ error: principle 309
10.3.10.3 Representation error: case study 310
10.3.10.4 Total uncertainties 310
10.3.10.5 Errors on physical observables 312
10.4 Results for $v_{\text{BDRS}}^{[\text{bare}(2)]}$: $L \leq 2$ partial waves with RG cutoffs 313
10.5 Results for $v_{\text{BDRS}}^{[\text{bare}(2)]}$: no RG cutoffs in the $^1\text{S}_0$ channel 316

10.1 $^1\text{S}_0$ channel: separable representation

Let us first present briefly results obtained by T. Lesinski using a parallel approach, that is a separable representation of $V_{\text{low}\,k}$ restricted to the $^1\text{S}_0$ partial wave [669]. The latter representation is motivated by the presence of a virtual state in the $^1\text{S}_0$ channel [1; 670]. This finite-range expression can be plugged in the particle-particle channel of Skyrme-EDF calculations using a new code written in a Bessel functions basis, while yielding to an accurate description for both matrix elements and phase shifts of the initial interaction. The separable interaction is defined as

$$v_{\text{sep}}(k,k') = \sum_{\alpha=1}^{R} g_\alpha(k)\,\lambda_\alpha\,g_\alpha(k')\,, \tag{10.1}$$

where R is the rank of the representation, typically 2-3 for low-momentum interactions with $\Lambda \lesssim 2.3\ \text{fm}^{-1}$, and the functions g are form factors. One possible definition for these form factors are exponential-polynomial expressions

$$g_\alpha(k) = \left[\sum_n x_{\alpha n}\left(\frac{a_\alpha^2\,k^2}{2}\right)^n\right]\exp\left(-\frac{a_\alpha^2\,k^2}{2}\right)\,, \tag{10.2}$$

where the sum over n runs on a small set of integer values, typically 4, and the total form factor is normalized such that $x_{\alpha n_{\text{min}}} = 1$. Some results concerning rank-2 and rank-3 representations of $V_{\text{low}\,k}$ for $\Lambda = 1.8\ \text{fm}^{-1}$ and $\Lambda = 2.5\ \text{fm}^{-1}$, respectively, are presented in Fig. 10.1. Numerical values for the parameters $\{a_\alpha, \lambda_\alpha, x_{\alpha n}\}$ are summarized on Tab. {10.1}. The very good description of the phase shifts by the separable representation is also seen on Fig. 10.2.

10.2 Explicit inclusion of renormalization group cutoffs

10.2.1 Motivations

An explicit introduction of the RG cutoff amounts to defining a *RG-induced* effective vertex in momentum space as

$$\tilde{V}^{[\text{ind}]}(\vec{k}_1,\vec{k}_2,\vec{k}_3,\vec{k}_4) \equiv \tilde{V}^{[\text{ind}]}(\vec{k}_i) = \tilde{V}_0(\vec{q})\,(2\pi)^3\,\delta(\vec{K}-\vec{K}\,')\times\tilde{g}(k)\,\tilde{g}(k')\,, \tag{10.3}$$

for a generic RG cutoff function $\tilde{g}^{(1)}$ (see Sec. 5.4.1), whereas $\tilde{V}_0$ denotes the momentum space representation of a local potential. Several arguments can be put forward for such an idea.

[1] In this section $\tilde{g}(k)$ will denote the momentum-space cutoff and $g(r)$ the associated coordinate-space one.

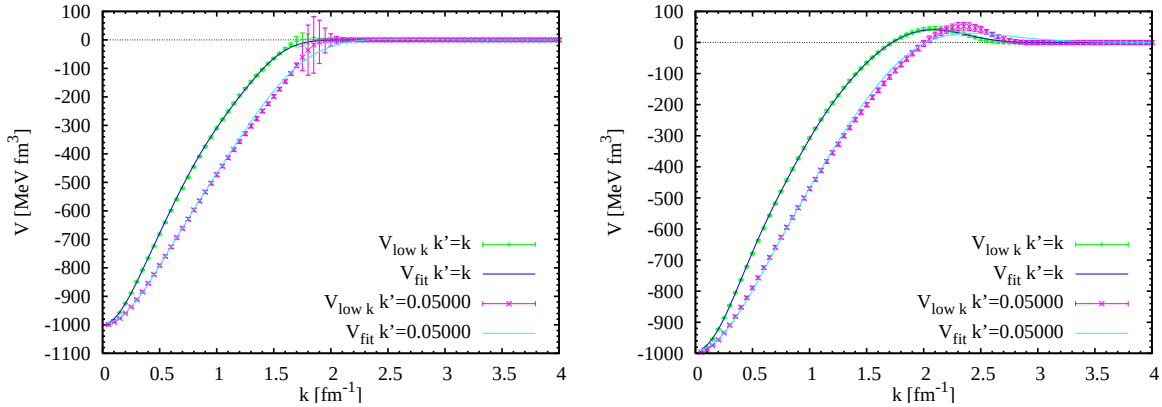

(a) $\Lambda = 1.8$ fm^{-1} with rank-2 fit (b) $\Lambda = 2.5$ fm^{-1} with rank-3 fit

Figure 10.1: Diagonal ($k = k'$) and off-diagonal ($k' \simeq 0$) matrix elements for a separable representation of $V_{\text{low}\,k}$ in the $^1\text{S}_0$ channel.

	$\Lambda = 1.8$ fm^{-1}		$\Lambda = 2.1$ fm^{-1}		
α	1	2	1	2	3
a_α [fm]	1.557932	1.758800	1.364033	1.161567	1.645158
$x_{\alpha 0}$	1.0		1.0		
$x_{\alpha 1}$	0.148392	1.0		1.0	
$x_{\alpha 2}$	0.340435	−0.556468	0.314835	−0.227809	1.0
$x_{\alpha 3}$	−0.058734	0.404733	−0.094650	−0.044524	0.287585
$x_{\alpha 4}$		−0.053844		0.015023	−0.272929
$x_{\alpha 5}$			−0.000430		0.056317
$\lambda_{\alpha\alpha}$ [MeV.fm^3]	−999.995	−998.5034	−992.5480	−1736.8452	223.2350

Table 10.1: Parameters for a separable representation of $V_{\text{low}\,k}$ at two cutoffs Λ.

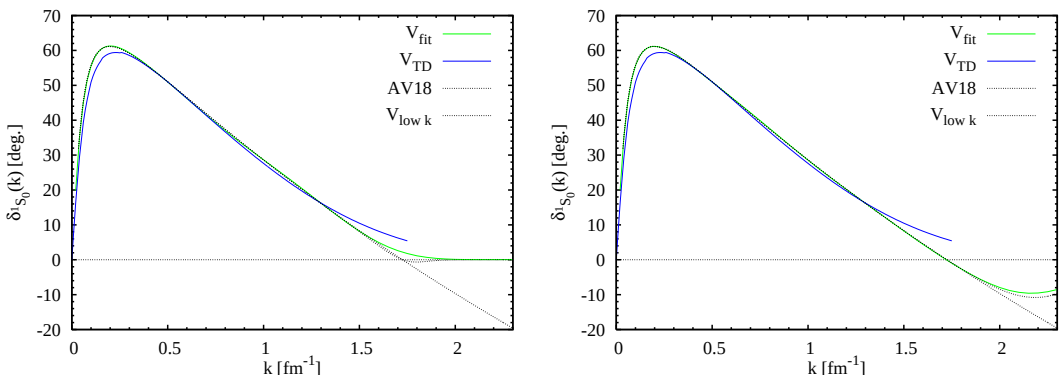

(a) $\Lambda = 1.8$ fm^{-1} with rank-2 fit (b) $\Lambda = 2.5$ fm^{-1} with rank-3 fit

Figure 10.2: $^1\text{S}_0$ phase shifts of $V_{\text{low}\,k}$ and its separable representation, with the same conventions as in FIG. 10.1.

- The RG formalism states that the relevant part of high-energy physics beyond the cutoff Λ is properly recast into the low-energy part that enters nuclear structure calculations. This means that there is actually no significance in using values of v_{BDRS} beyond Λ in the fit procedure. This argument can be extrapolated in the case of a smooth $V_{\mathrm{low}\,k}$.
- For reasonable values of Λ used in low-energy nuclear physics (around 2.1 fm^{-1}), matrix elements of $V_{\mathrm{low}\,k}$ present a sharp inflexion around Λ, where they go to zero. Such an inflexion cannot be reproduced by any gaussian parametrization, which is at the origin of the theoretical uncertainties defined in the following (large tolerance allowed around Λ). The introduction of RG cutoffs allows a better reproduction of this large curvature.
- This approach amounts to representing $V_{\mathrm{low}\,k}$, which is intrinsically non-local, by an interaction where the non-locality is explicitly factorized. However, such a factorization in momentum space does not lead to an equivalent factorization in coordinate space.
- The partial wave decomposition of a gaussian presents some peculiar behaviors, especially in the $^1\mathrm{S}_0$ channel. Indeed, if one considers a gaussian of arbitrary range $\mu_0 = 2.1$ fm, matrix elements as a function of the magnitude of the momentum transfer $|\vec{q}\,|$, represented in Fig. 10.3a, are negligible for $q \gtrsim 2.1$ fm^{-1}.

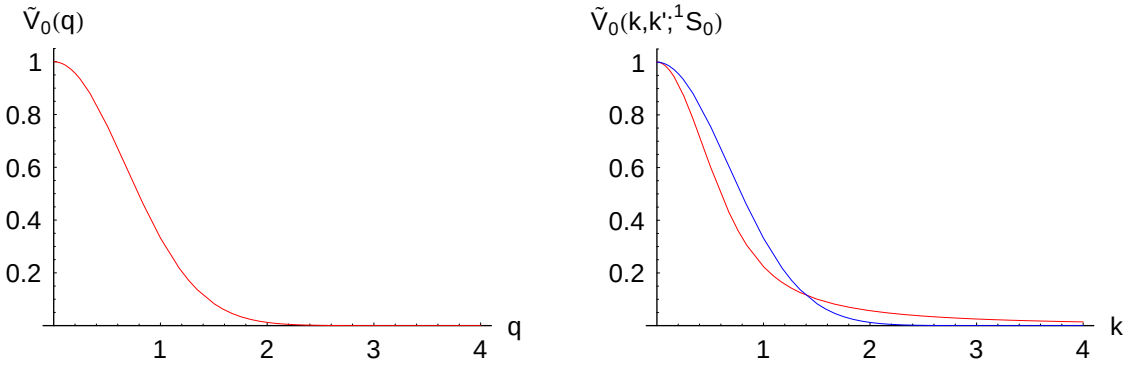

(a) As a function of the total momentum transfer q

(b) As a function of the entering relative momentum k in the $^1\mathrm{S}_0$ channel for diagonal (red) and off-diagonal (blue) matrix elements, without the phase factor

Figure 10.3: Matrix elements in momentum space of a simple gaussian.

However, the behavior of the matrix elements of such a gaussian in the $^1\mathrm{S}_0$ channel as a function of entering and outgoing momenta (k, k') is very different, as shown in Fig. 10.3b. Indeed, one has (i) non-negligible diagonal matrix elements up to $k \approx 3.5$ fm^{-1}, (ii) negligible off-diagonal matrix elements[(2)] for $k \gtrsim 2.1$ fm^{-1}. Such high-momentum components are necessary for a good reconstruction of the initial vertex. Let us consider as a toy model the initial vertex

$$\tilde{V}_0(\vec{q}) = \exp\left(-\frac{1}{4}\,\mu_0^2\,q^2\right)\,, \tag{10.4}$$

[2]Off-diagonal matrix elements are simple gaussians with same ranges as the initial vertex

where $\vec{q} = \vec{k} - \vec{k}\,'$, and the vector $\vec{k}$ is put on the $[0z)$ axis, which means, because of axial symmetry, that the only two relevant degrees of freedom for $\vec{k}\,'$ are its projections k'_x and k'_z on the x and z axis, respectively. From this starting point one can evaluate (i) the exact values for the potential $\tilde{V}_0(\vec{q})$ for several magnitudes of the vector $\vec{k}$ noted k_z, and (k'_x, k'_z), and (ii) the potential $\tilde{V}_0^{\text{reco}}(k_z, k'_x, k'_z)$, reconstructed from a partial wave expansion of $\tilde{V}_0(\vec{q})$. FIG. 10.4 shows a comparison between these two approaches, and one can see that for rather small values of k_z, the partial wave summation quickly converges to the original value of $\tilde{V}_0(\vec{q})$.

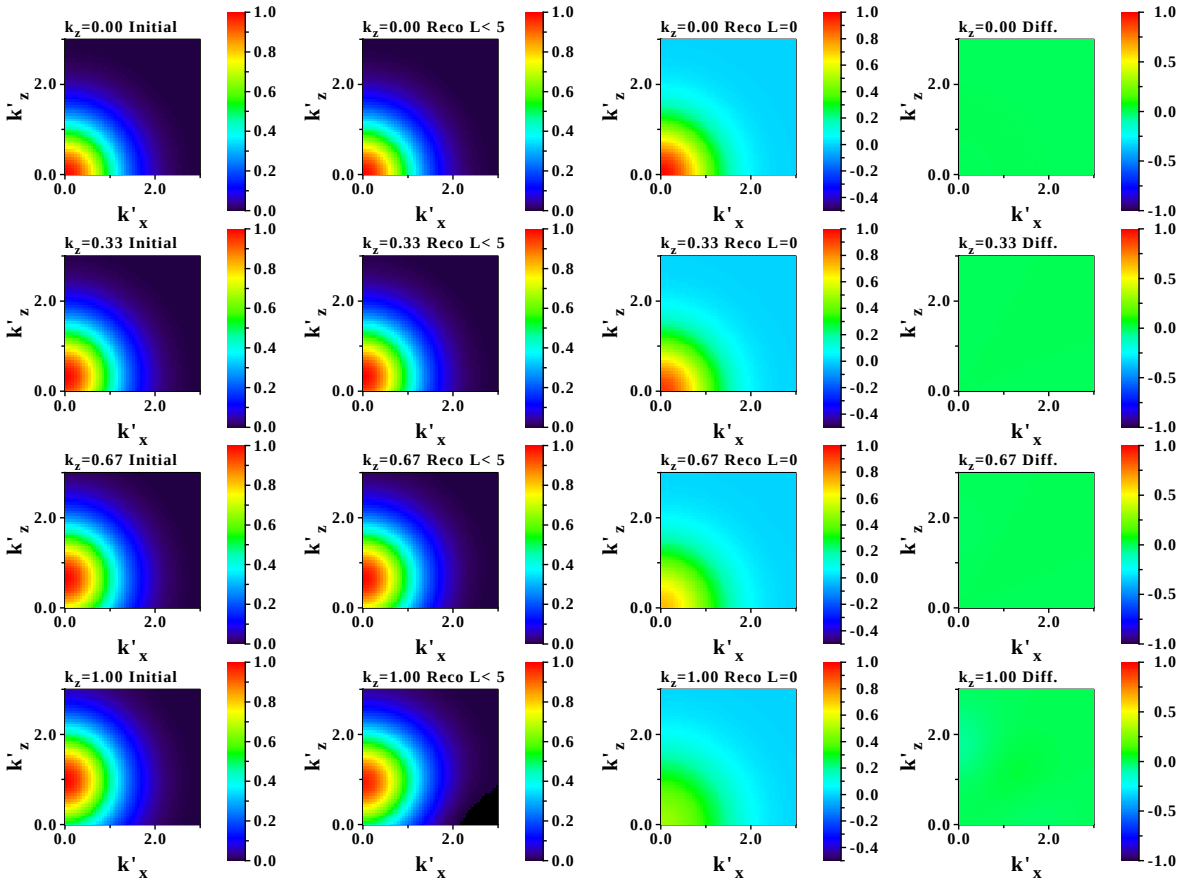

Figure 10.4: Toy model reconstruction of $\tilde{V}_0(\vec{q})$ from its partial wave expansion, for several values of k_z. From left to right panels: inital vertex, reconstructed vertex with $\ell < 5$ partial waves, $\ell = 0$ term without the phase factor, difference between the initial and reconstructed matrix elements using $\ell < 5$ partial waves.

One can also evaluate the reconstructed vertex $\tilde{V}_1^{\text{reco}}(k_z, k'_x, k'_z)$ from a partial wave expansion of $\tilde{V}_0(\vec{q})$ with a RG cutoff function enforced in each partial wave. Results are represented on FIGS. (10.5,10.6) with sharp and smooth RG cutoff functions. Low-k matrix elements are still very accurately reproduced. This proves that one can "artificially" deteriorate the high-k part of the matrix elements without affecting drastically matrix elements below the RG cutoff Λ.

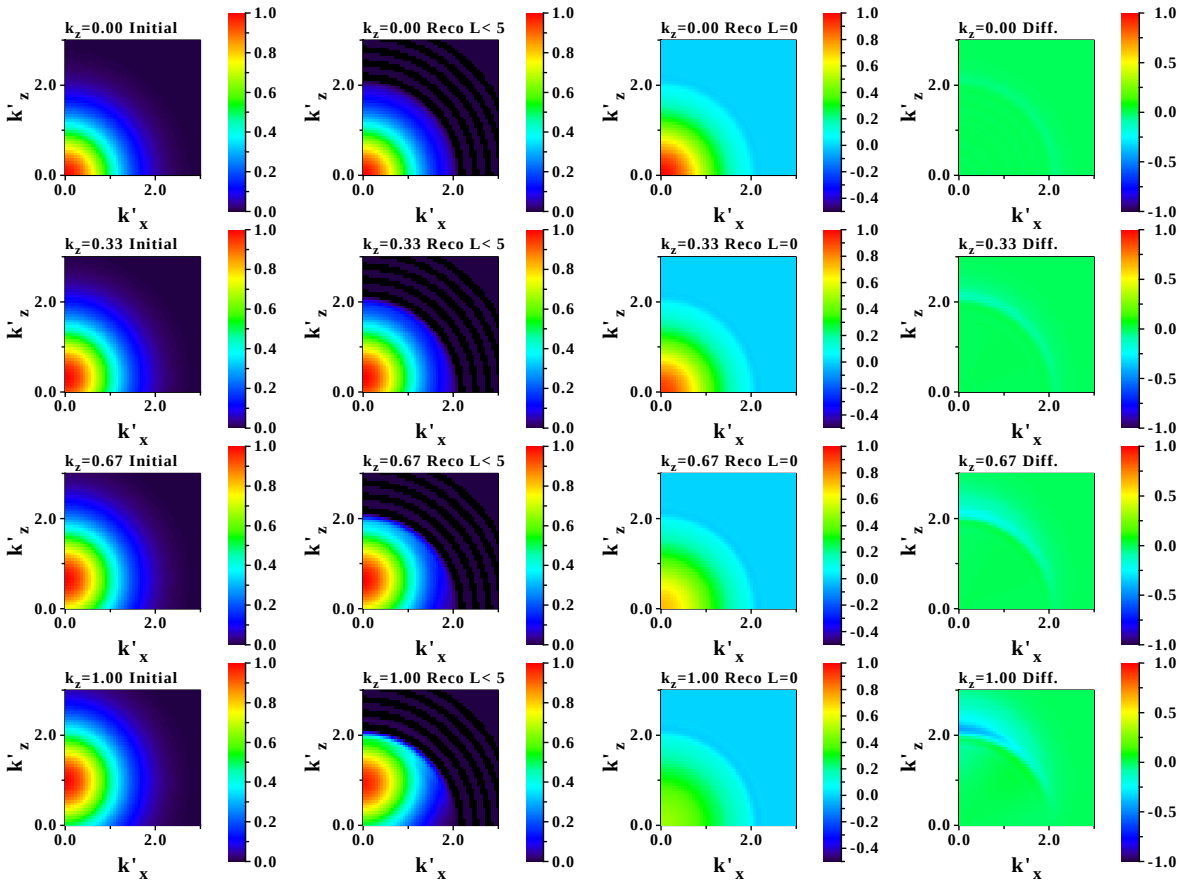

Figure 10.5: Same as in FIG. 10.4 but where partial wave matrix elements have a sharp RG cutoff at $\Lambda = 2.1$ fm^{-1}.

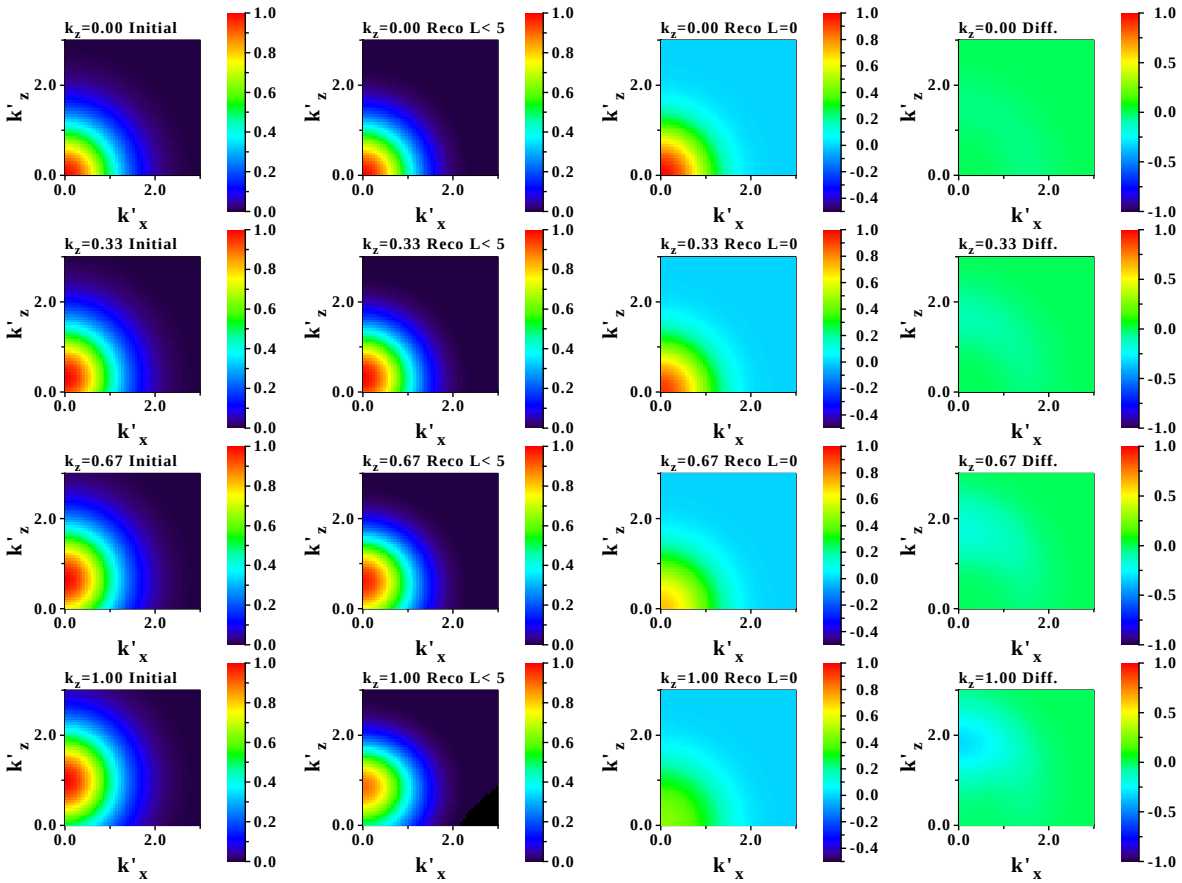

Figure 10.6: Same as in FIG. 10.4 but where partial wave matrix elements have a smooth exponential RG cutoff (SEC. 5.4.1) at $\Lambda = 2.1$ fm^{-1} with $n = 2$.

10.2.2 One-dimension toy model

The consequences of the introduction of RG cutoff functions in momentum space back into coordinate space must be evaluated, in particular whether it leads to a form which can be implemented in traditional structure codes or not. One starts from a toy model where all important features appear, i.e. simple 1D case ($d = 1$) with the central gaussian potential

$$\tilde{V}_0(q) = (\mu\sqrt{\pi})\,\exp\left(-\frac{1}{4}\,\mu^2\,q^2\right)\,, \tag{10.5}$$

And one aims at evaluating in coordinate space the RG-induced vertex

$$\tilde{V}^{[\mathrm{ind}]}(k_i) = \tilde{V}_0(q)\,(2\pi)\,\delta(K-K')\times\tilde{g}(k)\,\tilde{g}(k')\,. \tag{10.6}$$

Transformation rules read then

$$\tilde{V}_0^{[\mathrm{X}]}(k_i) = \int \mathrm{d}r_i\,e^{-i\,(r_1k_1-r_3k_3+r_2k_2-r_4k_r)}\,V_0^{[\mathrm{X}]}(r_i)\,, \tag{10.7a}$$

$$V_0^{[\mathrm{X}]}(r_i) = \frac{1}{(2\pi)^4}\int \mathrm{d}k_i\,e^{+i\,(r_1k_1-r_3k_3+r_2k_2-r_4k_r)}\,\tilde{V}_0^{[\mathrm{X}]}(k_i)\,. \tag{10.7b}$$

Let us first recall important properties for the 1D Dirac delta function, defined as the limit of nascent delta functions, that will be useful later on, i.e.

$$\delta(x) = \lim_{a\to 0}\delta_a(x)\,, \tag{10.8a}$$

$$\delta_a(x) = \frac{1}{\pi\,r}\,\sin\left(\frac{r}{a}\right)\,, \tag{10.8b}$$

$$\delta_a(x) = \frac{1}{a\sqrt{\pi}}\,e^{-r^2/a^2}\,. \tag{10.8c}$$

In particular, from Eq. (10.8b) one recovers

$$\langle\, r\,|\,r'\,\rangle = \frac{1}{(2\pi)}\int \mathrm{d}k\,e^{ik\,(r-r')} = \delta(r-r')\,. \tag{10.9}$$

10.2.2.1 Initial vertex in coordinate space

The uncorrected vertex

$$\tilde{V}_0^{[\mathrm{NC}]}(k_i) = (2\pi)\,\tilde{V}_0(q)\,\delta(K-K')\,, \tag{10.10}$$

reads immediately in coordinate space

$$\begin{aligned}
V_0^{[\mathrm{NC}]}(r_i) =& \frac{1}{(2\pi)^3}\int \mathrm{d}k\,\mathrm{d}k'\,\mathrm{d}K\,\mathrm{d}K'\,\tilde{V}_0(q)\,\delta(K-K') \\
&\times\exp\left[i\left(k(r_1-r_2)+\frac{K}{2}(r_1+r_2)-k'(r_3-r_4)-\frac{K'}{2}(r_3+r_4)\right)\right] \\
=& \frac{1}{(2\pi)^2}\,\delta\left(\frac{r_1+r_2-r_3-r_4}{2}\right)\int \mathrm{d}k\,\mathrm{d}k'\,\exp\left[i\left(k(r_1-r_2)-k'(r_3-r_4)\right)\right]\,\tilde{V}_0(q) \\
=& \frac{1}{(2\pi)^2}\,\delta\left(\frac{r_1+r_2-r_3-r_4}{2}\right) \\
&\times\int\frac{\mathrm{d}q\,\mathrm{d}q'}{2}\,\exp\left[i\left(\frac{q(r_1-r_2+r_3-r_4)}{2}+\frac{q'(r_1-r_2-r_3+r_4)}{2}\right)\right]\,\tilde{V}_0(q) \\
=& \frac{1}{(2\pi)}\,\frac{1}{2}\,\delta(R-R')\,\delta\left(\frac{r-r'}{2}\right)\int \mathrm{d}q\,\exp\left[\frac{iq(r_1-r_2+r_3-r_4)}{2}\right]\,\tilde{V}_0(q) \\
=& \frac{1}{(2\pi)}\,\delta(r_1-r_3)\,\delta(r_2-r_4)\int \mathrm{d}q\,e^{-i\,qr}\,\tilde{V}_0(q) \\
=& \delta(r_1-r_3)\,\delta(r_2-r_4)\,V_0(r)\,,
\end{aligned} \tag{10.11}$$

where

$$V_0(r) = e^{-\frac{r^2}{\mu^2}} \,. \tag{10.12}$$

10.2.2.2 RG cutoff function in coordinate space

The RG cutoff part from Eq. (10.6) reads

$$\tilde{V}^{[\mathrm{RG}]}(k_i) = \tilde{g}(k)\,\tilde{g}(k')\,. \tag{10.13}$$

This leads in coordinate space to

$$\begin{aligned} V^{[\mathrm{RG}]}(r_i) =& \frac{1}{(2\pi)^4}\int \mathrm{d}k\,\mathrm{d}k'\,\mathrm{d}K\,\mathrm{d}K'\,\tilde{g}(k)\,\tilde{g}(k') \\ & \times \exp\left[i\left(k(r_1-r_2)+\frac{K}{2}(r_1+r_2)-k'(r_3-r_4)-\frac{K'}{2}(r_3+r_4)\right)\right] \\ =& \delta(R)\,\delta(R')\,\frac{1}{(2\pi)}\int \mathrm{d}k\,e^{-i\,kr}\,\tilde{g}(k)\,\frac{1}{(2\pi)}\int \mathrm{d}k'\,e^{-i\,k'r}\,\tilde{g}(k') \\ =& \delta(R)\,\delta(R')\,g(r)\,g(r')\,, \end{aligned} \tag{10.14}$$

the RG functions in coordinate space being left to be evaluated.

10.2.2.3 RG-induced non-local vertex in coordinate space

Recovering the full RG-induced vertex in coordinate space $V^{[\mathrm{ind}]}(r_i)$ makes use of the convolution theorem. The latter reads for non-unitary Fourier transforms

$$\widetilde{(f*g)}(t) = \tilde{f}(\omega)\cdot\tilde{g}(\omega)\,, \tag{10.15}$$

where $[\cdot]$ is the normal product, and $[*]$ the convolution one defined as

$$(f*g)(t) = \int \mathrm{d}\tau\, f(\tau)\,g(t-\tau)\,. \tag{10.16}$$

One gets then

$$\begin{aligned} V_0^{[\mathrm{ind}]}(r_i) =& (V^{[\mathrm{NC}]} * V_0^{[\mathrm{RG}]})(r_i) \\ =& \int \mathrm{d}\tau_\mathrm{i}\,\mathrm{V}^{[\mathrm{NC}]}(\mathrm{r_i}-\tau_\mathrm{i})\,\mathrm{V}_0^{[\mathrm{RG}]}(\tau_\mathrm{i}) \\ =& \int \mathrm{d}\tau_i\,\delta(r_1-r_3-\tau_1+\tau_3)\,\delta(r_2-r_4-\tau_2+\tau_4)\,V_0(r_2-r_1-\tau_2+\tau_1) \\ & \times\delta\left(\frac{\tau_1+\tau_2}{2}\right)\,\delta\left(\frac{\tau_3+\tau_4}{2}\right)\,g(\tau_2-\tau_1)\,g(\tau_4-\tau_3) \\ =& \int \mathrm{d}\gamma\,\mathrm{d}\gamma'\,\delta\left(r_1-r_3-\frac{\gamma'-\gamma}{2}\right)\,\delta\left(r_2-r_4+\frac{\gamma'-\gamma}{2}\right)\,V_0\left(\frac{r+r'}{2}-\frac{\gamma+\gamma'}{2}\right)\,g(\gamma)\,g(\gamma') \end{aligned} \tag{10.17a}$$

$$=2\int \mathrm{d}\epsilon\,\mathrm{d}\epsilon'\,\delta\left(r_1-r_3-\epsilon'\right)\,\delta\left(r_2-r_4+\epsilon'\right)\,V_0\left(\frac{r+r'}{2}-\epsilon\right)\,g\left(\epsilon'-\epsilon\right)\,g\left(\epsilon'+\epsilon\right) \tag{10.17b}$$

$$=\delta\left(R-R'\right)\int \mathrm{d}\epsilon\,V_0\left(\frac{r+r'}{2}-\epsilon\right)\,g\left(\frac{r'-r}{2}-\epsilon\right)\,g\left(\frac{r'-r}{2}+\epsilon\right)\,, \tag{10.17c}$$

using the variable change

$$\left[\begin{array}{lll} \gamma & = & \tau_2 - \tau_1 \\ \gamma' & = & \tau_4 - \tau_3 \end{array}\right. \qquad \begin{array}{lll} \Gamma & = & \frac{1}{2}(\tau_1 + \tau_2) \\ \Gamma' & = & \frac{1}{2}(\tau_3 + \tau_4) \end{array} \quad \Leftrightarrow \left[\begin{array}{lll} \tau_1 & = & \Gamma - \frac{\gamma}{2} \\ \tau_3 & = & \Gamma' - \frac{\gamma'}{2} \end{array}\right. \qquad \begin{array}{lll} \tau_2 & = & \Gamma + \frac{\gamma}{2} \\ \tau_4 & = & \Gamma' + \frac{\gamma'}{2} \end{array} \tag{10.18a}$$

$$\left[\begin{array}{lll} \epsilon & = & \frac{\gamma'-\gamma}{2} \\ \epsilon' & = & \frac{\gamma'+\gamma}{2} \end{array}\right. \quad \Leftrightarrow \left[\begin{array}{lll} \gamma & = & \epsilon' - \epsilon \\ \gamma' & = & \epsilon' + \epsilon \end{array}\right. \tag{10.18b}$$

One sees that non-localities appear at the level of Eq. (10.17c) but are not expressed in terms of an explicit factorization of the kind

$$V_0^{[\mathrm{ind}]}(r_i) \equiv V(r)\, h(r_1 - r_3)\, h(r_2 - r_4)\,. \tag{10.19}$$

On the contrary, it is dubious that the expressions found for $V_0^{[\mathrm{ind}]}(r_i)$ can be implemented in existing EDF codes in a HO basis. Nevertheless, designing at first a RG-induced gaussian vertex remains of interest since it will lead to high-precision representations of the bare NN force $V_{\mathrm{low}\,k}$, setting reference points for studies without RG cutoff functions.

In the limit case $\tilde{g}(k) = 1$ one recovers easily Eq. (10.11) using Eq. (10.17a). In all other non-trivial cases, one can note that RG cutoff functions always verify

$$\tilde{g}(k) \underset{k \ll \Lambda}{\approx} 1 \qquad\qquad \tilde{g}(k) \underset{k \gg \Lambda}{\approx} 0\,, \tag{10.20}$$

i.e. associated Fourier transforms $g(r)$ will always be peaked around zero (see below). One sees that non-local induced vertices $V_0^{[\mathrm{ind}]}(r_i)$ will always correspond to rather small "non-local detunings" characterized for instance by the values of $(r_1 - r_3)$ or $(r_2 - r_4)$. That is, **the range in the non-local direction is expected to remain small**.

10.2.3 Applications

Let us now evaluate RG-induced vertices for the toy model case using the most common RG cutoff functions.

Sharp cutoff

For the sharp cutoff $V_{\mathrm{low}\,k}$, one has immediately

$$\tilde{g}(k) = \Theta(\Lambda - |k|)\,, \qquad\qquad g(r) = \frac{\sin(\Lambda\, r)}{\pi\, r}\,, \tag{10.21}$$

where one recovers the proper limits as the cutoff goes to infinity, since

$$\tilde{g}(k) \underset{\Lambda \to +\infty}{\longrightarrow} 1 \qquad\qquad g(r) \underset{\Lambda \to +\infty}{\longrightarrow} \delta(r) \quad (\text{from Eq. (10.8b)})\,. \tag{10.22}$$

While the expression of $V_0^{[\mathrm{ind}]}(r_i)$ does not seem to be analytical in this case, it can be numerically computed (see below). This cutoff function will be noted as g_∞, since this will be the limit of all smooth cutoff functions considered in this dissertation.

Smooth cutoff: exponential regulator

The smoothing parameter $\epsilon \in \mathbb{N}$ for the exponential regulator is noted n. Exponential RG cutoff functions read then

$$\tilde{g}_n(k) = \exp\left[-\left(\frac{k}{\Lambda}\right)^{2n}\right] \equiv \tilde{g}_n^1(k)\,, \tag{10.23}$$

and one gets

$$\tilde{g}_n^1(k) \underset{n\to+\infty}{\longrightarrow} \tilde{g}_\infty^1(k)\,, \qquad g_n^1(r) \underset{n\to+\infty}{\longrightarrow} g_\infty^1(r)\,, \tag{10.24a}$$

$$\tilde{g}_n^1(k) \underset{\Lambda\to+\infty}{\longrightarrow} 1\,, \qquad g_n^1(r) \underset{\Lambda\to+\infty}{\longrightarrow} \delta(r) \quad \text{(from Eq. (10.8c))}\,. \tag{10.24b}$$

In the simple gaussian case $n = 1$, we have immediately

$$g_1^1(r) = \frac{\Lambda}{2\sqrt{\pi}}\, e^{-\frac{1}{4}k^2\,\Lambda^2}\,. \tag{10.25}$$

That is the RG-induced vertex can be expressed as

$$\begin{aligned} V_0^{[\text{ind}]}(r_i) =& \delta\left(R - R'\right) \int \mathrm{d}\epsilon\, V_0\left(\frac{r+r'}{2} - \epsilon\right) g_1^1\left(\frac{r'-r}{2} - \epsilon\right) g_1^1\left(\frac{r'-r}{2} + \epsilon\right) \\ =& \delta\left(R - R'\right) \left[\frac{\Lambda^2\, e^{-\frac{1}{2}\Lambda^2\, r^{-2}}}{2\sqrt{2\pi}\sqrt{\Lambda^2 + \frac{2}{\mu^2}}}\right] \exp\left(-\frac{r^{+2}}{\mu^2 + \frac{2}{\Lambda^2}}\right) \\ \equiv& \delta\left(R - R'\right)\, h_\Lambda^1(r^-)\, h_\Lambda^2(r^+)\,, \end{aligned} \tag{10.26}$$

such that one has an explicit decorrelation between

- An "average" local vertex in terms of $r^+ \equiv (r + r')/2$, of range $\sqrt{\mu^2 + \frac{2}{\Lambda^2}}$.
- A non-local correction, which only depends on $r^- \equiv (r - r')/2$ with an effective range $\sqrt{2}/\Lambda$, which measures the non-locality of the RG-induced potential.

In the limit $\Lambda \to +\infty$, one recovers a pure local vertex, i.e.

$$\begin{aligned} h_\Lambda^1(r^-) \underset{\Lambda\to+\infty}{\sim}& \frac{1}{2}\left(\frac{\Lambda}{\sqrt{2}}\right) \frac{1}{\sqrt{\pi}} e^{-\left(\frac{\Lambda}{\sqrt{2}}\right)^2 r^{-2}}\,, \\ \underset{\Lambda\to+\infty}{\sim}& 2\,\delta(r^-) \quad \text{from Eq. (10.8c)}\,, \\ \underset{\Lambda\to+\infty}{\sim}& \delta(r' - r) \end{aligned} \tag{10.27a}$$

$$h_\Lambda^2(r^-) \underset{\Lambda\to+\infty}{\sim} V_0(r^+) = V_0(r)\,. \tag{10.27b}$$

For higher values of n, Fourier transforms of RG cutoff functions remain analytical, but are much more complicated. For instance

$$g_2^1(r) = \frac{1}{8\pi}\left(\Lambda^{5/2}\,\Gamma\left(\frac{5}{4}\right) {}_0\mathcal{F}_2\left(;\frac{1}{2},\frac{3}{2};\frac{\Lambda^4 r^4}{256}\right) - \Lambda^3 r^2\,\Gamma\left(\frac{3}{4}\right) {}_0\mathcal{F}_2\left(;\frac{5}{4},\frac{3}{2};\frac{\Lambda^4 r^4}{256}\right)\right)\,, \tag{10.28a}$$

$$\begin{aligned} g_3^1(r) =& \frac{\Lambda^5}{432}\Bigg(\frac{{}_0\mathcal{F}_4\left(;\frac{7}{6},\frac{4}{3},\frac{3}{2},\frac{5}{3};-\frac{\Lambda^6 r^6}{46656}\right)}{\Gamma\left(\frac{7}{6}\right)} - \frac{36\ {}_0\mathcal{F}_4\left(;\frac{2}{3},\frac{5}{6},\frac{7}{6},\frac{4}{3};-\frac{\Lambda^6 r^6}{46656}\right)}{\Lambda^2\sqrt{\pi}} \\ & - \frac{864\ {}_0\mathcal{F}_4\left(;\frac{1}{3},\frac{1}{2},\frac{2}{3},\frac{5}{6};-\frac{\Lambda^6 r^6}{46656}\right)}{\Lambda^4\,\Gamma\left(-\frac{1}{6}\right)}\Bigg)\,, \end{aligned} \tag{10.28b}$$

where $[{}_p\mathcal{F}_q]\,(a_1\dots a_p;b_1\dots b_q;x)$ are hypergeometric functions, i.e. functions defined in the form of hypergeometric series that read

$$c_0 = 1\,, \tag{10.29a}$$

$$\frac{c_{k+1}}{c_k} = \frac{P(k)}{Q(k)} = \frac{(k+a_1)(k+a_2)\dots(k+a_p)}{(k+b_1)(k+b_2)\dots(k+b_q)(k+1)}\,, \tag{10.29b}$$

such that

$$[{}_p\mathcal{F}_q]\,(a_1\dots a_p;b_1\dots b_q;x) = \sum_{k=0}^{\infty} c_k\, x^k\,, \tag{10.30a}$$

$$e^x = [{}_0\mathcal{F}_0]\,(;;x) = [{}_1\mathcal{F}_1]\,(a;a;x)\,, \tag{10.30b}$$

$$= \sum_{k=0}^{n} \frac{x^k}{k!} + \frac{x^{n+1}}{(n+1)!}\,[{}_1\mathcal{F}_1]\,(1;n+2;x)\,. \tag{10.30c}$$

Hypergeometric functions that enter the expressions of $g_n^i(r)$ remain however close to a cardinal sine in coordinate space. Using exponential RG cutoff leads in all cases to non-local potentials, where the non-local range that can be roughly represented by $(r'-r)$ remains small.

Indeed, and as seen in Fig. 10.7a where exponential RG cutoffs are represented in coordinate and momentum spaces, the "non-locality" does not extend significally beyond a few fms. Furthermore, the convergence $g_n^1 \underset{n\to+\infty}{\longrightarrow} g_\infty$ is seen graphically.

Smooth cutoff: alternative regulators

Previous arguments stand for other RG cutoff functions $g_\epsilon(r)$, such as the Woods-Saxon and hyperbolic tangent regulators defined by

$$\tilde{g}_\epsilon(k) = \frac{1}{1+\exp\left(\frac{k^2-\Lambda^2}{\epsilon^2}\right)} \equiv \tilde{g}_\epsilon^2(k)\,, \tag{10.31a}$$

$$\tilde{g}_\epsilon(k) = \frac{1}{2}\left[1+\tanh\left(\frac{\Lambda^2-k^2}{\Lambda\,\epsilon\,|k|}\right)\right] \equiv \tilde{g}_\epsilon^3(k)\,. \tag{10.31b}$$

These functions have all proper asymptotic behaviors, that is they verify

$$\tilde{g}_\epsilon(k) \underset{\epsilon\to+\infty}{\longrightarrow} \tilde{g}_\infty(k)\,, \qquad g_\epsilon(r) \underset{\epsilon\to+\infty}{\longrightarrow} g_\infty(r)\,, \tag{10.32a}$$

$$\tilde{g}_\epsilon(k) \underset{\Lambda\to+\infty}{\longrightarrow} 1\,, \qquad g_\epsilon(r) \underset{\Lambda\to+\infty}{\longrightarrow} \delta(r)\,, \tag{10.32b}$$

and their expressions $g_\epsilon^i(r)$ in coordinate space, although not analytical, can be numerically evaluated, as seen in Figs. (10.7b,10.7c) for a cutoff $\Lambda = 2.1$ fm^{-1}. Same conclusions than for exponential RG cutoffs hold, i.e. (i) the limited non-local range, and (ii) the convergence $g_\epsilon^i \underset{\epsilon\to+\infty}{\longrightarrow} g_\infty$.

Non-local vertices

RG-induced non-local vertices $V_0^{[\mathrm{ind}]}$, expressed as a function of r^+ and r^-, can then be evaluated, analytically for the exponential $n=1$ cutoff, and numerically for sharp and exponential $n>1$ cutoffs. Results are presented in Figs. (10.8,10.9), where one sees

- the convergence of the induced potential towards a Dirac function as a function of r^- when the RG cutoff goes to large values,

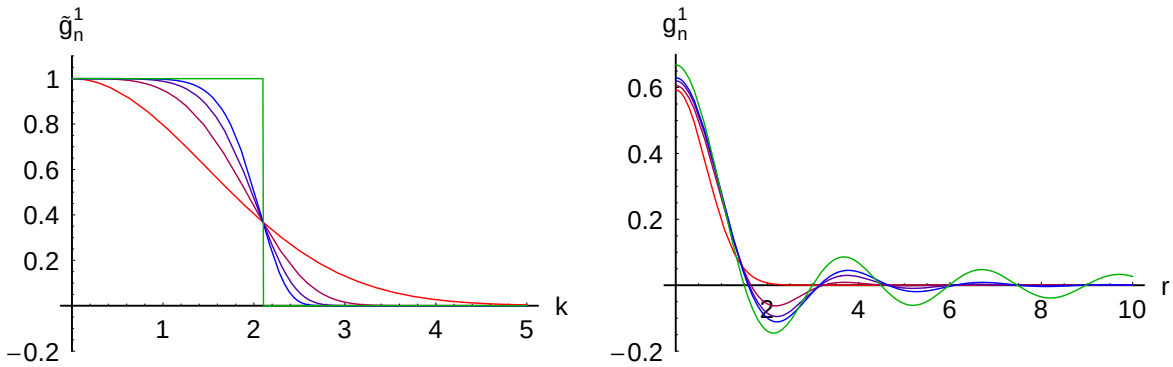

(a) Exponential cutoff g^1_n : (red) $n = 1 \ldots 4$ (blue)

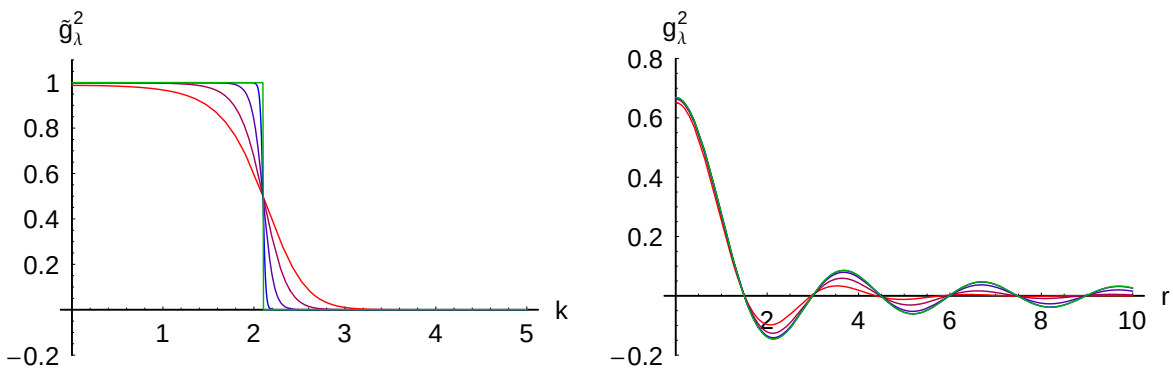

(b) Woods-Saxon cutoff g^2_ϵ : (red) $\epsilon = 1; 0.75; 0.5; 0.25$ (blue)

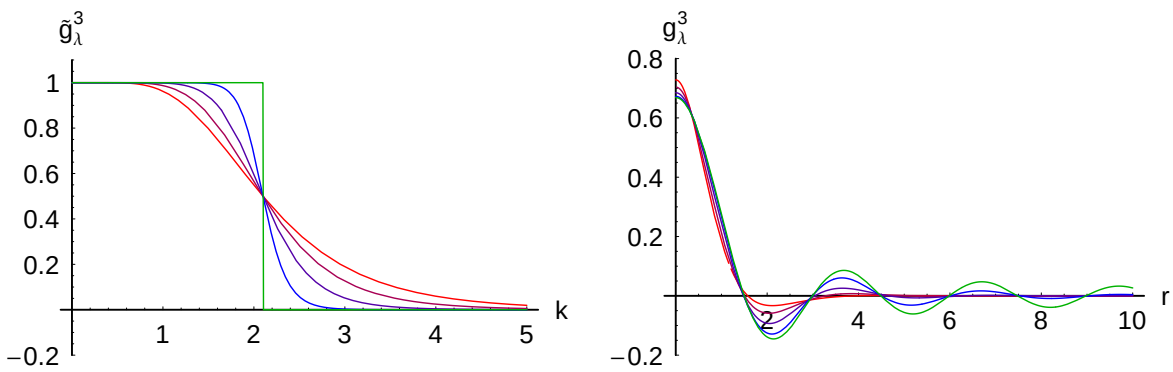

(c) Hyperbolic tangent cutoff g^3_ϵ : (red) $\epsilon = 1; 0.75; 0.5; 0.25$ (blue)

Figure 10.7: RG cutoff functions g^i_ϵ in momentum space (left) and Fourier transforms in coordinate space (right). The limit function g_∞ is represented in green.

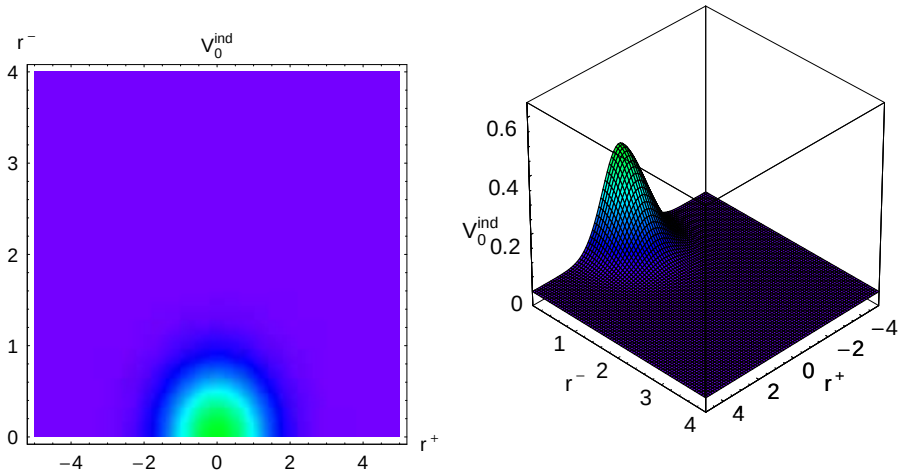

(a) $\Lambda = 2.0$ fm^{-1}

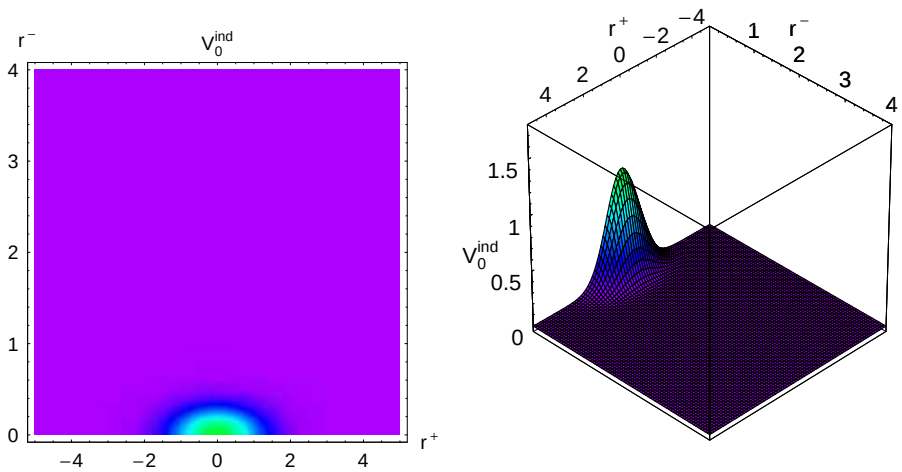

(b) $\Lambda = 5.0$ fm^{-1}

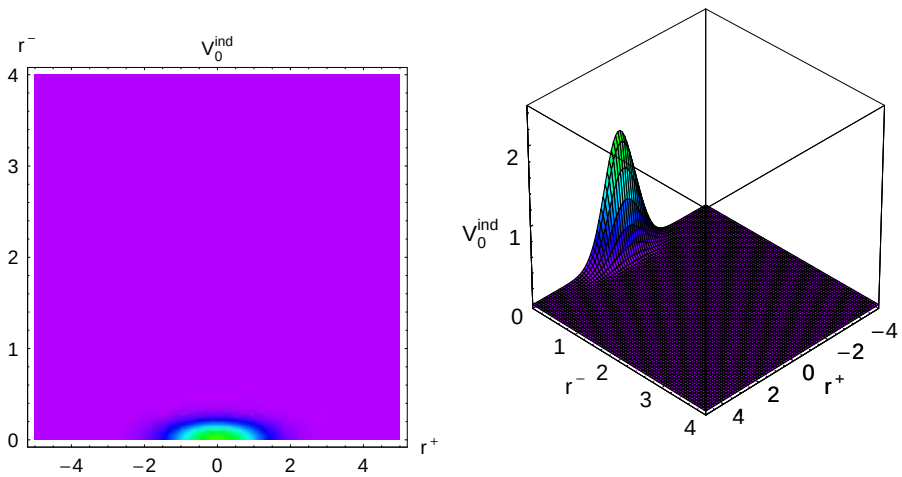

(c) $\Lambda = 8.0$ fm^{-1}

Figure 10.8: RG-induced non-local vertex in coordinate space as a function of $r^+ = (r' + r)/2$ and $r^- = (r' - r)/2$ for an exponential RG cutoff function with $n = 1$ and $\mu = 1.2$ fm.

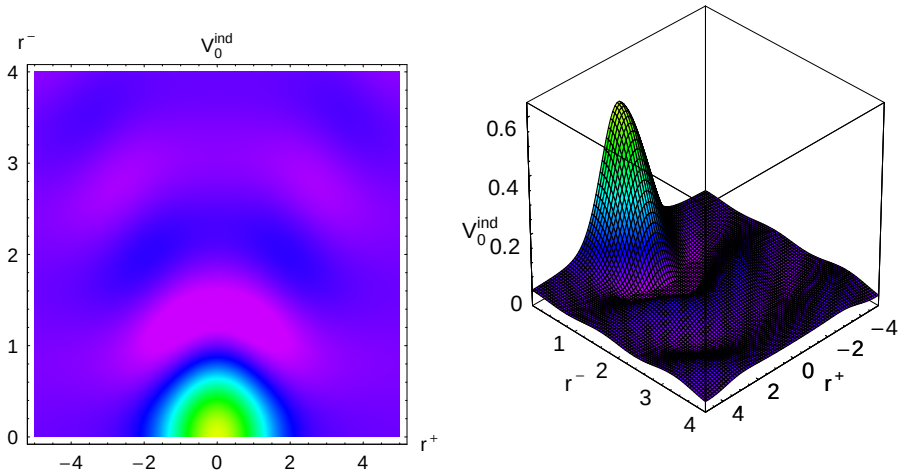

(a) $\Lambda = 2.0$ fm^{-1}

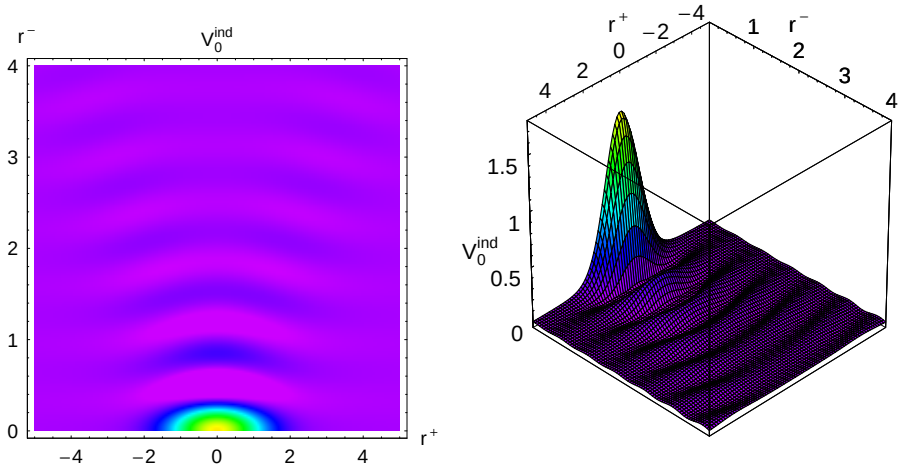

(b) $\Lambda = 5.0$ fm^{-1}

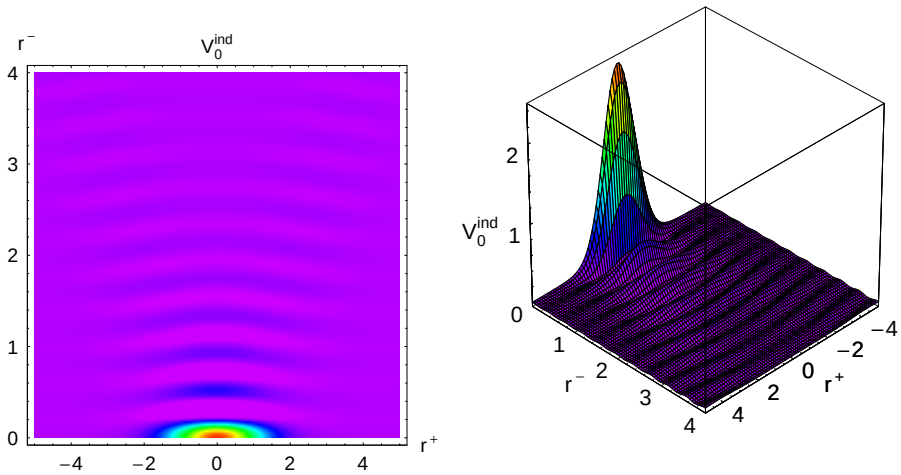

(c) $\Lambda = 8.0$ fm^{-1}

Figure 10.9: Same as in Fig. 10.8 for a sharp RG cutoff function. z scales are identical to the ones in Fig. 10.8 for each Λ value.

- a "ripple effect" in the sharp cutoff case. These cardinal sine-like oscillations seen in coordinate space are caused by the discontinuity of the sharp RG cutoff, and should also be observed when using standard smooth cutoffs that remain very close to a unit step function in momentum space. For these reasons, the cutoff function $\tilde{g}_1^1(k)$ (simple exponential) seems to be the more "physically sound". However such a function deteriorates the behavior of $V_{\text{low}\,k}$ at small momentum [491], and values of $n \sim 6-8$ are advised. Please note however that (i) such oscillations are smoothened out in the 3D case (Sec. 10.2.4), (ii) no real prescription exist to express non-local nuclear forces, the choice of r^+/r^- as variables of interest allows however to recover the proper limit cases, and (iii) such non-local vertices are specific of low-momentum interactions, since for large values of Λ non-local behaviors disappear. Indeed, for large Λ one notices that the RG-induced solution is very close to the non-induced one. Finally, one might try to define a RG cutoff function G_ϵ which verifies

$$\tilde{G}_\epsilon(k) \underset{\Lambda\to+\infty}{\longrightarrow} \tilde{G}_\infty(k)\,, \qquad \tilde{G}_\epsilon(k) \underset{\Lambda\to+\infty}{\longrightarrow} 1\,, \tag{10.33a}$$

$$\tilde{G}_\epsilon(|k| \lesssim \Lambda) \approx 1\,, \qquad \tilde{G}_\epsilon(|k| \gtrsim \Lambda) \approx 0\,, \tag{10.33b}$$

$$G_\epsilon(r) > 0\,, \tag{10.33c}$$

that might be complicated but would remove non-local oscillations at small Λ. The latter could be then implemented in existing RG codes since cutoffs are numerically evaluated at the beginning of the program once and for all. However, it seems that Eqs. (10.33a,10.33b) are exclusive with Eq. (10.33c).

10.2.4 Realistic RG-induced vertices

Let us now make brief comments concerning the generalization of the 1D toy model for a realistic nuclear interaction.

- All derivations from the toy model will hold for the 3D case, and final expressions in coordinate space will still involve Fourier transforms of the RG cutoff functions that are however more complicated because of angular dependencies. The only simple case is the gaussian RG cutoff, where results of the previous section stand. In all other cases the final convolution is a lot harder to treat.
- Equivalent derivations for spin-orbit and tensor terms are possible but are left pending at this point.
- In any cases, we still expect the apparition of non-local potentials in coordinate space, with the same features that arose in the toy model, i.e. (i) complex non-local dependencies, (ii) a limited range in the non-local direction characterized by $\vec{r}^{\,-} \equiv \vec{r} - \vec{r}\,'$, and (iii) vanishing non-local components at large RG cutoffs Λ.

Let us now make explicit some 3D cutoff functions.

Sharp RG cutoff

For the sharp cutoff function one gets immediately

$$\tilde{g}_\infty(k) = \Theta(\Lambda - |\vec{k}\,|)\,, \tag{10.34a}$$

$$\begin{aligned} g_\infty(r) =& \frac{1}{(2\pi)^3} \int \mathrm{d}\vec{k}\, e^{i\,\vec{k}\cdot\vec{r}}\, \tilde{g}_\infty(\vec{k}\,) \\ =& \frac{1}{(2\pi)^2} \int \sin(\theta)\,\mathrm{d}\theta \int k^2\,\mathrm{d}k\, e^{i\,kr\,\cos(\theta)}\,\Theta(\Lambda - k) \\ =& \frac{2}{(2\pi)^2} \int k^2\,\mathrm{d}k\, \frac{\sin(k\,r)}{k\,r}\,\Theta(\Lambda - k) \\ =& \frac{2}{(2\pi)^2}\, \frac{[\sin(\Lambda\,r) - \Lambda\,r\,\cos(\Lambda\,r)]}{r^3}\,. \end{aligned} \tag{10.34b}$$

$g_\infty(r)$ is represented in FIG. 10.10, alongside with the equivalent function obtained in the 1D case. The oscillatory behavior is still present, but is smoothened out which suggests a quenching of the non-local ripple effect in 3D, whereas the effective range of such a function is a little increased.

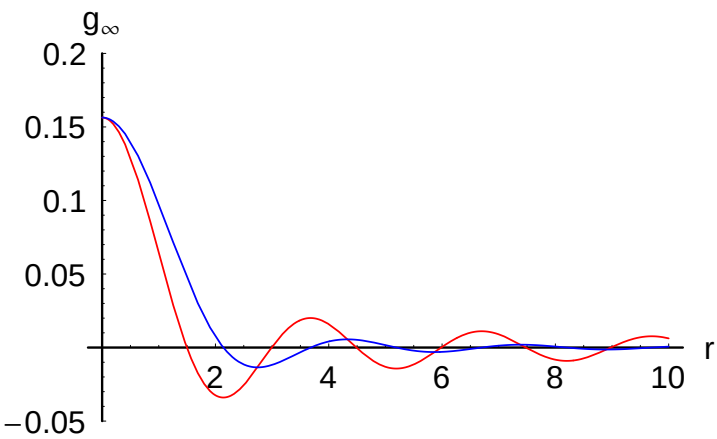

Figure 10.10: Sharp RG cutoff function g_∞ in coordinate space for the 3D (blue) and 1D (red) cases and $\Lambda = 2.1\ \mathrm{fm}^{-1}$. The 1D case is rescaled such that values at $r = 0$ are identical.

Smooth RG cutoff

For smooth exponential cutoffs one obtains

$$\tilde{g}_n(k) = \exp\left[-\left(\frac{k}{\Lambda}\right)^{2n}\right]\,, \tag{10.35a}$$

$$g_1(r) = \frac{\Lambda^3}{8\pi^{3/2}}\,\exp\left[-\frac{1}{4}\Lambda^2\,r^2\right]\,, \tag{10.35b}$$

$$g_2(r) = -\,\frac{\Lambda^3}{48\,\pi^2}\left(\Lambda^2\,r^2\,\Gamma\left(\frac{5}{4}\right)\,[{}_0\mathcal{F}_2]\left(;\frac{3}{2},\frac{7}{4};\frac{\Lambda^4\,r^4}{256}\right) - 8\,\Gamma\left(\frac{7}{4}\right)\,[{}_0\mathcal{F}_2]\left(;\frac{1}{2},\frac{5}{4};\frac{\Lambda^4\,r^4}{256}\right)\right)\,. \tag{10.35c}$$

These functions are represented in FIG. 10.11, where once again a reduction of oscillations at large r is observed in comparison with the 1D case.

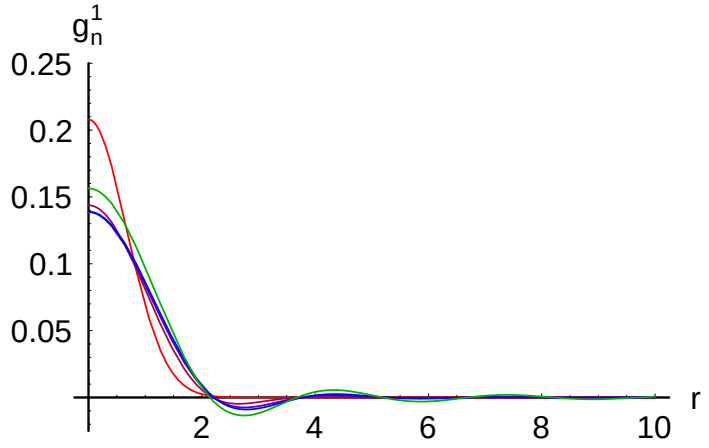

Figure 10.11: Smooth RG exponential cutoff functions g_n in the 3D case in coordinate space for $n = 1$ (red) up to $n = 4$ (blue) and $\Lambda = 2.1$ fm^{-1}. The limit function $g_\infty(r)$ is represented in green.

10.3 Results for $v_{\rm BDRS}^{[\rm bare(2)]}$: ^{1}S$_0$ channel with RG cutoffs

In all the following gaussian terms are ordered by increasing range, that is μ_1 will correspond to the shorter range and μ_N to the longest one. In this subsection $v_{\rm BDRS}^{[\rm bare(2)]}$ will denote the gaussian representation with explicit RG cutoffs. Unless precised, we will use for input a smooth neutron-neutron $V_{{\rm low}\,k}$ ($T_z = +1$). $N = 3$ gaussians have been used and allow a precise representation of matrix elements, whereas only six parameters are to be adjusted.

10.3.1 Fit setup

Prior to performing the actual fit, several quantities still are to be defined. The most important parameters of FITPACK are displayed in TAB. {10.2}. They correspond to rather standard parameters for a genetic algorithm, e.g. crossover and mutation probabilities of 80% and 20%, respectively. For a fit restricted to the ^{1}S$_0$ channel, only $2N$ parameters are to be adjusted, N being the number of gaussian terms in $v_{\rm BDRS}^{[\rm X]}$. Indeed, (i) spin-orbit and tensor coupling do not contribute to this particular channel, and (ii) only $S = 0$, $T = 1$ coupling constants have to be considered. For these reasons, a rather small population size, i.e. between 300 and 1000 simplexes, is enough.

The two-dimension k-mesh (k_i, k_j) that will be used is defined as a regular sampling of the interval $[0, \Lambda\sqrt{2}]$. In the case of a sharp RG cutoff for $V_{{\rm low}\,k}$, it corresponds to putting an equal constraint on non-zero matrix elements $(k, k') < \Lambda$ and zero matrix elements $(k, k') > \Lambda$. Indeed, the number of sampled points in both of these regions in the 2D mesh will be the same. Other choices for the mesh are possible, e.g. Gauss-Legendre quadrature points, but were not found to impact significantly the results. In any case, the introduction of RG cutoff fucntions for $v_{\rm BDRS}^{[\rm bare(2)]}$ alleviates this issue, which is obvious for instance using sharp cutoff functions.

Theoretical uncertainties $(\delta V_{{\rm low}\,k})_0^{001}(k_i, k_j; \Lambda) \equiv \delta V_{{\rm low}\,k}(k_i, k_j; \Lambda)$ that enter the cost function are defined in order to allow a different weighting of diagonal and off-diagonal matrix elements, that is to put more constraints on specific regions in (k, k') space, as introduced in SEC. 8.5. The general idea is (i) to put more constraints on diagonal matrix elements, since most physical observables are fully on-shell quantities, and (ii) to allow more freedom where $V_{{\rm low}\,k}$ has a large

curvature, since it cannot be sampled efficiently by a combination of "smooth" form factors. In that respect, one defines

$$\delta V_{\text{low}\,k}(k_i,k_j) \equiv \sigma_V(k_i,k_j)(V_{\text{low}\,k}^{\max} - V_{\text{low}\,k}^{\min})\mathcal{F}(k_i,k_j)\,, \tag{10.36a}$$

$$\sigma_V(k_i,k_j) \equiv \begin{cases} (\sigma_0) + (\sigma_+)\,\mathcal{G}\left[\dfrac{\Delta V_{\text{low}\,k}(k_i,k_j)}{\Delta V_{\text{low}\,k}^{\max}}\right]\,, \\ (\sigma_0) + (\sigma_-)\,\mathcal{G}\left[\dfrac{\Delta V_{\text{low}\,k}(k_i,k_j)}{\Delta V_{\text{low}\,k}^{\min}}\right]\,, \end{cases} \tag{10.36b}$$

$$\mathcal{F}(k_i,k_j) \equiv \frac{1+\kappa}{\kappa+\nu}\left[1 + (\kappa-1)\left|\frac{k_i-k_j}{k_i+k_j}\right|^{\nu}\right]\,, \tag{10.36c}$$

$$\mathcal{G}(X) \equiv X^{\beta}\,, \tag{10.36d}$$

where $Y^{\min}$ and $Y^{\max}$ denote respectively the minimum and maximum values of the quantity Y on the 2D mesh (k_i,k_j), whereas $\Delta V_{\text{low}\,k}(k_i,k_j)$ is the local curvature of $V_{\text{low}\,k}$ defined through a finite-difference expression for the Laplacian on the 2D momentum mesh by[3]

$$\Delta V_{\text{low}\,k}(k_i,k_j) = 2\left(\frac{V_{\text{low}\,k}(k_i,k_{j+1})}{\alpha_2(\alpha_2+\alpha_4)} + \frac{V_{\text{low}\,k}(k_{i-1},k_j)}{\alpha_1(\alpha_1+\alpha_3)} + \frac{V_{\text{low}\,k}(k_i,k_{j-1})}{\alpha_4(\alpha_2+\alpha_4)} + \frac{V_{\text{low}\,k}(k_{i+1},k_j)}{\alpha_3(\alpha_1+\alpha_3)} - \frac{V_{\text{low}\,k}(k_i,k_j)}{\alpha_1\alpha_3} - \frac{V_{\text{low}\,k}(k_i,k_j)}{\alpha_2\alpha_4}\right)\,, \tag{10.38a}$$

$$\alpha_1 = k_i - k_{i-1}\,, \qquad \alpha_2 = k_{j+1} - k_j\,, \tag{10.38b}$$

$$\alpha_3 = k_{i+1} - k_i\,, \qquad \alpha_4 = k_j - k_{j-1}\,. \tag{10.38c}$$

That is, (i) $\mathcal{F}(k_i,k_j,\Lambda)$ corresponds to the weighting between diagonal/off-diagonal components, while preserving an average value along the direction $k-k'$, (ii) $\mathcal{G}(X)$ defines the relative importance of high curvatures, i.e. mostly aroung the RG cutoff Λ, and (iii) $\sigma_V(k_i,k_j)$ relates the local Laplacian of $V_{\text{low}\,k}$ with a relative tolerance with respect to the total magnitude in the channel $(V_{\text{low}\,k}^{\max} - V_{\text{low}\,k}^{\min})$, $(\sigma_0)/(\sigma_+)/(\sigma_-)$ being the relative tolerances assigned to the points having zero, minimum and maximum curvatures, respectively. Typical values for the various parameters entering Eqs. (10.36a-10.36d) are found in Tab. {10.2}. An example of such error bars can be found on Fig. 10.12. As expected, one sees that more accuracy is demanded around the diagonal part of the interaction, with some freedom allowed around the cutoff Λ. In the following these theoretical uncertainties on the matrix elements will not be represented unless specified to not overload the graphics. Note that these uncertainties are defined up to an arbitrary multiplicative constant. Indeed, only the relative weighting of these errors matters in the minimization of the cost function.

10.3.2 Convergence issues

Fit attempts have been made in two steps. The first one consisted in a rough search for the optimal regions for the free parameters. In a second step the fit code is re-run with these approximate search regions. For values of the RG cutoff $\Lambda \lesssim 3.5$ fm^{-1}, initial limits which are accurate to constrain with efficiency the search space are summarized in Tab. {10.3} (Procedure I).

[3] For a uniform mesh the simpler formula

$$\Delta V_{\text{low}\,k}(k_i,k_j) = \frac{1}{\alpha^2}\left(V_{\text{low}\,k}(k_i,k_{j+1}) + V_{\text{low}\,k}(k_{i-1},k_j) + V_{\text{low}\,k}(k_i,k_{j-1}) + V_{\text{low}\,k}(k_{i+1},k_j) - 4V_{\text{low}\,k}(k_i,k_j)\right)\,, \tag{10.37a}$$

$$\alpha = k_i - k_{i-1}\,, \tag{10.37b}$$

can be applied.

FITPACK control parameters	
GA population size	750
Initial (relative) dispersion of simplexes	0.35
GA selection type	Biaised roulette
Elitism	True
GA number of simplexes in crossover	3
GA crossover rate	80%
GA mutation rate	20%
Simplex mutation blow-up ratio	5.
Number of simplex interations between GA step	5
GA stop: max variation of merit between simplexes	$10.^{-7}$
GA stop: max (relative) dispersion of best simplex	$10.^{-7}$

Theoretical uncertainties					
(σ_0)	0.1%	(σ_-)	1%	(σ_+)	0.2%
κ	1.5	ν	2.0	β	0.6

Table 10.2: Control parameters that enter the fit procedure, i.e. for FITPACK and the definition of theoretical uncertainties.

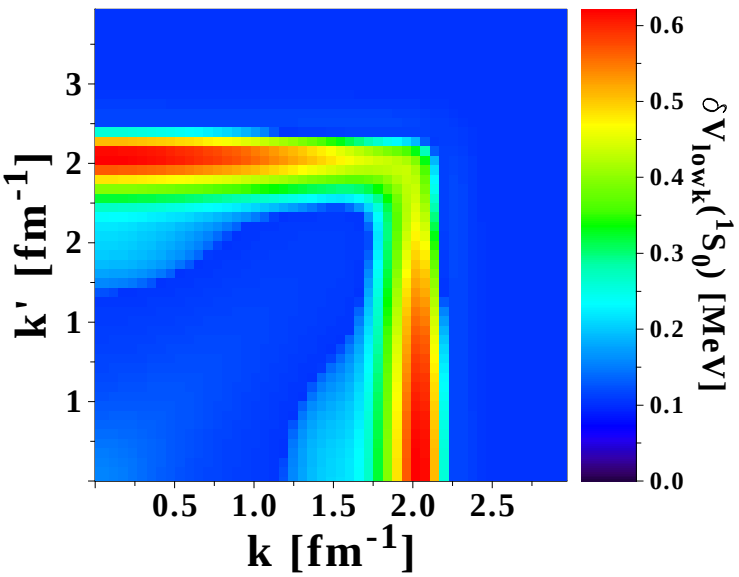

Figure 10.12: Definition of theoretical uncertainties on $V_{\text{low}\,k}$ for a smooth cutoff $\Lambda = 2.1\ \text{fm}^{-1}$.

	Procedure I		Procedure II		Procedure III	
	Min	Max	Min	Max	Min	Max
μ_1 [fm]	0.0	0.5	0.0	0.5	−0.1	0.5
C_1^{10} [MeV]	0.0	400000.0				
S_1^{10} [MeV.fm^3]			0.0	800.0	0.0	800.0
μ_2 [fm]	0.9	1.5	0.9	1.5	0.9	1.5
C_2^{10} [MeV]	−200.0	0.0				
S_2^{10} [MeV.fm^3]			−1500.0	−500.0	−1500.0	−500.0
μ_3 [fm]	2.6	3.8	2.6	3.8	2.6	3.8
C_3^{10} [MeV]	−10.0	10.0				
S_3^{10} [MeV.fm^3]			−500.0	0.0	−500.0	0.0

Table 10.3: Initial limits for parameters used in the fit of $V_{\rm low\,k}$ with three gaussians in the ^{1}S$_0$ channel, with different procedures detailed in the text.

With the fit procedure presented in Chap. 9, the convergence to the absolute minimum of the merit function χ^2 was very hard to reach, in particular for the parameter C_1^{01} associated with the shortest range μ_1. To illustrate this, 30 successive fits with the same initial limits have been done using $\Lambda = 1.8$ fm^{-1}, where the problem is more explicit. Optimized values of χ^2 presented in Fig. 10.13a are all very similar, as well as values of the ranges presented in Fig. 10.13b. It appears that $v_{\rm BDRS}^{[\rm bare(2)]}$ presents a (very) short, a medium and a long-range component, and this will be discussed more extensively later on. When looking at small variations of the fitted parameters, that is in logarithmic scale in Fig. 10.13d, medium and long ranges remain very stable, but important instabilities are seen for the short-range component. The latter are obvious when considering coupling constants C_i^{10}, presented in Figs. (10.13c,10.13e,10.13f). We find that the parameter μ_1 always hits the bottom hard limit $\mu = 0$ fm, while the associated coupling constant C_1^{10} hits the upper limit, whatever high the latter is set to.

The strength C_1^{10} tends to infinity when the associated range μ_1 goes to zero, i.e. a safe assumption is that one has been using inaccurate degrees of freedom. To solve this issue, we found one should adjust in place of C_i^{10} the zero-momentum coupling strengths for each term defined through

$$S_i^{10} \equiv (\mu_i\,\sqrt{\pi})^3\, C_i^{10}\,. \tag{10.39}$$

That is the ^{1}S$_0$ partial wave to be adjusted now reads

$$v_{\rm BDRS}^{[\rm X]}(^1S_0, k, k') = \frac{1}{2\pi^2}\sum_{i=1}^{N} S_i^{01}[\rho_0,\Lambda]\,\frac{\tilde{g}_0^i(k',k)}{4\pi}\,. \tag{10.40}$$

The latter are represented in Fig. 10.14, and are found to be almost identical for each set of fitted parameters. This suggests that **relevant degrees of freedom for a representation of $V_{\rm low\,k}$ when using explicit RG cutoff functions are indeed the parameters** $\{\mu_i, S_i^{10}\}$. Using these parameters instead of $\{\mu_i, C_i^{10}\}$, the fit limits can be now set to more reasonable values presented in Tab. {10.3} (Procedure II). To characterize further the relative impact of each gaussian term, we also introduce relative strengths at zero momentum R_i^{10} defined for each gaussian as

$$R_i^{10} \equiv \frac{|S_i^{10}|}{\sum_i |S_i^{10}|}\,. \tag{10.41}$$

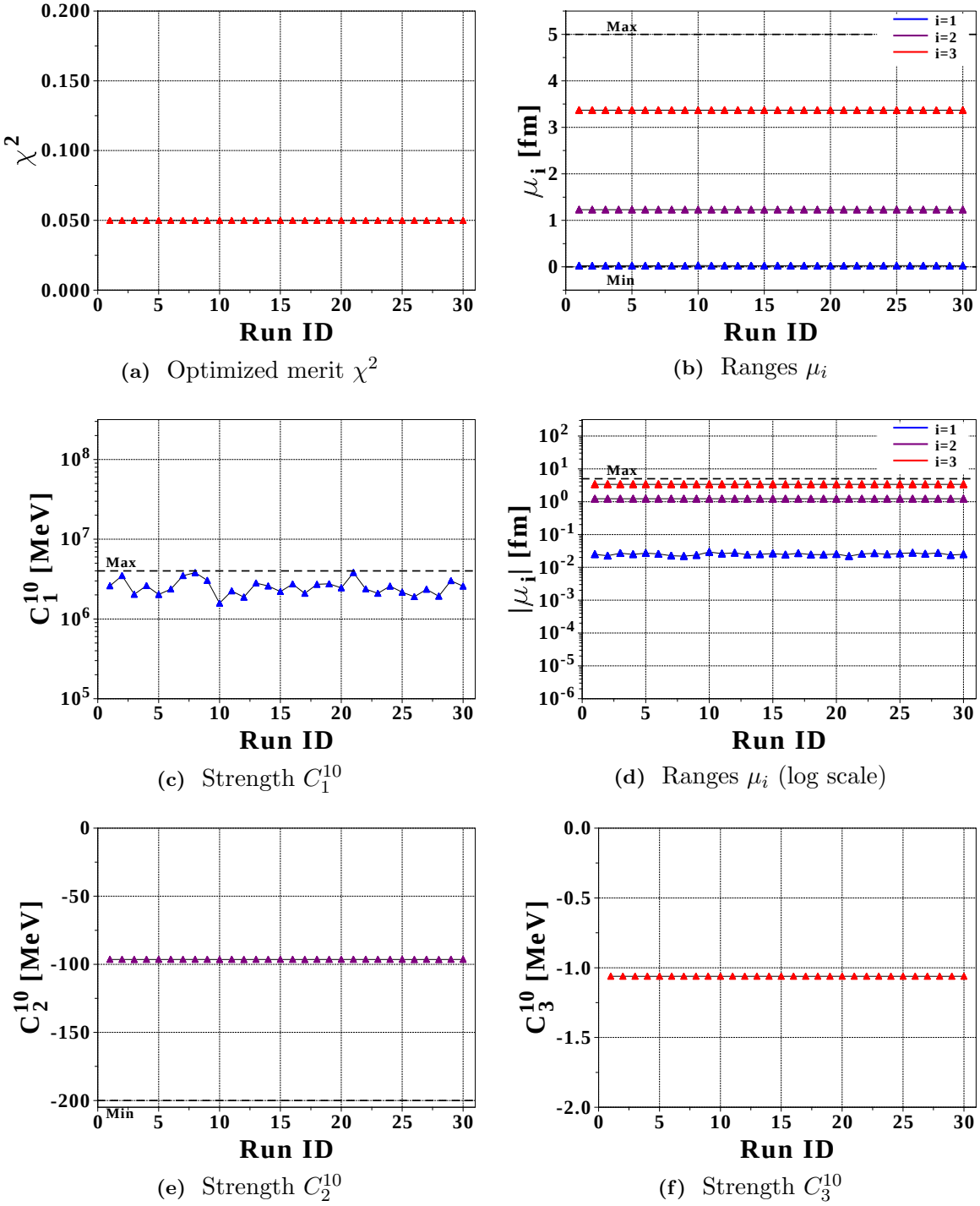

(a) Optimized merit χ^2

(b) Ranges μ_i

(c) Strength C_1^{10}

(d) Ranges μ_i (log scale)

(e) Strength C_2^{10}

(f) Strength C_3^{10}

Figure 10.13: Results for 30 different fits of the smooth neutron-neutron $V_{\text{low}\,k}$ with $N = 3$ gaussian terms and explicit RG cutoff functions.

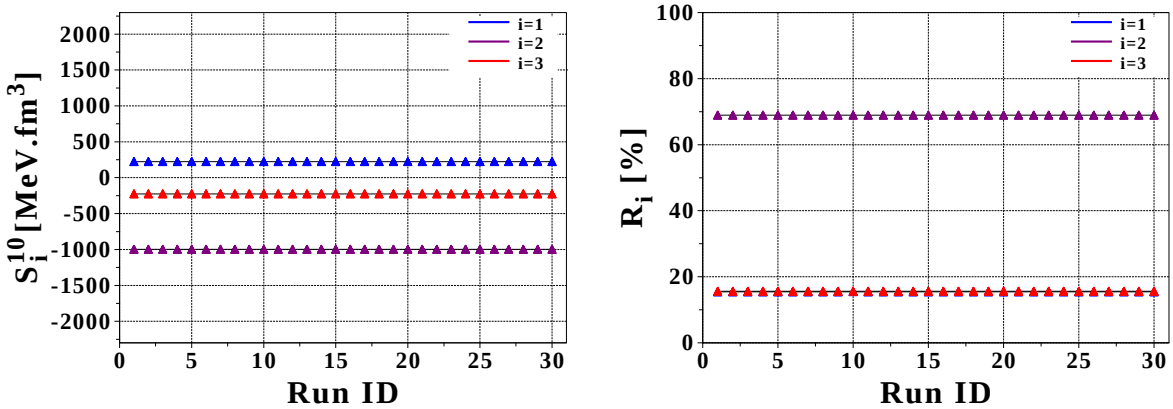

Figure 10.14: Coupling constants S_i^{10} and relative strengths R_i^{10} for 30 different fits using $\{\mu_i, C_i^{10}\}$ as degrees of freedom (see text).

Running once more 30 fits for $\Lambda = 1.8$ fm^{-1}, with these new degrees of freedom yields to quite different results presented in Fig. 10.15 and Tab. {10.4}. The average optimal value of χ^2 is slightly decreased, that is the change of degrees of freedom allowed a better optimization of the search process. However, while the value of S_1^{10} remains very stable and well within the pre-built hard limits, the associated range μ_1 still oscillates a lot (actually, more than in the previous case). Generally speaking, while the total merit is decreased, the spread of all parameters is found to be slightly increased, which is not promising.

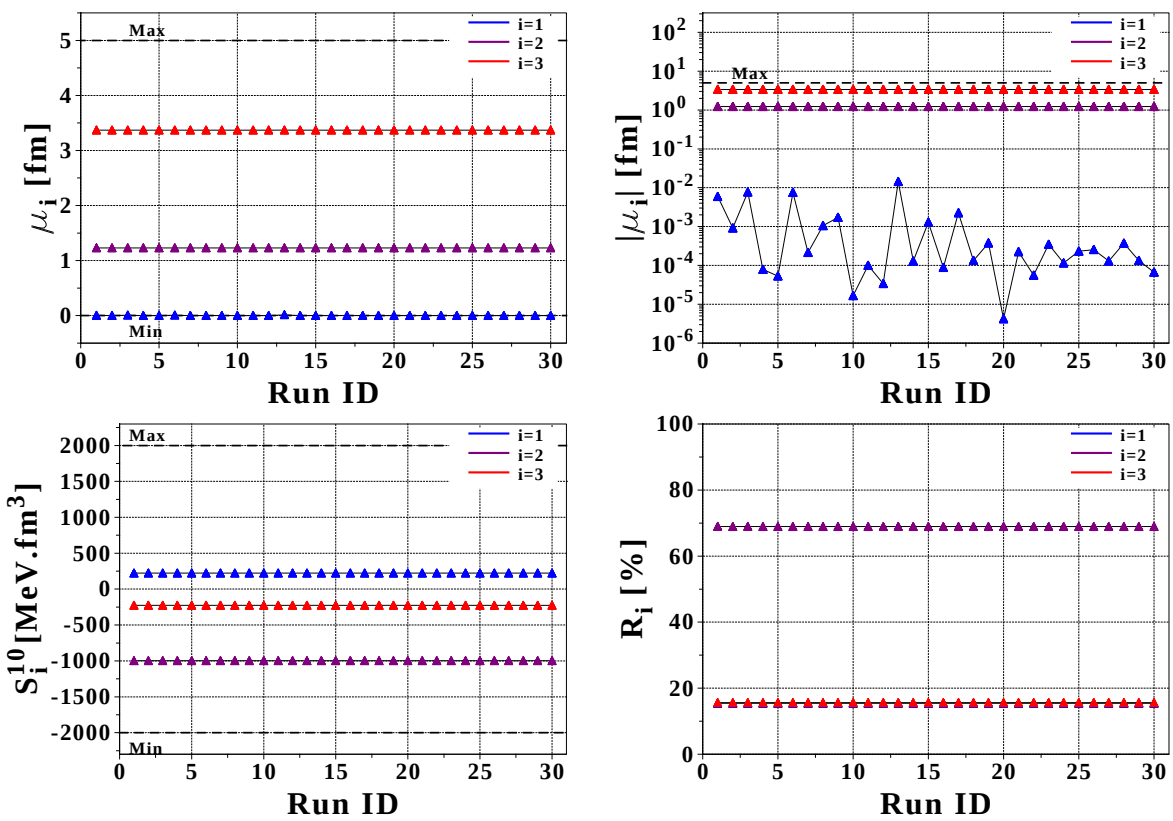

Figure 10.15: Same as in Fig. 10.13 with $\{\mu_i, S_i^{10}\}$ as degrees of freedom in the fit.

The oscillations of μ_1 come from the fact that it still hits the bottom hard limit $\mu_1 = 0$ fm. As a general principle, any fit results where one parameter hits a hard limits is subject to caution, since the stochastic exploration of phase space is not efficient around pre-built boundaries. To solve this problem, one can use an additional property of the representation $\{\mu_i, S_i^{10}\}$. In the latter, ranges μ_i are only used at even powers, that is one can do the actual fit while allowing ranges to be negative and keeping for "physical" parameters their absolute values. This allows to remove $\mu_1 = 0$ fm as a boundary. Thus we set the lower limit for μ_1 to -0.1 fm and ran again 30 fits with every other parameters kept to the same values (Procedure III).

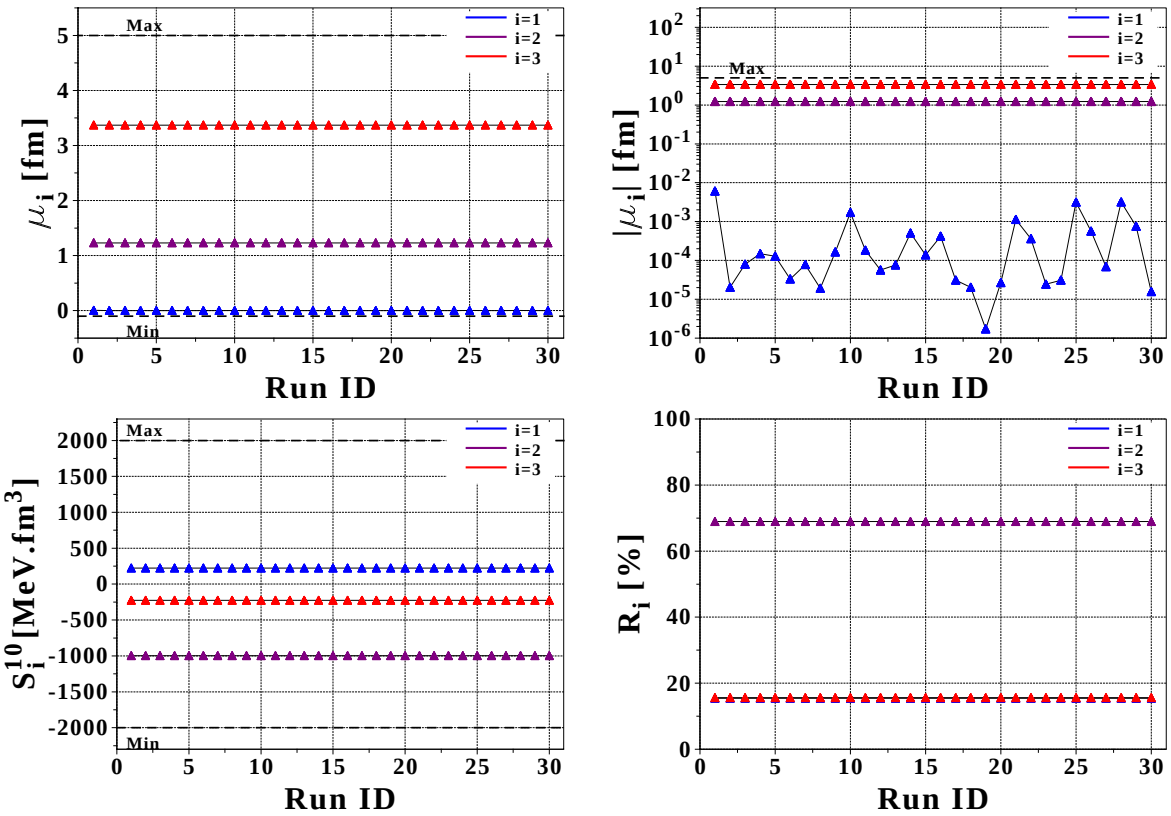

Figure 10.16: Same as in Fig. 10.15 with a negative lower limit for the ranges μ_i.

Final results are found in Fig. 10.16 and Tab. {10.4}. The optimized χ^2 is decreased by a few percents. Some oscillations still occur for μ_1, but with a much reduced dispersion. **Generally speaking, the latter procedure reduces the spread for each $\chi^2, \mu_i, S_i^{10}, R_i^{10}$ by about one order of magnitude**. Running 30 fits with randomized initializations leads now to almost identical values for the optimized merit χ^2. This proves a posteriori the efficiency of the genetic algorithm. Procedure III will be used in the remaining of this section, unless specified.

10.3.3 First results

Using the optimized fitting procedure, parameters $\{\mu_i, S_i^{10}\}$ are adjusted to reproduce the matrix elements of $V_{\text{low}\,k}$ in the $^1\text{S}_0$ partial wave. The results, presented in Fig. 10.17 for $\Lambda = 1.8$ fm^{-1}, are very encouraging since matrix elements of $v_{\text{BDRS}}^{[\text{bare}(2)]}$ are on top of $V_{\text{low}\,k}$ almost everywhere, at the pencil precision. To show this perfect agreement, scattering phase shifts in the $^1\text{S}_0$ channel as well as the INM gap equation of the fitted interaction are represented in Fig. 10.18, and agree perfectly with $V_{\text{low}\,k}$, even if these quantities were not constrained by the fit. The accuracy of the

		Procedure I		Procedure II	
		$\overline{X}$	ΔX	$\overline{X}$	ΔX
χ^2		0.0499398	0.0000145	0.0498379	0.0000064
μ_1	[fm]	0.02533	0.00177	0.00153	0.00315
C_1^{10}	[MeV]	2.5447×10^6	5.5467×10^5	1.8016×10^{16}	9.5316×10^{16}
S_1^{10}	[MeV.fm^3]	223.5328	0.0482	223.1919	0.0113
R_1^{10}	[%]	15.4456	0.0023	15.4292	0.0005
μ_2	[fm]	1.22926	0.00004	1.22952	0.00002
C_2^{10}	[MeV]	−96.4554	0.0121	−96.3698	0.0029
S_2^{10}	[MeV.fm^3]	−997.6655	0.0377	−997.4039	0.0269
R_2^{10}	[%]	68.9364	0.0020	68.9506	0.0011
μ_3	[fm]	3.36885	0.00078	3.36938	0.00019
C_3^{10}	[MeV]	−1.0617	0.0001	−1.0608	0.0003
S_3^{10}	[MeV.fm^3]	−226.0271	0.0107	−225.9531	0.0168
R_3^{10}	[%]	15.6180	0.0004	15.6201	0.0013

		Procedure III	
		$\overline{X}$	ΔX
χ^2		0.0498362	0.0000011
μ_1	[fm]	0.00058	0.00131
C_1^{10}	[MeV]	2.6125×10^{17}	1.4070×10^{18}
S_1^{10}	[MeV.fm^3]	223.1898	0.0053
R_1^{10}	[%]	15.4292	0.0003
μ_2	[fm]	1.22951	0.00001
C_2^{10}	[MeV]	−96.3701	0.0026
S_2^{10}	[MeV.fm^3]	−997.3945	0.0076
R_2^{10}	[%]	68.9502	0.0008
μ_3	[fm]	3.36930	0.00010
C_3^{10}	[MeV]	−1.0610	0.0001
S_3^{10}	[MeV.fm^3]	−225.9591	0.0098
R_3^{10}	[%]	15.6206	0.0006

Table 10.4: Optimization results for 30 fits with different procedures (see text): optimized merit χ^2, ranges μ_i, coupling constants C_i^{10}, zero-momentum coupling constants S_i^{10} and relative strengths at zero momentum R_i^{10}.

representation suggests that the symmetric matter EOS with $v_{\rm BDRS}^{[\rm bare(2)]}$ computed at different levels of MBPT complexity in place of $V_{{\rm low}\,k}$ will also provide identical saturation properties[4]. As a last check, a comparison of Weinberg eigenvalues and scattering parameters is done in TAB. {10.5}.

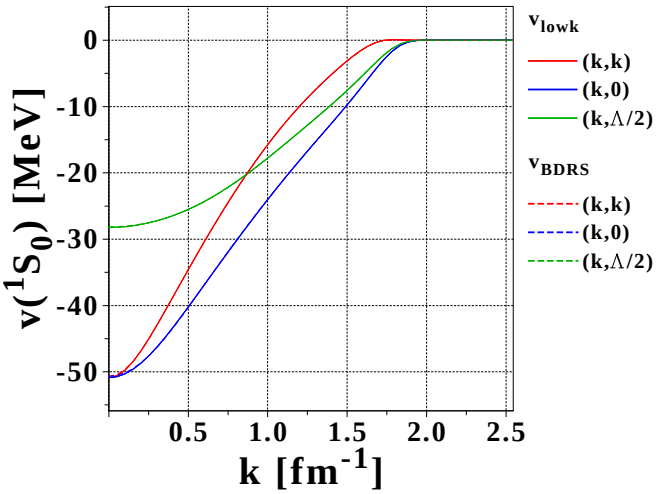

Figure 10.17: Matrix elements for neutron-neutron $V_{{\rm low}\,k}$ for smooth cutoff $\Lambda = 1.8$ fm^{-1} and $v_{\rm BDRS}^{[\rm bare(2)]}$ with $N = 3$ in the ^{1}S$_0$ channel.

	η_0	η_+	η_-	$a_0(nn)$ [fm]	r_0 [fm]
$V_{{\rm low}\,k}$ ($\Lambda = 1.8$ fm^{-1})	0.901	0.042	−0.011	−18.49	2.75
$v_{\rm BDRS}^{[\rm bare(2)]}$ ($\Lambda = 1.8$ fm^{-1})	0.901	0.042	−0.012	−18.43	2.81

Table 10.5: Comparison of Weinberg eigenvalues and scattering parameters for neutron-neutron $V_{{\rm low}\,k}$ at $\Lambda = 1.8$ fm^{-1} and fitted $v_{\rm BDRS}^{[\rm bare(2)]}$ with $N = 3$ in the ^{1}S$_0$ channel.

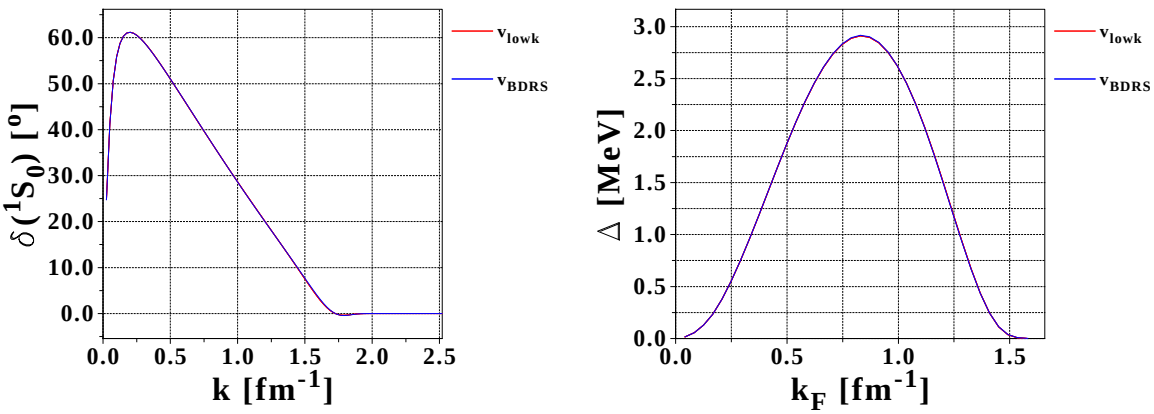

Figure 10.18: Scattering phase shifts and INM gap equation for neutron-neutron $V_{{\rm low}\,k}$ and $v_{\rm BDRS}^{[\rm bare(2)]}$ with $N = 3$ in the ^{1}S$_0$ channel.

[4]This supposes that such a quality of fit is achievable in other partial waves.

The latter results confirm a posteriori the assumption that RG cutoffs should be explicitly implemented in the fit procedure for high-precision representations for $V_{\rm low\,k}$, with the tradeoff that these representations might not be useable for finite nuclei structure codes. The accuracy of such a procedure stems from the fact that non-localities are explicitly included in $v_{\rm BDRS}^{[\rm bare(2)]}$ through the RG cutoff functions and shows that such a factorization of non-localities seems to be encoded in $V_{\rm low\,k}$.

Values for the fitted parameters can be found in Tab. {10.6}. It is found that the short range converges to extremely small values, while the coupling constant S_1^{10} remains rather stable around 225 MeV. It seems to be a safe approximation to take $\mu_1 \approx 0$ fm for values of Λ close to 1.8 fm^{-1}, that is the first gaussian component corresponds to a zero-range term. The latter can be understood in Fig. 10.19, where matrix elements of the fitted interaction are represented with and without the RG cutoff functions. It appears that the $\mu_1 \approx 0$ fm term acts as a "positive baseline" for matrix elements in momentum space. The latter are suppressed around Λ by the RG cutoff functions which provide the sharp inflexion point for $k, k' \approx \Lambda$. This zero-range term is expressed in coordinate space as

$$S_1^{10}\,\delta(\vec{r}\,) \approx 225\ \text{MeV.fm}^3\,\delta(\vec{r}\,)\,. \tag{10.42}$$

The deconvolution of this contact term into a RG induced-vertex can be easily evaluated using Eq. (10.18b), leading to a fully separable form

$$V_1^{[\rm ind]}(r_i) \equiv \mathcal{C}\,\delta(\vec{R}-\vec{R}\,')\,g(\vec{r}\,)\,g(\vec{r}\,')\,. \tag{10.43}$$

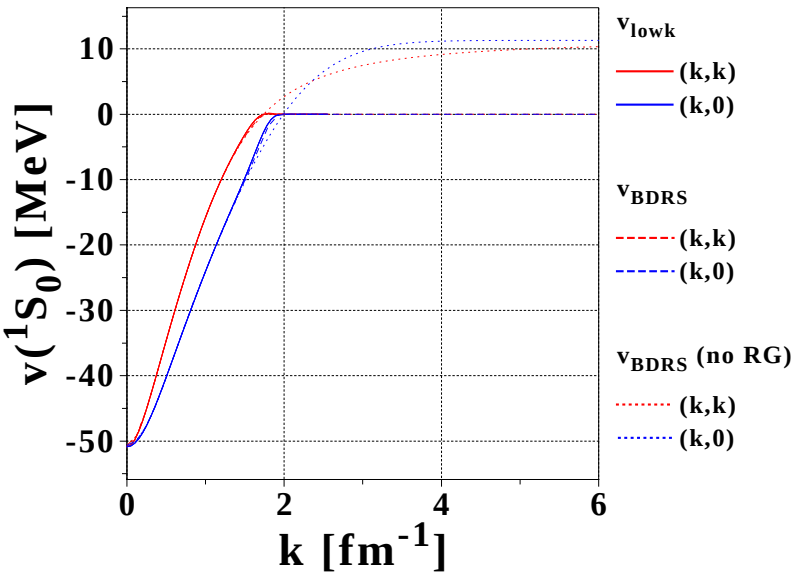

Figure 10.19: Matrix elements of $v_{\rm BDRS}^{[\rm bare(2)]}$ at $\Lambda = 1.8$ fm^{-1} with and without the RG cutoff functions.

On the other hand, the quantity R_i^{10} which measures the relative weights of each term shows that the main contribution to the potential in momentum space comes from the medium-range gaussian, while the other two components have almost exactly similar weights of the order of 15%. In particular this indicates that three gaussians are indeed needed for an accurate representation. The variable R_i^{10} is of interest as it proves that, for instance, the long-range term

has a very small absolute coupling constant C_3^{10}, but contributes significantly in momentum space.

When increasing slightly the RG cutoff Λ up to 2.1 fm^{-1}, one finds that the zero-range approximation breaks down ($\mu_1 \approx 0.1$ fm), but the idea of a "constant" baseline still holds. In both cases one obtains very high-accuracy representations of $V_{\text{low}\,k}$, as illustrated in FIG. 10.20.

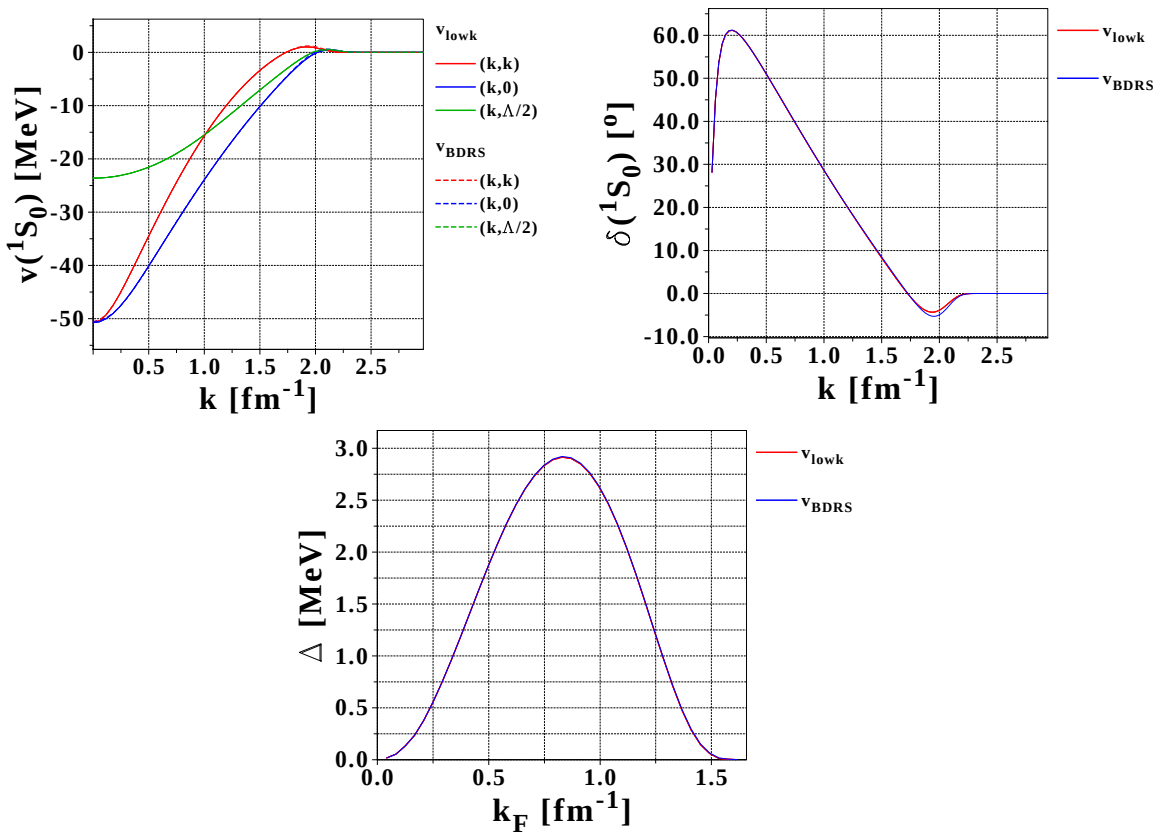

Figure 10.20: Same as in FIGS. (10.17,10.18) for $\Lambda = 2.1$ fm^{-1}.

10.3.4 Evolution with the RG cutoff Λ

The evolution of the fitted parameters $\{\mu_i, S_i^{01}\}$ as the RG cutoff runs down is found in FIG. 10.21 for a reasonable range of values for Λ.

The evolution of the optimized χ^2 as a function of Λ is not very meaningful *per se*, since theoretical uncertainties in the fit, thus the definition of the cost function, evolve with the RG cutoff. Indeed, uncertainties depend on the local Laplacian of matrix elements of $V_{\text{low}\,k}$. On the other hand, much information is gained from the evolution of different quantities as a function of Λ. The evolution of μ_1 in particular is peculiar in the low-Λ regime. It decreases smoothly with Λ before going abruptly to zero for $\Lambda \lesssim 2.1$ fm^{-1}. This might indicate the existence of a critical scale below which one "effective degree of freedom" has been integrated out. This critical point seems to occur at the frontier between domains where the RG function cuts off matrix elements in the $V < 0$ region or the $V > 0$ region, as indicated in FIG. 10.22 through the matrix elements of $V_{\text{low}\,k}$ at various values of Λ.

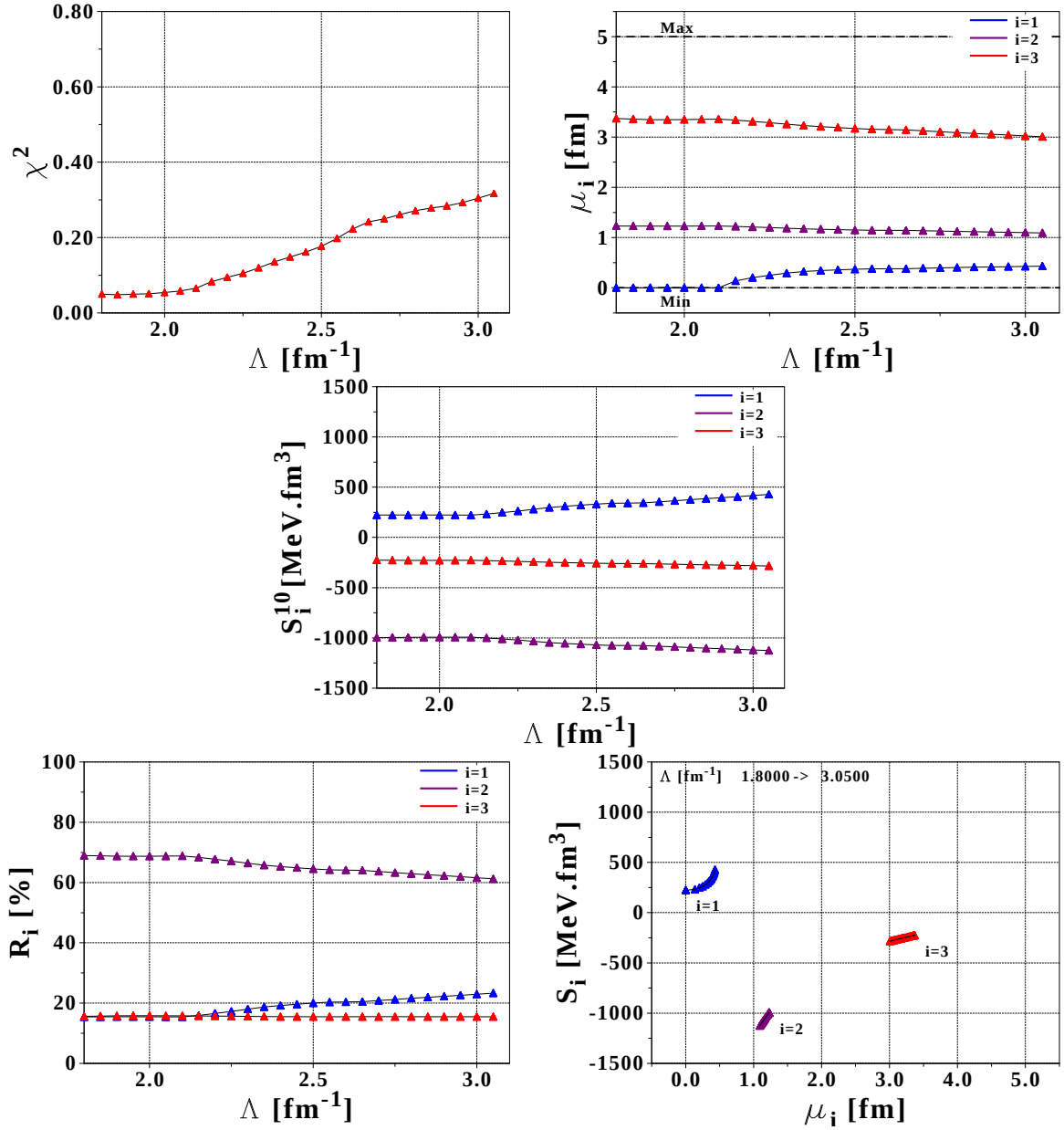

Figure 10.21: Parameters of the $v_{\rm BDRS}^{[\rm bare(2)]}$ at different Λ.

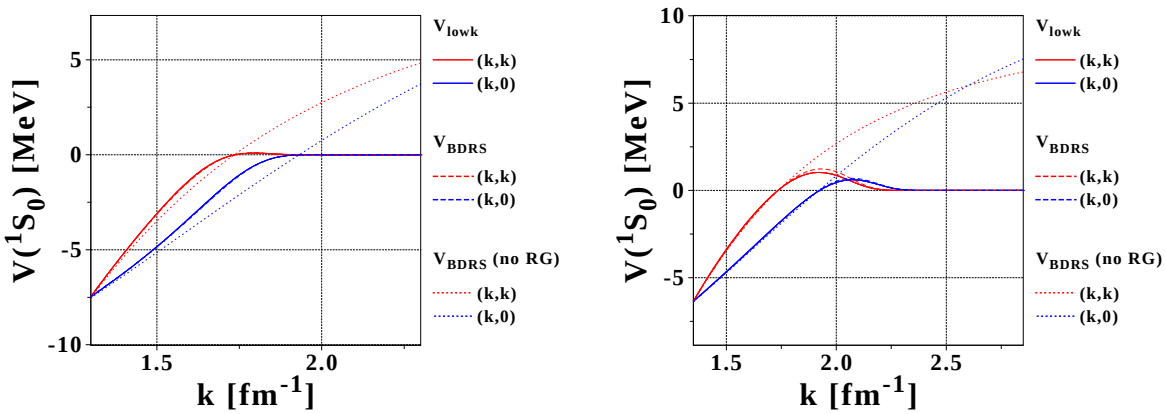

(a) $\Lambda = 1.8$ fm^{-1} ($V < 0$ RG cut) (b) $\Lambda = 2.1$ fm^{-1} ($V \approx 0$ RG cut)

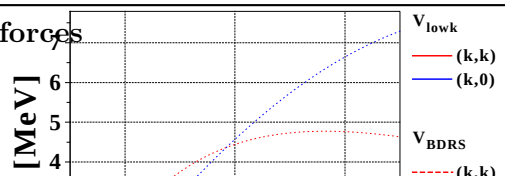

We will refer in the following to "zero-range regime" the region $\Lambda \lesssim 2.1$ fm^{-1}, where the short-range term μ_1 is consistent with zero. In this regime, values of the coupling constants S_1^{10}, thus relative strengths R_i^{10} are found to be almost constant.

For $\Lambda > 2.1$ fm^{-1}, the evolution of S_i^{10} is rather smooth. The general trend is that S_1^{10} associated with the shortest range increases (that is this term becomes more repulsive) while at the same time S_2^{10}, associated with the intermediate range, also increases (that is this term becomes more attractive), in something which resembles a see-saw mechanism. This could be investigated more closely by doing a principal component analysis of the results. Evolutions of R_1^{10} and R_2^{10} confirm that there is an "exchange of relative strength" between these two terms.

Meanwhile, the long-range part seems almost unaffected by a change of Λ. The latter information is confirmed by the evolution of R_3^{10} as a function of Λ which remains almost constant. This suggests that long-range physics is unaffected by the RG flow in the ^{1}S$_0$ channel, and might provide essential information concerning the central contribution from the long-range part of the nuclear interaction corresponding to OPE. In particular, a comparison between a true one-pion exchange (Yukawa potential) and the μ_3 term should be of interest.

		$\Lambda = 1.8$ fm^{-1}	$\Lambda = 2.1$ fm^{-1}	$\Lambda = 2.5$ fm^{-1}
χ^2		0.0498	0.0655	0.1769
μ_1	[fm]	0.0002	0.0011	0.3692
S_1^{10}	[MeV.fm^3]	223.19	222.27	331.69
R_1^{10}	[%]	15.43	15.41	20.01
μ_2	[fm]	1.2295	1.2304	1.1507
S_2^{10}	[MeV.fm^3]	−997.39	−992.69	−1069.72
R_2^{10}	[%]	68.95	68.82	64.52
μ_3	[fm]	3.3693	3.3573	3.1710
S_3^{10}	[MeV.fm^3]	−225.96	−227.44	−256.54
R_3^{10}	[%]	15.62	15.77	15.47

Table 10.6: Optimization results for different RG cutoff Λ for $v_{\rm BDRS}^{[\rm bare(2)]}$ (averaged on 30 fits).

10.3.5 Representation accuracy

An interesting quantity to compute is the errors bars magnitude necessary to have a $\chi^2 = 1$ fit, i.e. such that $v_{\rm BDRS}^{[\rm bare(2)]}$ accurately describes $V_{{\rm low}\,k}$ in the statistical sense. Such results are presented in Fig. 10.23 for $\Lambda = 2.1$ fm^{-1}. A maximum value $\left|\delta v(\chi^2 = 1)\right|^{\rm max} \approx 200$ keV and an average one $\left|\overline{\delta v}(\chi^2 = 1)\right| \approx 50$ keV are observed, that is the fitted $v_{\rm BDRS}^{[\rm bare(2)]}$ represents $V_{{\rm low}\,k}$ at the 50 keV level. Values of $\left|\overline{\delta v}(\chi^2 = 1)\right|$ as a function of Λ can be found in Fig. 10.24. The latter value increases with Λ which suggests that the accuracy of the current expression for $v_{\rm BDRS}^{[\rm bare(2)]}$ expressed in terms of (i) three gaussians, and (ii) a gaussian representation, deteriorates as the resolution scale increases. Given that we are mostly interested in representing $V_{{\rm low}\,k}$ at small RG cutoff for EDF calculations, this issue can be disregarded. Additionally, the level of accuracy of $v_{\rm BDRS}$ remains of the order of 200 keVs for $\Lambda = 3.5$ fm^{-1}, which remains satisfactory anyway.

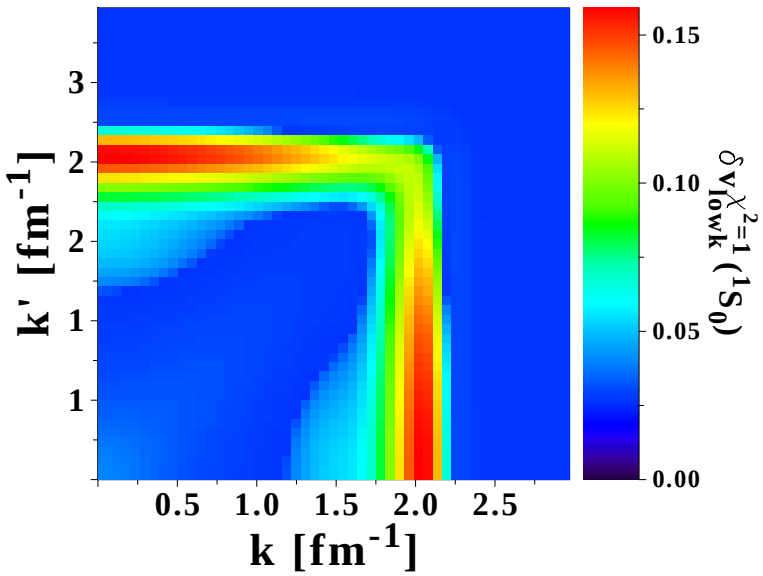

Figure 10.23: Rescaled theoretical error bars on $V_{\rm low\,k}$ such that $v_{\rm BDRS}^{[\rm bare(2)]}$ will be a $\chi^2 = 1$ fit at $\Lambda = 2.1$ fm^{-1}.

Such results are almost constant with small redefinitions of the error bars, which proves that the gaussian+RG representation is very precise.

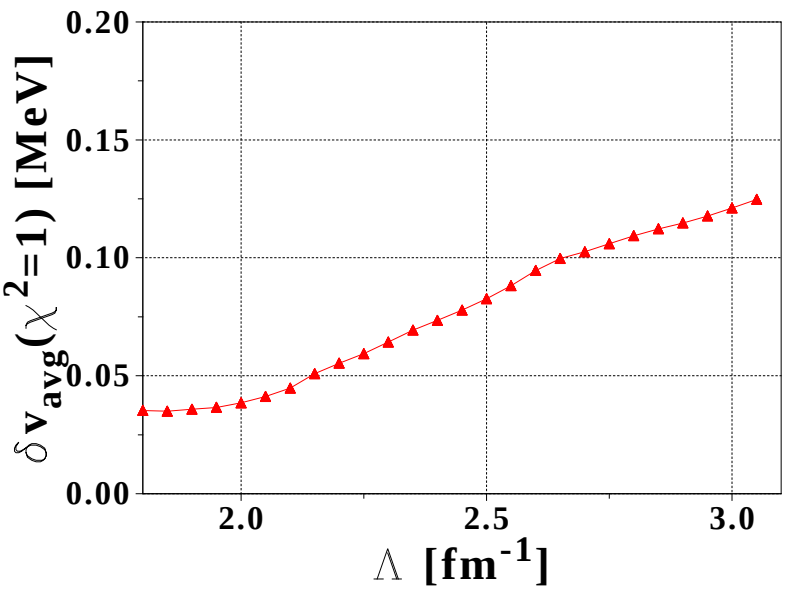

Figure 10.24: Average error $\left|\overline{\delta v}(\chi^2 = 1)\right|$ of theoretical error bars on $V_{\rm low\,k}$ such that $v_{\rm BDRS}^{[\rm bare(2)]}$ will be a $\chi^2 = 1$ fit as a function of Λ.

10.3.6 Impact of the RG cutoff function

A change of the RG cutoff function is supposed to affect only matrix elements of $V_{\rm low\,k}$ in the $k, k' \approx \Lambda$ region, except in extreme cases which have additional pathologies, such as an exponential regulator with very small n or a Woods-Saxon one with high ϵ. To investigate

this issue, $\{\chi^2, \mu_i, S_i^{10}, R_i^{10} \ldots\}$ have been computed for $\Lambda = 2.1$ fm^{-1}, with different RG cutoff functions $g(k)$ as listed below, that will be referred to as "Run ID" in this section and were represented in Fig. 5.12

1. Sharp cutoff.
2. Exponential cutoff $n = 2$,
3. Exponential cutoff $n = 3$,
4. Exponential cutoff $n = 4$,
5. Exponential cutoff $n = 5$,
6. Exponential cutoff $n = 6$,
7. Exponential cutoff $n = 7$,
8. Exponential cutoff $n = 8$,
9. Woods-Saxon cutoff $\epsilon = 1.00$,
10. Woods-Saxon cutoff $\epsilon = 0.80$,
11. Woods-Saxon cutoff $\epsilon = 0.60$,
12. Woods-Saxon cutoff $\epsilon = 0.40$,
13. Woods-Saxon cutoff $\epsilon = 0.20$.

Matrix elements of the fitted V_{BDRS} are represented in some of these test cases on Fig. 10.25, where in all cases a very good agreement between $v_{\text{BDRS}}^{[\text{bare}(2)]}$ and $V_{\text{low}\,k}$ is seen. Theoretical uncertainties are represented here, since they depend on the RG cutoff function, and are magnified by a factor of ten[5].

Optimization results, presented in Fig. 10.26, need to be commented on. Firstly, the convergence of all quantities for exponential regulators as a function of n is clearly seen. However, for small values of n (typically $2-3$) the reproduction of $V_{\text{low}\,k}$ seems at first very unaccurate from the value of the optimized χ^2. However in this situation the RG regulator cuts into the low-k region, which reduces the curvature of $V_{\text{low}\,k}$ and decreases theoretical uncertainties. As a consequence the overall value of the cost function χ^2 increases. Furthermore, numerical values for the fitted parameters are not very different from the other cases, which suggests that the unusually large value for χ^2 is meaningless.

For all these fits there is an overall agreement in terms of the decomposition of the total potential into

- a long-range part $\mu_3 \approx 3.2$ fm with a very small coupling constant, which varies a little depending on the RG cutoff function used for $V_{\text{low}\,k}$,
- a medium-range part $\mu_2 \approx 1.2$ fm, which is found to be the most stable with respect to the RG cutoff, and whose associated parameters (μ_2/C_2^{10}) are very close to the second gaussian of Gogny D1S,
- a short-range part which varies with the RG cutoff. The latter was to be expected, since short-range terms contribute the most to high-k matrix elements. Fig. 10.27 shows the shape of diagonal and off-diagonal terms for several values of the range μ with a simple gaussian. As expected, terms with lower values of μ will be much more affected by a change of the RG cutoff function.

[5] We recall here that only the relative magnitude of these uncertainties matter.

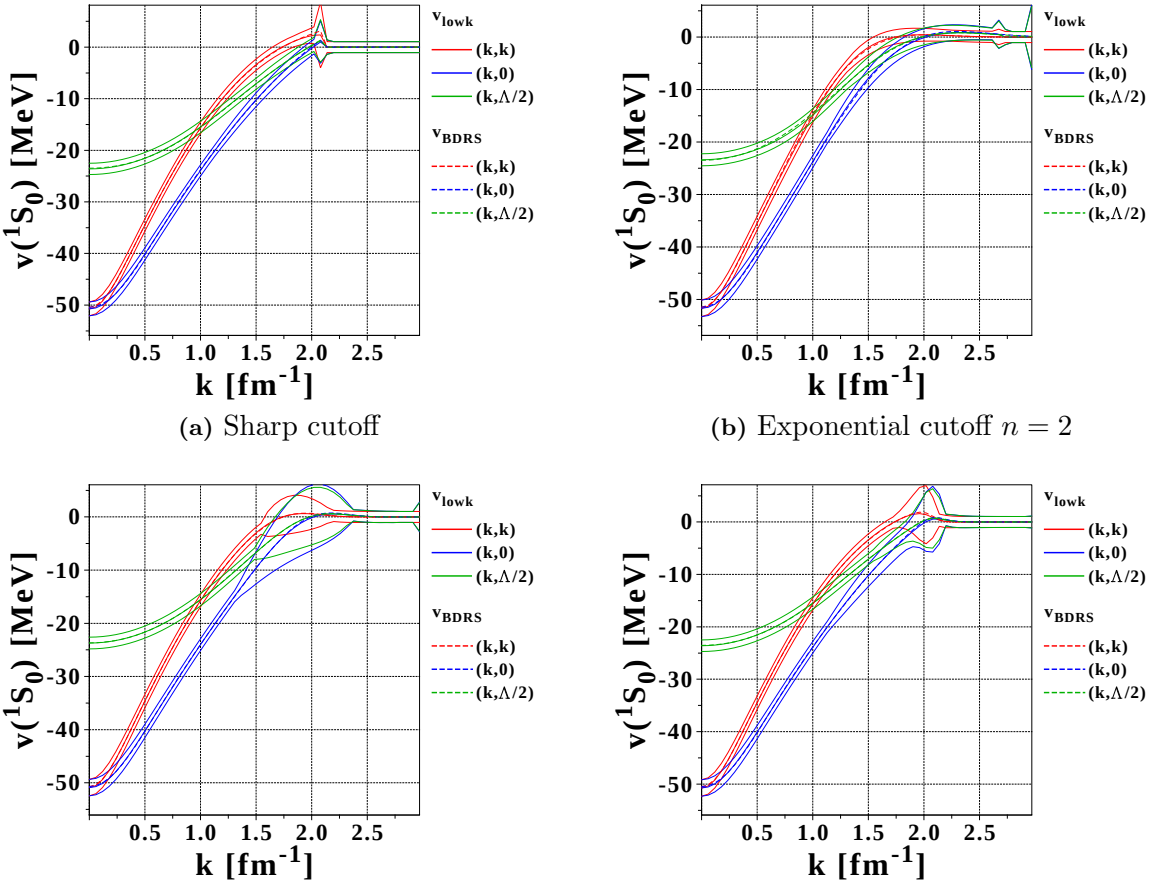

(a) Sharp cutoff (b) Exponential cutoff $n = 2$

(c) Exponential cutoff $n = 4$ (d) Woods-Saxon cutoff $\epsilon = 0.40$

Figure 10.25: Matrix elements of $v_{\rm BDRS}^{[\rm bare(2)]}$ adjusted on $V_{{\rm low}\,k}$ at $\Lambda = 2.1$ fm^{-1} with different cutoff schemes. Theoretical uncertainties have been magnified by a factor 10.

For all quantities, there is a good agreement between results for the Woods-Saxon regulators and the sharp one, which are very close in momentum space with the range of ϵ that we used. WS regulators used here are quite close to a step function. Different values of χ^2 are simply related to different theoretical uncertainties for $V_{{\rm low}\,k}$. The fast convergence of all quantities with exponential RG regulators as a function of increasing n is also seen. However, converged values differ from the ones in the WS/sharp cases. As an example, the long-range part of the interaction changes between WS and exponential regulators, the associated range by about 0.2 fm and the zero-momentum coupling constant S_3^{10} by about 30 MeV. However, the long-range relative strength R_3^{10} remains unchanged, which suggests that changes in $\{\mu_3, S_3^{10}\}$ compensate each other. Taking the sharp $V_{{\rm low}\,k}$ as a reference point, one finds that exponential regulators tend to underestimate the relative strength of the short-range component, while overestimating the one for the medium range. Such differences are related to the fact that $g_\epsilon(\Lambda) = 1/2$ for Woods-Saxon regulators, while $g_\epsilon(\Lambda) = 1/e$ for exponential ones as already outlined before. A study of error bars on these parameters will indicate that this is not a very serious issue (see Sec. 10.3.10).

As a conclusion, for small values of Λ, $V_{{\rm low}\,k}$ can therefore be very well represented, **independently of the RG cutoff function used**, by the sum of a contact term plus two gaussians of medium and long ranges. We suggest the diagrammatic representation from Fig. 10.28, where

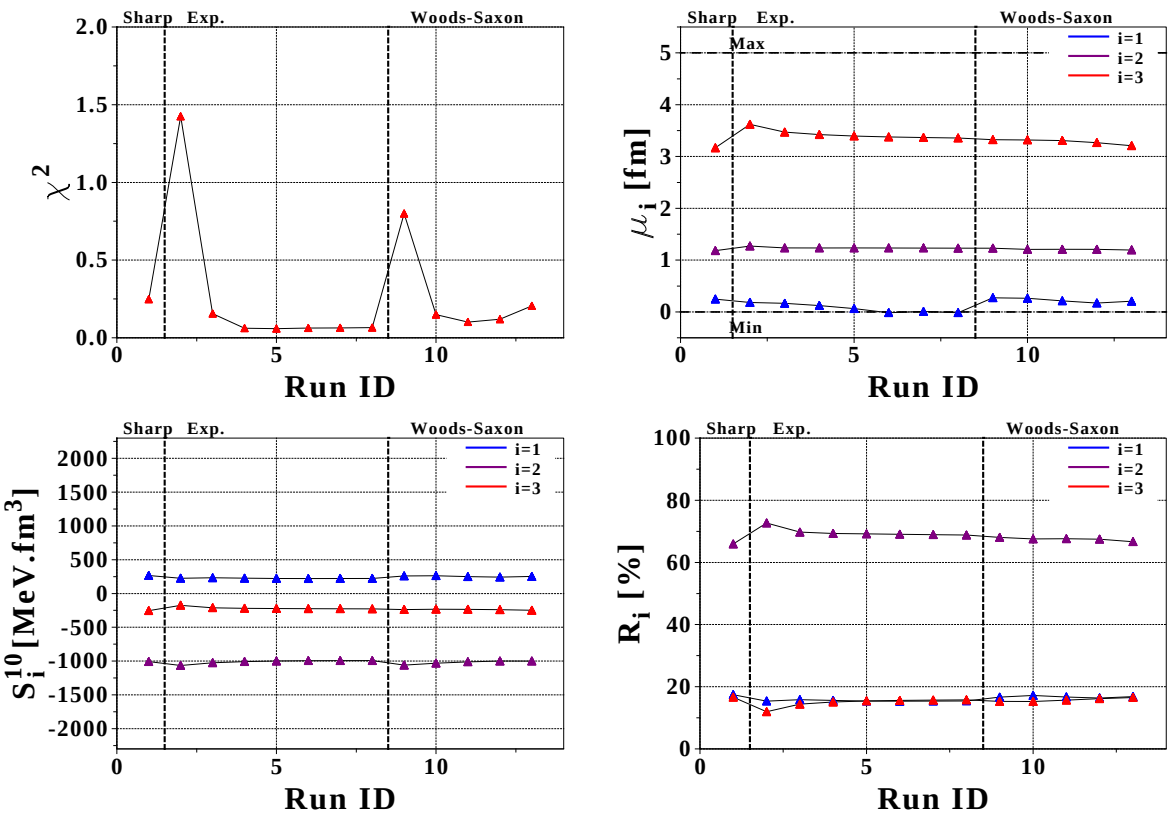

Figure 10.26: Evolution of the parameters of $v_{\mathrm{BDRS}}^{[\mathrm{bare}(2)]}$ fit from $V_{\mathrm{low}\,k}$ with different RG cutoff functions and $\Lambda = 2.1$ fm^{-1}.

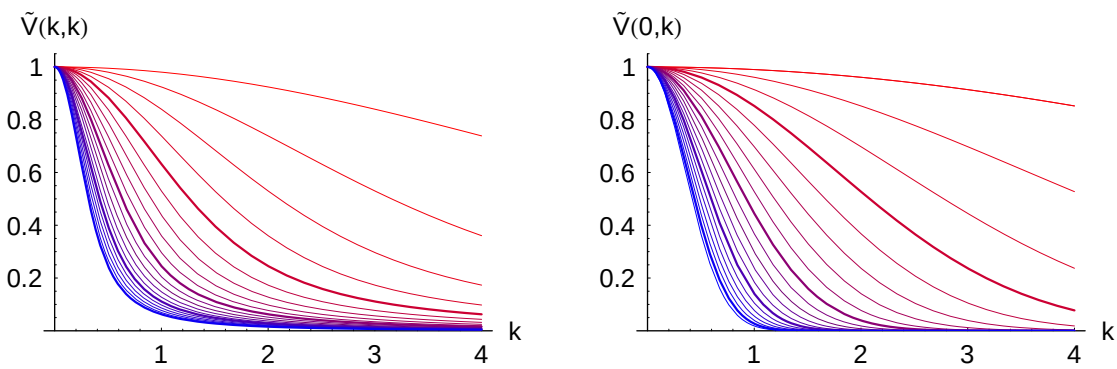

(a) Diagonal term (k, k) **(b)** Off-diagonal term $(0, k)$

Figure 10.27: Form factors of $v_{\mathrm{BDRS}}^{[\mathrm{bare}(2)]}$ in the $^1\mathrm{S}_0$ channel, for different effectives ranges $\mu = 0.2$(red)...4.0(blue) fm. Integer values of μ are highlighted in bold lines.

the cut on relative momenta of incoming and outgoing lines induced by the RG cutoff is explicited by the smooth red boundaries.

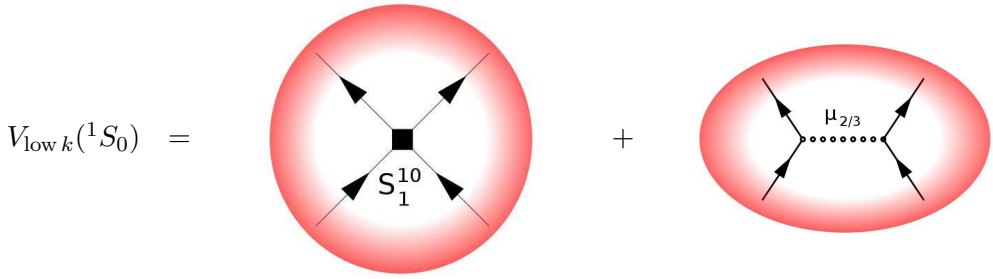

Figure 10.28: Diagrammatic representation of $V_{\rm low\,k}$ at small Λ.

		$v_{\rm BDRS}^{[\rm bare(2)]}$				Gogny D1S
		Sharp	Exp. $n=2$	Exp. $n=8$	WS $\epsilon=0.4$	
χ^2		0.2474	1.4252	0.0656	0.1194	
μ_1	[fm]	0.247	0.182	0.016	0.171	0.700
S_1^{10}	[MeV.fm^3]	266.35	225.29	222.43	242.35	364.47
R_1^{10}	[%]	17.43	15.37	15.42	16.36	24.05
μ_2	[fm]	1.182	1.271	1.230	1.208	1.200
S_2^{10}	[MeV.fm^3]	−1007.84	−1065.60	−992.79	−999.44	−1150.92
R_2^{10}	[%]	65.94	72.68	68.81	67.47	75.95
μ_3	[fm]	3.167	3.621	3.357	3.266	
S_3^{10}	[MeV.fm^3]	−254.15	−175.36	−227.50	−239.45	
R_3^{10}	[%]	16.62	11.96	15.77	16.16	

Table 10.7: Optimization results for $v_{\rm BDRS}^{[\rm bare(2)]}$ and different RG cutoff functions for $V_{\rm low\,k}$ at $\Lambda = 2.1$ fm^{-1}.

10.3.7 Evolution with the number of gaussians

Increasing the total number of gaussians is expected to increase the overall precision, thus decrease the total merit χ^2. Fits with increasing numbers of gaussians have been performed for $\Lambda = 2.1$ fm^{-1}. Results are presented in Fig. 10.29. The overall improvement of the reproduction of $V_{\rm low\,k}$ matrix elements is clearly seen as the number of gaussians used increases. For $N = 2$, one gets a quite unaccurate reproduction ($\chi^2 \approx 16.01$) since one gaussian is used for the zero-range baseline, and only one gaussian is effectively available. As N increases (i) the evolution of μ_i and R_i^{10} shows consecutive fragmentations of the long and medium ranges of the interaction from the $N = 3$ reference point, and (ii) the short-range term cannot be approximated by a zero-range term any more... On the other hand the fact that several gaussians have very close ranges shows

that one tries to reproduce higher-order components in k, i.e.

$$\exp\left[-\frac{(\mu(1+\epsilon)\,k)^2}{2}\right] - \exp\left[-\frac{(\mu\,k)^2}{2}\right] \approx -\epsilon\,(\mu\,k)^2\,\exp\left[-\frac{(\mu\,k)^2}{2}\right]. \tag{10.44}$$

Still, the non-uniqueness of a gaussian decomposition becomes more critical as N increases, and one tends to lose an interpretation of $v_{\rm BDRS}^{[\rm bare(2)]}$ in terms of physical degrees of freedom.

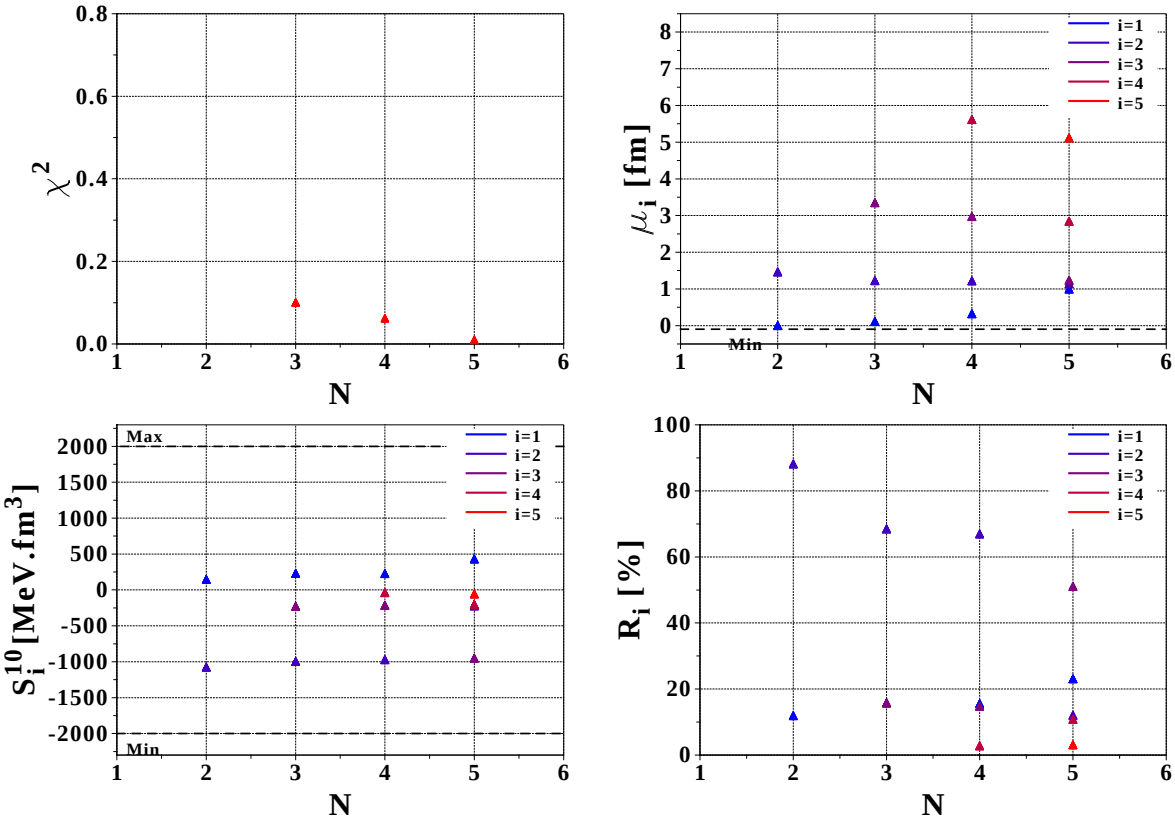

Figure 10.29: Evolution of the parameters of the $v_{\rm BDRS}^{[\rm bare(2)]}$ fit from $V_{{\rm low}\,k}$ with different number of gaussians N for $\Lambda = 2.1$ fm^{-1}.

One can evaluate the precision of the fit as well as areas of missing precision by computing the matrix elements differences $V_{{\rm low}\,k}(k,k') - v_{\rm BDRS}^{[\rm bare(2)]}(k,k')$, presented in Fig. 10.30. Increasing the number of gaussians in the fit greatly reduces the small structures that are observed, so there will be a tradeoff between the precision of the representation and the number of parameters involved. Of course, this is to be validated by the quality obtained on final observables. As far as pure vacuum-like observables (scattering phase shifts, deuteron properties...) are concerned, $N = 3$ is sufficient for $\Lambda \lesssim 3.5$ fm^{-1} as discussed previously. However it remains to assess the quality of the reproduction of observables which probe off-shell properties, e.g. the nuclear matter equation of state a second order in MBPT.

10.3.8 Isospin-symmetry breaking

To evaluate how well the isospin-symmetry breaking of the initial force can be approximated by $v_{\rm BDRS}^{[\rm bare(2)]}$, three fits have been performed to reproduce the matrix elements of $V_{{\rm low}\,k}$ at $\Lambda = 2.1$ fm^{-1}, starting from the nuclear part of AV18, that is without electromagnetic terms.

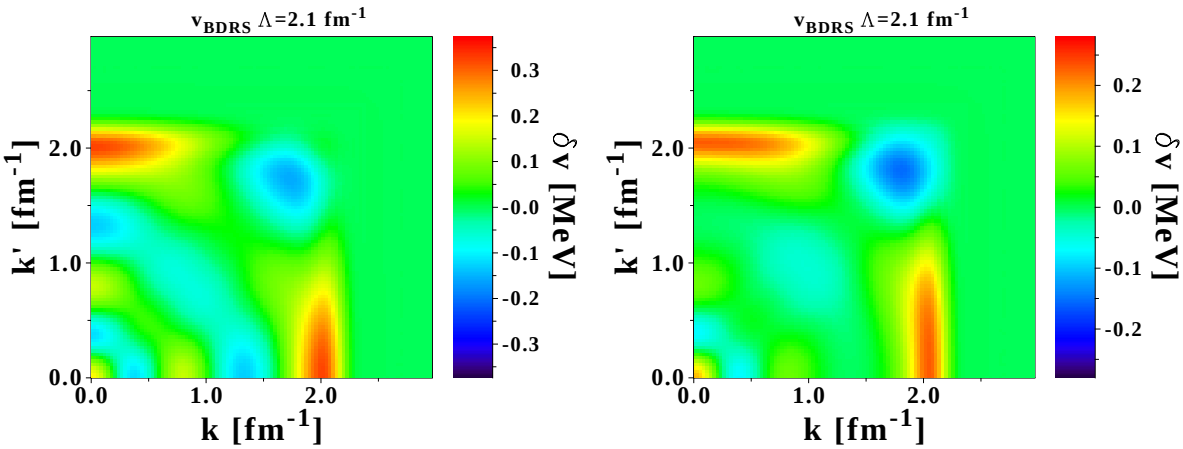

(a) $N = 3$ gaussians (b) $N = 6$ gaussians

Figure 10.30: $v_{\rm BDRS}^{[\rm bare(2)]}$ residuals in the ^{1}S$_0$ channel for $\Lambda = 2.1$ fm^{-1} and different numbers of gaussians. Note that color scales are different.

Results are presented in Tab. {10.8}[6].

In all three cases, $v_{\rm BDRS}^{[\rm bare(2)]}$ represents acurately $V_{{\rm low}\,k}$ at the cost of slight variations of the free parameters, which confirms that highly-precise parametrizations can be adjusted within this RG-induced framework. Furthermore

- relative strengths R_i^{10} do not depend on the isospin projection T_z. This would be in agreement with a meson exchange model where relative strengths of each diagram are only fixed by the exchange mesons mass ratios,
- the coupling strengths of the long-range term μ_3 (the "pion") is not affected at all by T_z, which would confirm the hypothesis that the long-range part of $V_{{\rm low}\,k}$ is well represented by a charge-independent OPE-like term,
- ranges and strengths of $v_{\rm BDRS}^{[\rm bare(2)]}$ change with T_z, in a way where the $T_z = 0$ interaction is always the weakest one in absolute value, and $T_z = \pm 1$ terms are roughly equal. This symmetry is more obvious for the long ranges (equal values for $\mu_{2/3}$ for $T_z = \pm 1$) than for the short one.

Note that in all cases such features should be strongly affected by the starting interaction $V_{{\rm low}\,k}$ derives from. A last comment can be made with respect to the fit strategy for the [bare(2)] level. In the case of the construction of an operatorial representation of the bare $V_{{\rm low}\,k}$ to be used in the pairing channel, one will have to choose the isospin projection T_z used as an input in the fit. Since proton-neutron pairing is usually neglected, we only need for $v^{\kappa\kappa}$ an accurate representation for neutron-neutron and proton-proton interactions. To our opinion, previous results suggest that, including theoretical error bars, the nuclear part of the NN force can be very well equivalently represented by fits of its $T_z = 0, \pm 1$ components. In that respect, the choice of T_z for the interaction constructed to represent $v^{\kappa\kappa}$, e.g. the pairing part of the nuclear EDF, will not be as critical as one could have expected.

[6] Small differences are observed for the neutron-neutron case in comparison with the results previously presented, because suppressing EM terms in AV18 also slightly affects the neutron-neutron potential.

		$T_z = -1$ (pp)	$T_z = 0$ (np)	$T_z = +1$ (nn)
		AV18		
a_0	[fm]	-17.164	-23.084	-18.818
r_0	[fm]	2.865	2.703	2.834
		$V_{\text{low}\,k}$		
a_0	[fm]	-17.156	-23.078	-18.809
r_0	[fm]	2.861	2.703	2.831
		$v_{\text{BDRS}}^{[\text{bare}(2)]}$		
a_0	[fm]	-17.115	-23.018	-18.762
r_0	[fm]	2.830	2.679	2.801
χ^2		0.1017	0.0771	0.0999
μ_1	[fm]	0.1344	0.0091	0.1101
S_1^{10}	[MeV.fm^3]	233.02	220.12	229.77
R_1^{10}	[%]	15.96	15.35	15.75
μ_2	[fm]	1.2241	1.2049	1.2237
S_2^{10}	[MeV.fm^3]	-997.32	-988.01	-999.13
R_2^{10}	[%]	68.30	68.91	68.49
μ_3	[fm]	3.3480	3.1879	3.3471
S_3^{10}	[MeV.fm^3]	-229.77	-229.79	-229.85
R_3^{10}	[%]	15.74	15.73	15.76

Table 10.8: Optimization results for different isospin projections for $V_{\text{low}\,k}$ at $\Lambda = 2.1$ fm^{-1} derived from the nuclear part only of AV18.

10.3.9 Comparison with separable interactions

FIG. 10.31 compares matrix elements for $v_{\text{BDRS}}^{[\text{bare}(2)]}$ and the rank-2 separable representation of $V_{\text{low}\,k}$ in the $^1\text{S}_0$ channel at $\Lambda = 1.8$ fm^{-1} [669]. While they both roughly provide very accurate (i) approximations of matrix elements of $V_{\text{low}\,k}$, and (ii) equivalent reproductions of physical observables such as scattering phase shifts, $v_{\text{BDRS}}^{[\text{bare}(2)]}$ seems to do a better job around the cutoff value Λ. The latter is best seen on FIG. 10.32, which shows residuals defined as

$$\delta v(k,k') = \left| V_{\text{low}\,k}(k,k') - v_{\text{sep/BDRS}}(k,k') \right| . \tag{10.45}$$

The total residual

$$\Delta_{\text{sep/BDRS}} v = \sqrt{\frac{2}{N(N+1)} \sum_{i<j}^{N} \left(V_{\text{low}\,k}(k_i,k_j) - v_{\text{sep/BDRS}}(k_i,k_j) \right)^2} , \tag{10.46}$$

can be evaluated for a common mesh $\{k_i \in [0, \Lambda\sqrt{2}], i = 1, 100\}$, and reads

$$\Delta_{\text{BDRS}} v \approx 28 \text{ keV} , \qquad \Delta_{\text{sep}} v \approx 604 \text{ keV} , \tag{10.47}$$

where only 6 free parameters are used for $v_{\text{BDRS}}^{[\text{bare}(2)]}$ instead of 12 for v_{sep}. This suggests that (i) the explicit treatment of non-localities that is done in both approaches is essential in the $^1\text{S}_0$

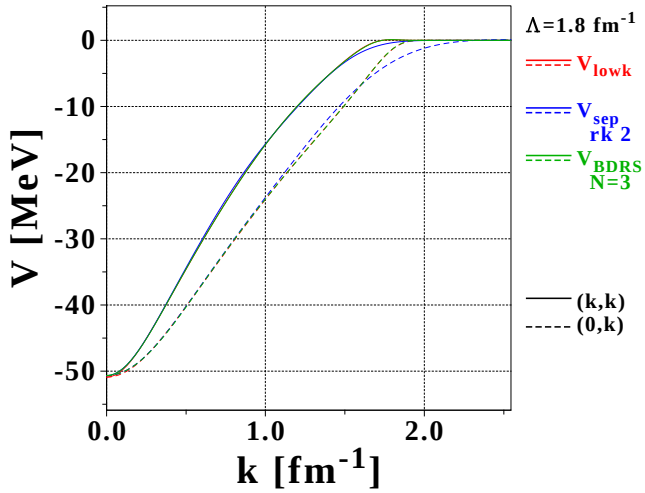

Figure 10.31: Matrix elements for $V_{\rm low\,k}$, $v_{\rm sep}$ and fitted $v_{\rm BDRS}^{[\rm bare(2)]}$ at $\Lambda = 1.8$ fm^{-1} in the ^{1}S$_0$ channel.

channel which presents a virtual di-nucleon state, (ii) at the tradeoff of a more complex scheme, $v_{\rm BDRS}^{[\rm bare(2)]}$ better approximates off-diagonal matrix elements while higher-order form factors are needed for $v_{\rm sep}$ [669], and (iii) in order to have a good description of the phase shifts, a good reproduction of matrix elements of the kind ($k \approx \Lambda, k' \lesssim \Lambda$) is not needed, and theoretical uncertainties can be raised in this region when necessary. This should turn out to be useful for the strict gaussian $v_{\rm BDRS}^{[\rm X]}$ (without RG cutoffs).

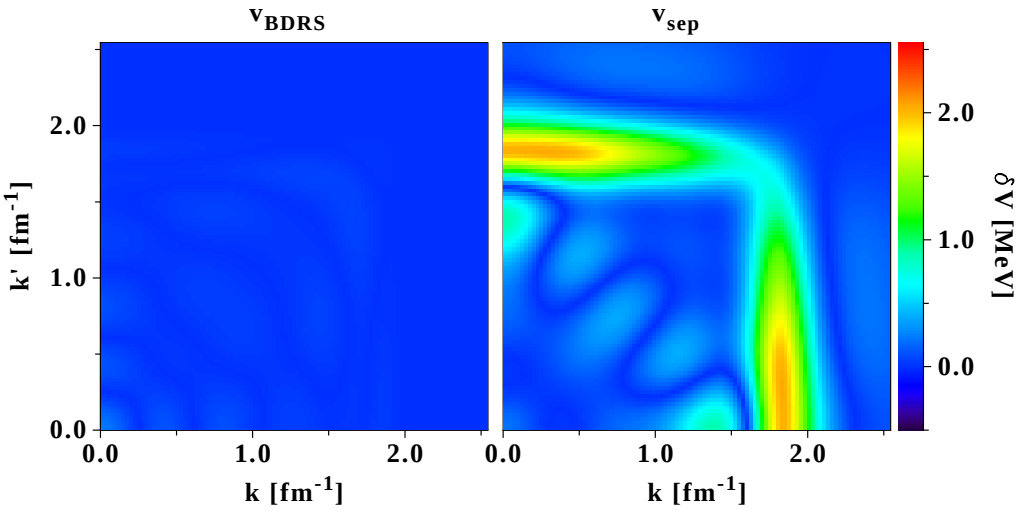

Figure 10.32: Residuals $\delta_{\rm sep/BDRS} v(k,k')$ in the ^{1}S$_0$ channel for $\Lambda = 2.1$ fm^{-1}.

10.3.10 Uncertainties analysis

Let us now turn to an essential feature that provides a new perspective to the results previously presented, i.e. a post-fit analysis in terms of confidence intervals. Uncertainties on the adjusted parameters $\{\mu_i, S_i^{10}\}$ can be essentially broken down into three different origins.

1. The *fit intrinsic error* that arises from the use of a stochastic algorithm with random initializations. That is, the final result might depend on the starting configuration of FITPACK.

2. The *representation error*, that is the uncertainty coming from the choice of the analytical expression of $v_{\text{BDRS}}^{[\text{bare}(2)]}$ as a sum of gaussian terms which is supposed to grasp the exact structure of $V_{\text{low}\,k}$.

3. The *input error* that comes from the small variations of $V_{\text{low}\,k}$ with respect to (i) changes in the RG cutoff function, and (ii) changes in the starting vacuum realistic interaction. Indeed, while $V_{\text{low}\,k}$ is usually considered in itself as a vacuum two-body force, we have to take into account such small variations, that are already well known [87] , when constructing a high-precision parametrization.

10.3.10.1 Fit intrinsic error

As shown in SEC. 10.3.2, the intrinsic dispersion of the fitted parameters on 30 fits with random initializations remains very small. This suggests that this source of error should be well under control in the procedure. To illustrate the latter point, we performed 30 fits by changing the convergence threshold $10^{-\epsilon}$ of FITPACK, which corresponds to (i) the (relative) merit dispersion between all simplexes, and (ii) the (relative) hypervolume of the best specimen. Results are presented in FIG. 10.33 for the dispersion σ_X and the relative dispersion σ_X/X of the optimal cost and the fitted parameters μ_i and S_i^{10}. As a striking result, one sees that the dispersion scales linearly with the convergence threshold, that is **the intrinsic precision of the fit can be set to any (arbitrary) small value by changing the control parameters of fitpack.** Given the precision chosen in the previous results ($\epsilon = 7$), one can thus safely disregard any error coming from the intrinsic precision of FITPACK. This can be confirmed a posteriori by the uncertainties that arise from other sources, that are of the order of a few percents, in comparison with the ones that one has to consider in the present case, that never exceed a few parts per million.

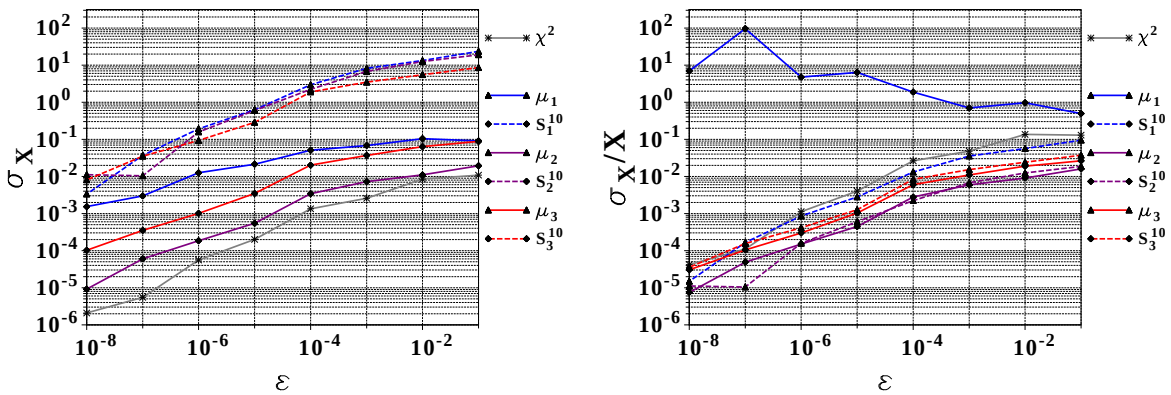

(a) Absolute errors σ_X (b) Relative errors σ_X/X

Figure 10.33: Relative and absolute dispersions for the fitted parameters and the optimized merit χ^2 as a function of the convergence threshold of FITPACK. The high relative dispersion for μ_1 stems from the fact that the optimized value of μ_1 corresponds to a zero-range term.

We notice finally, that the best (relative) precision is always obtained for the medium-range component $\{\mu_2, S_2^{10}\}$, while the worst one corresponds to the short-range term in $v_{\text{BDRS}}^{[\text{bare}(2)]}$.

10.3.10.2 Representation and $V_{\rm low\,k}$ error: principle

The last two sources of error will be treated using the bootstrap algorithm developed in collaboration with L. Illourmane that is presented in Sec. 9.6. Owing to the general principle of this method for error estimates, that is randomly resampling an initial data set with respect to a given statistics, we define a (arbitrary large) set of B variations of ^{1}S$_0$ matrix elements for $V_{\rm low\,k}$ that (i) remain close to the original one, and (ii) are used to perform an equivalent number of adjustments which provide theoretical errors on μ_i and S_i^{10} using the standard procedure from Sec. 9.6, i.e.

$$Y_i \in [(Y_i')_{\alpha B}, (Y_i')_{(1-\alpha)B}]\,, \tag{10.48}$$

$(Y_i')_{1\ldots B}$ corresponding to ordered values of the B fitted parameters. We define resampled matrix elements of $V_{\rm low\,k}$ as

$$\forall(i,j)\,, \qquad V_{\rm low\,k}^{[B]}(k_i,k_j) \equiv V_{\rm low\,k}(k_i,k_j) + \delta v^{[B]}(k_i,k_j)\,, \tag{10.49}$$

where the random deviations $\delta v^{[B]}$ are yet to be specified. We choose to use a form of *residuals resampling* which preserves a physical meaning, in the sense that the resampling is not performed independently bin by bin, but instead provides "smooth" random variation around the original $V_{\rm low\,k}$. The range of such variations depends on (i) the point of computation, e.g. we are precise for $k = k' \approx 0$ fm^{-1} diagonal components and allow more freedom for off-diagonal matrix elements around the RG cutoff Λ, and (ii) depends on the category of error that are probed. Indeed we define

$$\forall(i,j)\,, \qquad \delta v^{[B]}(k_i,k_j) \equiv \mathcal{R}^{[B]}(k_i,k_j) \times \delta v(k_i,k_j)\,, \tag{10.50}$$

where

- $\mathcal{R}^{[B]}$ is a random two-dimensional curve in $[-1,+1]$, that is a smooth curve where at each point (k_i,k_j) the probability law of $\mathcal{R}^{[B]}(k_i,k_j)$ is centered and of variance $1/2$[7]. The construction principle of such a curve relies on statistics and is detailed in Appendix F.2,
- $\delta v(k_i,k_j)$ is a (positive) error magnitude that defines the local range within which $V_{\rm low\,k}$ is resampled, defined as

$$\delta v(k_i,k_j) \equiv \left|V_{\rm low\,k}(k_i,k_j) - v_{\rm BDRS}^{[\rm bare(2)]}(k_i,k_j)\right| \qquad \text{for the representation error,} \tag{10.51a}$$

$$\delta v(k_i,k_j) \equiv \max_C \left|V_{\rm low\,k}(k_i,k_j;C) - v_{\rm BDRS}^{[\rm bare(2)]}(k_i,k_j)\right| \qquad \text{for the } V_{\rm low\,k} \text{ error,} \tag{10.51b}$$

  where $V_{\rm low\,k}(k_i,k_j;C)$ corresponds to the low-momemtum interaction calculated with a different RG cutoff function and/or a different starting vacuum interaction. Obviously both of these errors can be combined by taking for $\delta v(k_i,k_j)$ at each point the greatest value of all error sources.

Eq. (10.50) provides a way to evaluate variations of $v_{\rm BDRS}^{[\rm bare(2)]}$ between a small range of variations of $V_{\rm low\,k}$, i.e. assuming that the initial $V_{\rm low\,k}$ from which $v_{\rm BDRS}^{[\rm bare(2)]}$ is derived does not constitute an absolute reference. Note that the ideal approach would consist in taking the deviations $\delta v(k_i,k_j)$ within the alloted range *while strictly preserving the two-body observables constrained by the RG flow, e.g. the scattering phase shifts*[8]. We only use here as a first step a pure statistical

[7] Owing to the fact that a random variable never exceeds twice its variance, we obtain a random curve that remains at each point between -1 and $+1$ in average.

[8] A possible "quick & dirty" approach to this relatively complex problem would consist in rejecting all random resamplings that provide scattering phase shifts which exceed a certain value of residuals.

resampling, that lead to very small variations of such observables (see Sec. 10.3.10.5).

In the following we will use $B = 200$ resamplings which was found to be an accurate prescription, and will provide intervals at 90% confidence level, i.e. $\alpha = 0.05$.

10.3.10.3 Representation error: case study

To illustrate how the study of confidence intervals might provide essential informations, let us get back to the case where $v_{\rm BDRS}^{[\rm bare(2)]}$ was adjusted for different RG cutoff functions (Sec. 10.3.6). We had found that starting from AV18 and using different cutoffs, e.g. a sharp one and an exponential one, the free parameters of $v_{\rm BDRS}^{[\rm bare(2)]}$ where very close to each other but with small differences. Using the bootstrap procedure, the error bars associated with each parameter are found in Tab. {10.9} for $\Lambda = 2.1$ fm^{-1}. One finds that

- error bars for the coupling constants S_i^{10} are of the order of a few MeVs.fm^3, while error bars for the effective ranges are of the order of 0.05 fm except for the short range term. In all cases, error bars are much larger for the short-range term and the smallest for the medium-range one, which is (i) consistent with the previous interpretations, and (ii) similar to the situation of standard models of vacuum NN potentials for which the shortest range always corresponds to the most uncertain one,
- values for these error bars are, as expected, much larger than the intrinsic uncertainties (Sec. 10.3.10.1),
- **taking into account such uncertainties, the interactions $v_{\rm BDRS}^{[\rm bare(2)]}$ coming from a low-momentum interaction with a sharp and a smooth cutoff become almost non-exclusive.** When all levels or uncertainties are considered this becomes an exact result (see below). This suggests that $v_{\rm BDRS}^{[\rm bare(2)]}$ might be defined as a universal object, regardless of the cutoff procedure for $V_{{\rm low}\,k}$,
- their order of magnitude is also consistent with the small variations of $\{\mu_i, S_i^{10}\}$ as a function of T_z when CIB/CSB effects are included.

	Smooth			Sharp		
	Min	Fit	Max	Min	Fit	Max
μ_1 [fm]	0.000	0.000	0.117	0.203	0.246	0.292
S_1^{10} [Mev.fm^3]	221.32	222.27	230.70	251.05	266.19	288.17
μ_2 [fm]	1.222	1.230	1.233	1.164	1.182	1.195
S_2^{10} [Mev.fm^3]	−997.96	−992.69	−991.43	−1021.81	−1007.75	−996.78
μ_2 [fm]	3.327	3.357	3.379	3.115	3.168	3.211
S_2^{10} [Mev.fm^3]	−230.83	−227.45	−225.29	−262.33	−254.09	−247.54

Table 10.9: Representation error for the parameters of $v_{\rm BDRS}^{[\rm bare(2)]}$ computed for $V_{{\rm low}\,k}$ at $\Lambda = 2.1$ fm^{-1} for a sharp and a smooth cutoff.

10.3.10.4 Total uncertainties

Adding the uncertainties on the definition itself of $V_{{\rm low}\,k}$ can be one in two steps, i.e. (i) by computing associated error bars directly, or (ii) by combining errors on $V_{{\rm low}\,k}$ and on the

representation at the level of $\delta v(k_i, k_j)$. Uncertainties associated with the initial condition of the RG flow equations are expected to correspond to the largest uncertainties, given the order of magnitude within which $V_{\rm low\,k}$ is resampled. In that respect, we have used the bootstrap procedure in the following cases, starting from $V_{\rm low\,k}$ computed with a smooth cutoff at $\Lambda = 2.1$ fm^{-1}

1. representation error,
2. difference with $V_{\rm low\,k}$ coming from AV18 and a sharp cutoff ("cutoff uncertainty"),
3. difference with $V_{\rm low\,k}$ coming from CD-Bonn and a smooth cutoff ("vacuum force uncertainty"),
4. difference $V_{\rm low\,k}$ coming from CD-Bonn and AV18 and sharp/smooth cutoffs ("total $V_{\rm low\,k}$ uncertainty"),
5. error with respect to the representation and $V_{\rm low\,k}$ coming from CD-Bonn and AV18 and sharp/smooth cutoffs ("total uncertainty").

		Procedure				
		1	2	3	4	5
μ_1 [fm]	min	0.000	0.000	0.000	0.000	0.000
	max	0.117	0.137	0.304	0.294	0.299
S_1^{10} [Mev.fm^3]	min	221.32	221.06	214.07	213.53	214.11
	max	230.70	232.07	293.66	287.55	292.00
μ_2 [fm]	min	1.222	1.222	1.170	1.171	1.166
	max	1.233	1.233	1.249	1.253	1.251
S_2^{10} [Mev.fm^3]	min	−997.96	−1001.35	−1041.68	−1246.52	−1042.74
	max	−991.43	−991.17	−985.00	−978.20	−983.44
μ_2 [fm]	min	3.327	3.333	3.239	3.215	3.232
	max	3.379	3.371	3.441	3.453	3.460
S_2^{10} [Mev.fm^3]	min	−230.83	−230.65	−246.12	−250.26	−250.34
	max	−225.29	225.69	−215.66	−212.79	−212.58

Table 10.10: 90% Confidence intervals for the parameters of $v_{\rm BDRS}^{[\rm bare(2)]}$ computed for $V_{\rm low\,k}$ at $\Lambda = 2.1$ fm^{-1} and the procedures described in the text.

Results are presented in Tab. {10.10}. One observes that

- The uncertainty due to the RG cutoff function is of the same order as the representation error (procedures 1 and 2),
- When including variations associated with the initial RG condition one obtains larger uncertainties.

The latter results suggest a hierarchy of uncertainties for the fitted parameters of $v_{\rm BDRS}^{[\rm bare(2)]}$, i.e.

$$\delta Y_i^{[\rm intr]} \ll \delta Y_i^{[\rm representation]} \ll \delta Y_i^{[\rm V_{low\,k}]} \,. \tag{10.52}$$

Finally, one can compute total error bars for the parameters of $v_{\rm BDRS}^{[\rm bare(2)]}$ as a function of the RG cutoff Λ. Results, presented in Fig. 10.34, suggest that (i) the interpretation from Sec. 10.3.4 still stands regarding in particular the zero-range approximation of the short-range part of $v_{\rm BDRS}^{[\rm bare(2)]}$ in the low-Λ regime, (ii) ideal, that is rather large, phase regions for a linear refitting of

the parameters of $v_{\mathrm{BDRS}}^{[\mathrm{bare}(2)]}$ can be provided within such a framework. The confidence intervals obtained in the present work remain narrow, and the relative variations allowed for each adjusted parameter never exceed a few percents, which proves the robustness of the inital operatorial representation that remains stable versus small variations of the $V_{\mathrm{low}\,k}$ input within a physically sound interval. Additionally, the fact that these confidence intervals do not overlap with each other validates a choice of three well-defined gaussians. By adding more gaussians, as in Sec. 10.3.7, such intervals are expected to collide and any physically sound interpretation is lost. Finally, one sees a general trend where the magnitude of the confidence intervals increase with the resolution scale Λ, which suggests that an operatorial representation of *vlowk* with three gaussians remains only valid in a given interval for the RG cutoff, up to the point where the corresponding confidence intervals overlap with each other. Beyond that (i) more gaussians should be necessary, or (ii) the model should be tampered with. In any case, our model remains valid in the whole low-Λ regime which is of interest for EDF calculations.

Note however that in a statistical sense, the random variables μ_i and S_i^{10} are not independent, with correlations coming from (i) the non-orthogonality of gaussian functions, and (ii) intrinsic features of the gaussian+RG representation. In that respect one should keep in mind that the confidence intervals provided in this section must be complimented by a principal component analysis.

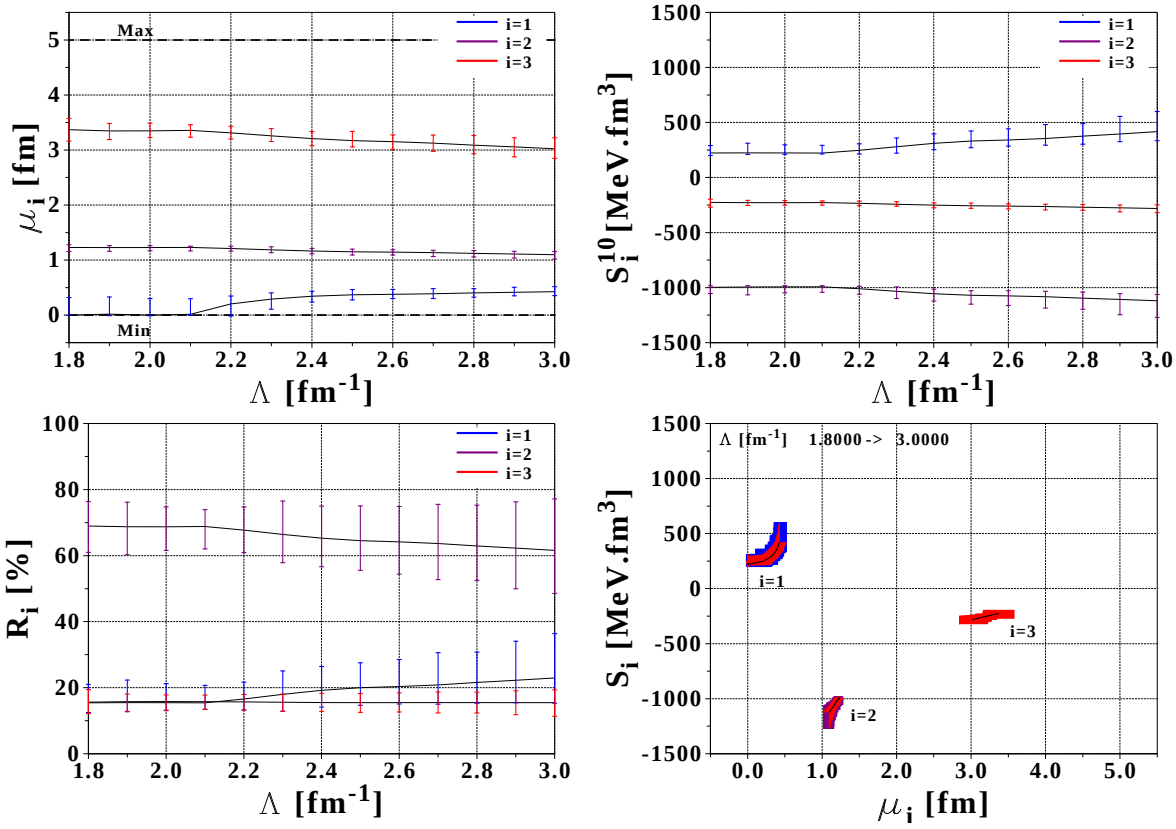

Figure 10.34: Parameters of the $v_{\mathrm{BDRS}}^{[\mathrm{bare}(2)]}$ at different Λ including error bars.

10.3.10.5 Errors on physical observables

The previous error bars on the (non-observable) parameters of $v_{\mathrm{BDRS}}^{[\mathrm{bare}(2)]}$ can be translated into uncertainties on the physical observables associated with $v_{\mathrm{BDRS}}^{[\mathrm{bare}(2)]}$, such as the scattering phase

shifts, the gap equation or the INM equation of state later on. Let $O(X_i)$ denote one of these quantities. Local uncertainties on $O(X_i)$ can be defined by

$$\forall\, i\,, \qquad O^{\min\,/\,\max}(X_i) = \min_{\alpha\in\mathcal{A}} / \max\left[O(X_i;\alpha)\right]\,, \tag{10.53}$$

where α denotes a set of parameters $\{\mu_i, S_i^{10}\}$ provided by the bootstrap analysis[9]. An example of such errors are provided by FIGS. (10.35,10.36,10.37) for the matrix elements, scattering phase shifts and the gap equation, respectively. These results suggest that the resampling procedure preserves in first approximation the two-body observables associated with the RG flow although it was not enforced at the level of the resampling procedure. On the other hand, it is of interest to study how these errors propagate into many-body observables that are not constrained by the RG approach, such as the INM EOS at various levels of complexity.

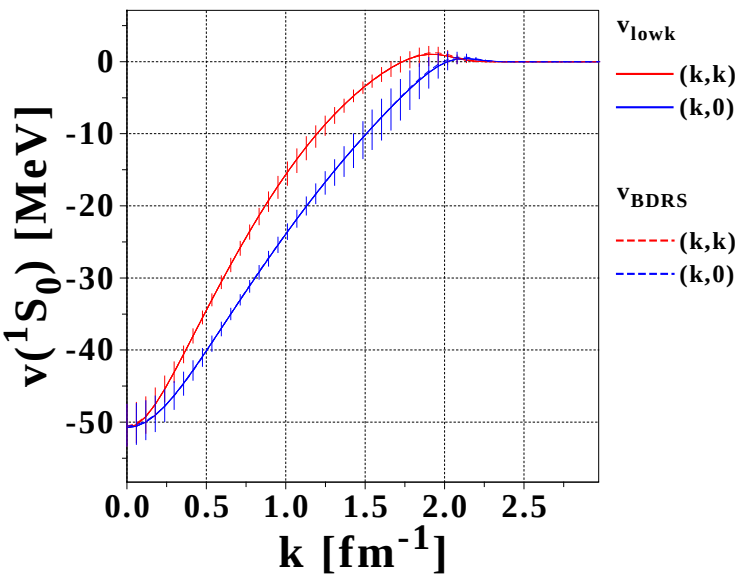

Figure 10.35: ^{1}S$_0$ Matrix elements of $v_{\rm BDRS}^{[{\rm bare}(2)]}$ including error bars magnified by a factor of ten, represented by vertical lines.

In the following, additional preliminary results are provided and highlight different paths along which our work has to be further developed. Only general guidelines will be given.

10.4 Results for $v_{\rm BDRS}^{[{\rm bare}(2)]}$: $L \leq 2$ partial waves with RG cutoffs

A first possible extension of the previous works concerns the generalization of the fitting process to all relevant partial waves in the two- (and three-body) domains. In this case, the general expression for $v_{\rm BDRS}^{[{\rm bare}(2)]}$ from SEC. 8.4.4.2 can be used. The number of degrees of freedom involved in the fitting procedure increases dramatically, and overfitting clearly becomes an issue. On the other hand, FITPACK has been designed specifically to handle such a complex optimization problem, baring some adjustement of its various parameters.

[9]Note that a naive approach would consist in using instead uncorrelated random resampling for each parameter within the phase space provided by the bootstrap analysis. However the latter case corresponds to completely removing all underlying correlations between the parameters, and for instance artificially modifies the well-constrained value of $v_{\rm BDRS}^{[{\rm bare}(2)]}$ for $k = k' = 0 = S_1^{10} + S_2^{10} + S_3^{10}$.

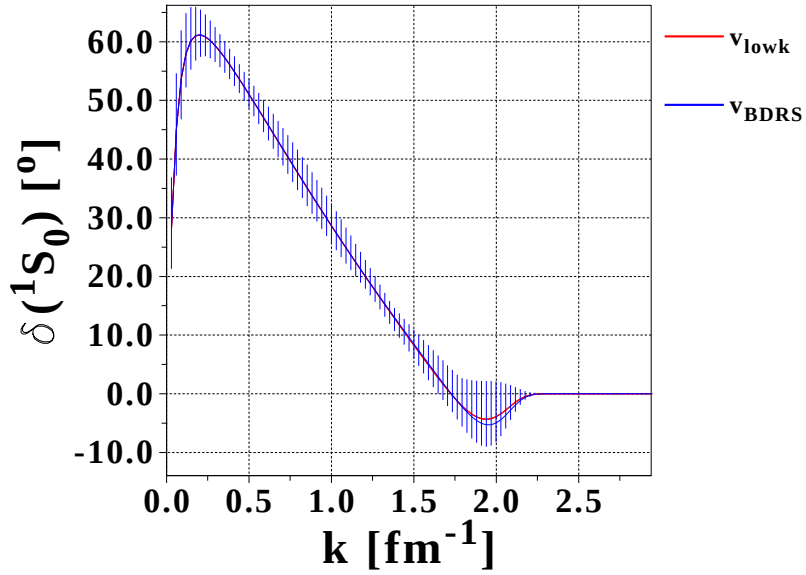

Figure 10.36: $^1S_0$ scattering phase shifts of $v_{\mathrm{BDRS}}^{[\mathrm{bare}(2)]}$ including error bars magnified by a factor of ten, represented by vertical lines.

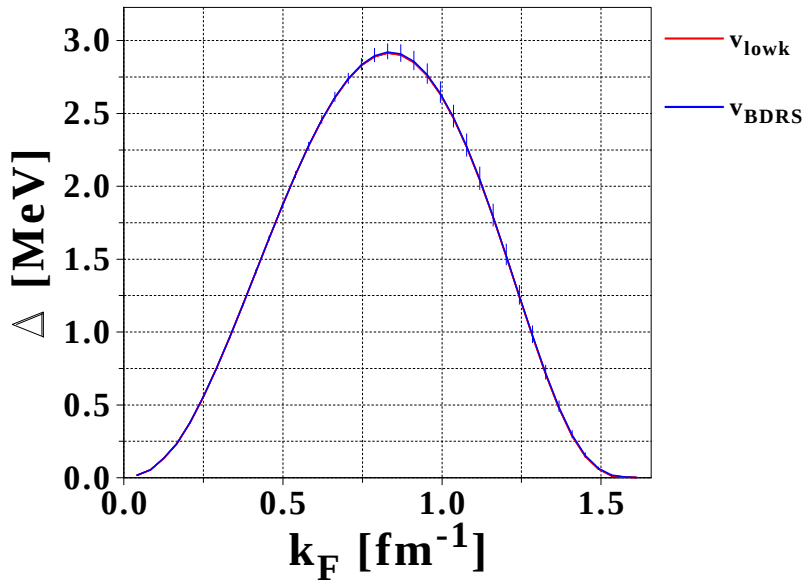

Figure 10.37: $^1S_0$ gap equation of $v_{\mathrm{BDRS}}^{[\mathrm{bare}(2)]}$ including error bars represented by vertical lines.

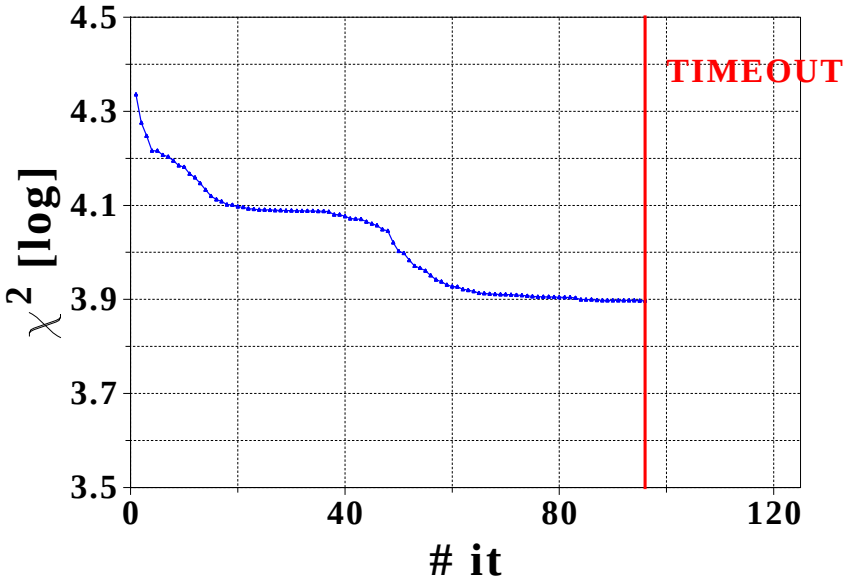

Figure 10.38: χ^2 of the RG-induced $v_{\mathrm{BDRS}}^{[\mathrm{bare}(2)]}$ fitting process using 11 partial waves as a function of the number of FITPACK iterations on the CCRT computer grid.

Having access to large-scale computing capabilities at the CCRT computer grid [657], preliminary adjustements have been performed using 256 CPU nodes and FITPACK in order to fit a gaussian vertex $v_{\mathrm{BDRS}}^{[\mathrm{bare}(2)]}$ that reproduces with three gaussian terms the two-body $V_{\mathrm{low}\,k}$ in all $L \leq 2$ partial waves. RG cutoffs at high momenta have been added in all channels using the same non-local momentum correction as in the previous section, considering that (i) they might provide better out-of-the box results, and (ii) the transformation back into coordinate space remains numerically possible. All 11 partial waves entering the fitting procedure have been given an equal weight in the total χ^2 function to be minimized[10]. The full optimization contains 21 parameters and about 15 minutes are needed between each genetic recombination process. FIG. 10.38 presents the evolution of the total χ^2 of the fit as a function of the number of iterations. The overall convergence of the process is clearly seen. On the other hand, the wall time limitation on the computer grid caused the whole process to timeout after about 48 hours of computation. Nevertheless, the resulting matrix elements shown in FIG. 10.40 already constitute very promising and encouraging results. Indeed

- in several partial waves (p waves, $^1D_2$...), a very good agreement between the fitted $v_{\mathrm{BDRS}}^{[\mathrm{bare}(2)]}$ and $V_{\mathrm{low}\,k}$ is already seen. The corresponding scattering phase shifts presented in FIG. 10.39 also reproduce very well experimental data,
- for the $^1S_0$ and $^3D_1$ channels, the optimization process does not seem to be fully converged, which might be a consequence of the undesired computation timeout. Nevertheless, the overall shape of these matrix elements gives reasonable hopes that an adequate representation of $V_{\mathrm{low}\,k}$ in these partial waves is possible,
- for the ϵ_1, $^3S_1$ and $^3D_2$ channels however the situation looks a little more complicated. Indeed, the rather large discrepancies between the matrix elements of $v_{\mathrm{BDRS}}^{[\mathrm{bare}(2)]}$ and $V_{\mathrm{low}\,k}$ might be explained by several reasons, that is (i) a non-converged fitting procedure, in

[10] This constitutes an arbitrary choice and several weighting functions might be envisioned instead, e.g. giving more weight to channel associated with smaller angular momenta or larger phase shifts.

which case a better global miminum could exist and has not been reached yet, or (ii) an intrinsic problem with the parametric definition of $v_{\mathrm{BDRS}}^{[\mathrm{bare}(2)]}$, in particular in the tensor channels where the modified gaussian vertex might not be an accurate momentum-space representation. The latter point particularly calls for additional studies, since a definite answer cannot be put forward given the scope of these preliminary results.

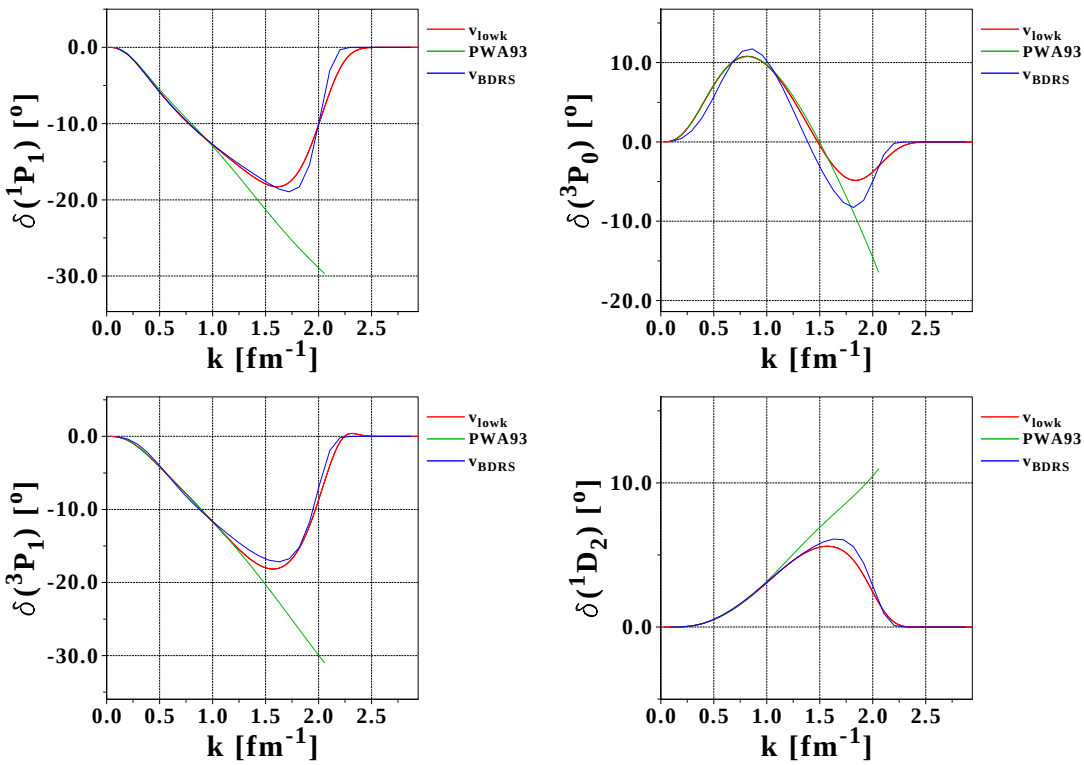

Figure 10.39: Phase shifts of $v_{\mathrm{BDRS}}^{[\mathrm{bare}(2)]}$ in various partial waves using RG cutoffs compared to the ones of $V_{\mathrm{low}\,k}$.

In any case, this example illustrates that a RG-induced momentum-space representation of $V_{\mathrm{low}\,k}$ is not only possible in the $^1S_0$ channel, but can also be generalized towards a more complete representation of the bare two-body vertex, while remaining a simple model with only a few parameters[(11)].

10.5 Results for $v_{\mathrm{BDRS}}^{[\mathrm{bare}(2)]}$: no RG cutoffs in the $^1\mathrm{S}_0$ channel

Similar preliminary results can also be given concerning another class of problem, that is the construction a full gaussian expression for $v_{\mathrm{BDRS}}^{[\mathrm{bare}(2)]}$ that can be directy plugged into existing nuclear structure codes. In this case the non-local momentum correction previously defined cannot be of help any more to quench high-momenta matrix elements, but the following proof of principle illustrates the kind of accuracy that can be expected nevertheless.

In this preliminary result only the $^1S_0$ channel is considered, aiming towards a gaussian representation of $V_{\mathrm{low}\,k}$ in the particle-particle channel instead of empirical representation such as Gogny D1S. Once again three gaussian terms are used in the fitting process. It appears that the choice of theoretical tolerances is now becoming critical regarding the accuracy of the

[11] The actual values of these parameters are not relevant in the present context and are not presented here.

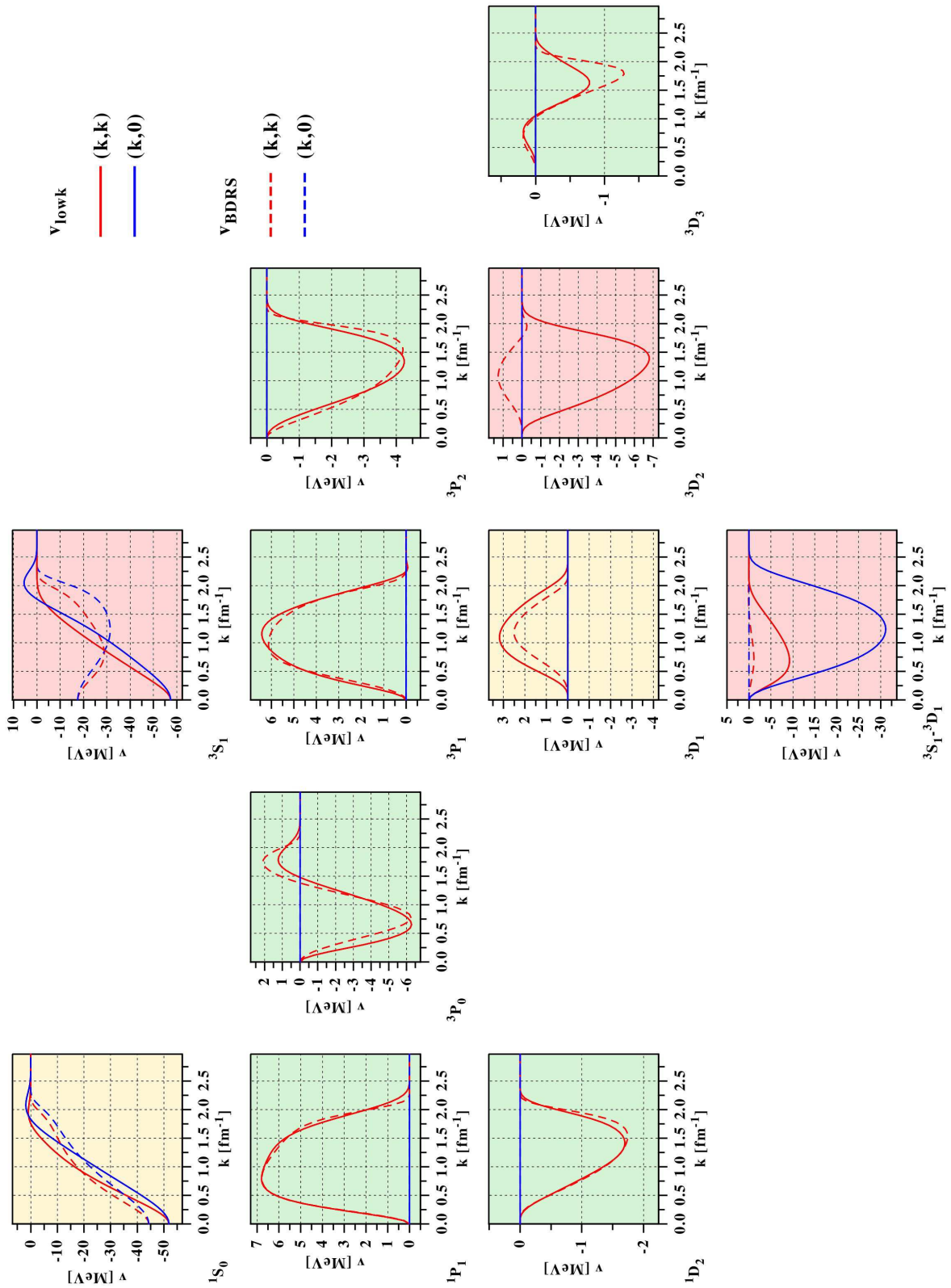

Figure 10.40: $v_{\rm BDRS}^{[\rm bare(2)]}$ matrix elements using RG cutoffs in all $L \leq 2$ partial waves ($T_z = 0$ if $T = 1$) compared to the ones of $V_{{\rm low}\,k}$.

final results. Using previous results, it appears that (i) both the RG-induced $v_{\rm BDRS}^{[\rm bare(2)]}$ and the separable interaction yield to similar accuracies in terms of physical observables such as scattering phase shifts, while having quite different deep off-diagonal matrix elements (see Sec. 10.3.9), (ii) increasing the number of gaussians in the RG-induced representation does not improve by much the accuracy of $v_{\rm BDRS}^{[\rm bare(2)]}$ in comparison with $V_{{\rm low}\,k}$ in this off-diagonal region (see Sec. 10.3.7), and (iii) the presence of small positive off-diagonal matrix elements does not affect the perturbative/non-perturbative behavior of a given bare interaction (see Sec. 7.6). For these reasons, we chose to keep the same expression as in Eq. (10.36a) for the theoretical uncertainties used in the fitting process, which provide more weighting to diagonal / small-momentum matrix elements.

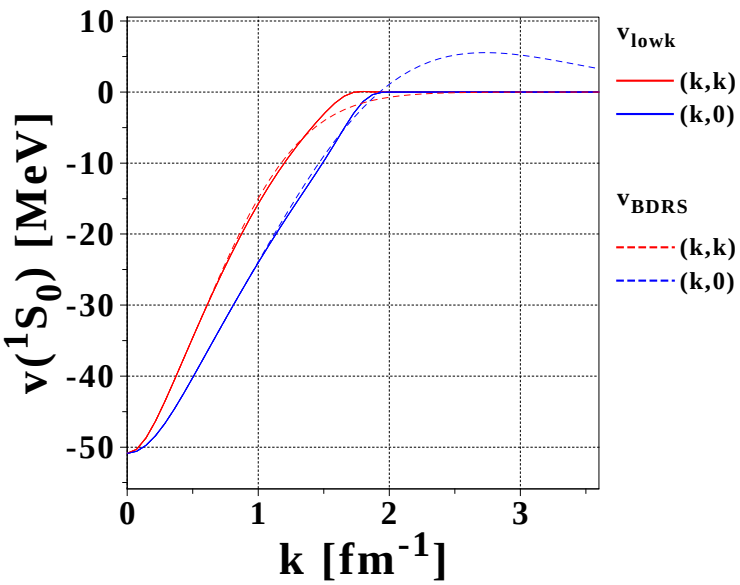

Figure 10.41: Matrix elements of the full gaussian $v_{\rm BDRS}^{[\rm bare(2)]}$ in the $^1S_0$ channel.

Fig. 10.41 shows the matrix elements of the fitted $v_{\rm BDRS}^{[\rm bare(2)]}$ in comparison with those of $V_{{\rm low}\,k}$, where one clearly sees that

- there is a very good overall agreement between the two models, in particular in the low-momentum region,
- the fitted $v_{\rm BDRS}^{[\rm bare(2)]}$ exhibits positive matrix elements that are localized in the off-diagonal region. While these may correspond to a signature of hard core repulsion, the results of Sec. 7.6 suggest that the magnitude of these matrix elements, which remains below $6-7$ MeVs, remains well within acceptable ranges concerning the perturbative many-body behavior of $v_{\rm BDRS}^{[\rm bare(2)]}$.

Futhermore, physical observables for this newly fitted $v_{\rm BDRS}^{[\rm bare(2)]}$ are presented in Figs. (10.42,10.43) look very promising since both the gap equation and the scattering phase shifts remain very close to those of $V_{{\rm low}\,k}$. The latter suggests that indeed a gaussian representation may indeed (i) carry out enough information embedded in the bare nucleon-nucleon force as shown in Tab. {10.11} where the physical properties of both the RG-induced and full gaussian $v_{\rm BDRS}^{[\rm bare(2)]}$ vertices appear to be in good agreement with those of $V_{{\rm low}\,k}$, and (ii) remain a realistic model for low-energy nuclear structure while keeping a simple and computationally-friendly structure. In addition Tab. {10.12} presents a summary of the ranges and strenghtes of the two approaches used to fit

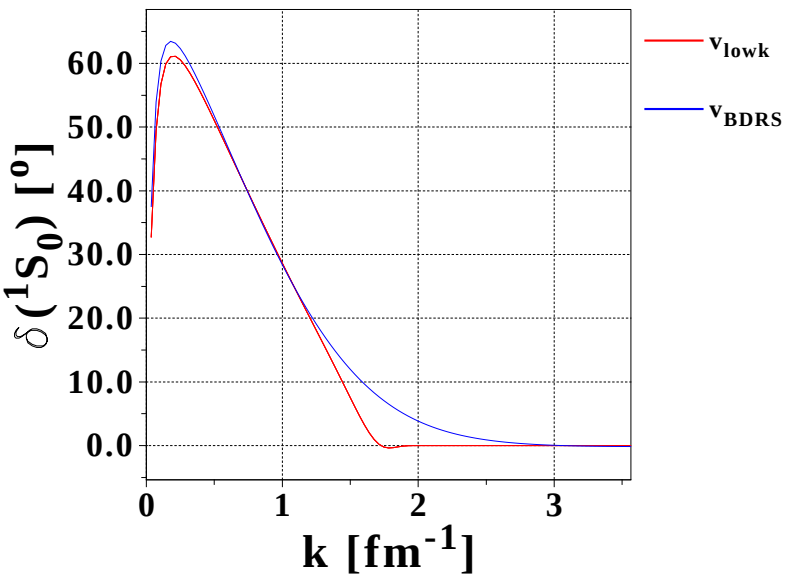

Figure 10.42: $^1S_0$ scattering phase shifts of the full gaussian $v_{\rm BDRS}^{[\rm bare(2)]}$.

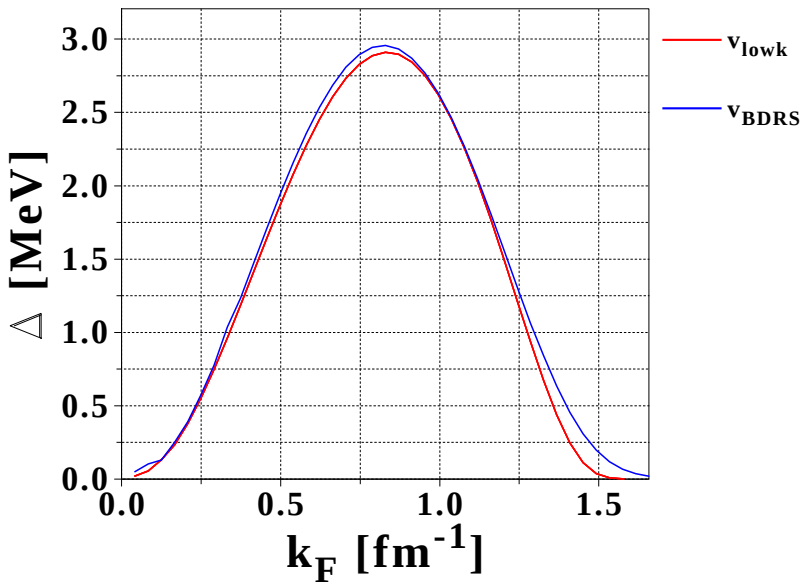

Figure 10.43: $^1S_0$ gap equation in symmetric nuclear matter of the full gaussian $v_{\rm BDRS}^{[\rm bare(2)]}$.

		$v_{\rm BDRS}^{[\rm bare(2)]}+RG$		$v_{\rm BDRS}^{[\rm bare(2)]}$		Gogny D1S	
μ_1 [fm]	S_1^{10} [MeV.fm^3]	0.006	223.2	0.863	−148.9	0.700	364.5
μ_2 [fm]	S_2^{10} [MeV.fm^3]	1.230	−997.4	1.212	−1748.9	1.200	−1150.9
μ_3 [fm]	S_3^{10} [MeV.fm^3]	3.369	−225.9	4.138	893.5	N/A	

Table 10.11: Ranges μ_i and strengthes S_i^{10} of $v_{\rm BDRS}^{[\rm bare(2)]}$ in the $^1S_0$ channel in the RG-induced approximation and the full gaussian representation, compared with the values of the Gogny D1S effective interaction.

	$V_{\rm low\,k}$	$v_{\rm BDRS}^{[\rm bare(2)]}+RG$	$v_{\rm BDRS}^{[\rm bare(2)]}$
a_0 [fm]	−18.5	−18.4	−22.2
r_0 [fm]	2.79	2.81	2.20
η_0	0.901	0.901	0.915
η_-	−0.011	−0.012	−0.046

Table 10.12: $^1S_0$ scattering length, effective range and Weinberg eigenvalues of $v_{\rm BDRS}^{[\rm bare(2)]}$ in the $^1S_0$ channel in the RG-induced approximation and the full gaussian representation, compared with the values obtained for $V_{\rm low\,k}$. As in Sec. 7.6, η_0 and η_- denote the largest and smallest eigenvalues of the scattering matrix, respectively.

$v_{\rm BDRS}^{[\rm bare(2)]}$ vertices in comparison with the ones of the Gogny D1S interaction. One may notice that for the full gaussian model the ranges of the first two gaussians of $v_{\rm BDRS}^{[\rm bare(2)]}$ look similar to those of D1S.

Conclusions

A large range of new perspectives for low-energy nuclear structure have been brought about by the recent advent of low-momentum vacuum interactions $V_{\text{low}\,k}$. For the first time, an explicit connection between realistic vacuum two- (and three-...) nuclear interactions and the nuclear energy density functional (EDF) that enters calculations of medium- and heavy-mass nuclei can be envisioned. This connection appears as a necessary step to improve the predictive power of EDF calculations for exotic nuclei far away from the valley of stability. In that respect, we have set up the first steps towards the construction of non-empirical EDFs based on effective two-body vertices, making use of recents achievements, namely

- low-momentum potentials that set a new paradigm for vacuum nuclear interactions, that reproduce low-energy two-body observables and constitute a starting point for perturbative many-body calculations,
- the construction of the three-body force in the context of chiral effective field theory, which can be transformed into density-dependent two body forces with a good precision,
- many-body calculations starting from such low-momentum two- and three-body forces, leading to a converged equation of state of symmetric nuclear matter at second order in many-body perturbation theory (MBPT) which displays good saturation properties in agreement with (i) empirical data and (ii) ab initio calculations using hard-core phenomenological potentials.

We have then proposed a possible connection between the effective two-body vertices $v^{\rho\rho}$ and $v^{\kappa\kappa}$ that act as basic ingredients in state-of-the-art EDF calculations and microscopic counterparts that are derived in the context of MBPT. More precisely, at lowest order in two-particle-irreducible vertices, $v^{\rho\rho}$ can be assimilated to the nuclear in-medium G-matrix computed from two- plus (averaged) three-body forces, and further reduced to second order in particle-particle ladders when starting from low-momentum interactions, whereas $v^{\kappa\kappa}$ is mapped onto the vacuum two-body force $V_{\text{low}\,k}$, possibly complemented by the contribution from the three-body force, i.e.

$v^{\rho\rho} \equiv$ 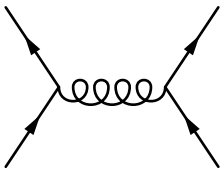 $v^{\kappa\kappa} \equiv$ 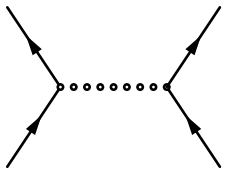 . (10.54)

The following step consists in constructing such vertices in a manner that is suitable for systematic EDF calculations of medium- and heavy-mass nuclei, i.e. such that some integrations at play can be computed analytically in opposition to using directly low-momentum interactions as they are numerically produced by the renormalization group flow equations. In that respect, we have introduced three possible strategies to ultimately compute $v^{\rho\rho}$ and $v^{\kappa\kappa}$, corresponding to different realizations of a so-called underlying v_{BDRS} non-empirical effective vertex. The

latter is introduced as a gaussian local expression that includes finite-range spin-orbit and tensor contributions and is suitable for EDF calculations in a HO basis. In the **strategy 1**, $v_{\rm BDRS}^{[\rm bare(2)]}$ represents the vacuum nucleon-nucleon force and three-body/MBPT effects that enter $v^{\rho\rho}$ and $v^{\kappa\kappa}$ need to be diagrammatically calculated and approximated by products of energy-dependent one-body densities, from which a quasi-local functional can be derived by applying the DME [593]. In **strategy 2**, $v_{\rm BDRS}^{[\rm bare(3)]}$ represents the sum of the vacuum two- and three-body forces, such that in-medium effects entering $v_{\rm BDRS}$ are encoded through complex density dependencies of its coupling constants. Again, MBPT effects must be calculated in a second step in this strategy. In **strategy 3** the effective vertices $v_{\rm BDRS}^{[\rho\rho]/[\kappa\kappa]}$ are constructed to represent $v^{\rho\rho}$ and $v^{\kappa\kappa}$ directly in infinite nuclear matter and thus resum in-medium correlations. These strategies correspond to resumming more and more in-medium effects into $v_{\rm BDRS}^{[\rm X]}$ at the level of infinite nuclear matter as one goes from **strategy 1** to **strategy 3**. The latter case corresponds to averaging the corresponding correlations in a homogenous system and simplifying accordingly finite nuclei calculations.

A fitting strategy of the free parameters of $v_{\rm BDRS}$ has been devised and relies on (i) a reproduction of matrix elements in a subset of partial waves where $v_{\rm BDRS}$ is matched on the vacuum two-body low-momentum interaction or more complex observables depending on the chosen strategy, and (ii) a new fitting algorithm that makes use of evolutionary techniques, i.e. based on a hybridation between simplex and genetic algorithms that can handle very complex optimization problems in high dimensionality. Note that in all envisioned strategies the matching is done at the vertex level where spin-orbit and tensor components contribute even in INM, whereas they may cancel out in the binding energy. This brings up new perspectives in comparison with other strategies where such components are adjusted a posteriori on finite nuclei data [147; 160; 595; 596].

The first set of results that have been presented relate to **strategy 1**, and highlight several areas of application for the non-empirical vertex $v_{\rm BDRS}^{[\rm bare(2)]}$

- **The possibility to devise a high-precision analytical representation of** $V_{{\rm low}\,k}$, when the local $v_{\rm BDRS}$ is complemented by a high-momentum cutoff function consistent with the cutoff functions entering the RG flow and thus incorporating explicitly the non-locality of $V_{{\rm low}\,k}$. While the structure of such a so-called *RG-induced* $v_{\rm BDRS}$ does not seem to be tractable in existing EDF codes, it allows a precise study of the ingredients that enter vacuum two-body forces. For instance, the $^1{\rm S}_0$ channel can be separated at small RG cutoff Λ into (i) a zero-range component stemming from the presence of a virtual di-nucleon state, and (ii) medium- and long-range parts that are well described by modified gaussians. The inclusion of theoretical error bars in this framework allows to describe $v_{\rm BDRS}^{[\rm bare(2)]}$ as a universal object, regardless of (i) the realistic nucleon-nucleon force $V_{{\rm low}\,k}$ is derived from, (ii) the cutoff procedure for high-momentum components that enters the RG flow equations, and (iii) other sources of uncertainties in the fitting procedure. Finally, one may note that the analysis, in particular concerning fits with increasing numbers of gaussians, suggests that incorporating higher-order components in k, k' in the definition of the matrix elements in momentum space, would allow a much better reproduction of low-momenutm interactions in the off-diagonal direction, e.g. in the $^1{\rm S}_0$ channel

$$v_{\rm BDRS}^{[\rm X]}(^1S_0, k, k') = (4\pi) \sum_{i=1}^{N} \mathcal{P}_i(k^2, k'^2)\, S_i^{01}[\rho_0, \Lambda]\, \frac{\tilde{g}_0^i(k', k)}{4\pi}\,, \tag{10.55}$$

where $\mathcal{P}_i$ are polynomials in k^2, k'^2 whose coefficients are free parameters that are to be adjusted, and that may differ in each partial wave. Of course such a fine tuning (i) is

very close to the construction of high-precision realistic NN models where in particular the short-range component is adjusted differently in each partial wave, and (ii) diverges from the initial goal to improve existing EDFs since the associated vertex in coordinate space becomes very complicated and cannot be easily implemented.

- The construction of a purely local gaussian expression for $v_{\rm BDRS}$ that can be directly put into existing EDF codes working in a harmonic oscillator basis, with the tradeoff that intermediate-energy observables such as the scattering phase shifts are slightly worsened.

While a whole field of study concerning accurate operatorial representations of $V_{{\rm low}\,k}$ remains opened, the ultimate goal of the present approach consists in computing finite nuclei. Let us now present short- and long-term prospects in that direction.

An immediate application envisioned in the context of **strategy 1** consists in using the non-empirical vacuum nucleon-nucleon force in the particle-particle part of the EDF, while keeping an empirical model such as Gogny D1S in the particle-hole channel. This approach was already followed with a separable representation of $V_{{\rm low}\,k}$ and led to pairing gaps in finite nuclei very close to experimental data [669]. In the present framework, similar calculations could be extended to deformed nuclei. In spherical nuclei it would be of interest to investigate the discrepancies in finite nuclei between separable and finite-range representations of the same initial object.

Then, on a longer time scale, the construction of the non-empirical effective vertex $v_{\rm BDRS}^{[\kappa\kappa]}$ in infinite nuclear matter, i.e. **strategy 3**, appears as the simplest approach to calculate finite nuclei using existing EDF codes. As a further extension of **strategy 3**, complex density dependencies of $v_{\rm BDRS}^{[\rho\rho]}$ (ρ_1, $\vec{s}_0$ and $\vec{s}_1$) can be envisioned. Obviously this would involve (i) complex fitting procedures using ab initio calculations of polarized INM, (ii) ameliorations of nuclear EDF codes to handle such dependencies. Such modifications should be of great interest in very exotic neutron-rich nuclei and for high-spin states.

Finally, a parallel approach must be ultimately envisioned, i.e. performing exact many-body calculations in finite nuclei using the vacuum force $v_{\rm BDRS}^{[{\rm bare}(2)]/[{\rm bare}(3)]}$ coming from **strategies 1 and 2**, corresponding to performing orbital-dependent EDF for which we have already set up general guidelines [593]. A parallel treatment of the latter two strategies will allow to evaluate the loss of precision that appear at each step, in particular in **strategy 3** where in-medium correlations are resummed into $v_{\rm BDRS}^{[\rho\rho]}$ in INM and transported to finite nuclei through a local density approximation.

Last but not the least, all strategies should/might be complemented by a linear refitting of the free parameters of the vertices $v_{\rm BDRS}^{[{\rm X}]}$ on finite nuclei data within the range provided by (i) the Λ-dependence of the coupling constants, and (ii) a study of theoretical error bars from resampling. This last step is of interest to have very accurate observables in the valley of stability, while keeping a predictive power for exotic nuclei.

Obviously, we have initiated a (very) long-term project, that requires additional manpower in order to come to maturity. While the very first results that we have obtained are very promising regarding (i) the capacity of $v_{\rm BDRS}$ to handle a very complex nuclear interaction structure, and (ii) the possibility to make high-precision fits and robust post-fit analysis in terms of error bars and correlations, much work is yet to be done before large-scale EDF calculations using non-empirical functionals that are fully derived from vacuum interactions are performed. Although such a challenge seems overwhelming, the ultimate goal really is worth the difficulties.

- [Hiro] Yata!

Bibliography

[1] G. E. Brown and A. D. Jackson: *The nucleon-nucleon interaction* (North-Holland, Amsterdam, 1976)

[2] R. Machleidt and I. Slauss: *The nucleon-nucleon interaction.* J. Phys. G: Nucl. and Part. Phys. **27** (2001) R69–R108

[3] R. B. Wiringa, V. G. J. Stoks and R. Schiavilla: *An accurate nucleon-nucleon potential with charge-independence breaking.* Phys. Rev. C **51** (1995) 38–51. arXiv:nucl-th/9408016

[4] H. Witała, W. Glöckle, D. Hüber, J. Golak and H. Kamada: *The cross section minima in elastic Nd scattering: a "smoking gun" for three nucleon force effects.* Phys. Rev. Lett. **81** (1998) 1183–1186. arXiv:nucl-th/9801018

[5] S. Nemoto, K. Chmielewski, S. Oryu and P. U. Sauer: *Discrepancy in the cross section minimum of elastic nucleon-deuteron scattering.* Phys. Rev. C **58** (1998) 2599–2602

[6] S. Kistryn *et al.*: *Systematic study of three-nucleon force effects in the cross section of the deuteron-proton breakup at 130 MeV.* Phys. Rev. C **72** (2005) 044006. arXiv:nucl-ex/0508012

[7] A. Nogga, H. Kamada and W. Glöckle: *Modern nuclear force predictions for the alpha particle.* Phys. Rev. Lett. **85** (2000) 944–947. arXiv:nucl-th/0004023

[8] A. Nogga, S. K. Bogner and A. Schwenk: *Low-momentum interaction in few-nucleon systems.* Phys. Rev. C **70** (2004) 061002. arXiv:nucl-th/0405016

[9] A. Faessler, S. Krewald and G. J. Wagner: *Is there evidence of three-body forces from violation of the Koltun energy sum rule?* Phys. Rev. C **11** (1975) 2069–2072

[10] J. Fujita and H. Miyazawa: *Pion Theory of Three-Body Forces.* Prog. Theor. Phys. **17** (1957) 360–365

[11] B. Loiseau and Y. Nogami: *Three-nucleon force.* Nucl. Phys. **B2** (1967) 470–478

[12] W. Zuo, I. Bombaci and U. Lombardo: *Asymmetric Nuclear Matter from Extended Brueckner-Hartree- Fock Approach.* Phys. Rev. C **60** (1999) 024605. arXiv:nucl-th/0102035

[13] A. Lejeune, U. Lombardo and W. Zuo: *Nuclear Matter EOS with a Three-body Force.* Phys. Lett. B **477** (2000) 45–50. arXiv:nucl-th/0102038

[14] W. Zuo, A. Lejeune, U. Lombardo and J. F. Mathiot: *Interplay of Three-Body Interactions in the EOS of Nuclear Matter.* Nucl. Phys. **A706** (2002) 418–430. arXiv:nucl-th/0202076

[15] W. Zuo, A. Lejeune, U. Lombardo and J. F. Mathiot: *Microscopic three-body force for asymmetric nuclear matter.* Eur. Phys. J. A **14** (2002) 469–475. arXiv:nucl-th/0202077

[16] F. Coester, S. Cohen, B. Day and C. M. Vincent: *Variation in Nuclear-Matter Binding Energies with Phase-Shift-Equivalent Two-Body Potentials.* Phys. Rev. C **1** (1970) 769–776

[17] R. Brockmann and R. Machleidt: *Relativistic nuclear structure. I. Nuclear Matter.* Phys. Rev. C **42** (1990) 1965–1980

[18] R. Brockmann and R. Machleidt: *Relativistic nuclear structure. I. Finite nuclei.* Phys. Rev. C **42** (1990) 1981–1988

[19] A. Sonzogni: *NNDC Chart of Nuclides* (2007)
URL http://www.nndc.bnl.gov/chart/

[20] H. A. Grunder: *Radioactive nuclear beam facilities in north America: Status and outlook.* Nucl. Phys. **A701** (2001) 43–48

[21] W. Henning: *RNB Facilities in Europe - Present and Future.* Nucl. Phys. **A746** (2004) 3–8

[22] H. Geissel, G. Müzenberg and K. Riisager: *Secondary Exotic Nuclear Beams.* Annu. Rev. Nucl. Part. Sci **45** (1995) 163–203

[23] D. J. Morrissey and B. M. Sherrill: *Radioactive nuclear beam facilities based on projectile fragmentation.* Phil. Trans. R Soc. London A **356** (1998) 1985–2006

[24] H. H. Gutbrod: *International Facility for Antiproton and Ion Research (FAIR) at GSI, Darmstadt.* Nucl. Phys. **A752** (2005) 457–469

[25] Y. Yano and T. Motobayashi: *Radioactive Isotope Beam Factory at RIKEN (RIBF).* Nucl. Phys. News **17** (2007) 5–10

[26] J. Vervier: *Status of the EURISOL project.* Nucl. Instr. and Meth. in Phys. Res. B **204** (2003) 759–764

[27] D. J. Morrissey: *The coupled cyclotron project at the NSCL.* Nucl. Phys. **A616** (1997) 45–55

[28] J. Vervier: *Recent achievements and experiments at the Louvain-la-Neuve radioactive nuclear beam facility.* Nucl. Phys. **A616** (1998) 97–106

[29] M. Gaelens, M. Huyse, M. Loiselet, G. Ryckewaert and P. Van Duppen: *Development of radioactive ion beams of light elements at ARENAS*^{3}. Nucl. Instr. and Meth. in Phys. Res. B **126** (1997) 125–129

[30] R. E. Laxdal *et al.*: *RNB post-accelerator for ISAC at TRIUMF - present and future.* Nucl. Phys. **A701** (2002) 647–650

[31] D. Habs *et al.*: *The REX-ISOLDE project.* Nucl. Phys. **A616** (1997) 29–38

[32] S. Gales: *SPIRAL2 at GANIL: A world leading ISOL facility at the dawn of the next decade.* Prog. Part. Nucl. Phys. **59** (2007) 22–31

[33] D. W. Stracener: *Status of radioactive ion beams at the HRIBF.* Nucl. Instr. and Meth. in Phys. Res. B **204** (2002) 42–47

[34] Committee on the Physics of the Universe: *Connecting Quarks with the Cosmos: Eleven Science Questions for the New Century* (The National Academies Press, Washington D.C., 2003)

[35] O. Sorlin and M.-G. Porquet: *Nuclear magic numbers: new features far from stability* (2008). unpublished, arXiv:0805.2561

[36] P. G. Hansen and B. Jonson: *The Neutron Halo of Extremely Neutron-Rich Nuclei.* Europhys. Lett. **4** (1987) 409–417

[37] A. S. Jensen, K. Riisager, D. V. Fedorov and E. Garrido: *Structure and reactions of quantum halos.* Rev. Mod. Phys. **76** (2004) 215–261

[38] I. Tanihata *et al.*: *Measurement of interaction cross sections using isotope beams of Be and B and isospin dependence of the nuclear radii.* Phys. Lett. B **206** (1985) 592–596

[39] M. Fukuda *et al.*: *Neutron halo in* ^{11}*Be studied via reaction cross sections.* Phys. Lett. B **268** (1991) 339–344

[40] I. Tanihata *et al.*: *Measurements of Interaction Cross Sections and Nuclear Radii in the Light p-Shell Region.* Phys. Rev. Lett. **55** (1985) 2676–2679

[41] I. Tanihata *et al.*: *Measurements of interaction cross sections and radii of He isotopes.* Phys. Lett. B **160** (1985) 380–384

[42] V. Rotival and T. Duguet: *New analysis method of the halo phenomenon in finite many-fermion systems: First applications to medium-mass atomic nuclei.* Phys. Rev. C **79** (2009) 054308. arXiv:nucl-th/0702050

[43] V. Rotival, K. Bennaceur and T. Duguet: *Halo phenomenon in finite many-fermion systems: Atom-positron complexes and large-scale study of atomic nuclei.* Phys. Rev. C **79** (2009) 054309. arXiv:0711.1275

[44] P. Delheij *et al.*: *The TITAN mass measurement facility at TRIUMF-ISAC.* Hyp. Int. **173** (2006) 123–131

[45] M. Mukherjee *et al.*: *ISOLTRAP: An on-line Penning trap for mass spectrometry on short-lived nuclides.* Eur. Phys. J. A **35** (2008) 1–29

[46] B. Schlitt *et al.*: *Schottky mass spectrometry at the heavy ion storage ring ESR.* Hyp. Int. **99** (1996) 117–125

[47] M. W. Kirson: *Global systematics of the Wigner energy.* Phys. Lett. B **646** (2007) 246–249

[48] H. Frisk: *Systematics of rotational bands with K=0 in odd-odd nuclei.* Z. Phys. A **330** (1988) 241–248

[49] A. Görgen *et al.*: *Shape Coexistence in Light Krypton Isotopes.* Acta Phys. Pol. B **36** (2005) 1281–1288

[50] M. Ionescu-Bujor *et al.*: *Shape coexistence in neutron-deficient Pb nuclei probed by quadrupole moment measurements.* Phys. Lett. B **650** (2007) 141–147

[51] K.-H. Schmidt *et al.*: *Relativistic radioactive beams: A new access to nuclear-fission studies.* Nucl. Phys. **A661** (2000) 221–267

[52] M. A. Caprio: *Structure of collective modes in transitional and deformed nuclei* (2005). Ph.D. Thesis, arXiv:nucl-ex/0502004

[53] D. Ackermann: *Superheavy elements at GSI - present and future.* Nucl. Phys. **A787** (2007) 353–362

[54] P. Möller, J. R. Nix, W. D. Myers and W. J. Swiatecki: *Nuclear Ground-State Masses and Deformations.* At. Data Nucl. Data. Tables **59** (2002) 185–381

[55] G. Royer and C. Gautier: *Coefficients and terms of the liquid drop model and mass formula.* Phys. Rev. **C73** (2006) 067302. arXiv:nucl-th/0608064

[56] J. L. Friar, G. L. Payne, V. G. J. Stoks and J. J. de Swart: *Triton calculations with the new Nijmegen potentials.* Phys. Lett. B **311** (1988) 4–8

[57] W. Glöckle and H. Kamada: *Alpha-particle binding energies for realistic nucleon-nucleon interactions.* Phys. Rev. Lett. **71** (1993) 971–974

[58] A. Nogga, D. Hüber, K. Hamada and W. Glöckle: *Triton binding energies for modern NN forces and the π-π exchange three-nucleon force.* Phys. Lett. B **A409** (1997) 19–25. arXiv:nucl-th/9704001

[59] B. S. Pudliner, V. R. Pandharipande, J. Carlson, S. C. Pieper and R. B. Wiringa: *Quantum Monte Carlo calculations of nuclei with $A \leq 7$.* Phys. Rev. C **56** (1997) 1720–1750. arXiv:nucl-th/9705009

[60] R. B. Wiringa: *Quantum Monte Carlo calculations for light nuclei.* Nucl. Phys. **A631** (1998) 70–90

[61] R. B. Wiringa, S. C. Pieper, J. Carlson and V. R. Pandharipande: *Quantum Monte Carlo calculations of A=8 nuclei.* Phys. Rev. C **62** (2000) 014001. arXiv:nucl-th/0002022

[62] K. Varga, Y. Suzuki, K. Arai and Y. Ogawa: *Microscopic description of light unstable nuclei with the stochastic variational method.* Nucl. Phys. **A696** (1998) 383–393

[63] Y. Suzuki, K. Varga and J. Usukura: *Stochastic variational methods in few-body systems.* Nucl. Phys. **A631** (1999) 91–110

[64] C. Ordonez, K. Arai, Y. Suzuki and K. Varga: *Microscopic four-cluster description of ^{10}Be and ^{10}C with the stochastic variational method.* Nucl. Phys. **A673** (2001) 122–142

[65] P. Navrátil and B. R. Barrett: *No-core shell-model calculations with starting- energy-independent multi-valued effective interactions.* Phys. Rev. C **54** (1996) 2986–2995. arXiv:nucl-th/9609046

[66] P. Navrátil and B. R. Barrett: *Shell-model calculations for the three-nucleon system.* Phys. Rev. C **57** (1998) 562–568. arXiv:nucl-th/9711027

[67] P. Navrátil and B. R. Barrett: *Large-basis shell-model calculations for p-shell nuclei.* Phys. Rev. C **57** (1998) 3119–3128. arXiv:nucl-th/9804014

[68] P. Navrátil, G. P. Kamuntavicius and B. R. Barrett: *Few-nucleon systems in translationally invariant harmonic oscillator basis.* Phys. Rev. C **61** (2000) 044001. arXiv:nucl-th/9907054

[69] K. Kowalski, D. J. Dean, M. Hjorth-Jensen, T. Papenbrock and P. Piecuch: *Coupled cluster calculations of ground and excited states of nuclei.* Phys. Rev. Lett. **92** (2004) 132501. arXiv:nucl-th/0310082

[70] D. J. Dean and Hjorth-Jensen: *Coupled-cluster approach to nuclear physics.* Phys. Rev. C **69** (2004) 054320

[71] G. Hagen, D. J. Dean, M. Hjorth-Jensen and T. Papenbrock: *Complex coupled-cluster approach to an ab-initio description of open quantum systems.* Phys. Lett. B **656** (2007) 169–173. arXiv:nucl-th/0610072

[72] G. Hagen *et al.*: *Coupled-cluster theory for three-body Hamiltonians.* Phys. Rev. C **76** (2007) 034302. arXiv:0704.2854

[73] G. Hagen, D. J. Dean, M. Hjorth-Jensen, T. Papenbrock and A. Schwenk: *Benchmark calculations for ^{3}H, ^{4}He, ^{16}O and ^{40}Ca with ab- initio coupled-cluster theory.* Phys. Rev. C **76** (2007) 044305. arXiv:0707.1516

[74] E. Caurier, G. Martínez-Pinedo, F. Nowacki, A. Poves and A. P. Zuker: *The Shell Model as Unified View of Nuclear Structure.* Rev. Mod. Phys. **77** (2005) 427–488. arXiv:nucl-th/0402046

[75] D. J. Dean, T. Engeland, M. Hjorth-Jensen, M. Kartamyshev and E. Osnes: *Effective interactions and the nuclear shell-model.* Prog. Part. Nucl. Phys. **53** (2004) 419–500. arXiv:nucl-th/0405034

[76] A. P. Zuker: *Three-body monopole corrections to the realistic interactions.* Phys. Rev. Lett. **90** (2003) 042502. arXiv:nucl-th/0209073

[77] M. Bender, P.-H. Heenen and P.-G. Reinhard: *Self-consistent mean-field models for nuclear structure.* Rev. Mod. Phys. **75** (2003) 121–180

[78] R. Machleidt, F. Sammarruca and Y. Song: *The Non-Local Nature of the Nuclear Force and its Impact on Nuclear Structure.* Phys. Rev. C **53** (1996) 1483–1487. arXiv:nucl-th/9510023

[79] R. Machleidt: *High-precision, charge-dependent Bonn nucleon-nucleon potential.* Phys. Rev. C **63** (2001) 024001. arXiv:nucl-th/0006014

[80] V. G. J. Stoks, R. A. M. Klomp, C. P. F. Terheggen and J. J. de Swart: *Construction of high quality NN potential models.* Phys. Rev. C **49** (1994) 2950–2962. arXiv:nucl-th/9406039

[81] M. Walzl, U.-G. Meißner and E. Epelbaum: *Charge-dependent nucleon nucleon potential from chiral effective field theory.* Nucl. Phys. **A693** (2001) 663–692. arXiv:nucl-th/0010019

[82] E. Epelbaum, U.-G. Meißner and W. Glöckle: *Nuclear forces in the chiral limit.* Nucl. Phys. **A714** (2003) 535–574. arXiv:nucl-th/0207089

[83] E. Epelbaum, W. Glöckle and U.-G. Meißner: *The two-nucleon system at next-to-next-to-next-to-leading order*. Nucl. Phys. **A747** (2005) 362–424. arXiv:nucl-th/0405048

[84] E. Epelbaum: *Few-nucleon forces and systems in chiral effective field theory*. Prog. Part. Nucl. Phys. **57** (2006) 654–741. arXiv:nucl-th/0509032

[85] B. Borasoy, E. Epelbaum, H. Krebs, D. Lee and U.-G. Meißner: *Lattice simulations for light nuclei: Chiral effective field theory at leading order*. Eur. Phys. J. A **31** (2007) 105–123. arXiv:nucl-th/0611087

[86] B. Borasoy, E. Epelbaum, H. Krebs, D. Lee and U.-G. Meißner: *Chiral effective field theory on the lattice at next-to-leading order*. Eur. Phys. J. A **35** (2008) 343–355. arXiv:0712.2990

[87] S. K. Bogner, T. T. S. Kuo and A. Schwenk: *Model-independent low momentum nucleon interaction from phase shift equivalence*. Phys. Rept. **386** (2003) 1–27. arXiv:nucl-th/0305035

[88] K. A. Brueckner: *Many-Body Problem for Strongly Interacting Particles. II. Linked Cluster Expansion*. Phys. Rev. **100** (1955) 36–45

[89] J. Goldstone: *Derivation of the Brueckner Many-Body Theory*. Proc. R. Soc. London Ser. A **239** (1957) 267–279

[90] I. Lindgren, S. Salomonson and B. Åsén: *The covariant-evolution-operator method in bound-state QED*. Phys. Rept. **389** (2004) 161–261

[91] I. Lindgren, S. Salomonson and D. Hedendahl: *Many-body-QED perturbation theory: Connection to the two-electron Bethe-Salpeter equation*. Can. J. Phys. **83** (2005) 183–218. arXiv:quant-ph/0502141

[92] R. J. Bartlett: *Many-Body Perturbation Theory and Coupled Cluster Theory for Electron Correlation in Molecules*. Ann. Rev. Phys. Chem. **32** (1981) 359–401

[93] S. Wilson: *Many-body perturbation theory of molecules*. In C. Thomson (Editor), *Theoretical Chemistry (Specialist Periodical Reports)* (Royal Society of Chemistry, London, 1981) pp. 1–48

[94] S. Wilson: *Many-Body Perturbation Theory and its Application to the Molecular Electronic Structure Problem*. In A. Hinchliffe (Editor), *Chemical Modelling: Applications and Theory: v. 1 (Specialist Periodical Reports)* (Royal Society of Chemistry, London, 2000) pp. 364–452

[95] S. Wilson: *Many-Body Perturbation Theory and its Application to the Molecular Electronic Structure Problem*. In A. Hinchliffe (Editor), *Chemical Modelling: Applications and Theory: v. 2 (Specialist Periodical Reports)* (Royal Society of Chemistry, London, 2002) pp. 329–390

[96] S. Wilson: *Many-Body Perturbation Theory and its Application to the Molecular Structure Problem*. In A. Hinchliffe (Editor), *Chemical Modelling: Applications and Theory: v. 3 (Specialist Periodical Reports)* (Royal Society of Chemistry, London, 2004) pp. 380–428

[97] S. Wilson: *Many-Body Perturbation Theory and its Application to the Molecular Structure Problem*. In A. Hinchliffe (Editor), *Chemical Modelling: Applications and Theory: v. 4 (Specialist Periodical Reports)* (Royal Society of Chemistry, London, 2006) pp. 470–524

[98] R. G. Paar and W. Yang: *Density Functional Theory of Atoms and Molecules* (Oxford University Press, Oxford, 1989)

[99] R. M. Dreizler and E. K. U. Gross: *Density Functional Theory* (Springer, Berlin, 1990)

[100] W. Kohn: *Nobel Lecture: Electronic structure of matter-wave functions and density functionals*. Rev. Mod. Phys. **71** (1999) 1253–1266

[101] N. Argaman and G. Makov: *Density Functional Theory – an introduction*. Am. J. Phys. **68** (2000) 69–79. arXiv:physics/9806013

[102] C. Fiolhais, F. Nogueira and M. Marques (Editors): *A Primer in Density Functional Theory*, *Lect. Notes Phys.*, vol. 620 (Springer, Heidelberg, 2003)

[103] P. Hohenberg and W. Kohn: *Inhomogenous electron gas.* Phys. Rev. **136** (1964) B864–B871

[104] W. Kohn and L. J. Sham: *Quantum Density Oscillations in an Inhomogeneous Electron Gas.* Phys. Rev. **137** (1964) A1697–A1705

[105] W. Kohn and L. Sham: *Self-Consistent Equations Including Exchange and Correlation Effects.* Phys. Rev. **140** (1965) A1133–A1138

[106] J. P. Perdew *et al.*: *Prescription for the design and selection of density functional approximations: More constraint satisfaction with fewer fits.* J. Chem. Phys. **123** (2005) 062201

[107] W. Heisenberg: *On the structure of atomic nuclei.* Z. Phys. **77** (1932) 1–11

[108] A. Bohr, B. R. Mottelson and D. Pines: *Possible Analogy between the Excitation Spectra of Nuclei and Those of the Superconducting Metallic State.* Phys. Rev. **110** (1958) 936–938

[109] A. Bohr and B. R. Mottelson: *Nuclear Structure* (Benjamin, New York, 1975)

[110] D. J. Dean and M. Hjorth-Jensen: *Pairing in nuclear systems: from neutron stars to finite nuclei.* Rev. Mod. Phys. **75** (2003) 607–656. arXiv:nucl-th/0210033

[111] B. L. Friman and O. V. Maxwell: *Neutron Star Neutrino Emissivities.* Astrophys. J. **232** (1979) 541–547

[112] S. Tsuruta: *Thermal properties and detectability of neutron stars. I. cooling and heating of neutron stars.* Phys. Rept. **56** (1979) 237–277

[113] T. Takatsuka and R. Tamagaki: *Effects of charged-pion condensation on neutron (3)P(2) superfluidity.* Prog. Theor. Phys. **97** (1997) 263–281

[114] S. Tsuruta: *Thermal properties and detectability of neutron stars. II. Thermal evolution of rotation-powered neutron stars.* Phys. Rept. **292** (1979) 1–130

[115] D. Page, M. Prakash, J. M. Lattimer and A. Steiner: *Prospects of detecting baryon and quark superfluidity from cooling neutron stars.* Phys. Rev. Lett. **85** (2000) 2048–2051. arXiv:hep-ph/0005094

[116] M. Baldo, Ø. Elgarøy, L. Engvik, M. Hjorth-Jensen and H. J. Schulze: $^3P_2 - ^3F_2$ *pairing in neutron matter with modern nucleon-nucleon potentials.* Phys. Rev. C **58** (1998) 1921–1928. arXiv:nucl-th/9806097

[117] L. N. Oliveira, E. K. Gross and W. Kohn: *Density-Functional Theory for Superconductors.* Phys. Rev. Lett. **60** (1988) 2430–2433

[118] B. Jancovici and D. H. Schiff: *The collective vibrations of a many-fermion system.* Nucl Phys. **58** (1964) 678–686

[119] D. M. Brink and A. Weiguny: *The generator coordinate theory of collective motion.* Nucl. Phys. **A120** (1968) 59–93

[120] A. L. Goodman: *Self-consistent symmetries of the Hartree-Fock-Bogoliubov equations in a rotating frame.* Nucl. Phys. **A230** (1974) 466–476

[121] H. J. Mang: *The self-consistent single-particle model in nuclear physics.* Phys. Rept. **18** (1975) 325–368

[122] P. Ring and P. Schuck: *The Nuclear Many-Body Problem* (Springer-Verlag, New-York, 1980)

[123] J.-P. Blaizot and G. Ripka: *Quantum Theory of Finite Systems* (MIT Press, Cambridge, MA, 1985)

[124] J. Dobaczewski, H. Flocard and J. Treiner: *Hartree-Fock-Bogolyubov description of nuclei near the neutron-drip line.* Nucl. Phys. **A422** (1984) 103–139

[125] C. Bloch and A. Messiah: *The canonical form of an antisymmetric tensor and its application to the theory of superconductivity.* Nucl. Phys. **39** (1962) 95–106

[126] B. Zumino: *Normal Forms of Complex Matrices.* J. Math. Phys. **3** (1962) 1055–1057

[127] J. Dobaczewski: *Generalization of the Bloch-Messiah-Zumino theorem.* Phys. Rev. C **62** (2000) 017301. arXiv:math-ph/0002034

[128] N. Tajima, H. Flocard, P. Bonche, J. Dobaczewski and P.-H. Heenen: *Diabatic effects in ^{186}Pb: A Generator coordinate analysis.* Nucl. Phys. **A542** (1992) 409–433

[129] K. Mühlhans, K.Neergård and U. Mosel: *Solution of the Hartree-Fock-Bogoliubov problem in the canonical representation.* Nucl. Phys. **A420** (1984) 204–220

[130] P.-G. Reinhard, M. Bender, K. Rutz and J. A. Maruhn: *An HFB scheme in natural orbitals.* Z Phys. A **358** (1997) 277–278. arXiv:nucl-th/9705054

[131] T. Duguet, P. Bonche, P.-H. Heenen and J. Meyer: *Pairing correlations. Part 1: description of odd nuclei in mean-field theories.* Phys. Rev. C **65** (2002) 014310. arXiv:nucl-th/0105049

[132] J. Dobaczewski, J. Dudek, S. G. Rohozinski and T. R. Werner: *Point symmetries in the Hartree-Fock approach: Symmetry-breaking schemes.* Phys. Rev. C **62** (2000) 014311. arXiv:nucl-th/9912073

[133] J. Dobaczewski, J. Dudek, S. G. Rohozinski and T. R. Werner: *Point symmetries in the Hartree-Fock approach: Densities, shapes and currents.* Phys. Rev. C **62** (2000) 014310. arXiv:nucl-th/9912072

[134] H. Goutte, J.-F. Berger, P. Casoli and D. Gogny: *Microscopic approach of fission dynamics applied to fragment kinetic energy and mass distributions in ^{238}U.* Phys. Rev. C **71** (2005) 024316. arXiv:nucl-th/0502002

[135] N. Dubray, H. Goutte and J.-P. Delaroche: *Structure properties of ^{226}Th and ^{256,258,260}Fm fission fragments: mean field analysis with the Gogny force.* Phys. Rev. C **77** (2008) 014310. arXiv:0712.0252

[136] J. Libert, M. Girod and J.-P. Delaroche: *Microscopic descriptions of superdeformed bands with the Gogny force: Configuration mixing calculations in the A≈190 mass region.* Phys. Rev. C **60** (1999) 054301

[137] M. Samyn, S. Goriely and J. M. Pearson: *Further explorations of Skyrme-Hartree-Fock-Bogoliubov mass formulas. I: Role of density dependence in pairing force.* Nucl. Phys. **A725** (2002) 69–81

[138] S. Goriely, M. Samyn, M. Bender and J. M. Pearson: *Further explorations of Skyrme-Hartree-Fock-Bogoliubov mass formulas. II: Role of the effective mass.* Phys. Rev. C **68** (2003) 054325. arXiv:nucl-th/0311086

[139] M. Samyn, S. Goriely, M. Bender and J. M. Pearson: *Further explorations of Skyrme-Hartree-Fock-Bogoliubov mass formulas. III: Role of particle-number projection.* Phys. Rev. C **70** (2004) 044309. arXiv:nucl-th/0409006

[140] S. Hilaire and M. Girod: *Large-scale mean-field calculations from proton to neutron drip lines using the D1S Gogny force.* Eur. Phys. J. A **33** (2007) 237–241

[141] T. H. R. Skyrme: *The nuclear surface.* Phil. Mag. **1** (1956) 1043–1054

[142] D. Vautherin and D. M. Brink: *Hartree-Fock Calculations with Skyrme's Interaction. I. Spherical Nuclei.* Phys. Rev. C **5** (1972) 626–647

[143] J. W. Negele and D. Vautherin: *Density-Matrix Expansion for an Effective Nuclear Hamiltonian.* Phys. Rev. C **5** (1972) 1472–1493

[144] J. W. Negele and D. Vautherin: *Density-matrix expansion for an effective nuclear hamiltonian. II.* Phys. Rev. C **11** (1975) 1031–1041

[145] X. Campi and A. Bouyssy: *A simple approximation for the nuclear density matrix.* Phys. Lett. B **73** (1977) 263–266

[146] K. W. Schmid and P.-G. Reinhard: *Center-of-mass projection of skyrme-hartree-fock densities.* Nucl. Phys. **A530** (1991) 283–302

[147] E. Chabanat, J. Meyer, P. Bonche, R. Schaeffer and P. Haensel: *A Skyrme parametrization from subnuclear to neutron star densities.* Nucl. Phys. **A627** (1997) 710–746

[148] J. C. Slater: *A simplification of the Hartree-Fock Method.* Phys. Rev. **85** (1951) 385–390

[149] J. S. Bell and T. H. R. Skyrme: *The nuclear spin-orbit coupling.* Phil. Mag. **1** (1956) 1055–1068

[150] T. H. R. Skyrme: *The effective nuclear potential.* Nucl. Phys. **9** (1959) 615–634

[151] T. H. R. Skyrme: *The spin-orbit interaction in nuclei.* Nucl. Phys. **9** (1959) 635–640

[152] E. Perlinska, S. G. Rohozinski, J. Dobaczewski and W. Nazarewicz: *Local density approximation for proton neutron pairing correlations: Formalism.* Phys. Rev. C **69** (2004) 014316. arXiv:nucl-th/0310005

[153] T. Duguet, M. Bender, K. Bennaceur, D. Lacroix and T. Lesinski: *Particle-Number Restoration within the Energy Density Functional formalism: are terms depending on non-integer powers of the density matrix viable?* To be published

[154] M. Bender, T. Duguet and D. Lacroix: *Particle-Number Restoration within the Energy Density Functional formalism.* To be published

[155] D. Lacroix, T. Duguet and M. Bender: *Particle-Number Restoration within the Energy Density Functional formalism: removing spurious contributions to non-diagonal energy kernels.* To be published

[156] J. Dobaczewski and J. Dudek: *Time-Odd Components in the Rotating Mean Field and Identical Bands.* Acta Phys. Pol. B **27** (1996) 45–58. arXiv:nucl-th/9510009

[157] J. R. Stone, J. C. Miller, R. Koncewicz, P. D. Stevenson and M. R. Strayer: *Nuclear matter and neutron-star properties calculated with the Skyrme interaction.* Phys. Rev. C **68** (2003) 034324

[158] T. Lesinski, M. Bender, K. Bennaceur, T. Duguet and J. Meyer: *The tensor part of the Skyrme energy density functional. I. Spherical nuclei.* Phys. Rev. C **76** (2007) 014312. arXiv:0704.0731

[159] T. Lesinski, K. Bennaceur, T. Duguet and J. Meyer: *Isovector splitting of nucleon effective masses, ab-initio benchmarks and extended stability criteria for Skyrme energy functionals.* Phys. Rev. C **74** (2006) 044315. arXiv:nucl-th/0607065

[160] E. Chabanat, P. Bonche, P. Haensel, J. Meyer and R. Schaeffer: *A Skyrme parametrization from subnuclear to neutron star densities. 2. Nuclei far from stablities.* Nucl. Phys. **A635** (1998) 231–256

[161] M. Beiner, H. Flocard, N. Van Giai and P. Quentin: *Nuclear ground-state properties and self-consistent calculations with the skyrme interaction (I). Spherical description.* Nucl. Phys. **A238** (1975) 29–69

[162] T. Lesinski: *Priv. comm.*

[163] F. Tondeur, M. Brack, M. Farine and J. M. Pearson: *Static nuclear properties and the parametrisation of Skyrme forces.* Nucl. Phys. **A420** (1984) 297–319

[164] S. Köhler: *Skyrme force and the mass formula.* Nucl. Phys. **A258** (1976) 301–316

[165] F. Tondeur: *Pairing with a delta interaction in the energy density nuclear mass formula.* Nucl. Phys. **A315** (1979) 353–369

[166] S. J. Krieger, P. Bonche, H. Flocard, P. Quentin and M. S. Weiss: *An improved pairing interaction for mean field calculations using skyrme potentials.* Nucl. Phys. **A517** (1990) 275–286

[167] G. F. Bertsch and H. Esbensen: *Pair correlations near the neutron drip line.* Ann. Phys. (NY) **209** (1991) 327–363

[168] N. Tajima, P. Bonche, H. Flocard, P.-H. Heenen and M. S. Weiss: *Self-consistent calculation of charge radii of Pb isotopes.* Nucl. Phys. **A551** (1993) 434–450

[169] J. Terasaki, P.-H. Heenen, P. Bonche, J. Dobaczewski and H. Flocard: *Superdeformed rotational bands with density dependent pairing interactions.* Nucl. Phys. **A593** (1995) 1–20

[170] J. Terasaki, R. Wyss and P. H. Heenen: *Onset of $T = 0$ pairing and deformations in high spin states of the $N = Z$ nucleus Cr-48.* Phys. Lett. B **437** (1998) 1–6. arXiv:nucl-th/9802045

[171] A. L. Goodman: *Proton-neutron pairing in $Z = N$ nuclei with $A = 76 \sim 96$.* Phys. Rev. C **60** (1999) 014311

[172] J. Dobaczewski *et al.*: *Mean-field description of ground-state properties of drip- line nuclei: Pairing and continuum effects.* Phys. Rev. C **53** (1996) 2809–2840. arXiv:nucl-th/9512008

[173] P. Bonche, H. Flocard, P.-H. Heenen, S. J. Krieger and M. S. Weiss: *Self-consistent study of triaxial deformations: Application to the isotopes of Kr, Sr, Zr and Mo.* Nucl. Phys. **A443** (1985) 39–63

[174] N. Tajima: *Canonical-basis solution of the Hartree-Fock-Bogoliubov equation on three-dimensional Cartesian mesh.* Phys. Rev. C **69** (2004) 034305. arXiv:nucl-th/0307075

[175] K. Bennaceur and J. Dobaczewski: *Coordinate-space solution of the Skyrme-Hartree-Fock-Bogolyubov equations within spherical symmetry. The program HFBRAD (v1.0).* Comp. Phys. Comm. **168** (2005) 96–122. arXiv:nucl-th/0501002

[176] J. Dobaczewski and J. Dudek: *Solution of the Skyrme-Hartree-Fock equations in the Cartesian deformed harmonic oscillator basis. (I) The method.* Comput. Phys. Commun. **102** (1997) 166–182. arXiv:nucl-th/9611035

[177] J. Dobaczewski and J. Dudek: *Solution of the Skyrme-Hartree-Fock equations in the Cartesian deformed harmonic oscillator basis. (II) The program HFODD.* Comput. Phys. Commun. **102** (1997) 183–209. arXiv:nucl-th/9611036

[178] J. Dobaczewski and J. Dudek: *Solution of the Skyrme-Hartree-Fock equations in the Cartesian deformed harmonic-oscillator basis. (III) HFODD (v1.75r): a new version of the program.* Comput. Phys. Commun. **131** (2000) 164–186. arXiv:nucl-th/0003003

[179] J. Dobaczewski and P. Olbratowski: *Solution of the Skyrme-Hartree-Fock-Bogolyubov equations in the Cartesian deformed harmonic-oscillator basis. (IV) HFODD (v2.07f): a new version of the program.* Comput. Phys. Commun. **158** (2004) 158–191. arXiv:nucl-th/0401006

[180] K. Bennaceur: *Priv. comm.*

[181] B. Gall, P. Bonche, J. Dobaczewski, H. Flocard and P.-H. Heenen: *Superdeformed rotational bands in the mercury region. A cranked Skyrme-Hartree-Fock-Bogoliubov study.* Z. Phys. A **348** (1994) 183–197. arXiv:nucl-th/9312011

[182] G. Dahlquist and Å. Björck: *Numerical Methods* (Prentice-Hall, Englewood Cliffs, NJ, 1974)

[183] D. Gogny: In J. de Boer and H. J. Mang (Editors), *Proceedings of the International Conference on Nuclear Physics.* Madrid (North-Holland, Amsterdam, 1973) p. 48

[184] D. Gogny: In G. Ripka and M. Porneuf (Editors), *Proceedings of the International Conference on Nuclear Self-Consistent fields.* International Center for Theoretical Physics, Trieste (North-Holland, Amsterdam, 1975) p. 333

[185] J. Dechargé and D. Gogny: *Hartree-Fock-Bogolyubov calculations with the D1 effective interaction on spherical nuclei.* Phys. Rev. C **21** (1980) 1568–1593

[186] J.-F. Berger, M. Girod and D. Gogny: *Time-dependent quantum collective dynamics applied to nuclear fission.* Comp. Phys. Comm. **63** (1991) 365–374

[187] M. Anguiano, J. L. Egido and L. M. Robledo: *Coulomb exchange and pairing contributions in nuclear Hartree-Fock-Bogoliubov calculations with the Gogny force.* Nucl. Phys. **A683** (2001) 227–254. arXiv:nucl-th/0008055

[188] F. Chappert: *Nouvelles paramétrisations de l'interaction nucléaire effective de Gogny* (2007). Ph.D. Thesis

[189] F. Chappert, M. Girod and S. Hilaire: *Unpublished* (2008)

[190] N. Schunck and J. L. Egido: *Continuum and Symmetry-Conserving Effects in Drip-line Nuclei Using Finite-range Forces.* Phys. Rev. C **77** (2008) 011301. arXiv:0710.0880

[191] M. Warda, J. L. Egido, L. M. Robledo and K. Pomorski: *Selfconsistent calculations of fission barriers in the Fm region.* Phys. Rev. C **66** (2002) 014310. arXiv:nucl-th/0203057

[192] J. Dobaczewski, M. V. Stoitsov and W. Nazarewicz: *Skyrme-hfb deformed nuclear mass table.* AIP Conf. Proc. **726** (1994) 51–56. arXiv:nucl-th/0404077

[193] M. V. Stoitsov, J. Dobaczewski, W. Nazarewicz and P. Borycki: *Large-scale self-consistent nuclear mass calculations.* Int. J. Mass. Spec. **251** (1996) 243–251. arXiv:nucl-th/0601040

[194] B. Sabbey, M. Bender, G. F. Bertsch and P. H. Heenen: *Global study of the spectroscopic properties of the first 2^+ state in even-even nuclei.* Phys. Rev. C **75** (2007) 044305. arXiv:nucl-th/0611089

[195] J. Terasaki and J. Engel: *Systematics of the first 2^+ excitation in spherical nuclei with the Skryme-QRPA* arXiv:0801.2346

[196] J. A. Sheikh and P. Ring: *Symmetry-Projected Hartree-Fock-Bogoliubov Equations.* Nucl. Phys. **A665** (2000) 71–91. arXiv:nucl-th/9907065

[197] J. L. Egido and P. Ring: *Symmetry conserving Hartree-Fock-Bogoliubov theory (I). On the solution of variational equations.* Nucl. Phys. **A383** (1982) 189–204

[198] M. Girod, K. Kumar, B. Grammaticos and P. Aguer: *Calculation of Nuclear Deformations and Collective Spectra Starting from a Density-Dependent, Finite-Range Nuclear Force.* Phys. Rev. Lett. **41** (1978) 1765–1768

[199] J. L. Egido and P. Ring: *Symmetry-conserving Hartree-Fock-Bogoliubov theory (II). Number-projected cranked Hartree-Fock-Bogoliubov calculations in the rare earth region.* Nucl. Phys. **A388** (1982) 19–36

[200] M. Anguiano, J. L. Egido and L. M. Robledo: *Particle number projection with effective forces.* Nucl. Phys. **A696** (2001) 467–493. arXiv:nucl-th/0105003

[201] M. Anguiano, J. L. Egido and L. M. Robledo: *Mean-field Based Approaches to Pairing Correlations in Atomic Nuclei.* Phys. Lett. B **545** (2002) 62–72. arXiv:nucl-th/0205017

[202] L. Próchniak and P. Quentin and D. Samsoen and J. Libert: *A self-consistent approach to the quadrupole dynamics of medium heavy nuclei.* Nucl. Phys. **A730** (2004) 59–79

[203] R. R. Rodríguez-Guzmán, J. L. Egido and L. M. Robledo: *Quadrupole collectivity of neutron-rich Neon isotopes.* Eur. Phys. J. A **17** (2003) 37–47. arXiv:nucl-th/0302008

[204] T. Duguet, M. Bender, P. Bonche and P.-H. Heenen: *Spectroscopy of heavy nuclei by configuration mixing of symmetry restored mean-field states: Shape coexistence in neutron-deficient Pb isotopes.* Phys. Lett. B **559** (2004) 201–206. arXiv:nucl-th/0302057

[205] M. Bender, P. Bonche and P.-H. Heenen: *Shape coexistence in neutron-deficient Kr isotopes: Constraints on the single-particle spectrum of self- consistent mean-field models from collective excitations.* Phys. Rev. C **74** (2006) 024312. arXiv:nucl-th/0607071

[206] M. Girod: *Unpublished*

[207] J.-F. Berger, L. Bitaud, J. Dechargé, M. Girod and K. Dietrich: *Superheavy, hyperheavy and bubble nuclei.* Nucl. Phys. **A685** (1984) 1–16

[208] T. Bürvenich, M. Bender, J. A. Maruhn and P.-G. Reinhard: *Systematics of fission barriers in superheavy elements.* Phys. Rev. C **69** (2004) 014307. arXiv:nucl-th/0302056

[209] A. S. Umar and V. E. Oberacker: *3-D unrestricted TDHF fusion calculations using the full Skyrme interaction.* Phys. Rev. C **73** (2006) 054607. arXiv:nucl-th/0603038

[210] A. S. Umar and V. E. Oberacker: *TDHF fusion calculations for spherical+deformed systems.* Phys. Rev. C **74** (2006) 024606. arXiv:nucl-th/0604010

[211] C. Simenel and B. Avez: *Time-dependent hartree-fock description of heavy ions fusion* (2007). arXiv:0711.0934

[212] S. Péru, J.-F. Berger and P.-F. Bortignon: *Giant resonances in exotic spherical nuclei within the RPA approach with the Gogny force.* Eur. Phys. J. A **26** (2005) 25–32. arXiv:nucl-th/0506022

[213] S. Fracasso and G. Coló: *Spin-isospin nuclear response using the existing microscopic Skyrme functionals.* Phys. Rev. C **76** (2007) 044307. arXiv:0704.2892

[214] S. Péru and H. Goutte: *Role of deformation on giant resonances within the QRPA approach and the Gogny force.* Phys. Rev. C **77** (2008) 044313. arXiv:0804.0130

[215] J. Dobaczewski and W. Nazarewicz: *Mean-Field and Pairing Properties of Exotic Nuclei: Exploring the Nuclear Landscape.* Prog. Theor. Phys. Suppl. **146** (2002) 70–83. arXiv:nucl-th/0203038

[216] M. Honma, T. Otsuka, B. A. Brown and T. Mizusaki: *Effective interaction for pf-shell nuclei.* Phys. Rev. C **65** (2002) 061301. ariv:nucl-th/0205033

[217] M. Honma, T. Otsuka, B. A. Brown and T. Mizusaki: *New effective interaction for pf-shell nuclei and its implications for the stability of the $N{=}Z{=}28$ closed core.* Phys. Rev. C **69** (2004) 034335. arXiv:nucl-th/0402079

[218] A. F. Lisetskiy, B. A. Brown, M. Horoi and H. Grawe: *New T=1 effective interactions for the $f_{5/2}$ $p_{3/2}$ $p_{1/2}$ $g_{9/2}$ model space: Implications for valence-mirror symmetry and seniority isomers.* Phys. Rev. C **70** (2004) 044314. arXiv:nucl-th/0402082

[219] *UNEDF Project*
URL http://www.uedf.org/

[220] G. A. Lalazissis, P. Ring and D. Vretenar (Editors): *Extended Density Functionals in Nuclear Structure Physics*, *Lect. Notes Phys.*, vol. 641 (Springer, Heidelberg, 2004)

[221] B. D. Chang: *Spin saturation and the Skyrme interaction.* Phys. Lett. B **56** (1975) 205–208

[222] S. Stringari, R. Leonardi and D. M. Brink: *Spin stability and magnetic polarizability with Skyrme's interaction.* Nucl. Phys. **A269** (1976) 87–90

[223] M. Kortelainen, J. Dobaczewski, K. Mizuyama and J. Toivanen: *Dependence of single-particle energies on coupling constants of the nuclear energy density functional* arXiv:0803.2291

[224] P. Klüpfel, P. G. Reinhard, T. J. Bürvenich and J. A. Maruhn: *Variations on a theme by Skyrme* (2008). arXiv:0804.3385

[225] G. Coló, H. Sagawa, S. Fracasso and P.-F. Bortignon: *Spin-orbit splitting and the tensor component of the Skyrme interaction.* Phys. Lett. B **646** (2007) 227–231. arXiv:nucl-th/0701015

[226] M. Zalewski, J. Dobaczewski, W. Satula and T. R. Werner: *Spin-orbit and tensor mean-field effects on spin-orbit splitting including self-consistent core polarizations.* Phys. Rev. C **77** (2008) 024316. arXiv:0801.0924

[227] J. Engel: *Intrinsic-Density Functionals.* Phys. Rev. C **75** (2007) 014306. arXiv:nucl-th/0610043

[228] N. Barnea: *Density functional theory for self-bound systems.* Phys. Rev. C **76** (2007) 067302. arXiv:0711.0963

[229] B. G. Giraud, B. K. Jennings and B. R. Barrett: *Existence of a Density Functional for an Intrinsic State* arXiv:0707.3099

[230] M. Bender and T. Duguet: *Pairing correlations beyond the mean field.* Int. J. Mod. Phys. E **16** (2007) 222–236. arXiv:nucl-th/0611031

[231] J. Dobaczewski, M. V. Stoitsov, W. Nazarewicz and P. G. Reinhard: *Particle-Number Projection and the Density Functional Theory.* Phys. Rev. C **76** (2007) 054315. arXiv:0708.0441

[232] G. Bruun, Y. Castin, R. Dum and K. Burnett: *BCS theory for trapped ultracold fermions.* Eur. Phys. J. D **7** (1999) 433–440

[233] A. Bulgac and Y. Yu: *Local Density Approximation for Pairing Correlations in Nuclei* (2001). arXiv:nucl-th/0109083

[234] A. Bulgac: *Local density approximation for systems with pairing correlations.* Phys. Rev. C **65** (2002) 051305(R)

[235] P. J. Borycki, J. Dobaczewski, W. Nazarewicz and M. V. Stoitsov: *Pairing renormalization and regularization within the local density approximation.* Phys. Rev. C **73** (2006) 044319. arXiv:nucl-th/0601054

[236] H. Esbensen, G. F. Bertsch and K. Hencken: *Application of contact interactions to Borromean halos.* Phys. Rev. C **56** (1997) 3054–3062

[237] T. Papenbrock and G. F. Bertsch: *Pairing in low-density Fermi gases.* Phys. Rev. C **59** (1999) 2052–2055

[238] M. Matsuo: *Spatial structure of neutron Cooper pair in low density uniform matters.* Phys. Rev. C **73** (2006) 044309. arXiv:nucl-th/0512021

[239] A. Bulgac: *Hartree-Fock-Bogoliubov Approximation for Finite Systems* (1999). arXiv:nucl-th/9907088

[240] A. Bulgac and Y. Yu: *Renormalization of the Hartree-Fock-Bogoliubov equations in the case of a zero range pairing interaction.* Phys. Rev. Lett. **88** (2002) 042504. arXiv:nucl-th/0106062

[241] Y. Yu and A. Bulgac: *Energy Density Functional Approach to Superfluid Nuclei.* Phys. Rev. Lett. **90** (2003) 222501. arXiv:nucl-th/0210047

[242] T. Duguet: *Bare vs effective pairing forces: A microscopic finite-range interaction for Hartree-Fock-Bogolyubov calculations in coordinate space.* Phys. Rev. C **69** (2004) 054317. arXiv:nucl-th/0311065

[243] F. Pistolesi and G. C. Strinati: *Evolution from BCS superconductivity to Bose condensation: Calculation of the zero-temperature phase coherence length.* Phys. Rev. B **53** (1996) 15168–15192

[244] F. V. De Blasio *et al.*: *Coherence length of neutron superfluids.* Phys. Rev. C **56** (1997) 2332–2335

[245] F. Pistolesi and G. C. Strinati: *Evolution from BCS superconductivity to Bose condensation: Role of the parameter $k_F\eta$.* Phys. Rev. B **49** (1994) 6356–6359

[246] M. Baldo, U. Lombardo and P. Schuck: *Deuteron formation in expanding nuclear matter from a strong coupling BCS approach.* Phys. Rev. C **52** (1995) 975–985

[247] D. E. González Trotter *et al.*: *A New Measurement of the $^1S_0$ Neutron-Neutron Scattering Length using the Neutron-Proton Scattering Length as a Standard.* Phys. Rev. Lett. **83**

(1999) 3788–3791. arXiv:nucl-ex/9904011

[248] N. Andrenacci, A. Perali, P. Pieri and G. C. Strinati: *Density-induced BCS to Bose-Einstein crossover.* Phys. Rev. B **60** (1999) 12410–12418. arXiv:cond-mat/9903399

[249] J. Dobaczewski, W. Nazarewicz and P.-G. Reinhard: *Pairing Interaction and Self-Consistent Densities in Neutron-Rich Nuclei.* Nucl. Phys. **A693** (2001) 361–373. arXiv:nucl-th/0103001

[250] E. Garrido, P. Sarriguren, E. Moya de Guerra and P. Schuck: *Effective density dependent pairing forces in the $T = 1$ and $T = 0$ channels.* Phys. Rev. C **60** (1999) 064312. arXiv:nucl-th/9909026

[251] C. Shen, U. Lombardo, P. Schuck, W. Zuo and N. Sandulescu: *Landau parameters of nuclear matter in the spin and spin-isospin channels.* Phys. Rev. C **67** (2003) 061302(R). arXiv:nucl-th/0212087

[252] L. G. Cao, U. Lombardo and P. Schuck: *Screening Effects in Superfluid Nuclear and Neutron Matter within Brueckner Theory.* Phys. Rev. C **74** (2006) 064301. arXiv:nucl-th/0608005

[253] J. Terasaki, F. Barranco, P.-F. Bortignon, R. A. Broglia and E. Vigezzi: *Effect of particle-phonon coupling on pairing correlations in nuclei.* Phys. Rev. Lett. **83** (2001) 2147–2150. arXiv:nucl-th/0109056

[254] J. Terasaki, F. Barranco, R. A. Broglia, E. Vigezzi and P.-F. Bortignon: *Solution of the Dyson equation for nucleons in the superfluid phase.* Nucl. Phys. **A697** (2002) 127–140. arXiv:nucl-th/0012024

[255] F. Barranco, R. A. Broglia, G. Coló, E. Vigezzi and P.-F. Bortignon: *Many-body effects in nuclear structure.* Eur. Phys. J. A **21** (2004) 57–60. arXiv:nucl-th/0304049

[256] G. Gori *et al.*: *Attractive and repulsive contributions of medium fluctuations to nuclear superfluidity.* Phys. Rev. C **72** (2005) 011302(R). arXiv:nucl-th/0502077

[257] M. V. Zhukov *et al.*: *Bound state properties of Borromean halo nuclei: ^{6}He and ^{11}Li.* Phys. Rept. **231** (1993) 151–199

[258] M. Zahar *et al.*: *Momentum distributions for $^{12,14}Be$ fragmentation.* Phys. Rev. C **48** (1993) R1484–R1487

[259] I. J. Thompson and M. V. Zhukov: *Structure and reactions of the $^{12,14}Be$ nuclei.* Phys. Rev. C **53** (1996) 708–714

[260] D. Bazin *et al.*: *One-Neutron Halo of ^{19}C.* Phys. Rev. Lett. **74** (1995) 3569–3572

[261] R. Kanungo, I. Tanihata, Y. Ogawa, H. Toki and A. Ozawa: *Halo structure in ^{19}C.* Nucl. Phys. **A701** (2002) 378–382

[262] M. V. Zhukov and I. J. Thompson: *Existence of proton halos near the drip line.* Phys. Rev. C **52** (1995) 3505–3508

[263] T. Minamisono *et al.*: *Proton halo of ^{8}B disclosed by its giant quadrupole moment.* Phys. Rev. Lett. **69** (1992) 2058–2061

[264] W. Schwab *et al.*: *Observation of a proton halo in ^{8}B.* Z. Phys. **A350** (1995) 283–284

[265] R. E. Warner *et al.*: *Evidence for a proton halo in ^{8}B: Enhanced total reaction cross sections at 20 to 60 MeV/nucleon.* Phys. Rev. C **52** (1995) R1166–R1170

[266] F. Negoita *et al.*: *^{8}B proton halo via reaction and breakup cross section measurements.* Phys. Rev. C **54** (1996) 1787–1797

[267] R. Kanungo *et al.*: *Possibility of a two-proton halo in ^{17}Ne.* Phys. Lett. B **571** (2003) 21–28

[268] H. Jeppesen *et al.*: *One- and two-proton removal from ^{15}O.* Nucl. Phys. **A739** (2004) 57–66

[269] R. Morlock *et al.*: *Halo Properties of the First 1/2$^+$ State in ^{17}F from the $^{16}O(p,\gamma)^{17}F$ Reaction.* Phys. Rev. Lett. **79** (1997) 3837–3840

[270] Z. Ren, A. Faessler and A. Bobyk: *Relativistic mean-field description of a proton halo in the first excited (1/2)$^+$ state of ^{17}F.* Phys. Rev C **57** (1998) 2752–2755

[271] C. J. Lin *et al.*: *Excitation Halo States of ^{12}B.* Chin. Phys. Lett. **18** (2001) 1183–1185

[272] Z. H. Liu *et al.*: *Asymptotic normalization coefficients and neutron halo of the excited states in ^{12}B and ^{13}C.* Phys. Rev. C **64** (2001) 034312

[273] J. G. Chen *et al.*: *Halo or skin in the excited states of some light mirror nuclei.* Eur. Phys. J. A **23** (2005) 11–17

[274] D. V. Fedorov, A. S. Jensen and K. Riisager: *Three-Body Halos. II. from Two- to Three-Body Asymptotics.* Phys. Rev. C **50** (1994) 2372–2383. arXiv:nucl-th/9409019

[275] F. Nunes, I. J. Thompson and R. C. Johnson: *Core excitation in three-body systems: Application to ^{12}Be.* Nucl. Phys. **A609** (1996) 43–73

[276] F. Nunes, J. A. Christley, I. J. Thompson, R. C. Johnson and V. D. Efros: *Core excitation in one neutron halo systems.* Nucl. Phys. **A596** (1996) 171–186

[277] J. M. Bang: *Few-body aspects of Borromean halo nuclei.* Phys. Rept. **264** (1996) 27–37

[278] K. Riisager, D. V. Fedorov and A. S. Jensen: *Quantum halos.* Europhys. Lett. **49** (2000) 547–553

[279] A. S. Jensen and M. V. Zhukov: *Few-body effects in nuclear halos.* Nucl. Phys. **A693** (2001) 411–423

[280] D. V. Fedorov, A. S. Jensen and K. Riisager: *General properties of halos.* Phys. Lett. B **312** (1993) 1–5

[281] A. S. Jensen and K. Riisager: *Towards necessary and sufficient conditions for halo occurrence.* Phys. Lett. B **480** (2000) 39–44

[282] D. V. Fedorov, A. S. Jensen and K. Riisager: *Three-body halos: Gross properties.* Phys. Rev. C **49** (1994) 201–212

[283] Y.-J. Liang *et al.*: *Coulomb effects on the formation of proton halo nuclei* (2007). arXiv:0708.0071

[284] K. Bennaceur, J. Dobaczewski and M. Ploszajczak: *Continuum effects for the mean-field and pairing properties of weakly bound nuclei.* Phys. Rev. C **60** (1999) 034308. arXiv:nucl-th/9905031

[285] K. Bennaceur, J. Dobaczewski and M. Ploszajczak: *Pairing anti-halo effect.* Phys. Lett. B **496** (2000) 154–160. arXiv:nucl-th/0008051

[286] I. Hamamoto and B. R. Mottelson: *Pair correlation in neutron drip line nuclei.* Phys. Rev. C **68** (2003) 034312

[287] I. Hamamoto and B. R. Mottelson: *Weakly bound $s_{1/2}$ neutrons in the many-body pair correlation of neutron drip line nuclei.* Phys. Rev. C **69** (2004) 064302

[288] I. Hamamoto: *Effective pair gap of weakly bound neutrons in deformed nuclei.* Phys. Rev. C **71** (2005) 037302

[289] S. Mizutori, J. Dobaczewski, G. A. Lalazissis, W. Nazarewicz and P.-G. Reinhard: *Nuclear Skins and Halos in the Mean-Field Theory.* Phys. Rev. C **61** (2000) 044326. arXiv:nucl-th/9911062

[290] K. Riisager, A. S. Jensen and P. Møller: *Two-body halos.* Nucl. Phys. **A548** (1992) 393–413

[291] T. H. Koopmans: *Über die Zuordnung von Wellenfunktionen und Eigenwerten zu den Einzelnen Elektronen Eines Atoms.* Physica **1** (1934) 104–113

[292] M. Grasso, S. Yoshida, N. Sandulescu and N. Van Giai: *Giant neutron halos in the non-relativistic mean field approach.* Phys. Rev. C **74** (2006) 064317. arXiv:nucl-th/0603060

[293] J. Meng and P. Ring: *A Giant Halo at the Neutron Drip Line.* Phys. Rev. Lett. **80** (1998) 460–463. arXiv:nucl-th/9612045

[294] B. Nerlo-Pomorska, K. Pomorski, J.-F. Berger and J. Dechargé: *The neutron halo in heavy nuclei calculated with the Gogny force.* Eur. Phys. J. A **8** (2000) 19–30

[295] S. Im and J. Meng: *Particles in classically forbidden area, neutron skin and halo, and pure neutron matter in Ca isotopes.* Phys. Rev. C **61** (2000) 047302. arXiv:nucl-th/0004010

[296] N. Sandulescu, L. S. Geng, H. Toki and G. C. Hillhouse: *Pairing correlations and resonant states in the relativistic mean field theory.* Phys. Rev. C **68** (2003) 054323. arXiv:nucl-th/0306035

[297] L. S. Geng, H. Toki and J. Meng: *A systematic study of Zr and Sn isotopes in the Relativistic Mean Field theory.* Mod. Phys. Lett. A **19** (2004) 2171–2190. arXiv:nucl-th/0312027

[298] M. Kaushik, D. Singh and H. L. Yadav: *Halo formation in neutron rich ca nuclei.* Acta Phys. Slov. **55** (2005) 181–196

[299] J. Terasaki, S. Q. Zhang, S. G. Zhou and J. Meng: *Giant halo in relativistic and non-relativistic approaches.* Phys. Rev. C **74** (2006) 054318. arXiv:nucl-th/0603005

[300] J. Dobaczewski, M. V. Stoitsov and W. Nazarewicz: *Skyrme-HFB deformed nuclear mass table.* AIP Conf. Proc. **726** (2004) 51–56. arXiv:nucl-th/0404077

[301] I. Angeli: *A consistent set of nuclear rms charge radii: properties of the radius surface R(N,Z).* Atomic Data and Nuclear Data Tables **87** (2004) 185–206

[302] G. Audi, A. H. Wapstra and C. Thibault: *The ame2003 atomic mass evaluation (I). Evaluation of input data, adjustment procedures.* Nucl. Phys. **A729** (2003) 129–336

[303] G. Audi, A. H. Wapstra and C. Thibault: *The ame2003 atomic mass evaluation (II). Tables, graphs and references.* Nucl. Phys. **A729** (2003) 337–676

[304] P. Lubiński *et al.*: *Composition of the nuclear periphery from antiproton absorption.* Phys. Rev. C **57** (1998) 2962–2973. arXiv:nucl-ex/9808005

[305] R. H. Helm: *Inelastic and Elastic Scattering of 187-Mev Electrons from Selected Even-Even Nuclei.* Phys. Rev. **104** (1956) 1466–1475

[306] M. Rosen, R. Raphael and H. Überall: *Generalized Helm Model for Transverse Electroexcitation of Nuclear Levels.* Phys. Rev. **163** (1957) 927–934

[307] R. Raphael and M. Rosen: *Electron Scattering from Deformed Nuclei.* Phys. Rev. C **1** (1970) 547–560

[308] J. Friedrich and N. Voegler: *The salient features of charge density distributions of medium and heavy even-even nuclei determined from a systematic analysis of elastic electron scattering form factors.* Nucl. Phys. **A373** (1982) 192–224

[309] D. Van Neck, A. E. L. Dieperink and M. Waroquier: *Natural orbitals, overlap functions, and mean-field orbitals in an exactly solvable A-body system.* Phys. Rev. C **53** (1996) 2231–2242

[310] D. Van Neck, M. Waroquier, A. E. L. Dieperink, S. C. Pieper and V. R. Pandharipande: *Center-of-mass effects on the quasi-hole spectroscopic factors in the* $^{16}O(e,e'p)$ *reaction.* Phys. Rev. C **57** (1998) 2308–2315. arXiv:nucl-th/9804067

[311] D. Van Neck and M. Waroquier: *Single-particle properties in self-bound systems.* Phys. Rev. C **58** (1998) 3359–3367

[312] J. Escher, B. K. Jennings and H. S. Sherif: *Spectroscopic amplitudes and microscopic substructure effects in nucleon capture reactions.* Phys. Rev. C **64** (2001) 065801. arXiv:nucl-th/0107011

[313] J. M. Bang, F. G. Gareev, W. T. Pinkston and J. S. Vaagen: *One- and two-nucleon overlap functions in nuclear physics.* Phys. Rept. **125** (1985) 253–399

[314] C. F. Clément: *Theory of overlap functions (I). Single particle sum rules and centre-of-mass corrections.* Nucl. Phys. **A213** (1973) 469–492

[315] C. F. Clément: *Theory of overlap functions (II). The overlap representation.* Nucl. Phys. **A213** (1973) 493–509

[316] A. E. L. Dieperink and T. de Forest, Jr.: *Center-of-mass effects in single-nucleon knock-out reactions.* Phys. Rev. C **10** (1974) 543–549

[317] D. Van Neck, M. Waroquier and K. Heyde: *On the relationship between single-particle overlap functions, natural orbitals and the one-body density matrix for many-fermion systems.* Phys. Lett. B **314** (1993) 255–259

[318] A. V. Shebeko, P. Papakonstantinou and E. Mavrommatis: *The one-body and two-body density matrices of finite nuclei with an appropriate treatment of the center-of-mass motion.* Eur. Phys. J. A **27** (2006) 143–155. arXiv:nucl-th/0602056

[319] M. Levy, J. P. Perdew and V. Sahni: *Exact differential equation for the density and ionization energy of a many-particle system.* Phys. Rev. A **30** (1984) 2745–2748

[320] M. Abramowitz and I. Stegun: *Handbook of Mathematical Functions* (Dover, New York, 1965)

[321] C. A. Bertulani, H.-W. Hammer and U. Van Kolck: *Effective Field Theory for Halo Nuclei: Shallow p-Wave States.* Nucl. Phys. **A712** (2002) 37–58. arXiv:nucl-th/0205063

[322] D. Berdichevsky and U. Mosel: *Detailed study of nuclear charge and mass densities (I). Surface and asymptotic properties.* Nucl. Phys. **A388** (1982) 205–229

[323] Y. K. Gambhir and S. H. Patil: *Neutron and proton densities in nuclei.* Z. Phys. **A321** (1985) 161–164

[324] Y. K. Gambhir and S. H. Patil: *Some characteristics of nuclear densities.* Z. Phys. **A324** (1986) 9–13

[325] A. Bhagwat, Y. K. Gambhir and S. H. Patil: *Nuclear densities in the neutron-halo region.* Eur. Phys. J. A **8** (2000) 511–520

[326] B. G. Giraud: *Density functionals in the laboratory frame.* Phys. Rev. C **77** (2008) 014311

[327] T. Duguet, P. Bonche, P.-H. Heenen and J. Meyer: *Pairing correlations. Part 2: Microscopic analysis of odd-even mass staggering in nuclei.* Phys. Rev. C **65** (2002) 014311. arXiv:nucl-th/0105050

[328] D. Van Neck, S. Verdonck, G. Bonny, P. W. Ayers and M. Waroquier: *Quasiparticle properties in a density functional framework.* Phys. Rev. A **74** (2006) 042501. arXiv:physics/0609037

[329] F. Nunes: *Priv. comm.*

[330] J. Meng, H. Toki, J. Y. Zeng, S. Q. Zhang and S.-G. Zhou: *Giant halo at the neutron drip line in Ca isotopes in relativistic continuum Hartree-Bogoliubov theory.* Phys. Rev. C **65** (2002) 041302(R)

[331] M. Matsuo, K. Mizuyama and Y. Serizawa: *Di-neutron correlation and soft dipole excitation in medium mass neutron-rich nuclei near drip line.* Phys. Rev. C **71** (2005) 064326

[332] J.-P. Blaizot, J.-F. Berger, J. Dechargé and M. Girod: *Microscopic and macroscopic determinations of nuclear compressibility.* Nucl. Phys. **A591** (1995) 435–457

[333] T. Myo, K. Katō, H. Toki and K. Ikeda: *Roles of the tensor and pairing correlations on the halo formation in* ^{11}*Li.* Phys. Rev. C **76** (2007) 024305. arXiv:0706.2911

[334] T. Otsuka, T. Matsuo and D. Abe: *Mean Field with Tensor Force and Shell Structure of Exotic Nuclei.* Phys. Rev. Lett. **97** (2006) 162501

[335] J. Dobaczewski: *Tensor interactions in mean-field approaches* (2006). arXiv:nucl-th/0604043

[336] B. A. Brown, T. Duguet, T. Otsuka, D. Abe and T. Suzuki: *Tensor interaction contributions to single-particle energies.* Phys. Rev. C **74** (2006) 061303(R). arXiv:nucl-th/0611019

[337] S. Q. Zhang, J. Meng, H. Toki, I. Tanihata and S.-G. Zhou: *Study of Proton Magic Even-Even Isotopes and Giant Halos of Ca Isotopes with Relativistic Continuum Hartree-Bogoliubov Theory.* Science in China Series **G46** (2003) 632–656. arXiv:nucl-th/0302032

[338] M. M. Sharma, M. A. Nagajaran and P. Ring: *Rho meson coupling in the relativistic mean field theory and description of exotic nuclei.* Phys. Lett. B **312** (1993) 377–381

[339] P.-G. Reinhard and H. Flocard: *Nuclear effective forces and isotope shifts.* Nucl. Phys. **A584** (1995) 467–488

[340] M. Yamagami: *Continuum effects for many-body correlations in nuclei close to the neutron drip line.* Phys. Rev. C **72** (2005) 064308

[341] M. Grasso, N. Sandulescu, N. Van Giai and R. J. Liotta: *Pairing and continuum effects in nuclei close to the drip line.* Phys. Rev. C **64** (2001) 064321. arXiv:nucl-th/0109058

[342] I. Hamamoto: *Priv. comm.*

[343] S. Weinberg: *Quasiparticles and the Born Series.* Phys. Rev. **131** (1963) 440–460

[344] I. Tanihata: *Nuclear studies with secondary radioactive beams.* Nucl. Phys. **A488** (1988) 113–126

[345] G. G. Ryzhikh and J. Mitroy: *Positronic lithium, an electronically stable Li-e^+ ground state.* Phys. Rev. Lett. **79** (1997) 4124–4126. arXiv:physics/9710044

[346] G. G. Ryzhikh, J. Mitroy and K. Varga: *The stability of the ground state for positronic sodium.* J. Phys. B: At. Mol. Opt. Phys. **31** (1998) L265–L271

[347] G. G. Ryzhikh, J. Mitroy and K. Varga: *The structure of exotic atoms containing positrons and positronium.* J. Phys. B: At. Mol. Opt. Phys. **31** (1998) 3965–3996

[348] M. W. J. Bromley and J. Mitroy: *Configuration-interaction calculations of PsH and e^+Be.* Phys. Rev. A **65** (2001) 012505

[349] M. W. J. Bromley and J. Mitroy: *Configuration-interaction calculations of positron binding to group-II elements.* Phys. Rev. A **65** (2002) 062505

[350] M. W. J. Bromley and J. Mitroy: *Configuration-interaction calculations of positron binding to zinc and cadmium.* Phys. Rev. A **65** (2002) 062506

[351] M. W. J. Bromley and J. Mitroy: *Positron and positronium interactions with Cu.* Phys. Rev. A **66** (2002) 062504

[352] J. Mitroy, M. W. J. Bromley and G. G. Ryzhikh: *Positron and positronium binding to atoms.* J. Phys. B: At. Mol. Opt. Phys. **35** (2002) R81–R116

[353] J. Mitroy: *Positron-Atom Complexes as Quantum Halo States.* Phys. Rev. Lett. **94** (2005) 033402

[354] J. Mitroy and G. G. Ryzhikh: *Improved binding energies for LiPs, e^+Be, NaPs and e^+Mg.* J. Phys. B: At. Mol. Opt. Phys. **34** (2001–2007) 2001

[355] J. Mitroy: *Expectation values of the e^+He(^{3}Se) system.* Phys. Rev. A **72** (2005) 032503

[356] J. Mitroy: *Expectation values of the e^+Li system.* Phys. Rev. A **70** (2004) 024502

[357] K. Varga and Y. Suzuki: *Precise solution of few-body problems with stochastic variational method on correlated Gaussian basis.* Phys. Rev. C **52** (1995) 2885–2905. arXiv:nucl-th/9508023

[358] K. Varga and Y. Suzuki: *Solution of few-body problems with the stochastic variational method: I. Central forces.* Comp. Phys. Comm. **106** (1997) 157–168. arXiv:nucl-th/9702034

[359] Y. Suzuki and K. Varga: *Approach to Quantum-Mechanical Few-Body Problems* (Springer, New York, 1998)

[360] P. Lubiński *et al.*: *Neutron Halo in Heavy Nuclei from Antiproton Absorption.* Phys. Rev. Lett **73** (1994) 3199–3202

[361] C. J. Horowitz, S. J. Pollock, P. A. Souder and R. Michaels: *Parity Violating Measurements of Neutron Densities.* Phys. Rev. C **63** (2001) 025501. arXiv:nucl-th/9912038

[362] A. Krasznahorkay *et al.*: *Neutron-skin thickness in neutron-rich isotopes.* Nucl. Phys. **A731** (2004) 224–234

[363] P. Kienle: *Medium energy antiproton absorption, a tool to study neutron halo nuclei.* Nucl. Instr. and Meth. in Phys. Res. B **214** (2004) 191–195

[364] K. Yako, H. Sagawa and H. Sakai: *Neutron Skin Thickness of ^{90}Zr Determined By Charge Exchange Reactions.* Phys. Rev. C **74** (2006) 051303(R). arXiv:nucl-ex/0609046

[365] J. M. Lattimer and M. Prakash: *The Physics of Neutron Stars.* Science **304** (2004) 536–542. arXiv:astro-ph/0405262

[366] A. W. Steiner, M. Prakash, J. M. Lattimer and P. J. Ellis: *Isospin Asymmetry in Nuclei and Neutron Stars.* Phys. Rept. **411** (2005) 325–375. arXiv:nucl-th/0410066

[367] P. Danielewicz: *Surface Symmetry Energy.* Nucl. Phys. **A727** (2003) 233–268. arXiv:nucl-th/0301050

[368] S. Yoshida and H. Sagawa: *Isovector nuclear matter properties and neutron skin thickness.* Phys. Rev. C **73** (2006) 044320

[369] I. Hamamoto: *Dominance of low-ℓ component in weakly bound deformed single-neutron orbits.* Phys. Rev. C **69** (2004) 041306(R)

[370] K. Yoshida and K. Hagino: *Role of low-ℓ component in deformed wave functions near the continuum threshold.* Phys. Rev. C **72** (2005) 064311. arXiv:nucl-th/0509068

[371] I. Hamamoto: *Pair correlation in deformed neutron-drip-line nuclei: The eigenphase formalism and asymptotic behavior.* Phys. Rev. C **73** (2006) 044317

[372] W. Horiuchi and Y. Suzuki: *^{22}C: S-Wave Two-Neutron Halo.* Phys. Rev. C **74** (2006) 034311. arXiv:nucl-th/0605055

[373] M. Andersson *et al.*: *Study of the pionic fusion reaction He_3 + He_3 → Li_6^*+π^+ at CELSIUS.* Phys. Scripta **T104** (2003) 105–106

[374] M. Lacombe *et al.*: *Parametrization of the Paris N-N Potential.* Phys. Rev. C **21** (1980) 861–873

[375] V. G. J. Stoks, R. A. M. Kompl, M. C. M. Rentmeester and J. J. de Swart: *Partial wave analaysis of all nucleon-nucleon scattering data below 350 MeV.* Phys. Rev. C **48** (1993) 792–815

[376] C. Van Der Leun and C. Alderlisten: *The deuteron binding energy.* Nucl. Phys. **A380** (1982) 261–269

[377] D. M. Bishop and L. M. Cheung: *Quadrupole moment of the deuteron from a precise calculation of the electric field gradient in D_2.* Phys. Rev. A **20** (1979) 381–384

[378] T. E. O. Ericson and M. Rosa-Clot: *The deuteron asymptotic D-state as a probe of the nucleon-nucleon force.* Nucl. Phys. **A405** (1983) 597–533

[379] N. L. Rodning and L. D. Knutson: *Asymptotic D-state to S-state ratio of the deuteron.* Phys. Rev. C **41** (1990) 898–909

[380] R. Roth *et al.*: *Hartree-Fock and Many-Body Perturbation Theory with Correlated Realistic NN-Interactions.* Phys. Rev. C **73** (2006) 044312. arXiv:nucl-th/0510036

[381] H. T. Coelho, T. K. Das and M. R. Robilotta: *Two-pion-exchange three-nucleon force and the ^3H and ^3He nuclei.* Phys. Rev. C **28** (1983) 1812–1828

[382] S. C. Pieper, V. R. Pandharipande, R. B. Wiringa and J. Carlson: *Realistic models of pion-exchange three-nucleon interactions.* Phys. Rev. C **64** (2001) 014001. arXiv:

nucl-th/0102004

[383] S. A. Coon and H. K. Han: *Reworking the Tucson-Melbourne three-nucleon potential.* Few Body Syst. **30** (2001) 131–141. arXiv:nucl-th/0101003

[384] R. Bieber *et al.*: *Three-Nucleon Force and the A_y Puzzle in Intermediate Energy $\vec{p}+d$ and $\vec{d}+p$ Elastic Scattering.* Phys. Rev. Lett. **84** (2000) 606–609

[385] K. Ermisch *et al.*: *Systematic investigation of the elastic proton-deuteron differential cross section at intermediate energies.* Phys. Rev. C **68** (2003) 051001. arXiv:nucl-ex/0308012

[386] N. Kalantar-Nayestanaki and E. Epelbaum: *The three-nucleon system as a laboratory for nuclear physics: the need for 3N forces* Commissioned article for Nuclear Physics News, arXiv:nucl-th/0703089

[387] S. K. Bogner, A. Schwenk, R. J. Furnstahl and A. Nogga: *Is nuclear matter perturbative with low-momentum interactions?* Nucl. Phys. **A763** (2005) 59–79. arXiv:nucl-th/0504043

[388] J. A. Nolen, Jr and J. P. Schiffer: *Coulomb Energies.* Ann. Rev. Nucl. Part. Sci. **19** (1969) 471–526

[389] S. A. Coon: *Chiral Symmetry and Low Energy Pion-Nucleon Scattering* (1999). arXiv:nucl-th/9903033

[390] G. Q. Li and R. Machleidt: *Charge-Asymmetry of the Nucleon-Nucleon Interaction.* Phys. Rev. C **58** (1998) 1393–1402. arXiv:nucl-th/9804023

[391] V. G. J. Stoks, P. C. van Campen, T. A. Rijken and J. J. De Swart: *Evidence for a large breaking of charge independence in the N-N interaction.* Phys. Rev. Lett. **61** (1988) 1702–1705

[392] G. Q. Li and R. Machleidt: *Charge-dependence of the nucleon nucleon interaction.* Phys. Rev. C **58** (1998) 3153–3162. arXiv:nucl-th/9807080

[393] E. M. Henley and G. A. Miller: *Meson theory of charge-dependent nuclear forces* (North-Holland, Amsterdam, 1979), pp. 405–434

[394] J. L. Friar, G. L. Payne and U. van Kolck: *Charge-Symmetry-Breaking Three-Nucleon Forces.* Phys. Rev. C **71** (2005) 024003. arXiv:nucl-th/0408033

[395] S. Okubo and R. E. Marshak: *Velocity dependence of the two-nucleon interaction.* Ann. Phys. **4** (1958) 166–179

[396] J. L. Friar: *Electromagnetic Energies of Nuclei and the Nuclear Compton Amplitude.* Ann. Phys. **96** (1976) 158–190

[397] G. J. M. Austen and J. J. de Swart: *An improved Coulomb potential.* Phys. Rev. Lett. **50** (1983) 2039–2042

[398] V. G. J. Stoks and J. J. De Swart: *The Magnetic moment interaction in nucleon-nucleon phase shift analyses.* Phys. Rev. C **42** (1990) 1235–1248

[399] W.-M. Yao *et al. (Particle Data Group)*: *Review of Particle Physics.* J. Phys. G: Nucl. and Part. Phys **33** (2006) 1–1232

[400] R. B. Wiringa, R. A. Smith and T. L. Ainsworth: *Nucleon Nucleon Potentials with and Without Δ(1232) Degrees of Freedom.* Phys. Rev. C **29** (1984) 1207–1221

[401] I. E. Lagaris and V. R. Pandharipande: *Phenomenological two-nucleon interaction operator.* Nucl. Phys. **A359** (1981) 331–348

[402] R. Machleidt: *The Meson Theory of Nuclear Forces and Nuclear Matter* (Wiley, New York, NY, 1986), pp. 71–173

[403] R. Machleidt: *The Meson theory of nuclear forces and nuclear structure*, vol. 19 (Plenum, New York, 1989)

[404] R. Machleidt, K. Holinde and C. Elster: *The Bonn Meson Exchange Model for the Nucleon Nucleon Interaction.* Phys. Rept. **149** (1987) 1–89

[405] S. Weinberg: *Effective chiral Lagrangians for nucleon-pion interactions and nuclear forces.* Nucl. Phys. **B363** (1991) 3–18

[406] C. Ordóñez, L. Ray and U. van Kolk: *The Two-Nucleon Potential from Chiral Lagrangians.* Phys. Rev. **C53** (1996) 2086–2105. arXiv:hep-ph/9511380

[407] U. van Kolk: *Effective field theory of nuclear forces.* Prog. Part. Nucl. Phys. **43** (1999) 337–418

[408] E. Epelbaum, W. Glöckle and U.-G. Meißner: *Nuclear forces from chiral Lagrangians using the method of unitary transformation. II: The two-nucleon system.* Nucl. Phys. **A671** (2000) 295–331. arXiv:nucl-th/9910064

[409] D. R. Entem and R. Machleidt: *Accurate Charge-Dependent Nucleon-Nucleon Potential at Fourth Order of Chiral Perturbation Theory.* Phys. Rev. C **68** (2003) 041001. arXiv:nucl-th/0304018

[410] G. P. Lepage: *How to renormalize the Schroedinger equation* arXiv:nucl-th/9706029

[411] U. van Kolk: *Few-nucleon forces from chiral Lagrangians.* Phys. Rev. C **49** (1994) 2932–2941

[412] E. Epelbaum *et al.*: *Three-nucleon forces from chiral effective field theory.* Phys. Rev. C **66** (2002) 064001. arXiv:nucl-th/0208023

[413] N. Kaiser: *Chiral 3π-exchange NN potentials: Results for representation-invariant classes of diagrams.* Phys. Rev. C **61** (1999) 014003. arXiv:nucl-th/9910044

[414] N. Kaiser: *Chiral 3π-exchange NN potentials: Results for diagrams proportional to g_A^4 and g_A^6.* Phys. Rev. C **62** (2000) 024001. arXiv:nucl-th/9912054

[415] N. Kaiser: *Chiral 3π-exchange NN potentials: Results for dominant next-to-leading order contributions.* Phys. Rev. C **63** (2001) 044010. arXiv:nucl-th/0101052

[416] N. Kaiser: *Chiral 2π exchange NN potentials: Two-loop contributions.* Phys. Rev. C **64** (2001) 057001. arXiv:nucl-th/0107064

[417] D. R. Entem and R. Machleidt: *Chiral 2π exchange at order four and peripheral NN scattering.* Phys. Rev. C **66** (2002) 014002. arXiv:nucl-th/0202039

[418] E. Epelbaum, W. Glöckle and U.-G. Meißner: *Improving the convergence of the chiral expansion for nuclear forces. I: Peripheral phases.* Eur. Phys. J. A **19** (2004) 125–137. arXiv:nucl-th/0304037

[419] E. Epelbaum, W. Glöckle and U.-G. Meißner: *Improving the convergence of the chiral expansion for nuclear forces. II: Low phases and the deuteron.* Eur. Phys. J. A **19** (2004) 401–412. arXiv:nucl-th/0308010

[420] E. Epelbaum: *Four-nucleon force using the method of unitary transformation.* Eur. Phys. J. A **34** (2007) 197–214. arXiv:0710.4250

[421] E. Epelbaum, H. Krebs and U.-G. Meißner: *Δ-excitations and the three-nucleon force* (2008). arXiv:0712.1969

[422] E. Epelbaum, H. Krebs and U.-G. Meißner: *Isospin-breaking two-nucleon force with explicit Delta-excitations* (2008). arXiv:0801.1299

[423] J. R. Bergervoet *et al.*: *Phase shift analysis of all proton-proton scattering data below T_{lab}=350 MeV.* Phys. Rev. C **41** (1989) 1435–1452

[424] M. J. Moravcsik, J. Pauschenwein and G. R. Goldstein: *Amplitude systems for spin-1/2 particles.* J. Phys. **50** (1989) 1167–1194

[425] V. G. J. Stoks and J. J. de Swart: *Comparison of potential models with the pp scattering data below 350 MeV.* Phys. Rev. C **47** (1992) 761–767. arXiv:nucl-th/9211013

[426] V. G. J. Stoks and J. J. de Swart: *Comparison of potential models with the np scattering data below 350 MeV.* Phys. Rev. C **52** (1995) 1698–1701. arXiv:nucl-th/9411002

[427] D. R. Entem and R. Machleidt: *Accurate nucleon nucleon potential based upon chiral perturbation theory.* Phys. Lett. B **524** (2002) 93–98. arXiv:nucl-th/0108057

[428] E. Epelbaum, W. Glöckle and U.-G. Meißner: *Improving the convergence of the chiral expansion for nuclear forces. II: Low phases and the deuteron.* Eur. Phys. J. A **19** (2004) 401–412. arXiv:nucl-th/0308010

[429] S. K. Bogner: *Priv. comm.*

[430] M. C. M. Rentmeester, R. G. E. Timmermans and J. J. de Swart: *Determination of the chiral coupling constants c_3 and c_4 in new pp and np partial-wave analyses.* Phys. Rev. C **67** (2003) 044001. arXiv:nucl-th/0302080

[431] D. Rozpedzik *et al.*: *A first estimation of chiral four-nucleon force effects in ^{4}He.* Acta Phys. Polon. B **37** (2006) 2889–2904. arXiv:nucl-th/0606017

[432] W. H. Dickhoff: *Scattering of dressed nucleons in nuclear matter.* Phys. Rev. C **58** (1998) 2807–2820

[433] W. H. Dickhoff, C. C. Gearhart, E. P. Roth, A. Polls and A. Ramos: *Phase shifts and in-medium cross-sections for dressed nucleons in nuclear matter.* Phys. Rev. C **60** (1999) 064319

[434] J. Winter: *Tensor spherical harmonics.* Lett. Math. Phys. **6** (1982) 91–96

[435] M. Jacob and G. Wick: *On the general theory of collisions for particles with spin.* Ann. Phys. **7** (1959) 404–428

[436] K. Erkelenz, R. Alzetta and K. Holinde: *Momentum space calculations and helicity formalism in nuclear physics.* Nucl. Phys. **A176** (1971) 413–432

[437] B. A. Lippmann and J. Schwinger: *Variational Principles for Scattering Processes. I.* Phys. Rev. **79** (1950) 469–480

[438] M. L. Goldberger: *Approximation Methods in the Theory of Scattering.* Phys. Rev, **84** (1951) 929–938

[439] L. A. L. Roriz and A. Delfino: *S-matrix pole trajectories for Yukawa potentials.* Phys. Rev. C **38** (1988) 607–610

[440] M. A. Morrison and A. N. Feldt: *Through scattering theory with gun and camera: Coping with conventions in collision theory.* Am. J. Phys. **75** (2007) 67–80

[441] J. M. Blatt and L. C. Biedenharn: *Neutron-Proton Scattering with Spin-Orbit Coupling. I. General Expressions.* Phys. Rev. **86** (1952) 399–404

[442] H. P. Stapp, T. J. Ypsilantis and N. Metropolis: *Phase-Shift Analysis of 310-Mev Proton-Proton Scattering Experiments.* Phys. Rev. **105** (1957) 302–310

[443] M. J. Seaton: *Coulomb functions for attractive and repulsive potentials and for positive and negative energies.* Comp. Phys. Comm. **146** (2002) 226–249

[444] N. Michel: *Precise Coulombnext term wave functions for a wide range of complex ℓ, η and z.* Comp. Phys. Comm. **176** (2006) 232–249

[445] C. M. Vincent and S. C. Phatak: *Accurate momentum-space method for scattering by nuclear and Coulomb potentials.* Phys. Rev. C **10** (1974) 391–394

[446] M. Walzl and U.-G. Meißner: *Elastic electron deuteron scattering in chiral effective field theory.* Phys. Lett. B **513** (2001) 37–45. arXiv:nucl-th/0103020

[447] J. R. Bergervoet, P. C. van Campen, W. A. van der Sanden and J. J. de Swart: *Phase shift analysis of 0-30 MeV pp scattering data.* Phys. Rev. C **38** (1988) 15–50

[448] L. L. Foldy and E. Eriksen: *Vacuum Polarization and Proton-Proton Scattering.* Phys. Rev. **98** (1955) 775–779

[449] J. Schwinger: . Phys. Rev. **72** (1947) 742

[450] H. A. Bethe: *Theory of the Effective Range in Nuclear Scattering.* Phys. Rev. **76** (1949) 38–50

[451] G. Breit, E. U. Condon and R. D. Present: *Theory of Scattering of Protons by Protons.* Phys. Rev. **50** (1936) 825–845

[452] L. Landau: *On the energy loss of fast particles by ionization.* J. Phys. (USSR) **8** (1944) 201–205

[453] G. Breit: *Relativistic Corrections for High-Energy p-p Scattering.* Phys. Rev. **99** (1955) 1581–1596

[454] M. Kohno: *Mesonic and relativistic corrections to the deuteron charge radius and quadrupole moment.* J. Phys. G: Nucl. and Part. Phys. **9** (1983) L85–L89

[455] R. Rosenfelder: *Coulomb Corrections to Elastic Electron-Proton Scattering and the Proton Charge Radius.* Phys. Lett. B **479** (2000) 381–386. arXiv:nucl-th/9912031

[456] K. Melnikov and T. van Ritbergen: *Three-Loop Slope of the Dirac Form Factor and the 1S Lamb Shift in Hydrogen.* Phys. Rev. Lett. **84** (2000) 1673–1676. arXiv:hep-ph/9911277

[457] I. Sick: *On the rms-radius of the proton.* Phys. Lett. B **576** (2003) 62–67. arXiv:nucl-ex/0310008

[458] S. Kopecky, P. Riehs, J. A. Harvey and N. W. Hill: *New Measurement of the Charge Radius of the Neutron.* Phys. Rev. Lett. **74** (1995) 2427–2430

[459] J. L. Friar, J. Martorell and D. W. L. Sprung: *Nuclear Sizes and the Isotope Shift.* Phys. Rev. A **56** (1997) 4579–4586. arXiv:nucl-th/9707016

[460] B. K. Jennings and S. D. Gupta: *Canonical partition function in nuclear physics.* Phys. Rev. C **62** (2000) 014901

[461] S. Ramanan, S. K. Bogner and R. J. Furnstahl: *Weinberg Eigenvalues and Pairing with Low-Momentum Potentials* (2007). arXiv:0709.0534

[462] E. C. G. Stueckelberg and A. Petermann: *Normalization of constants in the quanta theory.* Helv. Phys. Acta **26** (1953) 499–520

[463] M. Gell-Mann and F. E. Low: *Quantum electrodynamics at small distances.* Phys. Rev. **95** (1954) 1300–1312

[464] S.-K. Ma: *Introduction to the Renormalization Group.* Rev. Mod. Phys. **45** (1973) 589–614

[465] K. G. Wilson: *Renormalization group and critical phenomena. 2. Phase space cell analysis of critical behavior.* Phys. Rev. B **4** (1971) 3184–3205

[466] K. G. Wilson: *Renormalization group and critical phenomena. 1. Renormalization group and the Kadanoff scaling picture.* Phys. Rev. B **4** (1971) 3174–3183

[467] K. G. Wilson: *Nobel Lecture: The renormalization group and critical phenomena.* Rev. Mod. Phys. **55** (1983) 583–600

[468] K. G. Wilson and J. Kogut: *The renormalization group and the ϵ expansion.* Phys. Rept. **12** (1974) 75–199

[469] J. Polchinski: *Renormalization and Effective Lagrangians.* Nucl. Phys. **B231** (1984) 269–295

[470] C. Bervillier: *The Wilson-Polchinski exact renormalization group equation.* Phys. Lett. A **332** (2004) 93–100. arXiv:hep-th/0405025

[471] C. Wetterich: *Average action and the renormalization group equations.* Nucl. Phys. B **352** (1991) 529–584

[472] C. Wetterich: *Exact renormalization group equations for the average action and systematic expansions.* Int. J. Mod. Phys. S **9** (1994) 3571–3602

[473] N. N. Bogoliubov and D. V. Shirkov: *Introduction to the Theory of Quantized Fields* (Interscience, New-York, 1959)

[474] C. G. J. Callan: *Broken scale invariance in scalar field theory.* Phys. Rev. D **2** (1970) 1541–1547

[475] K. Symanzik: *Small distance behavior in field theory and power counting.* Comm. Math. Phys. **18** (1970) 227–246

[476] F. B. Anders: *On steady-state currents through nano-devices: a scattering-states numerical renormalization group approach to open quantum systems* arXiv:0802.0371

[477] L. P. Kadanoff: *Scaling laws for Ising models near T(c).* Physics **2** (1966) 263–272

[478] L. M. Smith and S. L. Woodruff: *Renormalization-Group Analysis of Turbulence.* Ann. Rev. Fluid Mec. **30** (1998) 275–310

[479] W.-X. Zhou and D. Sornette: *Renormalization Group Analysis of the 2000-2002 anti-bubble in the US S&P 500 index: Explanation of the hierarchy of 5 crashes and Prediction.* Physica A **330** (2003) 584–604. arXiv:physics/0301023

[480] M. V. Simkin and J. Olness: *Application of the renormalization group method in wireless market intelligence* (2001). arXiv:cond-mat/0108072

[481] T. T. S. Kuo and E. Osnes: *Folded-Diagram Theory of the Effective Interaction in Nuclei, Atoms and Molecules.* Springer Lect. Notes. Phys. **364** (1990) 100170

[482] K. Suzuki and S. Y. Lee: *Convergent Theory for Effective Interaction in Nuclei.* Prog. Theor. Phys. **64** (1980) 2091–2106

[483] S. K. Bogner, A. Schwenk, T. T. S. Kuo and G. E. Brown: *Renormalization Group Equation for Low Momentum Effective Nuclear Interactions* (2001). arXiv:nucl-th/0111042

[484] S. K. Bogner, T. T. S. Kuo, A. Schwenk, D. R. Entem and R. Machleidt: *Towards a unique low momentum nucleon nucleon interaction.* Phys. Lett. B **576** (2003) 265–272. arXiv:nucl-th/0108041

[485] F. Andreozzi: *Nonperturbative derivation of non-Hermitian and Hermitian effective interactions and operators.* Phys. Rev. C **54** (1996) 684–689

[486] S. Okubo: *Diagonalization of Hamiltonian and Tamm-Dancoff Equation.* Prog. Theor. Phys. **12** (1954) 603–622

[487] K. Suzuki: *General Relation between Hermitian and Non-Hermitian Forms.* Prog. Theor. Phys. **68** (1982) 246–260

[488] K. Suzuki and R. Okamoto: *Degenerate Perturbation Theory in Quantum Mechanics.* Prog. Theor. Phys. **70** (1983) 439–451

[489] S. K. Bogner and R. J. Furnstahl: *Variational Calculations using Low-Momentum Potentials with Smooth Cutoffs.* Phys. Lett. B **639** (2006) 237–241. arXiv:nucl-th/0602017

[490] S. K. Bogner and R. J. Furnstahl: *Variational Calculations of Nuclei with Low-Momentum Potentials.* Phys. Lett. B **632** (2006) 501–506. arXiv:nucl-th/0508022

[491] S. K. Bogner, R. J. Furnstahl, S. Ramanan and A. Schwenk: *Low-momentum interactions with smooth cutoffs.* Nucl. Phys. **A784** (2007) 79–103. arXiv:nucl-th/0609003

[492] S. D. Glazek and K. G. Wilson: *Renormalization of Hamiltonians.* Phys. Rev. D **48** (1993) 5863–5872

[493] S. D. Glazek and K. G. Wilson: *Perturbative renormalization group for Hamiltonians.* Phys. Rev. D **49** (1994) 4214–4218

[494] F. Wegner: *Flow-Equations for Hamiltonians.* Ann. Phys. (Leipzig) **3** (1994) 77

[495] S. Szpigel and R. J. Perry: *The similarity renormalization group* (2000). arXiv:hep-ph/0009071

[496] E. D. Jurgenson, S. K. Bogner, R. J. Furnstahl and R. J. Perry: *Decoupling in the Similarity Renormalization Group for Nucleon-Nucleon Forces* (2007). arXiv:0711.4252

[497] E. L. Gubankova, H.-C. Pauli and F. J. Wegner: *Light-cone Hamiltonian flow for positronium* (1998). arXiv:hep-th/9809143

[498] E. L. Gubankova: *Flow equations for the quantum electrodynamics on the light-front* (1999). Ph.D. thesis, arXiv:hep-th/9902103

[499] E. L. Gubankova, C.-R. Ji and S. R. Cotanch: *Flow equations for gluodynamics in the Coulomb gauge.* Phys. Rev. D **62** (2000) 074001. arXiv:hep-ph/0003289

[500] S. K. Bogner, R. J. Furnstahl and R. J. Perry: *Similarity Renormalization Group for Nucleon-Nucleon Interactions.* Phys. Rev. C **75** (2007) 061001. arXiv:nucl-th/0611045

[501] E. Anderson *et al.*: *Block Diagonalization using SRG Flow Equations.* Phys. Rev. C **77** (2008) 037001. arXiv:0801.1098

[502] B. Gabioud *et al.*: *The nn scattering length from the photon spectra of the reactions* $\pi^- d \to \gamma nn$ *and* $\pi^- p \to \gamma n$. Phys. Rev. Lett. **42** (1979) 1508–1511

[503] L. Köster and W. Nistler: *New determination of the neutron-proton scattering amplitude and precise measurements of the scattering amplitudes on carbon, chlorine, fluorine and bromine.* Z. Phys. A **272** (1975) 189–196

[504] G. G. Simon, C. Schmitt and V. H. Walther: *Elastic electric and magnetic e-d scattering at low momentum transfer.* Nucl. Phys. **A364** (1981) 285–296

[505] S. K. Bogner, R. J. Furnstahl, S. Ramanan and A. Schwenk: *Convergence of the Born Series with Low-Momentum Interactions.* Nucl. Phys. **A773** (2006) 203–220. arXiv:nucl-th/0602060

[506] S. K. Bogner *et al.*: *Convergence in the no-core shell model with low-momentum two-nucleon interactions.* Nucl. Phys. **A801** (2008) 21–42. arXiv:0708.3754

[507] W. H. Dickhoff and C. Barbieri: *Seld-consistent Green's function method for nuclei and nuclear matter.* Prog. Part. and Nucl. Phys. **52** (2004) 377–496. arXiv:nucl-th/0402034

[508] H. Müther and W. H. Dickhoff: *Pairing properties of nucleonic matter employing dressed nucleons.* Phys. Rev. C **72** (2005) 054313. arXiv:nucl-th/0508035

[509] H. A. Bethe: *Theory of nuclear matter.* Ann. Rev. Nucl. Part. Sci. **21** (1971) 93–244

[510] S. Fleming, T. Mehen and I. W. Stewart: *NNLO corrections to nucleon nucleon scattering and perturbative pions.* Nucl. Phys. **A677** (2000) 313–366. arXiv:nucl-th/9911001

[511] S. R. Beane, P. F. Bedaque, M. J. Savage and U. van Kolck: *Towards a perturbative theory of nuclear forces.* Nucl. Phys. **A700** (2002) 377–402. arXiv:nucl-th/0104030

[512] H. S. Köhler: *Theory of Finite Nuclei.* Phys. Rev. **137** (1965) B1145–B1157

[513] H. S. Köhler: *Many-body calculations for nuclei.* Nucl. Phys. **A139** (1969) 353–374

[514] B. D. Day: *Elements of the Brueckner-Goldstone Theory of Nuclear Matter.* Rev. Mod. Phys. **39** (1967) 719–744

[515] M. Gell-Mann and F. E. Low: *Bound states in quantum field theory.* Phys. Rev. **84** (1951) 350–354

[516] A. Messiah: *Mécanique Quantique* (Dunod, Paris, 1971)

[517] A. Fetter and J. D. Walecka: *Quantum Theory of Many-Particle Systems* (McGraw-Hill, New-York, 1971)

[518] K. A. Brueckner, C. A. Levinson and H. M. Mahmoud: *Two-Body Forces and Nuclear Saturation. I. Central Forces.* Phys. Rev. **95** (1954) 217–228

[519] K. A. Brueckner and C. A. Levinson: *Approximate Reduction of the Many-Body Problem for Strongly Interacting Particles to a Problem of Self-Consistent Fields.* Phys. Rev. **97** (1954) 1344–1352

[520] K. A. Brueckner, J. L. Gammel and H. Weitzner: *Theory of Finite Nuclei.* Phys. Rev. **110** (1958) 431–445

[521] K. A. Brueckner, A. M. Lockett and M. Rotenberg: *Properties of Finite Nuclei.* Phys. Rev. **121** (1958) 255–269

[522] B. H. Brandow: *Linked-Cluster Expansions for the Nuclear Many-Body Problem.* Rev. Mod. Phys. **39** (1967) 771–828

[523] H. Q. Song, M. Baldo, G. Giansiracusa and U. Lombardo: *Bethe-Brueckner-Goldstone Expansion in Nuclear Matter.* Phys. Rev. Lett. **81** (1998) 1582–1587

[524] B. H. Brandow: *Compact-Cluster Expansion for the Nuclear Many-Body Problem.* Phys. Rev. **152** (1966) 863–882

[525] R. L. Becker, A. D. Mackellar and B. M. Morris: *Brueckner Theory in an Oscillator Basis. I. The Method of Reference Bethe-Goldstone Equations and Comparison of the Yale, Reid (Hard-Core), and Hamada-Johnston Interactions.* Phys. Rev. **172** (1968) 1264–1290

[526] H. S. Köhler and R. J. McCarthy: *Calculation of ^{16}O binding energy (II).* Nucl. Phys. **A106** (1968) 313–322

[527] R. K. Tripathi, A. Faessler and A. D. MacKellar: *Self-Consistent Treatment of the Pauli Operator in the Brueckner-Hartree-Fock Approach.* Phys. Rev. C **8** (1979) 129–134

[528] P. Bozek and P. Czerski: *Thermodynamic consistency for nuclear matter calculations.* Eur. Phys. J. A **11** (2001) 271–275. arXiv:nucl-th/0102020

[529] P. Nozieres: *Theory of interacting Fermi sytems* (Westview Press, Boulder, CO, 1964)

[530] G. Baym: *Selfconsistent approximation in many body systems.* Phys. Rev. **127** (1962) 1391–1401

[531] D. J. Thouless: *Perturbation theory in statistical mechanics and the theory of superconductivity.* Ann. Phys. **10** (1960) 553–588

[532] R. Balian and N. R. Werthamer: *Superconductivity with Pairs in a Relative p Wave.* Phys. Rev. **131** (1963) 1553–1564

[533] N. N. Bogoliubov: *On a new method in the theory of superconductivity.* Nuovo Cimento **7** (1958) 794

[534] J. G. Valatin: *Comments on the theory of superconductivity.* Nuovo Cimento **7** (1958) 843–857

[535] E. M. Henley and L. Wilets: *Energy Gap in Nuclear Matter. I. Extended Theory.* Phys. Rev. **133** (1964) B1118–B1131

[536] *The CBM Experiment Introduction* (2007)
URL http://www.gsi.de/fair/experiments/CBM/1intro.html

[537] J.-P. Blaizot: *Theoretical overview: Towards understanding the quark-gluon plasma.* J. Phys. G: Nucl. and Part. Phys. **34** (2007) S243–S252. arXiv:hep-ph/0703150

[538] D. d'Enterria: *Quark-gluon matter.* J. Phys. G: Nucl. and Part. Phys. **34** (2007) S53–S81

[539] S. Hands: *The phase diagram of QCD.* Contemp. Phys. **42** (2001) 209–225. arXiv:physics/0105022

[540] M. G. Alford, A. Schmitt, K. Rajagopal and T. Schäfer: *Color superconductivity in dense quark matter* (2007). arXiv:0709.4635

[541] G. Colò, N. Van Giai, J. Meyer, K. Bennaceur and P. Bonche: *Microscopic determination of the nuclear incompressibility within the nonrelativistic framework.* Phys. Rev. C **70** (2004) 024307. arXiv:nucl-th/0403086

[542] M. Colonna, P. Chomaz and S. Ayik: *Mechanical and chemical spinodal instabilities in finite quantum systems.* Phys. Rev. Lett. **88** (2002) 122701. arXiv:nucl-th/0201070

[543] J. Margueron, J. Navarro and N. Van Giai: *Instabilities of infinite matter with effective Skyrme-type interactions.* Phys. Rev. C **66** (2002) 014303. arXiv:nucl-th/0204030

[544] P. Chomaz, M. Colonna and J. Randrup: *Nuclear spinodal fragmentation.* Phys. Rept. **389** (2004) 263–440

[545] S. Typel and B. A. Brown: *Neutron radii and the neutron equation of state in relativistic models.* Phys. Rev. C **64** (2001) 027302

[546] S. Kubis: *The nuclear symmetry energy and stability of matter in neutron star* arXiv:astro-ph/0611740

[547] J. M. Lattimer and M. Prakash: *Nuclear Matter and its Role in Supernovae, Neutron Stars and Compact Object Binary Mergers.* Phys. Rept. **333** (2000) 121–146. arXiv:astro-ph/0002203

[548] J. R. Stone and P. G. Reinhard: *The Skyrme Interaction in finite nuclei and nuclear matter.* Prog. Part. Nucl. Phys. **58** (2007) 587–657. arXiv:nucl-th/0607002

[549] P. Gögelein, E. N. E. van Dalen, C. Fuchs and H. Müther: *Nuclear matter in the crust of neutron stars derived from realistic NN interactions.* Phys. Rev. C **77** (2008) 025802. arXiv:0708.2867

[550] V. Baran, M. Colonna, V. Greco and M. Di Toro: *Reaction Dynamics with Exotic Beams.* Phys. Rept. **410** (2005) 335–466. arXiv:nucl-th/0412060

[551] M. Di Toro *et al.*: *Heavy ion collisions at relativistic energies: Testing a nuclear matter at high baryon and isospin density.* Nucl. Phys. **A782** (2007) 267–274. arXiv:nucl-th/0607031

[552] M. Baldo: *Nuclear methods and the nuclear equation of state.* Int. Rev. Nucl. Phys., Vol 9 (World Scientific, Singapore, 1999)

[553] G. C. Wick: *The Evaluation of the Collision Matrix.* Phys. Rev. **80** (1950) 268–272

[554] A. Lejeune, P. Grange, M. Martzolff and J. Cugnon: *Hot nuclear matter in an extended Brueckner approach.* Nucl. Phys. **A453** (1986) 189–219

[555] M. Baldo and F. Burgio: *Microscopic theory of the nuclear equation of state and neutron star structure.* Lect. Notes Phys. **578** (2001) 1–29. arXiv:nucl-th/0012014

[556] B. D. Day: *Current state of nuclear matter calculations.* Rev. Mod. Phys. **50** (1978) 495–521

[557] W. L. McMillan: *Ground State of Liquid* He^4. Phys. Rev. **138** (1965) A442–A451

[558] D. M. Ceperley, G. V. Chester and M. H. Kalos: *Exact Calculations of the Ground State of Model Neutron Matter.* Phys. Rev. D **13** (1976) 3208–3213

[559] B. Friedman and V. R. Pandharipande: *Hot and cold, nuclear and neutron matter.* Nucl. Phys. **A361** (1981) 502–520

[560] R. B. Wiringa, V. Fiks and A. Fabrocini: *Equation of state for dense nucleon matter.* Phys. Rev. C **38** (1988) 1010–1037

[561] A. Akmal, V. R. Pandharipande and D. G. Ravenhall: *The equation of state for nucleon matter and neutron star structure.* Phys. Rev. C **58** (1998) 1804–1828. arXiv:nucl-th/9804027

[562] M. I. Haftel and F. Tabakin: *Nuclear saturation and the smoothness of nucleon-nucleon potentials.* Nucl. Phys. **A158** (1970) 1–42

[563] M. Baldo: *Priv. comm.*

[564] S. Mallik, J. N. De, S. K. Samaddar and S. Sarkar: *S-matrix approach to equation of state of nuclear matter.* Phys. Rev. C **77** (2008) 032201. arXiv:0801.0498

[565] V. Soma and P. Bożek: *Nuclear matter with three-body forces from self-consistent spectral calculations* (2007). arXiv:0707.4380

[566] P. Bożek, D. J. Dean and H. Müther: *Correlations and effective interactions in nuclear matter.* Phys. Rev. C **74** (2006) 014303. arXiv:nucl-th/0604003

[567] P. C. Bhargava and D. W. L. Sprung: *Binding and saturation of nuclear matter by the reference spectrum method.* Ann. Phys. **42** (1967) 222–261

[568] A. Kallio and B. D. Day: *Accurate calculation of the reaction matrix in light nuclei and in nuclear matter.* Nucl. Phys. **A124** (1969) 177–198

[569] E. J. Irwin: (1963). Ph.D. thesis

[570] B. H. Brandow: *Foundations of the Nuclear Shell Model* (1964). Master's Thesis

[571] B. Frois and C. N. Papanicolas: *Electrn scattering and nuclear structure.* Ann. Rev. Nucl. Part. Sci. **37** (1987) 133–176

[572] W. D. Myers and W. J. Swiatecki: *Nuclear Masses and Deformations.* Nucl. Phys. **81** (1966) 1–60

[573] W. D. Myers and W. J. Swiatecki: *Average nuclear properties.* Ann. Phys. **55** (1969) 395–505

[574] W. D. Myers and W. J. Swiatecki: *Droplet model nuclear density distributions and single-particle potential wells.* Nucl. Phys. **A145** (1969) 387–400

[575] P. Möller and J. R. Nix: *Global nuclear-structure calculations.* Nucl. Phys. **A520** (1990) c369–c376

[576] P. Möller, J. R. Nix, W. D. Myers and W. J. Swiatecki: *Nuclear ground state masses and deformations.* Atom. Data Nucl. Data Tabl. **59** (1995) 185–381. arXiv:nucl-th/9308022

[577] C. Mahaux and R. Sartor: *Advances in Nuclear Physics*, vol. 20 (Plenum, New York, 1991)

[578] B. D. Day: *Three-body correlations in nuclear matter.* Phys. Rev. C **24** (1981) 1203–1271

[579] S. C. Pieper: *Quantum Monte Carlo Calculations of Light Nuclei.* Nucl. Phys. **A751** (2005) 516–532. arXiv:nucl-th/0410115

[580] D. G. Jenkins *et al.*: *T=0 and T=1 states in the odd-odd N=Z nucleus,* $^{70}_{35}Br_{35}$. Phys. Rev. C **65** (2002) 064307

[581] J. R. Schrieffer: *Theory of Superconductivity* (Benjamin, New York, 1964)

[582] T. Duguet: *Non-empirical pairing functional.* Eur. Phys. J. ST **156** (2008) 207–215. arXiv:0711.4386

[583] V. A. Khodel, V. V. Khodel and J. W. Clark: *Solution of the gap equation in neutron matter.* Nucl. Phys. **A598** (1990) 390–417

[584] K. Hebeler, A. Schwenk and B. Friman: *Dependence of the* $^1S_0$ *superfluid pairing gap on nuclear interactions.* Phys. Lett. B **648** (2007) 176–180. arXiv:nucl-th/0611024

[585] O. Elgarøy and M. Hjorth-Jensen: *Nucleon-nucleon phase shifts and pairing in neutron matter and nuclear matter.* Phys. Rev. C **57** (1998) 1174–1177

[586] U. Lombardo, P. Schuck and W. Zuo: *Self-energy Effects in the Superfluidity of Neutron Matter.* Phys. Rev. C **64** (2001) 021301. arXiv:nucl-th/0101042

[587] U. Lombardo and P. Schuck: *Size-shrinking of deuterons in very dilute superfluid nuclear matter.* Phys. Rev. C **63** (2001) 038201. arXiv:nucl-th/0011085

[588] P. Bożek: *Superfluid nuclear matter calculations.* Nucl. Phys. **A657** (1999) 187–215. arXiv:nucl-th/9902019

[589] P. Bożek: *Reduction of superfluid gap by scattering.* Phys. Rev. C **62** (2000) 054316. arXiv:nucl-th/0003048

[590] P. Bożek: *One-body Properties of Nuclear Matter with Off-shell Propagation.* Phys. Rev. C **65** (2002) 054306. arXiv:nucl-th/0201086

[591] K. Hebeler, T. Duguet and A. Schwenk: *Unpublished* (2008)

[592] S. Kümmel and L. Kronik: *Orbital-dependent density functionals: Theory and applications.* Rev. Mod. Phys. **80** (2008) 3–60

[593] V. Rotival, T. Duguet, S. K. Bogner and R. J. Furnstahl: *Work in progress*

[594] J. W. Negele: *The mean-field theory of nuclear structure and dynamics.* Rev. Mod. Phys. **54** (1982) 913–1015

[595] M. Baldo, P. Schuck and X. Viñas: *Kohn-Sham Density Functional Inspired Approach to Nuclear Binding* (2007). arXiv:0706.0658

[596] L. M. Robledo, M. Baldo, P. Schuck and X. Viñas: *Deformation properties of the BCP energy density functional* (2008). arXiv:0801.3765

[597] R. Machleidt: *Nuclear forces from chiral effective field theory* arXiv:nucl-th/0704.0807

[598] F. S. Acton: *Numerical Methods that Work, Revised Edition 1990* (Mathematical Association of America, Washington, DC, 1970)

[599] E. Polak: *Computationals Methods in Optimization* (Academic Press, New York, NY, 1971)

[600] R. P. Brent: *Algorithms for Minimization without Derivatives* (Prentice-Hall, Englewood Cliffs, NJ, 1973)

[601] P. E. Gill, W. Murray and M. H. Wright: *Practical Optimization* (Academic Press, New York, NY, 1981)

[602] J. E. Dennis and R. B. Schnabel: *Numerical methods for unconstrained optimization and Nonlinear Equations* (Prentice-Hall, Englewood Cliffs, NJ, 1983)

[603] N. Metropolis, A. W. Rosenbluth, M. N. Rosenbluth, A. H. Teller and E. Teller: *Equation of state calculations by fast computing machines.* J. Chem. Phys. **21** (1953) 1087–1092

[604] S. Kirkpatrick, C. D. Gelatt, Jr. and M. P. Vecchi: *Optimization by Simulated Annealing.* Science **220** (1983) 671–680

[605] V. Černý: *Thermodynamical approach to the traveling salesman problem: An efficient simulation algorithm.* J. Optim. Theory App. **45** (1985) 41–51

[606] J. H. Holland: *Adaptation in Natural and Artificial Systems: An Introductory Analysis with Applications to Biology, Control and Artificial Intelligence* (MIT Press, Cambridge, MA, 1975)

[607] K. DeJong: *An Analysis of the Behavior of a Class of Genetic Adaptative Systems* (1975). Ph.D. Thesis

[608] J. A. Nelder and R. Mead: *A Simplex Method for Function Minimization.* Comp. J. **7** (1965) 308–313

[609] D. E. Goldberg *et al.*: *Genetic Algorithms: A Bibliography* (1997). IlliGAL Report No. 97002
URL http://www.illigal.uiuc.edu/pub/papers/IlliGALs/97002.ps.Z

[610] S. L. S. Jacoby, J. S. Kowalik and J. T. Pizzo: *Iterative Methods for Nonlinear Optimization Problems* (Prentice-Hall, Englewood Cliffs, NJ, 1972)

[611] F. Gray: *Pulse code communication* (1953). U.S. Patent 2,632,058

[612] R. Caruana and J. D. Schaffer: *Representation and hidden bias: Gray vs. binary coding for genetic algorithms.* In J. E. Laird (Editor), *Proceedings of the* 5th *International Conference on Machine Learning* (Morgan Kaufmann Publishers Inc., San Francisco, CA, 1988) pp. 153–161

[613] U. K. Chakraborty and C. Z. Janikow: *An analysis of Gray versus binary encoding in genetic search.* Inf. Sci. **156** (2003) 253–269

[614] D. E. Goldberg and K. Deb: *A Comparative Analysis of Selection Schemes Used in Genetic Algorithms.* TCGA Report No. 90007 (1990)

[615] D. E. Goldberg: *Genetic Algorithms in Search, Optimization and Machine Learning* (Addison-Wesley, Reading, MA, 1989)

[616] D. E. Goldberg: *A note on Boltzmann tournament selection for genetic algorithms and population-oriented simulated annealing.* TCGA Report No. 90003 (1990)

[617] L. D. Whitley: *The genitor algorithm and selection pressure: Why rank-based allocation of reproductive trials is best.* In J. D. Schaffer (Editor), *Proceedings of the 3rd International Conference on Genetic Algorithms* (Morgan Kaufmann Publishers Inc., San Francisco, CA, 1989) pp. 116–123

[618] J. Baker: *Adaptive selection methods for genetic algorithms.* In J. J. Grefenstette (Editor), *Proceedings of the 2nd International Conference on Genetic Algorithms and their Applications* (Lawrence Erlbaum Associates, 1995) pp. 101–111

[619] G. Rudolph: *Convergence Analysis of Canonical Genetic Algorithms.* IEEE Trans. Neur. Net. **5** (1970) 96–101

[620] N. N. Schraudolph and R. K. Belew: *Dynamic Parameter Encoding for Genetic Algorithms.* Machine Learning **9** (1992) 9–21

[621] D. G. Kim and L. F. González Hernández: *Adaptive Precision Coding for Parameter Optimization Using Genetic Algorithms* (1997)
URL http://citeseerx.ist.psu.edu/viewdoc/summary?doi=10.1.1.53.2119

[622] K. M. Passino and S. Yurkovich: *Fuzzy Control* (Addison-Wesley-Longman, Menlo Park, CA, 1998)

[623] R. J. Streifel, R. J. Marks, II, R. Reed, J. J. Choi and M. Healey: *Dynamic fuzzy control of genetic algorithm parameter coding.* IEEE Trans. on Sys., Man, and Cyb. B **29** (1999) 426–433

[624] M. A. Lee and H. Takagi: *Dynamic control of genetic algorithms using fuzzy logic techniques.* In S. Forrest (Editor), *Proceedings of the 5th International Conference on Genetic Algorithms* (Morgan Kaufmann Publishers Inc., San Francisco, CA, 1993) pp. 76–83

[625] Z. Tu and Y. Lu: *A robust stochastic genetic algorithm (StGA) for global numerical optimization.* IEEE Trans. Evo. Comp. **8** (2004) 456–470

[626] D. Yuret and M. De La Maza: *Dynamic hill climbing: Overcoming the limitations of optimization techniques.* In *Proceedings of The Second Turkish Symposium on Artificial Intelligence and Neural Networks* (1993) pp. 208–212

[627] D. E. Goldberg, K. Deb, H. Kargupta and G. Harik: *Rapid, accurate optimization of difficult problems using fast messy genetic algorithms.* In S. Forrest (Editor), *Proceedings of the 5th International Conference on Genetic Algorithms* (Morgan Kaufmann Publishers Inc., San Francisco, CA, 1993) pp. 56–64

[628] S. Rajeev and C. S. Krishnamoorthy: *Discrete Optimization of Structures Using Genetic Algorithms.* J. Struct. Engrg. **118** (1992) 1233–1250

[629] W. T. Chan and T. F. Wa: *Road-Maintenance Planning Using Genetic Algorithms. I: Formulation.* J. Transp. Engrg. **120** (1994) 693–709

[630] R. Tuccillo and A. Senatore: *A genetic algorithm-based approach to radial flow impeller design.* Comput. Fluid Dyn. Aeropropulsion ASME **49** (1995) 51–62

[631] M. Sharif and R. Wardlaw: *Multireservoir Systems Optimization Using Genetic Algorithms: Case Study.* J. Comp. in Civ. Engrg. **14** (2000) 255–263

[632] Z. Y. Wu and A. R. Simpson: *Competent Genetic-Evolutionary Optimization of Water Distribution Systems.* J. Comp. in Civ. Engrg. **15** (1992) 89–101

[633] H. Hao and Y. Xia: *Vibration-based Damage Detection of Structures by Genetic Algorithm.* J. Comp. in Civ. Engrg. **16** (2002) 222–229

[634] A. M. Raich and T. R. Liszkai: *Improving the Performance of Structural Damage Detection Methods Using Advanced Genetic Algorithms.* J. Struct. Engrg. **133** (2007) 449–461

[635] S. J. Louis and C. Miles: *Playing to learn: case-injected genetic algorithms for learning to play computer games.* IEEE Trans. Evo. Comp. **9** (2005) 669–681

[636] B. A. Dike and R. E. Smith: *Application of genetic algorithms to air combat maneuvering.* TCGA Report No. 93002, University of Alabama, Tuscaloosa (1993)

[637] S. Mulgund, K. Harper, K. Krishnakumar and G. Zacharias: *Air combat tactics optimization using stochastic genetic algorithms.* IEEE Int. Conf. on Sys., Man, and Cyb. **4** (1998) 3136–3141

[638] H.-L. Fang: *Genetic Algorithms in Timetabling and Scheduling* (1994). Ph.D. Thesis

[639] T. P. Bagchi: *Multiobjective Scheduling by Genetic Algorithms* (Kluwer Academic Publishers, Boston, MA, 1999)

[640] S.-H. Chen: *Genetic Algorithms and Genetic Programming in Computational Finance* (Kluwer Academic Publishers, Dordrecht, 2002)

[641] L. Lin, L. Cao, J. Wang and C. Zhang: *The applications of genetic algorithms in stock market data mining optimisation* (WIT Press, Boston, MA, 2004), pp. 273–280

[642] M. Matilla-García: *Are trading rules based on genetic algorithms profitable?* Appl. Econ. Lett. **13** (2006) 123–126

[643] D. G. Ireland, S. Janssen and J. Ryckebusch: *A genetic algorithm analysis of N^* resonances in $p(\gamma, K^+)\Lambda$ reactions.* Nucl. Phys. **A740** (2004) 147–167

[644] C. Fernandez-Ramirez, E. Moya de Guerrra, A. Udias and J. M. Udias: *Properties of Nucleon Resonances by means of a Genetic Algorithm.* Phys. Rev. C **77** (2008) 065212. arXiv:0805.4178

[645] C. Winkler and H. M. Hofmann: *Determination of bound state wave functions by a genetic algorithm.* Phys. Rev. C **55** (1997) 684–687. arXiv:nucl-th/9412032

[646] J. M. Renders and H. Bersini: *Hybridizing genetic algorithms with hill-climbing methods for global optimization: Two possible ways.* In Z. Michalewicz, J. D. Schaffer, H.-P. Schwefel, D. B. Fogel and H. Kitano (Editors), *Proceedings of the 1st IEEE Conference on Evolutionary Computation* (IEEE Pres, San Francisco, CA, 1994) pp. 312–317

[647] R. Yang and I. Douglas: *Simple Genetic Algorithm with Local Tuning: Efficient Global Optimizing Technique.* J. Optim. Theory App. **98** (1998) 449–465

[648] J. Yen, J. C. Liao, B. Lee and D. Randolph: *A hybrid approach to modeling metabolic systems using a genetic algorithm and simplex method.* IEEE Trans. on Sys., Man, and Cyb. B **28** (1998) 173–191

[649] N. Durand and J.-M. Alliot: *A combined nelder-mead simplex and genetic algorithm.* In W. Banzhaf *et al.* (Editors), *Proceedings of the Genetic and Evolutionary Computation Conference (GECCO 1999)* (Morgan Kaufmann Publishers Inc., San Francisco, CA, 1999)

[650] M. Musil, M. J. Wilmut and N. R. Chapman: *A hybrid simplex genetic algorithm for estimating geoacousticparameters using matched-field inversion.* IEEE J. Oceanic. Engrg. **24** (1999) 358–369

[651] A.-R. Hedar and M. Fukushima: *Minimizing multimodal functions by simplex coding genetic algorithm.* Optim. Meth. & Soft. **18** (2003) 265–282

[652] L. J. Pit: *Parallel Genetic Algorithms* (1995). Ph.D. Thesis

[653] W. Gropp, E. Lusk and A. Skjellum: *Using MPI: portable parallel programming with the message-passing interface* (MIT Press, Cambridge, MA, 1994)

[654] W. Gropp, E. Lusk and A. Skjellum: *Using MPI, 2nd edition: portable parallel programming with the message-passing interface* (MIT Press, Cambridge, MA, 1994)

[655] *Open MPI: Open Source High Performance Computing*
URL http://www.open-mpi.org/

[656] *Performance Visualization for Parallel Programs*
URL http://www-unix.mcs.anl.gov/perfvis/

[657] *Centre de Calcul Recherche et Technologie*
URL http://www-ccrt.cea.fr/

[658] G.Saporta: *Probabilité, Analyses des Données et Statistique* (Technip, 2006)

[659] J.-M. Azaïs and J.-M. Bardet: *Le Modèle Linéaire par L'exemple* (Dunod, 2006)

[660] A. Antoniadis, J. Berruyer and R. Carmona: *Non-linear regression and applications* (Economica, 2001)

[661] B. Efron: *Bootstrap Methods: Another Look at the Jackknife.* Ann. Stat. **7** (1979) 1–26

[662] B. Efron: *Nonparametric estimates of standard error: The jackknife, the bootstrap and other methods.* Biometrika **68** (1981) 589–599

[663] B. Efron and R. J. Tibshirani: *An introduction to the bootstrap* (Chapman & Hall, 1993)

[664] A. C. Davison and D. Hinkley: *Bootstrap Methods and their Applications* (Cambridge University Press, Cambridge, UK, 1997)

[665] M. R. Chernick: *Bootstrap Methods: A Practitioner's Guide* (Wiley, New York, NY, 1999)

[666] A. C. Davison and D. Hinkley: *Bootstrap Methods and their Applications, 8th edition* (Cambridge University Press, Cambridge, UK, 2006)

[667] B. Efron: *The jackknife, the bootstrap, and other resampling plans* (Society for Industrial Mathematics, 1982)

[668] P. Hall: *Theoretical Comparison of Bootstrap Confidence Intervals.* Ann. Stat. **16** (1988) 927–953–204

[669] T. Lesinski: *Microscopic and Beyond-Mean-Field Constraints for a New Generation of Nuclear Energy Density Functionals* (2008). Ph.D. Thesis

[670] J. Haidenbauer and W. Plessas: *Separable representation of the Paris nucleon-nucleon potential.* Phys. Rev. C **30** (1984) 1822–1839

Résumé

La méthode de la fonctionnelle de la densité d'énergie (EDF) est un outil de choix pour l'étude de la structure nucléaire à basse énergie, car elle permet des calculs de noyaux finis aussi bien pour des systèmes stables connus expérimentalement dont les propriétés sont reproduites avec une bonne précision, que pour des noyaux qui ne peuvent encore être produits mais sont prédits théoriquement. Dans la première partie de cette thèse, une nouvelle méthode quantitative est introduite pour caractériser l'existence et les propriétés des halos dans les noyaux moyens et lourds, ainsi que pour étudier l'impact des corrélations d'appariement ou du choix de la fonctionnelle d'énergie sur leur formation. Il apparait que la solidité de ces résultats est limitée par le faible pouvoir prédictif des fonctionnelles utilisées jusqu'à présent qui sont ajustées sur des données expérimentales. Dans la seconde partie de ce mémoire, nous entreprenons la construction de fonctionnelles non-empiriques qui reposent sur un nouveau paradigme pour les forces nucléon-nucléon dans le vide, à savoir les interactions *low-momentum* engendrées par l'application des méthodes du groupe de renormalisation. Ces potentiels à cœur mou sont utilisés comme point de départ d'une stratégie à long terme faisant le lien entre les techniques modernes de résolution du problème à N corps et les méthodes EDF. Nous donnons ainsi des perspectives pour construire différentes réalisations d'un modèle non-empirique d'interaction $v_{\mathrm{BDRS}}^{[\mathrm{X}]}$ incluant les effets de milieu à différents niveaux d'approximation et pouvant être traité dans les codes dédiés à la structure nucléaire. Dans ce mémoire, la première étape de ce travail est initiée par l'ajustement d'une représentation opératorielle des forces *low-momentum* dans le vide réalisé au moyen d'un algorithme parallèle d'intelligence artificielle. Les premiers résultats mettent en valeur la possibilité d'incorporer la physique nécessaire à la structure de basse énergie dans ce vertex gaussien.

Abstract

The energy density functional (EDF) formalism is the tool of choice for large-scale low-energy nuclear structure calculations both for stable experimentally known nuclei whose properties are accurately reproduced and systems that are only theoretically predicted. We highlight in the present dissertation the capability of EDF methods to tackle exotic phenomena appearing at the very limits of stability, that is the formation of nuclear halos. We devise a new quantitative and model-independent method that characterizes the existence and properties of halos in medium- to heavy-mass nuclei, and quantifies the impact of pairing correlations and the choice of the energy functional on the formation of such systems. These results are found to be limited by the predictive power of currently-used EDFs that rely on fitting to known experimental data. In the second part of this dissertation, we initiate the construction of non-empirical EDFs that make use of the new paradigm for vacuum nucleon-nucleon interactions set by so-called low-momentum interactions generated through the application of renormalization group techniques. These soft-core vacuum potentials are used as a stepstone of a long-term strategy which connects modern many-body techniques and EDF methods. We provide guidelines for designing several non-empirical models $v_{\mathrm{BDRS}}^{[\mathrm{X}]}$ that include in-medium many-body effects at various levels of approximation, and can be handled in state-of-the art nuclear structure codes. In the present work, the first step is initiated through the adjustement of an operatorial representation of low-momentum vacuum interactions using a custom-designed parallel evolutionary algorithm. The first results highlight the possibility to grasp most of the relevant physics for low-energy nuclear structure using this numerically convenient gaussian vertex.